Dynamic Nuclear Polarization in Biomolecular Solid State NMR: Methods and Applications in Peptides and Membrane Proteins

By

Vikram Singh Bajaj

B.A., Biochemistry, University of Pennsylvania (2000)
M.S., Chemistry, University of Pennsylvania (2000)

Submitted to the Department of Chemistry
in partial fulfillment of the requirements for the degree of

Doctor of Philosophy in Chemistry
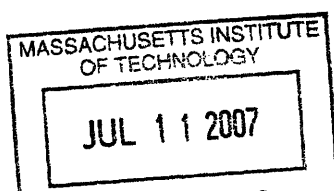
at the

MASSACHUSETTS INSTITUTE OF TECHNOLOGY

June 2007

Author . . . .
Department of Chemistry
May 21, 2007

Certified by . . . .
Robert G. Griffin
Professor, Department of Chemistry
Thesis Supervisor

Accepted by . . . .
Robert W. Field
Chairman, Department Committee on Graduate Students

This doctoral thesis has been examined by a committee of the Department of Chemistry as follows:

Professor Sylvia T. Ceyer ..../.............|...........
Chair

Professor Robert G. Griffin ....
Thesis Supervisor

Professor Keith A. Nelson ....

3

Dynamic Nuclear Polarization in Biomolecular Solid State NMR: Methods and Applications in Peptides and Membrane Proteins

by
Vikram Singh Bajaj

Abstract

Solid state NMR can probe structure and dynamics on length scales from the atomic to the supramolecular. However, low sensitivity limits its application in macromolecules. NMR sensitivity can be improved by dynamic nuclear polarization (DNP), in which electron polarization is transferred to nuclei. We present applications of magic angle spinning NMR that demonstrate its utility for the determination of structure at atomic resolution. We then present new techniques and instrumentation for DNP that permit these methods to be applied to larger systems such as membrane proteins.

These applications rest on several advances in instrumentation: millimeter-wave sources and conduits of power to the sample; low-temperature MAS probes incorporating millimeter-wave transmission; cryogenics and pneumatic control systems. We describe a 380 MHz DNP spectrometer incorporating a 250 GHz gyrotron oscillator and present the theory and operation of a 460 GHz gyrotron at the second harmonic of electron cyclotron resonance.

We have applied DNP to study trapped photocycle intermediates of the archael membrane protein bacteriorhodopsin, a light-driven transmembrane ion pump. We have observed the K photointermediate for the first time by NMR and found unexpected conformational heterogeneity in the L intermediate. With multidimensional correlation spectroscopy, we have assigned active site resonances in conformational mixtures of photointermediates of [U-^{13}C,^{15}N]-bR with high sensitivity. By using non-linear sampling of indirect dimensions, we have observed transient product of K accumulation. We present frequency-selective experiments for amino acid-selective assignments and the measurement of heteronuclear distances and torsion angles in [U-^{13}C,^{15}N]-bR and discuss the relevance of these results to its photocycle.

In addition, we describe several applications of solid state NMR, including a study of dynamic and structural phase transitions in peptides and proteins near the canonical glass transition temperature. We present resonance width experiments that can be used to measure homonuclear and heteronuclear dipolar couplings in uniformly labeled solids.

Finally, we discuss applications to amyloid fibrils, which are protein aggregates that are implicated in diseases of protein misfolding. We report the atomic resolution

structure of the disease-associated L111M mutant of $TTR_{105-115}$ in an amyloid fibril, and information about the supramolecular structure of fibrils from WT $TTR_{105-115}$.

Thesis Supervisor: Robert G. Griffin
Title: Professor, Department of Chemistry,
                      Director, Francis Bitter Magnet Laboratory

Acknowledgments

I am fortunate to have studied under excellent colleagues and advisors. Among them is Professor Robert Griffin; I am in his debt for allowing me to work on several broadly interesting projects during a formative period for solid state NMR and particularly for DNP, where our science has progressed from demonstration experiments in small molecules to routine applications in membrane proteins. I benefited greatly from the diversity of intellect that his lab brings to any problem: his collaborators are plasma physicists, structural biologists, biochemists, and engineers, and, as his students, we are educated in their disciplines as in our own. I learned from him that profound advances in magnetic resonance come through advances in instrumentation.

As an undergraduate, I spent one year in Professor Stanley Opella's laboratory at the University of Pennsylvania and was introduced to NMR by Suzana Straus, Gail Fanucci, and Sean Burns. I learned quantum mechanics from Professor Andrew Rappe and have since sought his counsel many times. I appreciate their willingness then and now to teach and advise me. During my first year in Professor Griffin's laboratory, I learned the practical aspects of magic angle spinning NMR by working with Christopher Jaroniec and Vladimir Ladizhansky. Chris and I solved the first structure at atomic resolution of an amyloid fibril; the results presented in Chapters 13 and 14 of this thesis are a continuation of that work. Vlad and I worked together on experiments for the measurement of homonuclear and heteronuclear dipolar couplings in solids, and some of that work is presented in Chapter 12.

The results described in Chapters 2-8 of my thesis all involve the development of instrumentation that has made high field DNP practical and routine. Because this instrumentation includes millimeter-wave sources and associated components, it was designed and built in close collaboration with Richard Temkin's group at MIT's Plasma Science and Fusion Center, and, specifically, with Melissa Hornstein, Kenneth Kreischer, Paul Woskov, Jagadishwar Sirigiri, Michael Shapiro, Ivan Mastovsky, and Bill Mulligan. I am particularly indebted to Melissa Hornstein for our collaboration on all the work discussed in Chapters 2-9. Our laboratory is staffed with research scientists and technicians whose skills and contributions were instrumental. They include our research scientists David Ruben, Christopher Turner, and Anthony Bielecki, our technicians Jeff Bryant, Ajay Thakkar, Peter Allen, and Michael Mullins, and our machinist, Ron Derocher. Dave lent his expertise to the interpretation of spectral purity measurements that appear in Chapter 5. Jeff, Ajay, Ron, and Peter were involved in the construction of the NMR spectrometer, MAS probe, and cryogenics described in Chapter 2. Chris provided valuable advice and insight into modern protein NMR experiments.

Through Professor Judith Herzfeld's group, I was fortunate to have access to a system in which solid-state NMR and DNP can be applied to biophysical problems that cannot be addressed by other techniques. The studies of bacteriorhodopsin presented in Chapters 9-10 result from a collaboration with her and one of her students, Melody Mak-Jurkauskas. Melody was also involved in modifications of the NMR probe presented in Chapter 2 to accommodate light irradiation of the sample.

I worked with Patrick van der Wel to obtain all the results in Chapter 11 of thesis, which involves a study of the effects of low temperature on the structure and dynamics of peptides and proteins by solid state NMR. In Chapter 12, I describe a family of related

7

Contents

List of Figures

radical. Note that electron-electron cross relaxation processes are significant at high radical concentrations. Adapted from Farrar *et al.*

intercepted (collected).

transmission line elements which produce isolation between each channel.

20

vacion pumps in the gray superconducting magnet, [center] corrugated transmission system with the directional coupler visible in the center of the photograph, and [right] 380 MHz NMR magnet is visible on the edge of the photo. The NMR probe is not visible since it is under the magnet. The view in this photo is from above the gyrotron and waveguide looking down.

(d) Photograph of the 250 GHz quasi-optical directional coupler. Forward power is coupled to the detector diode by means of a short dielectric taper, dielectric horn, and a circular-to-rectangular transition. An attenuator allows the power to be adjusted to the linear range of the diode. The detection circuit has been designed with high loss to avoid reflections across the beam splitter.

nonuniform spacing of the energy levels.

of power fluctuations from the setpoint.

25

"E" family of selective excitation pulses optimized for solid state NMR. Signals corresponding to the Schiff base are along the z-axis, and all other signals are allowed to dephase. Following rotation to the transverse plane, the ^{15}N magnetization arising from the Schiff base resonances evolves under the ^{15}N chemical shift during t1 and then is transferred selectively to retinal-C15 or K216-Cε by SPECIFIC CP. The ^{15}N and ^{13}C fields are chosen to provide spectrally selective, chemical-shift dependent transfer to either directly bonded carbon, while a ramp of 5-6% in the ^{13}C RF field results in quasi-adiabatic transfer with improved efficiency. Following an optional t2 evolution period under the ^{13}C chemical shift, further correlations are established by homonuclear mixing using proton-driven spin diffusion with an R^3 recoupling field or RFDR recoupling. Parameters were optimized using simplex optimization implemented in home-built NMR acquisition hardware and software (D. Ruben).

(B) light-adapted state ; (C) the K intermediate with residual bR_{568} and a short-lived side product with a 15N chemical shift like that of bR_{568}; (D) the L intermediate with residual bR_{568}; (E) the Mo state. . This spectrum in C was acquired in 45 minutes with a non-uniform sampling of t1 to capture the signal of the side-product of K formation that decays within 1-2 hrs at 90K. Details of this approach and the reconstruction of the spectrum will be provided in a separate publication.

axis, librational motions of the methionine side chain, rotamer interconversion of the leucine side chain, and three-fold hopping motion of the methyl groups.

(SPECIFIC CP). Aliphatic cross-peaks are generated by proton-driven spin diffusion with an R^3 recoupling field (DARR).

pronounced in the side chains. The ensembles are generated by selecting the five structures which represent the conformational space spanned by the 100 lowest energy conformers in the refined ensembles. Alignments are generated to all heavy atoms.

sequence of Figure 12-1(b) was used with the mixing time of 30 ms. Different cross peaks appear at different spinning frequencies, thereby demonstrating the selectivity of the polarization transfer. In (a) cross-peaks corresponding to the medium range V′-Vγ1 dipolar coupling (R=3.879 Å according to the crystal structure) appear in the spectrum, along with long-range couplings between the L′-Lδ1 (R=4.675 Å) and L′-Lδ2 (R=4.872 Å). These cross peaks are not present in (b) (note that the spinning frequency changes by just 100 Hz), but two additional cross-peaks appear between L′ and Vγ1 (R=6.464 Å) and V′ and Vγ2 (R=2.969 Å).

elements are not minimized. CSA parameters corresponding to amide ^{15}N and ^{13}Cβ were assumed.

freshly cleaved mica substrate.

to-backbone heteronuclear distances.

corresponding to parallel, parallel+1, and parallel+2 β-sheets. Note that out of register parallel b-sheets have inequivalent sets of intermolecular couplings which have been included in this simulation. T2=15ms, 360 MHz ^{1}H, 5.882 kHz MAS. The maximum filtering efficiency will vary depending on the magnitude of the T^{-2} relaxation, which is expected to be stronger in the amyloid fibril than in succinate.

List of Tables

Chapter 1   A Survey of Solid State NMR for Applications in Structural Biology

In contrast to widely employed techniques based on x-ray diffraction, spectroscopic probes of biological structure and dynamics do not require macroscopic order [1]. As such, they are routinely applied in a wide variety of noncrystalline samples, ranging in size from small peptides and proteins [2-21] to intact cells and living organisms (Figure 1-1). Spectroscopy in the condensed phase is nevertheless complicated because the Hamiltonian is generally characterized by a multitude of noncovalent and anisotropic interactions which, in the absence of some averaging process, render the spectra broad and featureless [22]. Within nuclear magnetic resonance, however, there are several such processes through which these complications can be circumvented: as will be described briefly, they include rapid molecular reorientation, in solution, and uniaxial alignment, or magic angle spinning (MAS), in solids. This thesis broadly concerns the application of MAS NMR methods to probe the structures of increasingly large biological molecules in the solid phase. Here, we will briefly review the process of structure determination by NMR.

nanocrystalline peptide   amyloid fibril   membrane protein   living cells
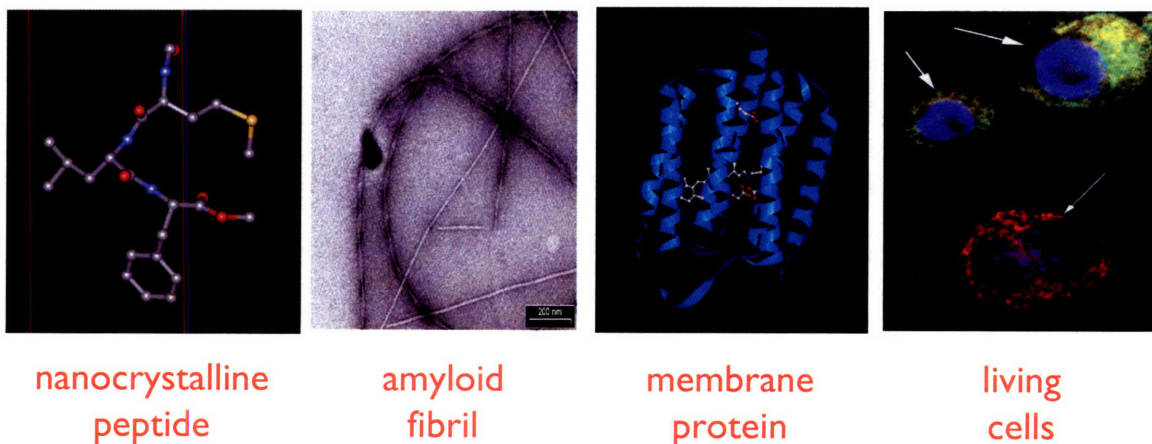
Figure 1-1: The range of samples to which solid state NMR methods can be applied.

Structure determination by solid state NMR benefits tremendously from the long history of solution state NMR in biology and biophysics. When a molecule is dissolved in solution, it can experience molecular reorientation on the timescale of the NMR experiment. If the motion is rapid enough, anisotropic interactions are averaged to their trace values, which are either zero (as in the case of the dipolar tensor, in Figure 1-4) or some finite isotropic value (as in the case of the chemical shift anisotropy, in Figure 1-3) [23]. The resulting spectra are characterized by narrow resonance linewidths. Indeed, in a dissolved protein consisting of thousands of unique resonances, it is generally possible to uniquely resolve and assign each one [24]. This, in large measure, is the responsible for the success of solution state NMR in structural biology. Where sample dissolution is impossible, the sample can be mechanically oriented along a single axis with respect to the external magnetic field, resulting in orientation-dependent values for the chemical shift and dipolar interactions. This approach has been applied extensively by Opella and co-workers for the structure determination of membrane proteins oriented in lipid bilayers or magnetically aligned bicelles [10-12, 25-27]; in the context of weak alignment, it has also been used by solution state NMR spectroscopists to measure residual dipolar couplings (RDCs) which supplement conventional interproton NOE restraints [28]. In the case of a static solid sample without uniaxial alignment, the full anisotropy of all interactions in manifest, and the spectra are generally broad and featureless. NMR spectra that result from these samples are illustrated in Figure 1-2.
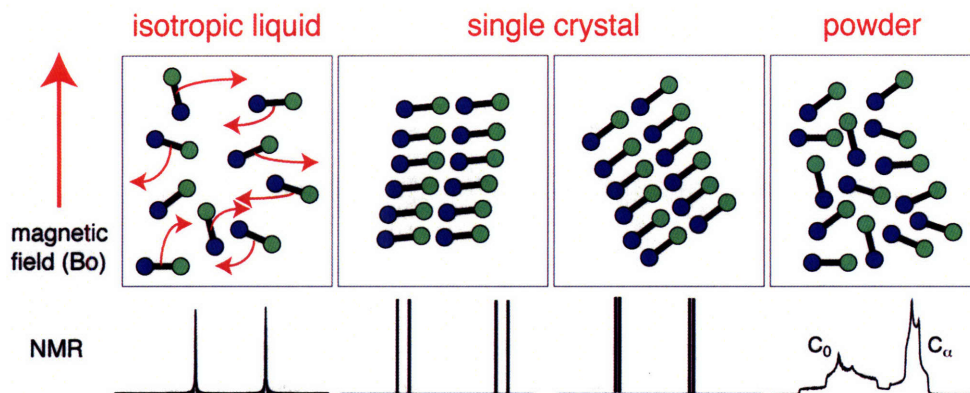
Figure 1-2: Schematic illustration of anisotropic and isotropic lineshapes in the NMR spectra of various samples.
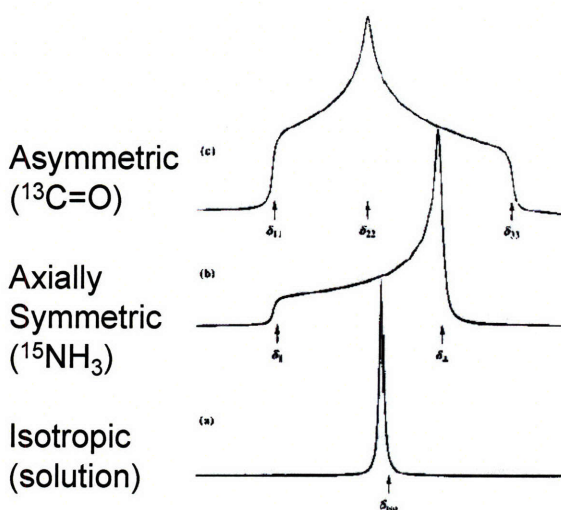
Figure 1-3: The chemical shift anisotropy.
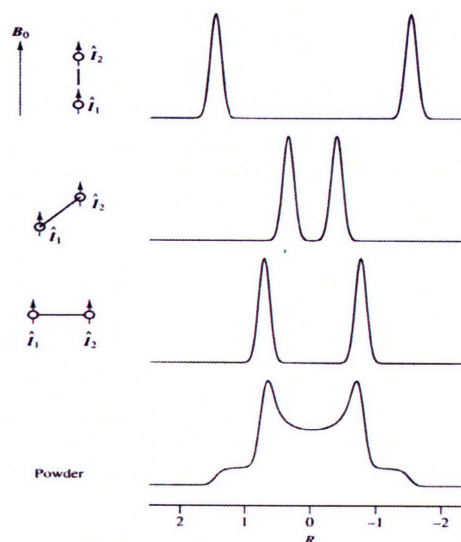
Figure 1-4: The dipolar coupling in solid-state NMR.

In powder samples, nuclear spin interactions which are inhomogeneous in the nomenclature of Maricq and Waugh [29, 30] can be averaged to isotropic values by fast spinning of the entire sample along one or more axes inclined with respect to the static magnetic field [31]. For second rank tensors such as the dipolar coupling and chemical shift anisotropy, this angle is the so-called magic angle of ~54.7°, and the experiment is called Magic Angle Spinning. Its effects on powder spectra are illustrated in Figure 1-5. In biomolecular solid state NMR applications, MAS is generally sufficient to give high

resolution, isotropic spectra of low-γ nuclei such as ^{13}C and ^{15}N, at least at currently employed field strengths up to 20 T [32, 33]. Magic angle spinning instrumentation has been developed with capabilities exceeding 70 kHz, and this technology has promising applications in the spectroscopy of abundant, high-γ nuclei such as ^{1}H, for experiments conducted at very high magnetic fields, for applications in paramagnetic molecules such as catalysts and metalloproteins, and for certain experiments at low or moderate magnetic fields [34-37]. For spatial averaging of tensors of higher rank, double-angle spinning methods have been developed; they have interesting applications in the spectroscopy of quadrupolar nuclei [38-40]. Finally, methods analogous to MAS but which instead involve electrical or mechanical turning of the magnetic field have recently been proposed for applications in low-field imaging and materials science [41].

$$^-OO^{13}C\text{-}^{13}CH_2\text{-}NH_3^+$$
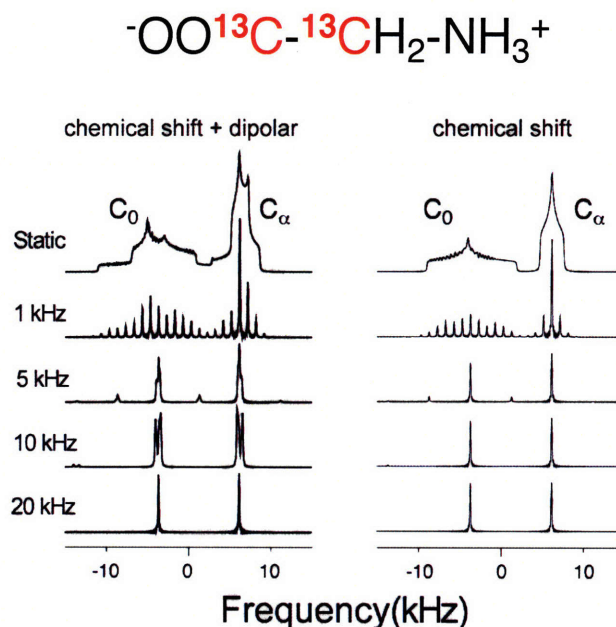
Figure 1-5: The effects of Magic Angle Spinning (MAS) on the NMR spectra of a powder.

Though MAS has the beneficial effect of producing isotropic, solution-like spectra which can lead to site-specific assignments, it also removes the structural information that is

encoded in anisotropic nuclear spin interactions. Dipolar couplings, in particular, indicate internuclear proximity through their $\sim r^3$ dependence on the distance between interacting atoms. In solution state NMR experiments, the proximity of nuclei is monitored indirectly through experiments based on cross-relaxation; while this is possible in solid state NMR, it is better to reintroduce dipolar couplings in order to directly and accurately measure structural distances [42]. The selective reintroduction of spin interactions averaged by MAS is called "recoupling." Recoupling experiments generally depend on a modulation of the spin part of the Hamiltonian by RF pulses. In a simple analogy, illustrated in Figure 1-6, periodic manipulation of the spin part of the Hamiltonian can interfere with the modulation imposed by MAS, resulting in a time-averaged non-zero value of the coupling of interest. A multitude of homonuclear and heteronuclear recoupling sequences have been developed [43-56], and many can be described by a formalism which considers the symmetry of the RF pulse sequence involved and the rotational symmetry properties of the recoupled spin interactions [43, 57, 58] to simplify calculation of the effective Hamiltonian.
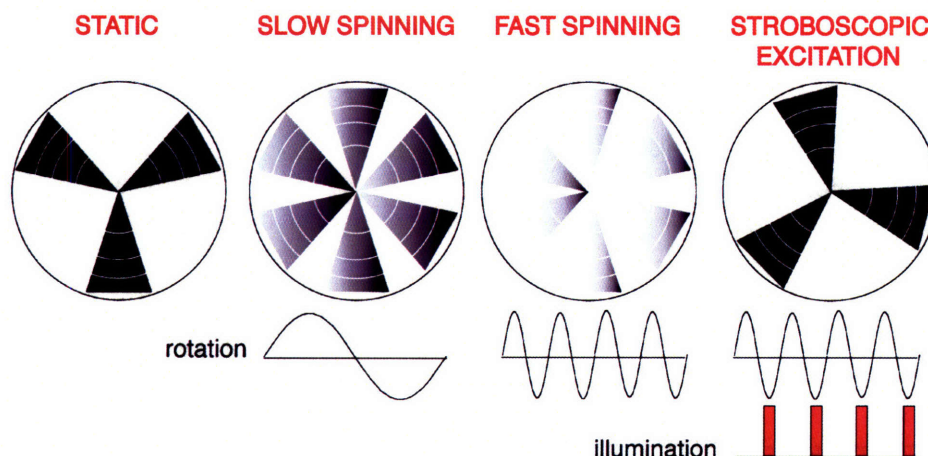
Figure 1-6: The effects of recoupling in magic angle spinning experiments.

In a spinning powder sample, it is therefore possible to manipulate the nuclear spin Hamiltonian and reintroduce spin interactions in a controlled manner, preserving both the resolution of isotropic spectra and the information carried by the anisotropic couplings. Following this approach, solid state NMR experiments have been developed to measure internuclear distances and torsion angles, in the latter case by the correlation of two anisotropic interactions whose orientation in the molecular frame are known *a priori* [59-66]. A multitude of applications in samples which are isotopically labeled at one or a few sites have been reported in the literature [67-72], and this has firmly established solid state NMR as a tool to probe the structures of arbitrarily large molecular complexes.

Selective Labeling

U-^{13}C,^{15}N Labeling

- Label scrambling possible
- Multiple samples required
- Measure specific constraints
- Experiments well-established
- Simple analytical treatments

- Fewer samples required
- High information content*
- multiple interactions
- Chemical Shift Resolution
- Dipolar Truncation: frequency-selective or commuting Hamiltonian
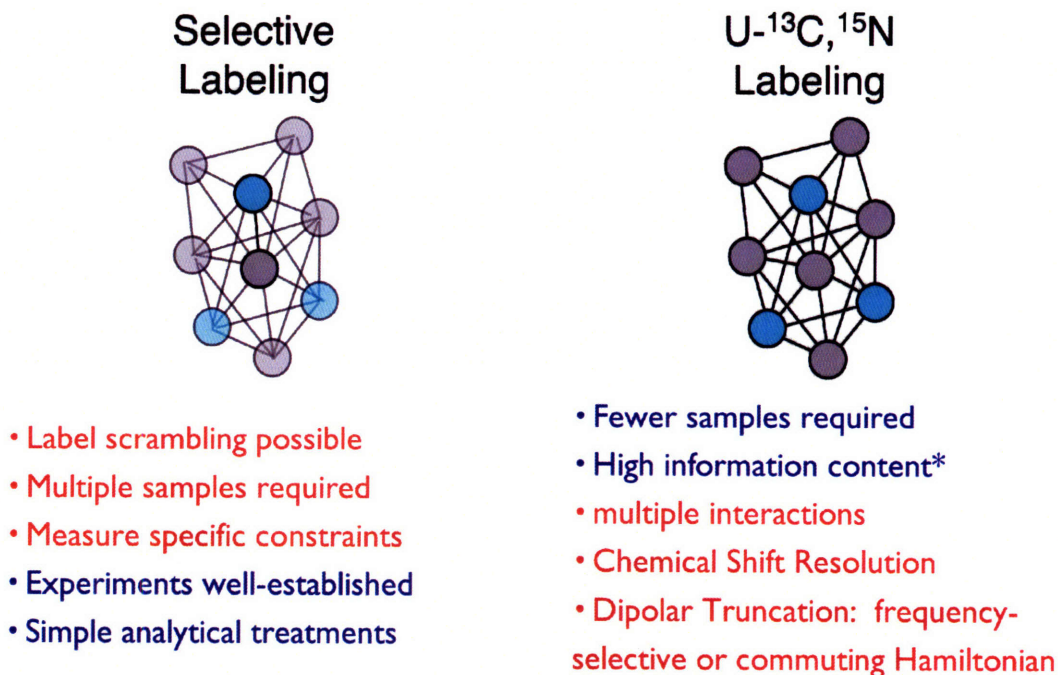
Figure 1-7: A comparison of selectively and uniformly labeled samples for solid-state NMR measurements.

The development of solid state NMR as a tool for the determination of total molecular structure, however, has required methods to measure constraints in samples which are multiply or uniformly isotopically labeled. As illustrated in Figure 1-7, it is possible to

simultaneously measure multiple constraints in a single uniformly labeled sample, albeit at the expense of increased complexity in the experiments and the spin dynamics they produce. Following successful approaches in solution state NMR, these solid state NMR methods must incorporate multidimensional chemical shift correlation periods. Correlation experiments, described in Figure 1-8, were first proposed by Jeener and later developed by Ernst and co-workers [73]. They involve creating one or more incrementable time dimensions, generally labeled t_1, t_2,... t_{n-1}, during which the system evolves under the chemical shift interaction of specific species. The evolution during successive t_n periods are correlated using "mixing" sequences, and finally the signal, carrying a phase corresponding to all previous evolution periods, is detected. Phase-sensitive detection is accomplished using one more schemes which involve orthogonal phase changes in the pulse sequence elements preceding or following each evolution period [74]. In the data processing step, the correlation between different periods is uncovered through n-dimensional Fourier transformation. Where the mixing sequences produce correlations through 1-bond dipolar couplings or J-couplings, the Fourier transform map traces the covalent topology of the molecule of interest. This can be applied, for example, to produce a spectrum in a $^{15}N,^{13}C$-labeled protein which correlates all the amide ^{15}N chemical shifts with those of the side chain carbons [24]. This so-called NCACX correlation experiment typically yields highly resolved solid state NMR spectra, even in proteins of > 100 residues [33, 75]. As illustrated in Figure 1-9, it is frequently applied in the process of assignment, in which chemical shifts of a protein are resolved and labeled in a site-specific manner through their correlations in multiple dimensions.
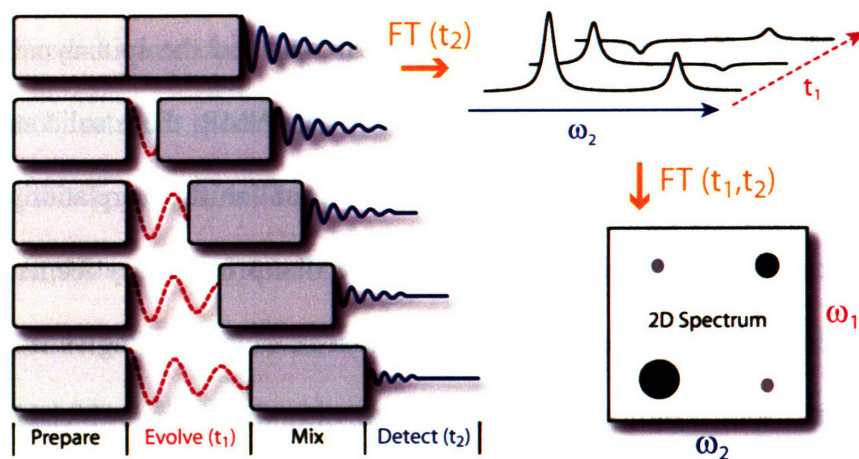
Figure 1-8: Schematic illustrating the principles of multidimensional chemical shift correlation.
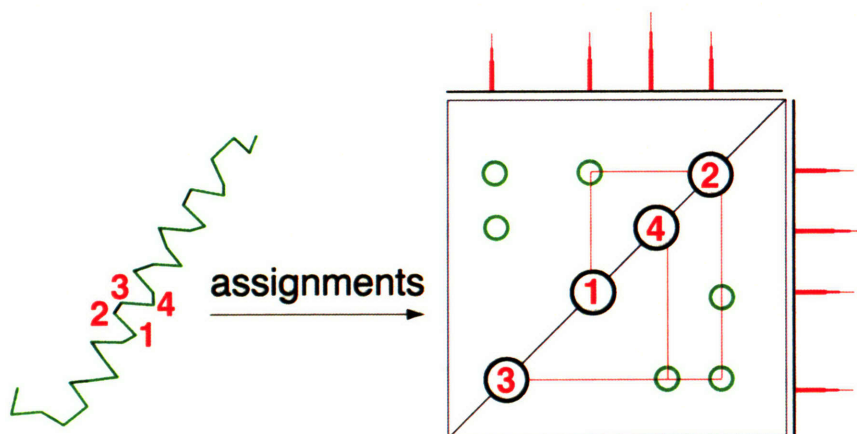
Figure 1-9: Chemical shift assignment through two-dimensional correlation spectroscopy.

Nearly complete chemical shift assignment is usually a prerequisite for the measurement of a set of constraints, in the form of distances and torsion angles (Figure 1-10), which are sufficient to refine a structure. In experiments intended for use in uniformly labeled samples, anisotropic interactions periods are added to chemical shift correlation experiments, but the Fourier transform is calculated only with respect to phase-sensitive dimensions. The result is a pseudo-nD spectrum in which the anisotropic spin dynamics are encoded in the time-varying cross peak intensities. A typical solid state NMR experiment of this type is shown in Figure 1-11, and most experiments presented in this

thesis follow its archetype. In the first stage, called "preparation", an initial traverse spin state is created on through polarization transfer from the ^{1}H via the cross polarization pulse sequence. The signal then evolves, during t_1, under the chemical shift of Spin 1; a recoupling sequence is then applied to reintroduce the dipolar interaction between Spin 1 and Spin 2, and the signal evolves during t_{mix} under the dipolar coupling. Finally, the signal evolves under the chemical shift of spins 1 and 2 during the detection period, t_2. The resulting multidimensional interferogram, if Fourier transformed with respect to t_2 and t_1 yields a series of 2D planes in which the intensity of the cross peaks between Spin 1 and Spin 2 is modulated by the recoupled dipolar coupling. These intensities can be extracted by integration, and the resulting dipolar mixing trajectories can be fit to a model that includes the dipolar coupling as one of its parameters.
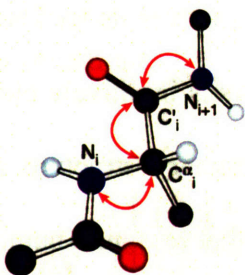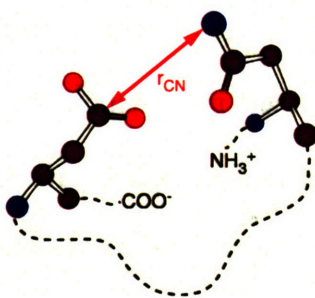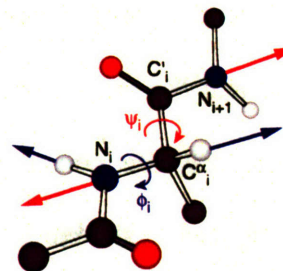
Figure 1-10: The variety of constraints measured in typical solid-state NMR experiments.
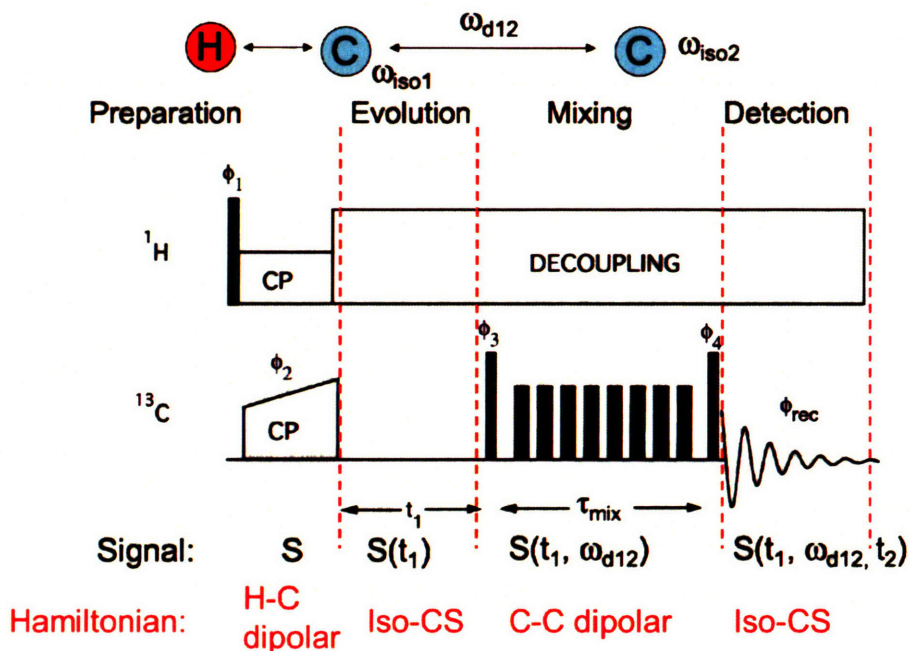
Figure 1-11: Components and modules of a typical solid-state NMR experiment.

The aim of these experiments, then, is to record enough constraints with sufficient accuracy to refine a detailed structure of the protein under study. To be precise, structure can be described at many levels: the global structure of a protein involves its backbone fold and the orientation of all partners in a multimeric complex. As is intuitively clear, short distance constraints between sites which are distant in primary structure are particularly valuable in fixing the global fold of a protein, and, for that reason, a number of solid state NMR methods have been developed which yield very many approximate constraints of this sort with high sensitivity [76-81]. They have been applied to determine the backbone fold of several microcrystalline systems [82-84]. However, the work presented in this thesis involves structure determination of peptides and peptide complexes or the measurement of chemically interesting parameters in a protein active site, and it is therefore more concerned with accurate local structure. The local conformational flexibility of a protein is usually expressed in terms of its internal heavy

54

atom coordinates: the ϕ, ψ, and ω backbone torsion angles and $\chi 1$, $\chi 2 \ldots \chi n$ angles describing the side chain. Internuclear distances can constrain one or more internal degrees of freedom, while torsion angle measurements are generally designed to measure one angle. If enough distances and torsion angles are recorded, the structure can be refined by a global optimization algorithm such as simulated annealing. As illustrated in Figure 1-11, NMR structures result from global optimization of a model that describes many *local* parameters, and this is an important advantage in some application over approaches based on diffraction. For example, in applications to trapped photocycle intermediates of the membrane protein bacteriorhodopsin, NMR is able to resolve and specifically measure structural parameters in the individual components of conformational mixtures. Diffraction measurements, in which each measurable parameter (a reflection) is a global observable of a macroscopic sample, cannot as easily be applied to samples which are locally disordered or which exist in a mixture of local conformations.
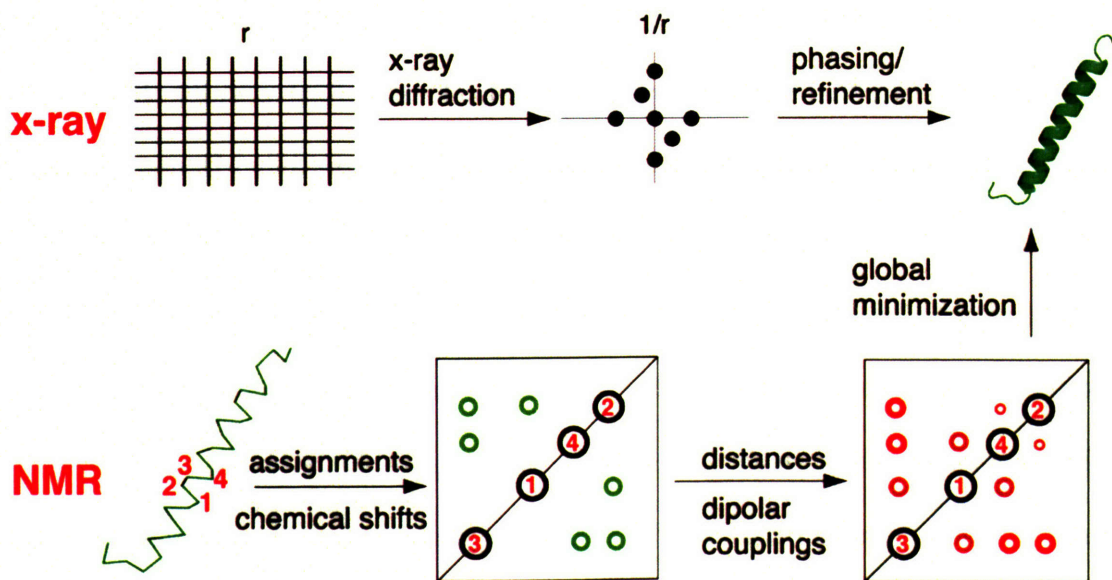
Figure 1-12: Structure determination by diffraction and NMR.

A number of examples illustrate the success of high-resolution solid-state NMR methods for atomic resolution structure determination. These include the refinement of a tripeptide structure [85], a recent structure of an amyloid fibril [86] and, in this thesis, the refinement of structures adopted by peptides at low temperatures, and finally the structure of a related amyloid fibril. These applications demonstrate that the protocols for structure determination in solid state NMR are now well established for systems of moderate size. The extension of these methods to larger systems, however, is not straightforward. In larger systems with many more unique chemical sites, the sensitivity per site decreases dramatically. A comparison of the sensitivity of solid-state NMR spectra recorded in a moderately sized system and a larger one, shown in Figure 1-13, clearly illustrates the problem. Since the experiments used to constrain the structure of the 11-residue amyloid fibril whose spectra are shown in Figure 1-13 can typically last ~7 days, their extension to a system with two orders of magnitude worse sensitivity is clearly impractical. This suggests that NMR sensitivity must be improved by one or two orders of magnitude in order for this successful protocol for structure determination to be applied routinely in macromolecular targets. Much of this thesis, then, is concerned with the development and initial applications of a sensitivity enhancement technique called Dynamic Nuclear Polarization, which can enhance NMR signals by two or three orders of magnitude through polarization transfer from electrons to nuclei.
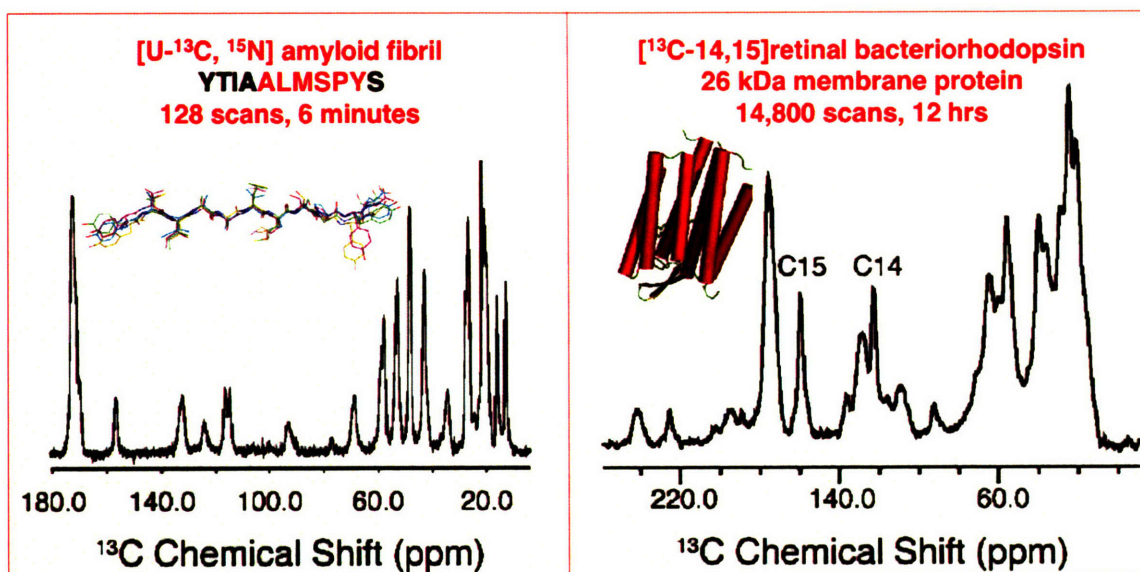
Figure 1-13: A comparison of the sensitivity of solid-state NMR acquisition in a system of moderate size (11-residues) and a large system (26 kDa membrane protein).

In Chapter 2 of this thesis, we review the major mechanisms of Dynamic Nuclear Polarization in high magnetic fields and describe the instrumentation required to perform DNP experiments, including the physics of microwave-generating vacuum electron devices. Chapters 3-5 deal with the development and controlled operation of a 250 GHz gyrotron oscillator and DNP/NMR spectrometer in the highest field DNP experiments performed to date. In Chapters 6-8, we describe the extension of this technology to even higher fields (corresponding to 700 MHz ^{1}H) through the development of a second harmonic gyrotron oscillator operating at 460 GHz. In Chapter 9, we describe initial biophysical applications of DNP to the study of photocycle intermediates of bacteriorhodopsin, including those which have not been previously observed by any technique. The work presented in Chapter 10 extends this methodology to uniformly ^{13}C,[15]N-labeled bacteriorhodopsin: we have made active site assignments even of the minor components of conformational mixtures of bR photocycle intermediates using DNP-enhanced multidimensional NMR and then used this information to perform

57

experiments which yield conformational constraints. Further, we show how the combination of non-linear sampling with DNP can be applied to study transient products of the bR photocycle. In Chapter 11, we study the protein glass transition using a model peptide whose high resolution structure is refined on the basis of solid state NMR restraints taken at low temperature. Chapter 12 discusses a family of experimental methods, collectively called "resonance width" measurements, in which homonuclear and heteronuclear dipolar couplings can be measured precisely and in a manner that accounts for the effects of relaxation. In Chapter 13, we present the atomic-resolution structure of of the L111M mutant of a peptide segment of transthyretin in an amyloid fibril. Finally, Chapter 14 describes experiments which probe the supramolecular architecture of an amyloid fibril on length scales ranging from the atomic to the microscopic.

References

[1]   Griffin, R. G., Dipolar recoupling and dynamic nuclear polarization in biological solids. *Abstracts of Papers of the American Chemical Society* **2000**, 219, U296-U296.

[2]   Jaroniec, C. P.; MacPhee, C. E.; Bajaj, V. S.; McMahon, M. T.; Dobson, C. M.; Griffin, R. G., High Resolution Molecular Structure of a Peptide in an Amyloid Fibril Determined by Magic Angle Spinning NMR Spectroscopy. *Proc. Nat'l. Acad. Sci.* **(submitted for publication) 2003**.

[3]   van der Wel, P. C. A.; Lewandoswki, J.; Griffin, R. G., Solid state NMR study of amyloid nanocrystals and fibrils formed by the peptide GNNQQNY from yeast prion protein Sup35p. *J. Am Chem. Soc* **2007**, (in press).

[4]   Bajaj, V. S.; Caproini, M.; MacPhee, C. E.; Dobson, C. M.; Griffin, R. G., Molecular Structure Determination of the L111M Amyloid Peptide from Transthyretin with Solid State NMR. *J. Am Chem. Soc* **2007**, (submitted for publication).

[5]   Tycko, R., Insights into the Amyloid Folding Problem from Solid-State NMR. *Biochemistry* **2003**, 42, (11), 3151-3159.

[6]   Petkova, A. T.; Ishii, Y.; Balbach, J. J.; Antzutkin, O. N.; Leapman, R. D.; Delaglio, F.; Tycko, R., Structural Model for Alzheimer's beta-Amyloid Fibrils Based on Experimental Constraints from Solid State NMR. *Proc. Nat'l Acad Sci* **2002**, 99, 16742-16747.

[7]   Jaroniec, C. P.; MacPhee, C. E.; Astrof, N. S.; Dobson, C. M.; Griffin, R. G., Molecular conformation of a peptide fragment of transthyretin in an amyloid fibril. *Proceedings of the National Academy of Sciences of the United States of America* **2002**, 99, (26), 16748-16753.

[8]   Tycko, R.; Antzutkin, O.; Balbach, J.; Ishii, Y.; Blanco, F.; Reed, J. In *Multiple-quantum NMR of Alzheimer's β-amyloid fibrils and other topics*, 41st Experimental Nuclear Magnetic Resonance Conference, Asilomar, CA, 2000; Asilomar, CA, 2000.

[9]   Tycko, R., Solid State NMR as a Probe of Amyloid Fibril Structure. *Curr. Opin. Chem. Biol.* **2000**, 4, 500.

[10]   Park, S. H.; Prytulla, S.; De Angelis, A. A.; Brown, J. M.; Kiefer, H.; Opella, S. J., High-resolution NMR spectroscopy of a GPCR in aligned bicelles. *Journal of the American Chemical Society* **2006**, 128, (23), 7402-7403.

[11]   Park, S. H.; De Angelis, A. A.; Nevzorov, A. A.; Wu, C. H.; Opella, S. J., Three-dimensional structure of the transmembrane domain of Vpu from HIV-1 in aligned phospholipid bicelles. *Biophysical Journal* **2006**, 91, (8), 3032-3042.

[12]   De Angelis, A. A.; Howell, S. C.; Nevzorov, A. A.; Opella, S. J., Structure determination of a membrane protein with two trans-membrane helices in aligned phospholipid bicelles by solid-state NMR spectroscopy. *Journal of the American Chemical Society* **2006**, 128, (37), 12256-12267.

[13]   Petkova, A. T.; Hatanaka, M.; Jaroniec, C. P.; Hu, J. G. G.; Belenky, M.; Verhoeven, M.; Lugtenburg, J.; Griffin, R. G.; Herzfeld, J., Tryptophan interactions in bacteriorhodopsin: A heteronuclear solid-state NMR study. *Biochemistry* **2002**, 41, (7), 2429-2437.

[14]   Lansing, J. C.; Tounge, B. A.; Jaroniec, C. P.; Pardoen, J. A.; Winkel, C.; Lugtenburg, J.; Belenky, M.; Herzfeld, J.; Griffin, R. G., Distortion of the chromophore of bacteriorhodopsin measured via solid state NMR. *Biophysical Journal* **2002**, 82, (1), 226a-226a.

[15]   Jaroniec, C. P.; Lansing, J. C.; Tounge, B. A.; Belenky, M.; Herzfeld, J.; Griffin, R. G., Internuclear distance measurements in uniformly C-13, N-15 labeled peptides and proteins. *Biophysical Journal* **2002**, 82, (1), 469a-469a.

[16]   Hatcher, M. E.; Hu, J. G. G.; Belenky, M.; Verdegem, P.; Lugtenburg, J.; Griffin, R. G.; Herzfeld, J., Control of the pump cycle in bacteriorhodopsin: Mechanisms elucidated by solid-state NMR of the D85N mutant. *Biophysical Journal* **2002**, 82, (2), 1017-1029.

[17]   Griffiths, J. M.; Bennett, A. E.; Engelhard, M.; Siebert, F.; Raap, J.; Lugtenburg, J.; Herzfeld, J.; Griffin, R. G., Structural investigation of the active site of bacteriorhodopsin: Geometric constraints on the roles of Asp-85 and Asp-212 in the proton pumping mechanism from solid-state NMR. *Biochemistry* **2000**, 39, 362-371.

[18]   Petkova, A. T.; Hu, J. G. G.; Bizounok, M.; Simpson, M.; Griffin, R. G.; Herzfeld, J., Arginine activity in the proton-motive photocycle of bacteriorhodopsin: Solid-state NMR studies of the wild-type and D85N proteins. *Biochemistry* **1999**, 38, (5), 1562-1572.

[19]   Hatanaka, M.; Hu, J. G.; Petkova, A. T.; Bizounok, M.; Verhoeven, M.; Lugtenburg, J.; Griffin, R. G.; Herzfeld, J., Active site changes in the early M -> late M transition of the photocycle of bacteriorhodopsin detected by ^{13}C-^{15}N REDOR NMR. *Biochemistry* **1999**.

[20]   Hu, J. G.; Sun, B. Q.; Hatcher, M. E.; Lansing, J. C.; Bizounok, M.; Griffin, R. G.; Herzfeld, J., Backbone structural changes during M-1 -> M-2 transition of bacteriorhodopsin detected by solid state NMR. *Biophysical Journal* **1998**, 74, (2), A292-A292.

[21]   Hu, J. G.; Sun, B. Q.; Bizounok, M.; Hatcher, M. E.; Lansing, J. C.; Raap, J.; Verdegem, P. J. E.; Lugtenburg, J.; Griffin, R. G.; Herzfeld, J., Early and late M intermediates in the bacteriorhodopsin photocycle: A solid-state NMR study. *Biochemistry* **1998**, 37, 8088-8096.

[22]   Mehring, M.; Pines, A.; Rhim, W.-K.; Waugh, J. S., High resolution NMR in solids. *J. Chem. Phys.* **1971**, 54, 3239-3246.

[23]   Abragam, A., *The Principles of Nuclear Magnetism*. Clarendon Press: Oxford, 1961.

[24]   Cavanaugh, J.; Fairbrother, W. J.; Palmer, A.; M.J, R.; Skelton, N. J., *Protein NMR Spectroscopy: Principles and Practice*. 2nd ed.; Academic Press: San Diego, CA, 2006.

[25]   Gu, Z. T.; Opella, S. J., Three-dimensional C-13 shift/H-1-N-15 Coupling/N-15 shift solid-state NMR correlation spectroscopy. *Journal of Magnetic Resonance* **1999**, 138, (2), 193-198.

[26]   Marassi, F. M.; Opella, S. J., NMR structural studies of membrane proteins. *Curr. Opin. Struct. Biol.* **1998**, 8, 640-648.

[27]   Opella, S. J., NMR and membrane proteins. *Nature Struct. Biol.* **1997**, 4, 845-848.

[28]   Tjandra, N.; Bax, A., Direct measurement of distances and angles in biomolecules by NMR in a dilute liquid crystalline medium. *Science* **1997**, 278, 1111-1114.

[29]   Maricq, M. M.; Waugh, J. S., NMR in rotating solids. *J. Chem. Phys.* **1979**, 70, 3300-3316.

[30]   Maricq, M.; Waugh, J. S., Rotational spin echoes and high resolution NMR in powders. *Chem. Phys. Lett.* **1977**, 47, (2), 327-329.

[31]   Andrew, E. R.; Bradbury, A.; Eades, R. G., Nuclear magnetic resonance spectra from a crystal rotated at high speed. *Nature* **1958**, 182, 1659.

[32]   Kolbert, A. C.; Griffin, R. G., 2-Dimensional Resolution of Isotropic and Anisotropic Chemical- Shifts in Magic Angle Spinning Nmr. *Chemical Physics Letters* **1990**, 166, (1), 87-91.

[33]   Baldus, M., Correlation experiments for assignment and structure elucidation of immobilized polypeptides under magic angle spinning. *Prog. NMR Spec.* **2002**, 41, (1-2), 1-47.

[34]   Ernst, M.; Samoson, A.; Meier, B. H., Low-power XiX decoupling in MAS NMR experiments. *Journal of Magnetic Resonance* **2003**, 163, (2), 332-339.

[35]   Ernst, M.; Samoson, A.; Meier, B. H., Low-power decoupling in fast magic-angle spinning NMR. *Chemical Physics Letters* **2001**, 348, (3-4), 293-302.

[36]   Pike, K. J.; Lemaitre, V.; Kukol, A.; Anupo, T.; Samoson, A.; Howes, A. P.; Watts, A.; Smith, M. E.; Dupree, R., Solid-State 17O NMR of Amino Acids. *J. Phys. Chem. B.* **2004**, (in press).

[37]   Wong, A.; Howes, A. P.; Pike, K. J.; Lemaitre, V.; Watts, A.; Anupold, T.; Past, J.; Samoson, A.; Dupree, R.; Smith, M. E., New limits for solid-state O-17 NMR spectroscopy: Complete resolution of multiple oxygen sites in a simple biomolecule. *J. Am Chem. Soc* **2006**, 128, 7744-45.

[38]   Kentgens, A. P. M.; van Eck, E. R. H.; Ajithkumar, T. G.; Anupold, T.; Past, J.; Reinhold, A.; Samoson, A., New opportunities for double rotation NMR of half-integer quadrupolar nuclei. *Journal of Magnetic Resonance* **2006**, 178, (2), 212-219.

[39]   Hung, I.; Howes, A. P.; Anupold, T.; Samoson, A.; Massiot, D.; Smith, M. E.; Brown, S. P.; Dupree, R., Al-27 double rotation two-dimensional spin diffusion NMR: Complete unambiguous assignment of aluminium sites in 9Al(2)O(3) center dot 2B(2)O(3). *Chemical Physics Letters* **2006**, 432, (1-3), 152-156.

[40]   Howes, A. P.; Anupold, T.; Lemaitre, V.; Kukol, A.; Watts, A.; Samoson, A.; Smith, M. E.; Dupree, R., Enhancing resolution and sensitivity of O-17 solid-state NMR through combining double rotation, H-1 decoupling and satellite modulation for biomolecular applications. *Chemical Physics Letters* **2006**, 421, (1-3), 42-46.

[41]   Meriles, C. A.; Sakellariou, D.; Moule, A.; Goldman, M.; Budinger, T. F.; Pines, A., High-resolution NMR of static samples by rotation of the magnetic field. *Journal of Magnetic Resonance* **2004**, 169, (1), 13-18.

[42]   Griffin, R. G., Dipolar recoupling in MAS spectra of biological solids. *Nature Struct. Biol.* **1998**, 5, 508-512.

[43]   Zhao, X.; Hoffbauer, W.; Guenne, J. S. a. d.; Levitt, M. H., Heteronuclear polarization transfer by symmetry-based recoupling sequences in solid-state NMR. *Solid State Nuclear Magnetic Resonance* **2004**, 26, 57-64.

[44]   Matsuki, Y.; Akutsu, H.; Fujiwara, T., Band-selective recoupling of homonuclear double-quantum dipolar interaction with a generalized composite 0 degrees pulse: application to C-13 aliphatic region-selective magnetization transfer in solids. *Journal of Magnetic Resonance* **2003**, 162, (1), 54-66.

[45]   Bjerring, M.; Nielsen, N. C., Solid-state NMR heteronuclear dipolar recoupling using off-resonance symmetry-based pulse sequences. *Chemical Physics Letters* **2003**, 370, (3-4), 496-503.

[46]   Jaroniec, C. P.; Tounge, B. A.; Herzfeld, J.; Griffin, R. G., Frequency selective heteronuclear dipolar recoupling in rotating solids: Accurate C-13-N-15 distance measurements in uniformly C-13,N-15-labeled peptides. *Journal of the American Chemical Society* **2001**, 123, (15), 3507-3519.

[47]   Jaroniec, C. P.; Tounge, B. A.; Rienstra, C. M.; Herzfeld, J.; Griffin, R. G., Recoupling of heteronuclear dipolar interactions with rotational-echo double-resonance at high magic-angle spinning frequencies. *Journal of Magnetic Resonance* **2000**, 146, (1), 132-139.

[48]   Hohwy, M.; Rienstra, C. M.; Jaroniec, C. P.; Griffin, R. G., Fivefold symmetric homonuclear dipolar recoupling in rotating solids: Application to double quantum spectroscopy. *J. Chem. Phys.* **1999**, 110, 7983-7992.

[49]   Rienstra, C. M.; Hatcher, M. E.; Mueller, L. J.; Sun, B. Q.; Fesik, S. W.; Griffin, R. G., Efficient multispin homonuclear double-quantum recoupling for magic-angle spinning NMR: ^{13}C-^{13}C correlation spectroscopy of U-^{13}C-Erythromycin A. *J. Am. Chem. Soc.* **1998**, 120, 10602-10612.

[50]   Gross, J. D.; Costa, P. R.; Griffin, R. G., Tilted n-fold symmetric radio frequency pulse sequences: Applications to CSA and heteronuclear dipolar recoupling in homonuclear dipolar coupled spin networks. *Journal of Chemical Physics* **1998**, 108, (17), 7286-7293.

[51]   Bennett, A. E.; Rienstra, C. M.; Griffiths, J. M.; Zhen, W. G.; Lansbury, P. T.; Griffin, R. G., Homonuclear radio frequency-driven recoupling in rotating solids. *Journal of Chemical Physics* **1998**, 108, (22), 9463-9479.

[52]   Gross, J. D.; Costa, P. R.; Griffin, R. G., Tilted n-fold Symmetric Radio Frequency Pulse Sequences: Applications to Chemical Shift Anistropy and Heteronuclear Dipolar Recoupling in Homonuclear Dipolar Coupled Spin Networks. *J. Chem. Phys.* **1997**, 108, 7286.

[53]   Fu, R.; Smith, S. A.; Bodenhausen, G., Recoupling of heteronuclear dipolar interactions in solid state magic-angle spinning NMR by simultaneous frequency and amplitude modulation. *Chem. Phys. Lett.* **1997**, 272, 361-369.

[54]   Mehta, M. A.; Gregory, D. M.; Kiihne, S.; Mitchell, D. J.; Hatcher, M. E.; Shiels, J. C.; Drobny, G. P., Distance measurements in nucliec acids using windowless dipolar recoupling solid state NMR. *Solid State Nucl. Mag. Reson.* **1996**, 7, (3), 211-228.

[55]   Levitt, M. H.; Oas, T. G.; Griffin, R. G., Rotary resonance recoupling in heteronuclear spin pair systems. *Isr. J. Chem.* **1988**, 28, 271-282.

[56]   Gullion, T.; Schaefer, J., Rotational Echo Double Resonance NMR. *J. Magn. Reson.* **1989**, 81, 196-200.

[57]   Brinkmann, A.; Levitt, M. H., Symmetry principles in the nuclear magnetic resonance of spinning solids: Heteronuclear recoupling by generalized Hartmann-Hahn sequences. *J. Chem. Phys.* **2001**, 115, 357-384.

[58]   Brinkmann, A.; Edén, M.; Levitt, M. H., Synchronous Helical Pulse Sequences in Magic-Angle Spinning NMR. Double Quantum Recoupling of Multiple-Spin Systems. *J. Chem. Phys.* **2000**, 112, 8539-8554.

[59]   Hong, M.; Gross, J. D.; Griffin, R. G., Site-resolved determination of peptide torsion angle phi from the relative orientations of backbone N-H and C-H bonds by solid-state NMR. *Journal of Physical Chemistry B* **1997**, 101, (30), 5869-5874.

[60]   SchmidtRohr, K., A double-quantum solid-state NMR technique for determining torsion angles in polymers. *Macromolecules* **1996**, 29, (11), 3975-3981.

[61]   Hohwy, M.; Jaroniec, C. P.; Lansing, J.; Rienstra, C. M.; Griffin, R. G., ^{13}C-^{1}H recoupling in the HCCH torsion angle experiment in solid-state NMR. *Chem. Phys. Lett.* **1999**.

[62]   Ladizhansky, V.; Jaroniec, C. P.; Diehl, A.; Oschkinat, H.; Griffin, R. G., Measurement of multiple y torsion angles in uniformly ^{13}C,^{15}N-labeled a-spectrin domain using 3D ^{15}N-^{13}C-^{13}C-^{15}N MAS dipolar-chemical shift correlation spectroscopy. *J. Am. Chem. Soc.* **2003,** in press.

[63]   Ladizhansky, V.; Veshtort, M.; Griffin, R. G., NMR determination of the torsion angle ψ in α–helical peptides and proteins: the HCCN dipolar correlation experiment. *J. Magn. Reson.* **2002,** 154, (2), 317-324.

[64]   Rienstra, C. M.; Hohwy, M.; Mueller, L. J.; Jaroniec, C. P.; Reif, B.; Griffin, R. G., Determination of multiple torsion angle-constraints in U-^{13}C, ^{15}N-labeled peptides: 3D ^{1}H-^{15}N-^{13}C-^{1}H dipolar chemical shift spectroscopy in rotating solids. *J. Am. Chem. Soc.* **2002,** 124, 11908-11922.

[65]   Feng, X.; Verdegem, P.; Lee, Y.; Sandstrom, D.; Eden, M.; Bovee-Geurts, P.; de Grip, W.; Lugtenburg, J.; de Groot, H.; Levitt, M., Direct Determination of a Molecular Torsion Angle in the Membrane Protein Rhodopsin by Solid-State NMR. *J. Am. Chem. Soc.* **1997,** 119, (29), 6853-6857.

[66]   Hong, M., Determination of Multiple Phi Torsion Angles in Solid Proteins by Selective and Extensive ^{13}C Labeling and Two-Dimensional Solid-State NMR. *J. Magnetic Reson.* **1999,** 139, 389-401.

[67]   Schaefer, J., REDOR-determined distances from heterospins to clusters of C-13 labels. *Journal of Magnetic Resonance* **1999,** 137, (1), 272-275.

[68]   Merritt, M. E.; Sigurdsson, S. T.; Drobny, G. P., Long-range distance measurements to the phosphodiester backbone of solid nucleic acids using ^{31}P-^{19}F REDOR NMR. *J. Am. Chem. Soc.* **1999,** 121, 6070-6071.

[69]   Jaroniec, C. P.; Tounge, B. A.; Rienstra, C. M.; Herzfeld, J.; Griffin, R. G., Measurement of C-13-N-15 distances in uniformly C-13 labeled biomolecules: J-decoupled REDOR. *Journal of the American Chemical Society* **1999,** 121, (43), 10237-10238.

[70]   Naito, A.; Nishimura, K.; Kimura, S.; Tuzi, S.; Aida, M.; Yasuoka, N.; Saito, H., Determination of the three-dimensional structure of a new crystalline form of N-acetyl-Pro-Gly-Phe as revealed by ^{13}C REDOR, x-ray diffraction, and molecular dynamics simulation. *J. Phys. Chem.* **1996,** 100, 14995-15004.

[71]   McDowell, L. M.; Lee, M. S.; McKay, R. A.; Anderson, K. S.; Schaefer, J., Intersubunit communication in tryptophan synthase by carbon-13 and fluorine-19 REDOR NMR. *Biochemistry* **1996,** 35, (10), 3328-3334.

[72]   Mcdowell, L. M.; Klug, C. a.; Studelska, D. R.; Tasaki, K.; Beusen, D. D.; Mckay, R. a.; Schaefer, J., Applications of Redor Nmr-Spectroscopy. *Journal of Cellular Biochemistry* **1995**, 18-18.

[73]   Jeener, J.; Meier, B. H.; Bachmann, P.; Ernst, R. R., Investigation of exchange processes by two-dimensional NMR spectroscopy. *J. Chem. Phys.* **1979**, 71, 4546-4553.

[74]   States, D. J.; Haberkorn, R. A.; Ruben, D. J., A two-dimensional nuclear Overhauser experiment with pure absorption phase in four quadrants. *J. Magn. Reson.* **1982**, 48, 286-292.

[75]   Petkova, A. T.; Baldus, M.; Belenky, M.; Hong, M.; Griffin, R. G.; Herzfeld, J., Backbone and Sidechain Assignment Strategies for Multiply Labeled Membrane Peptides and Proteins. *J. Magn. Resonance* **2003**, 160, 1-12.

[76]   Suter, D.; Ernst, R. R., Spectral spin diffusion in the presence of an extraneous dipolar reservoir. *Phys. Rev. B* **1982**, 25, 6038-6041.

[77]   Suter, D.; Ernst, R. R., Spin diffusion in resolved solid-state NMR spectra. *Phys. Rev. B* **1985**, 32, 5608-5627.

[78]   Meier, B. H., Polarization Transfer and Spin Diffusion in Solid-State NMR. *Advances in Magnetic and Optical Resonance* **1994**, 18, 1-116.

[79]   Takegoshi, K.; Nakamura, S.; Terao, T., C-13-H-1 dipolar-assisted rotational resonance in magic-angle spinning NMR. *Chemical Physics Letters* **2001**, 344, (5-6), 631-637.

[80]   Ohashi, R.; Takegoshi, K., Asymmetric C-13-C-13 polarization transfer under dipolar-assisted rotational resonance in magic-angle spinning NMR. *Journal of Chemical Physics* **2006**, 125, (21), -.

[81]   Crocker, E.; Eilers, M.; Ahuja, S.; Hornak, V.; Hirshfeld, A.; Sheves, M.; Smith, S. O., Location of Trp265 in metarhodopsin II: Implications for the activation mechanism of the visual receptor rhodopsin. *Journal of Molecular Biology* **2006**, 357, (1), 163-172.

[82]   Castellani, F.; van Rossum, B.-J.; Diehl, A.; Schubert, M.; Rehbein, K.; Oschkinat, H., Structure of a protein determined by solid-state magic-angle-spinning NMR spectroscopy. *Nature* **2002**, 420, 98-102.

[83]   Franks, W. T.; Zhou, D. H.; Wylie, B. J.; Money, B. G.; Graesser, D. T.; Frericks, H. L.; Sahota, G.; Rienstra, C. M., Magic-Angle Spinning Solid-State NMR Spectroscopy of the b1 Immunoglobulin Binding Domain of Protein G (GB1): 15N and 13C Chemical Shift Assignments and Conformational Analysis. *J. Am Chem. Soc* **2005**, 127, 12291.

[84]   Zech, S. G.; Wand, A. J.; McDermott, A. E., Protein Structure Determination by High-Resolution Solid-State NMR Spectroscopy: Application to Microcrystalline Ubiquitin. *J. Am. Chem. Soc.* **2005,** 127, (24), 8618-8626.

[85]   Rienstra, C. M.; Tucker-Kellogg, L.; Jaroniec, C. P.; Hohwy, M.; Reif, B.; McMahon, M. T.; Tidor, B.; Lozano-Perez, T.; Griffin, R. G., De novo determination of peptide structure with solid-state magic-angle spinning NMR spectroscopy. *Proceedings of the National Academy of Sciences of the United States of America* **2002,** 99, (16), 10260-10265.

[86]   Jaroniec, C. P.; MacPhee, C. E.; Bajaj, V. S.; McMahon, M. T.; Dobson, C. M.; Griffin, R. G., High-resolution molecular structure of a peptide in an amyloid fibril determined by magic angle spinning NMR spectroscopy. *Proceedings of the National Academy of Sciences of the United States of America* **2004,** 101, (3), 711-716.

Chapter 2   Dynamic Nuclear Polarization Of Biological Systems At High Magnetic Fields

Nuclear magnetic resonance in the solid phase is a powerful tool for the elucidation of local chemical environment; in combination with magic angle spinning (MAS), solid state NMR is also capable of delivering site-specific information about molecular topology and internuclear proximity. In favorable cases, the information derived from these experiments is sufficient for the total structure determination of biomolecules including peptides and proteins in the solid state. Nevertheless, a critical factor limiting the general applicability of these techniques is the inherently low sensitivity of the NMR experiment. Here, we review the application of dynamic nuclear polarization (DNP), a technique in which the greater spin polarization of the electrons is transferred to the nuclei, to enhance the sensitivity in solid state NMR spectroscopy of biomolecules in high magnetic fields.

2.1   Introduction: Sensitivity In Solid State NMR

Magnetic resonance has now emerged as a powerful and complementary technique to x-ray crystallography for the elucidation of molecular structure in atomic detail. In particular, nuclear magnetic resonance (NMR) in the solution state is an established and successful tool in structural biology, and recent methodological developments permit its application to systems of ever larger molecular weight [1][2]. Nevertheless, there are a number of interesting systems which can neither be readily crystallized for diffraction studies nor dissolved in sufficient concentrations for solution state NMR. Examples of particular importance include integral membrane proteins [3][4][5][6][7][8][9], protein

complexes or aggregates [10], amyloid fibrils [11][12][13][14][15], molecules in the cell wall or extracellular matrix [16], and natural or synthetic biomaterials [17][18]. For all these cases, solid state NMR methods can provide information about molecular geometry in the native biological or functional milieu, free from the requirement of crystallinity imposed by diffraction methods, and free from the requirements of solubility and molecular weight imposed by solution state NMR.

In order for an NMR spectrum to provide meaningful information at an atomic scale, each of its component resonances must be unambiguously assigned to a constituent nucleus of the molecule under study. For a molecule with multiple NMR-active sites, the extent to which this is possible is determined largely by the degree to which the transitions associated with the NMR Hamiltonian are mutually resolved. In general, the Hamiltonian is the sum of internal and external interactions which are anisotropic and whose magnitudes thus depend upon the orientation between interacting centers and the external magnetic field. The spectrum of a polycrystalline powder sample, in which all such orientations are represented, is therefore broad, unresolved, and generally devoid of site-specific information.

Molecules dissolved in solution typically undergo rotational diffusion which is fast on the time scale of NMR interactions. When this molecular reorientation is rapid and isotropic, many anisotropic elements of the spin Hamiltonian are either averaged to zero or to a finite trace, resulting in highly resolved NMR spectra. However, increased resolution is not the only result; since the width of resonance lines is reduced by at least three orders of magnitude by this process, the signal intensity and signal to noise ratio also increase by a similar factor. Because the spectra of abundant, high gyromagnetic

ratio nuclei (*e.g.* ^{1}H in biopolymers) are also well-resolved, it becomes possible to detect the spectra of dilute, low-gyromagnetic ratio nuclei such as ^{13}C and ^{15}N indirectly through their influence on the ^{1}H spins, resulting in even further improvements in signal to noise. Due to this degree of sensitivity, experiments involving three or four correlated dimensions are now routine. The latter fact in combination with techniques for uniform isotopic enrichment of samples has proven essential for the application of solution state NMR to the study of biological macromolecules.

Isotropic molecular reorientation is absent in the solid state, and the full anisotropy of the NMR Hamiltonian is manifest. Site-specific resolution of resonances in a solid state NMR spectrum is possible only in samples that are oriented with respect to an external director or in polycrystalline powders during magic angle spinning (MAS). In the first case, uniaxial orientation of the sample with respect to the static magnetic field has the effect of collapsing spatially anisotropic elements of the nuclear spin Hamiltonian to single, orientationally-dependent values [19]. Angular orientational constraints are then recovered through dipolar and chemical shift spectra which are typically recorded in a correlation experiment [20][21][22]. Because of this line-narrowing effect, spectra of oriented samples also exhibit far better sensitivity than those of the unoriented powder.

A more general route to high resolution NMR in the solid state is magic angle spinning, a technique in which the sample is tilted with respect to the static magnetic field and rotated rapidly about this tilted axis [23]. For the appropriate choice of tilt angle and in the limit of fast spinning, several anisotropic terms in the Hamiltonian such as the chemical shift and the dipolar coupling collapse to their trace, resulting in isotropic spectra which resemble those obtained in the solution state. However, this averaging is

not complete; for low gyromagnetic ratio nuclei, resonance lines in even microcrystalline samples exhibit inhomogeneous broadening, and, for abundant high-γ nuclei (such as ^{1}H), the homogeneous dipolar couplings continue to broaden the spectra. As a result, indirect detection experiments are not currently possible in the solid state, and signal to noise is often three orders of magnitude lower than in a comparable solution state experiment. This limits, in particular, the application of high-dimensionality pulse sequences, which are required to obtain assignments or multiple conformational constraints in multiply labeled samples [24][25][26][27] to systems which exhibit good sensitivity.

One technique which promises to alleviate this limitation is dynamic nuclear polarization (DNP), an experiment in which the greater polarization of the electrons is transferred to the nuclei prior to acquisition of an NMR spectrum. Previously applied to the problem of producing polarized targets for nuclear scattering experiments, DNP has recently been applied to solid-state NMR experiments both in static and spinning samples. Through a variety of polarization transfer mechanisms which depend on fixed, mobile, or transient paramagnetic centers and strong microwave irradiation, signal enhancements of up to three orders of magnitude have been reported. Many of these polarization transfer mechanisms depend on non-secular interactions which are strongly truncated at the high magnetic fields that are commonplace in biomolecular NMR, with the result that applications of DNP at high fields have been limited. Nevertheless, a variety of recent developments now permit the routine application of DNP as an adjunct to MAS in NMR experiments, even at elevated magnetic fields. The combined MAS/DNP experiment rests on two technologies: stable magic angle spinning at cryogenic temperatures and high microwave power output at millimeter or submillimeter

wavelengths. The latter requirement, in particular, has necessitated the development of cyclotron resonance masers (gyrotrons), which are capable of producing 10–50 W of microwave power at frequencies up to 460 GHz. Here, we briefly review the mechanisms responsible for electron-nuclear polarization transfer and discuss the instrumentation required to make use of this effect for sensitivity enhancement in solid state NMR.

2.2　Electron-Nuclear Polarization Transfer in Solids

Like most high-field EPR experiments, DNP is currently performed with radiation fields that are weak compared to the internal interaction Hamiltonian. The inhomogeneous interaction width can therefore be much larger than the available excitation bandwidth, and most experiments must be conducted with continuous wave (CW) radiation. Further, because the energies of EPR and NMR transitions differ by nearly three orders of magnitude, non-secular elements of the Hamiltonian which may be safely neglected for the electrons still contribute to the dynamics on a nuclear energy scale.

These factors complicate the treatment of electron-nuclear polarization transfer in solids; the problem has been approached from a variety of mathematical viewpoints, none of which provide an entirely satisfactory description of the phenomena involved. For historical reasons, DNP experiments based on continuous microwave irradiation (solid effect and thermal mixing) are generally discussed within the framework of spin temperature theory, which is a thermodynamic analog of perturbation theory [28][29][30][31][32][33][34][35][36][37]. Here, each constant of the motion in an unperturbed Hamiltonian is identified with a unique thermodynamic reservoir having a well-defined spin temperature. Small interactions which might otherwise be regarded as

perturbations then mediate temperature equilibration among these reservoirs. In this picture, dynamic nuclear polarization is a kind of Carnot cycle; the nuclear Zeeman reservoir is cooled by a direct or indirect interaction that transfers heat to the electron Zeeman reservoir. The enhancement is thus related to the heat capacity of the reservoirs, their initial temperatures, and the reversibility or adiabaticity of the polarization transfer process [38]. These treatments are in phenomenological agreement with experiment but afford little insight into the basis of the effect in terms of molecular parameters. Conversely, more recent DNP experiments involving transient irradiation of the electron-nuclear spin system resemble Hartmann-Hahn experiments in IS nuclear spin pairs and are therefore best understood entirely in the quantum mechanical picture [39][40][41][42]. These experiments require pulsed frequency and phase modulated microwave radiation; due to a lack of suitable sources at sub-terahertz frequencies, they have not been substantially applied at high magnetic fields.

A summary of the DNP experiments which are most relevant for existing and future applications in biomolecular solid state NMR appears in Figure 2-1.

Thermal Mixing	e⁻ ▭ ; ¹H —CP— TPPM	three-spin cross-relaxation
Solid Effect	¹³C/¹⁵N —CP—⟩⟩⟩	forbidden transitions $\Omega_S = \pm\omega_I$
Nuclear Rotating Frame DNP	e⁻ ▭ ; ¹H ▭—CP—TPPM ; ¹³C/¹⁵N —CP—⟩⟩⟩	forbidden transitions/ thermal mixing
Nuclear Orientation Via Electron Spin Locking	e⁻ ⎍---- ; ¹H —⟩⟩⟩	Hartmann-Hahn double resonance $\omega_{1S} = \omega_I$
Dressed State Solid Effect Electron-Nuclear CP	e⁻ ▭ ⎮ ⋁ ; ¹H ▭ ⊢—τ—⊢—τ—⊣	Hartmann-Hahn double resonance $\Omega_I = \pm\sqrt{\Omega_S^2 + \omega_{1S}^2}$

Figure 2-1. Pulse sequences for dynamic nuclear polarization (DNP) described in the text. Matching conditions are indicated for the microwave field, ω_{1S}, RF field, ω_{1I}, nuclear frequency, ω_I, and electron resonance offset, Ω_S.

2.2.1 Spin Thermodynamics in Paramagnetic Systems

Spin temperature theory is an approximate description of the quantum dynamics of an ensemble of interacting spins. It is valid only in the thermodynamic limit and is not concerned with the coherent properties of one or a few spins, but rather the average expectation values of observables over the entire ensemble. In this sense, the idea

follows directly from the concept of a density matrix.[1] For a large spin system defined by the Hamiltonian, H, and density matrix, σ, the entropy is

$$S = -kTr(\sigma \ln \sigma).$$ (2.1)

The distribution of states at equilibrium is one in which the entropy (2.1) is maximized. This maximization is subject to the constraints that both the total number of particles and total energy must be conserved, which leads to the variational formula,

$$\delta S = -k \ln \sigma - k - \lambda - \mu H = 0,$$ (2.2)

in which λ and μ are Lagrange multipliers which enforce these constraints. The solution to this optimization problem is the canonical (Boltzmann) ensemble [43],

$$\sigma = \frac{\exp\left(-\mu H / k\right)}{Tr\left\{\exp\left(-\mu H / k\right)\right\}}.$$ (2.3)

If we identify $\mu = 1/T$ as the inverse temperature, then (2.3) can be approximated to first order, as

$$\sigma \cong 1 - \frac{H}{kT}$$
$$= 1 - \mu H.$$ (2.4)

This is the so-called "high temperature limit."[2] Suppose now that we have a $S = \frac{1}{2}$ system whose Zeeman level populations, n_+ and n_-, are defined by the polarization,

$$P = n_+ - n_-.$$ (2.5)

If there is a Boltzmann equilibrium, then

---

[1] A more rigorous discussion of this connection is presented in Ch. 1 of [36].
[2] A normalization constant is required in (2.4), but it can be carried implicitly in the calculation of the trace.

$$\frac{n_+}{n_-} = \exp\left(\frac{E_+ - E_-}{kT_s}\right),$$ (2.6)

which gives

$$P = \tanh\left(\frac{\gamma\hbar B_0}{kT_S}\right)$$
$$\cong \frac{\gamma\hbar B_0}{kT_S}$$ (2.7)

in the high temperature limit. In other words, the probability of finding the ith state is proportional to e^{-E_i/kT_s}, where T_s is the spin temperature of the system. The idea of a spin thermodynamic reservoir having a temperature which is distinct from the lattice can only be valid if the processes establishing equilibrium within it are faster than those destroying it. Since many NMR experiments can produce non-equilibrium states which slowly reach equilibrium with the lattice, this criteria is often easily met. In fact, since spin systems can have complex interaction Hamiltonians, particularly where multiple spin species are involved, several independent Boltzmann equilibria might be satisfied on a limited time scale. More formally, suppose we have a Hamiltonian defined by several secular, mutually commuting terms which are constants of the motion on the time scale of spin-lattice relaxation. In that case, we would solve (2.2) subject to a Lagrange multiplier, λ_i, for each quasi-constant term. For example, a system consisting of an electron (S) and nuclear (I) spin together with the secular dipolar interaction between them H_D) is defined by

$$H = \omega_S S_z + \omega_I I_z + H_D$$ (2.8)

$$\sigma \cong 1 - \alpha S_z + \omega_I I_z + \gamma H_D.$$

In this case, there are three inverse spin temperatures, α, β, and γ, corresponding respectively to the temperatures of the electron Zeeman, nuclear Zeeman, and electron spin-spin thermodynamic reservoirs. Analogous spin temperatures can be derived in the interaction representation of the Hamiltonian, in which case they are called spin temperatures in the rotating frame [44]. The tendency for each to reach an equilibrium temperature with the lattice is described by

$$\dot{\alpha} = -\frac{1}{T_{1e}}(\alpha - \alpha_0) \tag{2.9}$$

$$\dot{\beta} = -\frac{1}{T_{1n}}(\beta - \beta_0)$$

$$\dot{\gamma} = -\frac{1}{T_{1D}}(\gamma - \gamma_0).$$

Spin-lattice relaxation is not the only mechanism which can result in change of spin temperature. In particular, we have neglected terms in (2.8) such as the non-secular dipolar interaction, which might produce matrix elements that couple these thermodynamic reservoirs (e.g. through the action of so-called "flip-flop" terms). To illustrate how these effects can lead to enhanced nuclear polarization, we will consider two examples: an electron-nuclear spin system consisting of electron and nuclear Zeeman thermodynamic reservoirs and an electron-electron-nuclear three spin system in which an additional spin temperature is introduced to account for interactions between the electrons. In both cases, it is straightforward to show that the electron and nuclear Zeeman reservoirs are coupled in such a way that the temperature (and hence polarization) of the nuclear spin system can be influenced by irradiation at or near the electron Larmor frequency. A diagram of these interaction reservoirs and the matrix

elements or relaxation mechanisms responsible for establishing equilibrium between them appears in Figure 2-2. Though it is in principle possible to estimate the DNP enhancement, the spin thermodynamic model incorporates many adjustable parameters which are difficult or impossible to measure at elevated magnetic fields, and therefore such estimates are of limited utility.
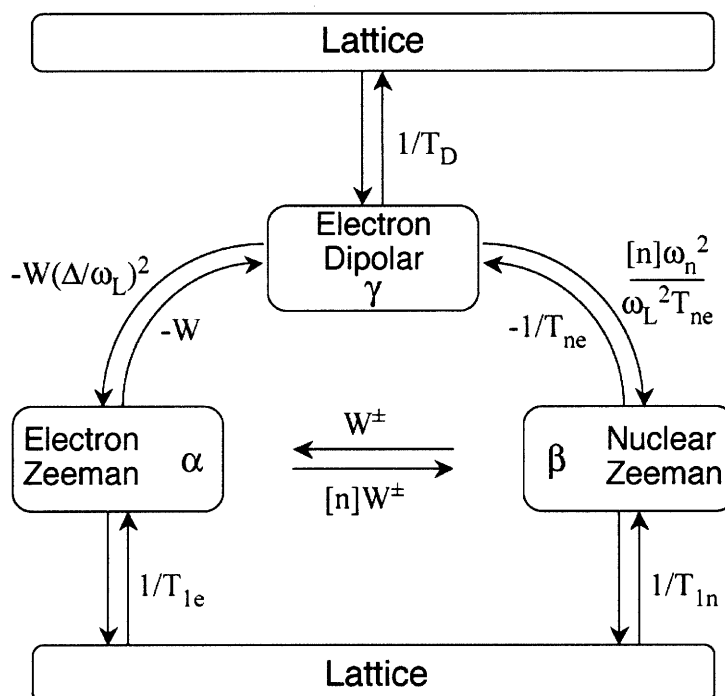
Figure 2-2. Spin thermodynamic description of coupled electron-nuclear multi-spin system. Matrix elements and/or relaxation processes responsible for spin temperature equilibration are labeled. Adapted from [33].

2.2.2 Solid Effect

In the simplest case, the non-secular hyperfine coupling between an electron and a nucleus can give rise to so-called "forbidden transitions" which involve coupled electron-nuclear spin flips. The relevant Hamiltonian for the electron-nuclear system is

$$H = \omega_S S_z + \omega_I I_z + C S_z I_+ + C^* S_z I_-, \tag{2.10}$$

where

$$C = -\frac{3}{2}\frac{\gamma_e^2 \hbar^2}{r^3}\sin\theta\cos\theta e^{-i\phi}, \qquad (2.11)$$

and (r,θ,ϕ) defines the relative orientation of the electron and nucleus. In the absence of the hyperfine coupling, the basis states of this system are product states such as $|++\rangle = |+\rangle \otimes |+\rangle$, and similarly for $|+-\rangle$, $|-+\rangle$, and $|--\rangle$. To first order, the hyperfine coupling results in an eigenstate mixing defined by,

$$|1\rangle = |++\rangle + q^*|+-\rangle \qquad (2.12)$$

$$|2\rangle = |+-\rangle + q|++\rangle$$

$$|3\rangle = |-+\rangle + q^*|--\rangle$$

$$|4\rangle = |--\rangle + q|-+\rangle,$$

where the mixing coefficient is given by

$$q = \frac{C}{2\omega_I}. \qquad (2.13)$$

This implies that there will be two new transitions, $|2\rangle \leftrightarrow |3\rangle$ and $|1\rangle \leftrightarrow |4\rangle$, which are forbidden in the absence of the perturbation. The first transition corresponds to an electron-nuclear flip-flop and occurs at $(\omega_S - \omega_I)$, while the second involves a two-spin flip and occurs at a frequency $(\omega_S + \omega_I)$. If one of these transitions can be selectively excited, the nuclear system will be polarized above thermal equilibrium. If the transition rate for the allowed transitions $|1\rangle \leftrightarrow |3\rangle$ and $|2\rangle \leftrightarrow |4\rangle$ is W_0, then that for the forbidden transitions will be qq^*W_0, which is much smaller than W_0 at high magnetic fields.

In the thermodynamic picture, these transitions couple the electron and nuclear thermodynamic reservoirs. Goldman has derived rate equations for the spin temperature of the electron Zeeman reservoir (in the rotating frame), nuclear Zeeman reservoir, and spin-spin interaction reservoir [36] which describe this process. For radiation near $\omega = (\omega_S - \omega_I)$ exciting transition $|2\rangle \leftrightarrow |3\rangle$ with probability W_+, or for radiation near $\omega = (\omega_S + \omega_I)$ exciting $|1\rangle \leftrightarrow |4\rangle$ with probability W_-, these are:

$$\dot{\alpha} = \frac{C_I}{\Delta} W_{\pm}[\mp \alpha \Delta + \beta \omega_I - \gamma(\Gamma_{\pm})] - \frac{1}{T_{1e}}(\alpha - \alpha_0) \qquad (2.14)$$

$$\dot{\beta} = -\frac{C_S}{\omega_I} W_{\pm}[\mp \alpha \Delta + \beta \omega_I - \gamma(\Gamma_{\pm})] - \frac{1}{T_{1n}}(\beta - \beta_0)$$

$$\dot{\gamma} = -W_{\pm}\frac{\Gamma_{\pm}}{D^2}[\mp \alpha \Delta + \beta \omega_I - \gamma(\Gamma_{\pm})] - \frac{1}{T_{1D}}(\gamma - \gamma_0),$$

where

$$\Gamma_+ = \omega_I - \omega_S + \omega \qquad (2.15)$$

$$\Gamma_- = \omega_I + \omega_S - \omega,$$

and $\Delta = \omega_S - \omega$), $C_S = N_S / (N_S + N_I)$, $C_I = N_I / (N_S + N_I)$, and N_S and N_I are the number of electron and nuclear spins, respectively.[3] The parameter D is a local frequency given by $D = \mathrm{Tr}(H_D^2) / \mathrm{Tr}(S_x^2)$. If $\omega = (\omega_S \pm \omega_I)$, then $\Gamma_{\pm} = 0$, and the terms in (2.14) involving the temperature of the spin-spin interaction reservoir are removed from the dynamics. At steady-state conditions (where $\dot{\alpha} = \dot{\beta} = 0$), and in the limit $C_S T_1 W_{\pm} \gg 1$, the polarization

[3] This is valid for the $I = \frac{1}{2}$, $S = \frac{1}{2}$ case.

becomes $P_I = \mp P_S$. Hence, the nuclear polarization can be as large as the electron polarization, but potentially of the opposite sign.

The forbidden transition probabilities responsible for the solid effect have also been estimated by Weis and co-workers [42] based on a derivation by Jeschke and Schweiger [45] in the context of coherence transfer in electron-nuclear spin systems. For the electron rotating frame Hamiltonian including secular, A, and non-secular, B, parts of the hyperfine coupling,

$$H = \Omega_S S_z + \omega_I I_z + A S_z I_z + B S_z I_x,\qquad(2.16)$$

the eigenvalues are

$$E_{1/2} = \frac{\omega_s}{2} \pm \frac{1}{2}\left(\omega_I + \frac{A}{2}\right)\cos(\eta_\alpha) \mp \frac{B}{4}\sin(\eta_\alpha)\qquad(2.17)$$

$$E_{3/4} = -\frac{\omega_s}{2} \pm \frac{1}{2}\left(\omega_I - \frac{A}{2}\right)\cos(\eta_\beta) \pm \frac{B}{4}\sin(\eta_\beta),$$

where

$$\eta_\alpha = \tan^{-1}\left(\frac{-B}{A + 2\omega_I}\right)\qquad(2.18)$$

$$\eta_\beta = \tan^{-1}\left(\frac{-B}{A - 2\omega_I}\right).$$

To explain the effects of microwave radiation, the Hamiltonian (2.16) including microwave excitation, $H_{mw} = \omega_{1S} S_x$, is diagonalized by the unitary transformation

$$U = \exp\left[-i\left(\eta_\alpha S^\alpha I_y + \eta_\beta S^\beta I_y\right)\right],^4 \text{ to give}$$

$$H = \Omega_S S_z + \omega_I I_z + A S_z I_z + \omega_1 \cos(\eta) S_x + 2\omega_1 \sin(\eta) S_y I_y,\qquad(2.19)$$

where $\eta = (\eta_\alpha - \eta_\beta)/2$.

The last two terms of (2.19) arise from the microwave excitation and are responsible for allowed and forbidden transitions, respectively. To make this more explicit, they can be re-written as

$$H_{mw} = \omega_1 \cos(\eta)S_x + \frac{1}{2}\omega_1 \sin(\eta)\left[S^+I^- + S^-I^+\right] - \frac{1}{2}\omega_1 \sin(\eta)\left[S^+I^+ + S^+I^+\right]. \quad (2.20)$$

The probability of an allowed transition is proportional to $\cos^2(\eta)$ and that of either forbidden transition to $\sin^2(\eta)$; the probability of exciting a forbidden transition therefore also declines approximately as B_0^2, which is in quantitative agreement with experimental results [42][46].

In order to achieve the theoretical solid effect enhancement, zero quantum and double quantum transitions at $(\omega_S + \omega_I)$ and $(\omega_S - \omega_I)$ must be mutually resolved, which implies that the EPR line width must be much smaller than ω_I. At high magnetic fields, EPR lines are inhomogeneously broadened due to the g-anisotropy, with the result that this condition does not hold for most radicals. Since the $\Delta(M) = \pm 2$ and $\Delta(M) = \pm 1$ transitions result in a polarization of equal magnitude but opposite sign, they will tend to cancel and limit the overall enhancement ("unresolved solid effect"). Experiments such as the integrated solid effect (ISE) [41], in which polarization transfer is accomplished by fast passage with an adiabatic magnetic field sweep, recover some of this lost enhancement at moderate magnetic fields. Even in radical systems which are not inhomogeneously broadened at elevated magnetic fields, the polarization transfer process will be slow due to its inverse dependence on B_0^2. This implies that it will compete with

---

[4] The polarization operators are $S^{a,b} = \frac{1}{2}(1 \pm S_z)$.

81

nuclear spin-lattice relaxation, and so the experiment is ideally conducted at cryogenic temperatures (where spin lattice relaxation is slow even in paramagnetically doped compounds). For these reasons, the solid effect is not the preferred mechanism of dynamic nuclear polarization in high fields.

2.2.3 Thermal Mixing

Thermal mixing is another DNP process which becomes operative exactly in the case when the EPR linewidth approaches or exceeds the nuclear Larmor frequency. However, the spin thermodynamic formalism of thermal mixing DNP requires either that the line broadening be entirely homogeneous in character or that fast electron-electron cross relaxation (spectral diffusion) within an inhomogeneously broadened line renders it effectively homogeneous on the time scale of spin-lattice relaxation [28][30][47]. In either case, the nuclear and electron Zeeman reservoirs are indirectly coupled by their mutual interaction with a reservoir corresponding to the secular part of the dipolar interaction Hamiltonian. Cooling of this latter reservoir can then result in increased nuclear polarization.

The concept of thermal mixing is closely related to the classical treatment of nuclear relaxation in paramagnetically doped solids. In such a solid, nuclear relaxation is greatly enhanced due to the coupling of the nuclei to paramagnetic centers which relax much more quickly. The element which almost entirely explains this relaxation process is the $S_z I_\pm$ term of the hyperfine interaction [34]. This is because transitions brought about by this coupling involve only a quantum of energy at the nuclear Larmor frequency, while other terms in the bilinear coupling $S \cdot I$ also involve energies on the scale of the electron Zeeman interaction. Suppose that the operator S_z fluctuates due to electron spin-lattice

relaxation with a correlation time of T_{1e}. Using semi-classical relaxation theory, Abragam has shown that [34]

$$\frac{1}{T_{1n}} = 4(q^2)\frac{\omega_n^2 T_{1e}}{1+\omega_n^2 T_{1e}^2},$$ (2.21)

where q has been previously defined in (2.13).

If the concentration of electrons is very high, fluctuations in S_z can also occur due to electron-electron "flip-flops", which occur at a rate T_{2e}. If this is the dominant relaxation process, then Goldman [37] argues that it is correct to replace T_{1e} in (2.21) with T_{2e}, giving

$$\frac{1}{T_{1n}} = 4(q^2)\frac{\omega_n^2 T_{2e}}{1+\omega_n^2 T_{2e}^2}.$$ (2.22)

Since $q^2 \propto 1/B_0^2$, this relaxation rate is dependent on the magnetic field. It is not, however, a mechanism for spin-lattice relaxation, as it serves only to couple the nuclear spins to the electron dipolar reservoir. Equation (2.22) does not consider the fact that two electrons involved in a T_2-type "flip-flop" process which then gives rise to a nuclear transition must differ in energy by the nuclear Larmor frequency in order for the total energy to be conserved. Wind [32] and Wenckebach [29] have suggested the following better estimate for this relaxation rate which explicitly accounts for energy conservation:

$$\frac{1}{T_{TM}} = 4|q|^2\frac{\omega_n^2 T_{2e}}{1+\omega_n^2 T_{2e}^2} \cdot \int_\infty^\infty \frac{g(\omega)g(\omega-\omega_n)}{g(0)}d\omega$$ (2.23)

Here, $g(\omega)$ is an EPR lineshape function.

In the context of the spin thermodynamic picture, this process couples the reservoir corresponding to the secular part of the dipolar interaction to that corresponding to the

Zeeman interaction of the nuclei. The rate of this heat transfer process is given by $1/T_{\text{TM}}$ in (2.23). The existence of this equilibrium implies that, if the dipolar interaction reservoir can be cooled, the nuclear reservoir will then also be cooled (and hence its polarization increased). Provotorov [48] has already defined the experimental conditions which can bring about a cooling of this reservoir. Under saturating microwave irradiation, there is an equilibrium between the electron Zeeman reservoir (in the rotating frame) and the dipolar reservoir, defined by the Provotorov equations,

$$\dot{\alpha} = -W(\alpha - \gamma) \tag{2.24}$$

$$\dot{\gamma} = -W\frac{\Delta}{\omega_L^2}(\gamma - \alpha),$$

where ω_L is the local resonance frequency, $W = \pi\omega_1^2 g(\Delta)$, $g(\Delta)$ is an electron lineshape function, and $\Delta = (\omega_e - \omega)$. Combining (2.24) and (2.23) results in a system of differential equations which governs the evolution of spin temperature in the coupled electron-electron-nuclear system. Neglecting spin-lattice relaxation, these are:

$$\dot{\alpha} = -W(\alpha - \gamma) \tag{2.25}$$

$$\dot{\beta} = -\frac{1}{T_{TM}}(\beta - \gamma)$$

$$\dot{\gamma} = -W\frac{\Delta}{\omega_L^2}(\gamma - \alpha) - \frac{C_n\omega_n^2}{\omega_L^2}\frac{1}{T_{TM}}(\gamma - \beta).$$

The physical interpretation of (2.25) is that off-resonance irradiation of the system can result in a cooling of the spin-spin interaction reservoir. This reservoir is then coupled to the nuclear Zeeman reservoir by an energy conserving three-spin process in which two

electrons differing in energy by $\hbar\omega_n$ "flip-flop" and bring about a nuclear transition. The net result is dynamic nuclear polarization.

The dependence of the DNP enhancement on the electron resonance offset is diagnostic of the thermal mixing DNP mechanism. In particular, since irradiation is required only at the frequency of allowed transitions, the position of maximum DNP enhancement should occur within the EPR lineshape; in the solid effect, by contrast, maximum enhancement should be obtained for resonant radiation of either the zero quantum or double quantum forbidden transitions, which occur at $(\omega_S \pm \omega_I)$. Figure 2-3 is an example of the field dependence of the thermal mixing DNP enhancement in a nitroxide-doped system at 250 GHz.
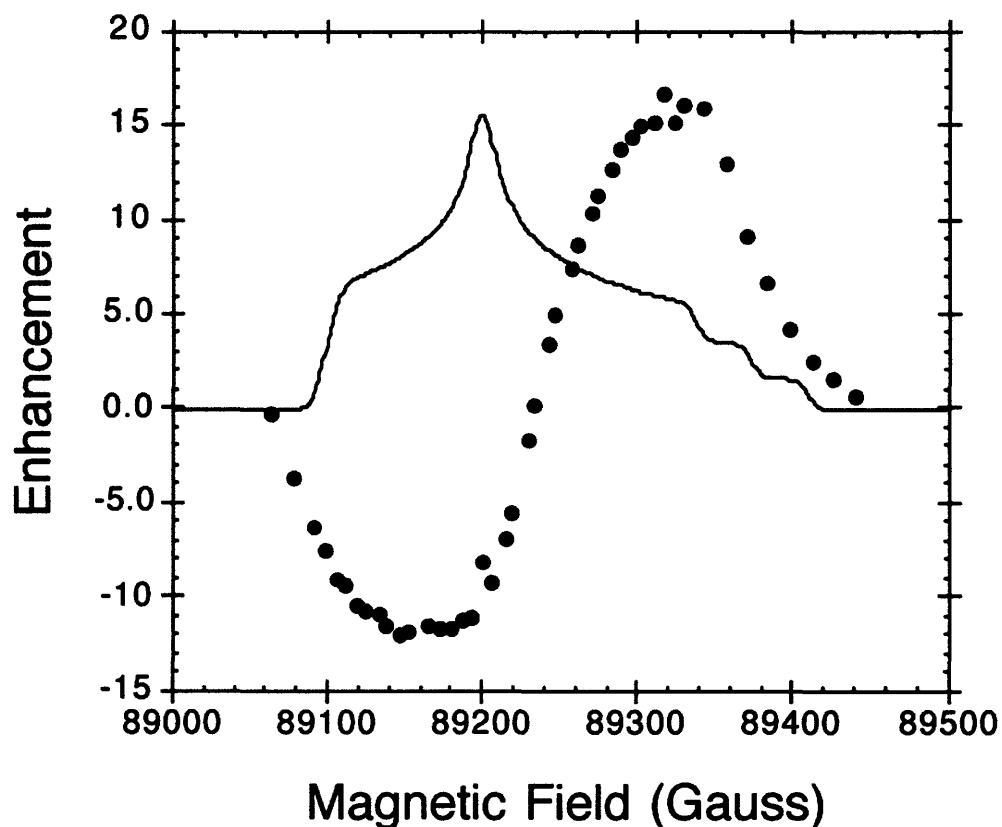
Figure 2-3. Magnetic field dependence of the thermal mixing DNP enhancement at 250 GHz in a static sample of [U-^{13}C]-glycine at 90 K, doped with 60 mM TEMPO. Adapted from [49].

2.2.4   Thermal Mixing at High Magnetic Fields

At high magnetic fields, the EPR lineshape in most organic radicals is dominated by the g-anisotropy; as such, the line broadening is inhomogeneous in nature, and Provotorov's treatment does not directly apply. Strong microwave irradiation in such systems will tend to produce non-uniform excitation of a single spin packet which is resonant with the microwave field ("hole burning") rather than uniform excitation. Nevertheless, signal enhancements of up to two orders of magnitude are still possible through a thermal mixing-like DNP mechanism at frequencies of up to 250 GHz [49]. As mentioned previously, Borghini [30], Atsarkin [47], and Abragam and Goldman [35] have suggested that fast electron-electron spectral diffusion can render the EPR line effectively homogeneous on the time scale of the relaxation processes which are responsible for DNP. However, it is unclear if these arguments apply at very high magnetic fields or in the moderate temperature regime, where spin-lattice relaxation is fast.

In order to investigate the role of spectral diffusion in DNP using inhomogeneously broadened radicals as the polarization source, Farrar and co-workers performed an electron-electron double resonance (ELDOR) experiment using a high-power 140 GHz gyrotron oscillator as a pump source and a pulsed, 139.50 GHz Gunn diode to generate the probe [46]. The results of these experiments (cf. Fig. 2-4) illustrate that cross-relaxation is significant at the radical concentrations which are required for high-field DNP experiments. By contrast, no cross relaxation is observed at radical concentrations which do not yield a DNP enhancement.
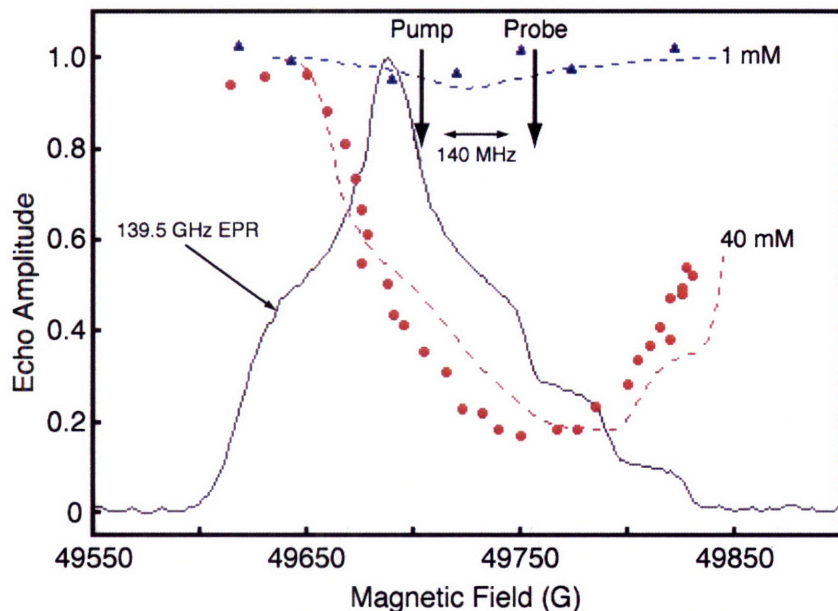
Figure 2-4. Results of 140 GHz ELDOR experiments for 1 mM (blue line) and 40 mM (red line) solutions of 4-amino-TEMPO in an aqueous medium, superimposed upon echo-detected EPR spectrum of the nitroxide radical. Note that electron-electron cross relaxation processes are significant at high radical concentrations. Adapted from [46].

These results suggest a phenomenological kinetic model for thermal mixing DNP at high magnetic fields, which is illustrated in Figure 2-5. Its principal feature is that the thermodynamic system corresponding to the electron Zeeman interaction is divided into a series of subsystems, each of which has a distinct spin temperature. These thermodynamic subsystems are in equilibrium through a distinct spectral diffusion or cross-relaxation process. Since there is no basis *a priori* to set the number of subsystems, this is an additional adjustable parameter of the model. As well, the "bin-to-bin" relaxation rate must be determined in a separate ELDOR experiment. In cases where these parameters of the model can be measured or estimated with good certainty, the DNP enhancement at high magnetic fields can be effectively simulated [50]. Since there is currently no theory to adequately account for the many parameters on which the model depends, it is less useful for the design of experiments or novel polarizing agents.

Nevertheless, the model provides insight into the dynamics of thermal mixing DNP, and it justifies the experimental conclusion that manipulation of radical concentration and sample temperature can result in large enhancements at high magnetic fields.
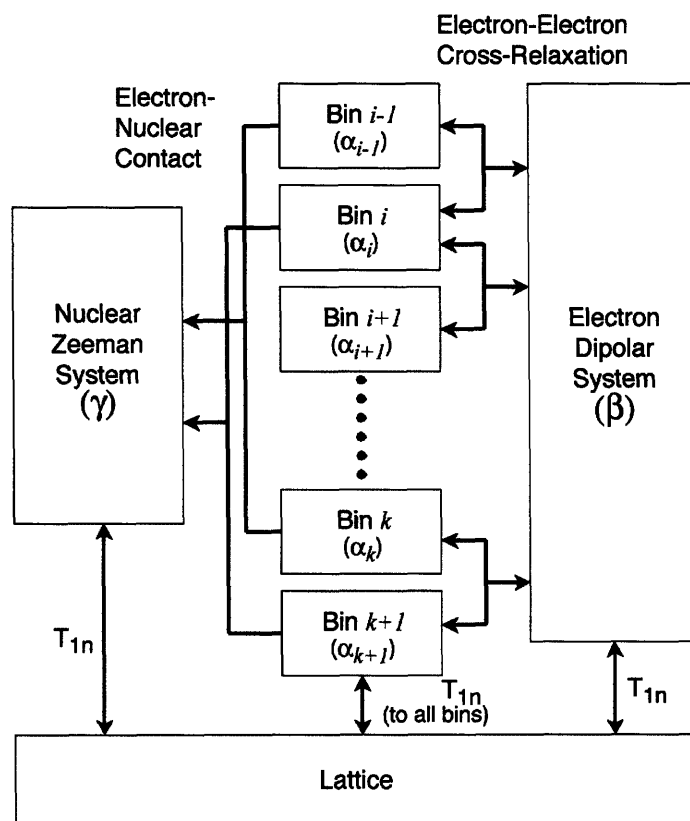
Figure 2-5. Phenomenological model of thermal mixing DNP at high magnetic fields. The dipolar interaction reservoir has been subdivided into a series of reservoirs, each having a unique spin temperature; fast electron cross-relaxation renders the dipolar system homogeneous on the time-scale of relaxation processes which give rise to dynamic nuclear polarization. Adapted from [46].

2.2.5 Cross Effect DNP[130]

Of the four commonly discussed DNP mechanisms–the Overhauser effect (OE), the solid effect (SE), the cross effect (CE), and thermal mixing (TM) [131, 132] – only the cross-effect and thermal mixing have proven useful for applications in high magnetic fields. The CE and TM are differentiated by whether or not the width of the EPR spectrum is governed by inhomogeneous broadening from the g-anisotropy and electronic cross

relaxation or by homogeneous broadening from the electron-electron dipolar coupling, respectively. As is clear from the preceding discussion, however, the basis for CE DNP effects in not adequately treated by approaches based on spin thermodynamics. Quantum mechanical approaches to the three-spin problem based on perturbation theory have been developed by Hu and co-workers [133] and will not be discussed. Our intention here is to summarize recent experimental evidence for aspects of the cross-effect DNP mechanism in mixtures of TEMPO and TRITYL radicals [130].

Both the CE and TM mechanisms rely on a three-spin electron–electron–nucleus process. Briefly, the microwave radiation flips an electron at ω_{1e} in the EPR spectrum that is coupled to a second electron at ω_{2e}. If the frequency separation satisfies the condition $|\omega_{2e} - \omega_{1e}| = \omega_n$ then a nuclear spin flip occurs concurrently, and the polarization of the nuclear spin reservoir is enhanced. Not surprisingly, the primary parameters that facilitate this three-spin process are the magnitude of the electron–electron dipolar coupling and the population of the electrons in the sample that satisfy the constraint $|\omega_{2e} - \omega_{1e}| = \omega_n$. To satisfy the first requirement, Hu and co-workers recently introduced biradical polarizing agents [134, 135] in which they tethered two TEMPO molecules with a chain of carbon atoms increasing the electron-electron dipolar coupling from ~1 MHz to 25 MHz [134]. In order to satisfy the frequency matching condition, they rely on the fraction of molecules in the sample that have correct relative orientation of the two TEMPO moieties that fortuitously leads to the correct g-tensor orientations. These biradicals exhibit improved DNP efficiency, the enhancement factors are a factor of 3-4 larger than observed with TEMPO (165 as opposed to 45), and they yield this

enhancement at an electron concentration (~10 mM) that is a factor of four lower than commonly used for TEMPO (40 mM).

There is another approach to satisfying the frequency matching condition mentioned above. It follows from the discussion above that the ideal polarizing agent for CE DNP experiments consists of two radicals with isotropic g-values separated by $|\omega_{e1} - \omega_{e2}| = \omega_n$. At the moment we are not aware of two radicals that rigorously satisfy this condition, but using a narrow line radical such as trityl or BDPA together with TEMPO is a reasonable approximation. In the case discussed here, the pseudo-isotropic line from trityl (Figure 2-6) is separated by 225 MHz (~80 Gauss) from the g_{yy} component of the TEMPO powder pattern that contains the maximal spectral intensity. This closely matches the ^1H Larmor frequency of 211 MHz and therefore the mixture serves as an excellent polarizing agent. Note that this separation will scale with ω_n and thus will also function at higher magnetic fields. Thus, this is a new avenue for designing better polarizing agents for high-field DNP.

(a)   **(b)**
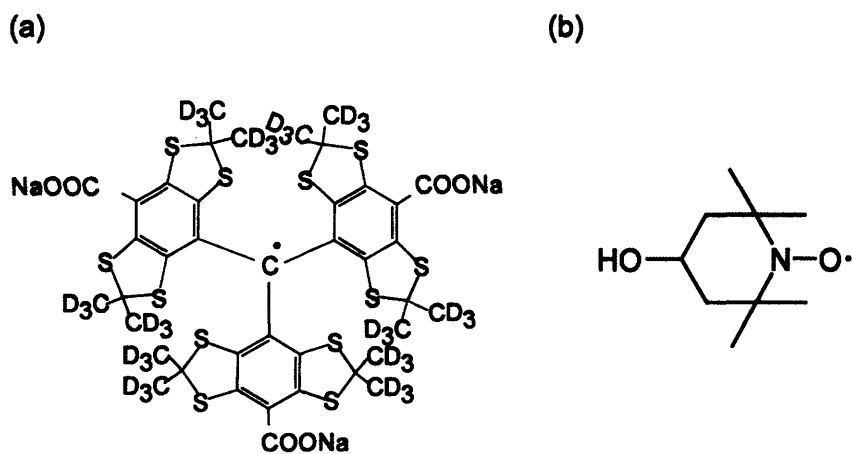
Figure 2-6. Molecular structures of (a) the trityl radical (molecular weight = 1080), which has principle g-values of g_{xx} = 2.0034, g_{yy} = 2.0031, and g_{zz} = 2.0027 [136], and (b) the 4-hydroxy-TEMPO radical (molecular weight = 172), which has principal g-values of g_{xx} = 2.0090, g_{yy} = 2.0061, and g_{zz} = 2.0021, and principal hyperfine A-values (^{14}N) of A_{xx} = 6.63 G, A_{yy} = 6.75 G, and A_{zz} = 36.63 G [137].

The upper traces of Figure 2-7 show the echo-detected EPR spectra (normalized) of 1 mM trityl, 1 mM TEMPO and a mixture of 0.5 mM trityl and 0.5 mM TEMPO in frozen $^2H_6$-DMSO/^2H_2O 60:40 w/w solutions. The EPR spectra corresponding to the frequency of the gyrotron (139.66 GHz) was obtained from shifting the recorded spectra (at 139.50 GHz) along the field axis by 57 G (160 MHz). The EPR spectrum of trityl had a peak at 49815 G and a line width (δ) of 15 G (42 MHz), reflecting the small axial asymmetry of the g-anisotropy at the radical center. Note the fact that the spectrum is not axially symmetric indicates that there is less than threefold symmetry at the central carbon. In contrast, TEMPO yielded a broad EPR line shape resulting from both g-anisotropy and anisotropic hyperfine interaction with the ^{14}N (I = 1) nucleus. The EPR spectrum, corresponding to 139.66 GHz irradiation, has a maximum at 49735 G, spanning 220 G (or 616 MHz) and featured three hyperfine steps on the high-field edge.

The lower panels of Figure 2-7 show the field-dependent ^1H enhancement profiles with 40 mM trityl radical, 40 mM TEMPO radical, and a 40 mM mixture of 50:50 trityl/TEMPO, respectively. Trityl, with δ (27 MHz) < ω_n (211 MHz for ^1H), leads to a SE polarization mechanism and well-resolved maxima and minima in the ^{13}C detected ^1H enhancements at 49891 and 49740 G, respectively. These field positions were ±75 G (or ±212 MHz, the ^1H Larmor frequency) from the EPR peak. The maximum ^1H enhancement from trityl was ~15, which is relatively small and consistent with the ω_n^{-2} dependence of the SE enhancement. In contrast TEMPO has $\delta > \omega_n$ and this leads to the TM mechanism dominating the polarization process with maximum positive and negative ^1H enhancements at 49798 and 49683 G, or ±161 MHz rather than $\omega_e \pm \omega_n$. As can be

seen from the figure the maximum ^{1}H enhancement from TEMPO was ~55, almost fourfold higher than that with trityl.

As expected, the ^{1}H enhancement profile changed drastically when half of the 40 mM TEMPO radicals were replaced by trityl. This sample yielded an even larger enhancement of ~162, which is threefold higher than with pure TEMPO. The positive enhancement peak was located at 49815 G, corresponding to the EPR peak of trityl. A smaller negative enhancement peak was found at 49740 G, corresponding to the EPR peak of TEMPO. The displacement of 76 G between the positive and negative enhancement peaks matched the ^{1}H Larmor frequency and is consistent with the CE mechanism. The field-dependent enhancement profiles for the SE and TM were simulated based on published theory [131, 138].
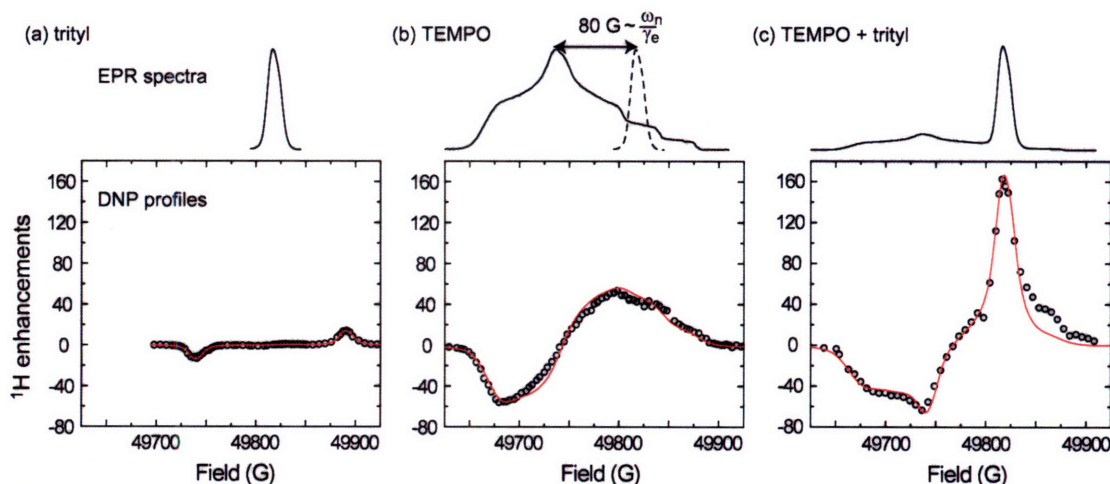
Figure 2-7. The pulse-echo-detected EPR spectra (upper traces) and proton DNP enhancement profiles (lower panels) at 139.66 GHz measured from (a) trityl (b) TEMPO and (c) TEMPO and trityl mixture (50:50). The EPR spectra represented a total radical concentration of 1 mM in frozen ^{2}H$_6$-DMSO/^{2}H$_2$O 60:40 w/w solutions at 20 K, whereas the DNP profiles were obtained from a total radical concentration of 40 mM in frozen ^{2}H$_6$-DMSO/^{2}H$_2$O/H$_2$O 60:34:6 w/w/w solutions at 90 K. The enhancement profiles are characteristic of the SE, TM, and CE mechanisms with paramagnetic species of trityl, TEMPO, and the mixture, respectively. The red line is a simulation of the experimental data.

Figure 2-8 illustrates the growth of the ^{13}C detected enhanced ^{1}H polarization during microwave irradiation at the optimal magnetic field (49815 G). The NMR signal

intensity grows exponentially with a time constant, $\tau_{DNP} \sim 5$ s and a steady-state ^1H signal enhancement, $\varepsilon = 162 \pm 20$. The random error arises from the low sensitivity of measurements conducted without DNP, which are required to calculate the DNP enhancement.
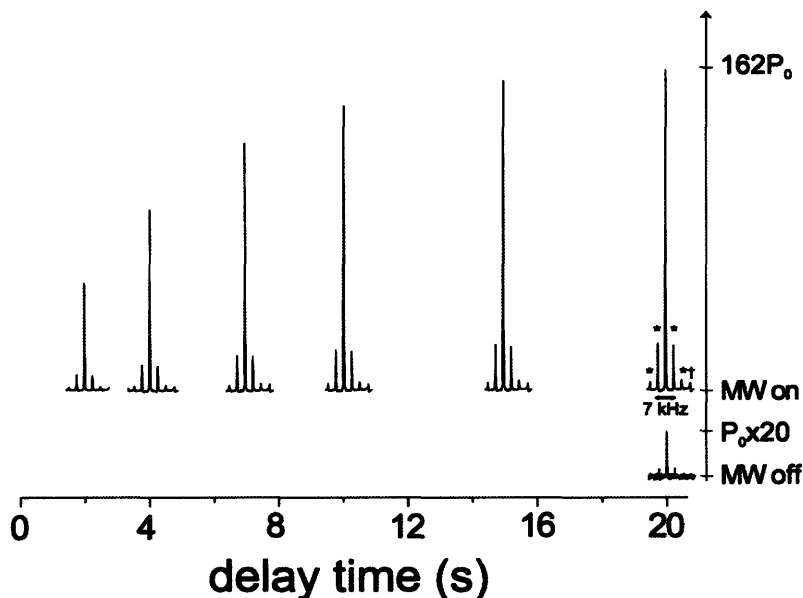
Figure 2-8. DNP–CPMAS ^{13}C-NMR signals of ^{13}C-urea with 40 mM 50:50 TEMPO/trityl mixtures with increasing length of microwave irradiation (139.66 GHz, ~1 W) at 49815 G. The asterisks indicate the spinning sidebands and the dagger marks the solvent peak. The growth of nuclear polarization is characterized by a time constant of ~5 s and a steady state ^1H enhancement of 162 ± 20.

Figure 2-9 illustrates the influence of the total electron concentration ([TEMPO] + [trityl]) on the DNP enhancement with 50:50 TEMPO/trityl mixtures at the magnetic field corresponding to the maximum enhancement. Not unexpectedly, the size of ε increases with the radical concentration, while the value of τ_{DNP} decreases. Beyond ~40 mM of radicals, the resulting paramagnetic broadening begins to eliminate a substantial number of the nuclei from observation, as evidenced by the attenuation of unenhanced NMR signals.
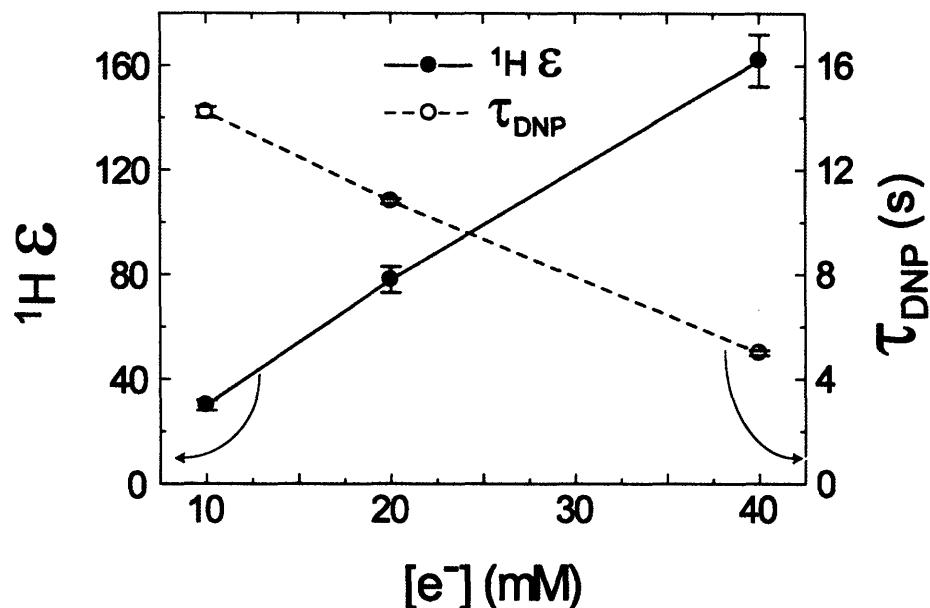
Figure 2-9. Radical concentration dependence of the measured proton enhancement (^{1}H ε) and buildup time constant (τ_{DNP}) from the 50:50 TEMPO/trityl mixture at 49815 G and 90 K.

The polarization mechanisms that dominate DNP processes in insulating solids—the SE, TM, or the CE–depends on the EPR line width of the paramagnetic species relative to the Larmor frequency of the nuclei being polarized. This behavior is well established in many previous experiments [131, 132, 139] and is illustrated again in Figure 2-7. In general, the SE dominates when $\delta < \omega_n$ (e.g., with trityl) and in samples where the EPR spectral width $\delta > \omega_n$ (TEMPO, biradicals and TEMPO/trityl mixtures) the TM and CE provide the polarization mechanism. The TM and CE mechanisms are further distinguished by whether the EPR spectrum is broadened by homogeneous or inhomogeneous interactions, respectively. The polarizing mechanism with TEMPO is thought to be TM or the CE depending on the radical concentration used. Although TEMPO presents an inhomogeneously broadened EPR spectrum at high fields, the electron dipolar bath for TM can be established via electron–electron cross-relaxation at high radical concentrations used in DNP experiments [30]. In contrast, low TEMPO

concentrations should limit the polarizing mechanism to the CE. For both the CE and TM, the required EPR frequency separation $|\omega_{2e} - \omega_{1e}| = \omega_n$ is satisfied when the g-tensor orientations of two dipolar coupled molecules in the sample randomly have the correct mutual orientations.

Our [139-141] and other [131] experiments have demonstrated that in high magnetic fields (>5T) the TM and CE mechanisms are more efficient than the SE and that the two class of mechanisms scale approximately as ω_0^{-1} and ω_0^{-2}, respectively. They also depend on the available microwave power and the electronic and nuclear relaxation times; consequently, high field DNP experiments employ high microwave powers available from gyrotron sources and are conducted at cryogenic temperatures, where the relaxation times are longer.. In principle, EPR frequency separations can be manipulated by controlling the orientations and principal values of the g-tensors of the dipolar coupled electrons. While the control of orientations is straightforward in single crystal systems, it is impossible to control orientation in powder samples where the relative orientation of g-tensors is a function of crystallite orientation. However, using mixtures of two radicals with maxima in their EPR spectra that correspond to the correct frequency separation is another approach to satisfying the CE matching condition. Thus, mixtures of TEMPO and trityl yield large improvements in the DNP ε since the desired g-value difference is achieved by the fact that one radical species with a small g-anisotropy and therefore a sharp EPR line is separated from the g_{yy} maxima in the TEMPO powder spectrum by the proper frequency.

The increase in ε with increasing concentration of TEMPO/trityl mixtures shown in Figure 2-9 illustrates the other requirement for an efficient three-spin process; in

particular, the average electron-electron dipole interaction needs to be strong for efficient DNP and it is reduced by the larger inter-radical distance that accompanies dilution. In the contrasting regime – at a higher radical concentration – the electron-nuclear paramagnetic broadening will not only reduce the resolution of NMR spectra, but will also diminish the number of observable nuclear spins, and therefore decrease the overall signal intensity. The electron–electron interactions at a low radical concentration could be optimized by chemically linking TEMPO and trityl radicals. The use of molecular linkers has proven successful for increasing the CE enhancement with two tethered TEMPO moieties from ~50 to ~165-290 depending on the experimental circumstances [134, 135]. Therefore, additional improvement of the DNP enhancement beyond the current maximum value of 162 observed with trityl-TEMPO mixtures is expected when these two species are successfully coupled.

The ideal polarizing agent for the CE consists of two dipolar-coupled electrons with narrow EPR spectra separated by ω_n. The CE from a broad inhomogeneous EPR spectrum may be attenuated by cancellation between electron pairs with EPR frequency separations of ω_n and $-\omega_n$, similar to the attenuation that occurs in the differential solid effect [142]. This differential effect limits the average DNP enhancement produced by participating electrons. In addition, because the microwave irradiation occurs at a fixed frequency and has a finite bandwidth, only a portion of the electrons under the broad EPR line shape participate in the CE process; the remainder contribute to paramagnetic nuclear relaxation and broadening. Combining TEMPO and trityl as the polarizing agent partially resolves the problems with differential CE enhancements and with non-participating radicals. Despite the broad EPR spectrum of TEMPO, the trityl resonance in the up field

part of the EPR spectrum of TEMPO caused the electron pairs to yield positive CE enhancements. Moreover, the narrow EPR line width of trityl increases the effectiveness of the microwave excitation at the trityl EPR transitions.

The choice of radical pairs that provide the desired EPR frequency separation for the CE is not limited to TEMPO and trityl, especially when a nuclear Larmor frequency different from ^{1}H is involved. For example, a hyperfine splitting (^{13}C, ^{15}N, ^{14}N, etc) could result in two narrow lines and the external magnetic field could be adjusted to match a nuclear Larmor frequency to this separation. However, hyperfine splittings are field independent so polarizing agents designed in this manner would be specific to a particular field and nucleus. In contrast, matching the nuclear Larmor frequency through g-value differences is independent of the external magnetic field and presents the possibility of an efficient, universal polarizing agent.

2.2.6   Spin Diffusion in Paramagnetically Doped Solids

Regardless of the DNP mechanism in question, our tacit assumption has been that the enhanced nuclear polarization is uniformly distributed throughout the sample. Were this not the case, the technique would be of limited utility for biomolecular NMR spectroscopy, as the polarizing agent is not expected to reach the hydrophobic core of a protein in the same concentration as exists in the bulk solvent. The spin diffusion mechanism is principally responsible for this transport of enhanced magnetization.

In organic solids, the protons form a homogeneously coupled network due to their high abundance and strong dipolar couplings, which are not significantly averaged at currently accessible MAS rates. In the context of a spin thermodynamic picture, this implies that the protons have a homogeneous polarization at long time scales. Local

perturbations in the proton polarization therefore propagate to the bulk with a characteristic time constant, a situation which is reminiscent of fluid-dynamical diffusion. Experimental evidence to support these ideas arose from the study of solids doped with fixed paramagnetic centers. As previously discussed, in these systems, the hyperfine interaction term $S_z I_+$ serves to couple electronic and nuclear spin-lattice relaxation; electronic spin-lattice relaxation causes fluctuations in S_z, which in turn brings about nuclear transitions. Since the dipolar interaction depends strongly on the distance between interacting centers, it is reasonable to assume that protons closest to the radical will relax very quickly, and those very far away from it will hardly feel its influence. However, this contradicts the experimental observation that even an exceedingly low concentration of paramagnetic spins can change the relaxation properties of all nuclei in the sample;[5] further, spin-lattice relaxation for all protons in such a sample is still characterized by monoexponential decay, albeit at a greatly accelerated rate in the presence of the impurities than in their absence.

In order to explain this, Bloembergen [51] proposed that proton magnetization, p, in such a solid obeys a diffusion equation,

$$\frac{\partial p}{\partial t} = D\nabla^2 p - C\sum_n \frac{1}{|r - r_n|^6}(p - p_0), \tag{2.26}$$

in which D is the diffusion constant, C is a term which arises from a correlation integral governing transitions caused by the $S_z I_+$ term of the dipolar coupling, $|r - r_n|$ is the distance between the nth nucleus and the paramagnetic center, and the sum is over all nuclei.[6] In the context of dynamic nuclear polarization, (2.26) implies that, even if only

---

[5] This applies particularly to abundant, tightly coupled nuclei such as ^{1}H.
[6] The equation is, of course, valid only for length scales on the order of several lattice spacings.

the nuclei which are close to a radical center are polarized, their polarization will rapidly diffuse to the bulk nuclei which are not coupled to the radical center.

According to this theory, there should also be a region close to the paramagnetic center in which no spin diffusion can take place. This "diffusion barrier" exists for those nuclei whose hyperfine coupling to an electron generates a resonance frequency shift which is large enough to remove them from the continuum of coupled nuclei in the bulk.[7] Though the idea of the diffusion barrier is reasonable even on quantum mechanical grounds, the experimental evidence for its existence is contradictory. Goldman [52] and other authors have obtained results which are clearly consistent with its existence, but King and co-workers [53] were able to demonstrate by direct observation that even nuclei which are very near to a paramagnetic center participate in spin diffusion processes with the bulk. Further, Jeschke *et al.* [45][54] and Weis and co-workers [42] (*vide infra*) suggest that strong hyperfine decoupling might exist in electron-nuclear spin systems which are irradiated in the vicinity of certain matching conditions. In the context of DNP applications, the existence of a spin diffusion barrier implies that some (abundant) proton spins will be removed from the spin diffusion network, and that some (dilute) spins of interest might not be observed in cross polarization experiments.

---

[7] This diffusion barrier can only exist if electronic spin lattice relaxation is slow.
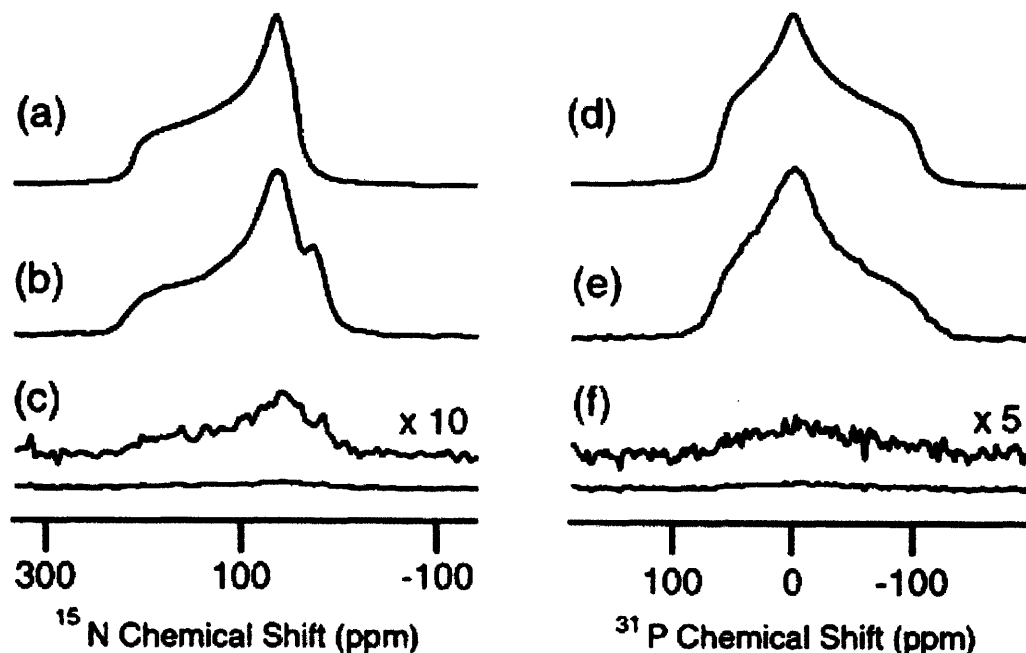
Figure 2-10: Calculated (a,d) and experimental (b,c and e,f) ^{15}N and ^{31}P powder spectra of *fd*-bacteriophage. Spectra in (b) and (e) are DNP-enhanced, while those in (c) and (f) were recorded without microwave irradiation; both were recorded with ^{1}H-^{13}C cross polarization. A signal enhancement of ~26 was observed in both cases, indicating that enhancements in the interior and exterior of the phage particle are identical. Parameters of the simulation and experiment are described in [55].

In practice, DNP experiments in biological systems are conducted with stable, soluble radicals that do not penetrate the hydrophobic core of a protein in appreciable concentrations. Spin diffusion from polarized nuclei to the bulk protons is therefore necessary for the success of these experiments, while the size or existence of a diffusion barrier is less material to their success. In order to test if spin diffusion continues to be effective in inhomogeneously broadened systems at high magnetic fields, Rosay and co-workers [55] designed an elegant experiment in an intact particle of *fd*-bacteriophage. Bacteriophage consists of a ^{15}N-containing protein capsid which surrounds a ^{31}P-rich nucleic acid core. The local proton magnetization inside and outside the core can therefore be detected indirectly through cross polarization from protons to ^{31}P and ^{15}N

respectively.[8] The result of such an experiment in a static sample of *fd*-bacteriophage is shown in Figure 2-10. The fact that proton enhancements detected inside and outside the particle are identical strongly suggests that spin diffusion continues to be effective in this system, although it is possible that the polarizing agent itself may have penetrated the viral core. In subsequent DNP experiments conducted with magic angle spinning in the soluble protein α-lytic protease and the membrane protein bacteriorhodopsin, resonances which can be unambiguously assigned to the interior of the protein are polarized to the same extent as those which are exposed to solvent.

No theory yet exists which adequately incorporates spin diffusion with DNP experiments at high magnetic fields. Using a theory which is strictly applicable only at low magnetic fields, Wind and co-workers have estimated the maximum enhancements that can result from the thermal mixing and solid effect DNP mechanisms [33]. These estimates are valid only under the assumption of a homogeneous EPR line shape characterized by a single line width, δ, and in the limit of fast proton spin diffusion. For the solid effect, the maximum enhancement is governed by

$$\varepsilon_{SE} \propto \frac{N_e T_{1n}}{b^3 \delta} \left(\frac{B_1}{B_0} \right)^2,$$

(2.27)

and, for thermal mixing,

$$\varepsilon_{TM} \propto \frac{N_e^2 T_{1e} T_{1n}}{b^3 \delta^2} \left(\frac{B_1^2}{B_0} \right),$$

(2.28)

where b is the radius of the spin diffusion barrier, N_e is the radical concentration, and all other parameters have been previously defined. Since these formulae depend on

---

[8] Nuclear cross polarization can be explained by quantum mechanical models in which only strongly coupled protons

parameters which cannot currently be measured at high magnetic fields, their complete validity is difficult to assess. However, the idea that solid effect enhancements scale more poorly with increasing magnetic field than those originating from a thermal mixing mechanism appears to be in qualitative agreement with experiment.

2.2.7   Thermal Mixing DNP with Magic Angle Spinning

The combination of thermal mixing DNP and magic angle spinning is so far the most promising method for signal enhancement in high resolution, multidimensional spectroscopy of biological systems. Its unique experimental requirements – both in the area of microwave radiation sources and cryogenic MAS equipment – are discussed in the second section of this review.

While MAS yields high-resolution spectra through averaging of anisotropic interactions such as the dipolar interaction, it does not appear to significantly disturb those interactions which are responsible for DNP; at the same time, paramagnetic line broadening is greatly reduced even at moderate MAS rates, with the advantage that high radical concentrations can be used. In glassy preparations of small molecules doped with the nitroxide radical 4-amino-TEMPO in concentrations of 40 – 60 mM, the predominant source of line broadening during MAS is inhomogeneous and arises from the conformational heterogeneity of the small molecule [58][49]. Though this form of inhomogeneous broadening cannot be eliminated for small molecules in glassy matrices, it has not been observed for adequately cryoprotected proteins at low temperatures [59]. Thermal mixing DNP is therefore a very general approach that should be effective in a

---

enter the spin dynamics and distant protons are not involved [56][57].

wide variety of systems with optimization of the polarizing agent and cryoprotection
conditions.
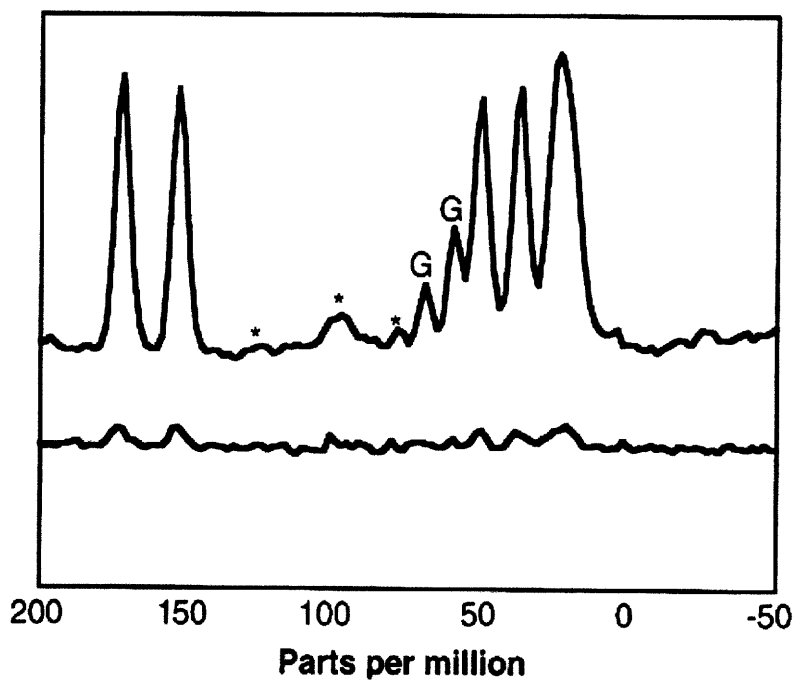
Figure 2-11: DNP-enhanced MAS spectrum of arginine doped with 40 mM 4-amino-TEMPO, taken at 55 K. The microwave source was a 140 GHz gyrotron oscillator developed at MIT. Adapted from [60].

At 140 GHz, using the thermal mixing DNP mechanism, Hall and co-workers have

obtained large DNP enhancements (Fig. 2-11) in small molecules during magic angle

spinning at the temperatures of liquid helium [60]. For experiments lasting longer than a

few hours, however, stable magic angle spinning cannot currently be maintained using

helium as the cooling source. Following the work of Rosay and co-workers [58][61],

thermal mixing DNP is now conducted with cooled nitrogen gas at temperatures in the

range 80 – 100 K, which results in stable experimental conditions at the expense of

smaller signal enhancements. In 1D MAS experiments conducted at ~90 K using a 140

GHz gyrotron oscillator as the microwave source and the thermal mixing DNP

mechanism, Rosay and co-workers have reported signal enhancements as large as 60

[58]. In MAS experiments of higher dimensionality, however, operating limitations of the 140 GHz gyrotron and cryogenic equipment have limited the enhancement to approximately 9–10 [61].

Quantitative MAS experiments which incorporate dipolar recoupling for the measurement or correlation of anisotropic interactions require reference stability of the DNP experiment of several percent at worst. Using a 250 GHz gyrotron-based DNP system designed for thermal mixing DNP experiments, we have recently demonstrated stable integration of DNP into magic angle spinning experiments where the variables of the experiment are controlled to high tolerances. In particular, Figure 2-12 illustrates the successful application of DNP for sensitivity enhancement in 2D correlation spectroscopy of the amino acid proline. Here, correlations were established both by proton-proton spin diffusion and by the dipolar recoupling sequence SPC5 [62]. The latter incorporates a double quantum coherence-selective phase cycle and therefore imposes strict demands of instrumental stability. In both cases, enhancements of 17–19 were obtained [49], and the result demonstrates the general applicability of this technique. Recent improvements in microwave delivery to the sample and in new polarizing agents have resulted in enhancements of ~40.
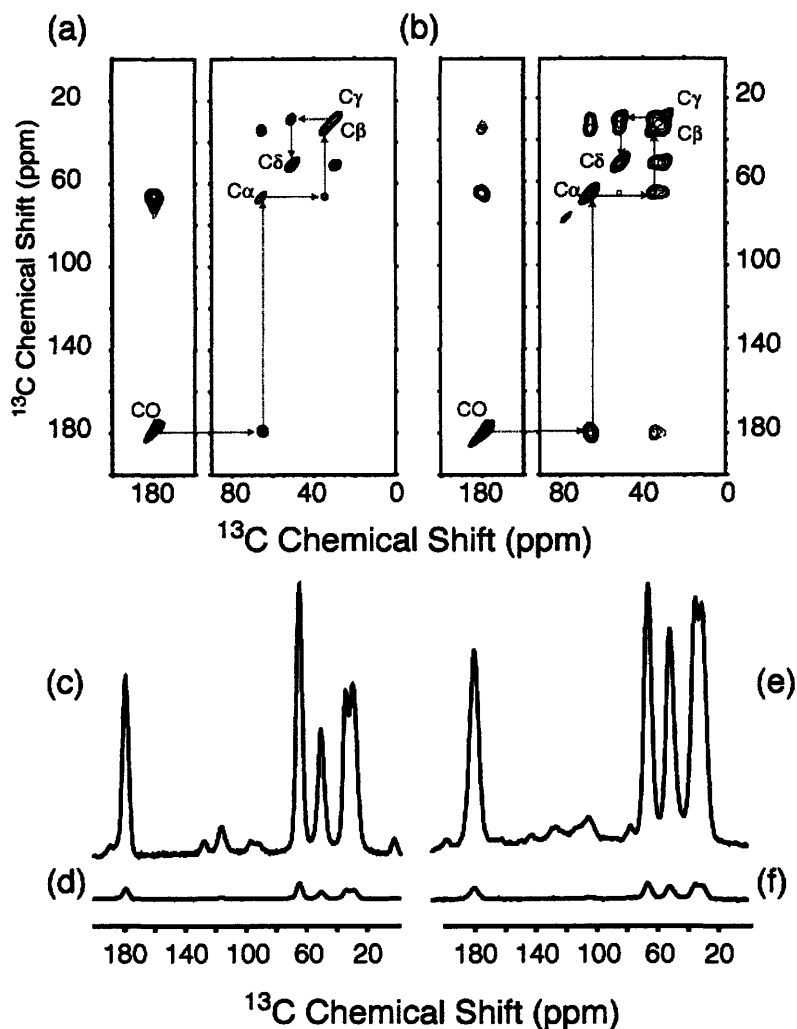
Figure 2-12: Two-dimensional ^{13}C-^{13}C correlation spectra of [U-^{13}C, ^{15}N]-proline. In (a), the SPC5 dipolar recoupling sequence was applied during a 1.33 ms mixing period. In (b), correlations were established by proton-driven spin diffusion for a mixing time of 10 ms. The DNP enhancement is approximately 17. In (c) and (d), we show one-dimensional ^{13}C MAS spectra obtained respectively with and without DNP, using SPC5 recoupling with a phase cycle that is selective for double-quantum coherence. Spectra in (e) and (f) are recorded with and without DNP respectively. Adapted from [49].

2.2.8 Rotating Frame DNP Methods

The exclusive use of laboratory frame mixing sequences for DNP experiments at high magnetic field imposes several experimental difficulties. First, since the polarization transfer process is slow, the experiment must be conducted at low temperatures in order to attenuate nuclear spin-lattice relaxation, which would otherwise compromise the

polarization transfer efficiency. Second, since these polarization transfer schemes rely on non-secular elements of the hyperfine Hamiltonian, we can expect that their efficiency will continue to decline at high magnetic fields.

In analogy to successful approaches for polarization transfer between high and low gyromagnetic nuclei in solids, several authors have attempted to apply analogs of Hartmann-Hahn double resonance to the problem of electron-nuclear polarization transfer. It is possible to conduct an ordinary DNP experiment in the presence of a strong nuclear spin lock, in which case the experiment is called "rotating frame DNP" [63][46], but still involves forbidden transitions. Next, Fritsch and co-workers [40] along with Henstra [41] have introduced experiments in the context of polarization transfer from photoexcited triplet spins in which DNP occurs by irradiation of allowed EPR transitions only, although the polarization transfer is still mediated by matrix elements which do not scale with the magnetic field. Finally, Weis and co-workers [42] have presented a DNP experiment requiring simultaneous off-resonance microwave and nuclear radiation satisfying a matching condition in an electron dressed state; these experiments can also be interpreted in analogy to experiments for chemical-shift selective polarization transfer between nuclei in solids [64][65][66]. They do not depend on anisotropic elements of the hyperfine Hamiltonian and therefore should be applicable at arbitrary magnetic fields with the appropriate instrumentation.

2.2.9 DNP in the Nuclear Rotating Frame

Both the thermal mixing DNP mechanism and the solid effect operate in the presence of a nuclear spin lock field; in this case, the enhanced nuclear polarization evolves along the quantization axis defined by the spin lock rather than I_z, and the thermal contact is said to

occur in the nuclear rotating frame [63]. This experiment originally arose from NMR studies of coal, in which cross-polarization dynamics tend to distort the ^{13}C line shapes due to a large distribution in $T_{1\rho}$ for different sites. Wind *et al.* realized that this distortion could be avoided if the natural paramagnetic impurities in coal were used as the ultimate polarization source in a nuclear rotating frame DNP experiment [63].

The nuclear rotating frame DNP (NRF DNP) experiment can be analyzed as an analog of the solid effect or thermal mixing. The degree of eigenstate mixing in a coupled electron-nuclear spin system in the nuclear laboratory frame [as in (2.13)] is proportional to a mixing coefficient,

$$q_{lab} = -\frac{3}{4}\frac{\gamma_e\gamma_n\hbar}{\omega_n^{lab}}\frac{1}{r^3}\sin\theta\cos\theta e^{-i\theta}, \qquad (2.29)$$

and, in the nuclear rotating frame, to

$$q_{NRF} = \frac{1}{4}\frac{\gamma_e\gamma_n\hbar}{\omega_n^{rot}}\frac{1}{r^3}\left(1-3\cos^2\theta\right). \qquad (2.30)$$

Since $\omega_n^{lab} >> \omega_n^{rot}$, the transition probability for forbidden transitions in the nuclear rotating frame will be greater than that in the laboratory frame; it should also depend far less on the magnetic field. Further, the kinetics of polarization build-up will be governed by the nuclear $T_{1\rho}$ rather than the T_1, and so the experiment can be recycled very quickly, resulting in a larger signal enhancement per unit time.

In order to explore potential applications of this technique at high magnetic fields, Farrar and co-workers [46] performed NRF DNP experiments at a magnetic field of 5 T. Here, the polarization source was the symmetric trityl radical, and microwave power was delivered by a Gunn diode without any kind of resonant structure, resulting in

approximately $1 - 5$ mW of power at the sample. Though an enhancement of 0.89 (*i.e.* less than unity) was obtained, the time-averaged enhancement,

$$\varepsilon = \frac{S_{on}}{S_{off}} \sqrt{\frac{T_{1\rho}^n}{T_1^n}} \tag{2.31}$$

with $T_{1\rho}^n = 27$ ms and T_1^n of several minutes at a temperature of 11 K, was ~197. In spite of this apparently large enhancement, the NRF DNP experiment has so far not been employed in high field DNP applications. This is mainly because it is impractical to recycle the experiment at a rate governed by $T_{1\rho}$ due to probe heating and other factors. Nevertheless, NRF DNP might have advantages over thermal mixing at extremely high magnetic fields.

2.2.10 Nuclear Orientation via Electron Spin Locking: Polarization Transfer from the Photoexcited Triplet State

In the context of studies of the polarization transfer process between photoexcited triplet states and nuclei, Fritsch *et al.* [40] and Henstra *et al.* [41] independently proposed an experiment based on Hartmann-Hahn transfer between electrons in the rotating frame and nuclei in the laboratory frame. The experiment has been called nuclear orientation via electron spin locking ("NOVEL") by the latter authors. Though the polarization transfer is necessarily fast, the experiment is not directly applicable at arbitrary magnetic fields; it depends on the non-secular, anisotropic hyperfine coupling and involves a matching condition $\omega_{mw} \cong \omega_H$, which requires unreasonable microwave field strengths at elevated magnetic fields. It nevertheless has motivated subsequent experiments which do not suffer from these limitations.

More importantly, the experiments have demonstrated that fundamental thermodynamic limits on the DNP enhancement can be overcome in an appropriately prepared system. The ultimate limitation on the enhancement arises from the Boltzmann polarization of the electrons. A second and somewhat related limitation arises from the fact that paramagnetic impurities, even in low concentrations, are an efficient mechanism for nuclear relaxation and also result in significant nuclear line broadening. As first suggested by Abragam, these limitations can be removed if the polarization source is a molecule which is paramagnetic only in its photoexcited triplet state and which relaxes rapidly to a diamagnetic ground state on a time scale which is long enough for the polarization transfer process to occur.

Triplet formation occurs by intersystem crossing from the first excited singlet state (*cf.* Fig. 2-13). At zero field, the Hamiltonian is then dominated by the magnetic dipole interaction between the electrons; it is generally written in a form which involves operators of total spin angular momentum, $S = S_1 + S_2$, and is called the "zero-field splitting,"

$$H_{ZFS} = \vec{S} \cdot \overleftrightarrow{D} \cdot \vec{S}.$$ (2.32)

The eigenstates of (2.32) are:

$$T_x = \frac{1}{\sqrt{2}}(\beta_1\beta_2 - \alpha_1\alpha_2)$$ (2.33)

$$T_y = \frac{i}{\sqrt{2}}(\beta_1\beta_2 + \alpha_1\alpha_2)$$ (2.34)

$$T_z = \frac{1}{\sqrt{2}}(\alpha_1\beta_2 - \beta_1\alpha_2), \tag{2.35}$$

where α and β are eigenfunctions of S_z.

Due to symmetry selection rules, these triplet sublevels are not populated according to the Boltzmann equilibrium after the triplet state is created, and the decay of the excited state to the ground state is also prevented (it is metastable). This means that there are two separate time constants that must be considered in such a system: one defining the decay of the triplet state and another defining the relaxation of the triplet state spin levels to reach thermal equilibrium with the lattice. In a sample subject to continuous light excitation, the triplet spin polarization will therefore be very high only if the triplet lifetime is considerably shorter than its spin-lattice relaxation time (or the time for polarization transfer). If the reverse is true, the average polarization will be dictated by the Boltzmann equilibrium, but the transient properties of the triplet state can still be exploited.

The system is also subject to the Zeeman interaction, which will define the quantization axis of the spin system at magnetic fields which are high enough for it to dominate the zero-field splitting. The Hamiltonian can be written (in fundamental units) as

$$H = \vec{S} \cdot \overset{=}{D} \cdot \vec{S} + B_0 \cdot \overset{=}{g} \cdot \vec{S}, \tag{2.36}$$

where $\overset{=}{g}$ is the g-anisotropy.
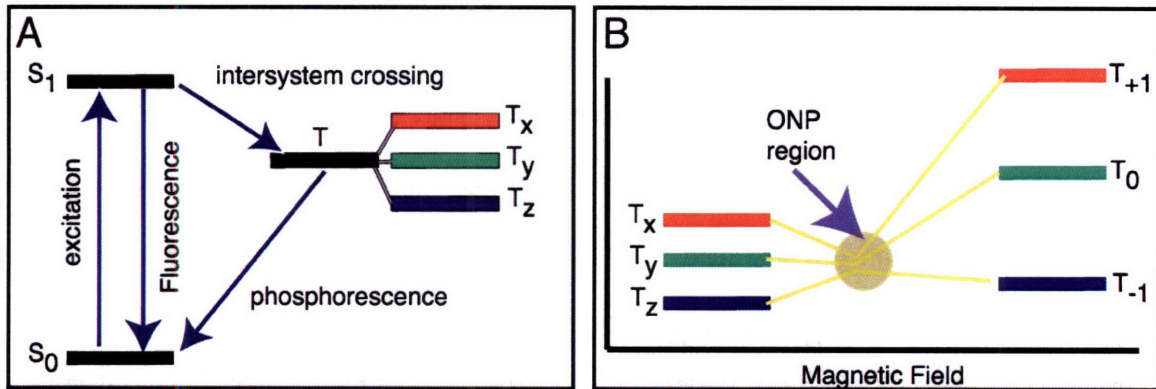
Figure 2-13: Triplet formation by intersystem crossing from the first excited singlet state, in (a), and the change in quantization axis of the spin Hamiltonian with increasing magnetic field in (b). In (b), note the region of near level-crossing in which low-field optical nuclear polarization can take place.

In the PAS of the ZFS tensor (*i.e.* the frame in which it is diagonal), the Zeeman interaction makes an off-diagonal contribution,

$$H = \begin{bmatrix} X & -igB_{0z} & igB_{0y} \\ igB_{0z} & Y & -igB_{0x} \\ -igB_{0y} & igB_{0x} & Z \end{bmatrix}, \tag{2.37}$$

where X, Y, and Z are the principal elements of the zero-field splitting tensor. Because of this fact, there will be an eigenstate mixing as the static magnetic field B_0 is increased; equivalently, the quantization axis of the nuclear spin Hamiltonian will gradually shift to that of the Zeeman interaction (*i.e.* the external magnetic field). At high magnetic fields, it is clear that the eigenstates of this Hamiltonian are, to a good approximation, those of the Zeeman interaction,

$$T_{+1} = (\alpha_1 \alpha_2) \tag{2.38}$$

$$T_0 = \frac{1}{\sqrt{2}} (\alpha_1 \beta_2 + \beta_1 \alpha_2) \tag{2.39}$$

$$T_{-1} = (\beta_1 \beta_2) \tag{2.40}$$

Three processes can transfer polarization to nuclei which are hyperfine coupled to the triplet. First, at intermediate magnetic fields, eigenstate mixing results in a complex energy spectrum; evolution of the spin system under this Hamiltonian after the creation of the triplet state can directly lead to nuclear polarization, an effect which has been called "optical nuclear polarization" (ONP) [67][68][69]. It is also possible to directly excite forbidden transitions with a resonant microwave field and produce a solid effect-like DNP process within the triplet state manifold. Such experiments have been reported by van Kesteren [39], by Hausser [69][70][71] and by Wenckebach and co-workers [41][72][73], where the mechanism has been called "microwave-induced optical nuclear polarization" (MI-ONP) by these authors. In single crystal guest-host complexes, large enhancements have been obtained using these mechanisms. However, a third and much more general technique involves polarization transfer using a modified Hartmann-Hahn condition. As mentioned previously, this experiment has been introduced in single crystals by Hausser [40] and Henstra [41] under the name "NOVEL" and has recently been extended to polycrystalline powders [74].

To demonstrate the existence of this phenomenon, Fritsch and co-workers [40] consider selective excitation of one transition within the triplet manifold. Since the width of the ESR spectrum is much larger than the available microwave excitation bandwidth, the $S = 1$, $I = \frac{1}{2}$ spin system under selective excitation behaves like a $S' = \frac{1}{2}$, $I = \frac{1}{2}$ spin system, where S' is a fictitious spin operator as introduced by Vega [75]. The experiment should therefore also be applicable to ordinary electron-nuclear spin pairs, where the radical is in a paramagnetic ground state. The Hamiltonian for the fictitious electron spin

(S) which is hyperfine coupled to the nuclear spin (I) and subjected to microwave radiation orthogonal to the static magnetic field is:

$$H = \omega_{0s}S_z + \omega_{0I} + 4C_1\cos(\omega_s t)S_x + H_{\text{HF}}, \tag{2.41}$$

where H_{HF} arises from the hyperfine coupling and is given by

$$H_{\text{HF}} = -C_1 C_2 A_{zi} I_i + 2C_1 A_{xi} S_x I_i + 2C_2 A_{yi} S_y I_i + 2C_1 C_2 A_{zi} S_z I_i. \tag{2.42}$$

In (2.42), $i = \{x,y,z\}$ and summation over the repeated index is implied. The constant terms are:

$$\alpha_z = \sqrt{(Y - X)^2 + 4(g_{zz}\gamma\hbar B_0)^2} \tag{2.43}$$

$$C_1 = \frac{1}{\sqrt{2}}\sqrt{1 - \frac{Y-X}{\alpha_z}}$$

$$C_2 = \frac{1}{\sqrt{2}}\sqrt{1 + \frac{Y-X}{\alpha_z}}.$$

Finally, $\hbar\,\omega_{0S} = E_m - E_1$, where E_m and E_1 are eigenvalues of the full triplet Hamiltonian (see Pratt [76]). In the interaction representation defined by a frame rotating at ω_S about z, and after truncation of oscillatory terms, (2.41) becomes:

$$H = \Omega_s S_z + \omega_{0I} I_z + 2C_1 \omega_{1S} S_x \tag{2.44}$$

$$H_{\text{HF}} = C_1 C_2 \left(2A_{zi}S_z I_i - A_{zi} I_i\right). \tag{2.45}$$

The spin dynamics are best analyzed in a titled frame defined by

$$\Theta_S = \arctan\left(\frac{2C_1\omega_{1S}}{\Omega_S}\right). \tag{2.46}$$

In this titled frame, the effective fields for spins S and I are given by

113

$$\Omega_S^{\text{eff}} = \sqrt{\Omega_S^2 + \left(2C_1\omega_{1S}\right)^2}$$ (2.47)

$$\Omega_I^{\text{eff}} = \omega_{0I} + C_1 C_2 A_{zz}.$$ (2.48)

Equating (2.47) and (2.48) yields the Hartmann-Hahn condition,

$$\sqrt{\Omega_S^2 + \left(2C_1\omega_{1S}\right)^2} = \omega_{0I} + C_1 C_2 A_{zz},$$ (2.49)

which implies $\omega_{1S} \approx \omega_{0I}$.

Using the effective Hamiltonian Hartmann-Hahn matching, Fritsch et $al.$ [40] also follow the time evolution of the density matrix to determine the proton polarization, $p_i(t)$,

$$p_i(t) = p_i(0) + \frac{1}{2}\sin^2(\Phi)\left[1 - \cos(\Omega t)\right]\left[P_s - p_i(0)\right],$$ (2.50)

where Ω and Φ are factors that depend on the hyperfine elements A_{zx} and A_{zy}. As is the case with nuclear cross-polarization, the proton magnetization is an oscillatory function whose period is set by the coupling strength. In this case, however, the coupling elements responsible for the polarization transfer are proportional to $S_z I_x$ and $S_z I_y$. Because these elements are non-secular, the transfer efficiency will decrease with increasing magnetic field; because they are anisotropic, NOVEL should also not operate in liquid solutions.

Further, the Hartmann-Hahn condition in (2.49) requires that the microwave field strength (in frequency units) be approximately equal to the nuclear Larmor frequency, a requirement which cannot be met for protons in elevated magnetic fields. At low magnetic fields (~100 mT), Fritsch and co-workers [40] have reported proton polarization as high as 30% in HHCP experiments from the photoexcited triplet state of dichlorobenzophenone. At the magnetic field of these experiments, the kinetics of the

optical pumping cycle are comparable to the polarization transfer time, allowing both to be repeated many thousand times within the nuclear T_1. It is clear that new polarization transfer schemes will be required for similar experiments to be conducted at higher magnetic fields.

2.2.11 Dressed State Solid Effect and Electron-Nuclear Cross Polarization

In applications at high magnetic fields, all the DNP mechanisms discussed so far suffer from one or two intrinsic limitations. First, nonsecular coupling elements are responsible for the polarization transfer, with the result that the polarization transfer becomes less efficient with increasing magnetic field. Second, the nuclear polarization evolves at a rate of T_{1n}; this implies, on the one hand, that the time-averaged sensitivity is lower than it might be if the process could occur with faster kinetics in the rotating frame and, on the other, that the T_{1n} must be reduced by manipulation of the sample temperature in order to attenuate spin-lattice relaxation processes which would otherwise limit the enhancement.

In fact, this situation is entirely analogous to the detection of spectra of dilute nuclei (*e.g.* ^{15}N, ^{13}C) in solid state NMR, which are insensitive both due to their low gyromagnetic ratios and long T_1. The solution to this problem in the domain of solid state NMR has involved pulsed cross-polarization. Here, a Hartmann-Hahn match is achieved in a doubly-rotating frame, resulting in rapid polarization transfer between protons and heteronuclei which depends only on the secular part of their dipolar coupling. For the case of off-resonant radiation of one or both spin species, a match between

effective fields can occur with diminished B_1 field requirements, albeit at the expense of introducing chemical shift dependent dynamics into the polarization transfer process.[9]

Weis and co-workers have made preliminary steps in applying similar concepts to the problem of electron-nuclear polarization transfer by near-resonant radiation of both the electrons and nuclei [42]. These experiments can be described either as a solid effect within an electron spin state that is dressed by the microwave field, or by using the conventional framework of cross-polarization in solids. The electron-nuclear cross-polarization experiment does not depend on the non-secular hyperfine coupling and can be repeated at a rate comparable to the electron T_1. Because it does not depend on the anisotropic hyperfine coupling, the experiment should also be applicable in liquid solutions, in which only the isotropic or Fermi contact component of the hyperfine coupling survives. In addition, Weis *et al.* have shown [42] that significant hyperfine decoupling occurs near this resonant matching, with the result that even protons relatively near the radical center can participate in bulk spin diffusion.

The mathematics of this process follows closely those of the laboratory-frame solid effect. The Hamiltonian in the electron rotating frame (2.16) is diagonalized as in (2.19). The microwave field in this frame is therefore given by (2.20). Since we are interested in the dynamics only at high magnetic fields, we can make the approximation $\eta \cong 0$ and diagonalize that part of the Hamiltonian which describes allowed EPR transitions only using the unitary transformation [45],

$$U = \exp\left[-i\left(\theta_\alpha S_y I^\alpha + \theta_\beta S_y I^\beta\right)\right], \tag{2.51}$$

where

---

[9] The narrow-band and band-selective sequences which result have been exploited in solid state NMR for spectral

$$\theta_\alpha = \left(\frac{-2\omega_{1s}}{A + 2\Omega_S} \right) \quad A + 2\Omega_S \geq 0 \tag{2.52}$$

$$\theta_\beta = \left(\frac{-2\omega_{1s}}{2\Omega_S - A} \right) \quad 2\Omega_S - A \geq 0$$

$$\theta_\alpha = \left(\frac{-2\omega_{1s}}{A + 2\Omega_S} \right) - \pi \quad A + 2\Omega_S < 0$$

$$\theta_\beta = \left(\frac{-2\omega_{1s}}{2\Omega_S - A} \right) - \pi \quad 2\Omega_S - A < 0.$$

The truncated Hamiltonian ($\eta = 0$ and taking only components of the microwave field which result in allowed transitions) then becomes

$$\tilde{H} = \Omega_S^{\text{eff}} S_z + \tilde{\omega}_I I_z + A^{\text{eff}} S_z I_z + B S_z I_x + \omega_{1S} S_x, \tag{2.53}$$

where

$$\tilde{\omega}_I = \omega_I \tag{2.54}$$

$$\Omega_S^{\text{eff}} = \frac{1}{2}\left[\left(\Omega_S + \frac{A}{2} \right) \cos(\Theta_\alpha) - \omega_{1S} \sin(\Theta_\alpha) \right]$$
$$+ \frac{1}{2}\left[\left(\Omega_S - \frac{A}{2} \right) \cos(\Theta_\beta) - \omega_{1S} \sin(\Theta_\beta) \right] \tag{2.55}$$

$$A^{\text{eff}} = \left(\Omega_S + \frac{A}{2} \right) \cos(\Theta_\alpha) - \omega_{1S} \sin(\Theta_\alpha)$$
$$- \left(\Omega_S - \frac{A}{2} \right) \cos(\Theta_\beta) - \omega_{1S} \sin(\Theta_\beta). \tag{2.56}$$

With these definitions, the eigenvalues of the (dressed) Hamiltonian are:

$$E_{1/2} = +\frac{\Omega_S^{\text{eff}}}{2} \pm \left(\frac{\omega_I}{2} + \frac{A^{\text{eff}}}{4} \right) \tag{2.57}$$

---

assignments [77][78][79].

117

$$E_{3/4} = -\frac{\Omega_S^{eff}}{2} \pm \left(\frac{\omega_I}{2} - \frac{A^{eff}}{4} \right).$$

It is now straightforward to demonstrate that simultaneous nuclear irradiation can bring about transitions between these states. The form of the RF Hamiltonian, $H_{RF} = w_{1I} I_x$, in the diagonal frame defined by (2.51) is:

$$H_{RF} = \omega_{1I} \cos(\theta) I_x + \frac{\omega_{1I}}{2} \sin(\theta) \left\{ \left[S^+ I^- + S^- I^+ \right] - \left[S^+ I^+ + S^- I^- \right] \right\}, \qquad (2.58)$$

where $\theta = (\theta_\alpha - \theta_\beta) / 2$. According to (2.58), there is then a close analogy between the effects of the microwave field and non-secular dipolar coupling, in the case of the laboratory frame solid effect, and the effects of radiofrequency irradiation in the truncated interaction frame which defines the electron dressed state. Specifically, irradiation of the nuclear spins can bring about zero-quantum and double-quantum transitions in the dressed state manifold; unlike in the laboratory frame case, however, the transition probabilities depend on experimental parameters and can therefore be adjusted to maximize the DNP effect. As with the conventional solid effect, the zero-quantum and double-quantum transitions give rise to polarization of the opposite sign and therefore must be selectively excited in order to yield a net gain in nuclear polarization. By following the evolution of the density matrix under the effective Hamiltonian, Weis *et al.* further demonstrate that the polarization resulting from either pathway is an oscillatory function of the mixing time, t_{sl}, with a frequency of $\omega_{1I} \cos(\theta_\alpha)$ [42]. Finally, one interesting consequence of this theory is that the microwave radiation partially decouples the hyperfine interaction. In the limit $A, B \square \omega_{1S}$, the nuclear transition frequencies are entirely independent of the hyperfine coupling. This implies that enhanced protons will

participate in free proton-proton spin diffusion to the bulk, since their resonance frequencies will not change dramatically due to the hyperfine interaction.

It is also worth mentioning that the same experiment can be described within the broader mathematical framework of Hartmann-Hahn cross-polarization. Unlike for NOVEL, in this case the polarization transfer dynamics are best treated in a doubly-rotating and titled frame defined by the electron and nuclear resonance offsets and excitation field strengths. For weakly coupled nuclei, the treatment is entirely analogous to that of narrow-band and band-selective "SPECIFIC CP" introduced by Baldus and co-workers [64] and Petkova *et al.* [65]. Hartmann-Hahn matching then occurs because of eigenstate degeneracy in the doubly-tilted Hamiltonian, where the matrix elements responsible for the process are now those of the hyperfine coupling rather than the heteronuclear dipolar coupling. Weis *et al.* have shown the relevant matching condition to be [66]

$$\Omega_I = \pm\sqrt{\Omega_S^2 + \omega_{1S}^2 - \tilde{\omega}_{1I}^2} \cong \pm\sqrt{\Omega_S^2 + \omega_{1S}^2}, \qquad (2.59)$$

and argue that, since $\Omega_I \geq \omega_{1S}$, the nuclear effective fields will be quantized approximately along the Zeeman axis, and so the nuclear polarization will evolve as I_z. The dynamics of the polarization build-up are largely governed by the nuclear spin lock field, ω_{1I}; however, in the limit of very large microwave field strengths, significant hyperfine decoupling effects will result in very long polarization transfer times.

The dressed state solid effect has not yet been observed directly in a DNP experiment. Due to experimental restrictions that are the focus of the second half of this paper, it has thus far only been practical to implement the experiment using a low-power solid-state microwave source in conjunction with a high-Q microwave cavity. The restricted sample

sizes in this experiment have complicated the detection of a useful NMR spectrum, and so Weis and co-workers instead chose to detect loss of electron magnetization rather than nuclear polarization [42][66]. The results of these experiments appear in Figure 2-14. Due to the potential experimental advantages of this technique, we anticipate that further experiments using DSSE/CP will become routine as high power gyroamplifiers become available.
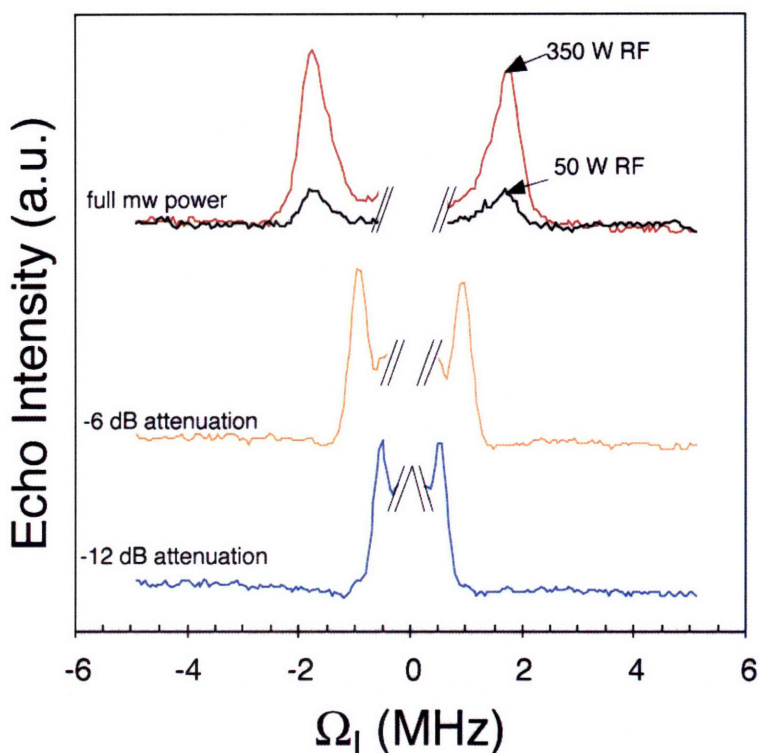
Figure 2-14: Modulation of EPR Echo intensity due to DSSE/CP effects in a sample of perdeuterated BDPA in a polystyrene matrix. In this experiment, the strength of the microwave spin lock field and nuclear spin lock were varied for a spin lock time of 3 μs. Adapted from [42].

2.3 Microwave Devices

With the exception of very specialized phenomena which occur in transiently coupled spin systems, electron-nuclear polarization transfer requires coherent microwave radiation at or near the electron Larmor frequency. For high field dynamic nuclear

polarization, the microwave B_1 field strength must also be on the order of a few megahertz. This necessitates either the use of a high power microwave source or a low power source in conjunction with a microwave cavity or other high-Q resonator. The latter requirement is not easily met for macroscopic samples undergoing magic angle spinning, and so current successful efforts have been directed towards fulfilling the former. DNP experiments based on analogs of Hartmann-Hahn polarization transfer impose the further requirement of coherent phase switching and pulse formation on the nanosecond timescale. This can be accomplished, in principle, either by gating of a high power source in combination with a network of delay lines and circulators to generate orthogonal phases, or by the amplification of a low power signal which has already been modulated using conventional microwave circuits operating at low powers.

For moderate frequency ranges (9–95 GHz), solid state devices exist which can satisfy these requirements [80]. The most useful example of these are two-port microwave diodes which convert a DC bias to RF power in the presence of a microwave cavity, examples of which include the Gunn diode and IMPATT diode. IMPATT oscillators, in particular, are capable of producing usable output power across a portion of the millimeter wave frequency band, but their output power in the submillimeter wave regime is limited. They will nevertheless continue to be useful as low power microwave sources for amplifiers operating at or below 140 GHz. Conversely, lasers operating in the near infrared have high peak output powers at extremely high frequencies, but they cannot efficiently produce the 5–10 W of power that is required for DNP in the moderate 140 GHz – 1 THz frequency range. In fact, the only suitable approaches for microwave generation satisfying these power and frequency requirements all involve vacuum

electron devices in which the kinetic energy of a beam of accelerated electrons is coupled to the radiation field, resulting in the emission of microwave radiation (*cf.* Fig. 2-15). High power microwave tube technology is routinely applied in communications [81], radar and radar countermeasures [82], plasma heating [83] and diagnostics [84], and more recently, electron spin resonance (ESR) [85].
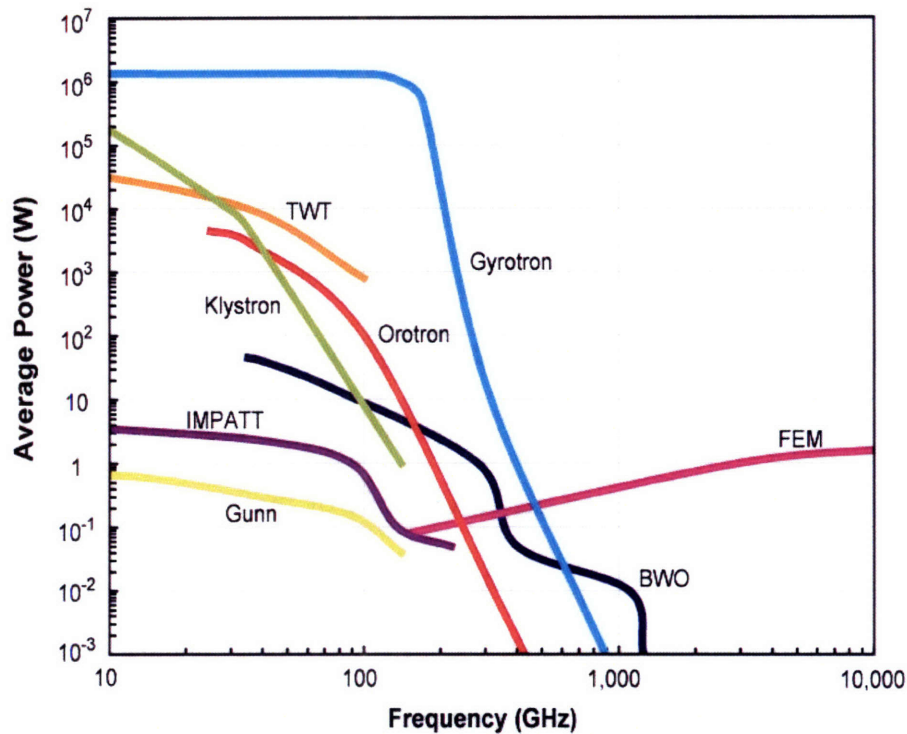
Figure 2-15: State-of-the-art in microwave sources, oscillators and amplifiers, including vacuum electron devices and solid-state devices.

The devices in Figure 2-15 consist of vacuum electron devices (VED), such as the traveling wave tube (TWT), klystron, backward wave oscillator (BWO), orotron, gyrotron, and free electron maser (FEM), and solid state sources, such as the Gunn diode and IMPATT diode. Of the VED's, the gyrotron and FEM are so-called "fast-wave" devices in which the wave phase velocity equals or exceeds the speed of light; the other

VED devices are "slow-wave" devices, for which the phase-velocity[10] is less than the speed of light. In slow-wave variants, the microwave interaction structure has dimensions comparable to the wavelength, while in fast-wave devices, the interaction occurs on a length scale much larger than the wavelength. For a constant output power, the energy density will increase as the wavelength decreases; since the high energy electron beam must travel close to the slow-wave microwave interaction structure, thermal loading will prevent the operation of these devices at high frequencies and high output powers. On the other hand, fast-wave devices such as the gyrotron (a type of cyclotron resonance maser) [86] do not suffer from this limitation and can continue to deliver high output powers into the sub-terahertz frequency band. Gyrotron oscillators have been successfully operated at frequencies as high as 889 GHz by Idehara and co-workers [87] and are shown in Figure 2-15.

One limitation of the gyrotron oscillator is that both the instantaneous bandwidth and the absolute frequency range are bounded. It arises from the fact that radiation is produced by coupling to a particular mode of a cavity or other interaction circuit, which has a well-defined frequency and a (usually high) Q. By consequence, the static magnetic field at the sample must be swept to change the electron resonance offset. This may be ameliorated by building tunable gyrotron resonators in which the cavity dimensions can be modulated in order to tune the frequency [88]. A more general solution might involve gyro-amplifiers based on traveling wave tubes, which do not suffer from this limitation. Further, their instantaneous bandwidth in pulsed mode is

---

[10] The phase velocity is the velocity with which a detector must move in order to measure a constant phase for a wave moving through the interaction structure after steady-state conditions have been reached. For a traveling electromagnetic wave, characterized by $\cos(\omega t - kz)$, the phase velocity is given by ω/k.

sufficient to excite the full breadth of the nitroxide EPR spectrum at moderate operating frequencies.

Finally, free electron maser (FEM) microwave sources have been built which are capable of short pulse operation with continuous tuning over a wide frequency range [89][90]. Conventional FEMs generally require highly relativistic electron beams and so are more expensive and much more complex than other sources, particularly for continuous-wave (CW) operation. By contrast, the orotron (or "ledatron") [91][92] is an FEM variant VED based on the Smith-Purcell effect, in which the transit of an electron beam close to a periodic grating generates a charge on the grating surface which interacts with the incident electron beam to produce radiation. In order to yield coherent radiation, the effect is generally produced within a reflective Fabry-Perot cavity in which a flat mirror is imprinted with the periodic grating. Orotrons have been successfully employed for spectroscopy applications in the submillimeter wave regime, where they can produce output powers of a few tens of milliwatts for pulse durations on the order of 100 ns [93]. Due to the limitations of FEMs and conventional slow-wave devices, we anticipate that gyrotrons operating at the fundamental cyclotron resonance frequency or its second harmonic will continue to be utilized in future DNP experiments. The closely related gyro-amplifier will also be useful in cases where coherent control over frequency and phase is required, but where the capability of CW operation must be preserved.

2.3.1 Solid State Microwave Oscillators and Amplifiers

The Gunn diode and the IMPATT diode are compact and efficient solid state sources which are useful throughout much of the microwave spectrum; however, above 95 GHz, their average power is limited (cf. Fig. 2-15) due to device size and properties of the

substrate. Both devices utilize carrier transit-time effects to achieve a negative resistance which, in combination with a tuned microwave circuit, can lead to oscillation or amplification. While IMPATT diodes can generally produce greater power, Gunn diodes have superior stability and noise properties, and so are extensively used in receivers and broadband amplifiers.

2.3.2   Gunn diodes

The unique band structure of compound semiconductors such as GaAs and InP gives rise to a negative differential mobility (NDM) effect in the presence of a strong electric field. In particular, the first conduction band occurs in a region of atypically low effective mass, and therefore high carrier mobility. At room temperature and in the absence of an electric field, most electrons lie in this low energy, high mobility conduction band. As the electric field is increased, the electron kinetic energy becomes comparable to the energy difference between the high and low mobility regions, and the adjacent conduction bands become populated (*cf.* Fig. 2-16). Above a certain threshold, the electron drift velocity begins to saturate in conventional semiconductors such as silicon. In GaAs, however, the drift velocity does not saturate and instead can decrease with increasing electric field, due to the population of low-mobility energy states. To see how negative resistance can arise, we note that current is related to the differential mobility, μ, by

$$J = qn\mu E, \tag{2.60}$$

where q is the charge, n is the number of charges per unit volume, E is the electric field, and the differential mobility is $\mu = dv/dE$. Since the electron drift velocity, v, is

decreasing with increasing electric field, μ is negative. The expression in (2.60) therefore requires that the current will decrease with an increasing electric field, which is equivalent to a negative resistance. The linear region of negative resistance is illustrated in Figure 2-17. A further consequence is that the space-charge distribution in a semiconductor operating above the threshold of NDM is fundamentally unstable. Consider a spatially localized perturbation (at point i), $\delta\rho$, to the carrier density, ρ, at $t = 0$. At a later time,

$$\delta\rho_i(t) = \delta\rho(0)e^{-t/\tau_r}, \tag{2.61}$$

where the relaxation time is given by $\tau_r = \varepsilon/qn\mu$ and ε is the permittivity. In a NDM semiconductor, μ is negative, and so the exponent τ_r is negative, and therefore the perturbation $\delta\rho$ will increase as a function of time instead of decaying. The degree to which this perturbation can grow is limited by the transit time through the semiconductor.
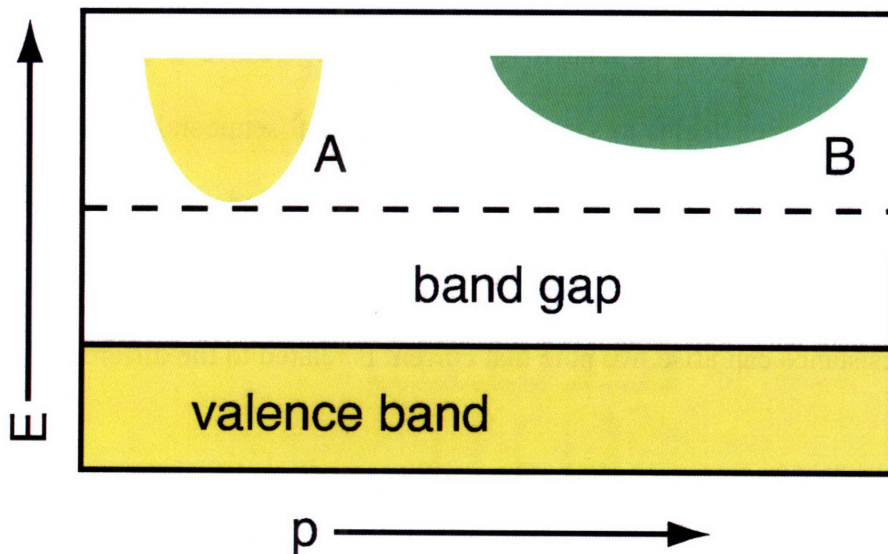
Figure 2-16: The band structure of direct-gap semiconductors such as GaAs or InP is characterized by a high mobility region (A) and a low mobility region (B) of higher effective mass.

These effects can be exploited (albeit with low power conversion efficiency) in the transit-time configuration of a Gunn diode [94][95], illustrated in Figure 2-17. Here, the operation of a Gunn diode in the region above the NDM threshold voltage results in the formation of a dipole domain for which carriers accumulate on one side and are depleted on the other. This dipole domain migrates across the device with a period approximately equal to the transit time, and then forms again at the cathode. A diode operated in this configuration can thus serve as an oscillator at a frequency which is fixed approximately by the inverse transit time. In practical circuits, however, the Gunn diode is coupled to a resonant circuit whose frequency is considerably greater than the inverse of the transit time. When operating in this mode, no dipolar domains form, and the Gunn diode behaves as a pure negative resistance.
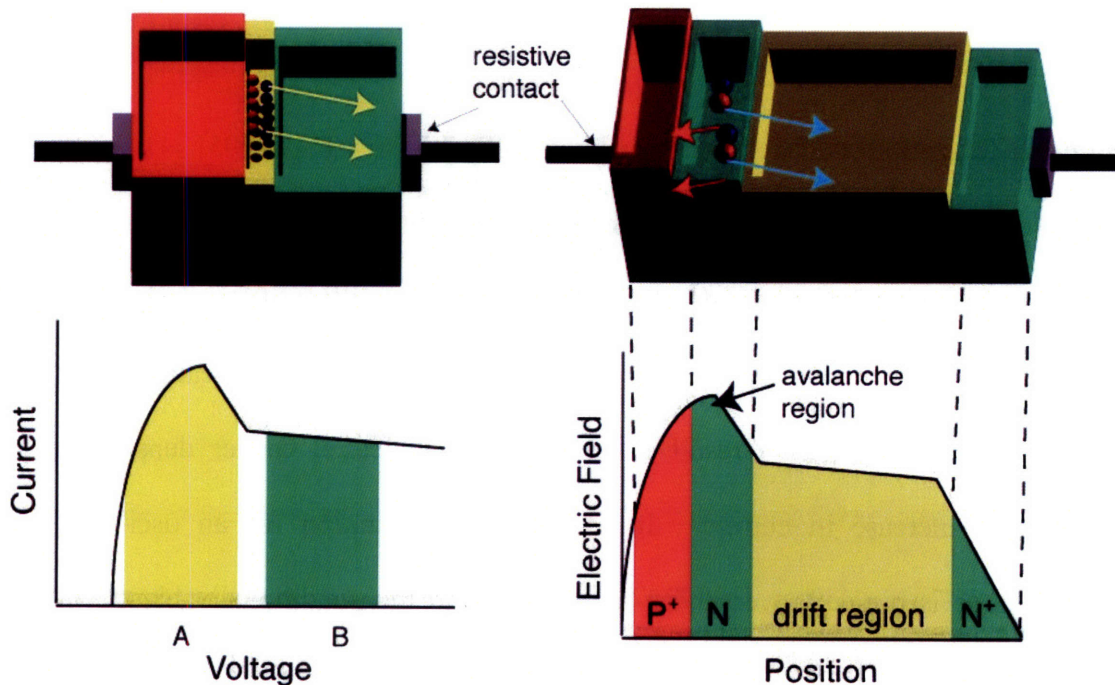
Figure 2-17: Schematic and electric field distribution of [left] the transit time configuration of a Gunn diode and [right] a typical IMPATT diode.

The Gunn diode has been successfully applied for DNP studies in conjunction with a high-Q resonator at 140 GHz for samples contained in microcapillary tubes [96] (*cf.* Fig. 2-18). Though the technique is not suitable for magic angle spinning studies, enhancements as high as 400 have been recovered at liquid helium temperatures.
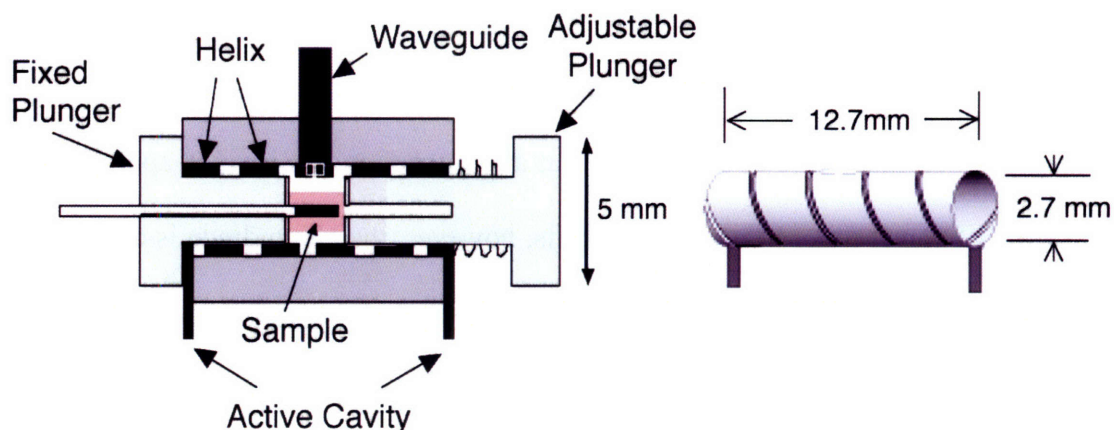
Figure 2-18: Resonator for DNP and ENDOR studies at 140 GHz. The resonator is tuned by means of an adjustable plunger. Adapted from [96].

2.3.3   IMPATT diodes

The impact-ionization avalanche transit time (IMPATT) diode [94][95] is a two-port microwave device in which transit time effects are utilized to produce a negative resistance. The simplest p^+nin^+-type[11] IMPATT diode is illustrated in Figure 2-17. When the diode is reverse-biased to near breakdown, avalanche multiplication effects in the region of a p^+n junction result in dramatically increased carrier density and a corresponding increase in current. In a typical configuration for an oscillator, an IMPATT diode is biased to very near breakdown, and then additionally biased with a small oscillating RF field. For some part of the RF cycle, avalanche breakdown will occur, and a current pulse will propagate through the device with a time constant that is

---

[11] Here, "i" refers to an intrinsic semiconductor region.

128

largely determined by the transit time in the intrinsic semiconductor region. If this transit time is long, the current can fall behind the voltage by a large phase, which is equivalent to a negative real resistance. Like the Gunn diode, then, the IMPATT diode can be used in a microwave resonant circuit to produce a microwave oscillator; unlike the Gunn diode, the IMPATT is an extremely noisy device. Though the IMPATT can produce significant power in the millimeter wave regime,[12] its efficiency declines steeply with frequency. We therefore do not anticipate its continued utility for DNP experiments above 140 GHz.

2.3.4   Gyrotron Theory

The gyrotron is a vacuum electron device which produces coherent microwave radiation with high efficiency through the unstable interaction of an electron beam and an electromagnetic field in a magnetic field. The theory of coherent radiation from an ensemble of relativistic electrons has been developed along quantum mechanical [97][98][99][100] and classical [100][101][102][103][104] lines. While the quantum theory of cyclotron resonance affords physical insight into the nature of the interaction, practical device design is greatly simplified by a classical fluid-dynamical theory, in which the electron beam is treated as a plasma, or by numerical solution of relativistic kinematical equations of motion for a number of test charges (so-called "ballistic" theory). Here, we will briefly review the salient physics of the gyrotron in both cases and discuss the practical consequences for the design of gyrotron oscillators operating in the millimeter and submillimeter wave bands.

---

[12] Commercially available single IMPATT sources can produce 50 mW at 150 GHz [80], and they can be combined in arrays for even greater output.

2.3.5 Quantum Mechanical Basis of the Cyclotron Resonance Maser

The gyrotron is an example of a cyclotron resonance maser; as suggested by its name, radiation occurs by stimulated emission within the quantized eigenspectrum of the electron in a magnetic field. The motion of a charged particle in a magnetic field has been treated first by Landau [105]. Briefly, the magnetic field, $\mathbf{B(r)}$, is defined up to the gradient of an arbitrary function through the vector potential, $\mathbf{A(r)}$,

$$\mathbf{B(r)} = \nabla \times \mathbf{A(r)}. \tag{2.62}$$

The Hamiltonian operator and the operator for the particle velocity are then given in (2.63) and (2.64):

$$H = \frac{1}{2m}(\mathbf{P} - e\mathbf{A})^2 \tag{2.63}$$

$$\mathbf{V} = \frac{1}{m}(\mathbf{P} - e\mathbf{A}), \tag{2.64}$$

where m is the mass. For $\mathbf{B(r)} = \hat{z}B_z$ and motion perpendicular to the magnetic field, (2.63) becomes

$$H = \frac{m}{2}\left(V_x^2 + V_y^2\right). \tag{2.65}$$

Commutators of elements of the velocity operator can be derived from canonical commutation relations; for the problem constructed, they are given in (2.66) and (2.67):

$$\left[V_x, V_z\right] = \left[V_y, V_z\right] = 0 \tag{2.66}$$

$$\left[V_x, V_y\right] = -i\frac{\hbar\Omega_c}{m}, \tag{2.67}$$

in which $\Omega_c = eB_z/m$ is the classical cyclotron resonance frequency.

130

The eigenspectrum of (2.65) can be obtained by analogy to the one-dimensional harmonic oscillator. In particular, we define

$$X = \sqrt{\frac{m}{\hbar\Omega_c}} V_x \tag{2.68}$$

$$P' = \sqrt{\frac{m}{\hbar\Omega_c}} V_y, \tag{2.69}$$

such that the operators X and P' now obey

$$[X, P'] = -i, \tag{2.70}$$

and the Hamiltonian (2.65) is now identical to that of the one-dimensional harmonic oscillator,

$$H = \frac{\hbar\Omega_c}{2}\left(X^2 + P'^2\right). \tag{2.71}$$

The eigenvalues of (2.65), defining motion in the plane orthogonal to the magnetic field, are

$$E = \left(n + \frac{1}{2}\right)\hbar\Omega_c. \tag{2.72}$$

This harmonic quantization of the energy of a charged particle moving in a homogeneous magnetic field is named for Landau [105]. We now consider the possibility that an ensemble of initially monoenergetic electrons can lose energy to an electromagnetic field in the presence of a strong magnetic field, a situation corresponding to stimulated emission. The energy absorbed by an electron from the radiation field over the interaction time, t, is

$$W = \hbar\left(\omega_{n,n+1}P_{n,n+1} - \omega_{n,n-1}P_{n,n-1}\right). \tag{2.73}$$

The transition probabilities, $P_{n,n+1}$ and $P_{n,n-1}$, which appear in (2.73) are given by expressions of the form

$$P_{n,n+1} = \frac{E_0^2 t^2}{\hbar^2} \mu_{n,n+1}^2 g_\omega\left(\omega_{n,n+1}\right),$$ (2.74)

where $\mu_{n,n+1}$ is the transition dipole moment for the harmonic oscillator, E_0 is the magnitude of the electric field, and $g_\omega(\omega_{n,n+1})$ is an approximate lineshape function, given by

$$g_\omega\left(\omega_{n,n+1}\right) \cong \frac{\sin^2\left[\left(\omega_{n,n+1} - \omega\right)t/2\right]}{\left[\left(\omega_{n,n+1} - \omega\right)t/2\right]^2},$$ (2.75)

where in (2.75), we have neglected the counter-rotating component of the electric field. Substituting (2.75) into (2.73), we can obtain an expression for the total energy absorbed by the electron in terms of fundamental parameters of the system:

$$W \cong \frac{e^2 E_0^2 t^2}{2m}\left\{n\left[g_\omega\left(\omega_{n,n+1}\right) - g_\omega\left(\omega_{n,n-1}\right)\right] + g_\omega\left(\omega_{n,n+1}\right)\right\}.$$ (2.76)

From (2.76), it is clear that energy can only be given up to the field if the quantity $[g_\omega(\omega_{n,n+1}) - g_\omega(\omega_{n,n-1})]$ is negative. However, we have already shown in (2.72) that the eigenvalues of the electron in a magnetic field are evenly spaced, hence $g_\omega(\omega_{n,n+1}) = g_\omega(\omega_{n,n-1}) = g_\omega(\Omega_c)$, which implies that W is purely absorptive. By this reasoning, there can be no loss of energy to the field and no cyclotron resonance maser effect unless the eigenspectrum of the electron in a magnetic field is anharmonic. Fortunately, such a situation can arise for a relativistic electron in a homogeneous magnetic field [97][98][99][100][106]. In this case, the electron obeys the Dirac equation,

132

$$\left(\gamma_\mu \partial_\mu + \frac{mc}{\hbar} \right) \psi = 0,$$

(2.77)

which, in the presence of an electromagnetic field, becomes

$$\left(\partial_\mu - \frac{ie}{\hbar c} A_\mu \right) \gamma_\mu \psi + \frac{mc}{\hbar} \psi = 0.$$

(2.78)

In (2.78), we have made the usual Gauge-invariant, Lorentz-covariant substitution for the electromagnetic field in the form $-i\hbar \partial_\mu \rightarrow -i\hbar \partial_\mu - eA_\mu / c$. In the correct gauge and using appropriate explicit representations of the matrices γ_μ, the problem in (2.78) can be solved in analogy to the Schrödinger harmonic oscillator using transformations very similar to those defined in (2.68) and (2.69) for the non-relativistic case. The solution to (2.78) requires that the kinetic energy of the electron be quantized according to

$$E \, \square \, m_0 c^2 \sqrt{\left[1 + 2 \left(n + \frac{1}{2} \right) \left(\frac{\hbar \Omega_c}{m_0 c^2} \right) \right]} - m_0 c^2,$$

(2.79)

where m_0 is the electron rest mass and all other parameters have been defined in the non-relativistic solution. The important consequence of this result is that the energy levels of the relativistic electron are not evenly spaced, and hence we can expect stimulated emission as defined in (2.76). Since $n\hbar \Omega_c / m_0 c^2$ is less than unity, (2.79) reduces to

$$E_{n+1} - E_n = \hbar \Omega_c = \hbar \frac{eB}{\gamma m},$$

(2.80)

where $\gamma = 1 + E_n / m_0 c^2$. For our purposes, this means that radiation can be produced from even a weakly relativistic beam of electrons, as shown in Figure 2-19. The gyrotron oscillator is one realization of a cyclotron resonance maser based on this effect.

133
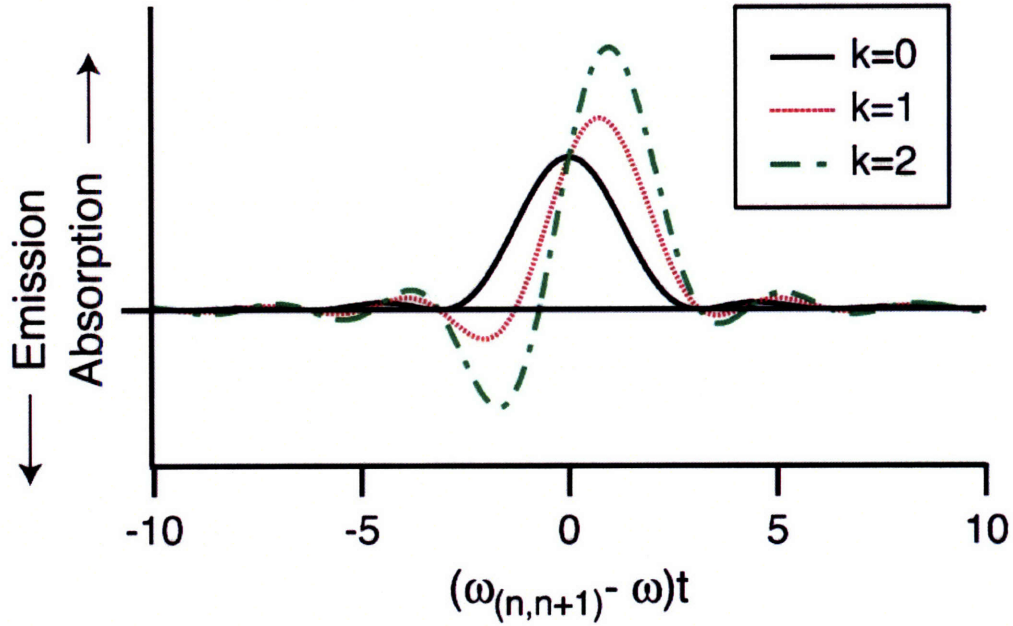
Figure 2-19: Cyclotron resonance for varying values of the parameter $k = n\hbar\Omega_c^2 / 2mc^2$ according to equation (2.76), where terms of order $\sim(\hbar\Omega_c/m_0c)^2$ have been neglected. Note that for a low energy beam, in which n is small, the non-relativistic limit ($k \cong 0$) is recovered in which pure absorption, and no gain, occurs.

2.3.6   Classical Description of the CRM Interaction

A gyrotron oscillator is a vacuum electron device in which a weakly relativistic electron beam is arranged to interact with transverse electric (TE) modes of a microwave resonant circuit in the presence of a strong magnetic field. The quantum mechanical approach we have previously introduced is insufficient to correctly describe the operation of this device; in particular, it is based on a time-dependent perturbation approach which does not account for non-linear interactions. Where n in (2.79) is large, we can apply the more convenient classical theory.

134
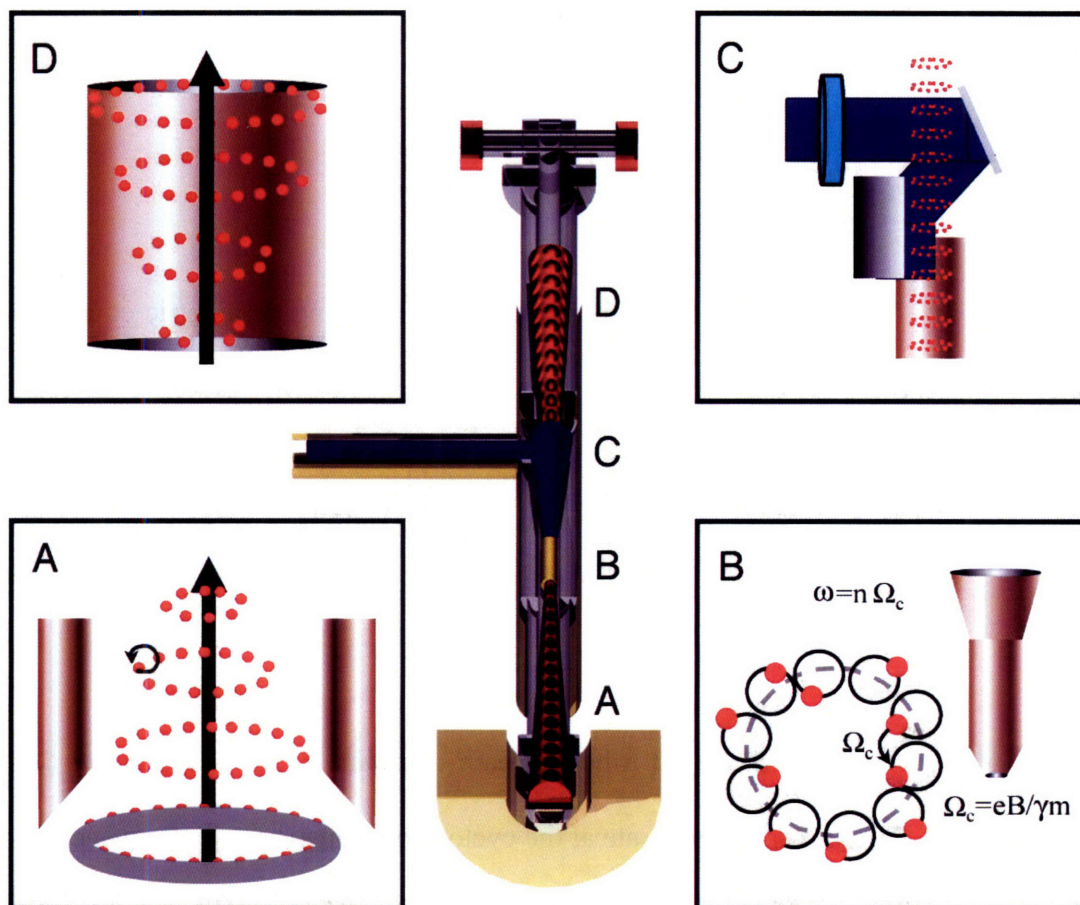
Figure 2-20: Schematic cross-section of a typical low-power gyrotron oscillator. (A) An annular electron beam leaves the cathode, accelerates towards the anode, and is compressed by the increasing static magnetic field. (B) Gyrating electrons interact with a mode of the interaction structure. (C) Microwave radiation is launched from a slotted waveguide, focused to a Gaussian beam, and steered toward a side vacuum window while the electron beam continues unimpeded. (D) The electron beam expands in the inhomogeneous stray field of the superconducting magnet and is intercepted (collected).

A schematic description of a typical gyrotron oscillator used for DNP appears in Figure 2-20. At one end of the vacuum tube, an annular electron beam is produced by a magnetron injection gun, and the beam is radially compressed as it enters the homogeneous region of the magnetic field. At the beginning of the interaction region (*e.g.* the cavity in a gyrotron oscillator), the electron beam is annular; it is initially unbunched and its constituent electrons are uniformly distributed azimuthally. A charged

135

particle moving through a magnetic field, **B**, with a velocity, **v**, experiences a Lorentz force,

$$\mathbf{F} = -e\mathbf{v} \times \mathbf{B} = \frac{d\mathbf{p}}{dt},$$

(2.81)

where $\mathbf{p} = \gamma m\mathbf{v}$. The charged particle then obeys the following parametric equations of motion:

$$x = x_0 + r_g \cos\left(\Omega_c t + \phi\right)$$

(2.82)

$$y = y_0 + r_g \sin\left(\Omega_c t + \phi\right)$$

$$z = z_0 + v_{\parallel} t.$$

Qualitatively, the particle traces out a helical path of radius r_g about a guiding center. The electrons in the annular beam gyrate at the cyclotron frequency (gyrofrequency),

$$\Omega_c = \frac{eB}{\gamma m},$$

(2.83)

where m and e are, respectively, the mass and charge of an electron, γ is the relativistic factor,

$$\gamma = \frac{1}{\sqrt{1 - v^2/c^2}},$$

(2.84)

and v is the electron velocity. The radius of this gyration is the gyro-radius, r_g, given by

$$r_g = \frac{v_\perp}{\Omega_c}.$$

(2.85)

We can understand the (fundamental) cyclotron resonance maser (CRM) interaction by examining the electrons in the phase space as a function of time. In order to do so, we regard the electron beam as a charged fluid or plasma, following the treatments in

[95][104]. Since the full development of this theory is beyond the scope of the present review, we will only travel far enough to illustrate the correspondence between classical and quantum mechanical pictures of the cyclotron resonance interaction. First, we observe that electrons obeying the equations of motion (2.82) have a velocity which is separable into an angular component orthogonal to the beam axis,

$$v_\perp = v_\perp\left(r,\phi\right),$$ (2.86)

and one parallel to it,

$$v_z = v_\parallel.$$ (2.87)

In this frame, both are constants of the motion and it is usually arranged that $v_\perp > v_\parallel$.

When the electron beam reaches the interaction region, it encounters the electric field of the resonator. Power transfer between the field and the beam is then related to the current density, $\mathbf{J}$, and electromagnetic field, $\mathbf{E}$, as

$$P = -\frac{1}{2}\text{Re}\left\{\int \mathbf{E}^* \cdot \mathbf{J} \, d\mathbf{r}\right\}.$$ (2.88)

It is useful to briefly consider the properties of the electron plasma which are necessary to produce stimulated emission. For the kth electron located at $(r, \phi_0 + \Omega t, 0)$ and moving with $v_\perp$ at $t = 0$, the electron current is spatially localized according to

$$J_\phi = -ev_\perp\delta\left(r - r_0\right)\delta\left[\phi - \left(\phi_0 + \Omega t\right)\right]\delta\left(z\right).$$ (2.89)

Re-writing (2.89) as a Fourier series with respect to ϕ gives

$$J_\phi = -\frac{ev_\perp}{2\pi}\delta\left(r - r_0\right)\delta\left(z\right)\sum_{n=-\infty}^{\infty} e^{in\left(\phi-\phi_0\right)-in\Omega t}.$$ (2.90)

The beam contains a large number, N, of electrons which are uniformly distributed in phase. In this case, (2.90) becomes

$$J_\phi = -\frac{ev_\perp}{2\pi}\delta(r-r_0)\delta(z)\sum_{n=-\infty}^{\infty}e^{in(\phi-\Omega t)}\sum_{k=1}^{N}e^{-in\phi_{0k}}. \tag{2.91}$$

This expression contains factors oscillating at the cyclotron frequency and its n harmonics. In order to evaluate (2.88) in this context, the integral must be taken over the entire phase space, which amounts to taking an ensemble average over all electron orbits. If the electrons are uniformly distributed in phase space, this integral will be zero over this domain. Thus, there can be no growing microwave field under these conditions.

As in the quantum mechanical case, it is a relativistic interaction which produces a non-uniform electron distribution and permits the generation of an oscillating RF field; however, in the classical theory, the electrons are distributed non-uniformly ("bunched") in their phase space, while, in the quantum theory, the eigenspectrum of a relativistic electron in a magnetic field is anharmonic.

In particular, the phase space of which we are now speaking is defined in the reference frame of the RF field (*e.g.* TE modes of an interaction cavity) (*cf.* Fig. 2-21). The electrons entering the cavity have an initially uniform azimuthal phase distribution and gyrate at the cyclotron frequency, Ω_c. Since the cyclotron frequency depends on the relativistic factor, γ, through (2.83), the electron will either gain or lose energy depending on its phase with respect to the RF field. Those electrons which are accelerated by the field gain energy, rotate at a lower frequency, and lag behind in phase; conversely, electrons which are decelerated by the field lose energy, rotate faster, and gain in phase. After a certain interaction time, the electrons are no longer uniformly distributed in phase. If the frequency of the RF electric field ω_{RF} is slightly larger than the electron cyclotron frequency Ω_c, the electrons give their rotational energy predominantly to the

growing RF field (Fig. 2-21). Practically, this condition can be met by tuning B_0 and the cavity radius. In the reverse case of $\Omega_c > \omega_{RF}$, the wave loses energy to the electrons, an effect which can be productively exploited to produce a gyrotron amplifier. After the energy is extracted from the electrons, they are no longer in phase (they lose their synchronism) with the RF wave, Ω_c has increased, and the interaction saturates.
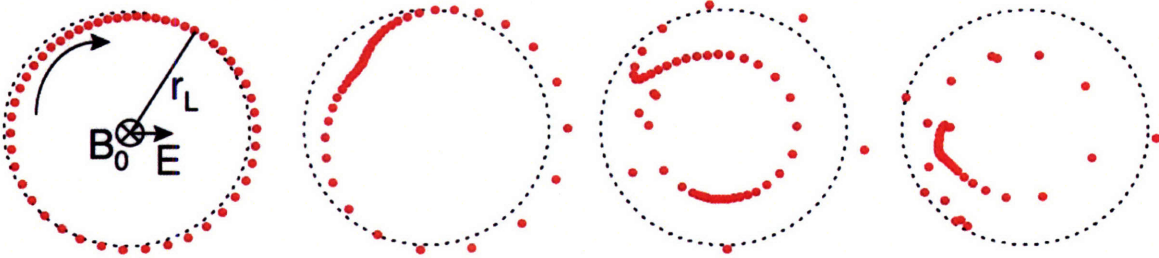
Figure 2-21: Simulation of a non-uniform electron phase distribution which occurs due to the interaction of a relativistic electron beam with a transverse electric field E, situated in a static magnetic field B_0. The beamlets, with Larmor radius r_L, are instantaneous slices in phase space corresponding to axial positions along the interaction structure.

A practical treatment of power transfer from the bunched electron beam to the RF field is complicated even in the small-signal limit. Straightforward evaluation of (2.88) involves the solution of Maxwell's equations for the electric field and the solution of relativistic-kinematic equations of motion for a series of test electrons to obtain electron trajectories, which give rise to a spatially-varying current density. This is called a "ballistic" theory of the gyrotron. In the more useful treatment of Chu and Hirshfield [103], Maxwell's equations still describe the electromagnetic field, but the electron beam is described by the relativistic Vlasov-Boltzmann equation, which is a distribution function for the electron velocity. The power transfer is then governed by

$$P = -\frac{1}{2}\text{Re}\left\{ \int e\mathbf{E}^* \cdot \mathbf{v} f(\mathbf{r},\mathbf{p},t) \, d\mathbf{r} \, d\mathbf{p} \right\}. \tag{2.92}$$

where $f(\mathbf{r}, \mathbf{p}, t)$ is a distribution function for the electron velocity.

Several other features of the gyrotron follow simply from this analysis. For example, any interaction circuit will have a finite Q which is related to its diffractive (Q_{diff}) and ohmic components (Q_{ohm}),

$$\frac{1}{Q} = \frac{1}{Q_{\text{diff}}} + \frac{1}{Q_{\text{ohm}}}. \tag{2.93}$$

The existence of a Q implies that dissipative processes will not permit a growing microwave field unless the electron beam current lies above a certain threshold. This threshold, called the "starting current," is obtained on energy conservation grounds by equating the relationship in (2.92) to that in

$$-\text{Re}\{P\} = \frac{\omega E}{Q}, \tag{2.94}$$

where E is the energy of the mode, and for a Gaussian axial field distribution in a cylindrical cavity of effective length L is given by [107][108]

$$I_{\text{start}} = 4.2 \times 10^3 \frac{I_0}{Q} \left(\pi \frac{v_{\perp 0}}{v_{\Box 0}} \right)^{2(n-3)} \left(\frac{L}{\lambda} \right)^{2n-5} \left(\frac{2^n n!}{n^n} \right)^2 \frac{\left(v_{mp}^2 - m^2 \right) J_m^2 \left(v_{mp} \right)}{J_{m\pm n}^2 \left(k_\perp r_{e0} \right)}. \tag{2.95}$$

Here, n is the harmonic number, I_0 is the normalized current parameter, v_{mp} is the pth zero of J'_m, m and p are the azimuthal and radial TE$_{mp}$ cavity mode eigenvalues, r_{e0} is the electron beam radius in the cavity, and $k_\perp$ is the cutoff wavenumber.

The results of such a linear calculation for a cylindrical cavity designed for a second harmonic 460 GHz gyrotron oscillator are shown in Figure 2-22. In a high frequency, low power gyrotron, it is generally desirable to have a high cavity diffractive Q to avoid competition between the many cavity modes and to produce a low starting current. This is particularly critical for harmonic gyrotron operation, where the design must take into

account competition with fundamental interaction modes that occur at lower starting currents. At the same time, a high diffractive Q will limit the efficiency, η, as

$$\eta \propto \frac{Q_{ohm}}{Q_{diff} + Q_{ohm}}.$$ (2.96)

In a cylindrical cavity, the ohmic Q, Q_{ohm}, is approximately related to the cavity radius, r_0, and the skin depth, $\delta_s = (\pi f \mu_0 \sigma)^{-\frac{1}{2}}$, by

$$Q_{ohm} \propto \frac{r_0}{\delta_s},$$ (2.97)

where μ_0 is the permeability of free space and σ is the electrical conductivity. Nevertheless, gyrotrons operate with high efficiency well into the submillimeter wave regime.
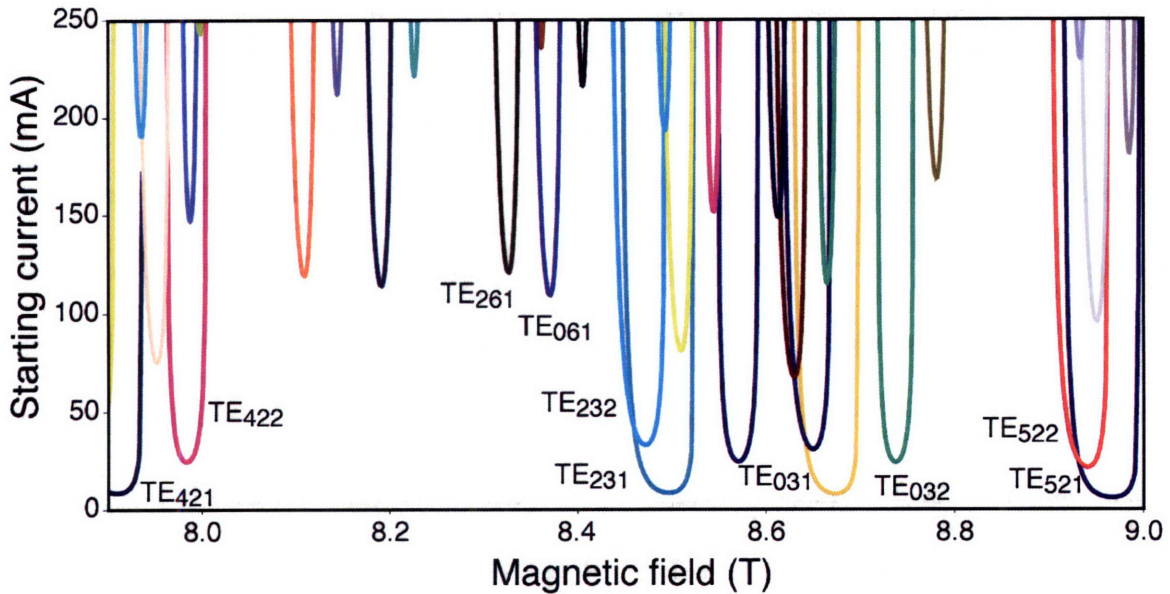
Figure 2-22: Mode plot (from linear theory [109]) for the cylindrical cavity employed in the 460 GHz gyrotron oscillator experiment. The second harmonic $TE_{0,6,1}$ mode is the desired mode of operation, and the $TE_{2,6,1}$ mode is the only other labeled second harmonic mode. Note that starting currents are higher for harmonic modes and those with higher axial numbers.

In summary, we have outlined the quantum mechanical and classical basis of electron cyclotron resonance and qualitatively discussed the principles which govern the operation

of CRM devices in the small amplitude limit. The design of actual microwave devices requires the careful consideration of non-linear effects which occur outside the limits assumed in the small amplitude theory. These effects are beyond the scope of this review, and the theory presently developed is sufficient to explain the design of a series of gyrotron oscillators (140–460 GHz) employed in DNP studies at MIT.

2.3.7   Gyrotron Engineering

The components of a typical gyrotron oscillator used for dynamic nuclear polarization studies at MIT are depicted in Figure 2-23. Here, the electron source is a magnetron injection gun, and the interaction circuit is always a tapered cylindrical cavity (though other designs are possible). In addition to these components, operation of the gyrotron in an ultrahigh vacuum for continuous duty cycles has required careful attention to electron beam collection, cooling, pumping efficiency, and control stability. The combination of these factors has resulted in the present dual-bore magnet design of Kreischer and co-workers [110][111], in which the microwave power is extracted in a Gaussian mode along an axis orthogonal to the direction of the electron beam propagation, while the electron beam is collected in a configuration that maintains continuous pumping efficiency in the region of the electron beam collector. The microwave power is monitored directly or indirectly through the electron beam current, and the electron gun heater is adjusted to keep it constant. It is transmitted by means of a smooth or corrugated waveguide and coupled optically to the NMR sample. A variety of ancillary control circuits are employed to guarantee the safe and unattended operation of the gyrotron for extended periods, which is a requirement for solid state NMR studies of biological systems. Finally, it is worth mentioning that what we will discuss here reflects

the current operating characteristics of MIT DNP gyrotrons; finding these operating conditions involves the experimental and theoretical exploration of many degrees of freedom, and the characteristics of the gyrotron during this "activation" phase improve with time.
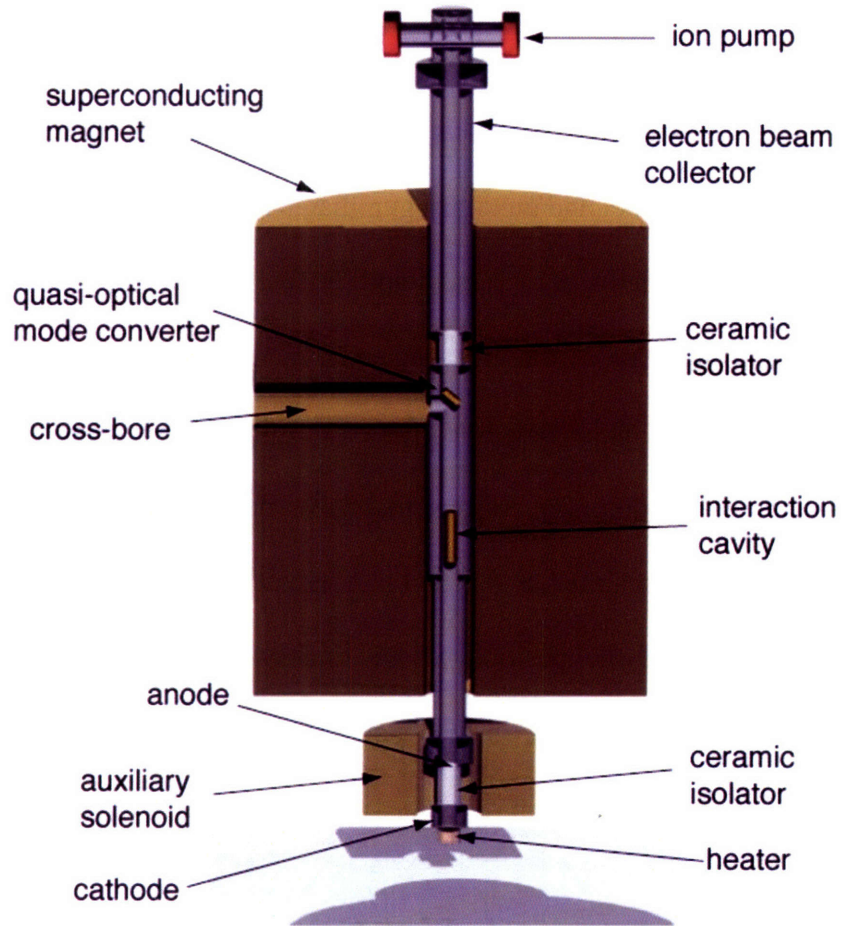
Figure 2-23: Pictorial cross-section of a typical gyrotron oscillator used for DNP.

2.3.8   Electron gun

The electron gun must produce an approximately monoenergetic beam of high energy electrons, and its characteristics influence all the operating parameters of the gyrotron. The gun is usually a magnetron injection gun (MIG), which is a thermionic device that

produces a hollow annular electron beam using a cylindrical cathode. Diode and triode MIG configurations have one or two anodes, respectively. When the temperature of the cathode is raised through the application of a small heating current, the electrons gain sufficient thermal energy to overcome the work function barrier. The cathode is biased with a high negative voltage relative to the anode, with the result that electrons ejected from the surface of the cathode are accelerated towards the anode at mildly relativistic velocities. At the same time, the electrons encounter the increasing axial magnetic field generated by the main magnet and auxiliary gun magnet; instead of impacting the anode, the electron beam is radially compressed and is free to propagate beyond the gun structure. The homogeneity of the electron beam is thereafter maintained due to the strong magnetic field, which also serves to convert most of the beam energy from axial to rotational degrees of freedom for reasons that have been previously discussed. The electron beam radius is minimal at the point of greatest magnetic field, B_0, which is arranged to coincide with the position of the microwave interaction structure. The minimal electron beam radius, r_{e0}, is then determined by the product of the cathode radius, r_K, and magnetic compression ratio,

$$r_{e0} = r_K \sqrt{\frac{B_K}{B_0}} \qquad (2.98)$$

where B_K is the cathode magnetic field. The nature of the electron beam is a critical variable in the operation of the gyro-device. Important metrics of electron beam quality include the α, which is the ratio of transverse to axial velocity, and the homogeneity of the electron velocity distribution. A large beam α is desirable, since it is only the rotational degrees of freedom which yield their energy to the microwave field, but it

should not be so large that the electrons do not have sufficient axial energy to propagate. In practical circuits, the electron gun is operated in a temperature-limited (saturated) emission regime. The beam current can be changed over a wide range by varying the temperature of the cathode. This feature allows for control of the microwave power independent of other variables of operation and is the principal mechanism by which output power is held constant in MIT DNP gyrotrons operating in continuous duty.

2.3.9 Interaction Cavity

The gyrotron interaction structure is the component in which rotational energy of the electron beam is converted to electromagnetic radiation. As such, the cavity must support one or more modes which are solutions to a wave equation for the electromagnetic field, subject to the appropriate boundary conditions. For a metallic cylindrical open resonator cavity [112], the principal boundary conditions are fixed by the cavity radius and nature of the input and output coupling, for which the most common configuration involves a downward taper at the input and an upward taper at the output.[13] This cavity configuration produces standing wave-like transverse electric (TE) modes whose electric and magnetic field components are characterized in the separable cylindrical solution space by a triplet of integers, $TE_{m,p,q}$, specifying their azimuthal, radial, and axial eigenvalues respectively. For example, the TE_{01q} modes have no azimuthal variations and one radial variation, and so resemble a hollow circle; as with all TE modes, the electric field remains transverse to the direction of propagation. Gyrotron cavities are generally overmoded, as the wave equation will have many TE-type solutions

---

[13] These boundary conditions are an evanescent wave at the input, propagating wave at the output, and vanishing tangential electric field at the cavity wall.

145

which fulfill the boundary conditions of the resonator. However, when operating near the cut-off of a desired TE mode, the gyrotron frequency depends very simply on the cavity radius and mode of operation, as

$$\omega \cong c\frac{v_{mp}}{r_0},$$

(2.99)

where v_{mp} is defined as in (2.95), and r_0 is the cavity radius.

Since the cavity cannot be made arbitrarily small to operate on the lowest order mode due to the thermal load of its interaction with a high energy electron beam, competition between parasitic modes and the design mode must be addressed explicitly in the design. Ideally, the electron beam should be placed at a position of maximum coupling to the electric field of the selected cavity mode in order to minimize the coupling to unwanted modes. In practice, however, the design of the cavity is a compromise involving ohmic losses in the cavity walls, mode competition, mode conversion, and starting current. This compromise is numerically addressed by solution of the axial wave equation [113],

$$\frac{d^2}{dz^2}E(z)+k_{\parallel}^2(z)E(z)=0,$$

(2.100)

for the RF field profile and the eigenfrequency, with the propagation factor

$$k_{\parallel}^2(z)=\left(\frac{\omega}{c}\right)^2-k_{\perp}^2(z)$$

(2.101)

subject to the appropriate boundary conditions for the electric field at the cavity inputs and walls. This treatment yields the diffractive Q as

$$Q_{\text{diff}}=\frac{\text{Re}(\omega)}{2\,\text{Im}(\omega)},$$

(2.102)

from which the efficiency and starting current for each mode can be estimated.

Several relevant conclusions follow from this analysis. First, since the mode plot of a typical resonator (*cf.* Fig. 2-22) is quite complicated, one might expect that the operating frequency can be effectively tuned simply by finding operating conditions for a series of modes which are distributed across the desired operating range [114]. However, since many parameters of operation, including the starting current, efficiency, magnetic field, and even the physical alignment of the resonator with respect to the electron beam, depend upon the choice of mode, this method of operation is inappropriate for DNP studies. A continuously tunable oscillator [88] has been designed based on mechanical modulation of a longitudinally split cavity during the experiment, but it remains to be seen if these approaches can be adapted to the requirements of DNP.

Second, it is clear that a gyrotron operating at the fundamental cyclotron resonance must produce a magnetic field which sets the electron cyclotron frequency very near to that of the microwave field. This implies that only second or higher harmonic designs will be practical at frequencies exceeding 500 GHz; indeed, though a 20 T magnet is commercially available, the prohibitive cost of such an instrument together with the desire for a general approach led to the design of a 460 GHz second harmonic gyrotron for MIT's high field DNP experiment. Operation at a higher harmonic mode further complicates the design when a conventional cylindrical cavity is used, because competition with fundamental modes must also be considered and avoided. Novel cavity designs based on analogs of optical photonic band-gap (PBG) structures [115] produce resolved, TE-like mode patterns, and it may be appropriate to consider them in future applications. Confocal cavities are another promising design, but as of this writing they

have not yet been successfully applied in higher harmonic gyrotron oscillators at MIT
[116].

2.3.10   Gyro-amplifier
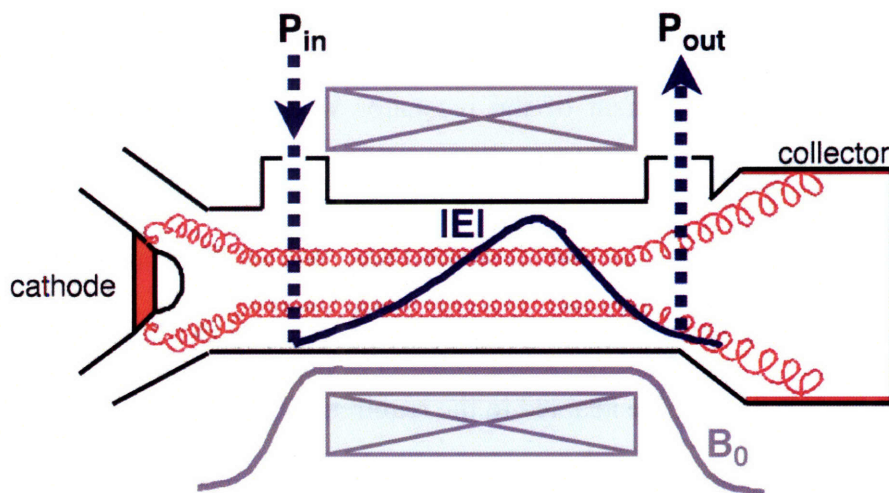
Figure 2-24: Cross-sectional schematic of a typical gyro-amplifier. In this design, the drive power is coupled into an input cavity and the amplified power is coupled out of a side cavity.

As we have mentioned previously, analogous considerations apply to the design of a gyrotron amplifier. In a gyro-amplifier, an additional drive input consisting of the signal to be amplified is coupled into an extended interaction region and allowed to modulate the electron beam. This requires either a physically longer interaction circuit (*e.g.* gyro-TWT) or one consisting of multiple cavities (*e.g.* gyro-klystron). In each case, the electron beam is involved in two sequential interactions: the first in which it takes energy from the input field, and a second in which it yields its rotational energy to the output field. Amplification is produced because the imprint of the first interaction modulates the output of the second. Gyrotron amplifiers can have much larger instantaneous and absolute bandwidth than gyrotron oscillators. As such, we anticipate that they will be extremely useful for time-domain DNP experiments based on analogs of Hartmann-Hahn

cross-polarization, and further that they will free the experiment from the requirement of a tunable static magnetic field. However, current gyro-amplifier designs will require a stable input drive signal source of approximately 100 mW to produce suitable output power in the 1–100 W range suitable for DNP studies. Such solid state and vacuum drive sources are not available above 140 GHz, nor are the switches and other components required to form a phase modulated network. Due to considerable academic and industrial interest in exploiting the radiation in the 0.3–10 THz regime for spectroscopy, film metrology, materials processing, remote sensing, and telecommunications, we believe that low power driver sources will be available in the future.

2.3.11   Microwave Extraction

The microwave field produced in the interaction cavity is rarely in an optimal form for transmission in a waveguide. As such, it is almost always necessary to transform the mode one or more times using waveguide or quasi-optical mode converters. The waveguide mode converter is usually a periodic structure; the effects of the periodicity in, for example, the radius of a waveguide are analyzed using a perturbation theoretical approach. The quasi-optical mode converter, by contrast, generally consists of a launcher and one or more focusing or correcting mirrors. It may be understood in terms of geometrical optics, but detailed designs require diffraction theory.

2.3.12   Quasi-optical mode converter

An elegant design of a quasi-optical mode converter consists of a step-cut waveguide antenna and a cylindrical parabolic mirror (*cf.* Fig. 2-25). This design is currently employed as an internal mode converter in both the MIT 250 GHz and 460 GHz gyrotron

experiments. For the appropriate slot length, the step-cut waveguide antenna, or the Vlasov-type launcher, radiates the TE_{0p} waveguide mode as a linearly polarized beam. The parabolic reflector then focuses the beam into a Gaussian shape.
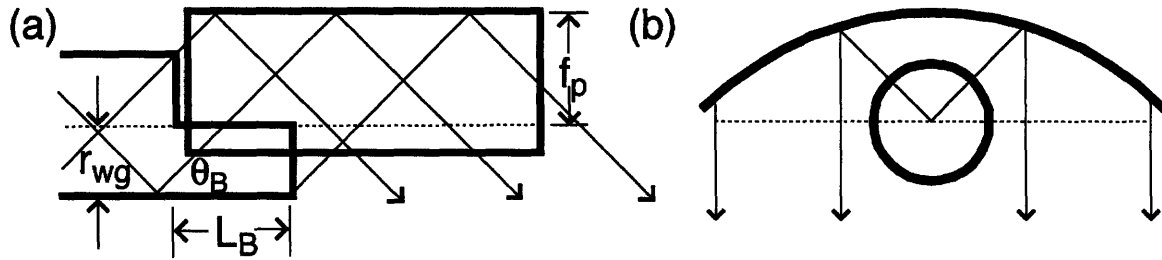
Figure 2-25: Sketch of the (a) side and (b) front view of a quasi-optical mode converter used in the 250 GHz and 460 GHz MIT DNP gyrotrons. Operation of the device is illustrated through geometric optics; test rays are launched from the slotted waveguide and then focused by a parabolic mirror. The slot length $L_B = 2r_{wg} \cot \theta_B$ is chosen such that the bounce angle $\theta_B = \sin^{-1}(k_\perp/k)$ is determined by the TE_{mp} waveguide mode, k is the wavenumber, and r_{wg} is the waveguide radius [117][118].

2.3.13 Waveguide mode converter

Efficient mode conversion can also occur in periodically perturbed waveguide structures [119]. In the case of a small perturbation, the wave equations remain cylindrically separable and a perturbation-theoretical treatment is sufficient. For example, to convert from the TE_{02} to the TE_{01} mode, only radial perturbations are needed, since the azimuthal mode number remains the same while the radial mode number is reduced. However, in order to achieve a TE_{01} to TE_{11} mode conversion, in which the azimuthal mode number is increased, the perturbations must have an angular component. A purely angular perturbation will not discriminate between modes which differ only in the radial direction. In general, a periodic repetition is therefore required to reinforce the desired mode. An example of a TE_{01} to TE_{11} mode converter operating on this principle

is shown in Figure 2-26. Due to its serpentine appearance, this device is colloquially referred to as a "snake" mode converter.
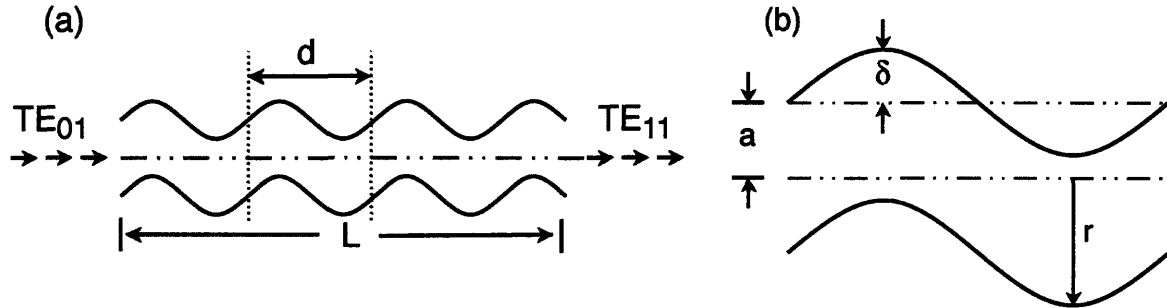
Figure 2-26: (a) Schematic of the TE_{01}- TE_{11} snake mode converter, where a is the waveguide radius, δ is the perturbation, $r(z) = a + \delta(z)$, d is a period, and L is the total length (b) close-up of one period. [120]

2.3.14 Output window

A variety of windows are employed in a typical installation to isolate different components of the DNP apparatus which would otherwise be linked through the microwave transmission system. They must be durable enough to handle high microwave powers and environmental exposure, including, in the case of a gyrotron window, ultrahigh vacuum conditions and, in the case of the probe window, cryogenic temperatures. The window must also transmit microwave power with minimal reflection and absorption. These criteria effectively limit the choice of window materials essentially to sapphire, quartz, diamond, and Teflon. For a material of known dielectric properties, transmission and reflection can be calculated according to simple Gaussian optical formulae at high frequencies. The thickness of the window is then chosen to optimize transmission by a quasi-optical model in which the window is regarded as a Fabry-Perot-type interferometer. The Fabry-Perot interferometer has a frequency-dependent transmission of power at normal incidence [121],

$$T = \left[1 + \frac{4R}{(1-R)^2} \sin^2 \left(\frac{2\pi d}{\lambda} \right) \right]^{-1} \qquad (2.103)$$

where R is the reflection coefficient given by $(n-1)^2/(n+1)^2$, n is the index of refraction, d is the thickness of the window, and λ is the wavelength in the medium or c/nf.

2.3.15 Electron Beam Collection and UHV

Only a fraction of the electron beam energy is transformed into that of the microwave field. The spent electron beam is therefore still energetic and must be kept away from fragile structures. At the same time, the beam must be collected in order to complete the high voltage circuit. Collection occurs because the electron beam expands as it enters the weakening stray field of the magnet and hence encounters the gyrotron tube wall. The mechanism of collection must take into account the thermal load of the interaction between the high energy electron beam and the wall, and also the need to maintain effective vacuum pumping efficiency in the region of the collector. In conventional gyrotron designs, the microwave power is extracted in a direction which is parallel to the direction of the electron beam. This implies that the linear distance between the cavity and the microwave output window must be very large in order to guarantee that the electron beam has been efficiently collected before the microwave beam encounters the fragile window. A consequence of this design is that the pumping efficiency in the neighborhood of the cavity and collector is very poor, and hence continuous duty operation is difficult.

The 250 GHz gyrotron oscillator designed by Kreischer and co-workers for DNP studies at 380 MHz overcomes these difficulties. Here, the microwave beam is extracted in a direction orthogonal to the electron beam by means of a reflector situated outside of

the electron beam path. The electron beam then immediately enters the stray field of the superconducting magnet and is efficiently collected in a short, water-cooled collector region. Two chemi-absorptive ion-pumps are located at a short linear distance from both the cavity and this collector region, and so very high pumping efficiency is maintained under all operating conditions. Indeed, a pressure less than 1×10^{-8} Torr can be maintained even during periods of CW operation lasting up to 120 hours. This innovation has therefore been critical to the successful application of gyrotron oscillators for DNP studies.

2.3.16 Magnetic Field

The gyrotron magnet must be chosen according to three considerations: first, the magnitude of the magnetic field must be such that the electron Larmor frequency is nearly equal to the desired microwave frequency or one of its sub-harmonics. For high frequency gyrotrons, this requires the use of a superconducting magnet. Second, the homogeneous region of the magnetic field must extend only to the dimensions of the interaction structure. Third, the field must become inhomogeneous in a controlled way in either direction from the position of the microwave cavity. In the input direction, it is the axial compression of the electron beam by the increasing magnetic field which is responsible for the successful operation of the electron gun; in the output direction, the distance over which the magnetic field becomes inhomogeneous determines the properties of the electron beam collector. For MIT gyrotron designs, in which the microwave power is extracted along an orthogonal axis, the magnet must have a second half-bore which lies slightly above the region of the magnet in which the cavity is situated. Finally, the field homogeneity and drift requirements are comparable to those

imposed by an NMR experiment. Just as in an NMR magnet, typical gyrotrons have auxiliary room temperature shimming solenoids which serve to tune the magnetic field in the region of the electron gun.

2.3.17 Microwave Waveguide Systems

The coupling of high power and high frequency microwave radiation to a sample is similar in principle but different in practice from the related problem of transmitting radiofrequency power to a load. In the latter case, even flexible coaxial transmission line can be used up to 30 GHz with relatively low loss; in the millimeter wave regime, however, propagation of power over a distance can only occur through guided structures. At high microwave frequencies (250 GHz and above), it is often possible to rely on quasi-optical radiation modes either in free space or through confined structures such as dielectric or corrugated waveguides which support them. Quasi-optical transmission has the additional advantage that microwave power can be manipulated using Gaussian-type optics such as focusing or reflecting mirrors and even lenses. Indeed, the use of hybrid optical and waveguide microwave transmission circuits has greatly simplified the design of magic angle spinning DNP probes at high microwave frequencies. As has been previously discussed, the gyrotron cavity output field is typically not in a Gaussian mode, which means that internal or external mode conversion is usually required. The design of an effective microwave transmission circuit will therefore require consideration of mode conversion efficiency, alignment tolerances, and effective coupling to a sample whose size is generally comparable to the wavelength. For reasons that we will now discuss, all these factors also argue in favor of a Gaussian transmission mode.

2.3.18 Attenuation in Cylindrical Waveguide

A useful waveguide must deliver power from source to load with minimal attenuation. If the waveguide is further coupled to an optical transmission section, then it must be free from mode conversion effects which would otherwise transform an initially quasi-Gaussian radiation field into a mixture of modes that would not propagate in the desired direction in free space. The theoretical loss of any straight, overmoded waveguide is almost completely ohmic. In experimental circumstances, power loss occurs through errors in the mechanism of input and output coupling, diffraction in components such as miter bends, and misalignment.

Specifically, power flow in a simple waveguide is of the form

$$P_T = P_0 e^{-2\alpha z}, \tag{2.104}$$

where α is an attenuation coefficient. On grounds of energy conservation, the rate of decrease of P_T must equal the time average power loss, P_L, per unit length,

$$P_L = -\frac{dP_T}{dz} = 2\alpha P_T. \tag{2.105}$$

The attenuation constant is defined as [122]

$$\alpha = \frac{\text{power lost per unit length}}{2(\text{power transmitted})} = \frac{P_L}{2P_T}$$

$$= \frac{\frac{1}{2} R_s \int_s |\mathbf{H}_{tan}|^2 \, ds}{2 \left[\frac{1}{2} \iint_A \mathrm{Re}\left(\mathbf{E} \times \mathbf{H}^* \right) \cdot \hat{z} \, dA \right]}, \tag{2.106}$$

where the surface resistivity, R_s, is given by $R_s = 1/\sigma \delta_s$, $\mathbf{H}_{tan}$ is the tangential component of the magnetic field at the surface, s is the waveguide contour, and A is the area

transverse to z, the waveguide axis. From the form of (2.106), it is immediately apparent that the loss in a waveguide is proportional to the square of the tangential component of the magnetic field at the waveguide wall. After all, it is only through the interaction with the waveguide wall that the microwave field can lose energy in this analysis. According to this argument, waveguide modes which concentrate power away from the walls will suffer less from ohmic losses than those which do not. Consider a hypothetical Gaussian mode: radiation in this mode is concentrated in the center of the waveguide and falls smoothly to zero in the radial direction away from it, and so it will have the lowest possible attenuation. This can be derived from a straightforward evaluation of (2.106) according to solutions for the field presented in Table 2.1, but we will only state the results here.

For TE modes, the attenuation constant is given by [122]:

$$\alpha = \frac{R_s}{\eta_0} \frac{v_{mp}^2/a^2 k^2 + m^2/v_{mp}^2 - m^2}{a\sqrt{1 - v_{mp}^2/a^2 k^2}}.$$

(2.107)

For TM modes the corresponding expression yields:

$$\alpha = \frac{R_s}{a\eta_0} \frac{1}{\sqrt{1 - v_{mp}^2/a^2 k^2}}.$$

(2.108)

where η_0 is the characteristic impedance ($\sim$377 Ω), the wavenumber is $k = \omega/c$, the cutoff wavenumber is $k_c = v_{mp}/a$, v_{mp} for the TE and TM fields is the pth zero of J'_m and J_m, respectively, and a is the waveguide radius.

Table 2.1: TE and TM fields in cylindrical smooth wall metallic waveguides [122]

	TE_{mp}	TM_{mp}
H_z	$k_c^2 J_m(k_c r)\cos m\phi$	0
E_z	0	$k_c^2 J_m(k_c r)\cos m\phi$
H_r	$-\gamma_{mp} k_c J'_m(k_c r)\cos m\phi$	$-\dfrac{ikm}{r}\eta_0 J_m(k_c r)\sin m\phi$
H_ϕ	$\gamma_{mp}\dfrac{m}{r} J_m(k_c r)\sin m\phi$	$-\dfrac{ikk_c}{\eta_0} J'_m(k_c r)\cos m\phi$
E_r	$ik\eta_0\dfrac{m}{r} J_m(k_c r)\sin m\phi$	$-\gamma_{mp} k_c J'_m(k_c r)\cos m\phi$
E_ϕ	$ik\eta_0 k_c J'_m(k_c r)\cos m\phi$	$\gamma_{mp}\dfrac{m}{r} J_m(k_c r)\sin m\phi$

Solutions for the TE_{11} and TM_{11} modes are presented in Table 2.2 and compared to an HE_{11} quasi-Gaussian mode, which is found to have lower loss. In actuality, a smooth-walled metallic waveguide cannot support a Gaussian mode. Instead, solutions to the wave equation subject to Gaussian-like profiles give rise to complicated mode distributions which are approximate linear combinations of TE and TM-like modes which propagate in the z direction. Since the attenuation of TE and TM modes differ, this implies that the true mode composition will depend on the length of the waveguide. If these effects are considered, the amount of power which can be transmitted in a Gaussian-like mode through a smooth wall waveguide will depend periodically on the length of the waveguide.

Table 2.2: Attenuation of modes in 1" OHFC copper cylindrical waveguide at 250 GHz

	TE_{11}	TM_{11}	HE_{11}
Waveguide type	Smooth	Smooth	Corrugated
v_{mp}	1.841	3.8317	2.405
α [nepers/m]	1.4×10^{-2}	3.3×10^{-2}	2.1×10^{-5}
α [dB/m]	1.2×10^{-1}	2.9×10^{-1}	1.9×10^{-4}

Dielectric and corrugated waveguides, by contrast, directly support the quasi-Gaussian HE_{11} mode and thus do not suffer from these limitations. Waveguide fields can be

viewed as superpositions of plane waves propagating at an angle ϕ relative to the waveguide axis. The electric and magnetic field components along the waveguide axis (E_z and H_z) are proportional to $\sin \phi$, which is in turn proportional to λ/a. It follows then that E_z and H_z become very small at high frequencies or large diameters. It is not correct to conclude, however, that the diameter of the waveguide can be made arbitrarily large. As we will show shortly, the diameter of the waveguide must be chosen carefully to guarantee loss-free coupling of radiation at the input end.

Fortunately, the tangential magnetic field can be eliminated by periodic linear or helical corrugation of the waveguide walls. Here, wall corrugations act like shorted radial transmission lines for a corrugation depth of $\lambda/4$, provided that the spacing between them is a fraction of the wavelength. Solutions to the wave equation subject to boundary conditions for a corrugated surface then give rise to quasi-Gaussian HE_{11}-type modes, which have very low fields at the waveguide walls and correspondingly low attenuation. The attenuation of the HE_{11} mode in corrugated waveguide of radius a is given by [123]

$$\alpha = \frac{0.00767 R_s}{k^2 a^3}.$$ (2.109)

The optimal radius for such a waveguide for coupling a given free-space Gaussian beam can be determined by calculating the efficiency of coupling the Gaussian beam, E_G, into the cylindrical waveguide by evaluating a simple geometrical overlap integral,

$$\eta = \frac{\left(\int_A E_{wg} E_G \, dA \right)^2}{\int_{-\infty}^{\infty} E_G^2 \, dA \int_A E_{wg}^2 \, dA},$$ (2.110)

where E_{wg} is the waveguide field and, for the corrugated case, $E_{wg} = E_{HE_{11}}$. The coupling efficiency is optimized (~98%) for a Gaussian beam with a waist that is 0.64 of the

158

waveguide radius, where the Gaussian beam waist is defined as the radius at which the peak intensity has dropped by $1/e^2$.

As a practical matter, corrugated waveguides can be constructed which are nearly free from attenuation even up to very high frequencies. The predominant sources of power loss are then misalignment or imperfection in other components of the transmission circuit.

2.3.19 Microwave Power and Mode Pattern Measurements

In order to align and calibrate microwave structures, reliable measurements must be made not only of the power of the radiation field, but also of its spatial variation. Even in the absence of direct information about the phase, such measurements can be combined with various reconstruction techniques to yield reliable estimates of the mode content of a microwave field. Absolute power measurements are generally made with a laser calorimeter; though the calorimeter absorption in the millimeter and sub-millimeter wave regime is limited, it is enhanced by the application of a microwave-absorbing paint, and the measured powers are corrected to account for its diminished absorbance. Radiation pattern measurements are made by automatic scans with a microwave diode detector through a lattice of points in three dimensional space [124]. Since the response of the diode is inherently non-linear, relative power is determined at each point by the automatic adjustment of a motorized attenuator to maintain a constant detector signal level. The degree of attenuation required is then a measure of the microwave power at that point. Sensitivity in such measurements can be improved by phase-sensitive lock-in detection, either by pulsing of the microwave source or by modulation of the microwave beam using a rotating blade ("chopper"). A scan of the TE_{01}-like mode pattern of the MIT 140

GHz gyrotron obtained using this technique is shown in Figure 2-27. As an alternative to such time-consuming schemes, an infrared camera can be used to image an irradiated substrate, albeit at a reduced signal to noise level. The spatial variation of IR irradiance across this substrate can then be related to temperature, and hence to the rate of energy absorption from the microwave beam.
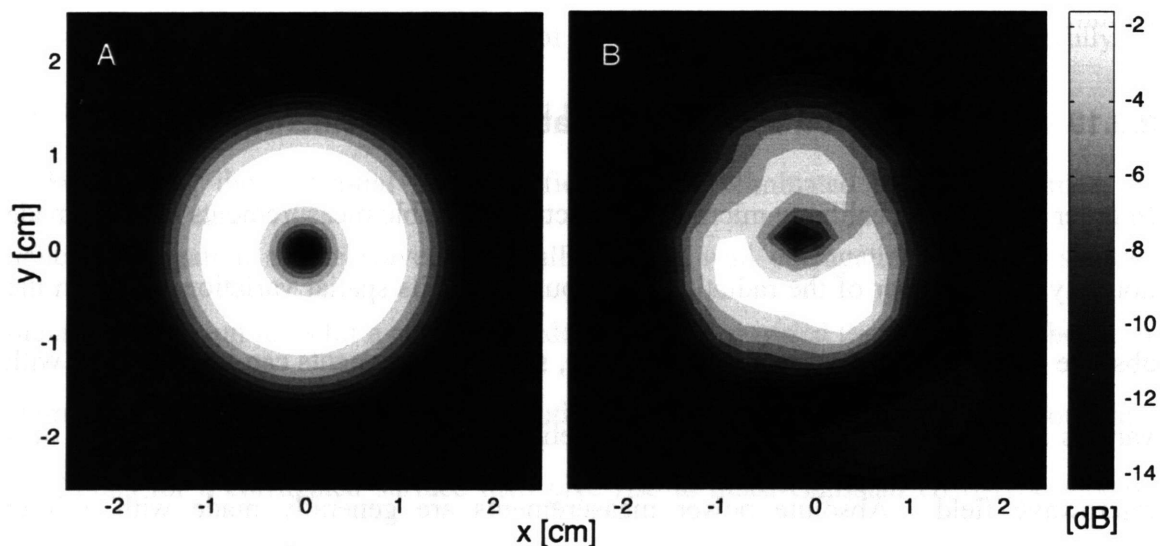
Figure 2-27: (a) E-field of theoretical TE_{01} mode pattern (b) a TE_{01}-like mode pattern radiated 5.08 cm from the output of the 140 GHz gyrotron oscillator and mapped using the automatic diode-detection scanner. Adapted from [125].

For the case of Gaussian beams, such radiation patterns can be readily interpreted in terms of simple geometric or Gaussian optics. However, the most general interpretation requires elaborate phase retrieval algorithms, some of which are described in [126][127]. In both cases, the result of such an analysis is a summation of radiation modes with appropriate phases and weights which give rise to the observed radiation pattern.

2.3.20 Gyrotron Control Systems

The application of dynamic nuclear polarization to quantitative measurements of internuclear distances and torsion angles requires reference stability of the DNP/MAS

signal of at least a few percent. A number of experimental variables can influence the stability of these experiments, but all data indicate that the instability is completely correlated with variations in the output power of the gyrotron and temperature variability in the sample chamber. At the same time, the gyrotron depends on a number of relatively complex systems for its safe operation; these include high voltage and potentially high current power supplies, ultrahigh vacuum systems, and water or air cooling. Even when these components are operating appropriately, the gyrotron can enter an unsafe mode of operation if its adjustable parameters fall outside safe limits. These parameters include, for example, the electron beam current and voltage, microwave output power, and, indirectly, the degree to which the beam is inappropriately intercepted by regions other than the collector. The control system must therefore automate the initialization, allow safe shutdown, and be capable of stable operation of the gyrotron over extended periods of, in the case of DNP studies, largely unattended operation.

In the case of MIT's 250 GHz and 460 GHz gyrotron oscillators, these objectives have been accomplished by a hybrid control system consisting of computer control of all power supplies and auxiliary systems involved with the gyrotron operation, together with safety interlocks that are electromechanical in nature and therefore independent of computer control. In addition to digital feedback from attached controlled devices, inputs to the control system include signals which are correlated to the collector current, body current (*i.e.* fraction of the electron beam current which does not reach the collector), pressure, microwave output power, thermal loads on critical components, and environmental temperature and humidity monitors. In the current implementation, initialization of the gyrotron is entirely automated. After emission commences, the

electron gun heater temperature is controlled to maintain a constant electron beam current, which in turn maintains a constant microwave power in the region of operation.

In an alternate mode of operation, the microwave power is directly monitored through a quasi-optical directional coupler and this is used as a control signal. Critical metrics of the tube condition during sustained operation include the pressure, efficiency, and thermal loads. If any of these parameters exceed safe limits or if other catastrophic failure occurs, the control system is capable of automatic and safe shutdown of the gyrotron. In practice, the 250 GHz gyrotron has operated in continuous duty for periods of up to 120 hours, during which time the tube pressure reaches a steady state and no deterioration of the microwave beam parameters has been observed. As an example, we show the stability of the gyrotron pressure and power in Figure 2-28 during sustained CW operation.
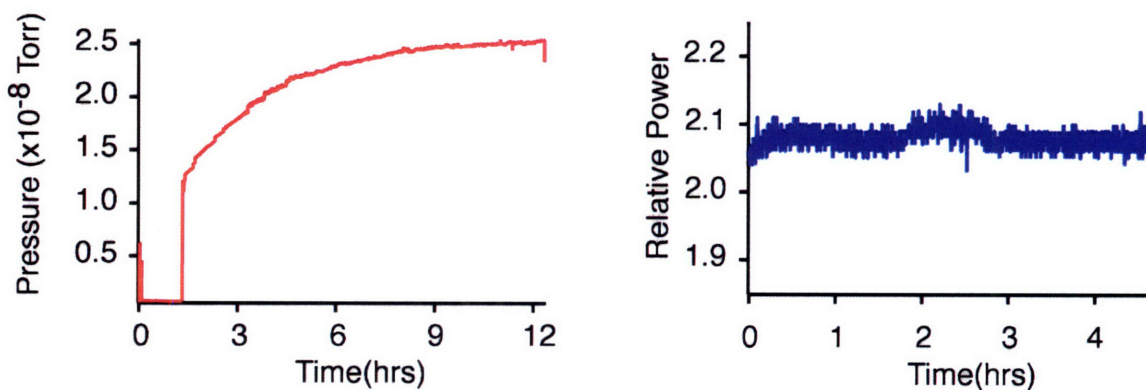
Figure 2-28: Stability of gyrotron pressure [left] and output power [right] during sustained CW operation.

2.3.21 Gyrotrons used in dynamic nuclear polarization

The previous discussion of gyrotron engineering principles is largely based on the design and successful operation of gyrotron oscillators for DNP studies at MIT; another product

of these studies is a gyrotron amplifier which is currently in an initial design phase. The operating characteristics of these gyrotrons are summarized in Table 2.3.

Table 2.3: Operating and design characteristics of MIT DNP gyrotrons

	140 GHz oscillator	250 GHz oscillator	460 GHz oscillator design	140 GHz amplifier design
Frequency (GHz)	140	250	460	140
Harmonic	1	1	2	1
Power – average (W)	10	25	50	100
Power – peak (W)	10	100	50	100
Gain (dB)	–	–	–	40
Bandwidth	–	150 kHz	–	>1 GHz
Pulse length	2 min.	CW	CW	2 ns
Repetition rate (kHz)	–	–	–	1
Duty factor	0.5	1	1	1
Mode	TE_{03}	TE_{03}	TE_{06}	–
Voltage (kV)	14	12	12	12
Magnetic field (T)	5	9	8.2	5

2.3.22   140 GHz gyrotron oscillator

The 140 GHz gyrotron oscillator (Fig. 2-30) is a first generation design capable of operating in long pulse (~60–120 s) operation for duty cycles approaching 50%. Internally, the gyrotron produces TE_{03} mode radiation which is converted to TE_{02} and then to TE_{01}, which is launched (cf. Fig. 2-29); an external snake-type mode converter (Fig. 2-26) is then used to produce TE_{11}-mode radiation, which is transmitted through a smooth-wall metallic waveguide structure. After a series of conversion steps, radiation reaches the sample eventually in fundamental mode waveguide.

The 140 GHz gyrotron oscillator has operated reliably in a variety of DNP experiments. However, the recent requirement of continuous duty (CW) operation for MAS/DNP experiments has suggested several design modifications which have been incorporated in a subsequent 250 GHz gyrotron oscillator. The principal shortcoming of

the 140 GHz design with respect to CW operation is the largely linear topology of the microwave tube, which results in low pumping efficiency. Since the collector region occurs before the radiation is extracted and at a large distance from the ion pumps, local increases in pressure appear to limit device operation. The device is therefore operated in a quasi-continuous mode involving pulses of 30-60 seconds at duty cycles approaching 50–60%.
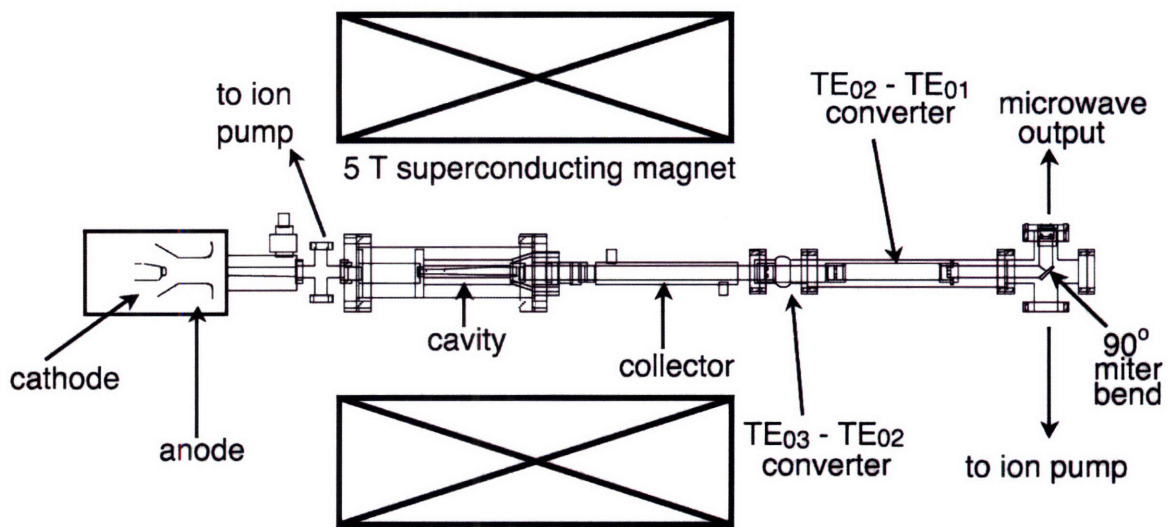
Figure 2-29: Cross-sectional schematic of the MIT 140 GHz DNP gyrotron oscillator.
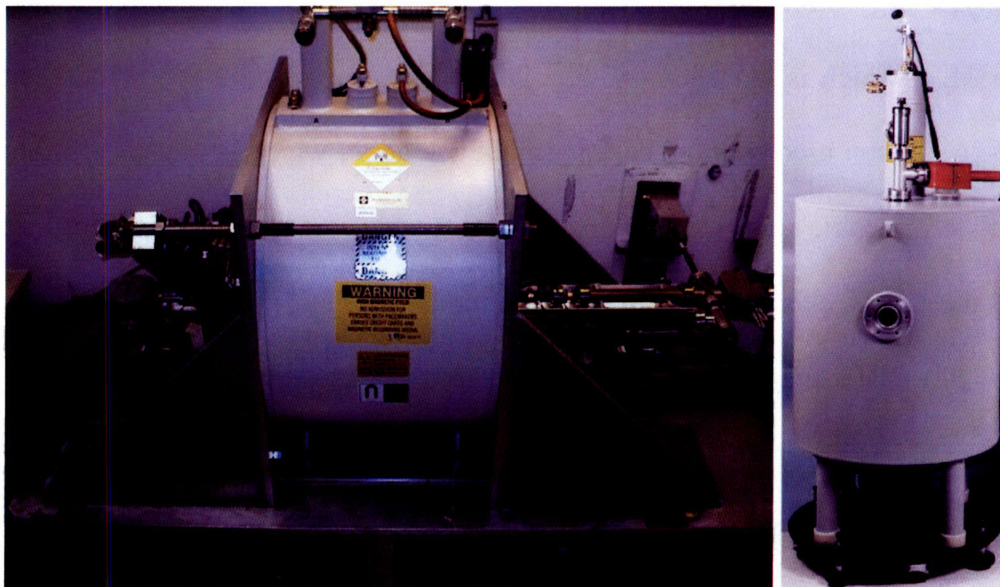
Figure 2-30: Photographs of the MIT 140 GHz [left] and 250 GHz DNP [right] gyrotron oscillators.

2.3.23   250 GHz gyrotron oscillator

In the period 1997-2000, Kreischer and co-workers designed and constructed a novel gyrotron oscillator for use in dynamic nuclear polarization studies [110][111]. This gyrotron operates at 250 GHz with a continuous duty cycle and peak output powers of 100 W. In conjunction with a control system incorporating various safety interlocks as has been previously described, this system has operated continuously for periods of up to 120 hours. Principal features of this design are depicted in Figures 2-23 and 2-30. These include a novel cross-bore topology in which the microwave power is extracted along an axis orthogonal to the electron beam propagation and prior to the electron beam collection. This allows for the location of fragile microwave circuits, such as the optical window, far from the energetic electron beam. At the same time, the beam can be collected in a compact, water-cooled collection region which is situated in a region of maximum pumping efficiency. As a result, the gyrotron is physically more compact and capable of higher duty cycle operation than its 140 GHz predecessor. Finally, the microwave transmission circuit is simpler: a single, quasi-optical internal mode converter produces a Gaussian microwave beam which can then be directly coupled to an overmoded smooth or corrugated waveguide structure.

2.3.24   Design of a 460 GHz gyrotron oscillator

The 460 GHz gyrotron oscillator design [125][128] is based largely on the previous 250 GHz gyrotron oscillator, which is in active use. A fundamental point of difference is that this gyrotron will operate at the second harmonic of cyclotron resonance, which has involved modifications in nearly all operating components and parameters. The gyrotron will operate in the TE_{06} mode; like the 250 GHz oscillator, an internal mode converter

will produce a Gaussian mode that will be coupled directly to a corrugated waveguide transmission system. Design parameters are listed in Table 2.3, and the characteristics of the interaction circuit have been previously addressed (*cf.* Fig. 2-22). More recent results from this gyrotron are presented in later chapters of this thesis.
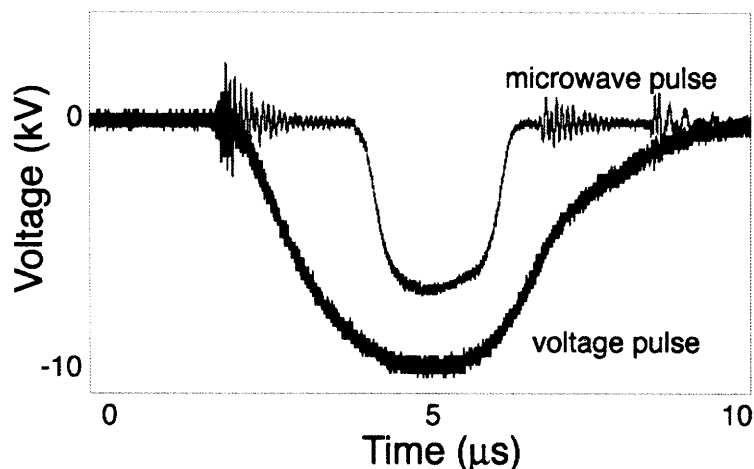
Figure 2-31: Short pulse operation of 460 GHz gyrotron in a fundamental mode.

2.3.25   Future Directions

A critical experimental deficit arises from the lack of coherent phase and frequency-switched radiation at submillimeter wave frequencies. In the context of DNP, it prevents the use of transient electron-nuclear cross-polarization techniques which do not rely on non-secular elements of the hyperfine Hamiltonian. A gyro-amplifier can satisfy this requirement. Due to its large intrinsic bandwidth, it will also be possible to tune the gyro-amplifier carrier frequency to optimize the DNP enhancement, a task which is currently accomplished by sweeping the static magnetic field. We plan to design and build a gyro-amplifier for DNP studies at 140 GHz (211 MHz ^{1}H). Preliminary parameters of this design are described in Table 2.3. Given the present lack of low power driver sources above 140 GHz, a complementary approach involves the design of a 330

GHz tunable gyrotron oscillator for DNP experiments at 500 MHz (^{1}H). This will not produce pulsed microwave radiation, but it will allow the DNP experiment to be performed with NMR magnets that do not incorporate sweep coils for large adjustments to the magnetic field.

2.4 Magic Angle Spinning

The routine incorporation of DNP into magic angle spinning (MAS) experiments introduces new challenges for probe design, as it becomes necessary to provide fast sample spinning at cryogenic temperatures along with high power RF irradiation at two or three frequencies and microwave irradiation near the electron Larmor frequency. At cryogenic temperatures, it is no longer possible to use room temperature air to drive pneumatic rotation of the sample, and instead cooled nitrogen or helium gas must be used. The MAS frequency and the temperature of the gas, and hence that of the sample, must be tightly regulated if quantitative NMR experiments are to be recorded. Finally, experiments in photoactive proteins such as bacteriorhodopsin require light excitation of the sample. Here, we briefly describe the 380 MHz Low Temperature MAS system developed for DNP experiments at 250 GHz. A complete description will be provided in a future publication.

2.4.1 Multiply Tuned Transmission Line DNP/MAS Probes

At 380 MHz / 250 GHz, MAS/DNP experiments are conducted with a remotely tuned probe which incorporates an air-dielectric coaxial transmission line [129]. The transmission line outer conductor is made from stainless steel to minimize thermal conduction, but is silver plated for improved electrical efficiency; a gold flash is applied to resist corrosion. The inner conductor has been assembled in several sections: nearest

the base of the probe, there is a stainless steel section, followed by a copper section in the region of the probe head whose purpose is to minimize the number of potentially ferromagnetic components near the coil. The coil is contained in a modified Varian, 4 mm stator. The probe is currently triply tuned for ^{1}H (380 MHz), ^{13}C (95 MHz) and ^{15}N (38 MHz) frequencies; the ^{13}C channel meets the main transmission line at a ^{1}H impedance node through a rigid coaxial line, the length of which is chosen to provide an inductive impedance in a convenient range to allow capacitive tuning and matching at the ^{13}C frequency. This probe design isolates the tuning and matching components of the probe from the cryogenic temperatures encountered at the sample coil. Further, with careful tuning of the electrical lengths, it provides greater than -30 dB isolation between all channels.
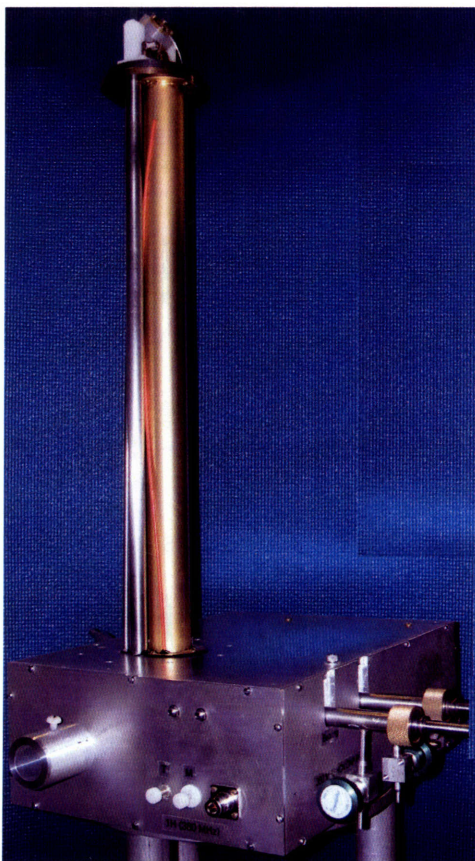
Figure 2-32: Photograph of assembled 250 GHz MAS probe with probe cap and dewar removed.
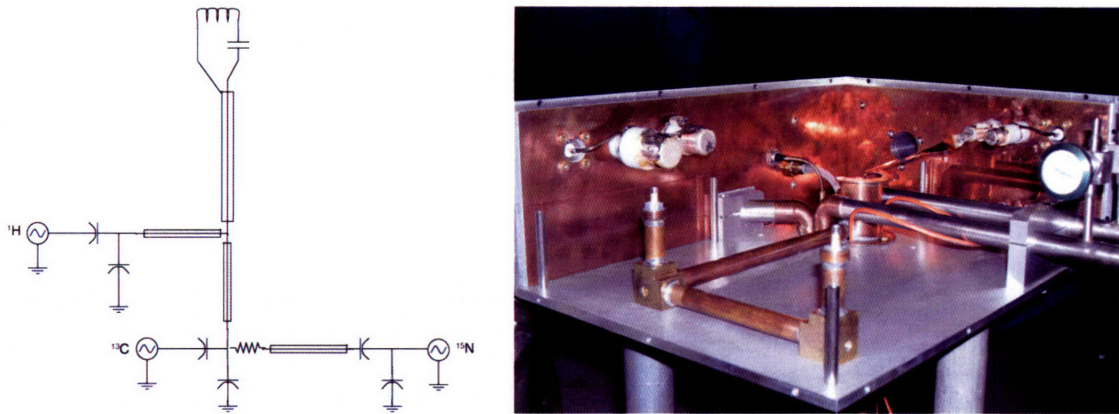
Figure 2-33: Probe schematic (left) and disassembled probe base showing transmission line elements which produce isolation between each channel.

Microwave power coupling is accomplished by a entirely quasi-optical transmission system. The transmitted microwaves reach the probe from the gyrotron through a corrugated HE_{11}-mode waveguide. At the base of the probe (Fig. 2-34), power is launched in a Gaussian mode, where it is focused by a parabolic reflection mirror and then steered to the RF center conductor by means of a flat mirror. The inner conductor of the RF transmission line also serves as a corrugated HE_{11}-mode waveguide for 250 GHz microwave radiation. Power reaches the sample after a miter bend (Fig. 2-34) which incorporates a microwave window made from a Teflon membrane whose thickness was chosen according to considerations in (2.103).

Next, cryogenic operation is achieved by cooling of both the drive and bearing gas. The cryogenic components of the probe itself are kept in a vacuum dewar, and the drive, bearing, and gas exhaust lines are vacuum jacketed. The vertical sections of the cold gas transfer lines enter the probe head in a region close to the coil. To minimize lineshape artifacts due to magnetic susceptibility, ferromagnetic contamination of the stainless steel, or work-induced ferromagnetism in the metal, these sections were constructed from composite fiberglass (G10) tubing. Insulation surrounds the probe components to

minimize convective coupling between the cold probe can and the warm probe base. During normal operation, the probe base remains near room temperature and the tuning is indefinitely stable.
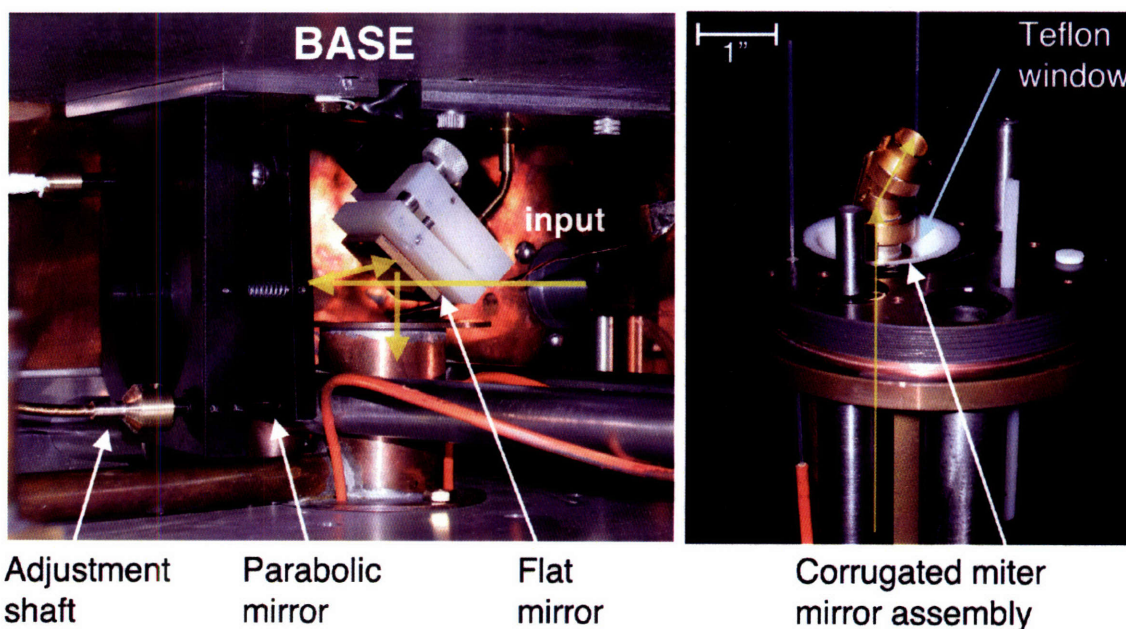
Figure 2-34: Photograph of the 250 GHz/380 MHz MAS probe. [left] In the base of the probe, the microwave beam enters through waveguide on the right-hand side. It is then focused by a concave mirror and steered into the vertical center conductor of the RF transmission line, which also serves as a waveguide. [right] The microwave beam reaches the sample through a corrugated miter bend at the complement of the magic angle. The sample is housed in a sapphire rotor, and no resonant cavity is used.
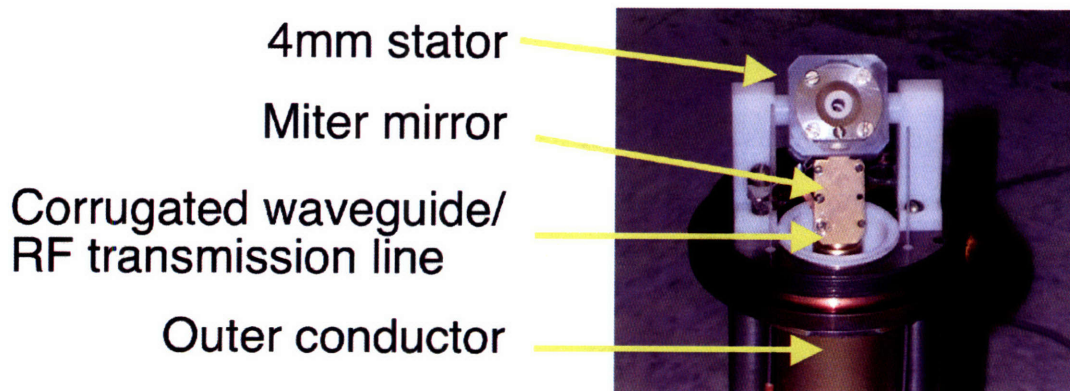
Figure 2-35: Photograph of the 250 GHz/380 MHz DNP probe which illustrates coupling of the microwave beam to the stator.

As mentioned previously, one of the initial applications of DNP involves the study of trapped photocycle intermediates of bacteriorhodopsin, as will be detailed elsewhere in this thesis. These experiments require cryogenic operation both to trap photocycle intermediates and for DNP; further, these intermediates are produced by irradiation of the sample at various visible wavelengths. Because the photointermediates decay rapidly in some cases, it is desirable to produce them *in situ*, which we accomplish by delivering laser light directly to the spinning sample through a multimode delivery system, illustrated in Figure 2-36. Variable wavelength light is produced using a dye laser which is pumped by a DPSS laser, as shown in Figure 2-37.
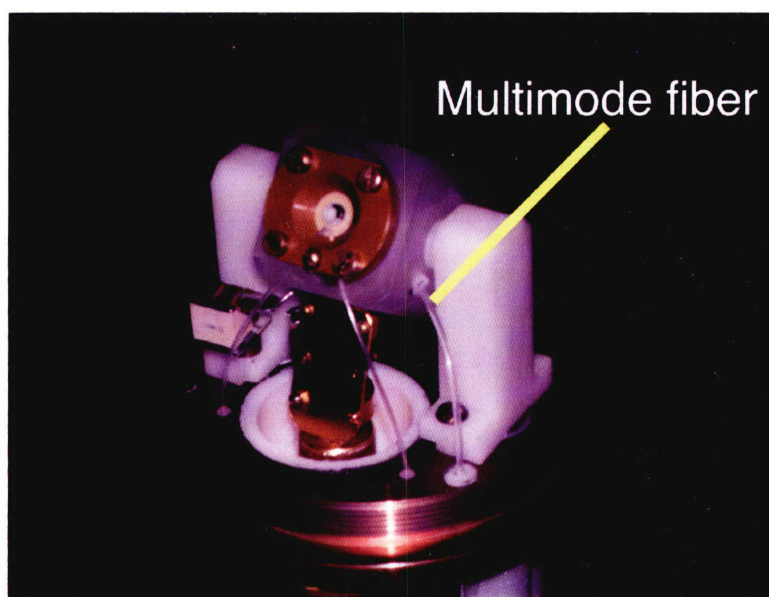
Figure 2-36: Photograph of the 250 GHz DNP probe head which illustrates coupling of laser light to the spinning sample through a multimode optical fiber.

Figure 2-37: System employed for variable-wavelength light irradiation of samples. It consists of a Coherent Verdi DPSS laser (6W, 532 nm) which pumps a Coherent 599 dye laser to produce longer wavelength red light.

2.4.2   Cryogenic MAS Control System

Since low temperature operation is achieved by cooling of the drive and bearing gas, cryogenic systems for MAS/DNP experiments must regulate both the gas pressure and temperature with sample temperature and spinning frequency being the critical control inputs. In the 90 K temperature range, the DNP enhancement is extremely sensitive to temperature variations, and so the temperature must be controlled to within 0.5 K.   In Figure 2-38, we illustrate, in schematic form, the control system which has allowed us to meet these tolerances for extended experiments. Here, spinning is accomplished by dry nitrogen gas which originates from vaporized liquid nitrogen. The drive and bearing gas streams are then taken through a heat exchanger which is immersed in liquid nitrogen. Prior to the heat exchange process, the drive and bearing gas pressures are independently controlled by a pneumatic controller; after the heat exchange process, cold drive and

bearing gases travel to the probe through transfer lines which incorporate integral 50 W heaters and temperature sensors. Thus, both the temperature and the pressure can be controlled for the drive and bearing gas lines independently. Since changes in the gas temperature can cause fluctuations in gas volume and hence perturb the MAS frequency, both the air pressure and temperature are controlled in software using a model which empirically accounts for the effects of this interplay. This approach has allowed us to conduct experiments of indefinite length.
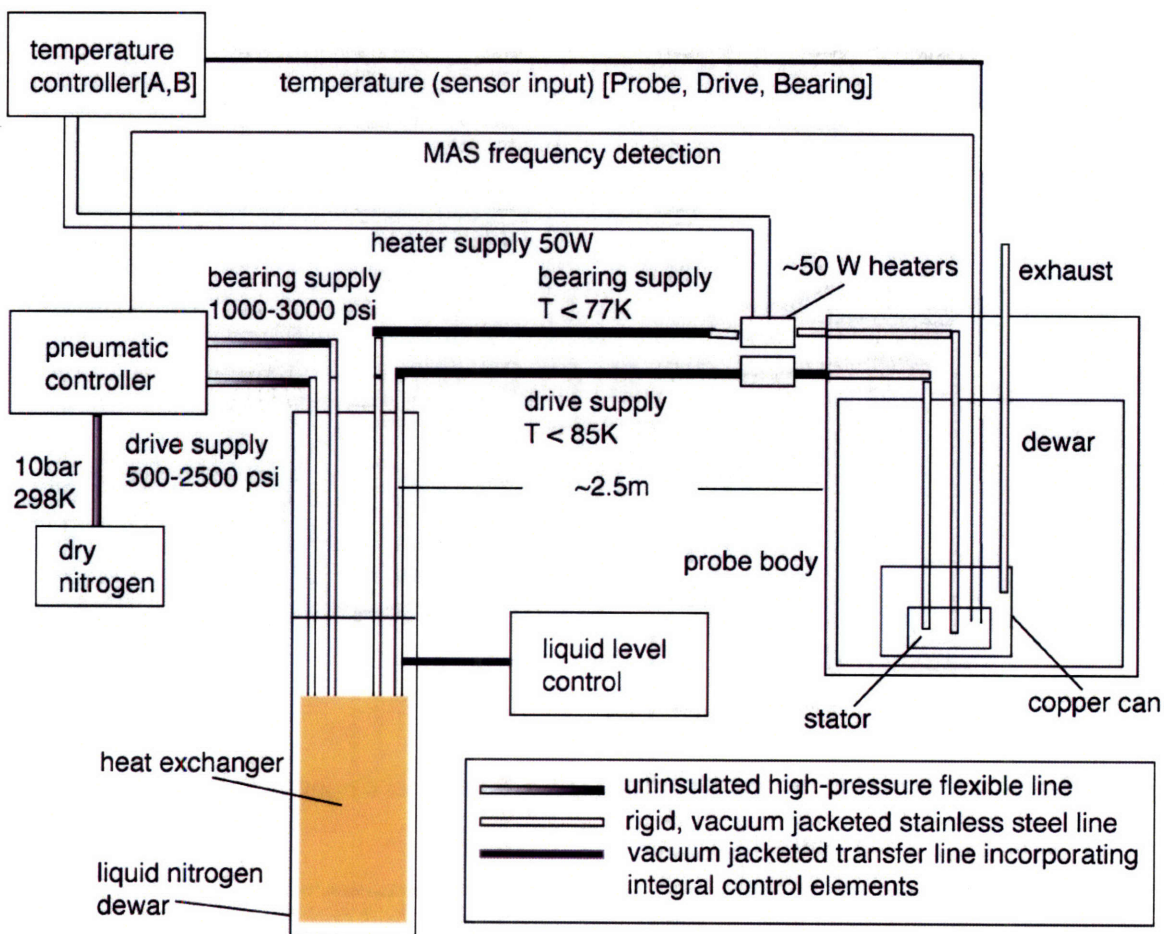
Figure 2-38: Cryogenic and MAS control system for 380 MHz/ 250 GHz DNP experiment at MIT.

integral heaters

heat exchanger
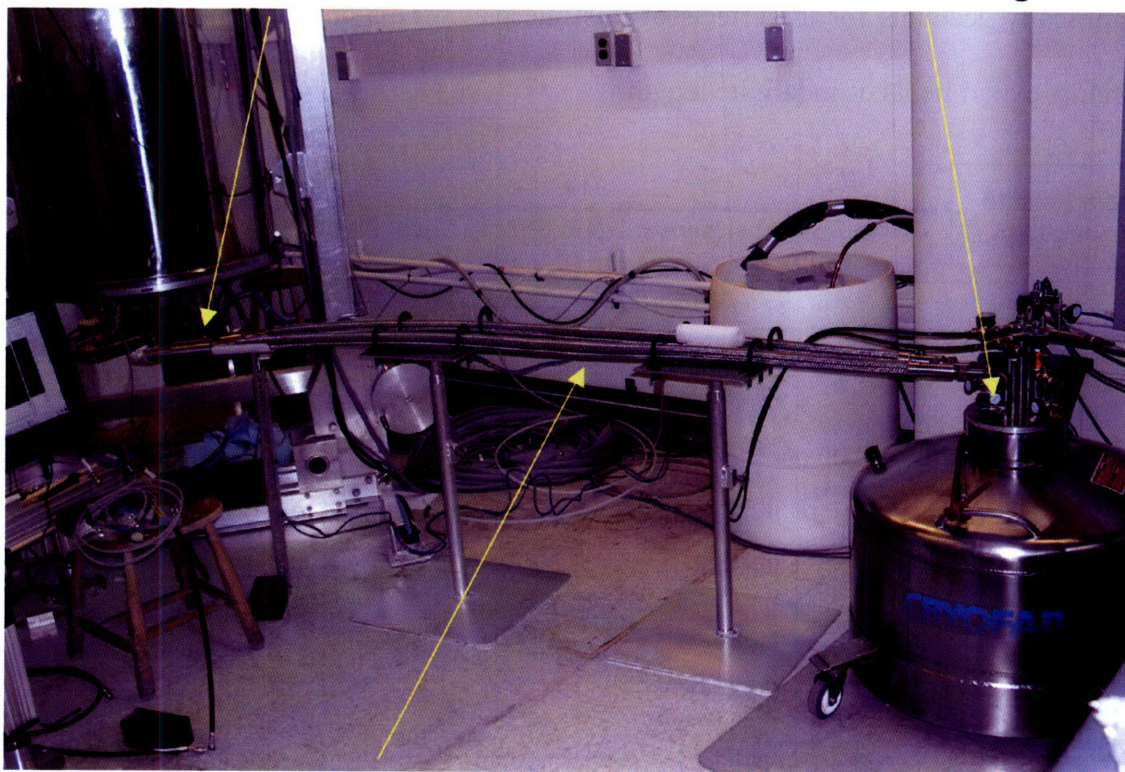
bearing and drive
gas transfer lines

dewar

Figure 2-39: Photograph of cryogenic MAS system.
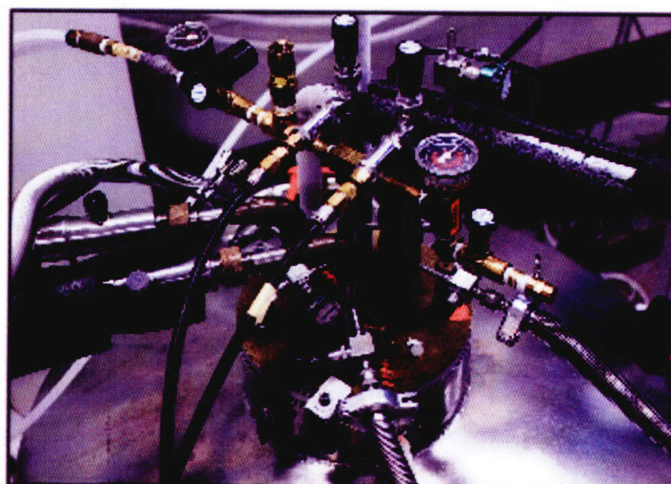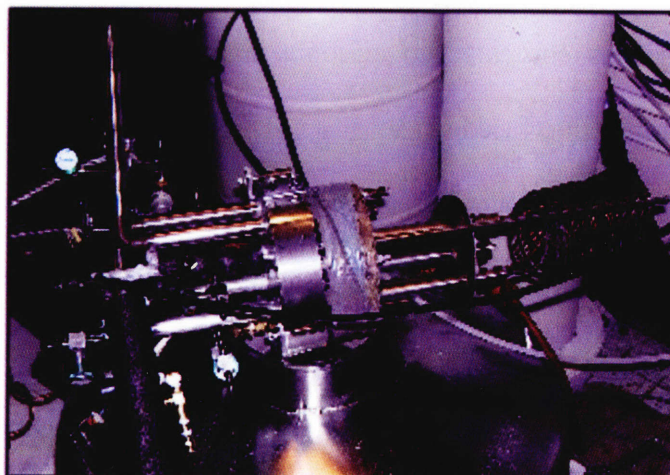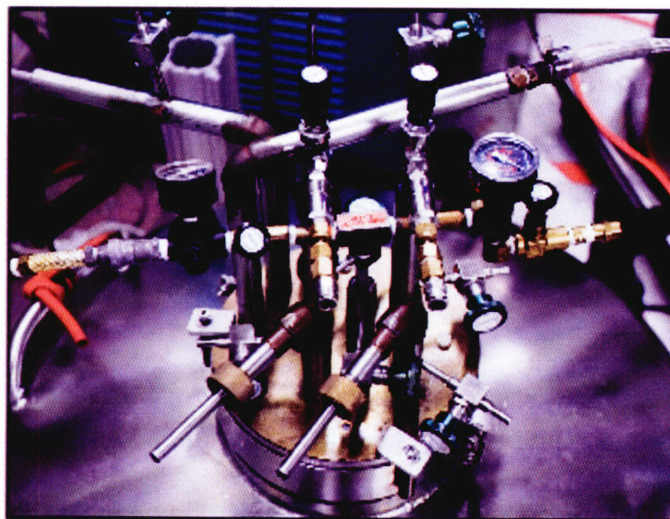
Figure 2-40: Photographs of heat exchanger used in cryogenic MAS experiments. (top) heat exchanger in dewar; (middle) heat exchanger internals are visible; (bottom) heat exchanger is connected to transfer lines during cryogenic MAS experiment.

2.4.3   Sample preparation

Sample preparation heavily influences the efficacy of the DNP process in biological samples.   At short microwave wavelengths, ordinary rotor materials such as zirconia have high indices of refraction and tend to absorb power; at the same time, the conductivity of frozen biological preparations is still high enough for skin depth effects to be important. Thus, the properties of the rotor material as well as its size can limit the DNP enhancement.   In practice, rotors made from crystalline sapphire have superior microwave properties as compared to zirconia, and superior physical properties for cryogenic use as compared to fused silica.

In Figure 2-41, we illustrate the typical sealing procedure for rotors which is performed prior to DNP experiments. Here, an ordinary vespel drive tip is modified with a small groove, approximately five thousandths of an inch deep, which serves as a channel for adhesive bonding of the drive tip to the rotor wall. The appropriate adhesive must be chosen empirically, but Hysol-type adhesives intended for use in aerospace applications have worked well in experiments conducted in the 77–100 K temperature range.

Ordinary sample spacers, which can be freely inserted into the rotor at room temperature, generally do not suffice. Instead, spacers are made whose dimensions are such that they must be cooled to liquid nitrogen temperatures prior to insertion into the rotor. In this way, they continue to fit tightly even at the low temperatures of these experiments. Of these, the top spacer is made with a cylindrical air hole that allows it to be inserted even after the opposing end of the rotor has been sealed by the drive tip,

bottom spacer, and sample. A small vespel screw is then driven into the hollow spacer to seal it.
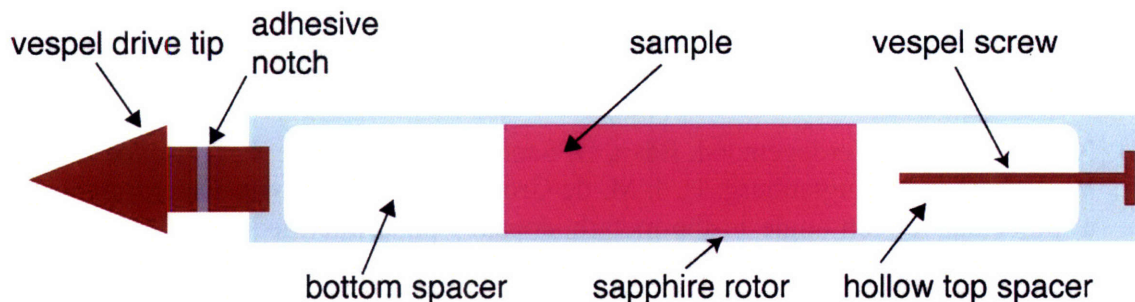
Figure 2-41: Procedure for sealing of sapphire rotors prior to DNP experiments.

The preparation of the biological sample itself involves cryoprotection to minimize inhomogeneous broadening. For soluble proteins, the cryoprotectant can be added directly, while, for membrane proteins, it has been incorporated by repeated cycles of resuspension and centrifugation. The optimization of cryoprotection conditions for DNP experiments is an area of current research.

2.5   References

[1] K. Pervushin, R. Riek, G. Wider, and K. Wüthrich. Attenuated T_2 relaxation by mutual cancellation of dipole-dipole coupling and chemical shift anisotropy indicates an avenue to NMR structures of very large biological macromolecules in solution. *Proc. Natl. Acad. Sci. USA*, 94(23):12366–12371, November 1997.

[2] V. Tugarinov, R. Muhandiram, A. Ayed, and L. E. Kay. Four-dimensional NMR spectroscopy of a 723-residue protein: Chemical shift assignments and secondary structure of malate synthase G. *J. Am. Chem. Soc.*, 124(34):10025–10035, August 2002.

[3] J. C. Lansing, M. Hohwy, C. P. Jaroniec, A. F. L. Creemers, J. Lugtenburg, J. Herzfeld, and R. G. Griffin. Chromophore distortions in the bacteriorhodopsin photocycle: Evolution of the H-C14-C15-H dihedral angle measured by solid-state NMR. *Biochemistry*, 41(2):431–438, December 2002.

[4] C. P. Jaroniec, J. C. Lansing, B. A. Tounge, M. Belenky, J. Herzfeld, and R. G. Griffin. Measurement of dipolar couplings in a uniformly ^{13}C, ^{15}N-labeled membrane protein: Distances between the Schiff base and aspartic acids in the active site of bacteriorhodopsin. *J. Am. Chem. Soc.*, 12341(51):12929–12930, December 2001.

[5] J. Herzfeld and J. C. Lansing. Magnetic resonance studies of the bacteriorhodopsin pump cycle. *Annu. Rev. Biophys. Biomol. Struct.*, 31:73–95, 2002.

[6] X. Feng, P. J. E. Verdegem, M. Eden, D. Sandstrom, Y. K. Lee, P. H. Bovee-Geurts, W. J. de Grip, J. Lugtenburg, H. J. M. de Groot, and M. H. Levitt. Determination of a molecular torsion angle in the metarhodopsin-I photointermediate of rhodpsin by double-quantum solid-state NMR. *J. Biomol. NMR*, 16(1):1–8, January 2000.

[7] X. Feng, M. Edén, A. Brinkmann, H. Luthman, L. Eriksson, A. Gräslund, O. N. Antzutkin, and M. H. Levitt. Direct determination of a peptide torsional angle Ψ by double-quantum solid-state NMR. *J. Am. Chem. Soc.*, 119(49):12006–12007, December 1997.

[8] A. McDermott, M. G. Zysmilich, and T. Polenova. Solid state NMR studies of photoinduced polarization in photosynthetic reaction centers: mechanism and simulations. *Solid State Nucl. Magn. Reson.*, 11(1-2):21–47, March 1998.

[9] R. R. Ketchem, W. Hu, and T. A. Cross. High-resolution conformation of gramicidin A in a lipid bilayer by solid-state NMR. *Science*, 261(5127):1457–1460, September 1993.

[10] J. D. van Beek, L. Beaulieu, J. Schäfer, M. Demura, T. Asakura, and B. H. Meier. Solid-state NMR determination of the secondary structure of Samia cynthia ricini silk. *Nature*, 405(6790):1077–1079, June 2000.

[11] R. Tycko, A. Petkova, N. Oyler, C. C. Chan, and J. Balbach. Probing the molecular structure of amyloid fibrils with solid state NMR. *Biophys.*, 82(1):913, January 2002.

[12] A. T. Petkova, Y. Ishii, and R. Tycko. Probing the structure of Alzheimer's beta amyloid fibrils by two-dimensional ^{13}C-^{13}C and ^{13}C-^{15}N solid state NMR methods. *Biophys.*, 82(1):1552, January 2002.

[13] C. P. Jaroniec, C. E. MacPhee, V. S. Bajaj, M. McMahon, C. M. Dobson, and R. G. Griffin. Structure of a peptide in an amyloid fibril determined by solid state NMR. In *Proc. 44th Conf. Exp. Nucl. Magn. Reson.*, Savannah, GA, April 2003.

[14] O. N. Antzutkin, J. J. Balbach, R. D. Leapman, N. W. Rizzo, J. Reed, and R. Tycko. Multiple quantum solid-state NMR indicates a parallel, not antiparallel, organization of β-sheets in Alzheimer's β-amyloid fibrils. *Proc. Natl. Acad. Sci. USA*, 97(24):13045–13050, November 2000.

[15] R. Tycko. Solid-state NMR as a probe of amyloid fibril structure. *Curr. Opin. Chem. Biol.*, 4(5):500–506, October 2000.

[16] S. J. Kim, L. Cegelski, D. R. Studelska, R. D. O'Connor, A. K. Mehta, and J. Schaefer. Rotational-echo double resonance characterization of vancomycin binding sites in *Staphylococcus aureus. Biochem.*, 41(22):6967–6977, June 2002.

[17] J. R. Long, W. J. Shaw, P. S. Stayton, and G. P. Drobny. Structure and dynamics of hydrated statherin on hydroxyapatite as determined by solid-state NMR. *Biochemistry*, 40(51):15451–15455, December 2001.

[18] J. R. Long, N. Oyler, G. P. Drobny, and P. S. Stayton. Assembly of α-helical peptide coatings on hydrophobic surfaces. *J. Am. Chem. Soc.*, 124(22):6297–6303, June 2002.

[19] S. J. Opella. NMR and membrane proteins. *Nat. Struct. Biol.*, 4(10):845–848, November 1997.

[20] A. Ramamoorthy and S. J. Opella. 2-dimensional chemical-shift / heteronuclear dipolar coupling spectra obtained with polarization inversion spin exchange at the magic angle and magic-angle sample spinning (pisemamas). *Solid State Nucl. Magn. Reson.*, 4(6):387–392, August 1995.

[21] F. M. Marassi, A. Ramamoorthy, and S. J. Opella. Complete resolution of the solid-state NMR spectrum of a uniformly ^{15}N-labeled membrane protein in phospholipid bilayers. *Proc. Natl. Acad. Sci. USA*, 94(16):8551–8556, August 1997.

[22] F. M. Marassi, C. Ma, J. J. Gesell, and S. J. Opella. Three-dimensional solid-state NMR spectroscopy is essential for resolution of resonances from in-plane residues in uniformly ^{15}N-labeled helical membrane proteins in oriented lipid bilayers. *J. Magn. Reson.*, 144(1):156–161, May 2000.

[23] E. R. Andrew, A. Bradbury, and R. G. Eades. Nuclear magnetic resonance spectra from a crystal rotated at high speed. *Nature*, 182:1659, 1958.

[24] R. G. Griffin. Dipolar recoupling in MAS spectra of biological solids. *Nat. Struct. Biol*, 5(7):508–512, July 1998.

[25] C. M. Rienstra, L. Tucker-Kellogg, C. P. Jaroniec, M. Hohwy, B. Reif, T. Lozano-Perez, B. Tidor, and R. G. Griffin. *De novo* determination of peptide structure with solid-state NMR spectroscopy. *Proc. Natl. Acad. Sci. USA*, 99(16):10260–10265, August 2002.

[26] C. P. Jaroniec, B. A. Tounge, J. Herzfeld, and R. G. Griffin. Frequency selective heteronuclear dipolar recoupling in rotating solids: Accurate [13]C-^{15}N distance measurements in uniformly ^{13}C, ^{15}N-labeled peptides. *J. Am. Chem. Soc.*, 123(15):3507–3519, April 2001.

[27] B. J. van Rossum, F. Castellani, K. Rehbein, J. Pauli, and H. Oschkinat. Assignment of the nonexchanging protons of the alpha-spectrin SH-3 domain by two- and three-dimensional [1]H-^{13}C solid-state magic-angle spinning NMR and comparison of

solution and solid-state proton chemical shifts. *ChemBioChem*, 2(12):906–914, December 2001.

[28] W. de Boer. Dynamic orientation of nuclei at low temperatures. *J. Low Temp. Phys.*, 22:185–212, 1976.

[29] W. Wenckebach, T. Swanenburg, and N. Poulis. Thermodynamics of spin systems in paramagnetic crystals. *Phys. Lett. Sec. C*, 14(5):181–255, November 1974.

[30] M. Borghini. Spin-temperature model of nuclear dynamic polarization using free radicals. *Phys. Rev. Lett.*, 20(9):419–421, 1968.

[31] P. S. Pershan. Cross relaxation in LiF. *Phys. Rev.*, 117(1):109–116, 1960.

[32] M. J. Duijvestijn, R. A. Wind, and J. Smidt. A quantitative investigation of the dynamic nuclear-polarization effect by fixed paramagnetic centra of abundant and rare spins in solids at room-temperature. *Physica B & C*, 138(1-2):147–170, March 1986.

[33] R. A. Wind, M. J. Duijvestijn, C. Van Der Lugt, A. Manenschijn, and J. Vriend. Applications of dynamic nuclear polarization in ^{13}C NMR in solids. *Prog. Nucl. Magn. Reson. Spectrosc.*, 17(33):33–67, 1985.

[34] A. Abragam. *Principles of Nuclear Magnetism.* Oxford Science Publications, 1961.

[35] Abragam and M. Goldman. *Nuclear Magnetism: Order and Disorder.* Oxford University Press, 1982.

[36] M. Goldman. *Spin Temperatures and Nuclear Magnetic Resonance in Solids.* Oxford Univ. Press, London, 1970.

[37] M. Goldman, S. F. J. Cox, and V. Bouffard. Coupling between nuclear Zeeman and electronic spin-spin interactions in dielectric solids. *J. Phys. C: Solid State Phys.*, 7(16):2940–2952, 1974.

[38] W. T. Wenckebach. Thermodynamics of dynamic nuclear polarization. *Nucl. Instrum. Methods Phys. Res., A Accel. Spectrom. Detect. Assoc. Equip.*, 356(1):1–4, March 1995.

[39] H.W. van Kesteren. *Microwave Induced Optical Nuclear Polarization.* PhD thesis, University of Leiden, 1985.

[40] R. H. Fritsch, H. Brunner, and K. H. Hausser. Triplet electron-proton cross-polarization by satisying a modified Hartmann-Hahn condition. *Chem. Phys.*, 151(2):261–278, March 1991.

[41] A. Henstra, P. Dirksen, and W. T. Wenckebach. Enhanced dynamic nuclear-polarization by the integrated solid effect. *Chem. Phys. Lett.*, 134(2):134–136, December 1988.

[42] V. Weis, M. Bennati, M. Rosay, and R. G. Griffin. Solid effect in the electron spin dressed state: A new approach for dynamic nuclear polarization. *J. Chem. Phys.*, 113(16):6795–6802, October 2000.

[43] R. K. Pathria. *Statistical Mechanics*. Butterworth-Heinemann, 1996.

[44] A. G. Redfield. Nuclear magnetic resonance saturation and rotary saturation in solids. *Phys. Rev.*, 98(6):1787–1809, June 1955.

[45] G. Jeschke and A. Schweiger. Generation and transfer of coherence in electron-nuclear spin systems by non-ideal microwave pulses. *Mol. Phys.*, 88(2):355–383, May 1996.

[46] C. T. Farrar, D. A. Hall, G. J. Gerfen, M. Rosay, J. H. Ardenkjaer-Larsen, and R. G. Griffin. High-frequency dynamic nuclear polarization in the nuclear rotating frame. *J. Magn. Reson.*, 144(1):134–141, May 2000.

[47] V.A. Atsarkin and M.I. Rodak. *Sov. Phys. - Uspekhi*, 15, 1972.

[48] B.N. Provotorov. Magnetic resonance saturation in crystals. *Soviet Physics JETP*, 14:1162, 1962.

[49] V. S. Bajaj, C. T. Farrar, M. K. Hornstein, I. Mastovsky, J. Vieregg, J. Bryant, B. Eléna, K. E. Kreischer, R. J. Temkin, and R. G. Griffin. Dynamic nuclear polarization at 9 T using a novel 250 GHz gyrotron microwave source. *J. Magn. Reson.*, 160(2):85–90, February 2003.

[50] C. T. Farrar, D. A. Hall, G. J. Gerfen, S. J. Inati, and R. G. Griffin. Mechanism of dynamic nuclear polarization in high magnetic fields. *J. Chem. Phys.*, 114(11):4922–4933, March 2001.

[51] N. Bloembergen. On the interaction of nuclear spins in a crystalline lattice. *Physica*, 15:386–426, 1949.

[52] M. Goldman. Thermal mixing between spin system solids. *Phys. Rev.*, 138(6A):A1668–A1674, June 1965.

[53] A. R. King, J. P. Wolfe, and R. L. Ballard. NMR of nuclei near a paramagnetic impurity in crystals. *Phys. Rev. Lett.*, 28(17):1099–1102, April 1972.

[54] G. Jeschke. Electron-electron-nuclear three-spin mixing in spin-correlated radical pairs. *J. Chem. Phys.*, 106(24):10072–10086, June 1997.

[55] M. Rosay, A. C. Zeri, N. S. Astrof, S. J. Opella, J. Herzfeld, and R. G. Griffin. Sensitivity-enhanced NMR of biological solids: Dynamic nuclear polarization of Y21M fd bacteriophage and purple membrane. *J. Am. Chem. Soc.*, 123(5):1010–1011, February 2001.

[56] V. Ladizhansky and S. Vega. Polarization transfer dynamics in Lee-Goldburg cross polarization nuclear magnetic resonance experiments on rotating solids. *J. Chem. Phys.*, 112(16):7158–7168, April 2000.

[57] V. Ladizhansky, E. Vinogradov, B. J. van Rossum, H. J. M. de Groot, and S. Vega. Multiple-spin effects in fast magic angle spinning Lee-Goldburg cross-polarization experimens in uniformly labeled compounds. *J. Chem. Phys.*, 118(12):5547–5557, March 2003.

[58] M. Rosay. *Sensitivity-Enhanced Nuclear Magnetic Resonance of Biological Solids.* PhD dissertation, Massachusetts Institute of Technology, Department of Chemistry, September 2001.

[59] A. McDermott and T. Igumenova. Studies of uniformly enriched proteins by solid state NMR. In *Proc. 44th Conf. Exp. Nucl. Magn. Reson.*, Savannah, GA, April 2003.

[60] D. A. Hall, D. C. Maus, G. J. Gerfen, S. J. Inati, L. R. Becerra, F. W. Dahlquist, and R. G. Griffin. Polarization-enhanced NMR spectroscopy of biomolecules in frozen solution. *Science*, 276(5314):930–932, May 1997.

[61] M. Rosay, V. Weis, K. E. Kreischer, R. J. Temkin, and R. G. Griffin. Two-dimensional ^{13}C-^{13}C correlation spectroscopy with magic angle spinning and dynamic nuclear polarization. *J. Am. Chem. Soc.*, 124(13):3214–3215, April 2002.

[62] M. Hohwy, C. M. Rienstra, C. P. Jaroniec, and R. G. Griffin. Fivefold symmetric homonuclear dipolar recoupling in rotating solids: Application to double quantum spectroscopy. *J. Chem. Phys.*, 110(16):7983–7992, April 1999.

[63] R. A. Wind, L. Y. Li, H. Lock, and G. E. Maciel. Dynamic nuclear-polarization in the nuclear rotating frame. *J. Magn. Reson.*, 79(3):577–582, October 1988.

[64] M. Baldus, A. T. Petkova, J. Herzfeld, and R. G. Griffin. Cross polarization in the tilted frame: assignment and spectral simplification in heteronuclear spin systems. *Mol. Phys.*, 95(6):1197–1207, December 1998.

[65] A. T. Petkova, M. Baldus, M. Belenky, M. Hong, R. G. Griffin, and J. Herzfeld. Backbone and side chain assignment strategies for multiply labeled membrane peptides and proteins in the solid state. *J. Magn. Reson.*, 160(1):1–12, January 2003.

[66] V. Weis. In *Proc. Chianti Workshop*, Chianti, Italy, 2000.

[67] J. P. Colpa and D. Stehlik. Optical nuclear polarization as a consequence of the non-crossing rule (level-anti-crossing): I. Analytical treatment of ONP in the level-crossing region. *Chem. Phys.*, 21(2):273–288, April 1977.

[68] J. P. Colpa, F. Seiff, and D. Stehlik. Magnetic-field dependence of phosphorescence intensity and optical nuclear-polarization (ONP) as a result of level-anti- crossing (LAC) and relaxation in excited triplet-states. *Chem. Phys.*, 33(1):79–91, October 1978.

[69] J. P. Colpa. Contribuation to the theory of microwave-induced optical nuclear-polarization (MI-ONP) - formal equivalence of microwave-induced and level-anticrossing optical nuclear- polarization - extremum values for polarization. *Chem. Phys.*, 91(3):425–433, December 1984.

[70] K. H. Hausser. Laser-induced dynamic nuclear-polarization. *Ber. Bunsen-Ges. Phys. Chem. Chem. Phys.*, 93(3):374–380, March 1989.

[71] D. Henrich, H. Brunner, R. H. Fritsch, and K. H. Hausser. Time-resolved microwave-induced optical nuclear-polarization. *Chem. Phys.*, 138(1):203–213, November 1989.

[72] A. Henstra, P. Dirksen, J. Schmidt, and W. T. Wenckebach. Nuclear-spin orientation via electron-spin locking (NOVEL). *J. Magn. Reson.*, 77(2):389–393, April 1988.

[73] A. Henstra, T. S. Lin, J. Schmidt, and W. T. Wenckebach. High dynamic nuclear-polarization at room-temperature. *Chem. Phys. Lett.*, 165(1):6–10, January 1990.

[74] K. Takeda, K. Takegoshi, and T. Terao. Dynamic nuclear polarization by photoexcited-triplet electron spins in polycrystalline samples. *Chem. Phys. Lett.*, 345(1-2):166–170, September 2001.

[75] S. Vega and A. Pines. Operator formalism for double quantum NMR. *J. Chem. Phys.*, 66(12):5624–5644, June 1977.

[76] D. W. Pratt. ODMR studies of excited triplet states in high field. In R. H. Clarke, editor, *Triplet State ODMR Spectroscopy: Techniques and Applications to Biophysical Systems*, chapter 3, pages 43–82. John Wiley & Sons, New York, 1982.

[77] S. K. Straus, T. Bremi, and R. R. Ernst. Resolution enhancement by homonuclear j decoupling in solid-state MAS NMR. *Chem. Phys. Lett.*, 262(6):709–715, November 1996.

[78] C. M. Rienstra, M. Hohwy, M. Hong, and R. G. Griffin. 2D and 3D ^{15}N-^{13}C-^{13}C NMR chemical shift correlation spectroscopy of solids: assignment of MAS spectra of peptides. *J. Am. Chem. Soc.*, 122(44):10979–10990, November 2000.

[79] M. Baldus. Correlation experiments for assignment and structure elucidation of immobilized polypeptides under magic angle spinning. *Prog. Nucl. Magn. Reson. Spec.*, 41(1-2):1–47, December 2002.

[80] ELVA-1 Millimeter Wave Division. IMPATT diodes and test fixtures IC & IM data sheet. URL. http://www.elva-1.spb.ru.

[81] Communications & Power Industries. Communications market. URL. http://cpii.com/communications.html.

[82] V. L. Granatstein, G. S. Nusinovich, M. Blank, K. L. Felch, R. M. Gilgenbach, H. Guo, H. Jory, N. C. Luhman Jr., D. B. McDermott, J. M. Rodgers, and T. A. Spencer. Gyro-amplifiers for millimeter wave radar. In R. J. Barker and E. Schamiloglu, editors, *High-power Microwave Sources and Technologies*, number 23 in IEEE Press series on RF and microwave technology, section 6.2.3, pages 163–166. Academic Press, New York, September 2001.

[83] K. Felch, H. Huey, and H. Jory. Gyrotrons for ECH applications. *J. Fusion Energy*, 9(1):59–75, March 1990.

[84] P. Woskoboinikow. Development of gyrotrons for plasma diagnostics. *Rev. Sci. Instr.*, 57(8):2113–2118, August 1986.

[85] S. Mitsudo, Aripin, T. Shirai, T. Matsuda, T. Kanemaki, and T. Idehara. High power, frequency tunable, submillimeter wave ESR device using a gyrotron as a radiation source. *Int. J. Infrared Millim. Waves*, 21(4):661–676, April 2000.

[86] C. J. Edgecombe, editor. *Gyrotron Oscillators: Their Principles and Practice*. Cambridge University Press, 1993.

[87] T. Idehara, I. Ogawa, S. Mitsudo, M. Pereyslavets, N. Nishida, and K. Yoshida. Development of frequency tunable, medium power gyrotrons (Gyrotron FU Series) as submillimeter wave radiation sources. *IEEE Trans. Plasma Sci.*, 27(2):340–354, April 1999.

[88] G. F. Brand and M. Gross. Continuously tunable, split-cavity gyrotrons. *Int. J. Infrared Millim. Waves*, 6(12):1237–54, December 1985.

[89] G. P. Gallerano, A. Doria, E. Giovenale, and A. Renieri. Compact free electron lasers: From Cerenkov to waveguide free electron lasers. *Infrared Phys. Technol.*, 40(3):161–174, June 1999.

[90] H. P. Freund and G. R. Neil. Free-electron lasers: vacuum electronic generators of coherent radiation. *Proc. IEEE*, 87(5):782–803, May 1999.

[91] K. Mizuno and S. Ono. The ledatron. In K. J. Button, editor, *Infrared and Millimeter Waves*, volume 1, chapter 5, pages 213–233. Academic Press, New York, 1979.

[92] R. P. Leavitt, D. E. Wortman, and H. Dropkin. Millimeter-wave orotron oscillation – Part I: Theory. *IEEE J. Quant. Electron.*, 17(8):1333–1340, August 1981.

[93] V. L. Bratman, B. S. Dumesh, A. E. Fedotov, Yu. A. Grishin, and F. S. Rusin. Broadband orotron operation at millimeter and submillimeter waves. *Int. J. Infrared Millim. Waves*, 23(11):1595–1601, November 2002.

[94] T. K. Ishii. *Handbook of microwave technology*, volume 1. Academic Press, San Diego, 1995.

[95] R. E. Collin. *Foundations for microwave engineering*. IEEE Press, 2001.

[96] V. Weis, M. Bennati, M. Rosay, J. A. Bryant, and R. G. Griffin. High-field DNP and ENDOR with a novel multiple-frequency resonance structure. *J. Magn. Reson.*, 140(1):293–299, September 1999.

[97] J. Schneider. Stimulated emission of radiation by relativistic electrons in a magnetic field. *Phys. Rev. Lett.*, 2(12):504–505, June 1959.

[98] A. Gaponov, M. I. Petelin, and V. K. Yulpatov. The induced radiation of excited classical oscillators and its use in high-frequency electronics. *Radiophysics*, 10(9-10):794–813, 1967.

[99] M. Petelin. Spontaneous and stimulated radiation of classical electrons. In R. A. Cairns and A. D. R. Phelps, editors, *Generation and Application of High Power Microwaves*, number 48 in Scottish Universities Summer Schools in Physics, chapter 2, pages 9–28. Institute of Physics Publishing, Bristol, December 1997.

[100] L. C. Robinson. *Physical Principles of Far-Infrared Radiation*, volume 10 of *Methods of Experimental Physics*, chapter 5, pages 230–264. Academic Press, New York, 1973.

[101] J. L. Hirshfield, I. B. Bernstein, and J. M. Wachtel. Cyclotron resonance interaction of microwaves with energetic electrons. *IEEE Int. J. Quant. Electron.*, 1(6):237–245, 1965.

[102] A. V. Gaponov. Interaction between electron fluxes and electromagnetic waves in waveguides. *Izv. VUZ Radiofizika*, 2(3):450–462, 1959.

[103] K. R. Chu and J. L. Hirshfield. Comparative study of the axial and azimuthal bunching mechanisms in electromagnetic cyclotron instabilities. *Phys. Fluids*, 21(3):461–466, March 1978.

[104] K. E. Kreischer and R. J. Temkin. Linear theory of an electron cyclotron maser operating at the fundamental. *Int. J. Infrared Millim. Waves*, 1(2):195–223, June 1980.

[105] L. D. Landau and E. M. Lifshitz. *Quantum Mechanics: Non-Relativistic Theory.* Pergamon, 1958.

[106] J. J. Sakurai. *Modern Quantum Mechanics.* Addison-Wesley, 1994.

[107] V. K. Yulpatov. In A. V. Gaponov-Grekhov, editor, *Gyrotron, collected papers,* page 26. Gorky: Inst. Applied Physics, 1981.

[108] G. S. Nusinovich. Linear theory of a gyrotron with weakly tapered external magnetic field. *Int. J. Electron.,* 64(1):127–135, January 1988.

[109] K. E. Kreischer. User's manual for LINEAR, a computer program that calculates the linear characteristics of a gyrotron. Technical Report PFC/RR/82-8, Massachusetts Institute of Technology, Plasma Fusion Center, Cambridge, MA, January 1982.

[110] K. E. Kreischer, C. T. Farrar, R. G. Griffin, R. J. Temkin, and J. Vieregg. The development of a 250 GHz CW gyrotron for EPR and NMR spectroscopy. In *Proc. 24th Int. Conf. Infrared Millim. Waves,* Monterey, CA, September 1999.

[111] K. E. Kreischer, C. Farrar, R. Griffin, R. Temkin, and J. Vieregg. A 250 GHz gyrotron for NMR spectroscopy. In *Proc. 27th IEEE Int. Conf. Plasma Sci.,* page 198, Monterey, CA, 2000.

[112] S. N. Vlasov, G. M. Zhislin, I. M. Orlova, M. I. Petelin, and G. G. Rogacheva. Irregular waveguides as open resonators. *Radiophys. Quant. Electron.,* 12(8):972–978, August 1969.

[113] A. W. Fliflet and M. E. Read. Use of weakly irregular waveguide theory to calculate eigenfrequencies, Q values, and RF field functions for gyrotron oscillators. *Int. J. Electron.,* 51:475–484, 1981.

[114] K. D. Hong, G. F. Brand, and T. Idehara. A 150-600 GHz step-tunable gyrotron. *J. Appl. Phys.,* 74(8):5250–5258, October 1993.

[115] J. R. Sirigiri, K. E. Kreischer, J. Machuzak, I. Mastovsky, M. A. Shapiro, and R. J. Temkin. Photonic-band-gap resonator gyrotron. *Phys. Rev. Lett.,* 86(24):5628–5631, June 2001.

[116] J. Sirigiri. *A Novel Wideband Gyrotron Traveling Wave Amplifier.* PhD dissertation, Massachusetts Institute of Technology, Department of Electrical Engineering and Computer Science, February 2003.

[117] S. N. Vlasov and I. M. Orlova. Quasioptical transformer which transforms the waves in a waveguide having circular cross section into a highly directional wave beam. *Radiophys. Quant. Electron.,* 17:115–119, 1974.

[118] S. N. Vlasov, M. A. Shapiro, and K. M. Likin. Geometrical optics of waveguide mode converters. *Opt. Commun.*, 88(4):455–463, April 1992.

[119] B. Z. Katsenelenbaum, L. Mercader del Rio, M. Pereyaslavets, M. Sorolla Ayza, and M. Thumm. *Theory of Nonuniform Waveguides: the cross-section method*, volume 44 of *Electromagnetic Waves*. The Institution of Electrical Engineers, London, 1998.

[120] J. Trulsen, P. Woskoboinikow, and R. J. Temkin. Circular waveguide mode converters at 140 GHz. Technical Report PSFC/RR-86-2, Massachusetts Institute of Technology, Plasma Fusion Center, Cambridge, MA, January 1986.

[121] H. A. Haus. *Waves and Fields in Optoelectronics*. Prentice-Hall, Englewood Cliffs, New Jersey, 1984.

[122] P. Bhartia and I. J. Bahl. *Millimeter wave engineering and applications*. John Wiley & Sons, 1984.

[123] J. L. Doane. Propagation and mode coupling in corrugated and smooth-wall circular waveguides. In K. J. Button, editor, *Infrared and Millimeter Waves*, volume 13, chapter 5, pages 123–170. Academic Press, New York, 1985.

[124] P. M. Borchard. Design of a data acquisitioning system for near- and far field scans of the gyrotron. Bachelor's project, Massachusetts Institute of Technology, Mechanical Engineering Department, May 1993.

[125] M. K. Hornstein. Design of a 460 GHz second harmonic gyrotron oscillator for use in dynamic nuclear polarization. Master's thesis, Massachusetts Institute of Technology, Department of Electrical Engineering and Computer Science, September 2001.

[126] J. P. Anderson, M. A. Shapiro, R. J. Temkin, and D. R. Denison. Phase retrieval of gyrotron beams based on irradiance moments. *IEEE Trans. Microwave Theory Tech.*, 50(6):1526–1535, June 2002.

[127] D. R. Denison, T. S. Chu, M. A. Shapiro, and R. J. Temkin. Gyrotron internal mode converter reflector shaping from measured field intensity. *IEEE Trans. Plasma Sci.*, 27(2):512–519, April 1999.

[128] M. K. Hornstein, V.S. Bajaj, R. G. Griffin, K. E. Kreischer, I. Mastovsky, M. A. Shapiro, and R. J. Temkin. Design of a 460 GHz second harmonic gyrotron oscillator for use in dynamic nuclear polarization. In *Proc. 27th Int. Conf. Infrared Millim. Waves*, San Diego, CA, September 2002.

[129] R. A. McKay. Probes for special purposes. In D. M. Grant and R. K. Harris, editors, *Encyclopedia of Nuclear Magnetic Resonance*, chapter 6, pages 3768–3771. John Wiley & Sons, New York, 1996.

[130] Hu, K.-N.; Bajaj, V. S.; Rosay, M. M.; Griffin, R. G., High Frequency Dynamic Nuclear Polarization Using Mixtures of TEMPO and Trityl Radicals. *J. Chem. Phys.* 2007, 126, 044512.

[131] Wind, R. A.; Duijvestijn, M. J.; Vanderlugt, C.; Manenschijn, A.; Vriend, J., Applications of Dynamic Nuclear-Polarization in C-13 Nmr in Solids. *Progress in Nuclear Magnetic Resonance Spectroscopy* 1985, 17, 33-67.

[132] Atsarkin, V. A., Dynamic polarization of nuclei in solid dielectrics. *Sov. Phys. Usp.* 1978, 21, 725-744.

[133] Hu, K.-N.; Griffin, R. G., Quantum Mechanical Theory of Dynamic Nuclear Polarization in Solid Dielectrics –Simulation of Electron-Electron-Nucleus Spin Systems with Relaxation. *J. Chem. Phys.* 2007, (submitted for publication).

[134] Hu, K.-N.; Yu, H.-h.; Swager, T. M.; Griffin, R. G., Dynamic nuclear polarization with biradicals. *Journal of the American Chemical Society* 2004, 126, (35), 10844-10845.

[135] Song, C.; Hu, K.-N.; Joo, C. G.; Swager, T. M.; Griffin, R. G., TOTAPOL-A biradical polarizing agent for dynamic nuclear polarization in aqueous media. 2006, accepted.

[136] Note:, *g-values of trityl (4-hydroxy-TEMPO) in frozen glycerol/water solutions are obtained from measurements of the powder EPR spectrum the FBML 140 GHz EPR spectrometer.*

[137] Grinberg, O. Y.; Dubinskii, A. A.; Lebedev, Y. S., Electron-Paramagnetic Resonance of Free-Radicals in a 2-Millimeter Range of Wave-Length. *Uspekhi Khimii* 1983, 52, (9), 1490-1513.

[138] Farrar, C. T.; Hall, D. A.; Gerfen, G. J.; Inati, S. J.; Griffin, R. G., Mechanism of dynamic nuclear polarization in high magnetic fields. *Journal of Chemical Physics* 2001, 114, (11), 4922-4933.

[139] Gerfen, G. J.; Becerra, L. R.; Hall, D. A.; Griffin, R. G.; Temkin, R. J.; Singel, D. J., High-Frequency (140 Ghz) Dynamic Nuclear-Polarization - Polarization Transfer to a Solute in Frozen Aqueous-Solution. *Journal of Chemical Physics* 1995, 102, (24), 9494-9497.

[140] Becerra, L. R.; Gerfen, G. J.; Temkin, R. J.; Singel, D. J.; Griffin, R. G., Dynamic Nuclear-Polarization with a Cyclotron-Resonance Maser at 5-T. *Physical Review Letters* 1993, 71, (21), 3561-3564.

[141] Bajaj, V. S.; Farrar, C. T.; Mastovsky, I.; Vieregg, J.; Bryant, J.; Elena, B.; Kreischer, K. E.; Temkin, R. J.; Griffin, R. G., Dynamic nuclear polarization at 9T using a novel 250 GHz gyrotron microwave source. *Journal of Magnetic Resonance* 2003, 160, (2), 85-90.

[142] Henstra, A.; Lin, T. S.; Schmidt, J.; Wenckebach, W. T., High Dynamic Nuclear-Polarization at Room-Temperature. *Chemical Physics Letters* 1990, 165, (1), 6-10.

Chapter 3　　　Dynamic Nuclear Polarization at 9 Tesla Using a Novel 250 GHz Gyrotron Microwave Source

In this communication, we report enhancements of nuclear spin polarization by Dynamic Nuclear Polarization (DNP) in static and spinning solids at a magnetic field strength of 9 Tesla (250 GHz for g=2 electrons, 380 MHz for ^{1}H). In these experiments, ^{1}H enhancements of up to 170±50 have been observed in 1-^{13}C-glycine dispersed in a 60:40 glycerol/water matrix at temperatures of 20 K; in addition, we have observed significant enhancements in ^{15}N spectra of unoriented *pf1*-bacteriophage. Finally, enhancements of ~17 have been obtained in two-dimensional ^{13}C-^{13}C chemical shift correlation spectra of the amino acid U-^{13}C, ^{15}N-proline during Magic Angle Spinning (MAS), demonstrating the stability of the DNP experiment for sustained acquisition and for quantitative experiments incorporating dipolar recoupling. In all cases, we have exploited the thermal mixing DNP mechanism with the nitroxide radical 4-amino-TEMPO as the paramagnetic dopant. These experiments are the highest frequency DNP experiments performed to date and indicate that significant signal enhancements can be realized using the thermal mixing mechanism even at elevated magnetic fields. In large measure, this is due to the high microwave power output of the 250 GHz gyrotron oscillator used in these experiments.

3.1 Introduction

During the last decade, a considerable variety of NMR techniques have been developed to constrain molecular structure in the solid state. In order to obtain site-specific resolution, these involve either uniaxial orientation of the sample with respect to the static magnetic field [1] or magic angle spinning (MAS) [2]. In the latter case, anisotropic dipolar and chemical shift interactions which encode structural parameters are modulated by the sample spinning and must be re-introduced to yield useful information. In particular, there are now a multiplicity of well-developed homonuclear and heteronuclear dipolar recoupling techniques [3], [4] useful as mixing sequences in chemical shift correlation spectroscopy [5], for distance measurements [6], and for the determination of torsion angles [7-11]. Recently, a complete atomic-resolution structure determined using these techniques has been reported in the literature [12].

In all cases, the applicability of these methods to larger systems and those in low abundance is currently limited by the necessity to directly observe signals of low gyromagnetic ratio (γ) nuclei, such as ^{13}C, ^{15}N, and ^{31}P, whose spectra are well-resolved. The indirect detection of dilute spin spectra through the more sensitive ^{1}H spins has not yet become generally practical in the solid state, due to strong homonuclear couplings among the protons [13-15]. As a result, solid state NMR is less sensitive by two or three orders of magnitude per unit time than solution state NMR. This inherent low sensitivity is a limiting factor in the application of multidimensional NMR methods to biological systems.

As a means to increase the sensitivity of these experiments, we have previously employed dynamic nuclear polarization (DNP) to enhance NMR signals in both static and

190

rotating solids at 5T [16-19]. DNP involves the irradiation of a coupled electron-nuclear spin system in the neighborhood of the electron Larmor frequency. According to a variety of polarization transfer mechanisms which rely on electron-nuclear hyperfine couplings alone (*e.g.* solid effect), or electron dipolar couplings in addition to hyperfine couplings to the nuclei (*e.g.* thermal mixing), nuclear signal enhancements on the order of γ_e/γ_N (~660 for ^{1}H nuclei and ~2600 for ^{13}C nuclei), are possible. In general, these experiments are conducted at low temperatures in order to attenuate competing spin-lattice relaxation processes which would otherwise compromise the polarization transfer efficiency. In earlier work, we have achieved ^{1}H signal enhancements ranging from 50-400 at a magnetic field of 5 T. However, it is desirable to apply DNP at higher fields (9-18 T) where NMR is commonly performed.

In this communication, we present preliminary results which illustrate the successful application of DNP at a magnetic field of 9 T in both static and rotating solids. In all cases, samples were dissolved or dispersed in frozen solutions of 60% glycerol and 40% water, and the source of electron polarization was the nitroxide radical 4-amino-TEMPO. We have obtained static 1H thermal mixing DNP enhancements of up to 170±50 for the amino acid 1-^{13}C-glycine at 20 K, and an enhancement of ~40 in an unoriented sample of U-[15]N-*pf1*-bacteriophage. Further, we have recorded two-dimensional [13]C-^{13}C chemical shift correlation spectra of U-^{13}C, ^{15}N-Proline in magic angle spinning dipolar recoupling experiments at 98-100K, with a DNP enhancement of 17.

3.2 Thermal Mixing DNP at High Fields

For systems in which the homogeneous EPR line width approaches the magnitude of the nuclear Larmar frequency, an energy conserving three-spin process is operative. Here, an allowed electron-electron mutual spin flip is accompanied by a nuclear spin flip; for the case of a non-equilibrium polarization among the electrons, this mode of relaxation can lead to the generation of enhanced nuclear polarization, a process which is referred to as thermal mixing. Thermal mixing is conventionally treated by a spin thermodynamic formalism in which the Hamiltonian for the coupled three-spin system is decomposed into several quasi-invariants of the motion, each of which has a distinct spin temperature. These are: the electron Zeeman spin reservoir (in the rotating frame), the electron spin-spin interaction reservoir, and the nuclear Zeeman bath. As shown by Provotorov [20], the electron Zeeman and spin-spin interaction reservoirs are in thermodynamic equilibrium when microwave radiation is applied. Off-resonance irradiation of the EPR line produces a non-equilibrium polarization state, which is equivalent to cooling of the electron spin-spin interaction reservoir. This spin-spin interaction reservoir is in thermal contact with the nuclear Zeeman system through the aforementioned three-spin process involving two electron spins and one nuclear spin, and so off-resonance irradiation of the EPR line can also produce a cooling of the nuclear Zeeman reservoir.

Treatments based on perturbation theory or a relaxation approach [21,22] both require that the homogeneous EPR line width (δ) be greater than the nuclear Larmor frequency (ω_n) for the thermal mixing DNP enhancement to be appreciable. If the enhanced nuclei are protons in an organic solid, the polarization is redistributed across the sample by spin diffusion which is fast on the time scale of the DNP experiment. In

the limit of fast spin diffusion and under the approximation of a homogeneous electron line shape, Wind *et al.* [23] have derived an expression for the dependence of the enhancement (ε) on the various experimental parameters, given by Equation (3.1).

$$\varepsilon = \frac{\gamma_e}{\gamma_n} \frac{N_e^2}{\delta^2} \left(\frac{B_{ie}^2}{B_0} \right) T_{1n} T_{1e} \tag{3.1}$$

Here B_{1e} is the microwave field strength, B_0 is the static magnetic field strength, N_e is the concentration of electrons, δ is the homogeneous EPR line width, and T_{1n} and T_{1e} are, respectively, the nuclear and electron spin-lattice relaxation times.

The assumptions inherent to this formulation are not satisfied under the conditions of the experiments described here. In particular, at high magnetic fields (*e.g.* 9 T), the EPR spectra of the nitroxide radicals used as polarizing agents in DNP experiments are inhomogeneously broadened by the g-anisotropy. The result is that there cannot be a single Zeeman spin temperature assigned to the electrons, and that equilibration of the nuclear and electron Zeeman reservoirs does not necessarily proceed through the dipolar system of the electrons. Farrar *et al.* [24] have recently presented a phenomenological interpretation of thermal mixing DNP at high fields which relaxes these assumptions. In the limit of a large electron concentration, this treatment suggests that electron cross relaxation, which is fast compared to the spin-lattice relaxation, can indirectly mediate spin temperature equilibration, effectively rendering the electron interactions homogeneous on the time-scale of the experiment. This treatment together with experimental data demonstrate that (3.1) is qualitatively valid. Although (3.1) suggests an inverse dependence of the DNP enhancement on the static magnetic field, we have been able to compensate for this dependence in our experiments, as follows:

1.   Far from saturation, the DNP enhancement qualitatively scales as B_{1e} and so the high output power of the 250 GHz gyrotron oscillator used in these experiments results in a large enhancement.

2.   Through manipulation of the sample temperature, nuclear spin-lattice relaxation has been attenuated. Thus, significant enhancements can be realized at temperatures of 10-20K. Although the MAS experiments are currently conducted near 77K, significant signal enhancements are also observed in that regime.

3.   A large radical concentration (60mM) was used in these experiments, with the result that electron-electron cross-relaxation is enhanced, and the thermal mixing DNP efficiency improved accordingly.

3.3   250 GHz Gyrotron Oscillator

In all experiments presented here, the source of microwave irradiation was a 250 GHz gyrotron (cyclotron resonance maser) designed for DNP experiments [25]. This instrument is capable of sustained (72-96 hr) operation at output powers of 10-15W, which results in approximately 3-4W of microwave power at the sample. The output power of the gyrotron is regulated to within 1% through a proportional control loop.

In a probe designed for static DNP experiments, microwave power from the 250 GHz gyrotron oscillator is coupled to the sample directly through an over-moded circular waveguide immediately below the NMR coil; no microwave resonant structure was used. Low temperature operation is achieved through a continuous flux of either nitrogen or helium gas near their respective boiling points. In the case of helium gas, dielectric breakdown limited the strength of ^{1}H decoupling which could be applied. MAS experiments were performed using a triple-channel transmission line probe incorporating

a microwave waveguide and a 4mM stator. Cryogenic operation was achieved by passing the drive and bearing nitrogen gas through a heat exchanger operating at liquid nitrogen temperatures. The temperature and pressure of the drive and bearing gas are actively regulated using multiple control loops implemented in software, with the result that the temperature is stable to within 1 K and the MAS frequency to within 5 Hz for extended operating periods. Finally, data acquisition and processing were accomplished using a custom-designed spectrometer and processing software (courtesy Dr. D.J. Ruben). Further details of the gyrotron and DNP spectrometer will be provided in a subsequent publication.

3.4 DNP CP of Static Samples

In the case of static samples, the sample and paramagnetic dopant were dissolved in a solution of glycerol and water and transferred to a 4mm quartz tube without further degassing. Provided that freezing is sufficiently rapid, the matrix forms a glass at the temperature of these experiments.
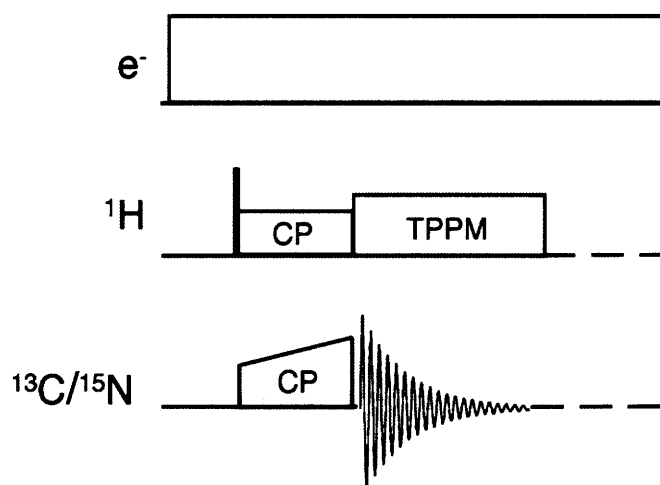
Figure 3-1: Cross-polarization with continuous microwave irradiation. In all cases, the resonance offset was set to maximize the ^{1}H enhancement.

$$\varepsilon = 170 \pm 50$$

^{13}C Chemical Shift (ppm)
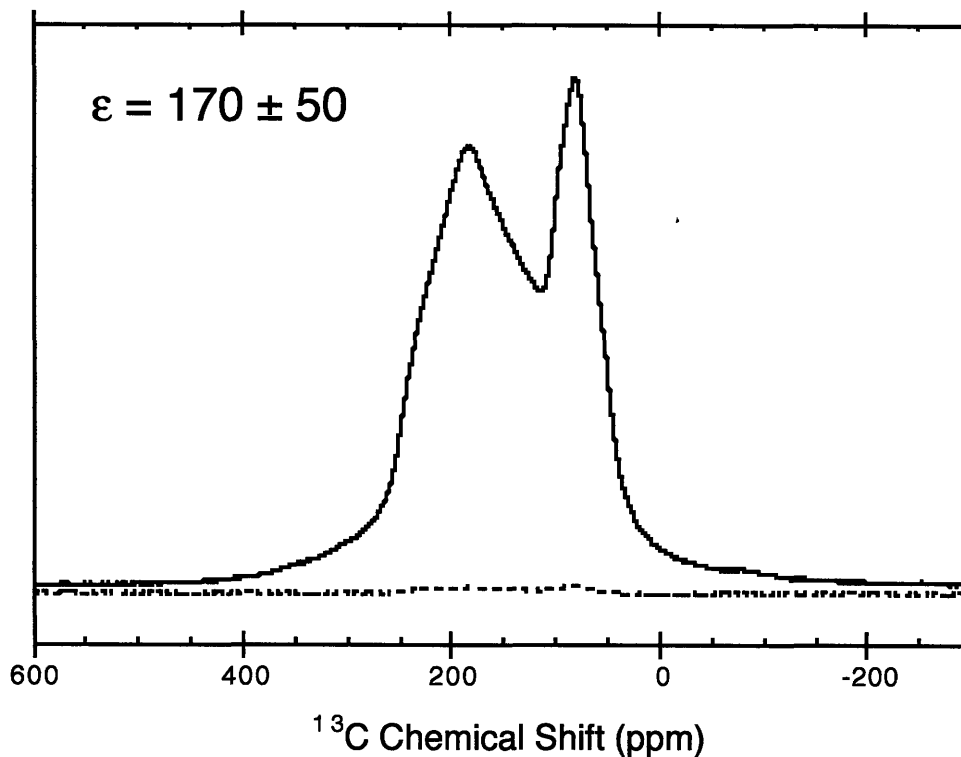
Figure 3-2: DNP CP spectra of static 1-^{13}C-glycine (0.39 M) dispersed in a 60:40 water/glycerol solution containing 80 mM 4-amino TEMPO at 20 K recorded with (solid trace) and without (dashed trace) microwave irradiation. A ^{1}H DNP enhancement of 170 ± 50 was observed with ~1.0 W of microwave power incident on the sample. Eight transients were recorded.

Experimental data were acquired using cross-polarization with continuous microwave irradiation (Figure 3-1). The offset from resonance (*vide infra*) was set to maximize the ^{1}H thermal mixing DNP enhancement. Accordingly, the reported enhancements are enhancements of the ^{1}H polarization detected indirectly through the dilute spins (^{13}C or ^{15}N). Previous results at 5 T demonstrate that proton polarization is homogeneously distributed through the sample by rapid proton spin diffusion on the timescale of the experiment [26]. Further, we have observed in these studies that the directly and indirectly detected 1H enhancements are identical. A representative static spectrum of 1-^{13}C-glycine is shown in Figure 3-2. The DNP enhancement of 170 ± 50 at 20K was achieved with a radical concentration of 80mM, and an enhancement of approximately 40 was also obtained in a sample of *pf1*-bacteriophage doped with

196

TEMPO at 60mM concentration (not shown). The enhancements obtained at 9 T from the glycine sample (Figure 3-2) are in the same order of magnitude as previous results obtained at 5 T [16], indicating that the inverse dependence of the thermal mixing enhancement on the static magnetic field has been overcome under the conditions of these experiments.
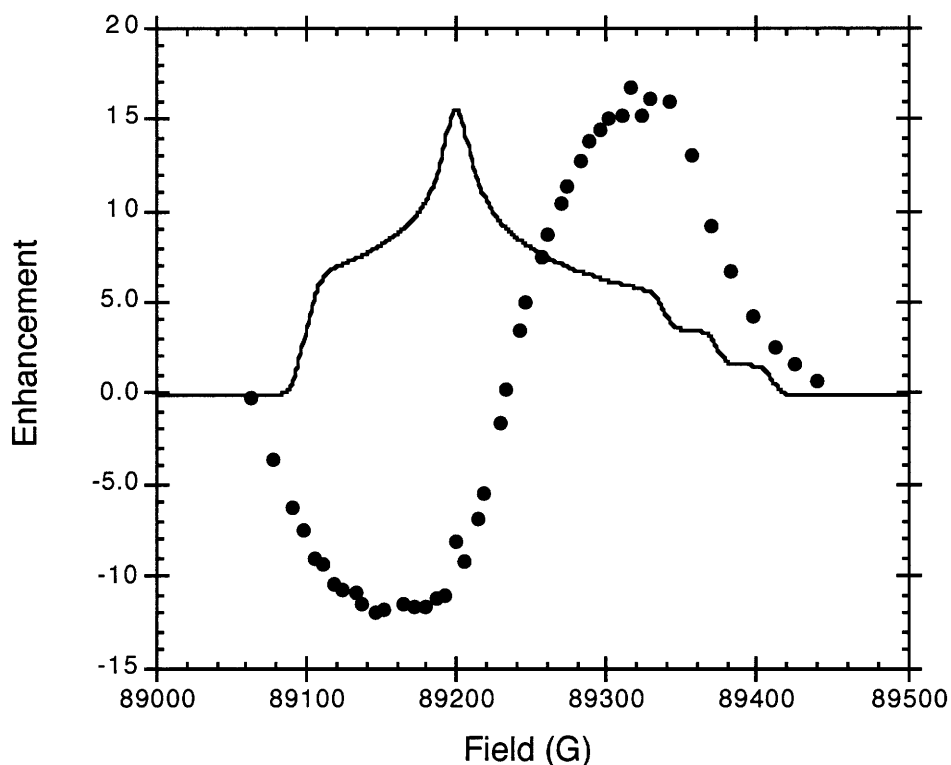
Figure 3-3: Dependence of the DNP enhancement (solid circles) on resonance offset, superimposed on the simulated 4-amino TEMPO EPR spectrum (solid trace). Because the gyrotron oscillator frequency is fixed, the static magnetic field was swept in this experiment.

In general, the DNP enhancement is strongly dependent upon the position of irradiation relative to the electron resonance. Since the gyrotron oscillator is fixed in frequency, the static magnetic field was swept from 89000 G to 89500 G (a Zeeman range which encloses the entire EPR line shape) in order to maximize the enhancement. In Figure 3-3, we show the field dependence of the DNP enhancement in a static sample

of 1-^{13}C-glycine doped with 60mM 4-amino-TEMPO at 90K together with a simulated EPR spectrum at 250 GHz. Since these spectra were acquired at a higher temperature and lower radical concentration than those in Figure 3-2, the DNP enhancement is lower. On the basis of these results, we have assigned the DNP effect observed here to the thermal mixing mechanism. In particular, the maximum DNP enhancement occurs within the EPR line shape, a fact which is consistent with the excitation of allowed EPR transitions and not forbidden ones.

3.5   DNP MAS Experiments at 9 T

A variety of techniques have been successfully applied to produce sensitivity enhancements in MAS spectra. These are based upon indirect detection of low γ nuclei during fast MAS [13,14], improved multiple pulse decoupling [15], or a combination of both [27]. Thermal mixing DNP is complementary to these methods, as the dynamics of electron nuclear polarization transfer do not involve any coherent manipulation of the nuclear spins. Further, DNP can produce signal enhancements of several orders of magnitude, albeit at the expense of considerable experimental complexity relative to other approaches. For the DNP/MAS experiments presented here, the sample, consisting of U-^{13}C, ^{15}N-Proline in a 60% glycerol matrix doped with 60mM TEMPO, was loaded into a 4mM sapphire rotor while still in the liquid state and frozen in situ. In Figure 3-5, we show two-dimensional chemical shift correlation spectra of proline taken using SPC5 homonuclear double-quantum mixing [28] (a) and proton-driven spin diffusion (b) (see Figure 3-4). In both cases, the DNP enhancement was approximately 17, and the microwave output power was stable to within 1%.

198
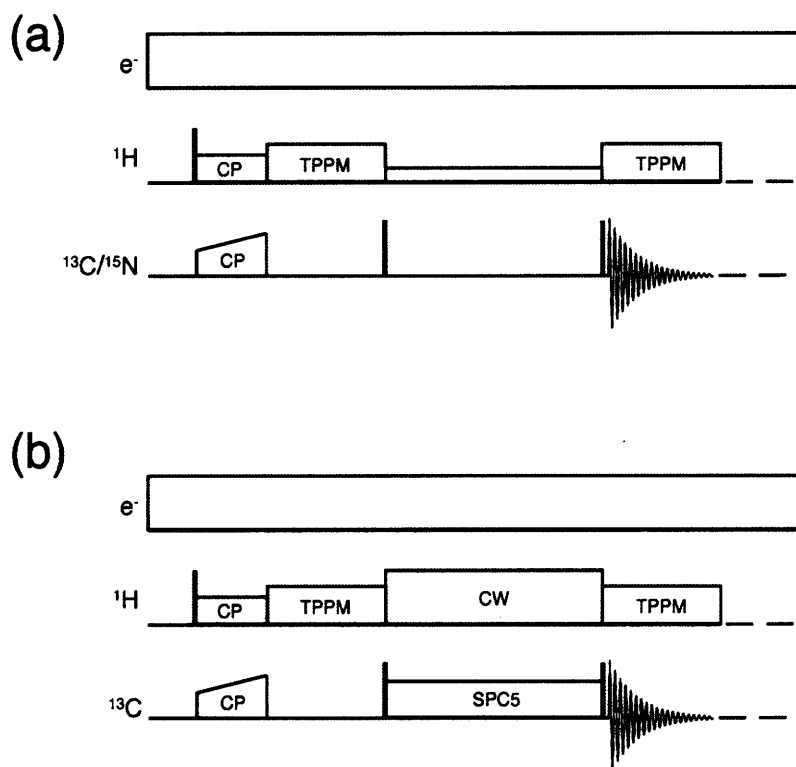
Figure 3-4: Sequences for two-dimensional homonuclear chemical shift correlation spectroscopy. Following cross polarization from ^{1}H-^{13}C, the system evolves under the ^{13}C chemical shift for a period t1. Correlations are established using mixing via (a) proton-driven spin diffusion or (b) SPC5 homonuclear double-quantum mixing as described elsewhere [28,31], and detected during t2.
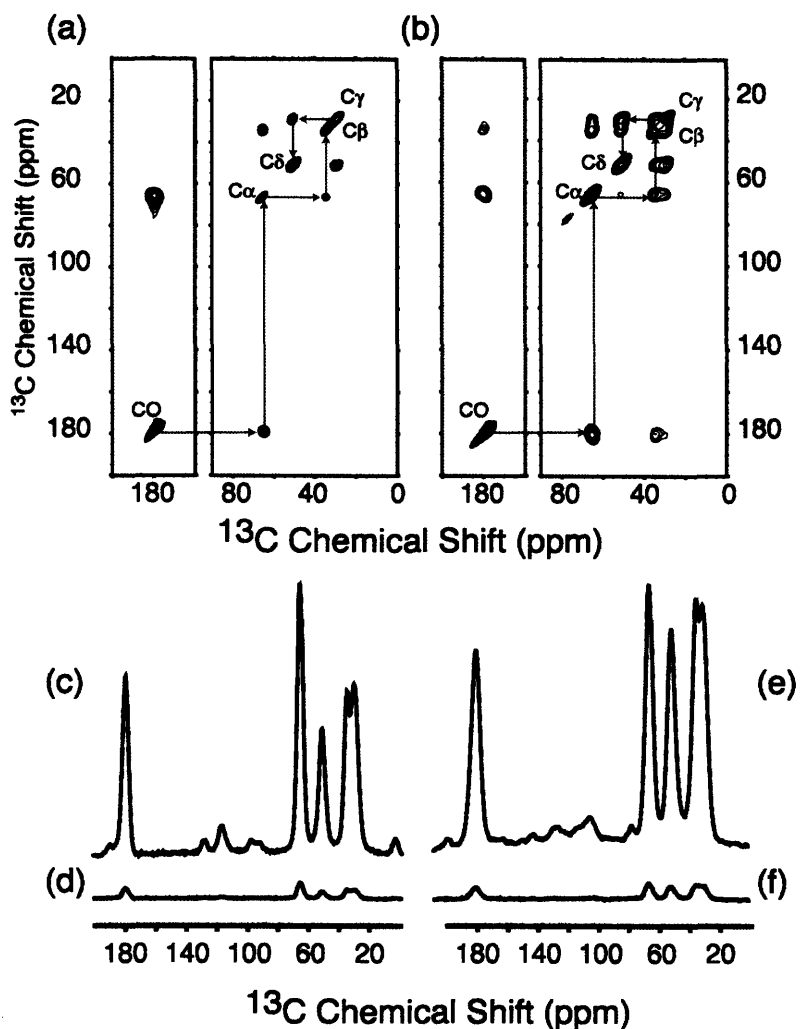
Figure 3-5: Two-dimensional ^{13}C-^{13}C correlation spectra of U-^{13}C,^{15}N-proline, in (a), the SPC5 dipolar recoupling sequence was applied during a double quantum mixing period. The MAS frequency was 6 kHz, the mixing time was 1.33 ms, and the temperature was regulated at 97 ± 0.8 K. In (b), correlations were established by proton-driven spin diffusion for a mixing time of 10ms. The MAS frequency was 7 kHz, and the temperature was unregulated but remained within the range 98-101K. In both cases, 16 transients were acquired for each of 128 increments in the t1 dimension, and the DNP enhancement was approximately 17. In (c) and (d), we show one dimensional ^{13}C MAS spectra obtained with and without DNP, respectively, using SPC5 recoupling with a double quantum phase cycle; (e) and (f) are CP spectra with and without DNP. The apparent intensity differences between the spectra in (c) and (e) are due to recoupling dynamics at short excitation times [3].

3.6   Conclusions

Using a 250 GHz gyrotron microwave source, we have obtained signal enhancements of

up to 170 ± 50 at a magnetic field strength of 9 T. These results illustrate that it is

feasible to manipulate experimental conditions including temperature, concentration and nature of paramagnetic dopant, and microwave power to obtain large enhancements of nuclear spin polarization even in elevated magnetic fields. A detailed study of these experimental parameters is currently in progress, and we are currently constructing a 460 GHz second harmonic gyrotron oscillator for DNP experiments at 16.5T (700 MHz ^{1}H) [29]. Finally, the routine incorporation of DNP into multidimensional correlation experiments, and, in particular, dipolar recoupling experiments, is now possible, and we are currently pursuing applications to the quantitative spectroscopy of biological systems.

3.7   References

[1] S. J. Opella, "NMR and membrane proteins", *Nature Structural Biology*, 4, 845-848, (1997)

[2] R.G. Griffin, "Structural studies of biological solids: Magic angle spinning and dipolar recoupling", *Nature of Structural Biology, NMR Supplement*, 508-512 (1998)

[3] A. E. Bennett, R. G. Griffin and S. Vega, "Recoupling of homo- and heteronuclear dipolar interactions in rotating solids", *NMR Basic Princ. Prog.*, 33, (1994)

[4] S. Dusold and A. Sebald, "Dipolar recoupling under magic angle spinning conditions", *Annual Reports on NMR Spectroscopy*, 185-264, (2000)

[5] M. Baldus, "Correlation experiments for assignment and structure elucidation of immobilized polypeptides under magic angle spinning", *Prog. Nucl. Magn. Reson. Spectrosc.*, 41, 1-47, (2002).

[6] C. P. Jaroniec, B. A. Tounge, J. Herzfeld and R. G. Griffin, "Frequency selective heteronuclear dipolar recoupling in rotating solids: Accurate ^{13}C–^{15}N distance measurements in uniformly ^{13}C, ^{15}N-labebed Peptides", *J. Am. Chem. Soc.*, 123, 3507-3519, (2001)

[7] K. Schmidt-Rohr, "Torsion angles in polymers", *Macromolecules*, 29, 3975-3981, (1996)

[8] X. Feng, Y. K. Lee, D. Sandström, M. Edén, H. Maisel, A. Sebald and M. H. Levitt, "Direct determination of a molecular torsional angle by solid-state NMR", *Chem. Phys. Lett.*, 257, 314-320, (1996)

[9] M. Hong, J. D. Gross and R. G. Griffin, "Site-resolved determination of peptide torsion angle phi from the relative orientations of backbone N-H and C-H bonds by solid-state NMR", *J. Phys. Chem. B*, 101, 5869-5874, (1997)

[10] P. R. Costa, J. D. Gross, M. Hong and R. G. Griffin, "Solid-state NMR measurement of Ψ in peptides: a NCCN 2Q-heteronuclear local field experiment", *Chem. Phys. Lett.*, 280, 95, (1997)

[11] V. Ladizhansky, M. Veshtort and R. G. Griffin, "NMR determination of the torsion angle Ψ in α-Helical peptides and proteins: The HCCN dipolar correlation experiment", *J. Magn. Reson.*, 154, 317-324, (2002)

[12] C. M. Rienstra, L. Tucker-Kellogg, C. P. Jaorniec, M. Hohwy, B. Reif, M. McMahon, B. Tidor, T. Lozano_Perez and R. G. Griffin, "*De Novo* determination of peptide structure with solid-state MAS NMR spectroscopy", *Proc, Nat'l. Acad. Sci.*, 99, 10260-10265, (2002)

[13] Y. Ishii and R. Tycko, "Sensitivity enhancement in solid state 15N NMR by indirect detection with high-speed magic angle spinning", *J. Magn. Reson.* 142, 199 (2000).

[14] B. Reif, C.P. Jaroniec, C.M. Rienstra, M. Hohwy and R.G. Griffin, "^{1}H-^{1}H correlation spectroscopy and distance measurements in a deuterated peptide," *J. Magn. Reson.* 151, 320-327 (2001).

[15] E. Vinogradov, P.K. Madhu, and S. Vega, "Proton spectroscopy in solid state nuclear magnetic resonance with windowed phase modulated Lee-Goldburg decoupling sequences", *Chem. Phys. Lett.* 354 (3-4), 193-202 (2002).

[16] G. J. Gerfen, L. R. Becerra, D. A. Hall, D. J. Singel and R. G. Griffin, "High frequency (140 GHz) dynamic nuclear polarization: Polarization transfer to a solute in frozen aqueous solution." *J. Chem. Phys.*, 102, 9494-9497, (1995)

[17] D. A. Hall, D. A. Maus, G. J. Gerfen, S. J. Inati, L. R. Beccera, F. W. Dahlquist and R. G. Griffin, "Polarization-enhanced NMR spectroscopy of biomolecules in frozen solution", *Science*, 276, 930-932, (1997)

[18] V. Weis, M. Bennati, M. Rosay, J. A. Bryant and R. G. Griffin, "High-field DNP and ENDOR with a novel multiple-frequency resonance structure", *J. Magn. Reson.*, 140, 293-299, (1999)

[19] M. Rosay, V. Weis, K. Kreischer, R. Temkin and R. G. Griffin, "Two dimensional ^{13}C-^{13}C correlation spectroscopy with magic angle spinning and dynamic nuclear polarization", *J. Amer. Chem Soc.*, 124, 3214-3215, (2002)

[20] B. N. Provotorov, "Magnetic resonance saturation in crystals", *Sov. Phys. JETP*, 14, 1126, (1962)

[21] W. T. Wenckebach, T. J. B. Swanenburg and N. J. Poulis, "Thermodynamics of spin systems in paramagnetic crystals", *Physics Reports*, 14, 181-255, (1974)

[22] M. J. Duijvestijn, R. A. Wind and J. Smidt, "A quantitative investigation of the dynamic nuclear polarization effect by fixed paramagnetic centra of abundant and rare spins in solids at room temperature", *Physica*, 138 B, 147-170, (1986)

[23] R. A. Wind, M. J. Duijvestijn, C. van der Lugt, A. Manenschijn and J. Vriend, "Applications of dynamic nuclear polarization in ^{13}C NMR in Solids", *Prog. NMR Spect.*, 17, 33-67, (1985)

[24] C. T. Farrar, D. A. Hall, G. J. Gerfen, S. J. Inati and R. G. Griffin, "Mechanism of dynamic nuclear polarization in high magnetic fields", *J. Chem. Phys.*, 114, 4922 – 4933, (2001)

[25] K. E. Kreischer, C. T. Farrar, R. G. Griffin and R. J. Temkin, "The use of a 250 GHz gyrotron in a DNP/NMR spectrometer", *Proc. 23rd Intl. Conf. Infrared and Millimeter Waves*, 357-141, (1998)

[26] M. Rosay, A. Zeri, N.S. Astrof, S.J. Opella, J. Herzfeld, and R.G. Griffin, "Sensitivity enhanced NMR of biological solids: Dynamic nuclear polarization of Y21M fd bacteriophage and purple membrane" *J. Am. Chem. Soc.* 123 1010-1011 (2001).

[27] P. K. Madhu, Xin Zhao and Malcolm H. Levitt, "High-resolution ^{1}H NMR in the solid state using symmetry-based pulse sequences", *Chem. Phys. Lett.* 346, 142-148 (2001)

[28] M. Hohwy, C.M. Rienstra, C. P. Jaroneic, and R.G. Griffin, "Fivefold Symmetric homonuclear dipolar recoupling in rotating solids: Application to double quantum spectroscopy," *J. Chem. Physics* 110, 7983 (1999).

[29] M. K. Hornstein, V.S. Bajaj, R. G. Griffin, K. E. Kreischer, I. Mastovsky, M. A. Shapiro, and R. J. Temkin, "Design of a 460 GHz second harmonic gyrotron oscillator for use in dynamic nuclear polarization," *Int. Conf. on Infrared and Millimeter Waves* (2002).

[30] D. Budil, K.A. Earle, W.B. Lynch, J.H. Freed, in: A.J. Hoff (Ed.), Advanced EPR: Applications in Biology and Chemistry, Elsevier, Amsterdam, 1989.

[31] C.M. Rienstra, M. Hohwy, M. Hong, and R.G. Griffin, "2D and 3D ^{15}N^{13}C^{13}C NMR chemical shift correlation spectroscopy of solids: Assignment of MAS spectra of peptides," *J. Am. Chem.* Soc. 122, 10979-10990 (2000).

Chapter 4   Corrugated Waveguide and Directional Coupler for CW 250 GHz Gyrotron DNP Experiments

A 250 GHz corrugated transmission line with a directional coupler for forward and backward power monitoring has been constructed and tested for use with a 25-watt CW gyrotron for dynamic nuclear polarization (DNP) experiments. The main corrugated line (22 mm internal diameter (i.d.), 2.4 m long) connects the gyrotron output to the DNP probe input. The directional coupler, inserted approximately midway, is a 4-port crossed waveguide beamsplitter design. Two beamsplitters, a quartz plate and 10-wire array, were tested with output coupling of 2.5% (-16 dB) at 250.6 GHz and 1.6% (-18 dB), respectively. A pair of mirrors in the DNP probe transferred the gyrotron beam from the 22 mm waveguide to an 8 mm helically corrugated waveguide for transmission the final 0.58 m distance inside the NMR magnet to the sample. The transmission line components were all cold tested with a 248 ± 4 GHz radiometer. A total insertion loss of 0.8 dB was achieved for $HE_{1,1}$ mode propagation from the gyrotron to the sample with only 1% insertion loss for the 22 mm diameter waveguide. A clean Gaussian gyrotron beam at the waveguide output and reliable forward power monitoring were achieved for many hours of continuous operation.

4.1   Introduction

The recent availability of multiwatt CW power at 250 GHz for dynamic nuclear polarization (DNP) [1] and other diagnostic applications has created a need for efficient,

205

moderate power transmission line and directional coupler components. Fundamental mode WR-03 waveguide components (0.86 x 0.43 mm inside dimensions) are not practical due to high insertion losses of $\geq$ 8 dB/m. High transmission efficiencies at 250 GHz can be achieved by using overmoded waveguide (cross section dimensions greater than a wavelength) or optical components. The most efficient overmoded waveguide mode is the $HE_{1,1}$ mode in corrugated waveguide [2]. This mode also ideally couples to a free space Gaussian beam, which is optimum for achieving the smallest possible diffraction limited spot sizes for maximizing power concentration or spatial resolution in an experiment.

Corrugated waveguide transmission lines are a well-established technology widely used with gyrotrons at lower frequencies. Some examples are the transmission lines at 110 GHz on the DIII-D tokamak [3], at 140 GHz on the ADSEX-Upgrade tokamak [4], and at 84 and 168 GHz on the Large Helical Device (LHD) stellarator [5]. In this report we extend this technology to 250 GHz.

In addition to efficient transmission, a directional coupler is required in most experiments to monitor forward and reflected power. In high power gyrotron transmission lines at lower frequencies this is typically accomplished with small coupling holes in the mirror of a miter bend. Practical considerations due to the high power levels and requirements for heat dissipation limit the coupling holes to linear arrays as used in the transmission lines at 110 GHz on DIII-D [6] and at 140 GHz on the Frascati Tokamak Upgrade [7]. To overcome the power coupling variations of a linear array when multiple modes are present in the transmission line, experiments with a two-dimensional array of holes in a copper film on a diamond substrate for heat dissipation have also been carried

out [8]. In the work presented here a quartz optical beam splitter, which is practical at moderate power levels, was implemented inside a straight section of corrugated transmission line to provide full beam cross section coupling of both forward and reflected power. Thin wires stretched across the waveguide aperture in place of the quartz were also tested as an alternative beamsplitter.
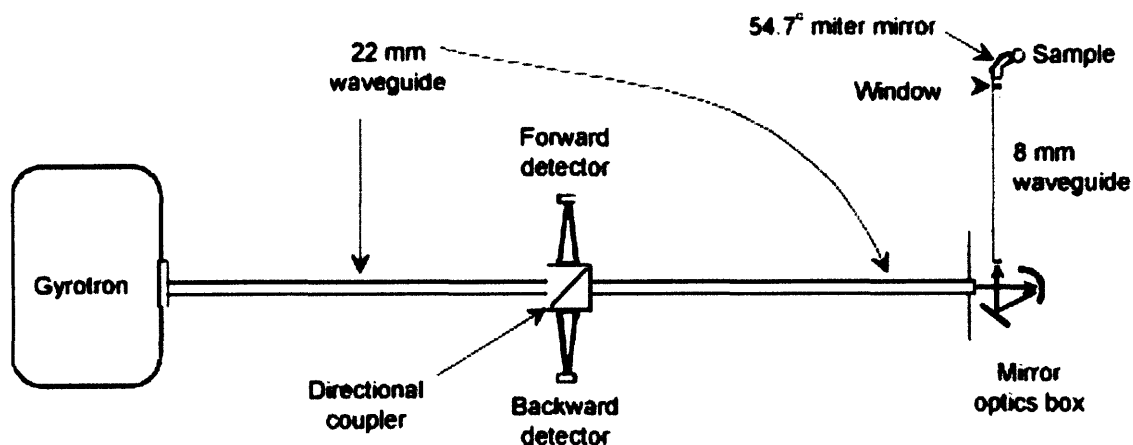
Figure 4-1: 250 GHz transmission line layout for DNP experiments.

4.2 Component Design

The layout and principal components of the 250 GHz transmission line for DNP experiments are illustrated in Figure 4-1. From the gyrotron the transmission line starts with a 22 mm diameter, 2.44 m long corrugated waveguide with a beamsplitter directional coupler near the middle. At the output of this waveguide a two-mirror optics unit focuses and directs the gyrotron beam into a smaller 8 mm diameter, 0.58 m long helically tapped corrugated waveguide. The two mirrors consist of a spherical 50 mm diameter, 50 mm focal length focusing mirror, and a 25 mm square flat steering mirror. At the sample end of the 8 mm waveguide a flat mirror, 54.7° mitered waveguide bend directs the beam to the cryogenically cooled sample. A PTFE (Teflon) window is located in the 8 mm straight waveguide just before the miter bend. The 8 mm waveguide and

sample are inside the bore of the magnet (not shown) for the DNP experiments. The 8 mm waveguide also serves the dual purpose of the central conductor of the coaxial line for the 30–300 MHz RF.

4.2.1 Waveguide

The choice of the main waveguide diameter was based on an analysis of the gyrotron output. An internal Vlasov converter inside the gyrotron transforms the $TE_{0,3}$ mode to a near Gaussian beam, launching it through a quartz window. Ray tracing analysis of the Vlasov coupler predicts a slightly elliptical beam waist at the window with minimum and maximum diameters of 10.04 and 13.72 mm. A calculation of coupling such an elliptical beam to a circular corrugated waveguide $HE_{1,1}$ mode as a function of waveguide diameter is shown in Figure 4-2. The coupling efficiency is optimal with a waveguide diameter of about 18 mm. A somewhat larger waveguide diameter of 22.2 mm (7/8 inch) was finally chosen after initial gyrotron output power measurements immediately outside the magnet dewar side bore showed greater power output coupling using a larger diameter waveguide due to the presence of higher order modes. The compromise for the calculated coupling to the $HE_{1,1}$ mode at this larger waveguide diameter is not significant, dropping only from 95% to 91%.

The 22 mm diameter corrugated waveguide was fabricated from many short aluminum tube sections with a wall thickness of 3.2 mm (1/8 inch). The circumferential wall corrugations were 0.3 mm (0.25 λ) deep and wide with a period of 0.4 mm (0.33 λ). Two 0.254 m long and fifteen 0.124 m long waveguide sections and one 0.064 m long directional coupler block were assembled with outer diameter clamps to achieve the desired waveguide length.
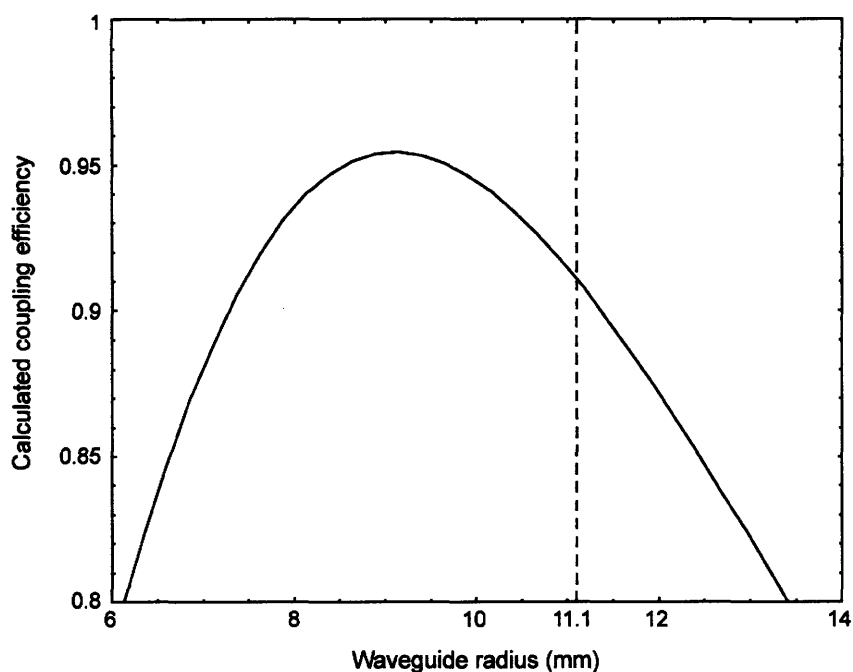
Figure 4-2: Calculated coupling efficiency of an elliptical Gaussian beam of 10.04 × 13.76 mm waist cross section to a circular waveguide $HE_{1,1}$ mode.

The 8 mm waveguide was fabricated from copper tubing with a short section of stainless steel tubing welded in the middle to act as a cryogenic thermal break. The internal corrugations were machined with a rifling tap having a pitch of 2.5 grooves per mm (3 per λ). The triangular groove depth was estimated to be between 1/4 λ and 1/8 λ.

The total polarization rotation for propagating a 250 GHz beam through this waveguide due to the helical groove was estimated to be < 3° using equation (2) in [9]. After machining, internal and external surfaces of this waveguide were flash coated with silver and then gold to provide good electrical conductivity to the RF and protection from corrosion.

4.2.2 Directional coupler

The directional coupler design, illustrated in Figure 4-3, uses crossed corrugated waveguides that are split along a diagonal of the crossed waveguide intersection to

accommodate a beamsplitter. The beamsplitter thickness and index of refraction determine the degree of reflective coupling from the main waveguide direction to the side waveguide ports. The reflectivity of a beamsplitter, assuming no absorption, is given by the standard formula [10]:
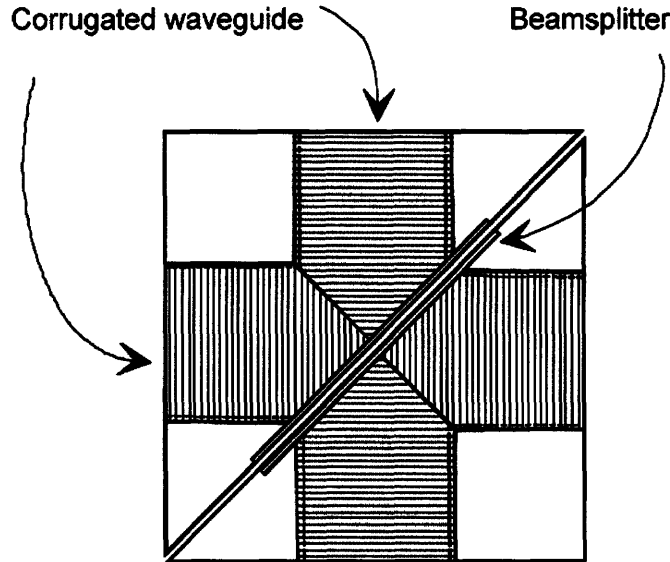
Figure 4-3: Design of the directional coupler fabricated from two corrugated waveguide corners that mate along the diagonal to hold the beamsplitter. One corner with a flat mirror along the diagonal would make a 90° waveguide miter bend.

$$\Re = \frac{4\rho\sin^2\frac{\delta}{2}}{(1-\rho)^2 + 4\rho\sin^2\frac{\delta}{2}}$$

(4.1)

where ρ is the surface reflection given by the Fresnel equations and δ is the phase difference between the beamsplitter front and back surfaces given by:

$$\delta = \frac{4\pi}{\lambda_0}nh\cos\theta_t$$

(4.2)

For the two orthogonal E-field polarizations parallel and perpendicular to the plane of incidence (the plane of Fig. 4-3):

210

$$\rho_{\parallel} = \left[\frac{\tan(\theta_i - \theta_t)}{\tan(\theta_i + \theta_t)} \right]^2 \qquad (4.3)$$

$$\rho_{\perp} = \left[-\frac{\sin(\theta_i - \theta_t)}{\sin(\theta_i + \theta_t)} \right]^2 \qquad (4.4)$$

where in the above equations θ_i and θ_t are the angle of incidence and transmission, respectively at the beamsplitter as related by Snell' law of refraction $\sin \theta_i = n \sin \theta_t$, n is the beamsplitter index of refraction, h is its thickness, and λ_0 is the gyrotron beam wavelength in vacuum.

A low coupling factor is achieved by a beamsplitter minimum in reflectivity. At 250 GHz fused quartz has an index of refraction of 1.955 [11] and for an incidence angle of 45° has a reflection minimum for a thickness of approximately 1 mm. Common microscope slides with this thickness and sufficient area (25 × 50 mm) to cover a 22 mm aperture at 45° are readily available and were used in the present experiments. Another advantage of this beamsplitter is that a visible laser beam can be introduced through a side port and its reflection off the beamsplitter can be aligned with the waveguide axis, facilitating downstream alignment of the transmission line and microwave optics.

A disadvantage of using a dielectric beamsplitter for signal coupling is that it is narrowband. Narrowband operation is not a limiting factor in this 250 GHz DNP experiment, since only the narrow gyrotron frequency is transmitted, but stability is important for monitoring power. Small changes to the beamsplitter parameters, for example due to thermal changes, could cause the coupling factor to drift. To overcome this potential limitation, experiments were carried out with thin wires stretched across the waveguide aperture as an alternative broadband beamsplitter approach.

4.2.3 Coupler with wires

(a)

(b)
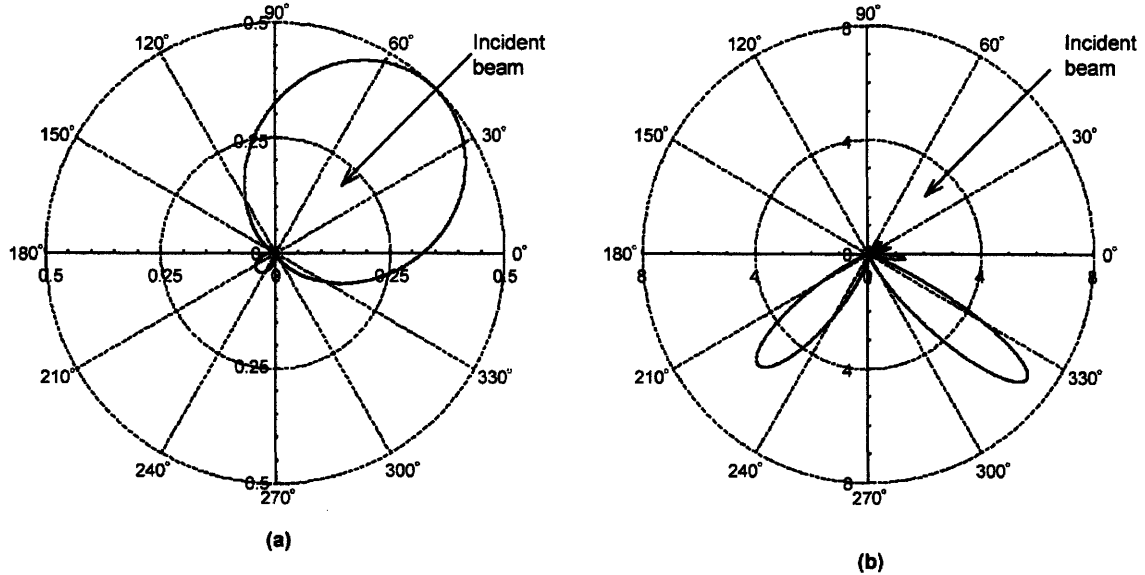
Figure 4-4: Scattered radiation patterns $(P_s/P_o \times 10^3)$ at 250 GHz by (a) one wire (36 gauge) and by (b) a ten wire array. The wires are arrayed with a spacing of 1/4 λ along the vertical axis of this figure with the wire axis normal to the figure plane. The incident beam is 45° from normal to the wire array plane with a $HE_{1,1}$ beam profile corresponding to corrugated waveguide with $ka = 58$.

The power scattered by a wire can be expressed as the product of its scattering cross section and the incident power density as:

$$P_S = \sigma P_D \qquad (4.5)$$

where σ has units of area and P_D has units of power per unit area. In the following analysis we will only consider the electric field polarization normal to the wire axis because the scattering cross-section is smaller for this orientation and we desire a small coupling factor. For an infinitely long, small radius, a, wire such that the condition $k_o\,a \ll 1$ is true the scattering cross-section is given by [12]:

$$\sigma_\perp = \frac{\pi^2 a \cos \Psi \left[(k_o a \cos \Psi)^3 \left(\frac{1}{2} \cos \phi \right)^2 \right]}{\cos^2 \Psi}$$ (4.6)

where Ψ is the angle between the incident beam and the normal to the wire axis and ϕ is the angle between the direction of the scattered signal and the plane containing the incident beam and wire. In our present coupler design for a wire stretched across the waveguide aperture perpendicular to the plane in Figure 4-3, $\Psi = 0°$ and $\phi = 90°$. A 36 gauge wire with $a = 63.5$ μm has a value $\sigma_\perp = 5.8 \times 10^{-3}$ mm^2 at 250 GHz ($k_o = 5.24$mm^{-1}).

The power density of the $HE_{1,1}$ mode inside a circular waveguide is best expressed in terms of the electric field density, E_D, as:

$$P_D = \frac{1}{2Z_o} E_D^2$$ (4.7)

where $Z_0 = (\mu_o / \varepsilon_o)^{1/2}$ is the impedance of free space and the electric field density is given by [2]:

$$E_D = \sqrt{\frac{2 P_o Z_o}{\pi}} \frac{1}{A} \frac{J_o \left(2.405 \frac{r}{A} \right)}{J_1 (2.405)}$$ (4.8)

where P_o is the power of the gyrotron beam, A is the waveguide radius, r is the radius coordinate inside the waveguide, and J_o and J_1 are Bessel functions.

According to (4.6), one wire will primarily backscatter the incident radiation (see the top of Figure 4-4). An array of wires is needed to impart directionality to the scattered signal away from the backward direction. The sum of the scattered electric field for an array of wire scatters can be calculated with the aid of the grating equation [13].

$$E_S = \sqrt{\sigma(\phi)}E_D(r_o)e^{ikr_o}\sum_{j=1}^{n}E_D(r_j)e^{ij\xi} \qquad (4.9)$$

where ξ is given by the grating equation as:

$$\xi = k_o d(\sin\theta_i + \sin\phi) \qquad (4.10)$$

and d is the spacing of the wires and

$$r_n = nd \text{ for } n \text{ odd or zero} \qquad (4.11)$$

$$r_n = \left(n + \frac{1}{2}\right)d \text{ for } n \text{ even.} \qquad (4.12)$$

Figure 4-5: View of 10-wire, gauge 36 beamsplitter stretched across the diagonal face of the corrugated 4-port directional coupler block.

The wire spacing needs to be less than the wavelength to minimize the number of side lobes in the radiation pattern. The radiation pattern for ten wires with a spacing of $0.25\,\lambda$ is shown in the lower part of Figure 4-4. The strongest radiation lobe is at about 83° to the incident beam with a scattering fraction of 0.0072 (-21.4 dB). The other strong

214

radiation lobe is in the forward direction and does not contribute to the output coupling into the side port. The 10-wire side port coupling is not as optimal as with the quartz beamsplitter due to the slight angular offset, but it would be broadband. Figure 4-5 shows the 10-wire beamsplitter implemented on the diagonal face of the split 4-port corrugated block for measurements described below.

4.3 Cold Tests

A 248 GHz heterodyne radiometer was used to test the transmission efficiency of the waveguide components with broadband thermal radiation. The radiometer obtained from Millitech used a tripled 88.67 GHz Gunn local oscillator (LO) that was frequency stabilized to a 100 MHz crystal quartz reference. The intermediate frequency (IF) amplifiers covered the 2–4 GHz range. A corrugated horn with an internal semi-angle of 2.5° and an output aperture of 18 mm provided an $HE_{1,1}$ mode field-of-view that was coupled to a 6.35 cm long 22 mm diameter corrugated waveguide section by a hollow acrylic plastic conical transition with an internal semi-angle of 4°. A second 12.4 cm long 22 mm diameter waveguide section was fixed relative to the first with a gap of about 1 cm for insertion of a chopper. A photograph of this setup is shown in Figure 4-6. The chopper permitted operation as a Dicke receiver [14] with lock-in amplifier phase sensitive detection. The double sideband (DSB) noise temperature was measured with a liquid nitrogen cooled thick (30 mm) pyramidal surfaced Eccosorb black body to be approximately T_r = 11,000 K past the chopper at the end of the 22 mm diameter waveguide. Though the theoretical measurement precision with this receiver as given by $T_r/(B\ t)^{1/2}$ [15] is 0.2°C for one second integration time (t = 1 s) and the full receiver DSB (B = 4 GHz), in practice it was at least several degrees due to electronics drift.
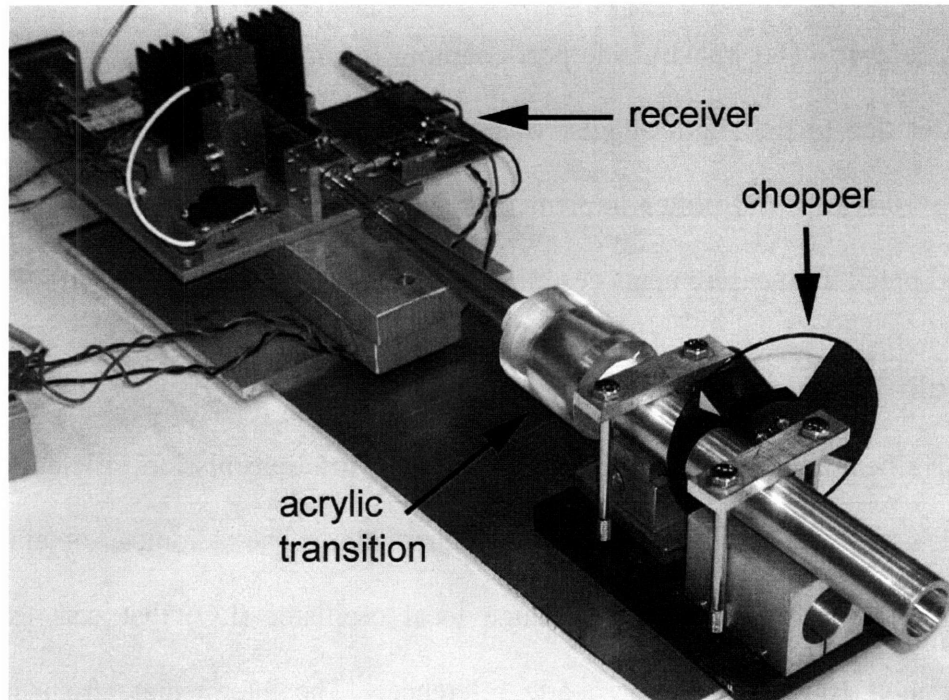
Figure 4-6: The 248 GHz heterodyne receiver used for cold test measurements.

The transmission efficiency of the 250 GHz corrugated waveguide components was determined by measuring the increase in receiver noise temperature as the components were added to the end of the receiver-chopper assembly. The results for the 22 mm waveguide and the two versions of the directional coupler are shown in Figure 4-7. The top plot (open circles) shows the transmission efficiency of the straight waveguide sections as they were built up to the full 2.4 m length without any directional coupler. A small linearly increasing insertion loss was observed that totaled 1% for the complete waveguide. This is probably an upper limit for $HE_{1,1}$ mode transmission efficiency, since it is likely that the receiver beam may have had some higher order mode content due to the acrylic transition and chopper waveguide gap.

In the next lower trace (solid circles) of Figure 4-7, a directional coupler using a 10-wire beamsplitter as described above was inserted into the 22 mm waveguide 1.37 m

from the receiver assembly. The measured loss of this coupler at the insertion location was 2.6%. In the lower trace (open squares) a directional coupler with a 1 mm thick quartz beamsplitter was inserted in the same position and measured a 6.8% insertion loss. Measurements of the noise temperature to the side port of the coupler for forward power coupling corresponded to 1.6% and 6.3% coupling fraction for the wire and quartz beamsplitters, respectively. Therefore some of the observed insertion loss is not coupled out to the monitoring port. A further measurement was made of the 4-port corrugated waveguide block without a beamsplitter and was found to have an insertion loss of about 0.5%. Consequently, the difference between the observed insertion loss and side coupling can be accounted for by the discontinuity of the crossed waveguide in the 4-port block.
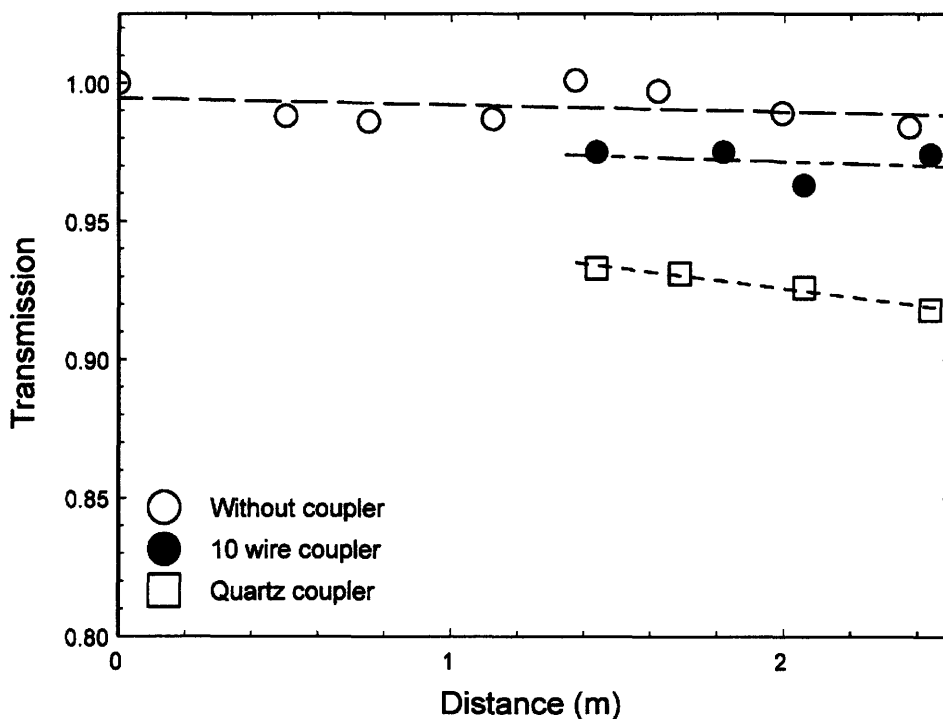
Figure 4-7: Cold test transmission measurements of the 22 mm diameter corrugated waveguide without and with two versions of the directional coupler.
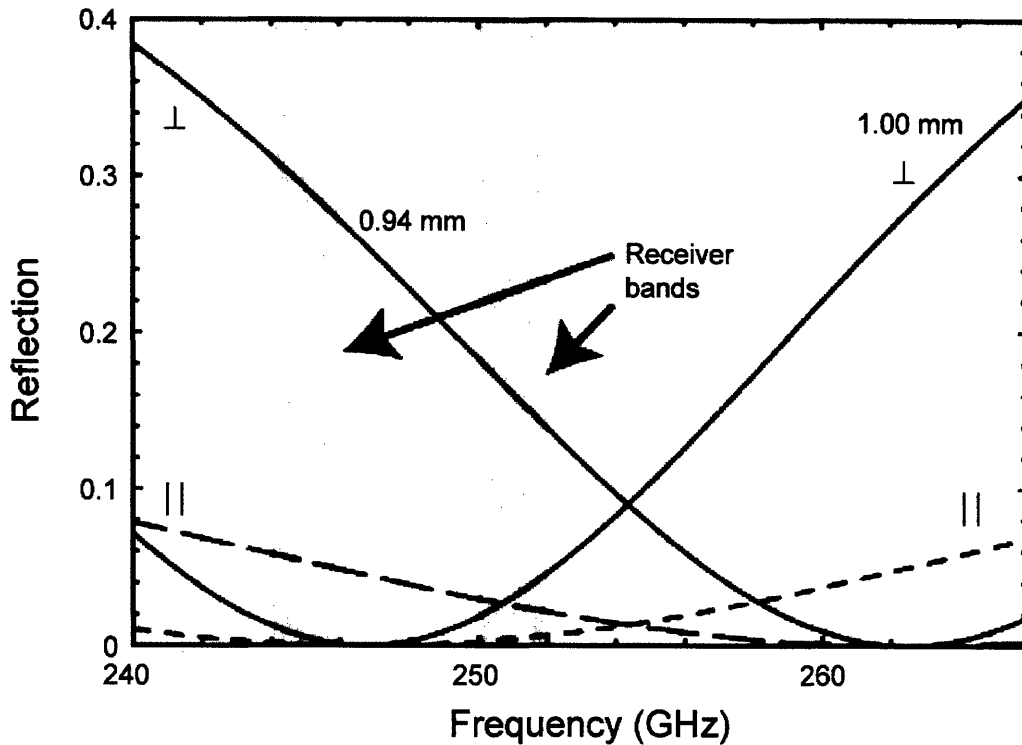
Figure 4-8: Calculated quartz (n=1.955) beamsplitter reflectivity for a beam incidence at 45° for the two orthogonal polarization cases and two thicknesses.

The measured coupling fraction of 1.6% (-18 dB) with the 10-wire beamsplitter is 3 dB larger than the calculation above. This difference may be due to the approximate nature of the calculation for $k_o a \ll 1$ where for the present case $k_o a = 0.33$.

The results for the coupler with the quartz beamsplitter can be understood with the aid of the calculations shown in Figure 4-8. The quartz reflectivity is a sensitive function of frequency and thickness. The beamsplitter thickness was measured to be 0.94 ± 0.02 mm, one of the cases plotted in Figure 4-8. Integrating the beamsplitter reflectivity over the detection bands of the receiver results in a reflectivity of 3.8 ± 2% for parallel polarization, the upper limit of which is close to the observed value. Rotating the quartz beamsplitter 90° on the waveguides axis to couple with the perpendicular polarization increased the measured coupling to 22%, which is also in agreement with the calculation of 22.2 ± 3% for a 0.94 mm thick beamsplitter. For comparison, the case for

a beamsplitter with a thickness of exactly 1 mm is also shown, which has a calculated parallel and perpendicular coupling of 0.24% and 1.7% respectively. Polishing the quartz beamsplitter to a precise thickness can be used to achieve almost any desired coupling factor less than -3 dB at a specific frequency.

Table 4.1: Cold test insertion loss measurement results with 248 ± 4 GHz radiometer

Component	Insertion Loss
22 mm waveguide, 2.44 m long	1%
Quartz coupler (6.3% coupling)	6.8%
10-wire coupler (1.6% coupling)	2.6%
4-port block w/o beamsplitter	0.5%
Transfer mirrors and 8 mm waveguide	$15 \pm 3\%$
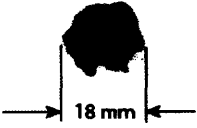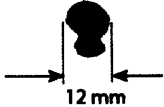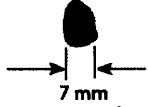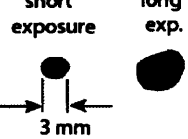
The insertion loss of the two mirrors that transfer the millimeter-wave beam from the 22 mm waveguide to the 8 mm waveguide and the 8 mm waveguide was also measured and found to be $15 \pm 3\%$. It is likely that most of this loss can be accounted for by non-optimal threaded groove parameters and an elliptical distortion of the millimeter-wave beam caused by the spherical focusing mirror that is used at about 30° off axis. Table 4.1 summarizes the cold test insertion loss measurements.

4.4 Measurements with Gyrotron

The 22 mm diameter corrugated waveguide with the quartz 4-port directional coupler was tested with the CW gyrotron beam. Power was measured with a Model 362 Scientech calorimeter and mode patterns were obtained with thermal burn paper backed by a flat sheet of Eccosorb to enhance absorption. The power measurements were not corrected for the actual millimeter-wave absorption by the calorimeter detector element [16]. Table 4.2 summarizes the results. The gyrotron power output was set to about 5 watts for these measurements, which is adequate for the DNP experiments and allows very stable

operation for periods of over 10 days. Operation with output power up to 25 watts is possible when long-term drift is not important.

Table 4.2: 250 GHz gyrotron beam measurements

Distance from Gyrotron Window (cm)	Burn Pattern	Power (W)
30 (no waveguide)	18 mm	-
38	18 mm	4.5
100	12 mm	-
132 (after quartz coupler)	7 mm	-
244	short exposure long exp. 3 mm	4.1

The top burn pattern was taken without any waveguide immediately outside the gyrotron magnet side port, about 30 cm from the gyrotron window. The irregular appearance of the beam indicates the presence of higher order modes. However, the nonlinear absorption properties of the thermal paper may exaggerate the content of higher order modes. In the next entry, a 38 cm long section of the 22 mm waveguide was brought into near contact with the gyrotron window and aligned to maximize the power output. At this point the beam is significantly distorted and elongated in the horizontal direction. The next measurement was made after 1 m of waveguide was added to the output of the gyrotron window. The beam now has evolved to two vertically separated

hot spots. In the next entry, with 132 cm of waveguide including the directional coupler the beam has become a smaller elliptically elongated spot. Finally, at the output of the full waveguide we have a single circular spot. Here two burn paper exposures are shown. The short exposure shows a small circular spot. In the longer exposure, the small circular spot has been burned from black to a lighter shade of gray making the outer regions of the beam visible, showing that the beam is circular over a large dynamic range. This suggests that the higher order gyrotron modes have been filtered from the beam by the 2.4 m long transmission through the corrugated waveguide. A power measurement of 4.1 watts was made at the waveguide output. This corresponds to an 11% loss relative to the first measurement of 4.5 watts near the gyrotron output.

The forward output coupling of the quartz directional coupler was also tested with the calorimeter. A coupled fraction of 2.5% was measured. This is lower than the cold test result because the quartz beamsplitter has a smaller reflectivity at the 250.55 GHz gyrotron frequency versus the two IF bands of the cold test receiver (*cf.* Figure 4-8). The gyrotron frequency was accurately established by harmonically mixing with a frequency counted and PLL-regulated Gunn oscillator and performing a Fourier transform measurement of the IF frequency on a digital oscilloscope.
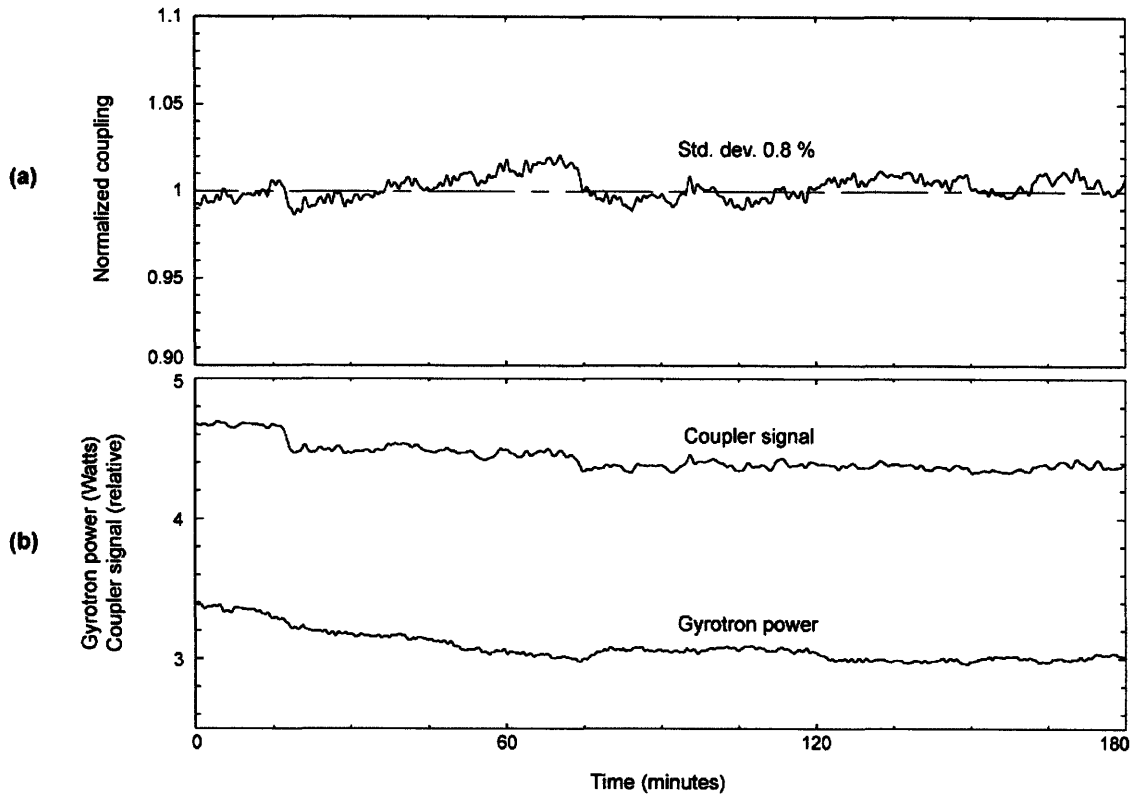
Figure 4-9: Three hour CW test of the quartz directional coupler stability, (a) normalized ratio of forward coupled signal and gyrotron power shown in (b).

A 3-hour test of the directional coupler was also carried out to determine thermal stability with the gyrotron beam. A detector diode in WR-3 waveguide was matched to the forward power monitoring port with a 2.5° corrugated horn from Millitech, a 4° hollow acrylic taper, and a short section of 22 mm dielectric waveguide similar to the setup of the 248 GHz radiometer described above. A thick pyramidal surfaced Eccosorb dump blocked the reflection monitoring port opposite the forward port for this test. The harmonic frequency measurement receiver was used to simultaneously monitor the gyrotron power in the main beam after the directional coupler by intercepting a small part of the beam at a distance. Figure 4-9 shows the results. The measured power levels are shown in Figure 4-9(b) and the normalized ratio of these signals is plotted in Figure 4-9(a). The coupling factor remains relatively stable over the three hour period. Drifts in

the detection electronics can explain the observed deviation of 0.8% in the coupling factor.

This directional coupler design will require careful matching of the detector diodes and/or isolation when both forward and backward detectors are simultaneously implemented because they view each other cross the beamsplitter.

4.5   Conclusions

A corrugated waveguide with a full cross-section directional coupler for use with a moderate power CW 250 GHz gyrotron for DNP experiments has been fabricated and successfully tested. Precise measurements of small insertion losses and coupling factors were made possible with the use of a wide bandwidth radiometer, 248 ± 4 GHz, for cold testing rather than a coherent source that would have had standing wave inaccuracies. The total transmission loss for an $HE_{1,1}$ mode from the gyrotron to the sample was found to be about 0.8 dB over a total distance of 3 m with a directional coupler, an optical change in waveguide diameter, a Teflon window, and a miter bend. The actual loss was about 1.1 dB due to the presence of higher order modes in the gyrotron beam. However, with 5 watts output at the gyrotron 4 watts can be readily coupled to the sample, more than adequate for the DNP experimental requirements. Most of the insertion loss of about 0.7 dB occurs in the 0.58 m long, 8 mm diameter waveguide inside the DNP magnet probe and the associated two mirrors that transfer the gyrotron beam from the 22 mm diameter waveguide. Future improvements in the performance of this section of the transmission line system are possible by replacing the spherical mirror with an off axis parabolic mirror and improved corrugation parameters. The main 22 mm diameter, 2.44

m long waveguide with optimum corrugations was found to have an upper limit for $HE_{1,1}$ mode transmission losses of only 1%.

The problem of monitoring forward power was solved with a 4-port crossed corrugated waveguide with a beamsplitter. Two types of beam splitters were tested, a narrow band thin quartz plate and a broadband 10-wire scattering array. The quartz plate has the advantage that a visible laser beam can be superimposed on the millimeter-wave beam for alignment, but it has a disadvantage that it may be susceptible to frequency drift of the coupling factor under thermal loading by the gyrotron beam. The 10-wire scattering array is broadband and the wires are good thermal conductors, potentially making the 10-wire array coupling factor more stable at higher power. Both beamsplitters cold tested about as predicted and in the present ~5 watt CW gyrotron tests the quartz beamsplitter did not reveal any problem with thermal drift. This directional coupler design along with the corrugated waveguide demonstrated here provide an efficient solution to the problem of transmitting and monitoring millimeter-wave beams at a frequency of 250 GHz.

4.6   References

[1] V. S. Bajaj, C. T. Farrar, M. K. Hornstein, I. Mastovsky, J. Vieregg, J. Bryant, B. Elena, K. E. Kreischer, R. J. Temkin, and R. G. Griffin, "Dynamic nuclear polarization at 9 Tesla using a novel 250 GHz gyrotron microwave source," *J. Magn. Reson.*, vol. 160, pp. 85–90, 2003.

[2] J. L. Doane, "Propagation and mode coupling in corrugated and smooth-walled circular waveguides," in *Infrared and Millimeter Waves*, K. J. Button, Ed. New York: Acadamic, 1985, vol. 13, ch. 5.

[3] R. W. Callis *et al.*, "The 6 MW, 110 GHz system for the DIII-D tokamak," in *IEEE Int. Plasma Science Conf. Rec.*, 2002, Abstract 02CH37340, pp. 294–294.

[4] F. Leuterer *et al.*, "Experience with the ECRH system of ASDEX-upgrade," *Fusion Eng. Des.*, vol. 53, pp. 485–489, 2001.

[5] H. Idei *et al.*, "Electron cyclotron heating scenario and experimental results on LHD," *Fusion Eng. Des.*, vol. 53, pp. 329–336, 2001.

[6] J. Doane *et al.*, "Quasi-Optic components in oversized corrugated waveguide for millimeter-wave transmission systems," presented at the 23rd Int. Infrared Millimeter-Waves Conf., T. J. Parker and S. R. P. Smith, Eds., Colchester, U.K., 1998.

[7] A. Simonetto *et al.*, "Directional couplers-polarimeters for high-power corrugated waveguide transmission lines," *Fusion Sci. Technol.*, vol. 40, pp. 247–251, 2001.

[8] C. P. Moeller, J. Lohr, and J. L. Doane, "The measured performance of a millimeter wave beam splitter," in *23rd Int. Infrared Millimeter-Waves Conf. Dig.*, R. J. Temkin, Ed., San Diego, CA, 2002, IEEE Catalog 02EX561, pp. 307–308.

[9] P. P. Woskov and C. H. Titus, "Graphite millimeter-wave waveguide and mirror for high temperature environments," *IEEE Trans. Microw. Theory Tech.*, vol. 43, no. 12, pp. 2684–2688, Dec. 1995.

[10] M. Born and E. Wolf, Principles of Optics, 5th ed. New York: Pergamon, 1975, sec. 7.6.

[11] J. W. Lamb, "Miscellaneous data on materials for millimeter and submillimeter optics," *Int. J. Infrared Millim. Waves*, vol. 17, pp. 1997–2034, 1996.

[12] G. T. Ruck, D. E. Barrick, W. D. Stuart, and C. K. Krichbaum, *Radar Cross Section Handbook*. New York: Plenum, 1970, vol. 1, ch. 4.

[13] M. Young, *Optics and Lasers: Including Fibers and Optical Waveguides*, 5th ed. New York: Springer, 2000, ch. 6.

[14] R. H. Dicke, "The measurement of thermal radiation at microwave frequencies," *Rev. Sci. Instrum.*, vol. 17, no. 7, pp. 268–275, 1946.

[15] M. E. Tiuri, *Radio Astronomy*, J. D. Krauss, Ed. New York: McGraw-Hill, 1970, ch. 7.

[16] F. B. Foote, D. T. Hodges, and H. B. Dyson, "Calibration of power and energy meters for the far infrared/ near millimeter wave spectral region," *Int. J. Infrared Millim. Waves*, vol. 2, pp. 773–782, 1981.

Chapter 5   250 GHz CW Gyrotron Oscillator for Dynamic Nuclear Polarization in Biological Solid State NMR

This chapter will appear in the following publication:

We describe the parameters and control characteristics of a gyrotron oscillator operating at 250 GHz for periods of up to 21 days with a 100% duty cycle. The 250 GHz gyrotron is the first gyro-device designed with the goal of seamless integration with an NMR spectrometer for routine dynamic nuclear polarization (DNP)-enhanced NMR spectroscopy. Multidimensional correlation spectra of the membrane protein bacteriorhodopsin recorded with DNP yield chemical shift assignments for several active site resonances and demonstrate the capabilities of this system in quantitative NMR experiments. Under extensive computer control, the gyrotron operates in continuous with a power stability of 1% and a frequency stability of better than 400 kHz. Power output is regulated through feedback control, which we have implemented by sampling the forward and reflected beam power using a quasi-optical directional coupler in overmoded corrugated waveguide. Radiation intensity patterns from the corrugated waveguide were measured using three techniques to confirm pure $HE_{1,1}$ mode content: thermal paper; a thermometric approach based on the temperature-dependent color of liquid crystalline media applied to a substrate; and, finally, imaging with a pyroelectric camera. Exploration of the operating characteristics of several fundamental modes reveals broadband continuous frequency tuning of up to 1.8 GHz as a function of the magnetic field alone. Oscillation of the 250 GHz gyrotron at the second harmonic of

cyclotron resonance begins at extremely low beam currents (as low 12 mA) at frequencies between 320-365 GHz. The low starting currents were attributed to an elevated cavity Q, which is confirmed by cavity thermal load measurements.

5.1   Introduction

Due to the excellent resolution in nuclear magnetic resonance (NMR) spectra, NMR has become the preferred spectroscopic approach for the solution of problems in many areas of physics, chemistry, biology, materials science, and more recently medicine. Its excellent resolution is a consequence of long nuclear relaxation times that are in turn a due to the small magnetic moments of the nuclear spins that couple weakly to the surrounding lattice. However, an additional effect of the size of these magnetic moments is that the sensitivity of NMR experiments is low when compared to other spectroscopic approaches. Further, since both high resolution solid state and solution NMR are utilized with increasing frequency in structural studies of macromolecular biological systems sensitivity continues to be an issue of paramount importance in the successful application of the technique.

Approaches to improving the sensitivity of NMR experiments have followed two avenues: innovations in instrumentation and in spectroscopic methodology. Outstanding examples of the former date from as early as the 1960's, when the appearance of laboratory computers enabled the implementation of Fourier transform NMR techniques resulting in signal-to-noise increases of 10-100 [1]. More recently, the development of superconducting magnets that operate at increasingly higher fields has improved sensitivity significantly, since the signal-to-noise per unit time scales as $\sim\omega_0^3$. Finally, in the last few years, cryogenically cooled probes with higher Q's in the r.f. coil and lower

noise figures in the detection r.f. preamplifiers have become routinely available, improving the sensitivity by a factor of 1.5-3 depending on the conductivity of the sample [2].

Examples of innovations in spectroscopic methodology that have improved sensitivity are also numerous. Some of the most successful approaches involve polarization transfer techniques, including cross polarization (CP) in solids [3, 4] and INEPT [5] transfers in solution, in which the polarization of a spin with a large magnetic moment is transferred to one with a smaller moment. Today, CP is an integral part of high resolution magic angle spinning (MAS) experiments in solids [6] and multiple INEPT transfers are present in essentially every biological solution NMR experiment [7]. In these approaches, the sensitivity is enhanced by a factor of (γ_I/γ_S) or about 4 for $I=^1H$ and $S=^{13}C$ and 10 when $S=^{15}N$. Another, and in fact the original, example of a polarization transfer experiment was proposed by Overhauser [8] and involved transfer of conduction electron polarization to nuclear spins in metals. Carver and Slichter [9, 10] verified Overhauser's hypothesis that such transfers and signal enhancements were possible with low field (3.03 mT) experiments performed on samples of Li metal and other materials with mobile electrons. During the 1970's the analogous nuclear Overhauser effect (NOE) was used extensively to increase sensitivity in spectra of low-γ species and is currently employed to estimate distances and to determine structures in solution NMR experiments.

Extension of electron-nuclear and other high polarization transfer experiments involving noble gases, para-hydrogen, semiconductors, or photosynthetic reaction centers [11-23] to contemporary solid state and solution experiments is very appealing, since it

could significantly enhance the sensitivity in a variety of NMR experiments. In particular, the theoretical enhancement for electron-nuclear polarization transfers is approximately $\sim(\gamma_e/\gamma_I)$, where now the ratio is $\sim$660, because of the large magnetic moment of the electron relative to the ^{1}H, making the theoretical gains in sensitivity large. Accordingly, during the 1960's and 1970's, there were extensive efforts to perform electron-nuclear polarization transfer in liquids [24, 25] and solids [26, 27], experiments that are collectively known as dynamic nuclear polarization (DNP). All of these experiments require that the electron paramagnetic resonance (EPR) spectrum be irradiated with microwaves that drive the exchange of polarization between the electrons and the nuclear spins. In the case of liquids, these are Overhauser effect transitions and in solids other mechanisms – the solid effect (SE), thermal mixing (TM) or the cross effect (CE) – dominate the polarization transfer process. Since DNP experiments require irradiation of the EPR spectrum, however, they were confined to relatively low magnetic fields because of the paucity of high frequency microwave sources. In particular, the microwave sources used in both the liquid and solid-state experiments were klystrons that operate $\leq$ 40 GHz, constraining DNP-MAS experiments to $\leq$ 60 MHz ^{1}H frequencies. Thus, if DNP was to move to higher fields employed in contemporary NMR experiments, then new instrumental approaches to producing microwaves were required.

To satisfy these requirements, we initiated efforts utilizing gyrotrons, a type of cyclotron resonance maser, as microwave sources for DNP experiments [28-30]. This choice was motivated by the fact that gyrotrons are fast wave devices [31], with interaction structures whose dimensions are large compared to the operating wavelength, and as such are capable of generating high powers (10-100 watts CW) for the extended

230

periods typical in acquisition of multidimensional NMR experiments. Because the gyrotron interaction involves a resonance between the r.f. modes of an electromagnetic cavity and an axial magnetic field, the gyrotron frequency can in principle be increased up to the available magnetic field strength. Further, the cavity can be much larger than the operating wavelength, so the power density does not increase with the gyrofrequency, resulting in long lifetimes and high reliability. We anticipate that gyrotrons will be used to at least the 1GHz ^{1}H NMR frequency regime (~660 GHz for electrons) or higher. A gyrotron was recently operated in pulsed mode at a frequency of a 1.03 THz [32].

In order to demonstrate the feasibility of employing gyrotrons in DNP experiments, we initially constructed a 140 GHz gyrotron oscillator that operates with a 211 MHz NMR spectrometer [30, 33]. This system permitted us to demonstrate DNP at 5T fields and to explore many important features of the experiments. For example, we established that cross effect DNP using biradical polarizing agents is the optimal mechanism [34-41] for high field experiments involving CW microwave radiation. Traditional approaches, based on the solid effect and thermal mixing, yield enhancements that are an order of magnitude smaller [38] or require high concentrations of polarizing agents that lead to electron-nuclear dipolar broadening [42]. In addition, the 140 GHz system permitted us to develop and refine a number of experimental techniques, for example MAS at 90 K and lower temperatures [42, 43]. Finally, over the last few years, research with the 140 GHz system led to increases in DNP enhancements from ~10 to ~300 [28, 35]. Nevertheless, this spectrometer is operating at a 5 T field, and as such is a low frequency instrument by present day NMR standards.

In order to move DNP experiments to higher fields, we have built two additional gyrotron oscillators operating at 250 and 460 GHz, corresponding to 380 and 700 MHz for ^{1}H NMR, respectively. A cursory description of the 250 GHz oscillator, initially designed and constructed by one of us (KEK), appeared elsewhere [44] and the 460 GHz oscillator is described in detail in other publications [45]. However, since the appearance of the brief description of the 250 GHz gyrotron, we have implemented many important changes to the system. In this paper we characterize the operation of the 250 GHz gyrotron oscillator with extensive measurements of several important operating parameters. We introduce two novel methods for imaging the millimeter wave beam and quantitatively determining its spectral purity. We have also demonstrated for the first time that the operating parameters of a gyrotron can be regulated under feedback control for indefinite and stable operation. For example, this is the first gyrotron for DNP that operates continuously (in true CW mode), and we have achieved uninterrupted and regulated CW operation for a period of 21 days, a record for any instrument operating in this frequency regime. In addition, we have integrated the device into a low temperature solid-state NMR spectrometer so that it now routinely performs multidimensional solid state NMR experiments on biological systems. Thus, the two of the primary goals of this paper are to provide a detailed description of this new piece of instrumentation for enhancing sensitivity in solid state NMR experiments – the 250 GHz gyrotron – and to provide examples illustrating the scientific possibilities with the enhanced sensitivity available with this equipment. For the latter goal we present in this paper DNP enhanced MAS spectra of the bacteriorhodopsin (bR) which is a 26 kD membrane protein embedded in a lipid bilayer that is a challenging test case for the DNP method. We chose

bR spectra, rather than spectra of a model compound such as urea or proline that we have used extensively in other papers demonstrating DNP [36, 46, 47], since it is a biologically important system that poses outstanding scientific questions and therefore addresses the applicability of DNP experiments to real systems. An additional important aim is to familiarize members of the magnetic resonance community with this instrumentation. In particular, while gyrotrons are well known in the microwave community, they are virtually unknown in the magnetic resonance community. Thus, the contents of this paper will serve to familiarize NMR and EPR community with the rudiments of gyrotron technology and facilitate propagation of the instrumentation to other laboratories.

An outline of the paper is as follows. In Section 5.2 we present DNP enhanced MAS NMR spectra of the membrane protein bacteriorhodopsin (bR) which demonstrate what is currently achievable with high frequency DNP experiments, including the first multidimensional spectra of a biological system acquired with DNP. The examples illustrate that it is possible to acquire spectra that are simply not accessible in the absence of DNP. Section 5.3 contains a brief discussion of the rf and microwave components of the 250 GHz/380 MHz DNP NMR spectrometer. This includes a mention of the millimeter wave transmission line, low temperature MAS probe, and cryogenics required, although we defer a complete description of these three components to other manuscripts. Section 5.4 provides a discussion of the theory of the operation of gyrotrons and a detailed description of eleven major components of the 250 GHz gyrotron and their function. Section 5.5 contains data on the operation of the gyrotron including power output as a function of beam current, spectral purity and quality, frequency pulling as a function of the magnetic field, and frequency and power output stability as a function of

several parameters. We also characterize the radiated mode of the microwave beam using two measurement techniques based on liquid crystal displays and pyroelectric camera technology. Finally, in Section 5.6 we consider the possibility of second harmonic operation in which the gyrotron frequency is twice that of the fundamental frequency in the same magnetic field. This is a feature of the 460 GHz system mentioned above and is important since generalization of second harmonic generation will reduce the cost of the magnet associated with future high frequency gyrotrons.

5.2   DNP Experiments on the Membrane Protein Bacteriorhodopsin

Two research areas where high resolution MAS experiments have proved especially successful are in studies of amyloid fibrils [48-50] [37, 51-54] and membrane proteins [42, 55-72], and in both of these cases low sensitivity currently limits the information that can be gleaned from the spectra. Accordingly, we recently demonstrated the use of DNP to enhance signal intensities in MAS spectra of amyloidiogenic nanocrystals [37] and we are currently utilizing DNP to improve the sensitivity of MAS spectra of the membrane protein bacteriorhodopsin (bR) [42]. In order to motivate the reader's interest in DNP, we present in this section DNP enhanced spectra of bR that illustrate some of the scientific experiments that are possible with the increased sensitivity that is currently available, and, as mentioned above, to address the issues of the applicability of the DNP technique to scientific questions involving membrane proteins.

Bacteriorhodopsin is a 248-residue integral membrane protein that functions as a light-driven proton pump. The protein encapsulates an *all-trans, 6-s-trans* retinylidene chromophore attached to the protein via a Schiff base linkage to Lys_{216} as it illustrated in Figure 5-1.
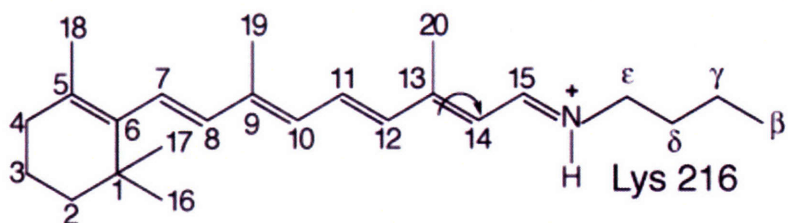
Figure 5-1: Nomenclature of ^{13}C sites of the retinal chromophore and Lys 216 side chain to which it is covalently attached. The arrow indicates that during the bR photocycle there is isomerization about the C13-C14 bond. In bR$_{568}$ the retinal is in an all-trans conformation and the Schiff base nitrogen is protonated, whereas in bR$_{555}$ (dark adapted bR) there are three retinal conformations present as shown by the DNP enhanced spectra in Figure 5-2 (*vide infra*).

The photoisomerization of the chromophore about the C13-C14 double bond initiates a vectorial proton transport process whose mechanism involves several discrete photocycle intermediates depicted in Figure 5-2. A knowledge of the precise molecular structure of the chromophore and the location of the adjacent amino acid sidechains in these intermediates could lead to a detailed understanding of the mechanism of proton translocation. Thus, the goal of the DNP enhanced MAS experiments is to provide the structures of these photointermediates.
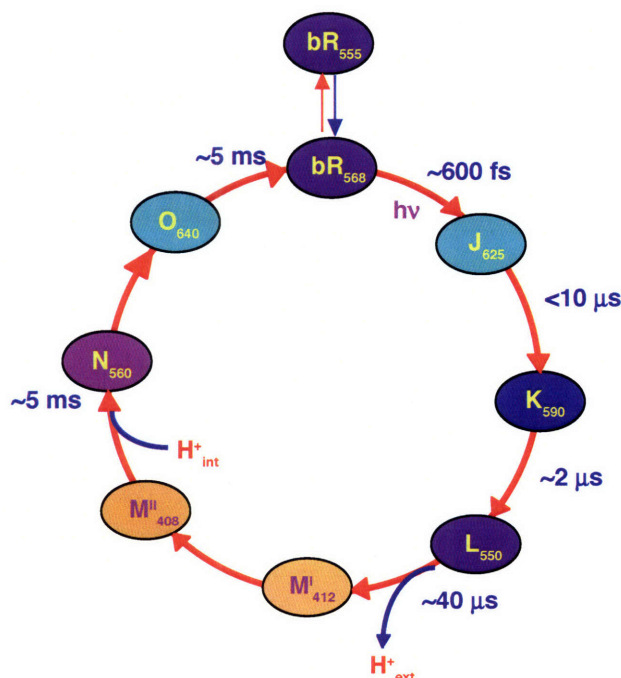
Figure 5-2: bR photocycle

235

In order to study a particular photocycle intermediate, the sample is irradiated with a

wavelength of light that maximizes its yield. The sample temperature is then lowered to

~90 K, a temperature that inhibits conversion of one intermediate to another and one

where DNP is efficient. Information about the sample preparation and conditions used to

generate and trap specific photocycle intermediates is provided elsewhere [59, 73-75]

[47]. Subsequently, one of a variety of dipolar recoupling experiments is performed

using DNP to enhance the sensitivity. At present we are observing enhancements of ~40

in the ^{1}H polarization at 250 GHz/380 MHz and this enhanced polarization is

subsequently transferred to ^{13}C or ^{15}N.

Typical pulse sequences for DNP enhanced MAS experiments are described in

several papers [29, 43, 46, 47] and the current generation experiment used to acquire the

multidimensional spectra presented here is illustrated in Figure 5-3.

250 GHz CW μwaves

^{1}H CP R^3 TPPM CW TPPM CW TPPM

^{13}C CP t2 t3

^{15}N CP t1 CP
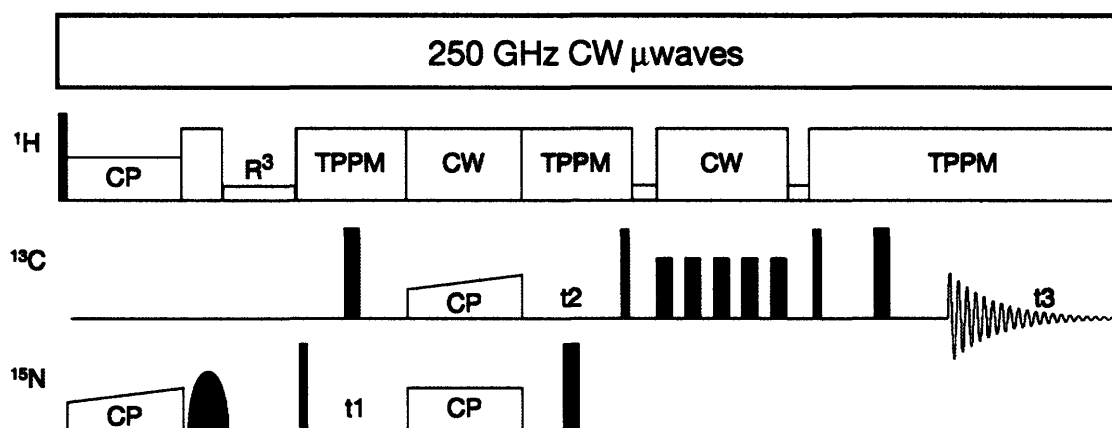
Figure 5-3: Pulse sequence for a 2D ^{15}N-^{13}C-^{13}C heteronuclear correlation experiment incorporating DNP. The EPR spectrum is continuously irradiated yielding a steady state enhanced ^{1}H polarization that is replenished during the recycle delay of the NMR experiment. Following ^{1}H-^{15}N cross-polarization, magnetization is labeled with the ^{15}N chemical shift and then transferred to the ^{13}C spins using band-selective ^{15}N-^{13}C cross polarization. Further homonuclear mixing is accomplished with a dipolar recoupling sequence such as RFDR or by proton-driven spin diffusion in the presence of an R^3 recoupling field (DARR/RAD) [76, 77] [78] [79]

236

Presently, all of our DNP experiments involve either pre- or continuous microwave irradiation, with the microwave frequency and/or magnetic field position in the EPR spectrum chosen to optimize the transfer of electron polarization to the ^{1}H spins. In the 140 GHz system mentioned above and the 250 GHz system considered here, the optimization is accomplished with a superconducting sweep coil, but in the future tunable gyrotrons [80] will likely become available. In the case of the 140 GHz/211 MHz system described previously, we generally employ long (~15-30 s) microwave pulses since the vacuum system in that gyrotron was not designed for true CW operation [30, 33] and the ^{1}H polarization appears in 3-5 T_1's [34, 37]. In contrast, the 250 GHz gyrotron operates in true CW mode – for example, it has operated continuously for a period of 21 days, but more typically we operate it for ~7 days continuously. Thus, in this case we apply microwaves continuously to maintain a steady state ^{1}H polarization. Subsequently, as illustrated in Figure 5-3, the enhanced ^{1}H polarization is transferred to the ^{13}C, ^{15}N, etc. spin reservoirs via cross polarization. We note that it is also possible to polarize the low-γ spins directly [27, 28, 81], but, because of the lower-γ the transfer process is slower and the slower spin diffusion among the low-γ nuclei limits the sphere of polarized nuclei to the vicinity of the paramagnetic center. Nevertheless, direct polarization of low γspins presents interesting scientific opportunities that have not yet been fully exploited.

Some typical DNP enhanced spectra obtained from bR are shown in Figures 5-4, 5-5 and 5-6 and illustrate the dramatic effect the increased signal to noise has on our ability to address scientific questions. In Figure 5-4 we show 1D ^{15}N spectra of ζ-^{15}N-Lysine-bR in the bR_{568} state that illustrate that DNP results in dramatically improved

signal-to-noise and reduced acquisition times, even with smaller sample quantities. As discussed elsewhere [55, 82][83] the chemical shift of the Schiff base is extremely sensitive to its local electrostatic environment, and therefore 1D spectra of a ζ-^{15}N-Lysine-labelled bR sample allow unambiguous assignment of each photocycle intermediate shown in Figure 5-2, even where multiple intermediates co-exist. Thus, spectra such as those illustrated in Figure 5-4 are of considerable interest. In the top trace we show the spectrum acquired at 200 K on a 317 MHz spectrometer without DNP using 160 μL of sample in a 5 mm rotor. The spectrum acquired, even after an extended period of data acquisition (10,000 scans, 3.5 days), illustrates the acute signal-to-noise problem that is present in MAS structural studies of membrane (and amyloid) proteins and why most of these experiments have been limited to 1D spectroscopy. In contrast, the lower spectrum was acquired at 90 K in a much shorter time period (384 scans, 30 minutes) from a 40 μL sample and displays excellent signal-to-noise suggestive of the possibility of multidimensional spectroscopy. The signal-to-noise enhancement for this spectrum
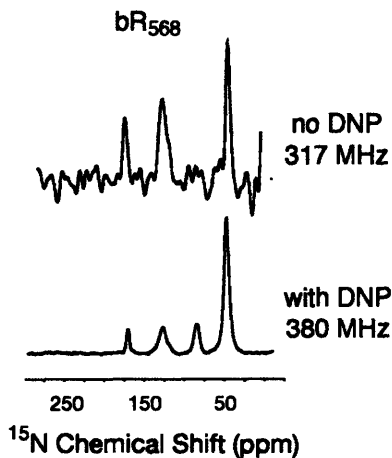
Figure 5-4: One dimensional ^{1}H decoupled ^{15}N MAS spectra of light adapted ζ-^{15}N-Lys-bR. *Top*: Spectrum acquired on a 317 MHz spectrometer using a 5 mm rotor with a 160 μL sample volume, 10,000 scans, 3.5 days (~5000 min) of data acquisition, T=200K *Bottom*: Spectrum acquired with DNP – 250 GHz microwave irradiation using a 4 mm rotor, 40 μL, T=90K, 384 scans, 30 minutes of data acquisition.

due to microwave irradiation is ~40 when compared to the spectrum obtained at 90 K without microwaves. However, since it was acquired at 90 K (as opposed to 200 K), the total enhancement, which we define as $\varepsilon^{\dagger}$, compared to the 317 MHz spectrum must also account for the increased polarization due to the Boltzmann factor [35]. Thus, $\varepsilon^{\dagger} = (200/90) \times 40 \approx 90$ as compared to the spectrum acquired on the 317 MHz spectrometer. This large signal enhancement permits us to record multidimensional spectroscopy with good signal-to noise in reasonable acquisition periods.

Figure 5-5 is an illustration of one of the initial 2D ^{15}N-^{13}C spectra obtained with the pulse sequence illustrated in Figure 5-3. As mentioned above the ^{15}N Schiff base signal is a sensitive reporter of the local electrostatic environment involved in proton translocation and its signal is well separated from the remainder of the ^{15}N signals in the spectrum of the protein. Thus, it is possible to selectively excite this resonance with a Gaussian pulse as it illustrated in Figure 5-3 and to subsequently transfer that magnetization to ^{13}C's in the retinal and lysine sidechain. Thus, following ^{1}H-^{15}N cross-polarization, magnetization is labeled with the ^{15}N chemical shift and then transferred to the ^{13}C spins using band-selective ^{15}N-^{13}C cross polarization. Subsequent homonuclear mixing is accomplished with a dipolar recoupling sequence such as RFDR or by proton-driven spin diffusion in the presence of an R^3 recoupling field (DARR/RAD). This procedure yields the spectrum shown in Figure 5-5 where we observe cross peaks between the ^{15}N Schiff base and C-15, C-14, C-13 and the methyl at C-20 on the retinal. By changing the offset frequency in the ^{15}N-^{13}C step we can transfer magnetization to the K216-Cε and K216-Cδ The spectrum in Figure 5-5 was recorded in approximately 12

hours and would not have been possible without the factor of ~90 signal enhancement
over our previous experiments mentioned above.
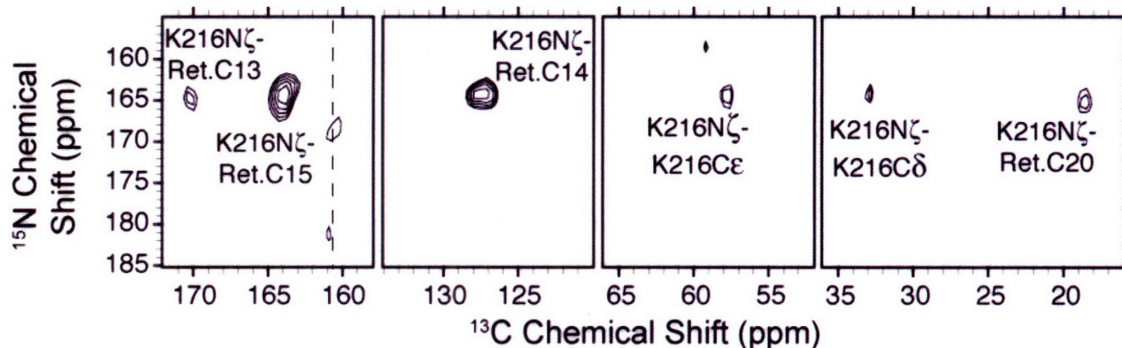
Figure 5-5: Schiff base region of 2D Lys-Nζ -Ret.-C15-CX correlation spectrum of [U-^{13}C, ^{15}N]-bR in the light adapted state. Multiple chemical shift assignments result from a single experiment.

As illustrated in Figure 5-2, bR undergoes a photocycle in response to absorption
of light and we are currently studying the spectra of the K, L and M intermediates with
the goal of determining their structure, results that will be described in detail elsewhere.
Also illustrated in Figure 5-2 is the fact that if bR is kept in the
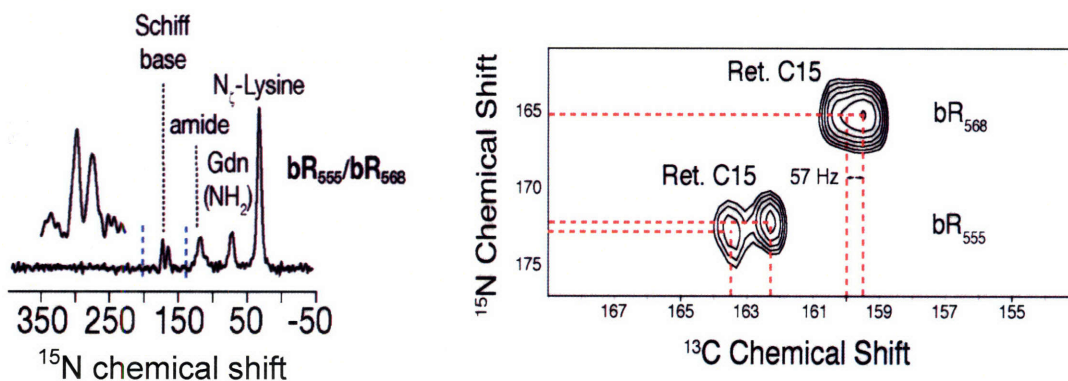
Figure 5-6: *[left]* 1D spectra of ζ-^{15}N-Lys-bR in the dark adapted state (bR$_{555}$/ bR$_{568}$) with Schiff base region shown in the inset. *[right]* 2D Lys-Nζ -Ret.-C15-CX correlation spectrum obtained from [U-^{13}C, ^{15}N]-bR in the dark adapted state. Note the presence of multiple conformers of bR$_{555}$ that are not visible in the 1D spectra and partial resolution of the J-doublet in C15 of bR$_{568}$.

dark an equilibrium mixture two species – bR_{555} and bR_{568} --forms. We initially reported the 1D ^{15}N spectrum of the bR_{555} / bR_{568} mixture [55] such as is shown in Figure 5-6 (*left*) and assigned the Schiff base line at 172 and 165 ppm to bR_{555} and bR_{568} respectively, based on their ~60:40 intensity ratio. Recently, it was suggested that bR_{555}/bR_{568} is heterogeneous and the three components of the bR trimer that exists in the bilayers may be inequivalent. The evidence for this suggestion is the observation that retinal binds with two different rates [84]. Thus, although the 1D spectrum of Figure 5-6 does not permit us to resolve this issue, the 2D ^{15}N-^{13}C spectrum shown in Figure 5-6 (*right*) that can be acquired with sensitivity enhanced DNP experiments clearly reveals two lines associated with the bR_{555} component of the mixture in agreement with the idea that the components of the trimer are inequivalent. There is also a splitting in the bR_{568} cross peak that may be due to heterogeneity, but it is also possible to interpret this as a ^{13}C-^{13}C J-coupling. In the K and L photointermediates we also observe conformational heterogeneity that may be of a different type.

In summary, the DNP enhanced MAS bR spectra presented illustrate that signal enhancements $\varepsilon^{\dagger}$ ~90 over spectra that we have published previously. This increase in sensitivity permits us to obtain 2D spectra of bR in a routine manner and to address interesting scientific issues such as the heterogeneity of the bR lattice. Finally, we emphasize that the spectra offer convincing evidence that cross effect DNP experiments using biradical polarizing agents provide significant enhancements in experiments involving a real membrane protein rather than a small molecule model system.

5.3   DNP/NMR Spectrometer

The 250 GHz/380 MHz DNP/NMR spectrometer is comprised of two collections of components belonging to the NMR and the microwave sections. This NMR components consist of a conventional triple resonance NMR console and a triple resonance transmission line probe based on the original design of McKay and Schaefer [85, 86] with an important exception discussed below. The console currently in use is from Cambridge Instruments and was designed by D.J. Ruben. The microwave section is composed of the gyrotron oscillator operating in a 9 T superconducting magnet, a corrugated waveguide that delivers the microwave power from the gyrotron to the probe, and a directional coupler for sampling the forward and reverse power. Finally, the NMR probe uses an air dielectric transmission line and the inner conductor of the line is a corrugated waveguide that ultimately transmits the microwaves to the sample. The DNP enhanced NMR experiment is performed in a second 9 T NMR magnet, located 2.4 m from the gyrotron magnet to minimize the overlap of the two fringe fields. The MAS probe typically operates at 90 K for the duration of the experiment, typically a few days. Figure 5-7(a) schematically illustrates the microwave components of the spectrometer that are clearly labeled, and in Figures 5-7(b) and 5-7(c) we show photographs of the equipment. In both photos the gray gyrotron magnet is visible on the left, the aluminum corrugated transmission line, supported on an inexpensive optical rail, can be seen running from the gyrotron towards the large NMR magnet located on the right side of the photo. The directional coupler is visible in this figure and is shown in more detail in Figure 5-7(d), and is discussed elsewhere [87]. The details of the construction of the

NMR probe will appear in separate publication. In this paper we focus on the design and operation of the gyrotron which is the major microwave component.
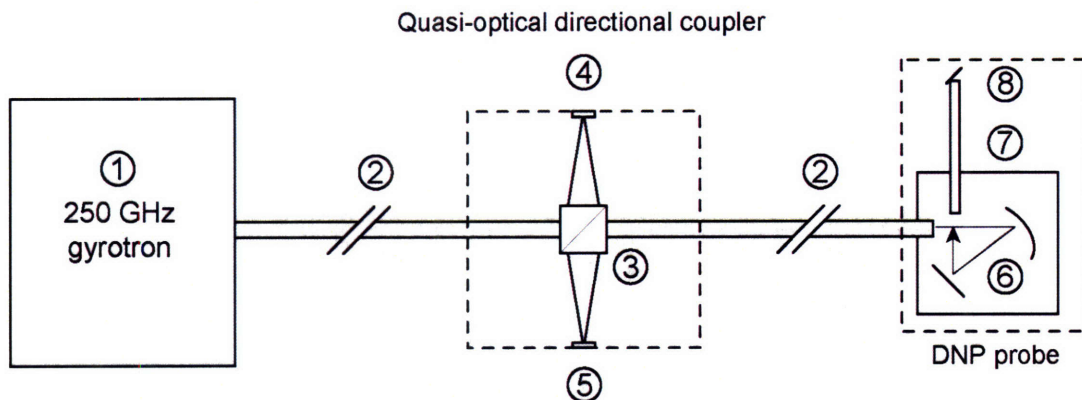
Figure 5-7(a): Schematic representation of the 250 GHz gyrotron, corrugated transmission system, and 380 MHz NMR probe. (1) 250 GHz gyrotron oscillator (2) Corrugated waveguide (22 mm i.d.). (3) Beam splitter; (4) Forward power detector; (5) Reflected power detector; (6) Focusing and reflecting mirror optics; (7) Helically corrugated waveguide (8 mm i.d.); and (8) Miter mirror.
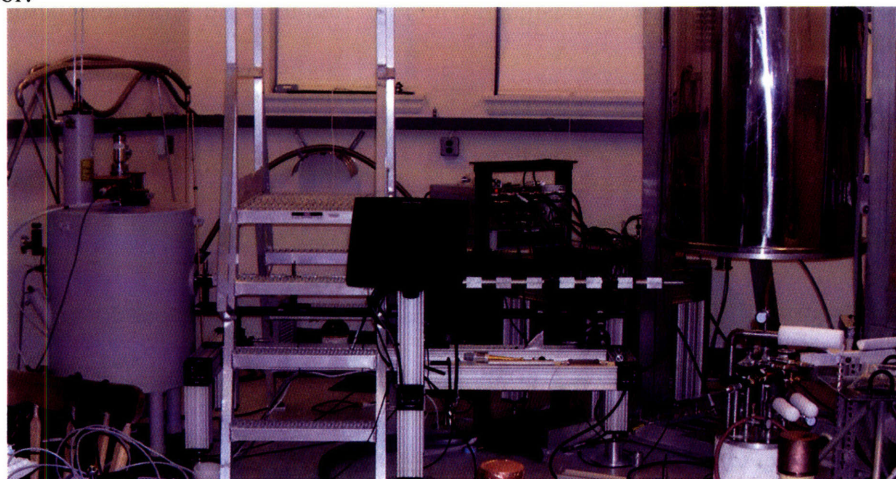
Figure 5-7(b): Side-view of the 250 GHz DNP spectrometer.
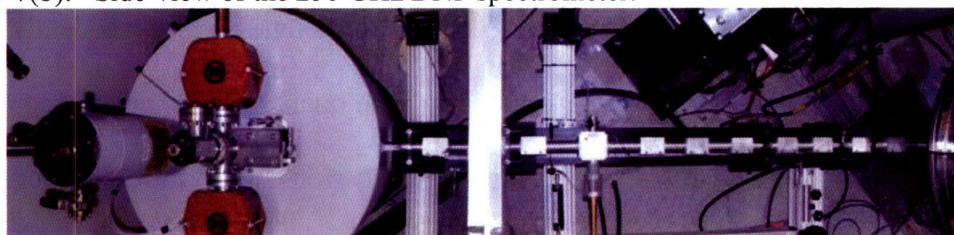
Figure 5-7(c): Composite photograph of the system illustrated schematically in Figure 5-7(a) *[left]* 250 GHz gyrotron the gyrotron tube is shown with Vacion pumps in the gray superconducting magnet, *[center]* corrugated transmission system with the directional coupler visible in the center of the photograph, and *[right]* 380 MHz NMR magnet is visible on the edge of the photo. The NMR probe is not visible since it is under the magnet. The view in this photo is from above the gyrotron and waveguide looking down.
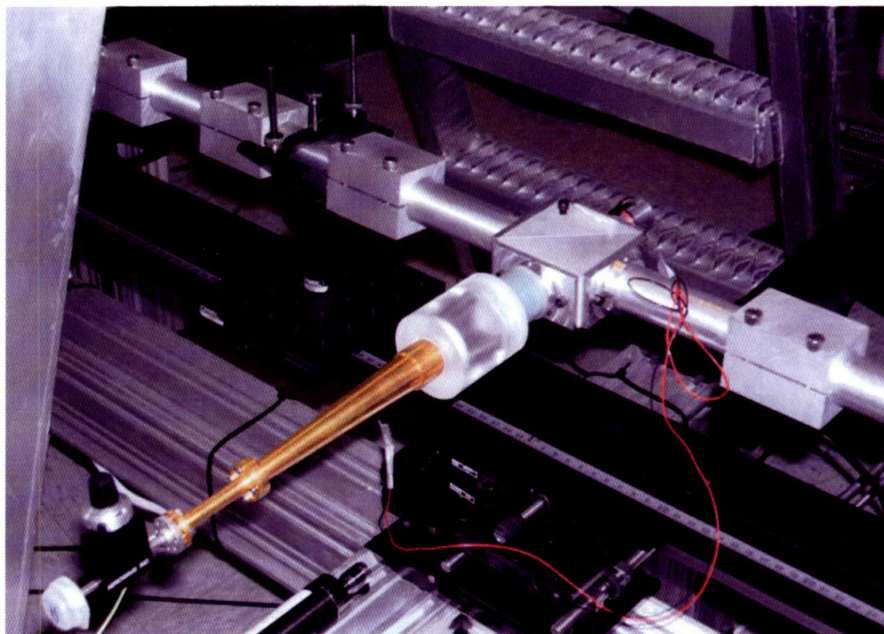
Figure 5-7(d): Photograph of the 250 GHz quasi-optical directional coupler. Forward power is coupled to the detector diode by means of a short dielectric taper, dielectric horn, and a circular-to-rectangular transition. An attenuator allows the power to be adjusted to the linear range of the diode. The detection circuit has been designed with high loss to avoid reflections across the beam splitter.

5.4   Gyrotron Oscillator

5.4.1 General Background

In this section, we provide a brief introduction to the design, theory, and operation of the 250 GHz gyrotron used in the DNP experiments described previously. We begin with an overview of the design and principles of operation of a gyrotron, and then consider the construction of the 250 GHz oscillator in detail. We subsequently discuss the theory of the operation of gyro-devices, from both quantum mechanical and classical perspectives. For more detailed and complete discussions of gyrotron principles and technology we refer the reader to one of the excellent introductory texts or review articles on this topic [31, 88-93].
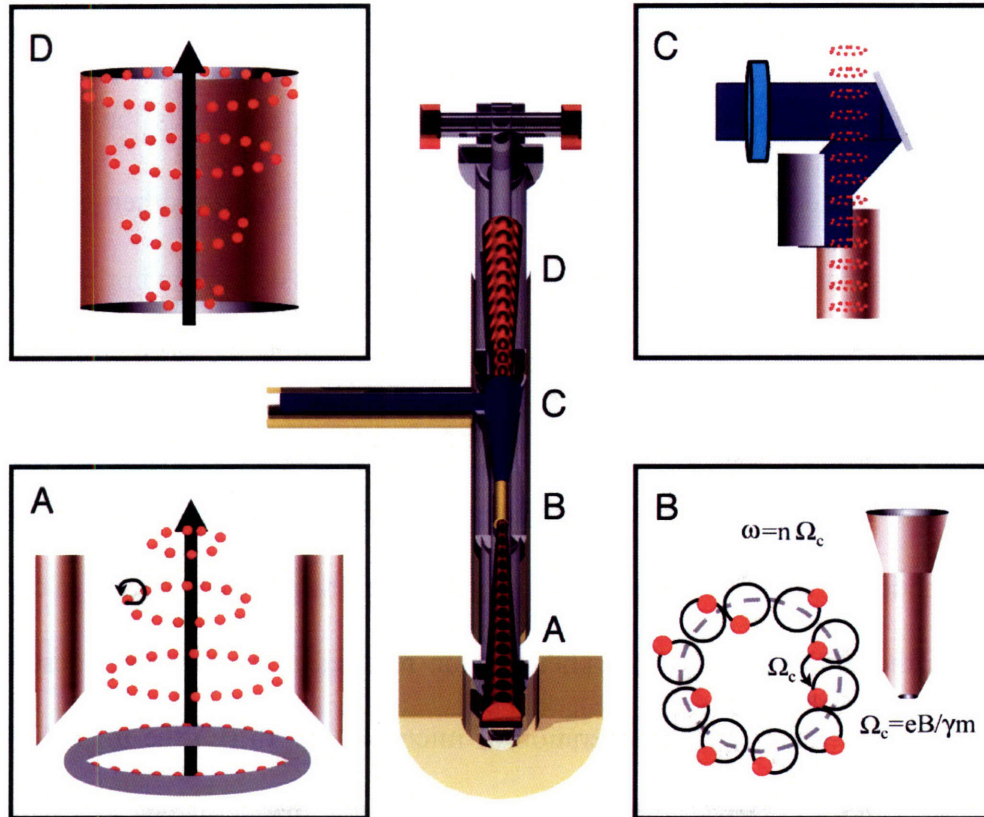
Figure 5-8: Schematic representation of the four major sections of a gyrotron tube that resides in the bore of a superconducting solenoid (see Figure 5.9). The central figure illustrates the assembled gyrotron tube and the four panels the function of each of the major sections. (A) shows the annular cathode of the electron gun from which the electrons are emitted and the cyclotron motion they undergo in the presence of the magnetic field. The red dots represent cross sections of the beam and a given point in time. In addition, the magnetic field adiabatically compresses the electron beam that it reaches the cavity with a radius optimized to interact with the cavity mode. (B) illustrates the cavity region where electron bunching leads to microwave generation. The electrons are depicted in the initial stage of the dephasing process. (C) shows the quasi-optical mode converter (consisting of a step-cut waveguide and steering mirror) that extracts the microwave beam and directs it an angle of 90° through the cross bore of the magnet and into the waveguide for sample irradiation. Note the energetic electron beam continues through the tube to the collector region. In (D) the electron beam is collected in a water-cooled collector.

A gyrotron is a vacuum electron tube that operates in a strong, static magnetic field. It functions as an electron cyclotron resonance maser that emits coherent radiation at the electron cyclotron frequency,

$$\omega_c = \frac{eB_0}{m\gamma}$$
(5.1)

or its harmonics ($s\omega_c$ with s an integer greater than one). Here e is the electron charge, m the electron mass, γ a relativistic mass factor (*see below*), and B_0 is the external DC magnetic field generated by a superconducting magnet. When other experimental constraints are satisfied, the frequency of the radiation, ω_c, is determined primarily by the strength of the magnetic field. An overview of the principal components of the gyrotron is shown schematically in Figure 5-8. An electron gun (A) contains a cathode which emits electrons that are accelerated by a voltage (~10-30 kV) applied between the anode and the cathode, moving them through the magnetic field where they precess in cyclotron motion. In the cavity region (B) a phenomenon referred to as bunching, described in more detail below, leads to the generation of microwaves. In (C) the microwaves are extracted by a mode converter through a cross bore in the magnet dewar and directed to the NMR sample through a waveguide. Finally, (D) shows the energetic electron beam impinging on a water-cooled collector.

The actual physical layout of the 250 GHz gyrotron oscillator is shown in Figure 5-9. While this gyrotron is constructed in a manner that is very similar to other demountable tube gyrotrons used in academic research, our desire to make it compact and compatible with operation in close proximity to an NMR spectrometer necessitated special design considerations.

Superconducting Magnet

A gyrotron operating at 1 GHz requires a peak magnetic field of 0.036γ Tesla, where γ is the relativistic mass factor defined below, and the magnetic field scales linearly with increasing frequency. Electrons accelerated in a potential of 10-100 kV are only

moderately relativistic (*i.e.* their energy is much smaller than the electron rest mass of
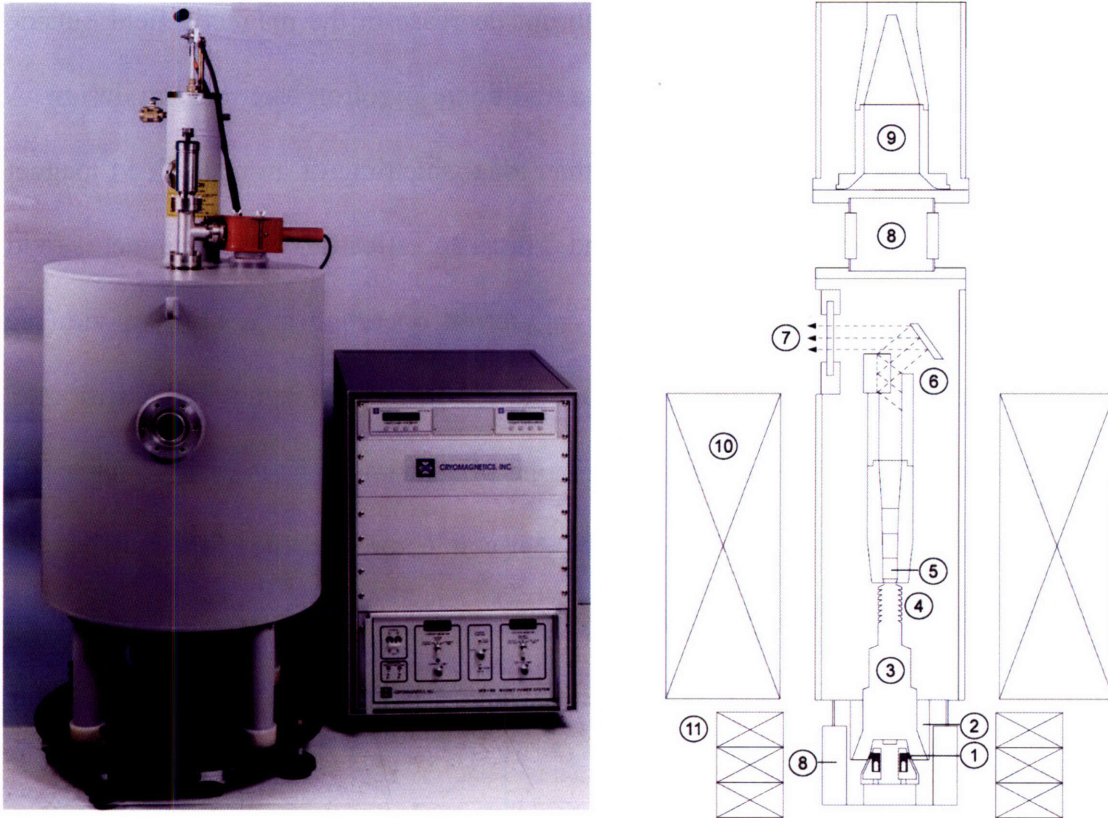
Figure 5-9: Left: photograph of the 250 GHz gyrotron and the superconducting magnet power supply. The high voltage/heater power supply and control electronics are hosted in an additional rack similar to the magnet power supply. Right: Schematic of a gyrotron tube indicating the key components. (1) cathode; (2) anode; (3) drift tunnel; (4) microwave absorber; (5) cylindrical resonant cavity; (6) quasi-optical mode converter; (7) output window; (8) high voltage ceramic insulator; (9) electron beam collector; (10) persistent superconducting magnet; (11) electromagnet.

511 kV), and so $\gamma \sim 1$. In this limit, the gyrotron operating frequency is ~28 GHz/Tesla.

Therefore, production of ~250 GHz microwaves requires a ~9 T gyrotron magnet.

The requirements for a gyrotron magnet are quite modest when compared to those of an NMR magnet. Most notably, the gyrotron oscillator requires that the cavity be located in a region spanning 10-30 free space wavelengths of the operating frequency and that the homogeneity over this region be ± 0.1 %. Outside of this "flat field" region of the solenoid, the magnetic field should decay with a $\sim 1/z^3$ (dipole) dependence, where z

is the distance along the solenoid axis. This dependence is especially important near the electron gun region for generation of a high quality beam. Thus, a typical actively shielded NMR magnet, which exhibits an abrupt decrease in the magnetic field outside the flat field region, is not compatible with a traditional gyrotron electron gun design. A partially shielded magnet with more radial than axial shielding or an unshielded magnet is desirable in a gyrotron system. The second critical specification for the magnet is field drift, and, typically, the frequency drift of a gyrotron operating in a TE_{mp1} mode (*see below*) is at least of an order of magnitude lower than the magnet field drift rate. Nevertheless, with current technology a drift rate of ~0.01 ppm/hr is easily obtained in NMR magnets fabricated from NbTi and Nb_3Sn conductor, and therefore matches the drift of the gyrotron to the drift of the NMR magnet. This is most desirable for applications of gyrotrons to DNP experiments where it is desirable to maintain a stable irradiation position in the EPR spectrum.

Electron Gun

The electron beam is generated in a diode electron gun with an annular thermionic emitter and a hollow anode. In order to avoid poisoning of the emitter when the tube is operated in true CW mode, it is necessary to maintain the vacuum at a base pressure $<10^{-9}$ Torr. The electron beam is born at a finite magnetic field generated from the decaying field of the main superconducting magnet and a local room temperature copper solenoid (10 and 11 respectively, in Figure 5-9). The electron gun is very similar to that used in a magnetron tube and hence is referred to as a magnetron injection gun (MIG). The 250 GHz gyrotron uses a diode electron gun because it is simple to fabricate and requires a single power supply, but it is not unusual to have a triode electron gun for more precise

control of the electron beam properties. The electron beam is adiabatically compressed as it traverses up the magnetic hill created by the main superconducting magnet and achieves the final beam radius in the resonator which is appropriate for exciting the desired interaction mode. The section through which the electron beam drifts during its compression is called the beam tunnel (3 in Figure 5-9) and is designed to suppress the generation of any spurious interaction modes that can compromise the beam quality. For this purpose, the beam tunnel has slotted tubes and rings of lossy ceramics to lower the quality factor and prevent excitation of spurious oscillations.

Cavity Resonator

The heart of the microwave generation system is a cavity resonator formed by a profiled cylindrical waveguide open at both ends. The simplest manifestation of the resonator is a straight cylinder with a downtaper through which the electron beam enters the resonator and an uptaper through which the electron beam and the generated microwave radiation exit. The cavity operates in a TE_{mpq} mode where m, p and q are the number of azimuthal, radial and axial variations of the mode respectively. Gyrotrons typically operate in a TE_{mp1} mode, which has a single axial variation of the field and results in high efficiency microwave generation and a stable output frequency. The frequency is determined by the radius of the straight section of the cavity and is only weakly dependent on the operating voltage, current or magnetic field. Hence, the operating mode is often designated as TE_{mp} with the understanding of one axial variation (q=1). The 250 GHz gyrotron operates typically in the TE_{032} mode because the TE_{032} mode frequency in this case is closer to the desired electron excitation frequency corresponding to 380 MHz ^{1}H frequency.

249

Mode converter

The microwave radiation is generated in a high order cavity mode such as the TE_{03} which cannot be easily extracted from the gyrotron tube and most importantly cannot be transmitted over a simple waveguide transmission line which may involve switches, bends, directional couplers and other elements. Hence, the operating mode is transformed into a linearly polarized free space TEM_{00} Gaussian beam in the tube using an internal mode converter (6, in Figure 5-9) and then extracted from the tube. The mode converter is designed using quasioptical techniques and consists of a launcher which in this case is waveguide with a step-cut to radiate the operating mode in the radial direction. The radiation is collected by a parabolic reflector that focuses it on another mirror or a series of mirrors that direct the beam out of the gyrotron tube radially through a vacuum window. In the 250 GHz tube, the mode converter has two mirrors that include the parabolic reflector facing the launcher. A second crucial function performed by the mode converter is the separation of the electron beam from the microwave radiation. This allows the electron beam to be collected in a simple collector that is described in the next section.

In many gyrotron designs the collector and output window are located above the magnet dewar and therefore the mode converter requires multiple mirrors – sometimes four or more – to eventually direct the radiation out of the tube over the top of the superconducting magnet dewar. To reduce the number of mirrors in the 250 GHz gyrotron a cross bore as shown in Figure 5-9 (left). The cross bore simplifies the mode converter design while allowing the magnet dewar to have sufficient volume to satisfy the helium hold time requirements. However, the cross bore requires precise alignment

of the tube and the internal mode converter to extract the radiation out through the narrow opening, but it has been used successfully in the 250 GHz gyrotron considered here and in the 460 GHz device described elsewhere.

Collector

The spent electron beam exiting the cavity is separated from the microwaves by the internal mode converter and is allowed to expand adiabatically in the decaying field of the superconducting magnet. After the beam radius is sufficiently large, it is collected on a water-cooled collector. The beam is allowed to expand in order to maintain the thermal load on the collector at ≤ 100 W/cm^2. Since the gyrotron typically operates at ~5% efficiency, the remaining power in the beam (12 kV x 20 mA ~250 watts) is dissipated in the collector, where a water flow rate of few gallons per minute is sufficient to extract the generated heat. The ceramic break (8, in Figure 5-9) allows independent measurement of the collector current from any body current which can be generated due to premature beam interception.

Control System

The control system consists of both electromechanical and digital controls and interlocks. Electromechanical interlocks involving the gyrotron tube pressure, coolant flow, and ambient temperature and humidity are implemented using power control hardware which also controls uninterruptible power (UPS) service to critical aspects of the experiment. Digital controls and interlocks are implemented in a combination of LabVIEW interface elements (National Instruments Inc.) operating under a Windows PC environment and, for some functions, in C++ programs. Digital I/O occurs via UDP over ethernet network

or through RS-232C/GPIB terminal servers (National Instruments Inc.). Analog I/O is accomplished through integrated data acquisition boards (Computerboards Inc.; National Instruments Inc.). Analog signal conditioning is limited to high-voltage isolation, amplification of signals, and low-pass audio filtering; further signal conditioning and parameter estimation is performed in software. Finally, standard microwave components such as video detectors, attenuators, and scalar horns etc. were purchased from Millitech Inc., Pacific Millimeter, and Aerowave and incorporated into the system. The transmission line has other specialized components that are described in the later sections.

5.4.2 Theory

As mentioned above the gyrotron can operate either as an oscillator or amplifier and it functions by converting the transverse kinetic energy of a moderately relativistic electron beam into electromagnetic radiation. Specifically, when the beam current in the device exceeds threshold (the starting current of the oscillation), then the resonant interaction of the cyclotron mode of the electron beam and the electromagnetic mode of the cavity resonator leads to energy exchange.

Cyclotron Mode: The electron beam supports cyclotron modes that obey the dispersion relation,

$$\omega = v_z k_z + \frac{s\omega_c}{\gamma}, \tag{5.2}$$

where ω is the radiation frequency, k_z is the wave vector, v_z is the axial electron velocity, s is the cyclotron harmonic number, and γ is the relativistic mass factor,

$$\gamma = \frac{1}{\sqrt{1 - v^2 / c^2}} \tag{5.3}$$

Here $v = \sqrt{v_x^2 + v_y^2 + v_z^2} = \sqrt{v_\perp^2 + v_z^2}$ is the total electron velocity. The beam pitch factor

$\alpha = (v_\perp / v_z)$ determines the transverse energy in the electron beam, where $v_\perp$ and v_z are

the parallel and perpendicular velocities respectively of the electron beam with respect to

the external DC magnetic field B_0. Specifically, (5.2) and (5.3) are a statement that the

radiation frequency ω lies near to the cyclotron frequency, but that it is upshifted by the

Doppler term, $v_z k_z$. The Doppler term arises because the synchronous precession of the

electrons is in turn perturbed by the oscillating electromagnetic field. While the Doppler

term in the resonance condition indicates that the radiation frequency can, in principle, be

much higher than the cyclotron frequency, gyrotrons typically operate in the regime

$k_z v_z \ll \omega_c$. This prevents velocity spread of the electron beam from broadening the

width of the output radiation and reducing the gain. In addition, we note from (5.2) and

(5.3) that as $v \to c$ (as the energy increases) then γ increases and the frequency of the

radiation ω decreases. This leads to bunching and the conversion of beam power to

microwaves (*see below*).

Waveguide Mode: The cavity resonator used in a gyrotron supports a transverse

electric (TE) electromagnetic wave with the following dispersion relation:

$$\frac{\omega^2}{c^2} = k^2 = k_\perp^2 + k_z^2 \tag{5.4}$$

where $k_\perp = v_{mp} / R$, R is the waveguide radius, c is the speed of light, v_{mp} is the pth root

of $J'_m(x) = 0$, $J_m(x)$ is the Bessel function of order m, and k_z is the axial wave number of

the TE$_{mpq}$ mode in the waveguide. For a simple right circular cylinder resonator, $k_z = q\pi/L$, where q is an integer and L is the cavity length. For a more general cavity shape, k_z is obtained by solving for the appropriate cavity eigenmode.

The condition for excitation of the electron cyclotron maser instability requires simultaneously satisfying both the resonance condition and the wave equation, that is (5.2) and (5.4) above, and this is illustrated graphically using the uncoupled ω-k diagram in Figure 5-10. In the figure, the dispersion relations of both the waveguide mode and the cyclotron resonance mode are shown. The gyrotron instability is excited near the point of intersection of the beam-wave and waveguide dispersion relation.
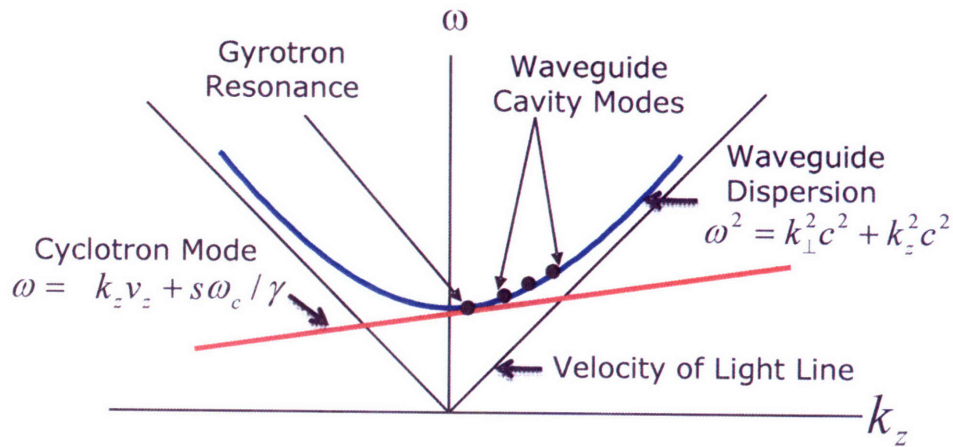
Figure 5-10: The uncoupled dispersion relations for the electron beam (cyclotron mode) and the waveguide mode (waveguide dispersion). Cyclotron maser emission can occur when the two modes coincide, as shown in the figure by the arrow at gyrotron resonance.

Quantum Theory of Gyrotrons

The gyrotron interaction can be explained understood quantum mechanically by considering the energy levels of an electron placed in a homogeneous magnetic field. For a nonrelativistic electron, the energy levels in a DC magnetic field were solved by Landau and are harmonically quantized according to [94, 95]

$$E_n = (n + \frac{1}{2})\hbar\omega_c , \qquad (5.5)$$

where n is the quantum number. These levels are evenly spaced and do not yield stimulated emission. On the other hand, a solution of the Dirac equation for an electron in a homogeneous magnetic field shows, in the weakly relativistic limit, that the energy eigenspectrum is given by:

$$E_n = mc^2[1 + (2n+1)(\frac{\hbar\omega_c}{mc^2})]^{1/2} - mc^2 \qquad (5.6)$$

[96, 97] As shown in Figure 5-11, these levels are not harmonic, because the relativistic cyclotron frequency (ω_c/γ) decreases with increasing energy (*i.e.*, v→c and γ increases). Stimulated emission is possible in a manifold of unequally spaced states, and this is the gain mechanism of the gyrotron oscillator.. The emission frequency is slightly higher than the cyclotron frequency as shown in the example below.
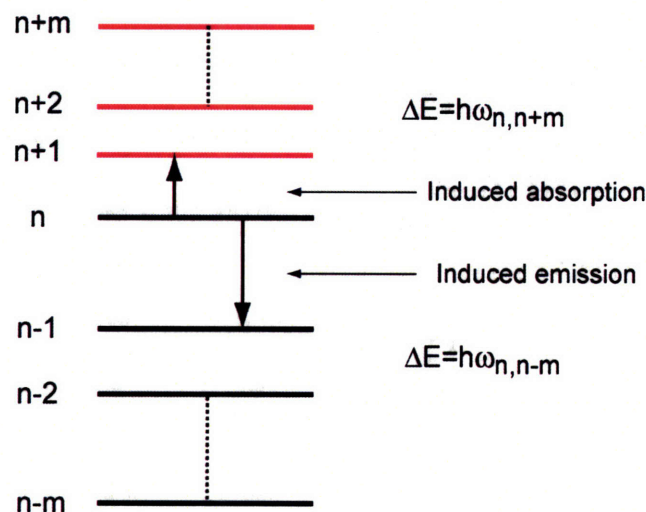
Figure 5-11: The energy spectrum of a relativistic gyrating electron showing the nonuniform spacing of the energy levels.

Following the approach of Robinson [97], one can show the net energy absorption of weakly relativistic electrons to be

255

$$W = \frac{N_n q^2 \xi_0^2 t^2}{2m} \left[\frac{\sin^2(\Gamma)}{\Gamma^2} + \frac{n\hbar\omega_c^2 t}{2m_0 c^2} \frac{1}{\Gamma} \left\{ \frac{2\sin^2(\Gamma)}{\Gamma^2} - \frac{\sin(2\Gamma)}{\Gamma} \right\} \right], \tag{5.7}$$

where N_n is the number of electrons in the nth state, q is the charge of an electron, ξ_0 is the amplitude of the electromagnetic field in a uniform resonator of length L, t is the interaction time (equal to L/v_z), m is the rest mass of an electron and Γ is half of the relative phase shift of the electrons with respect to the electromagnetic wave, defined as

$$\Gamma = (\omega_{n,n+1} - \omega)t/2. \tag{5.8}$$

In Fig. 5-12 the absorption (W) is plotted as a function of Γ for different values of the factor F defined as

$$F = \frac{n\hbar\omega_c^2 t}{2mc^2} = \frac{1}{2}\left(\frac{n\hbar\omega_c}{mc^2} \right)(\omega_c t) \tag{5.9}$$

In this equation for F, the quantity in parentheses can be identified as the ratio of the electron kinetic energy to the electron rest mass energy and the second term in the parentheses is 2π times the number of cyclotron orbits in the resonator. The condition for emission, as shown in Fig. 5-12, is that the value of F be large compared with unity. This can occur when the weakly relativistic electrons execute many orbits in the gyrotron resonator ($N = (\omega_c t) \gg 1$).

256
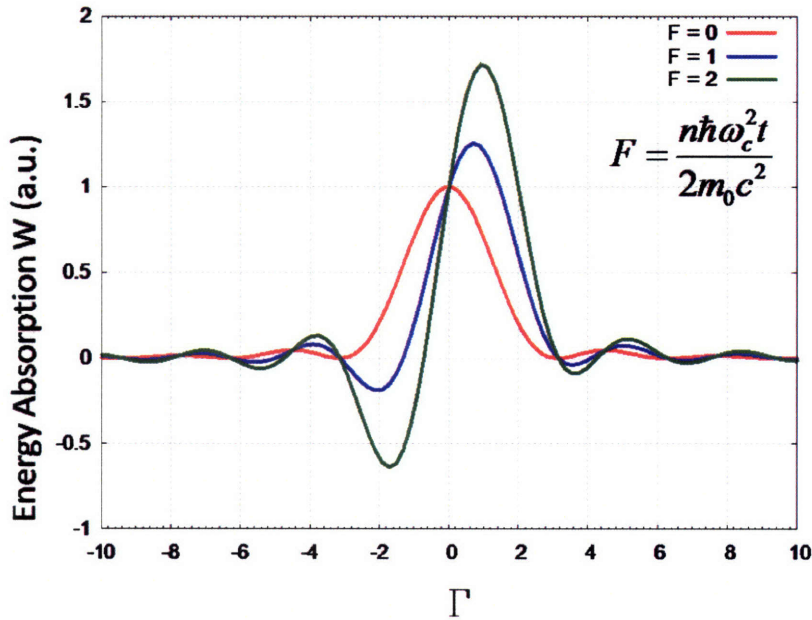
Figure 5-12: The energy absorption, E_0, (in arbitrary units) of an electron passing through a uniform resonator, as a function of the detuning from resonance. The plots are shown for different values of the parameter F. Significant energy emission ($E < 0$) requires a value of F~2. F increases with both the electron energy (electrons that are more relativistic) and the number of cyclotron orbits in the interaction region.

For moderately relativistic electrons (F>0), a proper choice of Γ, which is related to the detuning as [$\Gamma/2 = (\omega_c - \omega)t$] can lead to negative absorption or gain. In practice, for a resonator mode, the frequency ω is constant and the magnetic field is changed to vary ω_c and satisfy the beam/wave resonance condition.

However, we note that a 10 to 100 keV electron possesses an energy $\sim 10^8$ times the energy of the cyclotron photons (100 GHz = $\sim 4 \times 10^{-3}$ eV). Since the energies are large compared to the photons, the gyrotron can also be understood with classical theory, especially for the nonlinear regime.

Phenomenological Description of Gyrotron Interaction

The gyrotron interaction can also be described as a typical process in a vacuum electron device (microwave tube), where, under the force of the electromagnetic field, the

257

phenomenon of electron bunching occurs in phase space. In this process, the electrons, whose phases are initially randomly distributed,, either acquire or lose phase because of the non-uniform perturbation of the oscillating electromagnetic field. Thus, the bunched electrons are eventually decelerated to generate electromagnetic radiation. Let us consider a hollow annular gyrating electron beam drifting through a waveguide supporting a TE_{01} mode and immersed in a static background magnetic field as shown in Figure 5-13.
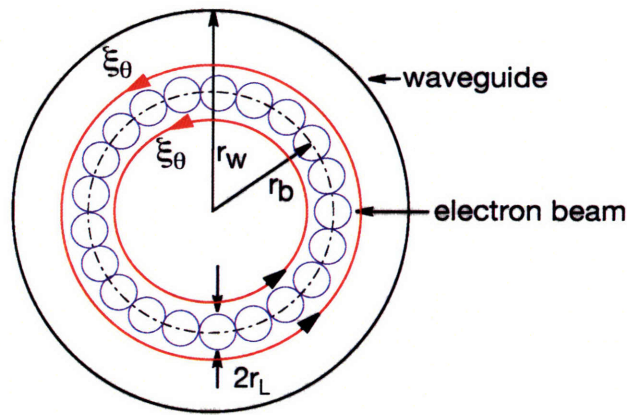
Figure 5-13: Schematic of the cross-section of a gyrotron interaction region at the resonator, showing the annular electron beam of radius r_b, consisting of electron beamlets of radius r_L. r_w specifies the radius of the resonator and ξ_θ is the azimuthal electric field.

The gyrating electrons with Larmor radii of $r_L = v_\perp / (\omega_c / \gamma)$ are located on a circle of radius r_b (the electron beam radius). The electrons are initially emitted from a cathode of much larger radius, but in passing from the electron gun, situated in a lower magnetic field region, to the resonator, in a higher field region, they are adiabatically compressed to a final radius of r_b, as shown in Figure 5-8 and 5-13 and also discussed below. When they enter the interaction region the electrons are initially randomly distributed in phase space. But, due to relativistic effects the cyclotron frequency of the electron decreases as

they gain energy and increases as they lose energy, resulting in bunching as shown in Figure 5-14.
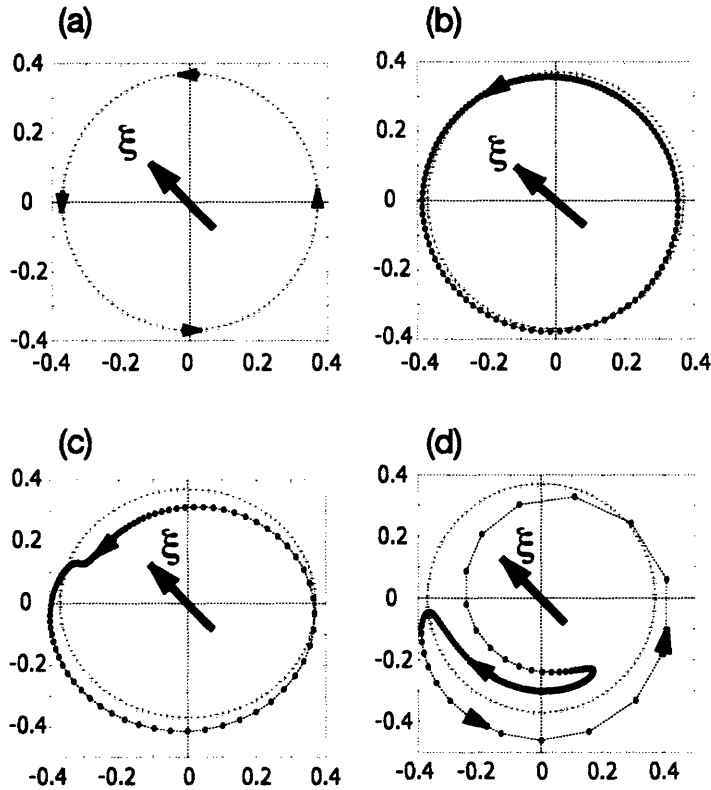
Figure 5-14: The sequence of bunching, its evolution and eventual energy extraction in a gyrotron. (from J. Sirigiri, PhD thesis MIT, 2002).

Each panel of this figure shows a snapshot of the electron distribution at a series of time steps taken at an integer multiple of the E- field oscillation so that the E- field appears stationary. The dots in the panels show the electrons within one of the beamlets shown in Figure 5-13. In (a) the electrons are initially randomly distributed in phase space and have equal Larmor radii. In (b) and (c) the electromagnetic field accelerates half the electrons , and they gain energy and are retarded in phase space due to the decrease in cyclotron frequency due to their increased relativistic mass. The other half are decelerated by the electric field, lose energy and are accelerated in phase space due to an increase in their cyclotron frequency. Furthermore, the Larmor radii of the faster gyrating

electrons decrease, while those of the slower gyrating electrons increase, resulting in a change in the shape of each beamlet as shown above. The bunch continues to grow as the electron beam traverses the cavity as shown in (c). If the frequency of the electromagnetic field is slightly higher than the cyclotron frequency the bunch slips in phase with respect to the wave and eventually ends up in the decelerating phase of the electromagnetic field (where the bunch is moving parallel to the electric field) as shown in (d). The electrons end up as a bunch in the decelerating phase, giving up their energy to the electromagnetic field, resulting in energy extraction.

5.5   Characterization of the 250 GHz Gyrotron

In multidimensional magnetic resonance experiments it is important to have the experimental variables such as rf power levels stable to 1% since signal averaging requires that the spectrum must be reproducible from scan to scan. Similarly, in an experiment incorporating DNP, the enhancement depends on the power output, the frequency stability, and spectral purity of the gyrotron radiation and this places constraints on the operational stability of the device. In order to understand the manner in which these three parameters vary, we have systematically investigated the performance of the 250 GHz oscillator under a variety of test conditions. In particular, we have measured the power output as a function of voltage, current, magnetic field, and temperature, and observed the fluctuation of the power as a function of time. The stability of the frequency is monitored simultaneously in these experiments. The spectral purity of the radiation was measured with a combination of heterodyne and homodyne techniques that assess the average and instantaneous purity of the gyrotron emission. The results demonstrate that the gyrotron can operate safely under feedback control with a power

stability <1%, typically for periods of 10 days. The spectral purity is excellent, showing a bandwidth of <10 ppm determined by the local oscillator bandwidth in the heterodyne experiments and no strong contaminating resonances in the homodyne experiment.

5.5.1 Power and Frequency Stability

Figure 5-15 illustrates the output power of the 250 GHz gyrotron as a function of magnetic field and beam current and in Figures 5-15(a) and 5-16 we show the frequency as a function of magnetic field, gun field and applied voltage. Normally the gyrotron operates in the $TE_{0,3,2}$ mode (to be discussed further below) with a beam voltage of 12.2 kV and beam current of 15-30 mA. The operating mode corresponds to the output frequency that maximizes the DNP enhancement for a ^1H NMR frequency of 380 MHz, but operation in other modes is possible. In addition, the oscillation appears at a low current and generates a sufficient amount of output power for DNP. Figure 5-15 illustrates that the power output does not vary dramatically with magnetic field, and thus with a stable superconducting magnet (drift < 0.01 ppm/hr) the power output should not be affected by changes in the magnetic field. Nevertheless, in our particular system the accumulated magnet drift necessitates the adjustment of the magnetic field every few months.

Figure 5-15(b) depicts the variation of the output power of the $TE_{0,3,2}$ operating mode with beam current. In this regime, the output power is a linear function of the beam current, suggesting that feedback control of the beam current could be sufficient to regulate the output power. However, fluctuations in other gyrotron operating parameters over long time scales modify this linear correlation, and so regulation of the beam current alone is insufficient to guarantee stable output power. In Figure 5-15(b) we show a

maximum CW output power of 7 W that is achieved at beam parameters of 26 mA and 12.2 kV, yielding an efficiency of 2.2%. Output powers of up to 25 W have been observed in the $TE_{0,3,1}$ mode (beam voltage and current of 11.8 kV and 49 mA, corresponding to 4.4 % efficiency) during hour-long CW operation [44].
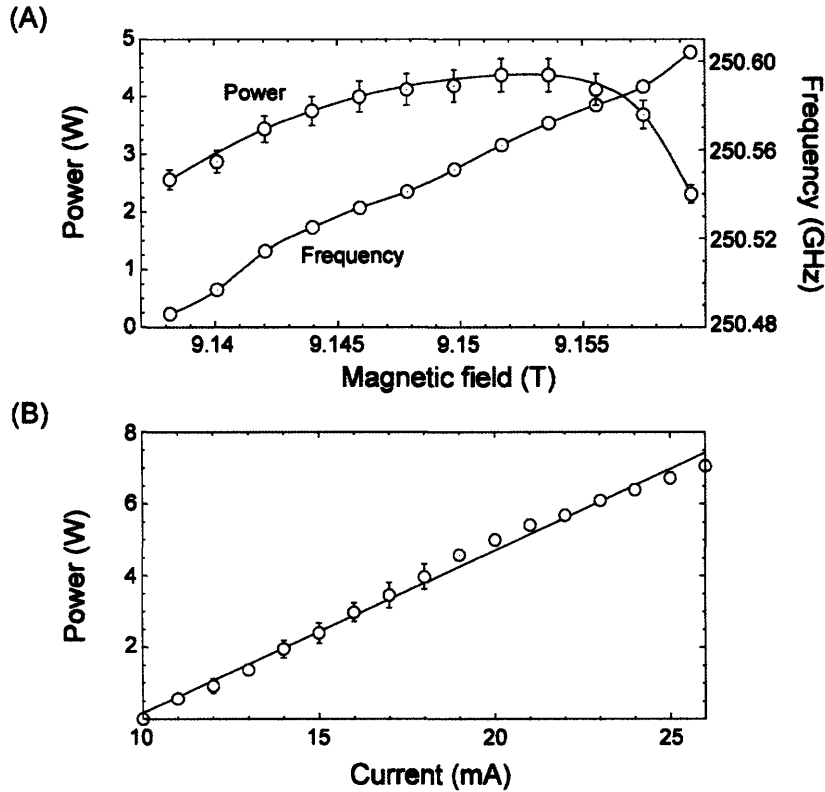
Figure 5-15: (a) Frequency and power of the operating $TE_{0,3,2}$ mode as a function of magnetic field. (b) Power in the $TE_{0,3,2}$ mode as a function of beam current. Power measurements were performed with a Scientech laser calorimeter that has been calibrated for millimeter waves.

5.5.2 Frequency Pulling

The dependence of the gyrotron frequency on experimental parameters is of interest for two reasons. First, it is important to have the frequency stable in the CW DNP experiments discussed here since the enhancement in solid effect, thermal mixing and cross effect experiments [38] is strongly dependent on the position of irradiation in the EPR spectrum. Second, it would be useful to be able to tune a gyrotron oscillator across

the breadth of the EPR spectrum, a feature that is discussed elsewhere [45] and mentioned in Chapter 6, Section 6.4. Here we discuss relatively small variations of the output frequency, which we term frequency pulling, that describe the variation of frequency as a function of beam voltage, cathode parameters, and magnetic field while the gyrotron is operating in the $TE_{0,3,2}$ mode. These effects were observed and discussed previously [98-100]. As illustrated in Figures 5-15(a) and 5-16(a,b,c) the gyrotron operating frequency (and the microwave power output) is sensitive to variations in the main or auxiliary magnetic fields, the beam voltage, or beam current, and the cavity temperature (data not shown). Measurements of the frequency pulling characteristics of the 250 GHz gyrotron were performed using a heterodyne receiver system consisting of a WR-3 harmonic mixer and a K-band local oscillator (18-28 GHz) along with signal conditioning and data acquisition instruments. The local oscillator is stabilized to within 1 Hz using a phase-locked loop (PLL), and these measurements used the 11th harmonic of the oscillator and are limited only by the phase noise of this source.

The data in Figure 5-16 show that when the gyrotron is operating in the $TE_{0,3,2}$ mode, we observe that changes in the main magnetic field by 0.02 T, the cathode magnetic field by 20 gauss, and the beam voltage by 250 V result in frequency pulling while still maintaining acceptable power output. Individually tuning the beam voltage and gun magnetic field in these ranges resulted in 14 and 25 MHz of frequency tuning, respectively, while the main magnetic field yields the widest tuning amounting to 118 MHz. This wider tuning range is a result of the use of the second longitudinal mode as the operating mode. In Figure 5-16(a), the experimentally observed magnetic tuning is compared to nonlinear theory simulated in MAGY using experimental parameters with

good agreement. The dependence of the operating frequency on external parameters is summarized in Table 5.1. We also examined the effects of changing the cavity temperature assuming it to be that of the thermally regulated coolant at the cavity inlet.
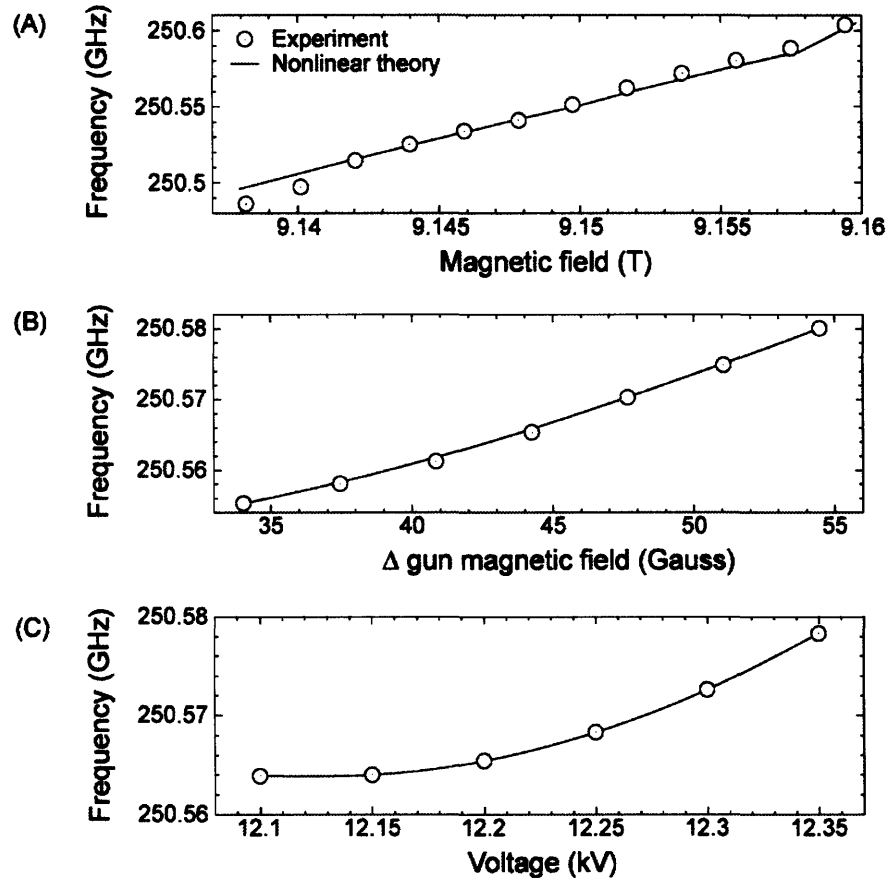
Figure 5-16: Frequency pulling in the $TE_{0,3,2}$ mode as a function of (a) the main magnetic field, (b) the gun magnetic field, and (c) the beam voltage. Simulations were conducted in MAGY [101].

Table 5.1: Dependence of frequency on operating parameters

Parameter	Sensitivity
Magnetic field	5.3 GHz/T
Beam voltage	86 MHz/kV
Cathode magnetic field	12.3 GHz/T
Cavity temperature	<1.0 MHz/°C

These results demonstrate that the gyrotron operating frequency is most sensitive to variations in the magnetic field. At this frequency, DNP typically requires frequency stability of less than 1 MHz for experiments lasting up to ten days, which limits the

maximum permissible magnetic field drift to 0.08 ppm/hr under these operating conditions. To achieve these magnetic field control tolerances, the superconducting magnet must operate in persistent mode, and, in the 250 GHz DNP installation, the magnet must be recharged approximately monthly to counteract its intrinsic drift. Currently, the magnet drift and the capacity of the magnet cryogenic dewar are the only factors which limit the length of continuous operation.

5.5.3 Spectral Purity

In magnetic resonance experiments it is important to have not only a source with excellent frequency stability over time, but also one that is spectrally pure. For example, if the local oscillator in an NMR spectrometer is noisy then it will degrade the signal to noise of the instrument. In the case of DNP experiments, if the noise bandwidth of the gyrotron is comparable to the EPR linewidth, then it may comprise experiments that depend on frequency selective excitation. Thus, it is important to know the spectral purity of the 250 GHz oscillator, and, accordingly, we have performed two experiments to investigate its bandwidth. These experiments are similar to other investigations of the spectral linewidth in gyrotrons discussed earlier [102, 103]. The radiation produced by the gyrotron has a finite linewidth that can be attributed to both intrinsic and extrinsic sources [104, 105]. The intrinsic linewidth arises from the natural emission line width, shot noise, which is white noise, and flicker noise, which has a $1/f$ power spectrum. Extrinsic sources of noise are those coupled into the system by variations of external operating parameters such as the beam voltage, magnetic fields, or coolant circuit temperature. We have analyzed the spectral purity of the CW gyrotron emission using a combination of heterodyne and homodyne measurements. During these measurements,

the gyrotron operated in CW mode with feedback regulation of the beam current rather than the microwave power.

The gyrotron linewidth in the $TE_{0,3,2}$ operating mode was measured using the phase-locked K-band oscillator and heterodyne receiver system used to measure the frequency stability together with a spectrum analyzer as a detector. The data shown in Figure 5-17(a), are an average of 32 frequency sweeps lasting 0.5 s each and yield an estimated linewidth of ~300 kHz, which is close to the detection limit set by the phase noise of the local oscillator circuit at its 11th harmonic. This is comparable to the linewidths reported in other measurements [102].

(A)

(B)
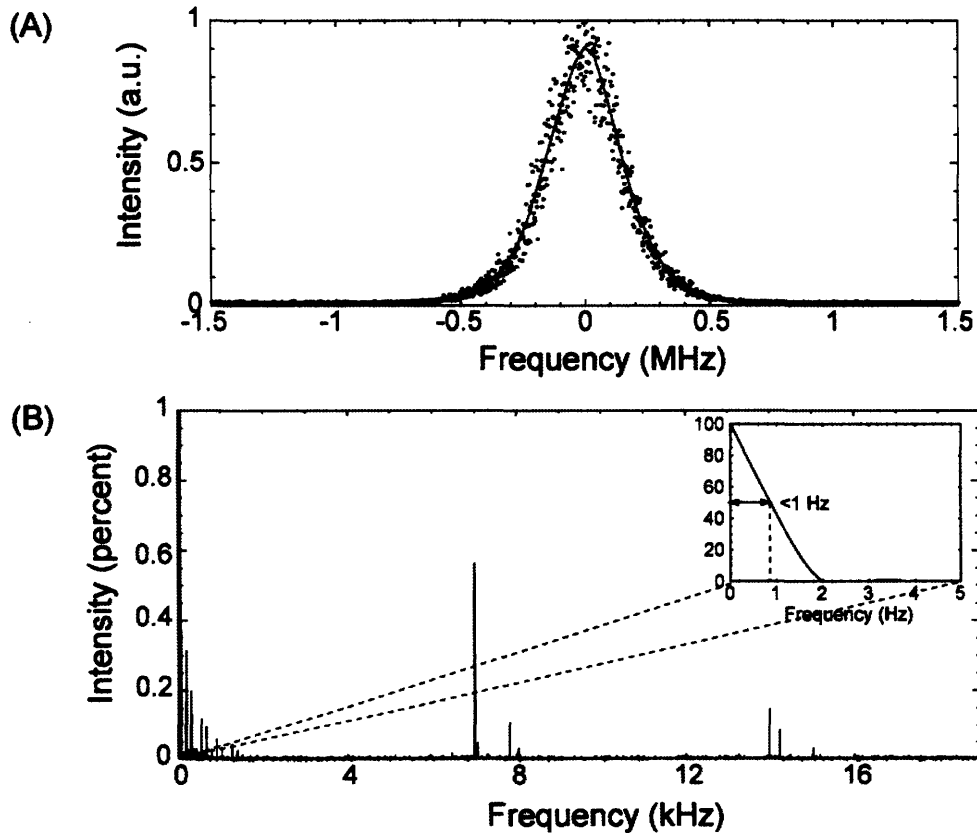
Figure 5-17: (a) Linewidth measurement of the operating $TE_{0,3,2}$ mode using the heterodyne frequency measurement system. (b) Homodyne measurement in $TE_{0,3,2}$ mode. The offset panel illustrates the natural emission linewidth.

While the heterodyne measurement is sensitive to the time-averaged absolute line width, the instantaneous modulation of a high frequency signal is best detected by demodulation using a homodyne technique [106] . We have measured the homodyne emission spectrum of the 250 GHz gyrotron using a diode detector and an oscilloscope (LeCroy, Model LT354) capable of sampling for several tens of seconds of acquisition. Typical data, shown in Figure 5-17(b), are processed by zero-order baseline correction in the time-domain to eliminate any DC level artifacts and then Fourier-transformed without further apodization. All contaminating sidebands in the homodyne spectrum are less than 1% of the intensity of the DC component. Specifically, there is a manifold of signal sidebands with 7 kHz periodicity that arises from the switching frequency of the power supply, and a manifold of sidebands at 60 Hz that arises from AC line modulation of either the detector or the gyrotron beam. Thus there is no low frequency noise in the frequency spectrum of the radiation that is <300 kHz. The heterodyne measurement of the gyrotron linewidth is therefore limited either by the phase noise of the local oscillator circuit or by extrinsic fluctuations in the operating parameters on the long time scale of the heterodyne measurement. Neither measurement shows the presence of significant parasitic modes or oscillations. We note that homodyne measurement is an approach to detect these oscillations and they have been detected at ~400 MHz in the operation of the 460 GHz gyrotron [107].

5.5.4 Radiation Patterns

Millimeter wave power is produced in the gyrotron cavity where it exist in a confined transverse electric (TE) mode. By contrast the propagation of the millimeter beam in free space is convenient only for a Gaussian beam. Therefore, a type of antenna, called a

mode converter, is used to efficiently couple radiation in the cavity mode to a free space Gaussian mode. The mode converter, consisting of a step-cut waveguide launcher and a cylindrical focusing mirror, also serves to separate the millimeter wave power from the energetic electron beam as is illustrated in Figure 5-9(a), thus protecting fragile structures such as the millimeter wave output window. The Gaussian beam is then directly coupled to an overmoded $HE_{1,1}$ corrugated waveguide [87] which contains a quasi-optical beamsplitter that acts as a directional coupler (See Figure 5-7 for details). At the terminus of the waveguide, the millimeter wave beam propagates again in free space and is optically focused into a smaller corrugated waveguide for delivery to the sample. A miter bend at the complement of the magic angle (35.3°) is located at the end of the corrugated waveguide and allows for efficient coupling of the radiation into the sample [⑧ in Figure 5-9]. Because the $HE_{1,1}$ mode in corrugated waveguide couples efficiently to free space Gaussian propagation, $HE_{1,1}$ mode purity is essential to efficient power delivery in this system. The presence of parasitic higher-order modes may otherwise compromise the experiment by introducing additional sensitivity to misalignment or vibration in the base of the NMR probe. Finally, the directional coupler that uses a beam splitter will only operate correctly for $HE_{1,1}$ mode. For these reasons, we have analyzed the mode purity of the 250 GHz transmission system using three techniques: thermal paper, temperature-dependent liquid crystalline media, and a pyroelectric camera. The analysis of thermal burn patterns and calorimeter power measurements is discussed elsewhere [87] and suggests that initial higher order mode content amounts to 10% of the total coupled millimeter wave power but is filtered by the waveguide, resulting ultimately in a Gaussian-like beam at the waveguide terminus.

Millimeter wave mode patterns are most accurately mapped with motorized scanning devices, but these are difficult to use in the presence of the large fringe field of the 9 T wide-bore NMR magnet. Therefore, we have employed the temperature-dependent color of liquid crystalline media applied to a substrate transparent to millimeter waves as an indirect calorimetric measurement of the radiation pattern [108]. This method does not require any magnetic or moving components such as optical choppers or positioning motors and is easily scaled to arbitrary beam dimensions. With proper calibration, liquid crystal thermometry can provide sub-micron resolution and temperature accuracy approaching 0.1°C [109, 110]. In these experiments, we used a commercially available (Edmund Optics, Barrington, N.J.) liquid crystalline formulation that is sparsely applied to a thin polyethylene substrate. Since the substrate is nearly transparent at 250 GHz, while the encapsulated liquid crystalline particles are not, the measurement samples the millimeter wave radiation without perturbing the field structure and without excessive bleeding due to background absorption. Liquid crystal formulations that are sensitive to different temperature ranges can be combined in separate measurements to improve the overall dynamic range of the method. We employed a cross-polarized illumination and detection system to minimize optical reflections from the surface of the substrate. Collinear alignment of the substrate and camera was accomplished with the aid of a laser beam injected through the directional coupler and therefore aligned along the axis of the waveguide. Detection was accomplished through the use of an RGB-mode camera operating at 30 frames per second with a resolution of 640 x 480 pixels (Logitech, Inc.) arranged coaxially with the millimeter wave beam and normal to the surface of the LC substrate. Data were

processed by first subtracting dark frame images to remove systematic artifacts and then averaging video frames over 333 ms to improve the sensitivity of the measurement. White light color calibration was accomplished through subsequent measurement of a white reflective paper. Finally, the images were converted from the RGB to an HSI color space and the incident power at each pixel was extracted by integrating images taken at different times.

In total, 16 seconds of video were taken at each of three positions (see Figure 5-18) along the axis of the waveguide: (a) at 30 cm from the gyrotron window; (b) immediately before the directional coupler (120 cm from the gyrotron window); and, (c), between the directional coupler and the waveguide terminus (200 cm from the gyrotron window). In Figure 5-18(a), the gyrotron radiation is captured at the cross-bore exit unguided, resulting in some interference with the beam propagation. Figure 5-18(b) shows that the beam contains a small sidelobe, which is also seen in the pyroelectric measurements, and Figure 5-18(c) demonstrates that a relatively pure Gaussian mode is coupled to the NMR probe at the waveguide terminus. The Gaussian beam widths recovered in these measurements are systematically 5-8% higher than those obtained on the basis of pyroelectric measurements, partly because the measurement plane was 1.5" from the terminus of the waveguide. In both cases, the experimental errors were assumed to be normally distributed; the values are reported at the 95% confidence interval, and the intervals were recovered from the covariance matrix of the fit.
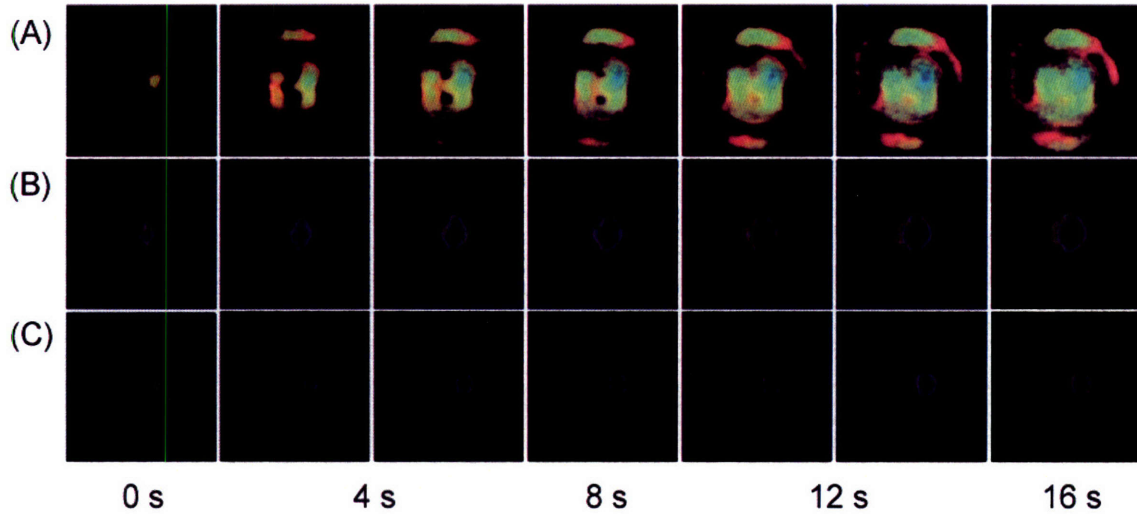
Figure 5-18: Radiated intensity of the gyrotron output while operating in the $TE_{0,3,2}$ mode as recorded on liquid crystal media for (a) at the gyrotron bore and (b) after 120 cm of waveguide and (c) after 200 cm of corrugated waveguide as described in the text.

Pyroelectric camera

We have also used a pyroelectric camera to image the mode pattern. The advantage of this approach is its simplicity and linearity and therefore it is a well established technique in laser mode pattern measurements. The major disadvantage is that a magnetic motor is required to power the chopper and the small detector size which does not permit complete imaging of the beam. We employed a pyroelectric camera (Spiricon Pyrocamera III, Model No. PY-III-C-B, Serial No. 30507) consisting of a 124 x 124 element pyroelectric array with a 12.4 mm x 12.4 mm active area to measure the radiation pattern 190 cm along the waveguide axis. During these measurements, the gyrotron was operating in CW mode with an output power of less than 2 W to avoid damaging the detector. The CW beam was modulated at 24 Hz with an optical chopper integrated into the pyroelectric camera. The chopper motor and other magnetic components within the camera restricted its use to locations with an acceptable fringe magnetic field. The camera body was aligned with the millimeter wave beam using a laser beam injected into the waveguide through the directional coupler, and the detector element was assumed to

be aligned with respect to the camera enclosure. The detector element is recessed 0.6"

from the enclosure, which was aligned with the terminus of the waveguide in these

measurements. Since the detector area does not cover the entire aperture of the

waveguide, the detector gain was set near the threshold of saturation to maximize the

dynamic range of the measurement. All measurements were conducted in the absence of

daylight to reduce background levels of infrared radiation. Data were processed by

subtraction of a separately recorded dark frame to eliminate systematic dead pixel

artifacts and background noise, followed by averaging of 32 captured frames to improve

the sensitivity of the measurement. Near wavelengths corresponding to the pixel spacing

(~0.1 mm), a rectilinear diffraction pattern becomes visible. Comparative measurements

of another gyrotron oscillator operating in several modes from 150-460 GHz confirm that

this is an artifact of the pixel spacing [111], and fitting of the images with and without

image processing to eliminate these artifacts gives identical results for the case of a

nearly Gaussian beam. These results are summarized in Figure 5-19, where Figure 5-

19(a) is of the raw data, Figure 5-19(b) is a plot of the best-fit Gaussian, and Figure 5-

19(c) is the fitting residual. The measurements indicate a small sidelobe and a slightly

elliptical beam (*cf.* Table 5.2), in good agreement with the liquid crystal data and close to

theoretical expectations.

Table 5.2: Gaussian parameters of the radiation field from Figures 5-18 and 5-19.

Measurement parameter	LC method	LC plane (theoretical width)	Pyroelectric camera	Camera plane (theoretical width)	Beam waist (theory)
x $1/e^2$	7.7 ± 0.2	7.29	7.25 ± 0.02 mm	7.04	6.99 mm
y $1/e^2$	7.0 ± 0.1	7.29	6.60 ± 0.02 mm	7.04	6.99 mm
Ellipticity (y/x)	0.90	-	0.91	-	-
Ellipticity (%)	9%	-	9%	-	-
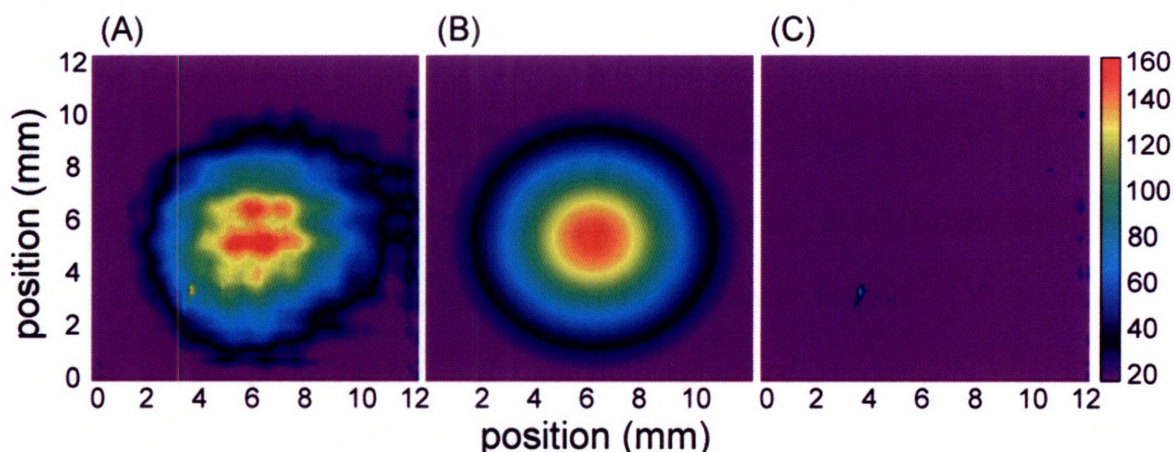
Figure 5-19: Planar section of the radiation intensity as recorded by a pyroelectric camera. (a) is the intensity 190 cm along the waveguide axis (b) is a Gaussian fit of the intensity data and (c) is the residual of the fit. The intensity is described on a linear scale in arbitrary units.

5.5.5 CW Long-term Stability and Control

Long term signal averaging is an essential feature of most magnetic resonance experiments, including experiments involving DNP. Thus, it is important that the gyrotron be capable of functioning for extended periods of unattended operation. During this period the power stability and therefore the fluctuations in the DNP enhancements should be $\leq 1\%$ in order for multidimensional experiments to function properly. Accordingly we have assembled a control system described in detail in Appendix 1 that permits operation for periods of > 10 days with the output stability specified above. At the present time the length of an experiment is limited by the intrinsic drift of the superconducting magnet and the volume of the cryogen dewar, which must be refilled approximately every 10-11 days.

Data from a representative 10-day CW run using 4.5 W of output power are contained in Table 5.3 and illustrated in Figure 5-20. During the period all metrics of the gyrotron operation remained within acceptable tolerances for DNP experiments. The

273

electron beam parameters and vacuum parameters are those reported by the high voltage gun and ion pump power supplies, respectively, and the heater parameters are reported by a low-voltage power supply integrated into the high voltage gun supply. Power is coupled into the millimeter wave diode using the directional coupler apparatus depicted in Figure 5-7(d), and the measured values are corrected for the DC offset of the amplification and signal conditioning circuit. The proportionality of the sampled millimeter wave power and the absolute power over long time scales was demonstrated in [87] and was verified in this experiment by monitoring with a second calibrated diode which externally sampled the millimeter wave beam power at a high data rate to facilitate the analysis. The millimeter wave frequency was measured using the phase-locked heterodyne detection system discussed earlier.

Table 5.3: Stability of the 250 GHz operating parameters during CW operation

Technical parameter	Average value	Standard deviation	(%)
Filament voltage (V)	3.274	0.004	0.1
Filament current (A)	4.515	0.008	0.2
Beam voltage (kV)	12.090	0.047	0.4
Pressure (10^{-9} Torr)	3.430	0.019	0.5
Frequency (GHz)	250.559348	0.000359	0.000143
Power (diode units (mV))	229.75	1.94	0.8

Note from Table 5.3 that the power was stable to ~0.8% and the other parameters were well below this level including the frequency which showed a stability of 1.6 ppm.
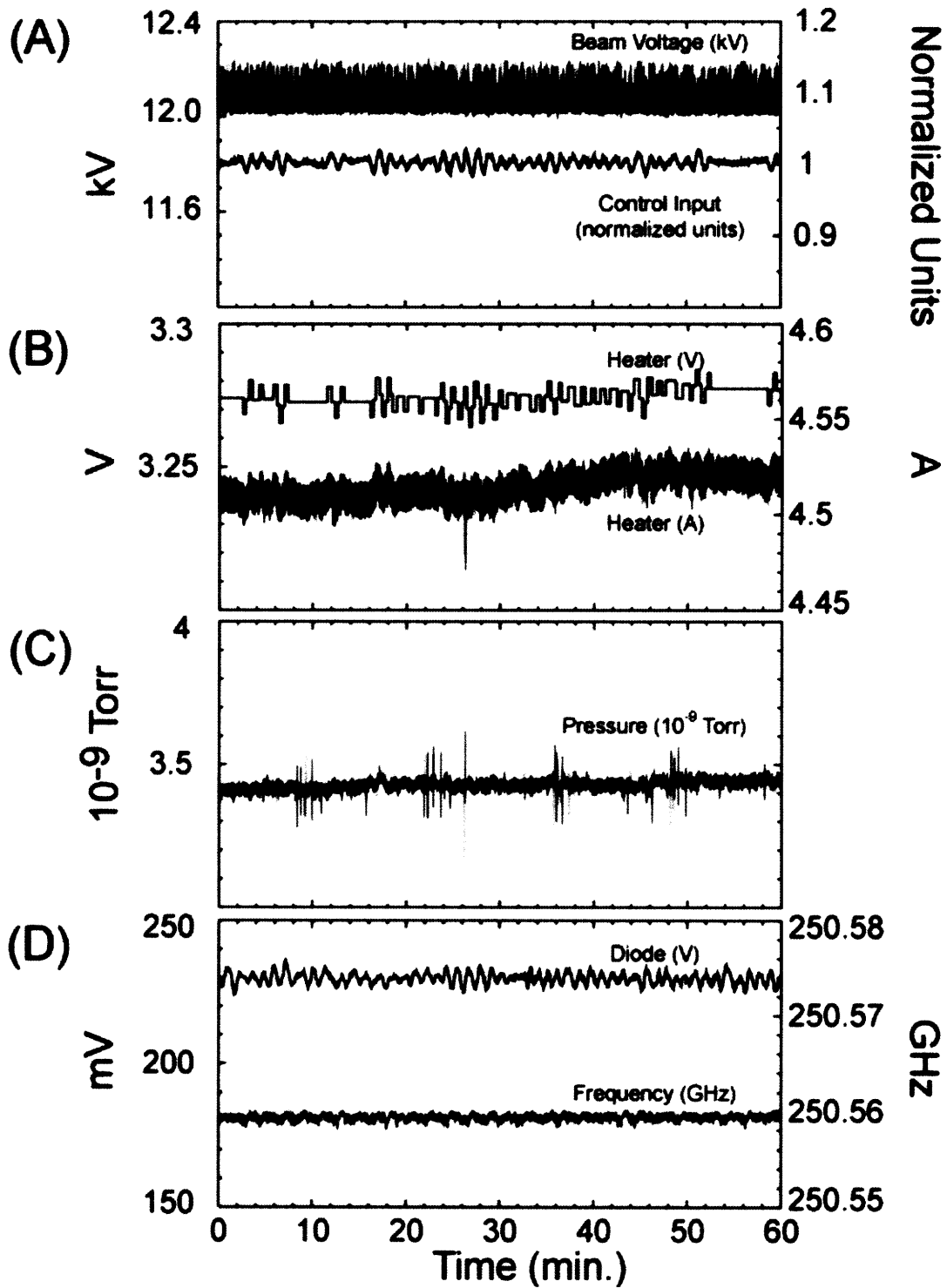
Figure 5-20: Stability of the $TE_{0,3,2}$ operating mode over a representative hour of a long experiment. (a) beam voltage and control input, (b) heater voltage and current, (c) pressure, and (d) power and frequency. These parameters were measured with the directional coupler shown in Figure 5-7(d) as described in the text.
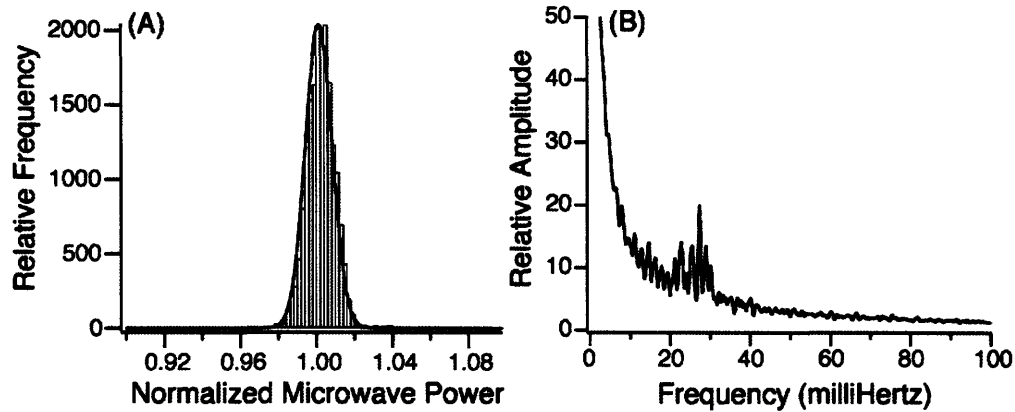
Figure 5-21: (a) Statistical analysis of power fluctuations from setpoint. The solid line is a Gaussian fit to the data. The control system was set to maintain the output power within a 1% tolerance. (b) Frequency-domain analysis of power fluctuations from the setpoint.

After a period of thermal equilibration of the heater, initial operation of the gyrotron at constant power requires higher heater voltages and produces higher tube pressures than is observed at equilibrium. Approximately two hours after initial CW emission with regulation of the output power, the operating parameters and tube pressure stabilize to a steady-state value about which there are only minor fluctuations. Uncontrolled operation of the gyrotron, on the other hand, results in oscillations of the output power with an overall increase in the output power after a period of equilibration. For this and other reasons, the correlation between beam current and output power is not precise, and therefore regulation of the beam current alone is sufficient to guarantee regulation of the output power only on very short time scales. Finally, while the measured tube pressure rapidly returns to its base resting value after termination of an experiment [Figure 5-22(c)], the gyrotron remains extremely sensitive to its operating history. We have found that regular operation of the gyrotron reduces the length of the initial equilibration period and improves the stability of operation.

Three factors limit the controlled operation of the gyrotron oscillator. First, the speed of the control circuit is currently limited by the need to perform signal conditioning

and parameter estimation in software for a number of synchronously monitored analog signals including those involved in the safety interlock circuits. This effectively limits the cycle rate of the control circuit to 0.1 - 0.2 Hz with acceptable interactive performance and interrupt handling on our hardware. Next, the minimum increment and gain of the heater power supply limits control accuracy. Finally, the transient response of the heater circuit limits the degree to which rapid changes in the millimeter wave output power can be regulated by changes in the cathode heater. Figure 5-22 shows typical response curves for a sudden positive or negative step in the heater voltage (from 3.6 V to 3.7 V or the reverse). Note that there is a small-amplitude oscillatory modulation of the output signal on a 1-10 s time scale even in the absence of feedback regulation, which suggests that this noise is the result of power supply fluctuations or fluctuations in the pulsatile chiller circuit. The transient response of the cathode heater is characterized by a process dead time of 57 ± 8.5 s and a time constant of nearly 120 s, while we wish to regulate the gyrotron output power on the 1-10 s time scale. Proportional control alone results either in a long settling time and a large error at steady state or in highly oscillatory behavior with respect to fluctuations in the process variables. In order to achieve effective control with this transient response, we implemented a heuristic three-term error controller that gives the standard transfer function , $G(s)$, of the form

$$G(s) = \frac{K_3 s^2 + K_2 s + K_1}{s} \qquad (5.10)$$

where the K_i are parameters determined pseudo empirically and s is the transform variable. We have implemented a process signal prefilter (bandpass filter) whose transfer function is

$$F_{bp}(s) = \frac{A_0 \beta s}{s^2 + \beta s + \omega_0^2} \tag{5.11}$$

when the signal is outside a confidence band around the setpoint. Here b is the bandwidth and w_0 is the center frequency, while A_0 is chosen to give the control parameters convenient units. The error signal is set to zero when the power lies within the confidence band, resulting in no change to the controller output.
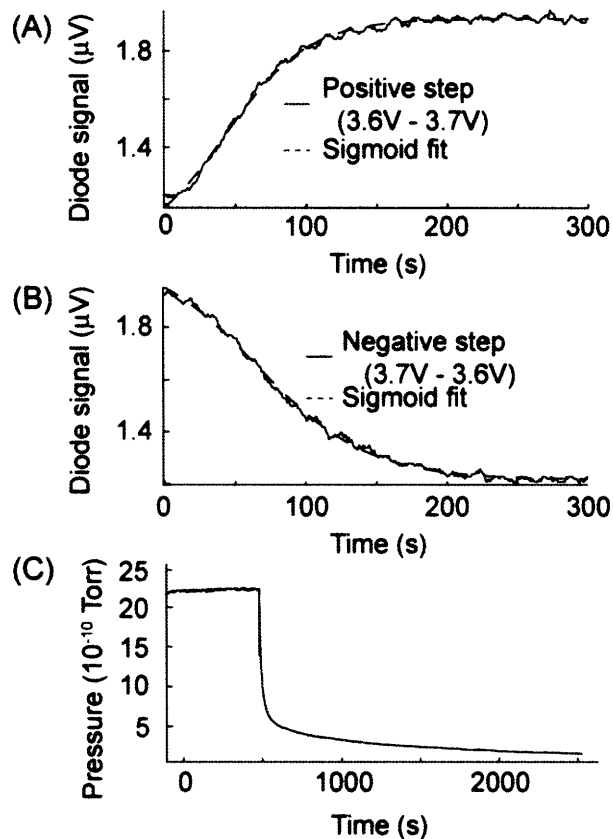
Figure 5-22: Representative transient response of the gyrotron to (a) positive and (b) negative step in the control voltage. The dashed line is a sigmoidal fit to the data from which optimal PID parameters were estimated. Note oscillations in the output power which persist even though the system is not under proportional regulation for these measurements. (c) Response of the system to termination of running power supplies following thirteen hours of CW operation.

The initial parameters, K_i, of the three-term controller were estimated using a Ziegler-Nichols PID tuning rule from the transient response data in Figure 5-22 without need for further empirical optimization. Automatic, on-line re-tuning of the control

278

coefficients was triggered whenever the steady-state error exceeded a user-selectable threshold, thus allowing the control system to adapt to changing operating conditions. The bandpass prefilter was implemented in software, and its parameters were chosen to eliminate aliasing artifacts and line noise. The confidence band around the setpoint was set to account for minor oscillations in the signal amplitude at short time scales which are apparent in Figure 5-21(a) and (b); the confidence band also serves to limit control changes so that the power can be controlled within a preset tolerance even with the long cycle times of this control system. A statistical analysis of excursions of the process variable from its setpoint over the 10-day experiment, shown in Figure 5-21(a), shows that power fluctuations are normally distributed and that the tolerances of the DNP experiment are met by the control system. The distribution of data reflects the confidence interval, which, in this case, was set to 1%. A frequency-domain analysis, shown in Figure 5-21(b), also suggests that the residual error is time-dependent with a frequency of approximately 28 mHz, a fact which is clearly visible by inspection of Figure 5-20(a) and (d).

The optimal control parameters are extremely sensitive to operating history of the device, and regular operation of the gyrotron is required to avoid the need for periodic recalibration.

5.6 Second Harmonic Operation

By far the most expensive component of the 250 GHz and other gyrotrons is the superconducting magnet, and, as DNP experiments proceed to higher frequencies, the cost of the magnet for an oscillator operating in fundamental mode increases dramatically. In particular, at millimeter wave frequencies of ≤ 263 GHz (corresponding

to ≤400 MHz NMR frequencies) it is possible to use magnets constructed from NbTi conductor that are relatively inexpensive. However, the successful experiments described in Section 2 above suggests that it would be desirable to move DNP/NMR to higher fields to take advantage of the increased resolution. Thus, we anticipate that DNP experiments in the 700-900 MHz regime, corresponding to millimeter wave frequencies of 460-591 GHz, will become desirable in the immediate future and this could require a magnet based on Nb_3Sn where the conductor cost are much higher. Thus, the most economical approach to generating millimeter wave power at these frequencies would be to employ an oscillator in which the frequency is doubled and in this case for all ^{1}H NMR frequencies ≤800 MHz it should be possible to use NbTi based magnets. Second harmonic operation has recently been demonstrated in a 460 GHz CW gyrotron oscillator for DNP, which operates in a 9 T magnet [107, 111] .

This argument provided the rationale for us to performed a parametric study of mode excitation in the 250 GHz DNP gyrotron in order to optimize the efficiency of fundamental mode operation and to verify the potential for operation at the second harmonic of cyclotron resonance. For this study, the Gamma high voltage gun power supply was replaced by a pulsed modulator, and the gyrotron operated with 1-3 μs pulses with a frequency of approximately 1 Hz. Operating parameters including the cavity and gun magnetic fields, beam current, and beam voltage were varied to map out the operating characteristics of several second harmonic modes and fundamental modes in their vicinity. The electron beam voltage and current were varied up to 15 kV and 120 mA while the main magnetic field was varied up to 9.2 T and the gun magnet up to ±8.5 x 10^{-2} T with respect to the cathode field.

Four unique transverse second harmonic modes were observed from 5.8 to 6.6 T with starting current as low as 12 mA. The oscillation frequency at a given magnetic field and voltage along with the starting currents for the $TE_{0,4,1}$, $TE_{2,4,1}$, $TE_{3,4,1}$ (and $TE_{3,4,2}$), and $TE_{1,5,1}$ modes are enumerated in Table 5.4. Figure 5-23 summarizes the experimental starting current data as a function of magnetic field recorded for resonant cavity modes from 5.8 to 9.2 T and up to 120 mA beam current (open symbols denote fundamental modes and filled symbols denote second harmonic modes). It is of particular interest that the three harmonic modes detailed in the experiment, the $TE_{2,4,1}$, $TE_{0,4,1}$, and $TE_{3,4,1}$, begin to oscillate at unusually low currents between 12-15 mA, and that the $TE_{3,4,2}$ second harmonic mode begins to oscillate at 47 mA.

Table 5.4: Second harmonic modes observed in the 250 GHz gyrotron.

Mode	Frequency (GHz)	Magnetic field (T)	Voltage (kV)	Start current (mA)
$TE_{2,4,1}$	323.67	5.84	7.3	12
$TE_{0,4,1}$	327.41	5.90	7.8	15
$TE_{3,4,1}$	358.42	6.48	8.6	15
$TE_{3,4,2}$	358.81	6.50	8.6	47
$TE_{1,5,1}$	365.26	6.60	8.8	-
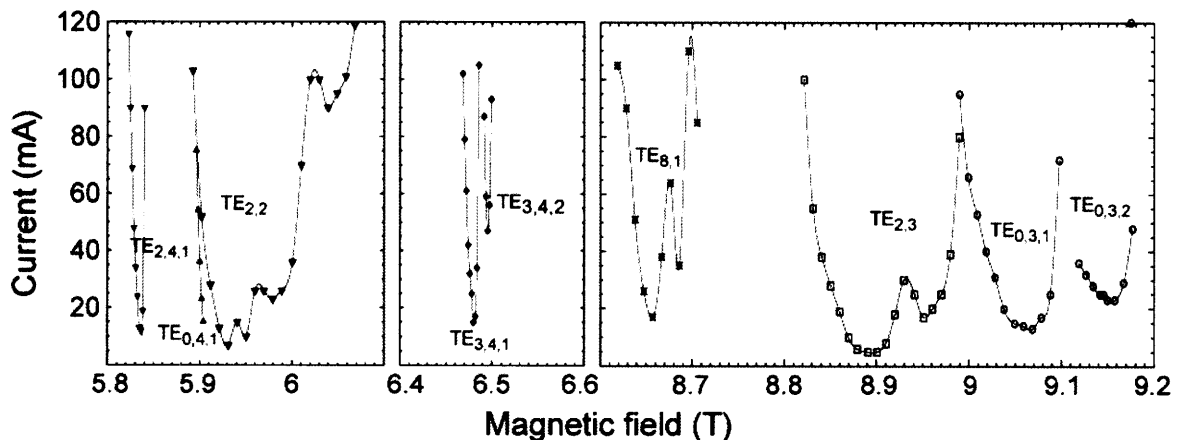
Figure 5-23: Summary of experimental starting current data recorded for resonant cavity modes from 5.8 to 9.2 T and up to 120 mA. Open symbols denote fundamental modes and solid symbols denote second harmonic modes.

As has been reported previously for the fundamental modes of a 460 GHz second harmonic gyrotron oscillator [45], we observe broadband continuous frequency tuning with variation of the magnetic field alone. Figure 5-24 summarizes the experimental frequency tuning as a function of magnetic field recorded near the starting current for resonant cavity modes from 5.8 to 9 T (open symbols denote fundamental modes and filled symbols denote second harmonic modes). Data for the $TE_{2,4,1}$, $TE_{0,4,1}$, $TE_{3,4,1}$, and $TE_{3,4,2}$ second harmonic modes is shown in addition to the $TE_{2,2}$, $TE_{8,1}$, and $TE_{2,3}$ fundamental modes. Table 5.5 summarizes the frequency tuning of the modes shown in Figure 5-24, where, notably, 1.8 GHz tuning has been observed in the $TE_{2,2}$ mode and 1.4 GHz in the $TE_{8,1}$, and only tens of megahertz of tuning in the second harmonic modes. The magnetic frequency tuning of the fundamental modes has been previously analyzed in detail [45].
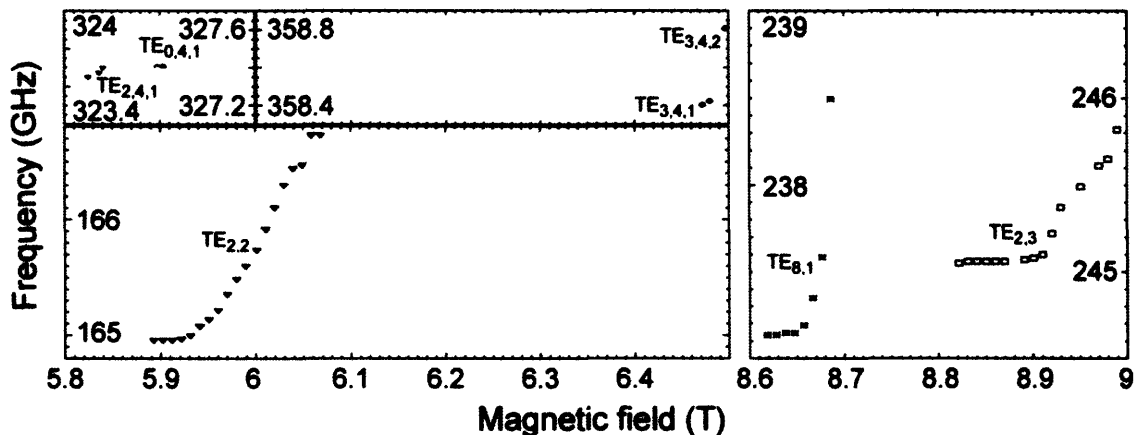
Figure 5-24: Summary of experimental frequency tuning data recorded for resonant cavity modes from 5.8 to 9 T near their starting currents. Open symbols denote fundamental modes and solid symbols denote second harmonic modes.

Table 5.5: Frequency tuning for the observed modes between 5.8 and 9 T in the 250 GHz gyrotron.

$TE_{m,p,q}$	Harmonic	Δf (GHz)
$TE_{2,4,1}$	2	0.05
$TE_{0,4,1}$	2	-
$TE_{2,2,1}$	1	1.77
$TE_{3,4,1}$	2	0.02
$TE_{3,4,2}$	2	-
$TE_{8,1,1}$	1	1.36
$TE_{2,3,1}$	1	0.77

The expected starting currents for the 250 GHz gyrotron second harmonic modes and the $TE_{8,1}$ fundamental mode calculated using linear theory, in Table 5.6, are much higher than the experimentally observed starting currents shown in Figure 5-23, while the experimental oscillation frequencies are nevertheless close to those obtained from cold-cavity simulations. There are several possible explanations for this phenomenon. First, the performance of the diode-type electron gun used in these experiments, which has been previously analyzed in detail [45], is characterized by large changes in the beam pitch factor and velocity spread as a function of beam voltage and magnetic field. However, linear theory and non-linear simulations using MAGY, shown in Figure 5-25, suggest that the effects of velocity spread alone cannot account for the lower starting currents. Second, we consider potential effects on the starting current of coupling to an off-axis beam, which may optimize the coupling coefficient for some modes, and was first contemplated due to the location of the oscillator magnet within the fringe field of a 9 T NMR magnet. The design beam radius of 1.018 mm effectively couples the electron beam to the second radial maximum of the $TE_{0,3}$ mode.

Table 5.6: Minimum start current, and magnetic field and frequency for minimum starting current of $q=1$ modes from linear theory [112] vs. experiment.

$TE_{m,p,q}$	Experiment			Theory		
	B_0 (T)	I_{st} (mA)	f (GHz)	B_0 (T)	I_{st} (mA)	f (GHz)
$TE_{2,4,1}$	5.84	12	323.67	5.85	272	323.537
$TE_{0,4,1}$	5.90	15	327.41	5.92	361	327.301
$TE_{2,2,1}$	5.93	7	165.00	5.95	15	164.889
$TE_{3,4,1}$	6.48	15	358.42	6.49	226	358.286
$TE_{3,4,2}$	8.66	17	237.19	8.66	252	237.062
$TE_{8,1,1}$	8.89	5	245.07	8.93	9	244.966
$TE_{2,3,1}$	9.06	13	250.10	9.12	9	249.973

The coupling to the experimentally observed $TE_{8,1}$ whispering gallery mode should be poor except for interaction with electrons in the vicinity of the cavity wall, but, in the experiment, the mode has a low starting current. An analysis of all the starting current data and a geometrical analysis of coupling factors in the presence of beam offset shows that no single beam offset can explain all the starting current data and, further, the magnitude of the beam offset required to optimize the coupling factors would result in beam interception at the cavity down-taper or in the ceramic drift region which precedes it. A third possibility is that the cavity diffractive Q is elevated over the design value, either through a manufacturing defect or another mechanism. In order to explore this possibility, we have measured the RF efficiency of the 250 GHz gyrotron through thermal load measurements of the cavity coolant loop (see Table 5.7). Using a cavity diffractive Q of 6,000, which was obtained from cold cavity simulations, and assuming that the conductivity of the electroformed cavity is half that of ideal copper, the expected RF efficiency for the 250 GHz $TE_{0,3,1}$ mode is approximately 62%. In fact, according to the thermal load measurements in Table 5.7, the actual RF efficiency is closer to 21%, suggesting that the conductivity of the cavity has been overestimated by a factor of 25 (which is unlikely) or that the diffractive Q is six times higher than the design value.

Table 5.7: Thermal load measurements of the 250 GHz gyrotron in the TE$_{0,3,1}$ mode.

Beam power (W)	Cavity load (W)	Collector load (W)	Calorimeter (W)	RF efficiency (%)
48	0	37	0	-
96	0	85	0	-
144	11	127	3	21.43
192	24	150	5.7	19.23
240	31	189	8.4	21.38
288	37	221	10.3	21.75
336	47	260	12	20.34
384	51	292	13.9	21.37
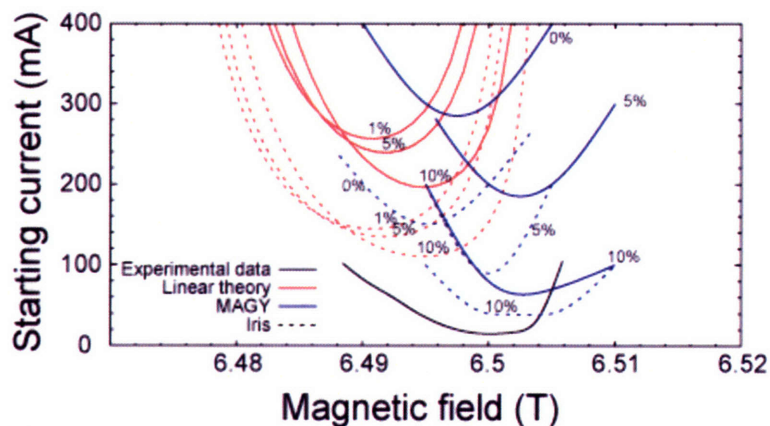
Figure 5-25: Starting currents for the second harmonic TE$_{3,4,1}$ mode using linear and non-linear theory and for the case of the design cavity (lines) and with an iris added before the output uptaper (dotted lines). The percentages indicate the velocity spread simulated.

We note that a broad family of manufacturing defects commonly encountered at discontinuities in the cavity mandrel radius can increase cavity diffractive Q, particularly for second harmonic modes, while leaving the resonant mode frequencies largely unchanged. These effects are illustrated in Figures 5-25 and 5-26.
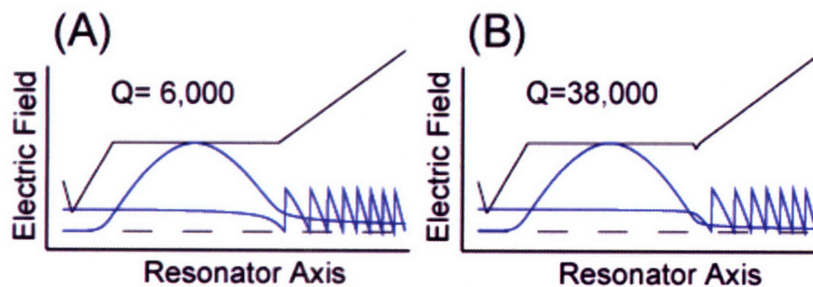
Figure 5-26: Cold cavity simulation showing the cavity and RF profile for the 250 GHz gyrotron cavity (a) without and (b) with an iris.

5.7 Conclusions

A computer-controlled stable CW source, the 250 GHz gyrotron was the first gyro-device specifically designed with the purpose of seamless integration into an NMR spectrometer [44, 47]. During the course of this work, the 250 GHz gyrotron has been operated continuously for a period of 21 days yielding a power stability of <1% and frequency stability of better than 400 kHz (1.6 ppm). The gyrotron output power is controlled through feedback regulation of power sampled through a quasi-optical directional coupler implemented in an overmoded corrugated waveguide. We have mapped radiation patterns at various locations along the axis of the waveguide and demonstrated using two techniques that a pure Gaussian mode is effectively coupled to the sample. Further, a parametric study of mode excitation in the 250 GHz gyrotron oscillator has revealed broadband continuous frequency tuning of up to 1.8 GHz through variation of the main magnetic field alone. Several second harmonic modes were observed in the range 325-365 GHz, and they are characterized by unusually low starting currents (as low as 12 mA). The low starting currents were attributed to an elevated cavity Q, a fact that is also suggested by cavity thermal load measurements.

The performance of the gyrotron control system is currently limited by the cycle time of the hardware, which is dominated by the need to synchronously sample multiple analog signals. Improvements in this approach, involving asynchronous digital sampling of slowly-varying signals and asynchronous sampling of analog signals, have been demonstrated in a 460 GHz gyrotron control system [111].

5.8 Appendix

As mentioned in Section 5.5 the gyrotron is employed in 3D DNP/NMR experiments and requires a control system to maintain the power stability for the extended periods involved. In this Appendix we provide detailed block diagrams of the control system developed for this purpose.

The major components of the 250 GHz gyrotron control system are illustrated in schematic form in Figure 5-27 aspects of the event-driven architecture of the software control system are illustrated in Figure 5-28. Its principal function is to regulate the microwave output power by changing the heater voltage.
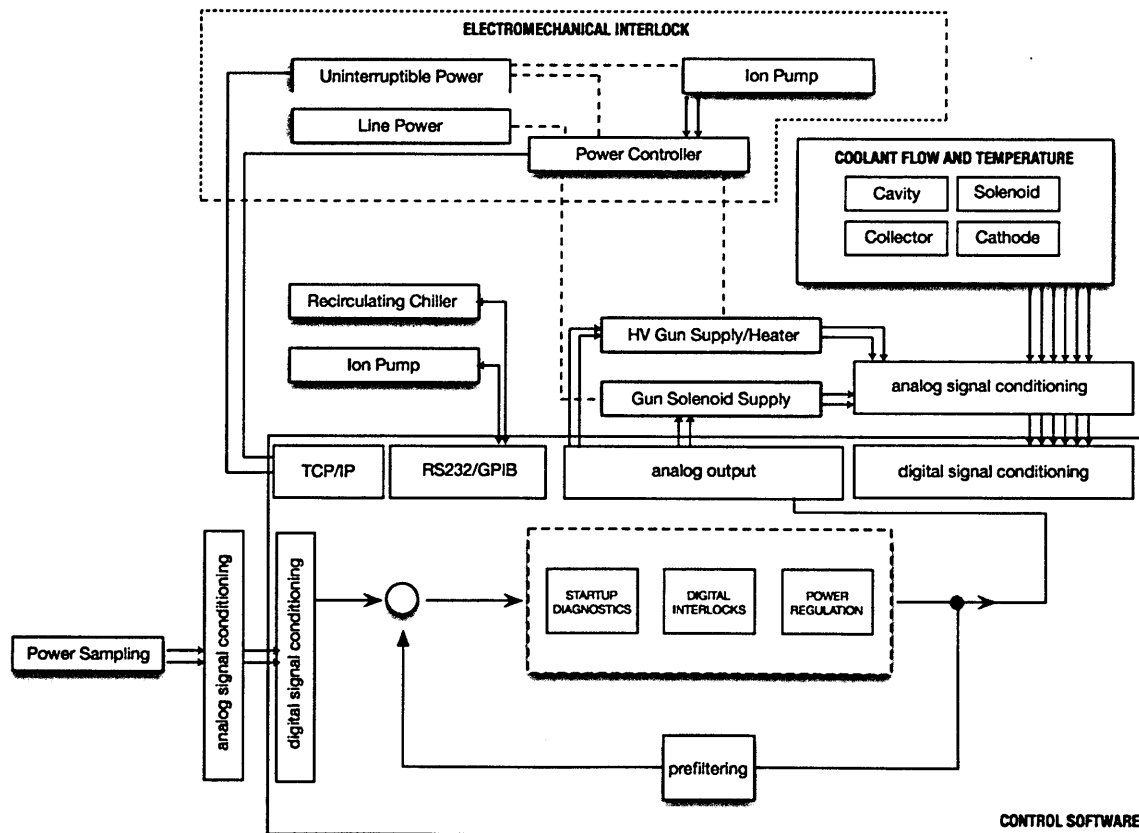
Figure 5-27: Block diagram illustrating major components of the 250 GHz gyrotron control system.

287
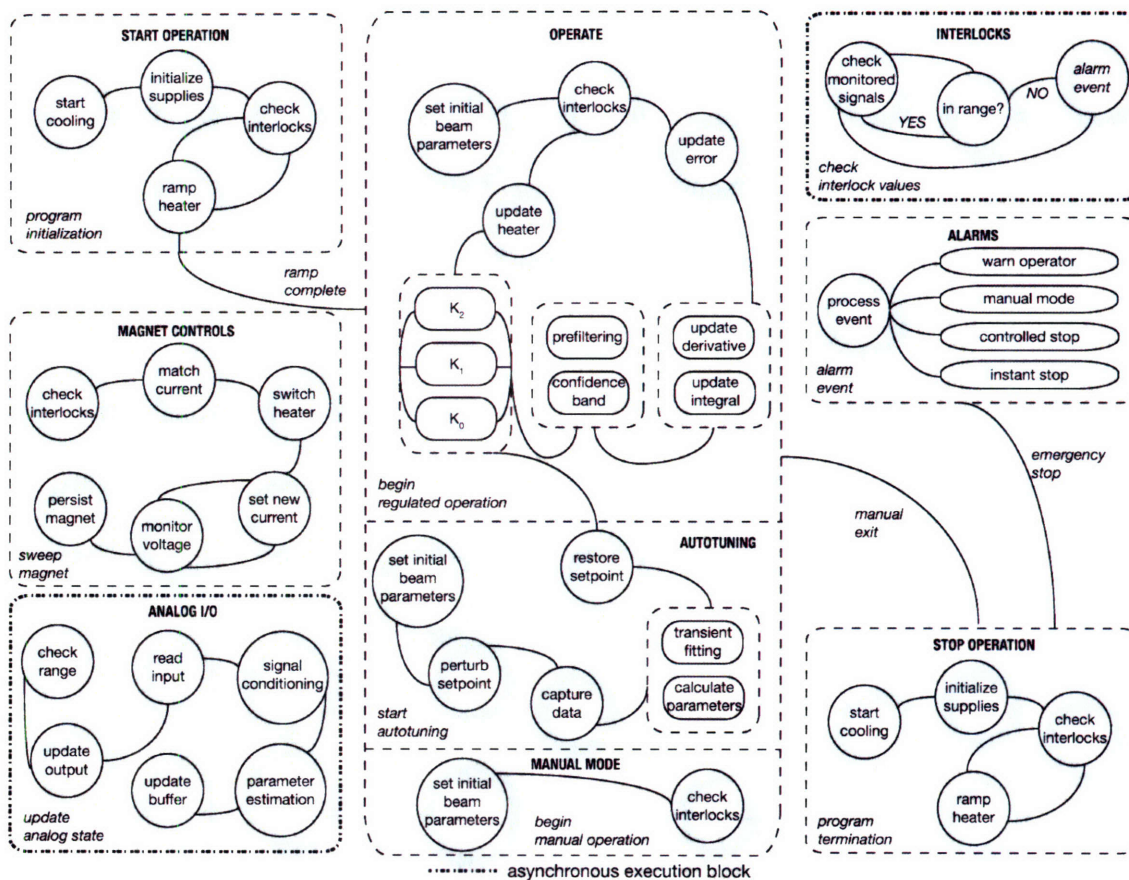
Figure 5-28: State machine indicating common processing functionality of the 250 GHz control system. Transitions between blocks occur in response to events passed through a global message queue and are not explicitly illustrated. Each block has access to a global variable space and message queue, and concurrent execution blocks are indicated. Analog I/O is blocking.

5.9 References

[1]   Ernst, R. R.; Anderson, W. A., Application of Fourier Transform Spectroscopy to Magnetic Resonance. *Review of Scientific Instruments* **1966,** 37, 93-102.

[2]   Styles, P.; Soffe, N.; Scott, C.; Cragg, D.; Row, F.; White, D.; White, P., A High-Resolution NMR Probe in Which the Coil and Preamplifier are Cooled with Liquid Helium. *Journal of Magnetic Resonance* **1984,** 60, 397-404.

[3]   Hartmann, S. R.; Hahn, E. L., Double Resonance in the Rotating frame. *Phys. Rev.* **1962,** 128, 2042-2053.

[4]   Pines, A.; Gibby, M. G.; Waugh, J. S., Proton-enhanced NMR of dilute spins in solids. *J. Chem. Phys.* **1973,** 59, 569-590.

[5]   Morris, G.; Freeman, R., Enhancement of Nuclear Magnetic Resonance Signals by Polarization Transfer. *J. Am Chem. Soc* **1979,** 101, 760-762.

[6]   Schaefer, J.; Stejskal, E. O., ^{13}C Nuclear Magnetic Resonance of Polymers Spinning at the Magic Angle. *J. Am. Chem. Soc.* **1976,** 98, 1031-1032.

[7]   Cavanaugh, J.; Fairbrother, W. J.; Palmer, A.; M.J, R.; Skelton, N. J., *Protein NMR Spectroscopy: Principles and Practice*. 2nd ed.; Academic Press: San Diego, CA, 2006.

[8]   Overhauser, A. W., Polarization of Nuclei in Metals. *Phys. Rev.* **1953,** 92, 411-415.

[9]   Carver, T. R.; Slichter, C. P., Experimental Verification of the Overhauser Nuclear Polarization Effect. *Phys. Rev.* **1956,** 102, 975-980.

[10]   Carver, T. R.; Slichter, C. P., Polarization of Nuclear Spins in metals. *Physical Review* **1953,** 92, 212-213.

[11]   Duckett, S. B.; Sleigh, C. J., Applications of the parahydrogen phenomenon: A chemical perspective. *Progress in Nuclear Magnetic Resonance Spectroscopy* **1999,** 34, (1), 71-92.

[12]   Natterer, J.; Bargon, J., Parahydrogen induced polarization. *Progress in Nuclear Magnetic Resonance Spectroscopy* **1997,** 31, 293-315.

[13]   Navon, G.; Song, Y. Q.; Room, T.; Appelt, S.; Taylor, R. E.; Pines, A., Enhancement of solution NMR and MRI with laser-polarized xenon. *Science* **1996,** 271, (5257), 1848-1851.

[14]   Fitzgerald, R. J.; Sauer, K. L.; Happer, W., Cross-relaxation in laser-polarized liquid xenon. *Chemical Physics Letters* **1998,** 284, (1-2), 87-92.

[15]   Cherubini, A.; Payne, G. S.; Leach, M. O.; Bifone, A., Hyperpolarising C-13 for NMR studies using laser-polarised Xe-129: SPINOE vs thermal mixing. *Chemical Physics Letters* **2003,** 371, (5-6), 640-644.

[16]   Pavlovskaya, G. E.; Cleveland, Z. I.; Stupic, K. F.; Basaraba, R. J.; Meersmann, T., Hyperpolarized krypton-83 as a contrast agent for magnetic resonance imaging. *Proceedings of the National Academy of Sciences of the United States of America* **2005,** 102, (51), 18275-18279.

[17]   Goto, A.; Hashi, K.; Shimizu, T.; Miyabe, R.; Wen, X. G.; Ohki, S.; Machida, S.; Iijima, T.; Kido, G., Optical pumping NMR in the compensated semiconductor InP : Fe. *Physical Review B* **2004,** 69, (7).

[18]   Barrett, S. E.; Tycko, R.; Pfeiffer, L. N.; West, K. W., Directly Detected Nuclear-Magnetic-Resonance of Optically Pumped Gaas Quantum-Wells. *Physical Review Letters* **1994,** 72, (9), 1368-1371.

[19]   Michal, C. A.; Tycko, R., Nuclear spin polarization transfer with a single radio-frequency field in optically pumped indium phosphide. *Physical Review Letters* **1998,** 81, (18), 3988-3991.

[20]   McDermott, A.; Zysmilich, M. G.; Polenova, T., Solid state NMR studies of photoinduced polarization in photosynthetic reaction centers: mechanism and simulations. *Solid State Nuclear Magnetic Resonance* **1998,** 11, (1-2), 21-47.

[21]   Polenova, T.; McDermott, A. E., A coherent mixing mechanism explains the photoinduced nuclear polarization in photosynthetic reaction centers. *Journal of Physical Chemistry B* **1999,** 103, (3), 535-548.

[22]   Prakash, S.; Alia; Gast, P.; de Groot, H. J. M.; Jeschke, G.; Matysik, J., Magnetic field dependence of photo-CIDNP MAS NMR on photosynthetic reaction centers of Rhodobacter sphaeroides WT. *Journal of the American Chemical Society* **2005,** 127, (41), 14290-14298.

[23]   Goez, M.; Mok, K. H.; Hore, P. J., Photo-CIDNP experiments with an optimized presaturation pulse train, gated continuous illumination, and a background-nulling pulse grid. *Journal of Magnetic Resonance* **2005,** 177, (2), 236-246.

[24]   Hausser, K. H.; Stehlik, D., Dynamic Nuclear Polarization in Liquids. *Advances in Magnetic Resonance* **1968,** 3, 79.

[25]   Müller-Warmuth, W.; Meise-Gresch, K., Molecular Motions and Interactions as Studied by Dynamic Nuclear Polarization in Free Radical Solutions. *Advances in Magnetic Resonance* **1983,** 11, 1-45.

[26]   Atsarkin, V. A., Dynamic Polarization of Nuclei in Solid Dielectrics. *Soviet Physics Solid State* **1978,** 21, 725-744.

[27]   Wind, R. A., Applications of Dynamic Nuclear Polarization in ^{13}C NMR in Solids. *Progress in NMR Spectroscopy* **1985,** 17, 33-67.

[28]   Becerra, L. R.; Gerfen, G. J.; Temkin, R. J.; Singel, D. J.; Griffin, R. G., Dynamic Nuclear Polarization with a Cyclotron Resonance Maser at 5 T. *Physical Review Letters* **1993,** 71, (21), 3561-3564.

[29]   Gerfen, G. J.; Becerra, L. R.; Hall, D. A.; Singel, D. J.; Griffin, R. G., High Frequency (140 GHz) Dynamic Nuclear Polarization : Polarization Transfer to a Solute in Frozen Aqueous Solution. *J. Chem. Phys.* **1995,** 102, 9494.

[30] Becerra, L. R.; Gerfen, G. J.; Bellew, B. F.; Bryant, J. A.; Hall, D. A.; Inati, S. J.; Weber, R. T.; Un, S.; Prisner, T. F.; McDermott, A. E.; Fishbein, K. W.; Kreischer, K. E.; Temkin, R. J.; Singel, D. J.; Griffin, R. G., A Spectrometer for Dynamic Nuclear Polarization and Electron Paramagnetic Resonance at High Frequencies. *J. Magn. Reson. A* **1995,** 117, 28-40.

[31] Felch, K. L.; Danly, B. G.; Jory, H. R.; Kreischer, K. E.; Lawson, W.; Levush, B.; Temkin, R. J., Characteristics and Applications of Fast-Wave Gyrodevices. *Proceedings of the IEEE* **1999,** 87, 752-781.

[32] Idehara, T.; Tsuchiya, H.; Watanabe, O.; Agusu, L.; Mitsudo, S., The First Experiment of a THz Gyrotron with a Pulse Magnet. *Intl. J. Infrared and Millimeter Waves* **2006,** 27, 319-331.

[33] Joye, C. D.; Griffin, R. G.; Hornstein, M. K.; Hu, K.-N.; Kreischer, K. E.; Rosay, M.; Shapiro, M. A.; Sirigiri, J. R.; Temkin, R. J.; Woskov, P. P., Operational Characteristics of a 14 Watt, 140 GHz Gyrotron for Dynamic Nuclear Polarization. *IEEE Transactions on Plasma Science* **2006,** 34, 518-523.

[34] Hu, K.; Yu, Y.-y.; Swager, T.; Griffin, R. G., Dynamic Nuclear Polarization with Biradicals. *J. Am. Chem. Soc.* **2004,** 126, 0000-0000.

[35] Joo, C.-G.; Hu, K.-N.; Bryant, J. A.; Griffin, R. G., In Situ Temperature Jump High-Frequency Dynamic Nuclear Polarization Experiments: Enhanced Sensitivity in Liquid-State NMR Spectroscopy
. *J. Am Chem. Soc* **2006,** 128, 9428-9432.

[36] Song, C.; Hu, K.-N.; Swager, T. M.; Griffin, R. G., TOTAPOL – A Biradical Polarizing Agent for Dynamic Nuclear Polarization Experiments in Aqueous Media. *J. Am Chem. Soc* **2006,** 128, 11385-90.

[37] van der Wel, P. C. A.; Hu, K.-N.; Lewandoswki, J.; Griffin, R. G., Dynamic Nuclear Polarization of Amyloidogenic Peptide Nanocrystals: GNNQQNY, a Core Segment of the Yeast Prion Protein Sup35p
. *J. Am Chem. Soc* **2006,** 128, 10840-10846.

[38] Hu, K.-N.; Bajaj, V. S.; Rosay, M. M.; Griffin, R. G., High Frequency Dynamic Nuclear Polarization Using Mixtures of TEMPO and Trityl Radicals. *J. Chem. Phys.* **2007,** 126, 044512.

[39] Hu, K.-N.; Griffin, R. G., Quantum Mechanical Theory of Dynamic Nuclear Polarization in Solid Dielectrics –Simulation of Electron-Electron-Nucleus Spin Systems with Relaxation. *J. Chem. Phys.* **2007,** (submitted for publication).

[40]   Hu, K.-N.; Griffin, R. G., Quantum Mechanical Theory of Dynamic Nuclear Polarizaton in Solid Dielectrics: I- Analytical Approach. *J. Chem. Phys.* **2007,** (submitted for publication).

[41]   Hu, K.-N.; Song, C.; Yu, H.-h.; Swager, T. M.; Griffin, R. G., High-Frequency Dynamic Nuclear Polarization Using Biradicals: A Multifrequency EPR Lineshape Analysis. *J. Chem. Phys.* **2007,** (submitted for publication).

[42]   Rosay, M.; Lansing, J. C.; Haddad, K. C.; Bachovchin, W. W.; Herzfeld, J.; Temkin, R. J.; Griffin, R. G., High Frequency Dynamic Nuclear Polarization in MAS Spectra of Membrane and Soluble Proteins. *J. Am. Chem. Soc.* **2003,** 125, 13626-27.

[43]   Hall, D. A.; Maus, D. C.; Gerfen, G. J.; Inati, S. J.; Becerra, L. R.; Dahlquist, F. W.; Griffin, R. G., Polarization-Enhanced NMR Spectroscopy of Biomolecules in Frozen Solution. *Science* **1997,** 276, 930-932.

[44]   Kreischer, K. E.; Farrar, C.; Griffin, R. G.; Temkin, R. J.; Vieregg, J. In *Development of a 250 GHz CW Gyrotron for EPR and NMR Spectroscopy,* Proceedings of the 24th International Conference on Infrared and Millimeter Waves, Monterey, CA, 1999; Lombardo, L., Ed. UC Davis: Monterey, CA, 1999; pp TU-A3.

[45]   Hornstein, M. K.; Bajaj, V. S.; Griffin, R. G.; Kreischer, K. E.; Mastovsky, I.; Shapiro, M. A.; Sirigiri, J. R.; Temkin, R. J., Second Harmonic Operation at 460 GHz and Broadband Continuous Frequency Tuning of a Gyrotron Oscillator. *IEEE Transactions on Electron Devices* **2005,** 52, 798-807.

[46]   Rosay, M.; Weis, V.; Kreischer, K. E.; Temkin, R. J.; Griffin, R. G., Two-dimensional C-13-C-13 correlation spectroscopy with magic angle spinning and dynamic nuclear polarization. *Journal of the American Chemical Society* **2002,** 124, (13), 3214-3215.

[47]   Bajaj, V. S.; Farrar, C. T.; Hornstein, M. K.; Mastovsky, I.; Vieregg, J.; Bryant, J.; Elena, B.; Kreischer, K. E.; Temkin, R. J.; Griffin, R. G., Dynamic nuclear polarization at 9T using a novel 250 GHz gyrotron microwave source. *J. Mag. Res.* **2003,** 160, 85-90.

[48]   Lansbury, P. T.; Costa, P. R.; Griffiths, J. M.; Simon, E. J.; Auger, M.; Halverson, K. J.; Kocisko, D. A.; Hendsch, Z. S.; Ashburn, T. T.; Spencer, R. G. S.; Tidor, B.; Griffin, R. G., Structural Model for the b Amyloid Fibril: Interstrand Alignment of an Antiparallel b Sheet Comprising a C-terminal Peptide. **1995,** 2, 990-997.

[49]   Jaroniec, C. P., C.E. MacPhee, N.S. Astrof, C.M. Dobson, R.G. Griffin,, Molecular Conformation of a Peptide Fragment of Transthyretin in an Amyloid Fibril. *Proc. Nat'l. Acad. Sci.* **2002,** 99,, 16748-16753.

[50]   Jaroniec, C. P.; MacPhee, C. E.; Bajaj, V. S.; McMahon, M. T.; Dobson, C. M.; Griffin, R. G., High Resolution Molecular Structure of a Peptide in an Amyloid Fibril Determined by MAS NMR Spectroscopy. *Proc. Nat'l. Acad. Sci.* **2004**, 101, 711-716.

[51]   Siemer, A. B.; Ritter, C.; Ernst, M.; Riek, R.; Meier, B. H., High-Resolution Solid-State NMR Spectroscopy of the Prion Protein HET-s in Its Amyloid Conformation. *Angew. Chem. Int. Ed.* **2005**, 44, 2–5.

[52]   Tycko, R., Insights into the Amyloid Folding Problem from Solid-State NMR. *Biochemistry* **2003**, 42, (11), 3151-3159.

[53]   Heise, H.; Hoyer, W.; Becker, S.; Andronesi, O. C.; Riedel, D.; Baldus, M., Molecular-level secondary structure, polymorphism, and dynamics of full-length alpha-synuclein fibrils studied by solid-state NMR. *Proc. Nat'l. Acad. Sci.* **2005**, 102, 15871-15876.

[54]   van der Wel, P. C. A.; Lewandoswki, J.; Griffin, R. G., Solid state NMR study of amyloid nanocrystals and fibrils formed by the peptide GNNQQNY from yeast prion protein Sup35p. *J. Am Chem. Soc* **2007**, (in press).

[55]   Harbison, G. S.; Herzfeld, J.; Griffin, R. G., Solid-State ^{15}N Nuclear Magnetic-Resonance Study of the Schiff-Base in Bacteriorhodopsin. *Biochemistry* **1983**, 22, (1), 1-5.

[56]   Harbison, G. S.; Smith, S. O.; Pardoen, J. A.; Courtin, J. M. L.; Lugtenburg, J.; Herzfeld, J.; Mathies, R. A.; Griffin, R. G., Solid-State C-13 Nmr Detection of a Perturbed 6-S-Trans Chromophore in Bacteriorhodopsin. *Biochemistry* **1985**, 24, (24), 6955-6962.

[57]   Harbison, G. S.; Roberts, J. E.; Herzfeld, J.; Griffin, R. G., Solid-State Nmr Detection of Proton-Exchange between the Bacteriorhodopsin Schiff-Base and Bulk Water. *Journal of the American Chemical Society* **1988**, 110, (21), 7221-7223.

[58]   Griffiths, J. M.; Lakshmi, K. V.; Bennett, A. E.; Raap, J.; Vanderwielen, C. M.; Lugtenburg, J.; Herzfeld, J.; Griffin, R. G., Dipolar Correlation NMR-Spectroscopy of a Membrane-Protein. *J. Am. Chem. Soc.* **1994**, 116, (22), 10178-10181.

[59]   Hu, J. G.; Griffin, R. G.; Herzfeld, J., Synergy in the Spectral Tuning of Retinal Pigments - Complete Accounting of the Opsin Shift in Bacteriorhodopsin. *Proceedings of the National Academy of Sciences of the United States of America* **1994**, 91, (19), 8880-8884.

[60]   Jaroniec, C. P.; Lansing, J. C.; Tounge, B. A.; Belenky, M.; Herzfeld, J.; Griffin, R. G., Measurement of dipolar couplings in a uniformly C-13,N-15-labeled membrane protein: Distances between the Schiff base and aspartic acids in the active site of

bacteriorhodopsin. *Journal of the American Chemical Society* **2001**, 123, (51), 12929-12930.

[61]   Cross, T. a.; Opella, S. J., Solid-State Nmr Structural Studies of Peptides and Proteins in Membranes. *Current Opinion in Structural Biology* **1994**, 4, (4), 574-581.

[62]   Chekmenev, E. Y.; Waddell, K. W.; Hu, J.; Gan, Z. H.; Wittebort, R. J.; Cross, T. A., Ion-binding study by O-17 solid-state NMR spectroscopy in the model peptide gly-gly-gly at 19.6 T. *Journal of the American Chemical Society* **2006**, 128, (30), 9849-9855.

[63]   Denny, J. K.; Wang, J. F.; Cross, T. A.; Quine, J. R., PISEMA powder patterns and PISA wheels. *Biophysical Journal* **2001**, 80, (1), 370A-370A.

[64]   Cross, T. A.; Arseniev, A.; Cornell, B. A.; Davis, J. H.; Killian, J. A.; Koeppe, R. E.; Nicholson, L. K.; Separovic, F.; Wallace, B. A., Gramicidin channel controversy - revisited. *Nature Structural Biology* **1999**, 6, (7), 610-611.

[65]   Pascal, S. M.; Cross, T. a., Structure of an Isolated Gramicidin-a Double Helical Species by High-Resolution Nuclear-Magnetic-Resonance. *Journal of Molecular Biology* **1992**, 226, (4), 1101-1109.

[66]   Salgado, G. F. J.; Struts, A. V.; Tanaka, K.; Krane, S.; Nakanishi, K.; Brown, M. F., Solid-state H-2 NMR structure of retinal in metarhodopsin I. *Journal of the American Chemical Society* **2006**, 128, (34), 11067-11071.

[67]   Kobayashi, M.; Fujiwara, T.; Brown, M. F.; Akutsu, H., Solid-state H-2 NMR studies of DMPC membranes containing subunit c of E. Coli ATP synthase. *Biophysical Journal* **2005**, 88, (1), 141A-141A.

[68]   Salgado, G. F. J.; Struts, A. V.; Tanaka, K.; Fujioka, N.; Krane, S.; Nakanishi, K.; Brown, M. F., Deuterium solid-state NMR of aligned rhodopsin: POPC membranes sheds new light on retinal conformation. *Biophysical Journal* **2005**, 88, (1), 203A-204A.

[69]   Subramaniam, V.; Alves, I. D.; Salgado, G. F. J.; Lau, P. W.; Wysocki, R. J.; Salamon, Z.; Tollin, G.; Hruby, V. J.; Brown, M. F.; Saavedra, S. S., Rhodopsin reconstituted into a planar-supported lipid bilayer retains photoactivity after cross-linking polymerization of lipid monomers. *Journal of the American Chemical Society* **2005**, 127, (15), 5320-5321.

[70]   Zhang, W. Y.; Sato, T.; Smith, S. O., NMR spectroscopy of basic/aromatic amino acid clusters in membrane proteins. *Progress in Nuclear Magnetic Resonance Spectroscopy* **2006**, 48, (4), 183-199.

[71]   Crocker, E.; Eilers, M.; Ahuja, S.; Hornak, V.; Hirshfeld, A.; Sheves, M.; Smith, S. O., Location of Trp265 in metarhodopsin II: Implications for the activation mechanism of the visual receptor rhodopsin. *Journal of Molecular Biology* **2006**, 357, (1), 163-172.

[72] Smith, S. O., Solid-state NMR approaches for probing the structure and dynamics of membrane proteins. *Biophysical Journal* **2005**, 88, (1), 542A-542A.

[73] Hu, J. G.; Griffin, R. G.; Herzfeld, J., Interactions between the protonated Schiff base and its counterion in the photointermediates of bacteriorhodopsin. *J. Am. Chem. Soc.* **1997**, 119, (40), 9495-9498.

[74] Hu, J. G.; Sun, B. Q.; Griffin, R. G.; Herzfeld, J., Solid state NMR study of the L-intermediate in bacteriorhodopsin. *Biophysical Journal* **1996**, 70, (2), SU432-SU432.

[75] Balashov, S. P.; Ebrey, T. G., Trapping and spectroscopic identification of the photointermediates of bacteriorhodopsin at low temperatures. *Photochemistry and Photobiology* **2001**, 75, 453-62.

[76] Bennett, A. E.; Ok, J. H.; Griffin, R. G.; Vega, S., Chemical-Shift Correlation Spectroscopy in Rotating Solids - Radio Frequency-Driven Dipolar Recoupling and Longitudinal Exchange. *Journal of Chemical Physics* **1992**, 96, (11), 8624-8627.

[77] Bennett, A. E.; Rienstra, C. M.; Griffiths, J. M.; Zhen, W. G.; Lansbury, P. T.; Griffin, R. G., Homonuclear radio frequency-driven recoupling in rotating solids. *Journal of Chemical Physics* **1998**, 108, (22), 9463-9479.

[78] Takegoshi, K.; Nakamura, S.; Terao, T., C-13-H-1 dipolar-assisted rotational resonance in magic-angle spinning NMR. *Chemical Physics Letters* **2001**, 344, (5-6), 631-637.

[79] Morcombe, C. R.; Paulson, E. K.; Gaponenko, V.; Byrd, R. A.; Zilm, K. W., H-1-N-15 correlation spectroscopy of nanocrystalline proteins. *Journal of Biomolecular NMR* **2005**, 31, (3), 217-230.

[80] Brand, G. F.; Gross, M., Continuously Tunable Split-Cavity Gyrotrons. *International Journal of Infrared and Millimeter Waves* **1985**, 6, 1237-54.

[81] Ardenkjær-Larsen, J. H.; Fridlund, B.; Gram, A.; Hansson, G.; Hansson, L.; Lerche, M. H.; Servin, R.; Thaning, M.; Golman, K., Increase in signal-to-noise ratio of >10,000 times in liquid-state NMR. *Proc. Nat'l Acad. Sci. USA* **2003**, 100, 10158–10163.

[82] Degroot, H. J. M.; Harbison, G. S.; Herzfeld, J.; Griffin, R. G., Nuclear Magnetic-Resonance Study of the Schiff-Base in Bacteriorhodopsin - Counterion Effects on the N-15 Shift Anisotropy. *Biochemistry* **1989**, 28, (8), 3346-3353.

[83] Herzfeld, J.; Tounge, B., NMR probes of vectoriality in the proton-motive photocycle of bacteriorhodopsin: evidence for an 'electrostatic steering' mechanism. *Biochimica Et Biophysica Acta-Bioenergetics* **2000**, 1460, (1), 95-105.

[84]   Friedman, N.; Ottolenghi, M.; Sheves, M., Heterogeneity Effects in the Binding of all-trans Retinal to Bacterio-opsin. *Biochemistry* **2003**, 42, 11281-88.

[85]   McKay, R. A., Probes for Special Purposes. In *Encyclopedia of Nuclear Magnetic Resonance*, Grant, D. M.; Harris, R., Eds. John Wiley and Sons: New York, 1996; Vol. 6, pp 3768-71.

[86]   Schaefer, J.; McKay, R. A. Multituned Single Coil Transmission Line Probe for Nuclear Magnetic Resonance Spectrometer. 5,861,748, 1999.

[87]   Woskov, P. W.; Bajaj, V. S.; Hornstein, M. K.; Temkin, R. J.; Griffin, R. G., Corrugated Waveguide and Directional Coupler for CW 250 GHz Gyrotron DNP Experiments. *IEEE Transactions on Microwave Theory and Techniques* **2005**, 53, 1863-69.

[88]   Nusinovich, G. S., *Introduction to the Physics of Gyrotrons*. Johns Hopkins University Press: Baltimore, MD 21218-4363, 2004; p 335.

[89]   Kartikeyan, M. V.; Borie, E.; Thumm, M. K. A., *Gyrotrons: High Power Microwave Sources and Technologies*. Springer: New York, 2004; p 227.

[90]   Nusinovich, G. S.; Barker, R. J.; Luhmann, N. C.; Booske, J. H., *Modern Microwave and Millimeter-Wave Power Electronics* Wiley-IEEE Press: 2005; p 872.

[91]   Cairns, R. A.; Phelps, A. D. R., *Generation and Application of High Power Microwaves*. Taylor & Francis London, 1997.

[92]   Granatstein, V. L.; Alexeff, I., *High-Power Microwave Sources*. Artech House Publishers: 1987.

[93]   Edgcombe, C. J., *Gyrotron Oscillators: Their Principles and Practice* CRC Press: 1993; p 423.

[94]   Griffiths, D. J., *Introduction to Quantum Mechanics, 2e*. Pearson Prentice Hall: Upper Saddle River, NJ, 2005; p 468.

[95]   Gasiorowicz, S., *Quantum Physics, 3e*. John Wiley and Sons: 2003.

[96]   Schneider, J., Stimulated Emission of Radiation by Relativistic Electrons in a Magnetic Field. *Phys. Rev. Letters* **1959**, 2, 504-505.

[97]   Robinson, L. C., *Physical Principles of Far-infrared Radiation*. Academic Press: New York, 1973; Vol. 10, p 230-264.

[98] Kreischer, K. E.; Danly, B. G.; Woskoboinikow, P.; Mulligan, W. J.; Temkin, R. J., Frequency Pulling and Bandwidth Measurements of a 140 GHz Pulsed Gyrotron. *Int. J. Electronics* **1984,** 57, 851-862.

[99] Fliflet, a. W.; Read, M. E.; Chu, K. R.; Seeley, R., A Self-Consistent Field-Theory for Gyrotron Oscillators - Application to a Low Q Gyromonotron. *International Journal of Electronics* **1982,** 53, (6), 505-521.

[100] Brand, G. F.; Douglas, N. G.; Gross, M.; Ma, J. Y. L.; Zhiyi, C., Frequency Detuning Measurements in a Low-Power Gyrotron. *International Journal of Infrared and Millimeter Waves* **1983,** 4, (6), 891-900.

[101] Botton, M.; Antonsen, T. M.; Levush, B.; Nguyen, K. T.; Vlasov, A. N., MAGY: A Time-Dependent Code for Simulation of Slow and Fast Microwave Sources. *IEEE Trans. Plasma Sci.* **1998,** 26, (3), 882-892.

[102] Woskoboinikow, P., Development of Gytotrons for Plasma Diagnostics. *Rev. Sci. Instrum.* **1986,** 57, 2113-18.

[103] Machuzak, J. S.; Woskoboinikow, P.; Mulligan, W. J.; Cohn, D. R.; Gerver, M.; Guss, W.; Mauel, M.; Post, R. S.; Temkin, R. J., 137-GHz gyrotron diagnostic for instability studies in Tara. *Rev. Sci. Instrum.* **1986,** 57, 1983-85.

[104] Nusinovich, G. S.; Dumbrajs, O., Technical noise in gyroklystrons and phase-locked gyrotron oscillators. *Phys. Plasmas* **1997,** 4, 1424-33.

[105] Dumbrajs, O.; Nusinovich, G. S., Effect of technical noise on radiation linewidth in free-running gyrotron oscillators. *Phys. Plasmas* **1997,** 4, 1413-23.

[106] Okoshi, T.; Kikushi, K.; Nakayama, A., Novel method for high resolution measurement of laser output spectrum. *Elect. Lett.* **1980,** 16, 630-631.

[107] Hornstein, M. K. A Continuous-Wave Second Harmonic Gyrotron Oscillator at 460 GHz. Ph.D., Mass. Institute of Technology, Cambridge, MA 02139, 2005.

[108] Carmel, Y.; Chu, K. R.; Read, M. E.; Granatstein, V. L.; Faillon, G.; Boulanger, P.; Kammerer, E.; Mourier, G., A Technique to Identify Electromagnetic Modes in Oversize Waveguides. *IEEE Transactions on Microwave Theory and Techniques* **1984,** 32, 1493-95.

[109] Azar, K.; Benson, J. R.; V.P. Manno In *Liquid crystal imaging for temperature measurement of electronic devices*, Proceedings Seventh Annual IEEE Semiconductor Thermal Measurement and Management Symposium (Cat. No.91CH2972-8), Phoenix, AZ, 1991; Phoenix, AZ, 1991; pp 22-33.

[110] Farina, D. J., Making Surface Temperature Measurements Using Liquid Crystal Thermography. *Electronics Cooling* **1995,** 1, 10-15.

[111] Hornstein, M. K.; Bajaj, V. S.; Griffin, R. G.; Temkin, R. J., Continuous-wave operation of a 460-GHz second harmonic gyrotron oscillator. *Ieee Transactions on Plasma Science* **2006,** 34, (3), 524-533.

[112] Yeddulla, M.; Nusinovich, G. S.; Antonsen, T. M., Start currents in an overmoded gyrotron. *Phys. Plasmas* **2003,** 10, 4513-4520.

Chapter 6   Second Harmonic Operation at 460 GHz and Broadband Continuous Frequency Tuning of a Gyrotron Oscillator

We report the short pulse operation of a 460 GHz gyrotron oscillator both at the fundamental (near 230 GHz) and second harmonic (near 460 GHz) of electron cyclotron resonance. During operation in a microsecond pulse length regime with 13 kV beam voltage and 110 mA beam current, the instrument generates several watts of power in two second harmonic modes, the $TE_{2,6,1}$ at 456.15 GHz and the $TE_{0,6,1}$ at 458.56 GHz. Operation in the fundamental modes, including the $TE_{0,3,1}$ mode at 237.91 GHz and the $TE_{2,3,1}$ at 233.15 GHz, is observed at output powers up to 70 W. Further, we demonstrate broadband continuous frequency tuning of the fundamental modes of the oscillator over a range of more than 2 GHz through variation of the magnetic field alone. We interpret these results in terms of smooth transitions between higher order axial modes of the resonator.

6.1   Introduction

The terahertz or submillimeter band of the electromagnetic spectrum, corresponding to frequencies between 300 and 3,000 GHz, is of considerable interest for applications in spectroscopy, communications, high-resolution RADAR, and imaging [1], [2]. Potential applications are nevertheless frustrated by a historical dearth of sources that yield

appreciable powers in this frequency regime. On the one hand, near-infrared lasers are capable of delivering moderate peak power at very high frequencies, but they do not yet scale to intermediate frequencies; on the other hand, conventional vacuum electron devices such as the klystron and traveling wave tube (TWT) operate at very high output powers in the tens of gigahertz, but the physical dimensions of their interaction structures (*i.e.* the region of interaction with the electron beam) necessarily scale with the wavelength. The resulting increase in power density with increasing frequency limits the reliability and utility of these devices above 140 GHz.

Gyrotrons, by contrast, do not suffer from these limitations. Unlike so-called "slow-wave" microwave devices, "fast-wave" devices such as gyrotron oscillators and amplifiers rely on a resonance between the modes of an interaction structure (such as the transverse electric modes of a cylindrical cavity) and the electron beam in a magnetic field. The resonator can be overmoded and, as such, can have physical dimensions which are much larger than the operating wavelength. This permits high peak and average power operation even at elevated frequencies without risk of damage to the interaction structure [2]. Indeed, gyrotrons routinely achieve megawatt power levels at frequencies between 100 and 170 GHz, where plasma heating for fusion is the driving application [4]. The highest frequency achieved by a gyrotron oscillator to date is 889 GHz at Fukui University in Japan [5]. At the University of Electronic Science and Technology of China in Chengdu, a gyrotron successfully produced the third harmonic at 35 GHz [6]. Second harmonic operation of a Soviet gyrotron was demonstrated at 326 GHz with the power level of 1.5 kW at continuous duty [7]. More recent applications in spectroscopy, such as high field dynamic nuclear polarization (DNP) [8] and electron paramagnetic

resonance (EPR) require lower peak power, but high average power continuous duty (7-10 days CW) operation and high stability of the frequency and output power.

Superconducting magnet technology is one limiting factor in high frequency gyrotron design. At fields up to 10 T, magnets which have wide room temperature bores generally employ the NbTi superconducting technology; from 10 T to 22 T (corresponding to a range of fundamental electron cyclotron frequency from 280 to 616 GHz), it is necessary to use the Nb_3Sn conductor which elevates the cost of the superconducting magnet. This limitation can be alleviated by operating the gyrotron at a harmonic of electron cyclotron resonance, for which the nth harmonic will deliver n times the fundamental frequency for a given magnetic field. However, the harmonic interaction is inherently less efficient than the fundamental interaction due to elevated ohmic losses. It also suffers from the additional complication of mode competition and requires much higher beam currents in order to initiate oscillation. To a large extent, these difficulties can be reduced through appropriate design.

In this work, we report microsecond pulsed results from a 460 GHz gyrotron oscillator designed to operate continuously at the second electron cyclotron harmonic at low voltages and output powers of between several watts and several tens of watts. Further, we have demonstrated that continuous tuning of the gyrotron oscillator over a range of nearly 2 GHz at constant output power is possible by changing the magnetic field and implementing feedback control on the beam current. The gyrotron oscillator design will also permit the precise control of the output power and frequency that is necessary for applications to sensitivity-enhanced magnetic resonance spectroscopy through dynamic nuclear polarization (DNP). Originally employed to produce spin

polarized targets for nuclear scattering experiments, DNP is a technique through which the greater Zeeman polarization of the electrons is transferred to the nuclei, in this case to enhance the sensitivity of a subsequent NMR experiment by up to two orders of magnitude. DNP requires irradiation of the sample with 1–10 W of power near the electron Larmor frequency (which is close to the electron cyclotron frequency) [8]. This technology will extend the applicability of DNP techniques to frequencies much higher than was previously possible.

6.2   Gyrotron design considerations and construction

The design of the 460 GHz gyrotron oscillator is based on a previous 250 GHz oscillator built at MIT for DNP experiments [9]–[11], with the additional goal that it operate at the second electron cyclotron harmonic. This design is described in [12] and [13]. Challenges associated with second harmonic operation were addressed with novel designs for many components of the tube. Critical operational features of this design include the ability to efficiently generate second harmonic radiation at relatively low voltages and currents, low starting currents, reduced ohmic losses for higher efficiency, and isolated excitation of a second harmonic mode without competition from fundamental modes.

Table 6.1: Gyrotron design parameters

Frequency	460 GHz	Perp. velocity spread	4%
Magnetic field	8.4 T	Velocity pitch factor	2
Harmonic number	2	Magnetic compression	28
Mode	$TE_{0,6,1}$	Electron beam radius	1 mm
Accelerating voltage	12 kV	Cavity diffractive Q	31,100
Beam current	100 mA	Cavity ohmic Q	19,400
Cathode radius	5.4 mm	Total cavity Q	12,000
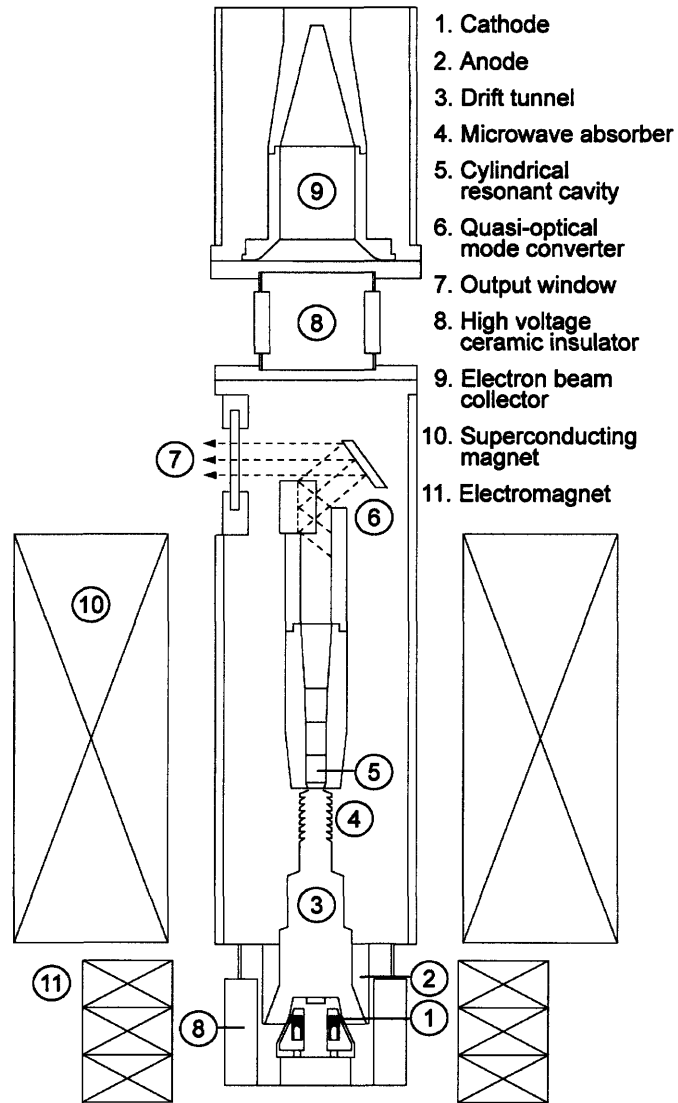
Figure 6-1: Cross-sectional schematic of the cylindrically symmetric 460 GHz gyrotron tube, not shown to scale, indicating key components. The gyrotron tube is approximately 1.4 m long and the magnet bore diameter is 7.62 cm.

A schematic of the 460 GHz gyrotron system is shown in Fig. 6-1. The axis of the gyrotron tube and electron beam lie along the vertical bore of a 9.2 T superconducting magnet, while the microwave power is extracted via a quasi-optical mode converter through an auxiliary, horizontal, room temperature bore which intersects with the main bore above the main coil of the superconducting magnet. The dual-bore arrangement allows for efficient separation of the microwave beam from the electron beam, resulting in increased vacuum pumping conductance to the lower portion of the tube, a feature

which is critical for continuous duty operation. It also reduces ohmic losses in the output waveguide, simplifies the window design, and allows the spent electron beam to be collected in a highly compact and water-cooled collector region which is far from any fragile microwave or waveguide structure. The total length of the gyrotron tube is therefore only 1.4 m. Sets of two-axis horizontal alignment stages are located both under the electron gun and around the collector and are used to align the gyrotron tube with respect to the magnetic field of the superconducting magnet thereby aligning the electron beam.

The experiment employs a low voltage, diode-type electron gun whose design is modeled after the gun employed in a successful 250 GHz gyrotron experiment [11]. The low operating voltage of less than 15 kV eliminates the need for cumbersome oil cooling and high voltage insulation and reduces the possibility that ionizing radiation will be produced. The reduced complexity of this gun design is achieved at the expense of an increased sensitivity of the electron beam velocity pitch factor and velocity spread to the exact operating parameters. For that reason, characteristics of the electron gun were studied using the EGUN electron optics and gun design program [14] and optimized for the intended operating regime. Figure 6-2(a) depicts a typical simulation of the trajectories followed by electrons accelerated by a 12 kV potential in a gently tapered magnetic field reaching a maximum of 8.4 T in the cavity. The transverse rms velocity spread and beam α reach 4% and 2, respectively, in the region of the cavity for the design parameters optimized for second harmonic operation. For operating parameters corresponding to excitation of fundamental modes observed in this experiment, EGUN simulations predict large variations in the velocity spread and velocity pitch ratio with

changes in the beam voltage and the magnetic field. The results of an EGUN study of this gun over a broader range of operating voltages and magnetic fields are shown in Figure 6-2(b) and (c).
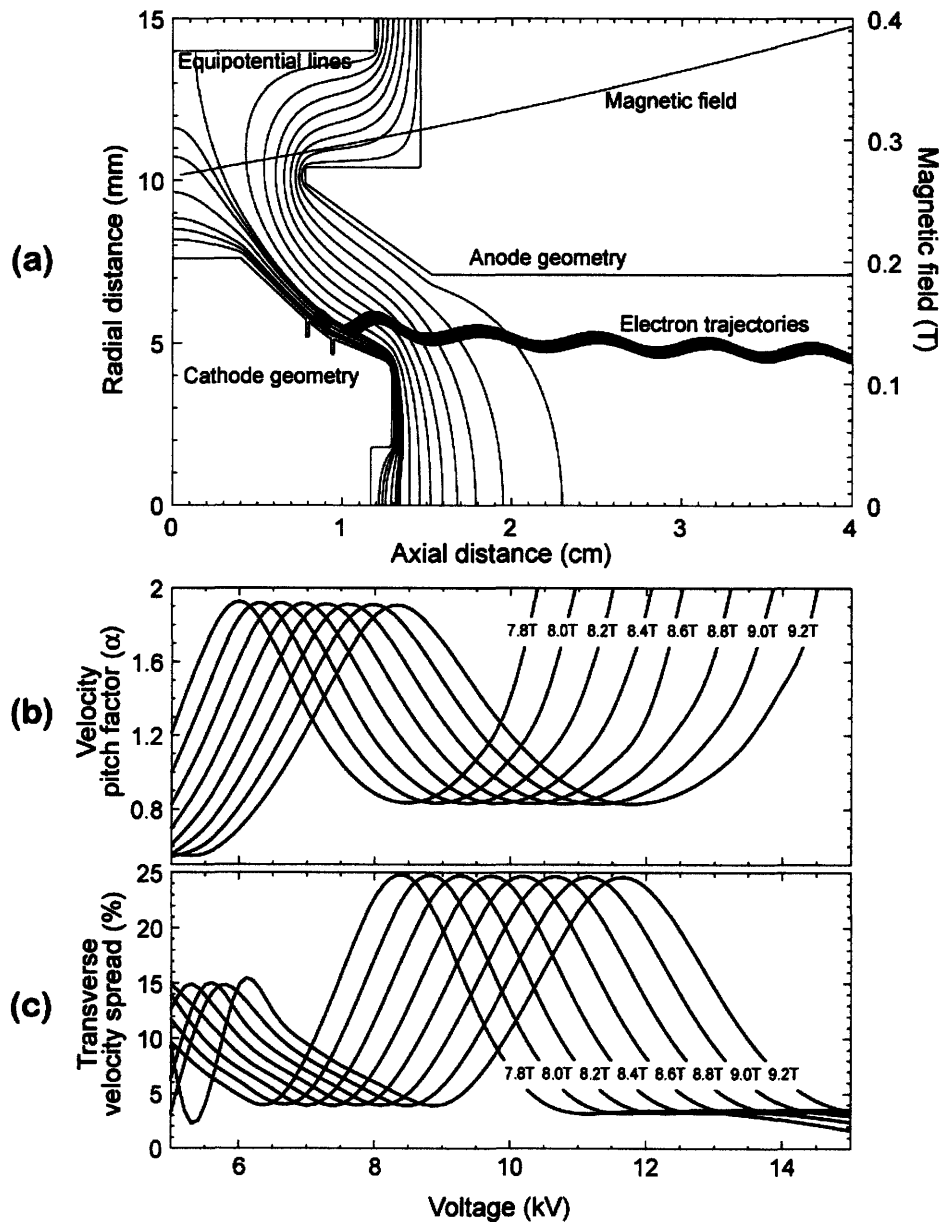
Figure 6-2: Simulation of the evolution of the transverse and axial velocities of the electrons accelerated at 12 kV in the 460 GHz gyrotron experiment using the EGUN electron optics and gun design program. (a) The electron trajectories, equipotential lines, cathode and anode geometries, and applied magnetic field of the gun region. (b) Velocity pitch factor and (c) transverse velocity spread for the low-voltage, diode-type gun used in the 460 GHz gyrotron experiment. Each curve is derived from EGUN simulations of the gun geometry conducted as a function of voltage and magnetic field.

305

In practice, the electron beam parameters such as the velocity pitch factor and velocity spread can be experimentally tuned by an electromagnet shim coil situated around the electron gun through changing the magnetic compression, the ratio of axial magnetic field at the cavity and cathode. Also known as the "gun coil", it reaches a maximum magnetic field of 8.5×10^{-2} T on axis and serves to fine tune the electron beam characteristics.
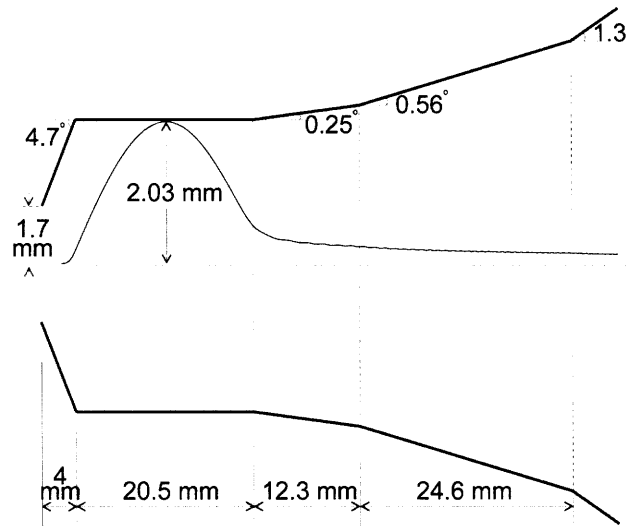
Figure 6-3: Cross-sectional schematic, not drawn to scale, of the 460 GHz gyrotron cavity with the axial radiation field profile for the second harmonic $TE_{0,6,1}$ resonator mode.

The resonant gyrotron interaction structure is a tapered cavity that was optimized for the $TE_{0,6,1}$ second harmonic eigenmode at 460 GHz using a cold cavity (electron beam absent) simulation code described in Section 6.4.2 [15]. Figure 6-3 is a cross-sectional schematic of the tapered cavity, consisting of a straight section of length 20.5 mm and circular cross-section of radius 2.03 mm joined to a linearly uptapered section at three discrete slopes at the exit (0.25, 0.56, and 1.3°) and a linearly downtapered section at the entrance of 4.7°, showing the axial profile of the design mode. Mode conversion in the

input taper was not detected by simulation. The gyrotron cavity was electroformed from OFC copper using an aluminum mandrel precision machined to a 5 µm tolerance and 0.2 µm finish.

The quasi-optical mode converter, optimized for the $TE_{0,6}$ mode, serves to convert the waveguide radiation into a free-space Gaussian beam in addition to separating the electron beam from the RF beam. The mode converter consists of a step cut waveguide launcher, a focusing mirror, and a flat reflecting mirror.

Table 6.1 summarizes the gyrotron and cavity design parameters. Notably, the gyrotron was designed for low voltage and current (12 kV, 100 mA) operation in a single second harmonic higher order mode. The DNP experiment requires moderate peak powers but continuous duty cycle operation for periods lasting 7-10 days, during which the output power and frequency must be stable to within 1% and at least 5 MHz respectively. We selected the $TE_{0,6,1}$ design mode on the basis of its isolation from competing fundamental modes and because the electron gun can easily generate a 1 mm beam radius in the cavity, which couples to the third maximum of the transverse field distribution.

Auxiliary equipment includes a recirculating chiller with three separate channels to water cool the electron beam collector, gun coil, and to maintain a constant cavity temperature, which is required for gyrotron frequency stability.

6.2.1 Theory

The electromagnetic radiation in a gyrotron is produced by the interaction of a mildly relativistic gyrating electron beam and transverse electric (TE) wave near cutoff in an

overmoded cavity resonator situated in a DC magnetic field. The oscillation frequency ω

of a $TE_{m,p,q}$ mode of a cylindrical cavity of effective length L and radius r_0 is given by

$$\frac{\omega^2}{c^2} = k^2 = k_\perp^2 + k_z^2 \qquad (6.1)$$

where $k_\perp$ $(= v_{mp}/r_0)$ and k_z $(q\pi/L \ll k_\perp)$ are the transverse and longitudinal propagation

constants of the $TE_{m,p,q}$ wave, c is the velocity of light, v_{mp} is the pth root of $J'_m(x)$, and m,

p, and q are, respectively, the azimuthal, radial, and axial mode numbers. The resonance

condition for the excitation of the cyclotron resonance maser instability is satisfied when

ω and k_z in (6.1) satisfy the beam mode dispersion relation,

$$\omega - k_z\beta_{z0}c \approx n\omega_{c0} \qquad (6.2)$$

where ω_{c0} $(=eB_0/\gamma\, m_e)$ is the relativistic cyclotron frequency, $\gamma = (1 - \beta_{z0}^2 - \beta_{\perp0}^2)^{-1/2}$ is the

relativistic mass factor, m_e and e are the electron rest mass and charge, $\beta_{\perp0}$ and β_{z0} are,

respectively, the transverse and longitudinal velocities of the electrons normalized to the

velocity of light, n is the cyclotron harmonic number, B_0 is the magnitude of the static

axial magnetic field, and the subscript "0" denotes that the value is taken at the start of

the interaction region.

The starting current is defined as the minimum electron beam current needed to

overcome the dissipative processes in the cavity and excite a given transverse electric

mode. This threshold is obtained on energy conservation grounds by equating the

dissipative relationship implied in

$$P = \frac{\omega W}{Q} \qquad (6.3)$$

with the beam-wave power transfer governed by

$$P = -\frac{1}{2}\mathrm{Re}\left\{ \int \mathbf{E}^* \cdot \mathbf{J} \, dr \, d\mathbf{p} \right\} \tag{6.4}$$

where W is the stored energy of the mode, $\mathbf{E}$ is the cavity electric field, $\mathbf{J}$ ($= e \, \mathbf{v} \, f(\mathbf{r},\mathbf{p},t)$) is the current density, and $f(\mathbf{r},\mathbf{p},t)$ is the electron distribution function. For both the fundamental and second electron cyclotron harmonic, the starting current, in amperes, for a Gaussian axial field profile with a single axial maximum, as a function of the magnetic field detuning is given by [16]:

$$I_{\mathrm{start}}(\Delta,\mu) = 8.56 \times 10^4 \frac{\exp\left[1/8\,(\mu\Delta)^2\right]}{\mu^2 \left(\mu^2\Delta - 4n\right)} \left(\frac{\gamma_0}{Q_T}\right) \beta_{\perp 0}^{2(3-n)} \times \left(\frac{L}{\lambda}\right) C_{m,p}^{-2} \tag{6.5}$$

where the length parameter μ is defined by

$$\mu \equiv \pi \frac{\beta_{\perp 0}^2}{\beta_{\parallel 0}} \frac{L}{\lambda} \tag{6.6}$$

the magnetic field detuning Δ is given by

$$\Delta = \frac{2}{\beta_{\perp 0}^2}\left(1 - n\frac{\omega_{c0}}{\omega}\right) \tag{6.7}$$

the beam-wave coupling factor $C^2_{m,p}$ is given by

$$C_{m,p}^2 = \frac{J_{m\pm n}^2\left(k_\perp R_e\right)}{\left(v_{mp}^2 - m^2\right)J_m^2\left(v_{mp}\right)} \tag{6.8}$$

and R_e is the electron beam radius. The "$\pm$" sign in (6.8) refers to the counter- and co-rotating $\mathrm{TE}_{m,p}$ waves, respectively.

A similar theory, derived for the case of fixed sinusoidal axial field profiles, can be applied to calculate linear starting currents for higher order axial modes [17].

6.2.2 Operation at the second harmonic

Operation of a gyrotron at the second harmonic of the electron cyclotron resonance, which results in approximately twice the fundamental frequency for a given magnetic field, is attractive even when magnet technology is not a limiting factor. Nevertheless, it suffers from three principal challenges: high ohmic losses, which reduce the efficiency, high start currents, which require higher beam power than our experimental design allows, and finally, mode competition. Of these, mode competition from fundamental modes whose starting currents are inherently lower is the primary concern. Due to the density of the mode structure in an overmoded resonator, particularly when higher order longitudinal modes are included, mode competition must be explicitly addressed in the design [18].

The ratio of the second electron cyclotron harmonic, $I_{2\omega_c}$, to the fundamental starting current, I_{ω_c}, can be approximated from (6.5) as follows;

$$\frac{I_{2\omega_c}}{I_{\omega_c}} = \frac{(L/\lambda)^2_{\omega_c}}{(L/\lambda)^2_{2\omega_c}} \times \frac{1}{\beta^2_{\perp 0}} \times \frac{Q_{\omega_c}}{Q_{2\omega_c}} \times \frac{\left(C_{m,p}\right)^2_{\omega_c}}{\left(C_{m,p}\right)^2_{2\omega_c}} \tag{6.9}$$

where the subscript ω_c denotes the fundamental mode quantities and $2\omega_c$ the second harmonic. The first term is approximately 1/4 since the number of wavelengths in a cavity of fixed length L is approximately twice as large at second harmonic as at the fundamental. Due to the low voltage used to accelerate the electrons, the second term, which incorporates the normalized transverse velocity of the electrons, is large; it is about 25 for velocity pitch factor equal to 2 at 12 kV. In practice, this can be mitigated through a design in which the second harmonic Q is large with respect to the competing fundamental mode. In this experiment, the value of the third factor is about 1/3. The

fourth factor is the ratio of beam-wave coupling factor $C^2_{m,p}$ of the modes and depends on the beam radius. It is generally greater than unity because the v_{mp}^2 term is smaller at the fundamental than at the second harmonic. In summary, the minimum starting current for the second harmonic modes is generally at least several times higher than the minimum starting current for the fundamental modes.

In lowering the start current through lengthening the cavity, we encounter an elevated diffractive Q,

$$Q_{\text{diffractive}} \propto \left(\frac{L}{\lambda} \right)^2 \tag{6.10}$$

which directly leads to increased ohmic losses in the cavity by

$$\eta \propto \frac{Q_{\text{ohmic}}}{Q_{\text{diffractive}} + Q_{\text{ohmic}}} \tag{6.11}$$

where η is the total efficiency. In reality, the cavity design must be a compromise between several factors.

6.3   Second Harmonic Experiment

The initial experiments were performed using pulses with duration of approximately 3 μs. The free parameters of the experiment include the electron beam voltage and current, main magnetic field, gun magnetic field, and the alignment of the vacuum tube with respect to the room temperature bore of the superconducting gyrotron magnet. The electron beam voltage and current were varied up to 15 kV and 160 mA while the main magnetic field was varied up to 9.2 T and the gun magnet up to $\pm 8.5 \times 10^{-2}$ T with respect to the cathode field. All measurements were taken at the end of a 2 m long copper waveguide of 2.54 cm inner diameter, which couples to the output window.

Figure 6-4 shows an example of typical oscilloscope traces of the electron beam voltage, collector current, and RF signal for the experiment. In this case we show the fundamental $TE_{0,3,1}$ mode. The noise and distortions to the pulse shape are due to power supply ripple and the transient response of connecting cables. A small droop in the voltage pulse causes a small corresponding droop in the microwave pulse.
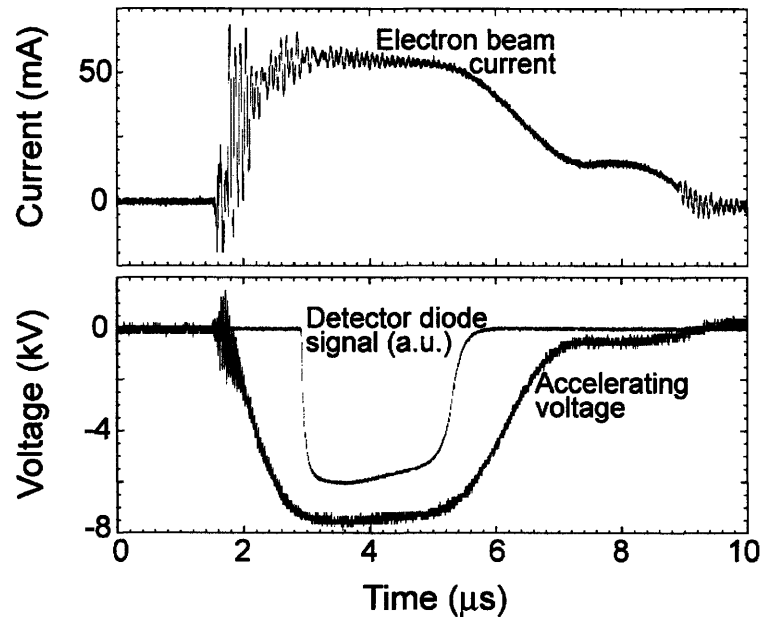
Figure 6-4: Oscilloscope microwave signal, beam voltage and collector current traces of the fundamental $TE_{0,3,1}$ mode at 237.91 GHz and main magnetic field of 8.58 T. The RF signal is recorded with a broadband WR-3 (220-325 GHz) detector diode. The voltage and current traces are measured through inductively couples probes (Rogowsky coils).

6.3.1 Start oscillation current

The starting current curves for all modes experimentally observed are shown in Fig. 6-5. Five fundamental modes are depicted with open shapes ranging in frequency from 157 to 246 GHz and two second harmonic modes near 460 GHz are shown with filled shapes. Data in each mode were collected at the unique voltage which was optimal for its excitation. The conditions are labeled in Fig. 6-5.
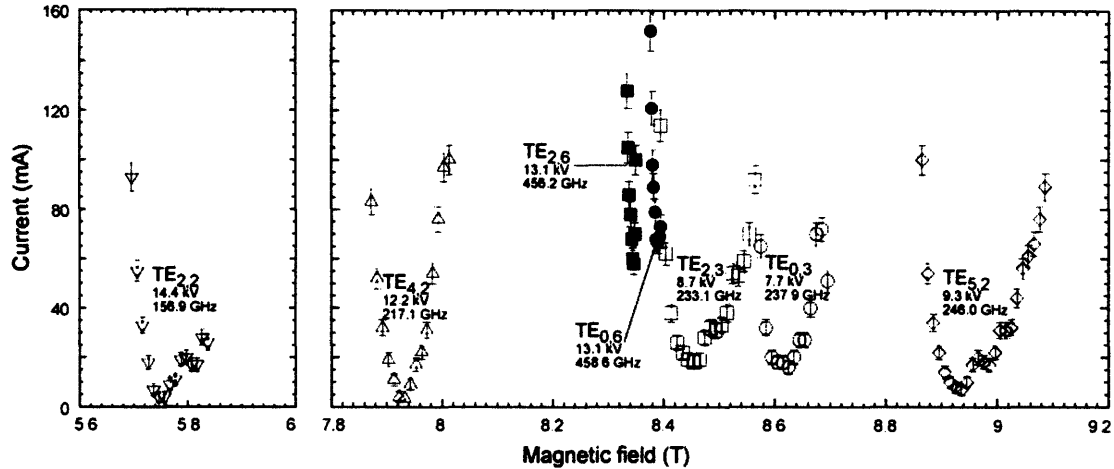
Figure 6-5: Summary of experimental starting current data recorded for resonant cavity modes from 5.6 to 9.2 T and up to 15 kV and 160 mA. Open symbols denote fundamental modes and filled-in symbols denote second harmonic modes.

6.3.2 Power

Peak power measurements were made during the microsecond pulsed experiment using both a laser calorimeter and a pyroelectric detector. The calorimeter head surface was coated with an absorbing layer of paint and re-calibrated for millimeter wavelengths.

Figure 6-6(a) depicts measured peak power data of the fundamental $TE_{0,3,q}$ modes around 238 GHz as a function of beam current and magnetic field. A pyroelectric detector was used to measure the radiation, and the beam voltage was fixed at 9 kV with microsecond pulse lengths and a repetition rate of approximately 30 Hz. The data were confirmed with calorimetric measurements. Nearly 70 W of peak power were recorded at 237.9 GHz with an efficiency of over 7%.

Initial pulsed power measurements of the $TE_{2,6,1}$ (456.15 GHz) second harmonic mode indicate signal strengths of several watts with 13 kV and 110 mA. The $TE_{2,6,1}$ mode was found experimentally to be more isolated from fundamental modes than the $TE_{0,6,1}$ second harmonic design mode, which was also observed in [19], [20].

313
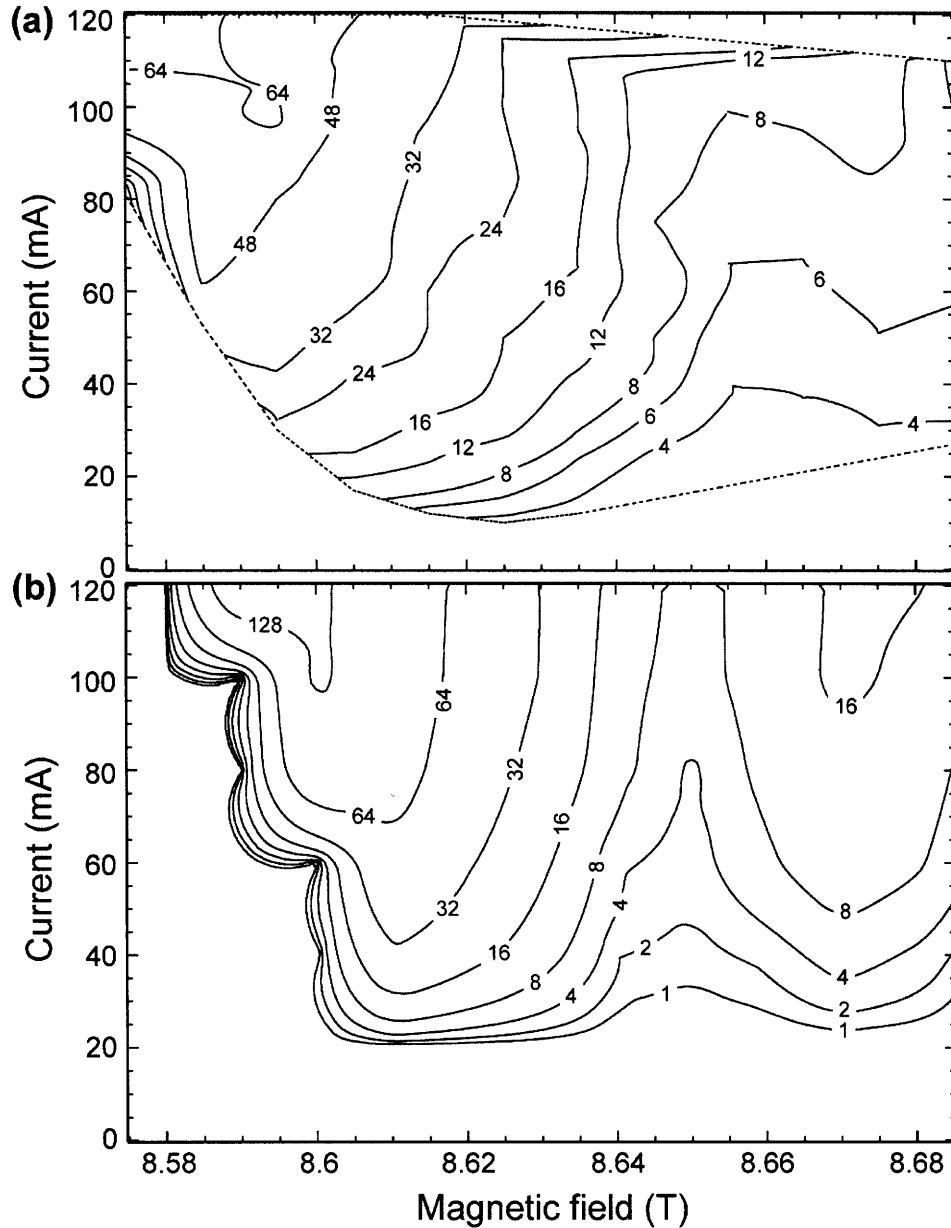
Figure 6-6: Contour plot of (a) measured peak power data of the fundamental $TE_{0,3,q}$ modes in watts as a function of beam current and magnetic field using a pyroelectric detector. The electron gun was pulsed for several microseconds at a repetition rate of approximately 30 Hz with 9 kV. The power level was calibrated using a calorimeter. (b) MAGY simulated power at experimental conditions.

6.3.3 Linear theory and MAGY simulations

With the linear theory previously described in Section 6.2.1, we can proceed to analyze

the start current data from Fig. 6-5. In all cases, we use the beam parameters that were

derived from EGUN simulations. We have observed two second harmonic modes in

314

these experiments, the $TE_{2,6,1}$ and $TE_{0,6,1}$, for which theoretically predicted and experimentally measured starting currents show good agreement (Figure 6-7). For each mode, we have also calculated the theoretical magnetic field which minimizes the start current and compared it to experiment (Table 6.2). Finally, we are able to calculate a cavity radius of 2.041 mm to obtain the best fit to the data. This value is 0.3% larger than the design value of 2.035 mm and the difference is within the manufacturing accuracy of the cavity.

Table 6.2: Minimum start current, and magnetic field and frequency for minimum starting current of q=1 modes from linear theory [21] using EGUN calculated parameters of Fig. 6-2(b) and (c) vs. experiment

$TE_{m,p,q}$	Experiment			Theory		
	B_0 (T)	I_{st} (mA)	f (GHz)	B_0 (T)	I_{st} (mA)	f (GHz)
$TE_{2,2,1}$	5.747	4	156.90	5.746	4	156.89
$TE_{4,2,1}$	7.933	2	217.10	7.926	4	217.09
$TE_{2,6,1}$	8.346	58	456.15	8.345	58	456.15
$TE_{0,6,1}$	8.388	67	458.56	8.390	67	458.56
$TE_{2,3,1}$	8.454	18	233.15	8.433	27	233.15
$TE_{0,3,1}$	8.625	16	237.91	8.605	7	237.92
$TE_{5,2,1}$	8.936	7	246.00	8.915	14	246.01

It is clear that the $TE_{m,p,1}$ modes are excited at the magnetic fields predicted by linear theory [21]. However, the fundamental modes in the experiment have multiple local minima which form a continuous manifold of accessible cavity oscillation states, each one producing monochromatic emission. This phenomenon, which is due to higher order longitudinal states, will be more fully discussed in Section 6.4. In short, for fundamental modes, the occurrence of overlapping $TE_{m,p,q}$ (where q is larger than one) higher order axial modes broadens the magnetic excitation range. Finally, the very low values of start current observed in the fundamental modes are described by linear theory.

In Table 6.2, the experimental start current values of seven observed modes are compared with values calculated from [21] using beam parameters from Fig. 6-2, diffractive Q from cold cavity theory, and all other values from experiment. The agreement is good, and discrepancies might be explained by the uncertainties in the beam alpha, diffractive Q, and experimental conditions such as beam radius and alignment.
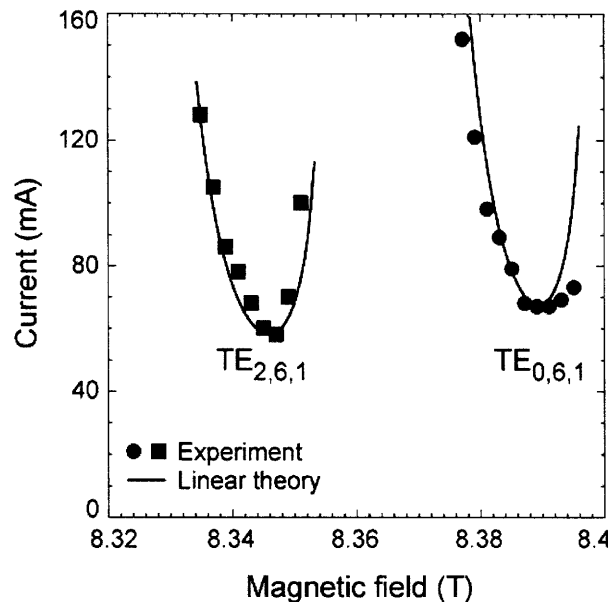
Figure 6-7: Second harmonic $TE_{2,6,1}$ and $TE_{0,6,1}$ start oscillation current data (points) compared with linear theory (solid lines) at 13.1 kV.

Nonlinear modeling has been performed using the time-dependent simulation code MAGY, developed jointly at the University of Maryland and the Naval Research Laboratory [22]. In MAGY, the resonator transverse fields are expanded in a normal mode basis of waveguide modes, and the axial field structure is solved self-consistently in the slowly time-varying approximation. In all the simulations presented here, one or two TE modes were used in the basis. In order to observe steady state dynamics, all modes were forced to oscillate at the frequencies obtained from self-consistent simulations in an iterative adjustment procedure which employs the slope of the field

316

phase evolution as an estimator. The cavity geometry was defined with an axial grid step of 9.8×10^{-3} cm (1041 points), and with half the conductivity of ideal copper. We have chosen physical parameters to describe the geometry and thermal properties of the beam. This includes, for all simulations, pitch angle, velocity spread, guiding center radius and (where applicable) the spread in guiding centers which was obtained from EGUN simulations presented in Fig. 6-2(b) and (c). We have systematically increased the EGUN-derived velocity spread according to [23] to account for cathode uniformity, thermal variations, and other effects not explicitly modeled in EGUN. The simulation geometry also involves a slightly tapered magnetic field derived from experimental measurement of the axial field profile. The simulation time step was taken to be 50-150 ps, and we ran the code for 200-2,000 iterations to reach a converged steady state solution.

In simulations of the $TE_{0,3}$ fundamental mode, MAGY qualitatively reproduces the experimentally observed power distribution [Fig. 6-6(b)] but predicts much higher power output than was actually observed. The remaining differences might arise due to higher ohmic losses in the cavity, diffractive and coupling losses in the quasi-optical mode converter, and reduced coupling to the output waveguide, which were not studied in detail in this experiment.

6.4 Broadband continuous frequency tuning experiment

Broadband continuous frequency tuning was observed as a function of magnetic field for all fundamental modes. A long cavity design was utilized in order to reduce the start current for the second harmonic, in order to meet excitation criteria for a low power gun. In addition to lowering the start current for second harmonic modes, the length of the

cavity permits multiple radiation maxima along the axial length of the cylindrical waveguide resonator to be excited. That is, in addition to the $TE_{m,p,1}$ modes that we expect to excite, there exist a series of $TE_{m,p,q}$ modes where the q is larger than one. These higher order axial modes can be excited at magnetic fields just above those where the $TE_{m,p,1}$ modes are reached. The practical consequence of this is that continuous frequency tuning on the order of several gigahertz has been observed for each of the fundamental modes excited in this gyrotron. A continuous bandwidth of 410 MHz around 31.8 GHz has been previously observed using higher order axial modes, up to q=5, in a two-stage gyrotron amplifier experiment at the University of Maryland [24]. Several experiments in electron paramagnetic resonance (EPR) and dynamic nuclear polarization (DNP) might be dramatically simplified with a tunable oscillator that exploits this property.

6.4.1 Experimental data

The experimental gyrotron frequency corresponding to magnetic field tuning in the range 5.6 - 9.2T is shown in Fig. 6-8. The frequency was measured using a heterodyne receiver system which operates on a high harmonic of an 18-26 GHz YIG-tuned local oscillator. The local oscillator was frequency-locked using a PLL circuit, resulting in frequency measurement accuracy which is limited only by the harmonic phase noise of the local oscillator.
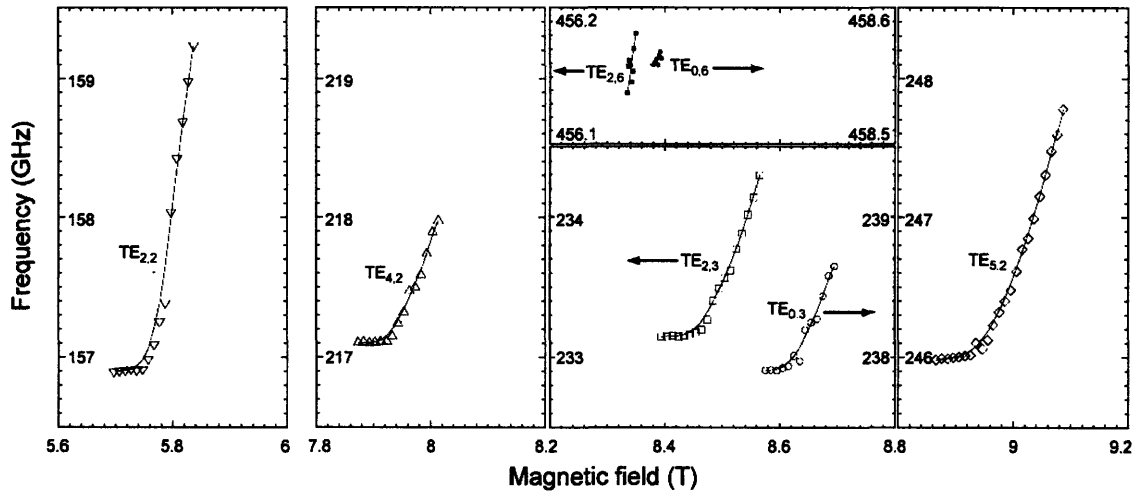
Figure 6-8: Summary of experimentally measured frequency vs. magnetic field for the modes in Fig. 6-5.

The data were taken concurrently with the data from Fig. 6-5, in which the beam current was set near the threshold of oscillation for each mode. Further, the data in each $TE_{m,p}$ mode were taken at unique voltages which are labeled on Fig. 6-5. We observe continuous frequency tuning in each fundamental mode across a range of magnetic fields. The frequency tuning bandwidth is relatively large, notably with 1.8 GHz tuning at the 246 GHz $TE_{5,2,q}$ modes and 2.34 GHz tuning at the 157 GHz $TE_{2,2,q}$ modes. Further, the data show that a significant amount of power can be maintained across the frequency tuning range of a given mode. This is illustrated for the $TE_{0,3,q}$ modes in Fig. 6-6(a), where the power measurements are taken as a function of the magnetic field and electron beam current. We can conclude that an average power of at least 5 W can be maintained from 237.9 to 238.6 GHz. Finally, the second harmonic modes do not tune by more than 20-30 MHz, which implies that the long-term frequency will be stable towards drift in the magnetic field. This follows from Fig. 6-7 where we have shown that only the first axial variation of the second harmonic modes has been excited in this experiment. This is important in the intended application of this device.

319

6.4.2 Discussion

Prior to further analysis, we note that the mechanism of frequency tuning is qualitatively similar for each fundamental mode. Figure 6-9 is a plot of the experimental data from the fundamental modes of Figs. 6-6 and 6-8, normalized to one magnetic field axis. That is, the data from each $TE_{m,p,q}$ mode family are normalized to the magnetic field value which yields minimum start current for the mode. The frequency axis in the lower plot is then normalized with respect to the frequency of the first axial mode at that magnetic field.
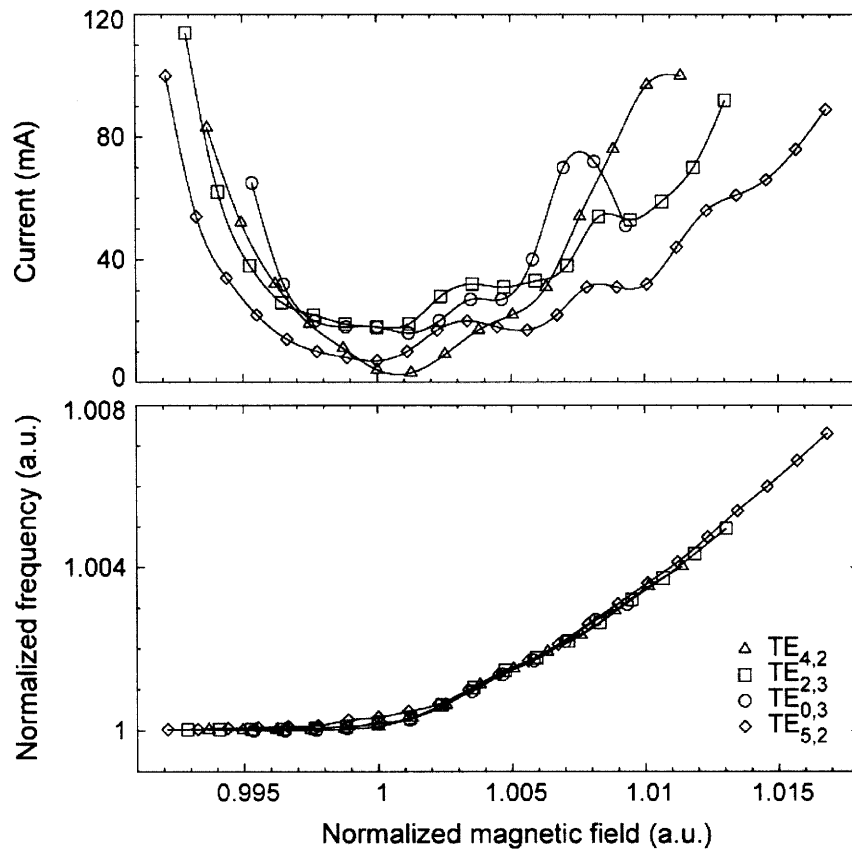
Figure 6-9: Start oscillation currents and frequency tuning normalized to the frequency at the minimum start current versus magnetic field normalized to the field at the minimum start current of fundamental modes from 7.8 to 9.2 T.

The start currents and normalized frequency tuning with respect to magnetic field resemble each other in functional form. For instance, in the upper plot, the local minima of the start oscillation current curves fall at approximately the same magnetic field values; in the lower plot, the frequency tuning rate, df/dB, is identical for each family of modes.

For the following discussion, we therefore focus our attention on the $TE_{5,2}$ mode, which displays broad frequency tuning in isolation from other fundamental and second harmonic modes. First, using weakly irregular waveguide (so-called "cold cavity") theory [15], we can calculate the resonator eigenfrequencies, Q values, and axial field functions of TE modes by solving a one-dimensional wave equation of the form

$$\left[\frac{d^2}{dz^2} + k_z^2(z)\right]f(z) = 0 \qquad (6.12)$$

where f is the longitudinal profile function and z is the longitudinal coordinate, with the boundary conditions of a cutoff wave in the input and propagating wave at the output. The analysis relies upon the dimensions of the cavity as well as the indices of the $TE_{m,p}$ mode, but neglects coupling to other modes and the perturbing effects of the electron beam. Calculated field profiles lose the distinction between consecutive axial modes, approximating the continuous behavior observed in the experiment.

Using the cold cavity frequencies and axial field profiles corresponding to the $TE_{5,2,1}$ – $TE_{5,2,5}$ modes, we have applied linear theory [21] to calculate their corresponding magnetic fields. These five calculated eigenfrequencies are shown in Fig. 6-10 as solid circles, where each eigenfrequency is located at the magnetic field corresponding to the theoretical minimum starting current of that eigenmode. This value of magnetic field is selected because, at the minimum starting current, the effect of

dispersion due to the electron beam is negligible and the linear theory should be valid. Since these data are indeed taken near the threshold of the starting current, the agreement between theory and experiment is very good.
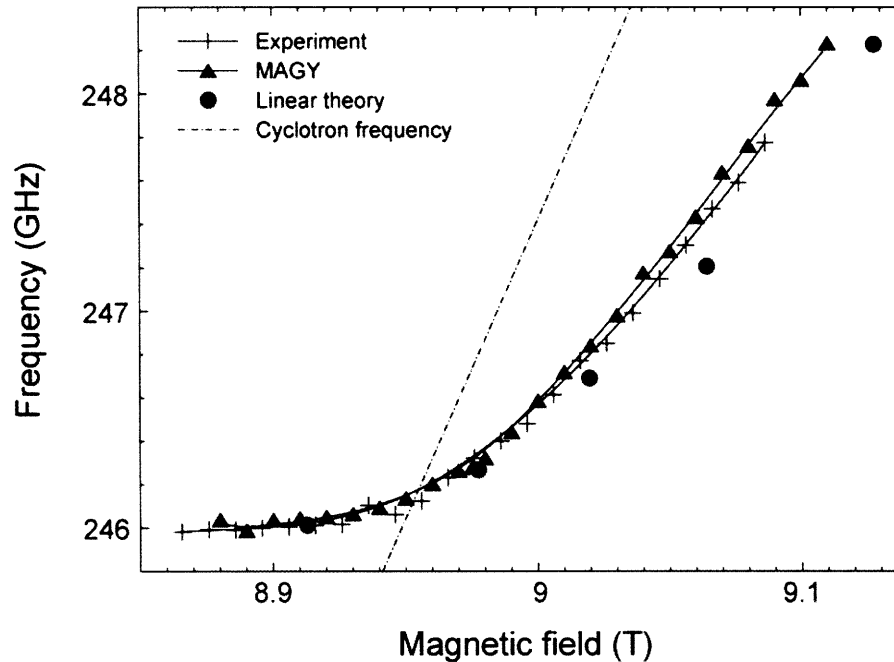
Figure 6-10: Linear theory (solid circles) and MAGY simulation (solid triangles) using EGUN calculated parameters of the frequency tuning of the $TE_{5,2,q}$ modes compared to the experiment (+). The dotted line is the relativistic cyclotron frequency.

However, the linear theory alone cannot completely describe the dynamics of the beam-wave interaction for reasons that have been previously enumerated. For example, the observation of continuous frequency tuning even between frequencies corresponding to the discrete axial modes of the cold cavity theory cannot be easily explained within the framework of linear theory. We therefore again apply the non-linear, time-dependent theory as implemented in MAGY to model the operating characteristics of this gyrotron. Using the EGUN-derived beam pitch ratio and the adjusted perpendicular velocity spread to model thermal properties of the electron beam as previously described, the self-consistent MAGY simulations quantitatively predict continuous frequency tuning and

monochromatic emission in the $TE_{5,2}$ mode. The agreement between experiment and the predictions of MAGY as shown in Fig. 6-10 is better than for the linear theory, even though the former depends on fewer adjustable parameters.
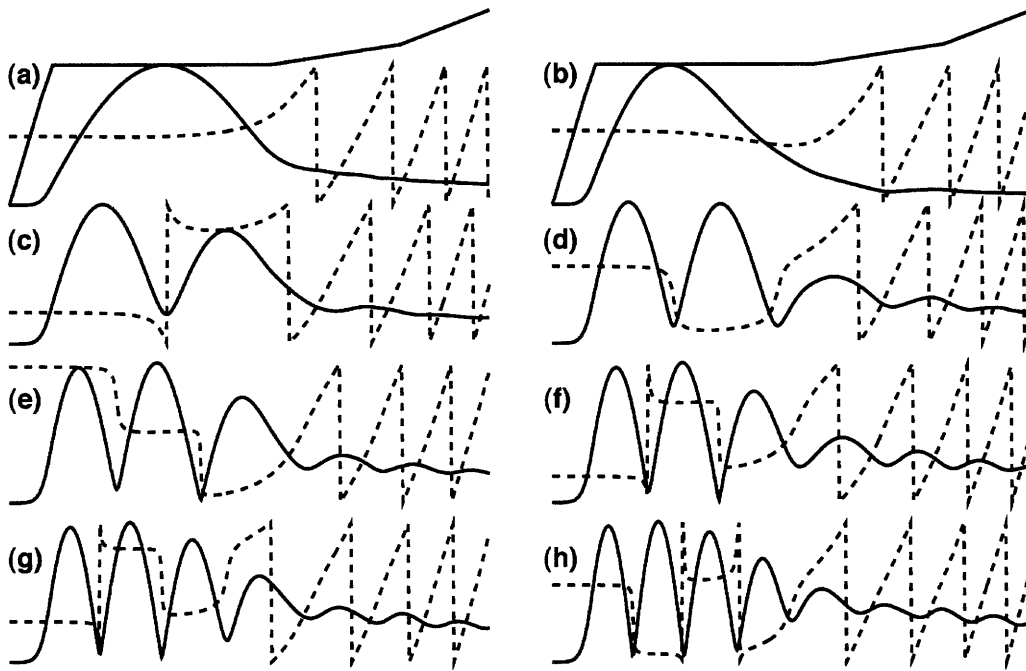
Figure 6-11: Self-consistent axial field profiles for $TE_{5,2,q}$ modes with $q \geq 1$ as calculated from MAGY. The cavity geometry is indicated above each column, and we have displayed the normalized voltage amplitude. The frequency increases from 246.0 GHz in (a) to 248.1 GHz in (h).

Detailed analysis of the axial field structures predicted by MAGY (Figure 6-11) reveal a continuous transition from lower to higher order axial modes, and this is the basis of the observed frequency tuning. The self-consistent axial field structures resemble those obtained from the cold cavity theory.

6.5   Conclusion

The 460 GHz experiment has successfully demonstrated that a gyrotron can efficiently produce several watts of average power in submillimeter wavelengths at low voltage. In addition, continuous broadband frequency tuning of the gyro-oscillator has been

demonstrated, and we have presented non-linear and linear analyses of the results. The gyrotron is currently being processed for CW second harmonic generation at 460 GHz. We note that, due to the inhomogeneous frequency dispersion of the interactions responsible for dynamic nuclear polarization effects in paramagnetically doped solids, either the microwave source frequency or the static magnetic field in the NMR spectrometer must be varied over a broad range to optimize the experiment. Performing the latter currently requires high homogeneity superconducting magnets in the 9–16 T range which incorporate a persistent sweep coil. Future oscillator designs which could exploit the broad tunability features described here might eliminate this complication of the experiment while still preserving the advantages of simple, low-voltage, CW operation.

6.6   References

[1] F. C. de Lucia, "Science and technology in the submillimeter region," *Opt. Photon. News*, vol. 14, no. 8, pp. 44–50, Aug. 2003.

[2] D. van der Weide, "Applications and outlook for electronic terahertz technology," *Opt. Photon. News*, vol. 14, no. 4, pp. 48–53, Apr. 2003.

[3] K. Felch, B. Danly, H. Jory, K. Kreischer, W. Lawson, B. Levush, and R. Temkin, "Characteristics and applications of fast-wave gyrodevices," *Proc. IEEE*, vol. 87, no. 5, pp. 752–81, May 1999.

[4] R. Callis, W. Cary, S. Chu, J. Doane, R. Ellis, K. Felch, Y. Gorelov, H. Grunloh, J. Hosea, K. Kajiwara, J. Lohr, T. Luce, J. Peavy, R. Pinsker, D. Ponce, R. Prater, M. Shapiro, R. Temkin, and J. Tooker, "Maturing ECRF technology for plasma control," *Nucl. Fus.*, vol. 43, no. 11, pp. 1501–1504, Nov. 2003.

[5] T. Idehara, I. Ogawa, S. Mitsudo, M. Pereyslavets, N. Nishida, and K. Yoshida, "Development of frequency tunable, medium power gyrotrons (Gyrotron FU series) as submillimeter wave radiation sources," *IEEE Trans. Plasma Sci.*, vol. 27, no. 2, pp. 340–354, Apr. 1999.

[6] H. Li, Z. Xie, W. Wang, Y. Luo, P. Du, X. Den, H. Wang, S. Yu, X. Niu, L. Wang, and S. Liu, "A 35-GHz low-voltage third-harmonic gyrotron with a permanent magnet system," *IEEE Trans. Plasma Sci.*, vol. 31, no. 2, pp. 264–271, Apr. 2003.

[7] N. Zaytsev, T. Pankratova, M. Petelin, and V. Flyagin, "Millimeter- and submillimeter-wave gyrotrons," *Radiophys. Quantum Electron.*, vol. 19, pp. 103–104, 1974.

[8] V. Bajaj, C. Farrar, M. Hornstein, I. Mastovsky, J. Vieregg, J. Bryant, B. Elena, K. Kreischer, R. Temkin, and R. Griffin, "Dynamic nuclear polarization at 9 Tesla using a novel 250 GHz gyrotron microwave source," *J. Mag. Res.*, vol. 160, no. 2, pp. 85–90, Feb. 2002.

[9] K. Kreischer, C. Farrar, R. Griffin, and R. Temkin, "The use of a 250 GHz gyrotron in a DNP/NMR spectrometer," in *Proc. 23rd Int. Conf. Infrared Millimeter Waves*, 1998, pp. 357–341.

[10] K. E. Kreischer, C. T. Farrar, R. G. Griffin, R. J. Temkin, and J. Vieregg, "The development of a 250 GHz CW gyrotron for EPR and NMR spectroscopy," in *Proc. 24th Int. Conf. Infrared Millimeter Waves*, 1999.

[11] K. E. Kreischer, C. Farrar, R. Griffin, R. Temkin, and J. Vieregg, "A 250 GHz gyrotron for NMR spectroscopy," in *Proc. 27th Int. Conf. Plasma Sci.*, 2000, p. 198.

[12] M. K. Hornstein, "Design of a 460 GHz second harmonic gyrotron oscillator for use in dynamic nuclear polarization," Master's thesis, Mass. Inst. Technol., Depart. Elect. Eng. Comput. Sci., Cambridge, 2001.

[13] M. K. Hornstein, V. Bajaj, R. G. Griffin, K. E. Kreischer, I. Mastovsky, M. A. Shapiro, and R. J. Temkin, "Design of a 460 GHz second harmonic gyrotron oscillator for use in dynamic nuclear polarization," in *Proc. 27th Int. Conf. Infrared Millim. Waves*, R. J. Temkin, Ed., San Diego, CA, Sep. 2002, IEEE Cat. no. 02EX561, pp. 193–4.

[14] W. Herrmannsfeldt, "EGUN: An electron optics and gun design program," Stanford Linear Accelerator Center, Stanford, CA, Tech. Rep. SLAC-0331 UC-28, 1988.

[15] A. W. Fliflet and M. E. Read, "Use of weakly irregular waveguide theory to calculate eigenfrequencies, values, and RF field functions for gyrotron oscillators," *Int. J. Electron.*, vol. 51, no. 4, pp. 475–484, Oct. 1981.

[16] B. Danly and R. J. Temkin, "Generalized nonlinear harmonic gyrotron theory," *Phys. Fluids*, vol. 29, no. 2, pp. 561–567, Feb. 1986.

[17] K. Kreischer and R. Temkin, "Mode excitation in a gyrotron operating at the fundamental," *Int. J. Infrared Millim. Waves*, vol. 2, no. 2, pp. 175–196, Mar. 1981.

[18] I. Zarnitsina and G. Nusinovich, "Stability of single-mode self-excited oscillations in a gyromonotron," *Radiophys. Quantum Electron.*, vol. 17, no. 12, pp. 1418–1424, Dec. 1974.

[19] T. Idehara, T. Tatsukawa, I. Ogawa, T. Mori, H. Tanabe, S. Wada, G. Brand, and M. Brennan, "Competition between fundamental and second-harmonic operations in a submillimeter wave gyrotron," *Appl. Phys. Lett.*, vol. 58, no. 15, pp. 1594–1596, Apr. 1991.

[20] T. Idehara and Y. Shimizu, "Mode cooperation in a submillimeter wave gyrotron," *Phys. Plasmas*, vol. 1, no. 10, pp. 3145–3147, Oct. 1994.

[21] M. Yeddulla, G. Nusinovich, and T. Antonsen, "Start currents in an overmoded gyrotron," *Phys. Plasma*, vol. 10, no. 11, pp. 4513–4520, Nov. 2003.

[22] M. Botton, T. Antonsen, B. Levush, K. Nguyen, and A. Vlasov, "MAGY: A time-dependent code for simulation of slow and fast microwave sources," *IEEE Trans. Plasma Sci.*, vol. 26, no. 3, pp. 882–892, Jun. 1998.

[23] K. Kreischer, T. Kimura, B. Danly, and R. Temkin, "High-power operation of a 170 GHz megawatt gyrotron," *Phys. Plasmas*, vol. 4, no. 5, pp. 1907–1914, May 1997.

[24] J. Zhao, G. Nusinovich, H. Guo, J. Rodgers, and V. Granatstein, "Axial mode locking in a harmonic-multiplying, inverted gyrotwystron," *IEEE Trans. Plasma Sci.*, vol. 28, no. 3, pp. 597–605, Jun. 2000.

Chapter 7   Continuous-Wave Operation of a 460 GHz Second Harmonic Gyrotron Oscillator

We report the regulated CW operation of a second harmonic gyrotron oscillator at output power levels of over 8 W (12.4 kV and 135 mA beam voltage and current) in the $TE_{0,6,1}$ mode near 460 GHz. The gyrotron also operates in the second harmonic $TE_{2,6,1}$ mode at 456 GHz and in the $TE_{2,3,1}$ fundamental mode at 233 GHz. CW operation was demonstrated for a one-hour period in the $TE_{0,6,1}$ mode with better than 1% power stability, where the power was regulated using feedback control. Non-linear simulations of the gyrotron operation agree with the experimentally measured output power and RF efficiency when cavity ohmic losses are included in the analysis. The output radiation pattern was measured using a pyroelectric camera and is highly Gaussian, with a beam waist ellipticity of 4%. The 460 GHz gyrotron will serve as a millimeter-wave source for sensitivity-enhanced nuclear magnetic resonance (dynamic nuclear polarization) experiments at a magnetic field of 16.4 T.

7.1   Introduction

The submillimeter wave regime is lacking in high average power devices. While gyrotrons deliver the highest average power in this band, there have been very few CW gyrotron experiments at high frequencies. Only six CW gyrotrons from Univ. Sydney [1], Fukui Univ. [2], IAP [3], [4], and MIT [5], [6] generate frequencies above 250 GHz at output powers ranging from a fraction of a Watt to a kilowatt.

The gyrotron is a vacuum electron device that is capable of producing high average power at the fundamental or an harmonic of the electron cyclotron frequency through an interaction between a mildly relativistic electron beam and electromagnetic field in a static DC magnetic field. Design at high frequency, second harmonic, and low beam power is challenging because the latter two involve lower gain than at fundamental modes and all three necessitate higher Q cavities. Furthermore, ohmic loss is a limiting factor in the design of high Q cavities, which are necessary to lower starting currents to the operating range of the low power electron gun

While the physics of a gyrotron can be nearly completely characterized in short pulse (microsecond to millisecond) operation, many nontrivial engineering issues remain which must be addressed in the design of a high frequency continuous-wave gyrotron. These include passing an energetic electron beam through a narrow interaction structure, the design of a robust collector that can dissipate high average power, a cooling circuit, and a sufficient vacuum pumping conductance throughout the tube. The goal of this experiment is to successfully generate several watts of CW power at the second harmonic $TE_{0,6,1}$ mode near 460 GHz, a level sufficient to perform biological experiments using sensitivity-enhanced nuclear magnetic resonance (NMR) through dynamic nuclear polarization (DNP) [7] at 16.4 T.

7.2   Experiment

The gyrotron is shown schematically in Fig. 7-1. We have previously characterized the operation of this gyrotron in short pulse operation [5]. In the present study, we have employed a CW DC power supply in place of the pulse forming network and found stable operating parameters for continuous duty operation. The parameters of the CW operation

are summarized in Table 7.1. During the transition from short pulse to CW operation, the heater temperature was held constant and the emission current increased over time with increasing cathode voltage at continuous duty, resulting in the successful outgassing of the collector. The collector has dissipated in excess of 2.0 kW of electron beam power, sufficient to achieve the nominal operating parameters of 12.4 kV and 100 mA, with no adverse effects.

1. Cathode
2. Anode
3. Drift tunnel
4. Microwave absorber
5. Cylindrical resonant cavity
6. Quasi-optical mode converter
7. Output window
8. High voltage ceramic insulator
9. Electron beam collector
10. Superconducting magnet
11. Electromagnet
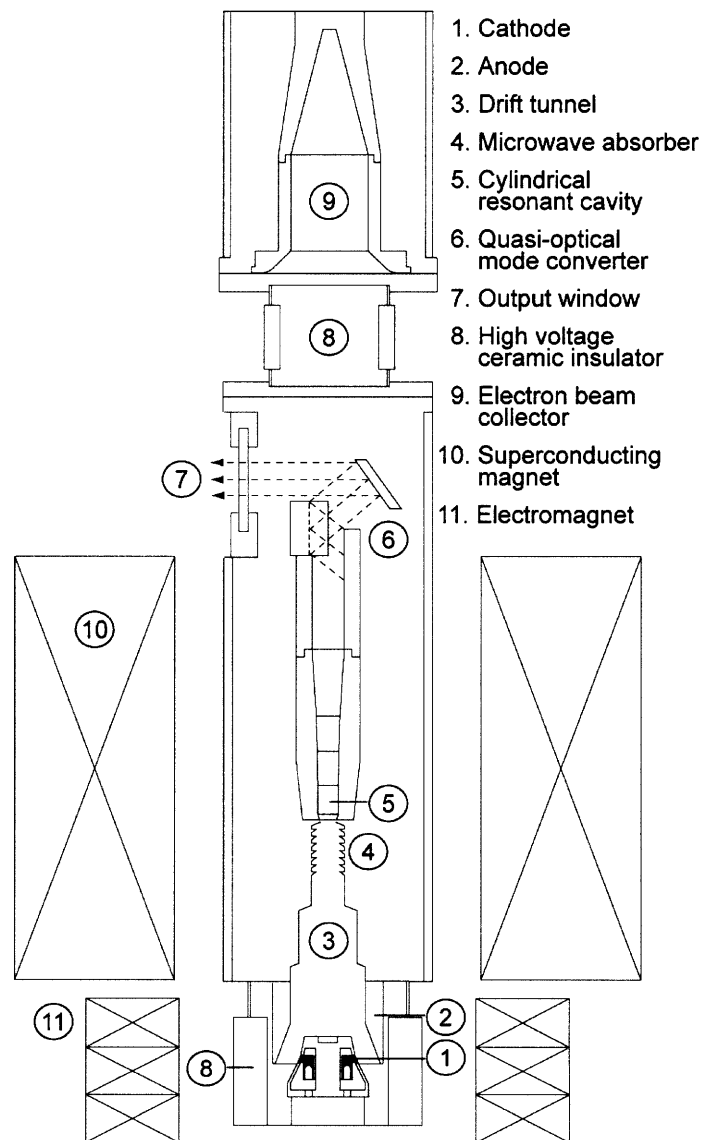
Figure 7-1: Cross-sectional schematic of the cylindrically symmetric 460 GHz gyrotron tube, not shown to scale, indicating key components. The gyrotron tube is approximately 1.4 m long and the magnet bore diameter is 7.62 cm.

329

Table 7.1: CW experimental operating parameters

Experimental parameters	Min.	Max.
Duty cycle (%)	–	100
Beam voltage (kV)	0	15
Beam current (mA)	0	140
Main magnetic field (T)	8.3	8.7
Δ cathode magnetic field (mT)	-85	85

A parametric study of the second harmonic design mode and neighboring modes involves independent variation of the electron beam voltage and current, main magnetic field, gun magnetic field, and the alignment of the vacuum tube with respect to the room temperature bore of the superconducting gyrotron magnet. The electron beam voltage and current were independently varied up to 15 kV and 140 mA while the main magnetic field was varied up to 8.7 T and the gun magnet up to $\pm 8.5 \times 10^{-2}$ T with respect to the cathode field. All measurements were taken at the end of a 2 m long copper waveguide of 2.54 cm inner diameter, which couples directly to the output window, unless otherwise specified.

7.2.1 Mode Map

A mode map was generated to chart the regions of parameter space in which the modes in the vicinity of the $TE_{0,6,1}$ design mode can be excited (cf. Fig. 7-2). In the region of interest, we observed only two second harmonic modes, the $TE_{2,6,1}$ and $TE_{0,6,1}$, and one competing fundamental mode, the $TE_{2,3,q}$. To determine the operational limits of each mode, the main and cathode magnetic fields were varied for fixed beam parameters of 12.4 kV and 100 mA during CW operation.
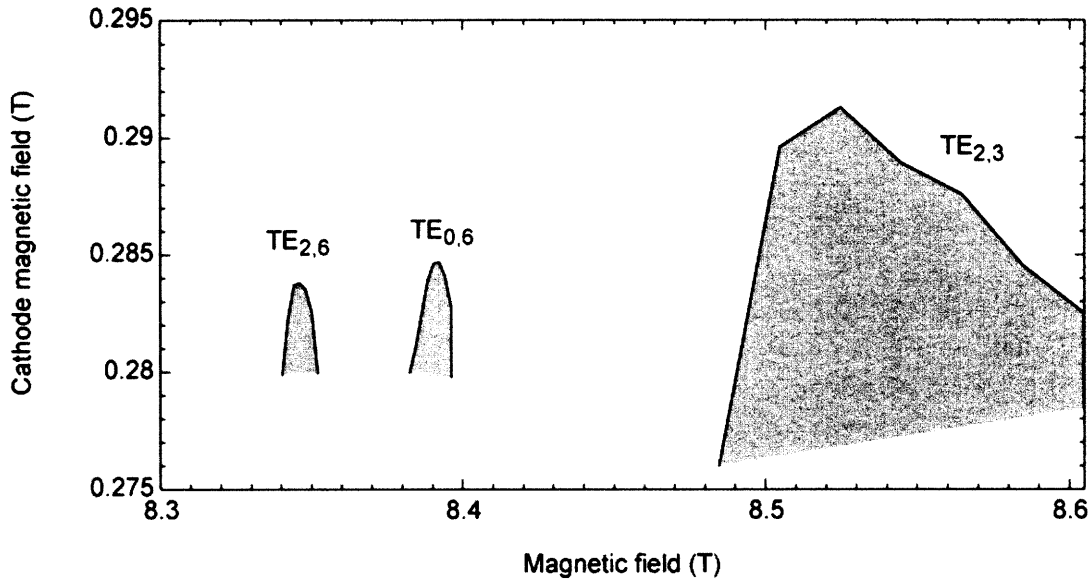
Figure 7-2: Mode map for the design mode and nearby competing fundamental $TE_{2,3}$ mode for the cavity and cathode magnetic fields operating CW at 12.4 kV and 100 mA.

We find that the modes are spaced well apart and there are few possibilities of simultaneous mode excitation in the present gyrotron in CW operation. This result differs from the observation in the short pulse experiment [5], in which the neighboring $TE_{2,6,1}$ mode was experimentally favored over the design $TE_{0,6,1}$ second harmonic mode due to interference from the fundamental $TE_{2,3,q}$ mode, which was excited at the rise and fall of the pulse, which saturated the $TE_{0,6,1}$ signal at high magnetic fields. The high efficiency region is located in the lower left of each of the three mode spaces.

7.2.2 Second Harmonic

The CW power in the operating mode was measured using a calorimeter (Scientech, Inc.) that was recalibrated for millimeter wavelengths. The variation of the output power of the $TE_{0,6,1}$ design mode with beam current is depicted in Fig. 7-3(a). After oscillations begin around 77 mA, the power is linear with beam current, indicating that saturation of

331

the interaction has not been reached. A maximum CW output power of 8.4 W is achieved at beam parameters of 135 mA and 12.4 kV, yielding an efficiency of 0.5%.
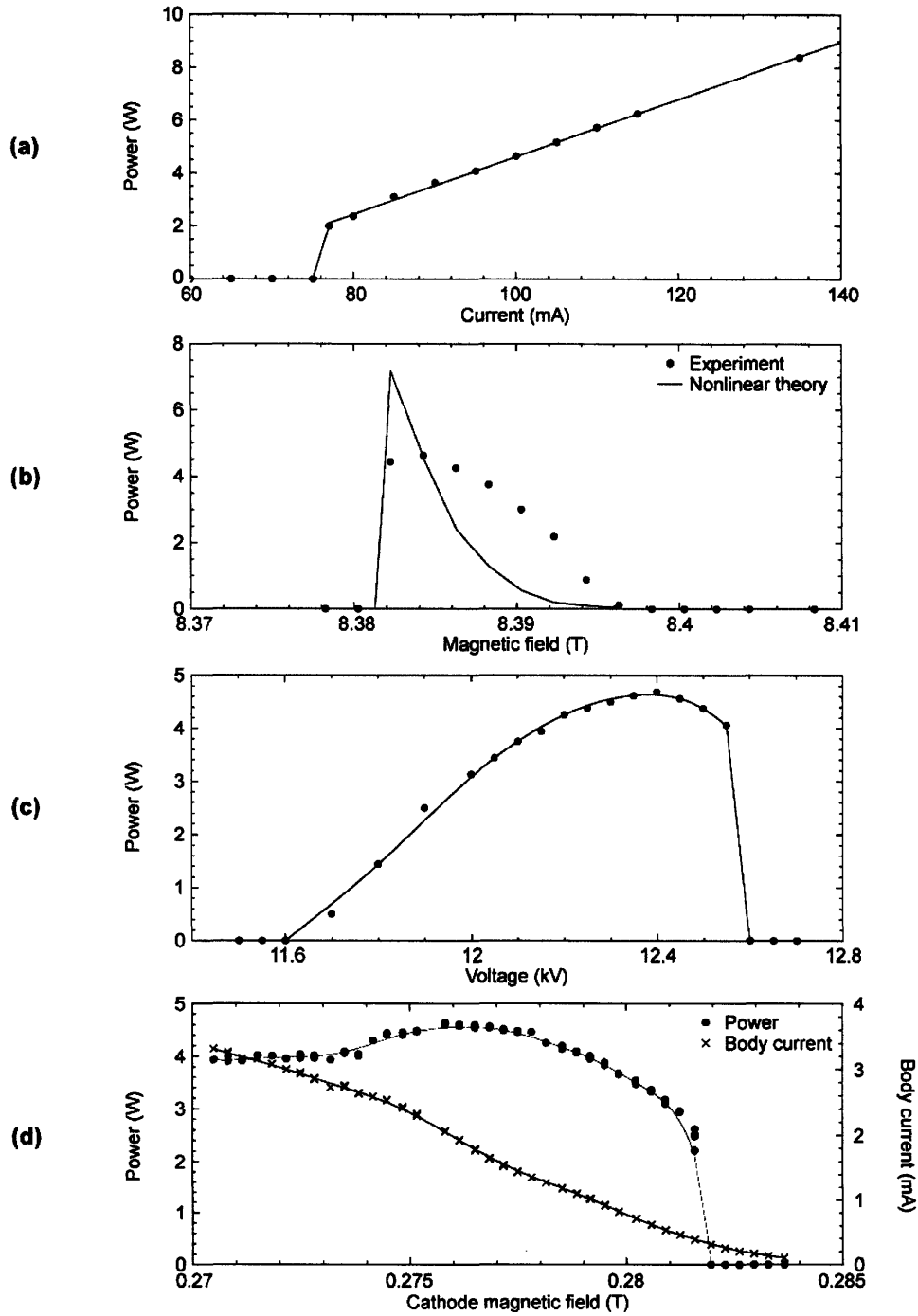
Figure 7-3: CW output power in the $TE_{0,6}$ second harmonic mode as a function of (a) beam current, (b) main magnetic field, (c) voltage, and (d) cathode magnetic field. The magnetic tuning (b) is compared with nonlinear theory from MAGY simulations, and in (a), (c), and (d) the lines are added as a guide.

In Fig. 7-3(b) the experimentally measured continuous duty power of the design $TE_{0,6,1}$ mode with varying magnetic field is compared with the theoretical results from MAGY, a self-consistent nonlinear code developed by the University of Maryland and the Naval Research Laboratory [8]. In the theoretical model we assumed 30% losses in the quasi-optical mode converter. A conductivity one-fifth that of ideal copper is used based on cavity thermal load measurements of the second harmonic $TE_{0,6,1}$ mode. The following parameters of the electron gun operation were obtained through EGUN simulations: the guiding center spread is 5.5%, the transverse velocity spread is 6%, and the pitch factor is 2.4 [5]. At beam parameters of 100 mA and 12.4 kV, a power of nearly 5 W is recorded. However, the theory shows a slightly elevated power of 7 W indicating that either the mode converter is less efficient than previously assumed or that the beam quality is below that which is expected. There is no present explanation for the difference in width of the theoretical and experimental curves.

The power was optimized as a function of beam voltage [Fig. 7-3(c)], yielding an optimum beam voltage of 12.4 kV. In our diode electron gun, the electron velocity pitch factor changes rapidly with cathode magnetic field, along with other factors such as main magnetic field and cathode voltage [5]. This rapid change is illustrated in Fig. 7-4. A first-order attempt at holding the alpha (ratio of transverse to longitudinal velocity of the electrons) constant was made in the voltage optimization measurement by maintaining a constant body current signal. The small but nonzero body current is attributed to reflected electrons originating from an unusually high alpha, and is less than 2% of the total beam current in most cases. Since we do not have an alpha probe in our experiment, an experimental illustration of the change in alpha with cathode magnetic field can be

inferred from the change in body current and is shown in Fig. 7-3(d). Here, both the power and body current are shown as a function of changing cathode magnetic field. The body current increases from zero to four milliamperes with decreasing cathode magnetic field (increasing alpha) while the power increases with decreasing cathode magnetic field (increasing alpha and increasing beam compression) until a point where the overall beam quality suffers.
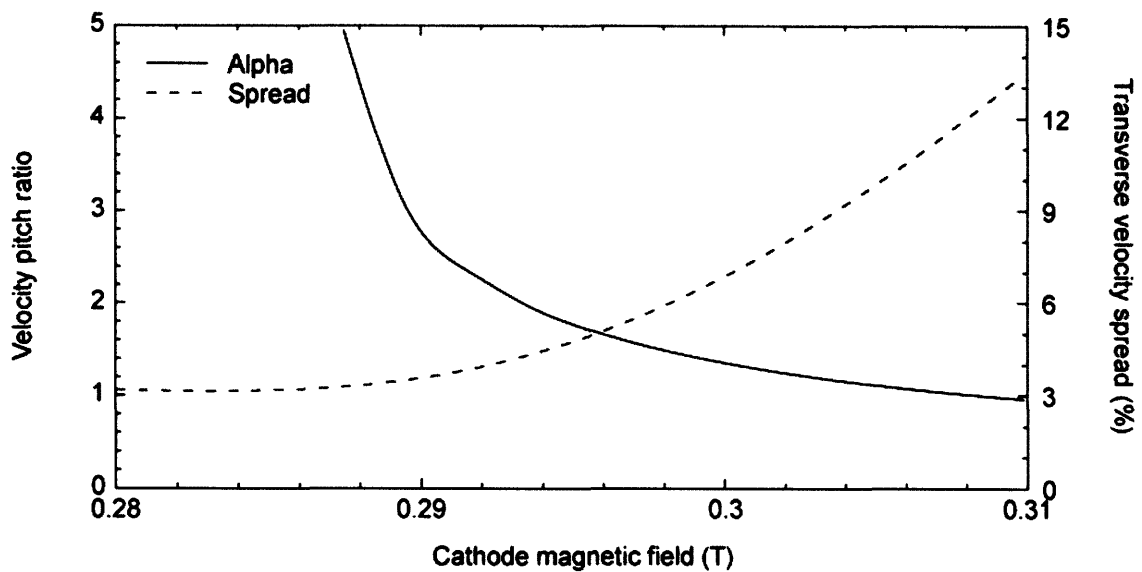
Figure 7-4: EGUN simulations for varying cathode magnetic fields at 12.4 kV and 100 mA.

7.2.3 Frequency Pulling

The dependence of the emission frequency on the operating parameters is an important metric of the frequency stability of the gyrotron. The DNP application requires approximately 5 MHz frequency stability near 460 GHz (corresponding to 700 MHz ^{1}H). While the gyrotron frequency at the nominal operating parameters is 458.56 GHz, in the present paper it is referred to as either 459 GHz or "near 460 GHz." The dependence of the emission frequency of the $TE_{0,6}$ design mode on the operating parameters such as the beam current, main magnetic field, beam voltage, and cathode magnetic field was

characterized using a heterodyne frequency system. The heterodyne receiver system is highly accurate due to a phased locked loop which is capable of stabilizing the local oscillator to 1 Hz (Phase Matrix EIP 578B). Only a single parameter was varied for each measurement in order to simulate operation. While the beam voltage is not likely to change during operation, the control of the output power feedback will cause the beam current to vary in response to fluctuations in the output power. While in persistent mode, the main magnetic field will drift downward at a specified rate (ppm/hour) over long periods of time and the cathode magnetic field may vary due to heating of the gun coil.

Table 7.2: Frequency dependence on operating parameters

Parameter	Sensitivity
Beam current	0.4 MHz/mA
Magnetic field	3.0 GHz/T
Beam voltage	50 MHz/kV
Cathode magnetic field	1.3 GHz/T

The measured frequency pulling characteristics of the gyrotron are plotted in Fig. 7-5 and the frequency dependence on operating parameters is summarized in Table 7.2. The total frequency change observed is within 30 MHz. Linear theory predicts that the pulling effects on frequency by the magnetic field are proportional to ω/Q [9].
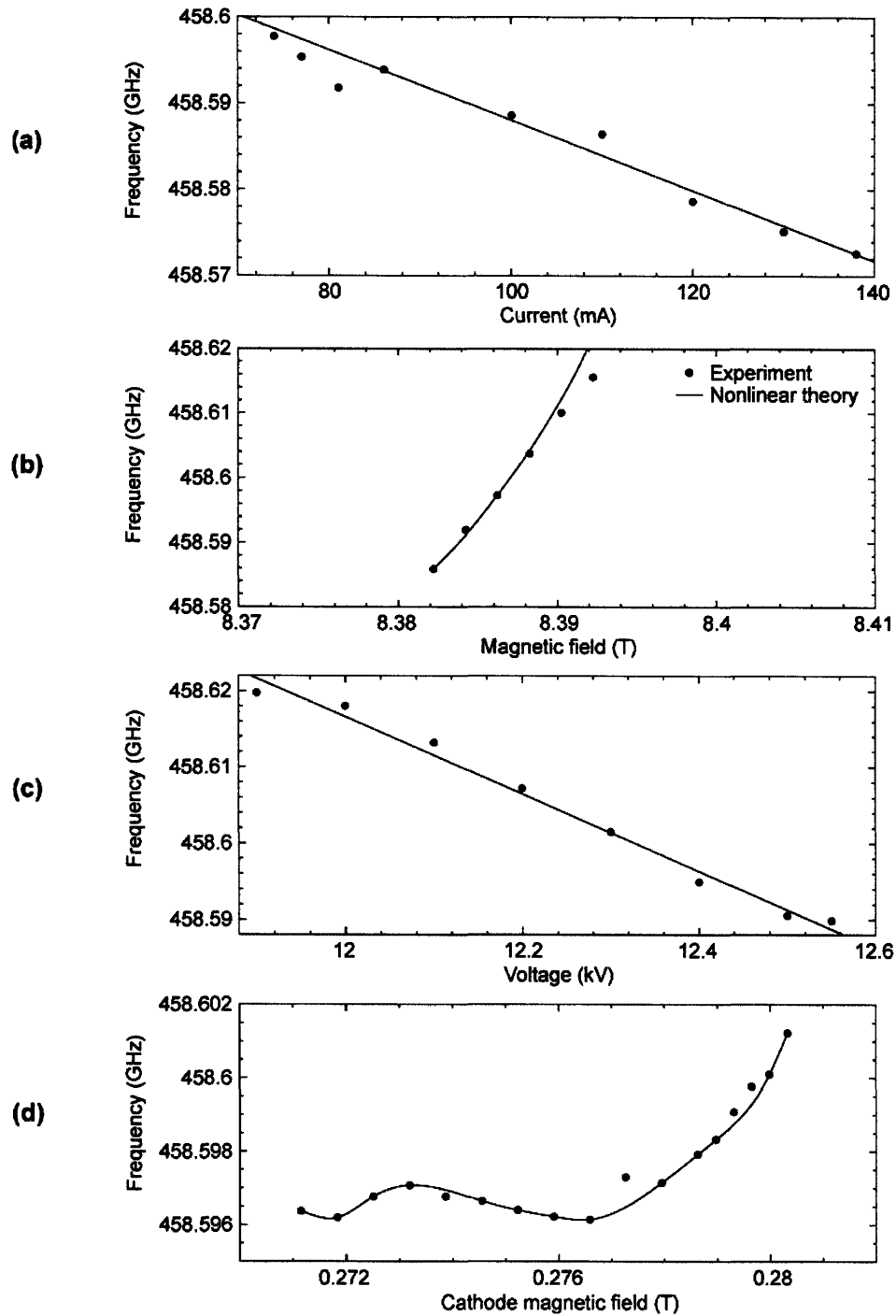
Figure 7-5: Frequency tuning of the $TE_{0,6}$ second harmonic mode with (a) beam current, (b) main magnetic field, (c) voltage, and (d) cathode magnetic field. The magnetic frequency tuning (b) is compared with nonlinear theory from MAGY simulations, and in (a), (c), and (d) the lines are added as a guide.

The frequency pulling effects of the cathode voltage V_c and main magnetic field B in Figs. 7-5(b) and (c) have opposing slopes. For a given beam current, the observed

shift in emission frequency resulting from changes of either the main magnetic field or the beam voltage is due to the effect on the cyclotron frequency, ω_c ($= eB/\gamma \, m_e$), where γ (=1+V_c/511) is the relativistic factor, and the cathode voltage V_c is in kilovolts. If the magnetic field alone is varied, the resulting frequency pulling will have a positive slope, and if the voltage is varied, the frequency pulling will have a negative slope. However, in theory over small values, coordinated changes in both the magnetic field and cathode voltage may leave the cyclotron frequency unchanged such that there is no change in the emission frequency. The same nonlinear theory (MAGY) as was used to simulate the power as a function of magnetic field yields results for the frequency pulling, which are compared with experimental data in Fig. 7-5(b) with coinciding slope.

7.2.4 Ohmic Losses

At high frequencies, a significant portion of the power generated in the cavity is not extracted and is instead deposited in the cavity walls in the form of ohmic heating. These ohmic losses are given by the ratio of diffractive to ohmic Q multiplied by the output power,

$$P_{\text{ohmic}} = \frac{Q_{\text{diffractive}}}{Q_{\text{ohmic}}} P_{\text{out}} \tag{7.1}$$

where

$$Q_{\text{diffractive}} = 4\pi \frac{(L/\lambda)^2}{1 - |R_{1,2}|} \tag{7.2}$$

$$Q_{\text{ohmic}} = \frac{r_0}{\delta} \left(1 - \frac{m^2}{v_{mp}^2} \right) \tag{7.3}$$

The method, materials, and process of fabrication of the cavity are the main contributions to the experimental value of the ohmic losses. For example, the properties of the material (in our case copper), in particular the electrical conductivity and surface roughness, as well as machining anomalies such as irises, in essence determine the ohmic losses. The theoretical RF efficiency, diffractive Q, and conductivity for the second harmonic $TE_{0,6,1}$ mode are given in Table 7.3. The RF efficiency is the fraction of output power with respect to the total power generated in the cavity. With an initial value near 40% at the conductivity of ideal copper (5.8×10^7 S/m), the RF efficiency rapidly decreases as the quality of copper degrades. By contrast, the RF efficiency decreases rapidly with increasing diffractive Q.

A measurement of the ohmic losses in the $TE_{0,6}$ second harmonic design mode of the 460 GHz gyrotron was made possible by the data acquisition capabilities of the computerized control system. By measuring the flow rate and change in temperature of the cavity cooling water, the amount of power transferred from the cavity to the water could be calculated. The temperature of the cavity cooling water was simultaneously measured at both the inlet and outlet of the cavity with separate thermistors, where the measurement was taken as spatially close to the cavity as possible to prevent heat transfer between the cooling hose and the ambient. Assuming that the water is in good thermal contact with the cavity and that the cavity is thermally isolated from any other source of heat internal or external to the tube (such as the collector which is isolated by a ceramic insulator), this is equivalent to measuring the thermal load on the cavity. A period of up to several minutes was allowed for thermal equilibrium to be reached.

Table 7.3: Design and measured parameters from the ohmic loss measurement of the gyrotron cavity at 458.6 GHz

	Design	Measured
Conductivity $\times$ (5.8×10^7 S/m)	0.5	0.25
Diffractive Q	31,000	47,000
RF efficiency (%)	32	24

Table 7.4: Measured and theoretical ohmic losses in the gyrotron cavity at 458.6 GHz

Output power (W)	Cavity thermal load (W)	RF efficiency (%)
0	0	–
2.5	7.9	24.0
3.75	12.1	23.6
4.1	13.5	23.3

Using wet calorimetry, the ohmic power distribution was measured for CW gyrotron output powers up to 4 W. The output microwave power was measured using dry calorimetry. The results of these measurements are shown in Table 7.4. The RF efficiency is nearly constant with output power and the cavity thermal load is linear with output power. The observed RF efficiency of 24% is approximately 8% less than the theoretical value. The effective electrical conductivity required to match the experimental results ranges between one-quarter and one-fifth that of ideal copper. An increase in the cavity diffractive Q from 31,000 to 47,000 might also explain the increased cavity losses, and this might result from errors in the manufacture of the shallow output taper. The design and measured values for the ohmic loss measurement are summarized in Table 7.3. The measured quantities are given such that the value reflects a single parameter change in either electrical conductivity or diffractive Q. Both the increase in diffractive Q and decrease in conductivity are within reasonable bounds

and in reality it is probably a combination of the two factors contributing to the slightly elevated ohmic losses.

7.2.5 Spectral Purity

The radiation produced by the gyrotron has a finite linewidth which can be attributed to both intrinsic (natural) and extrinsic (technical) sources. The fluctuations of the technical parameters which dominate over the natural noise sources cause the broadening of the radiation linewidth in gyrotrons [10], [11]. Among these technical or operating parameters are the beam voltage, beam current, and external magnetic field.
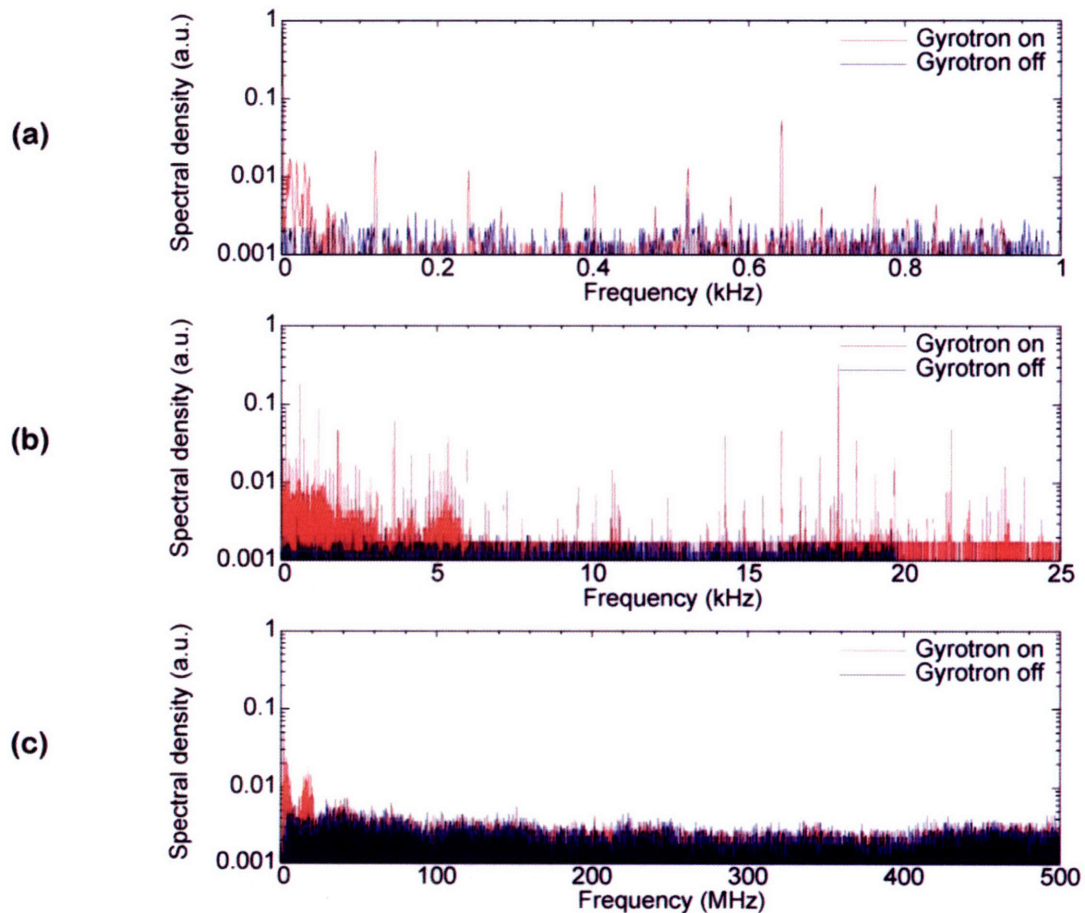
Figure 7-6: Homodyne measurements of the technical noise for the second harmonic $TE_{0,6,1}$ mode.

The 460 GHz time domain signal is an amplitude modulated (AM) signal which can be demodulated yielding both the linewidth and technical noise of the device. An overmoded horn directed at the gyrotron output beam coupled a sample of the gyrotron radiation into the homodyne receiver. In our case, the main center line frequency of the gyrotron acts as a local oscillator; this frequency beats with any other frequencies that are generated by the gyrotron in the harmonic mixer, including those generated by spurious or competing gyrotron modes. The receiver consists of a mixer followed by three intermediate frequency (IF) amplifiers whose amplification bandwidth is from approximately 0.1–1,000 MHz, and a low pass filter with 520 MHz cutoff frequency. Thus, the intermediate frequencies between 0.1 and 520 MHz are amplified, digitized, and passed through an FFT.

The results of homodyne measurements on the $TE_{0,6,1}$ mode over 1 kHz, 25 kHz, and 500 MHz bands are shown in Figure 7-6. Since the amplifiers do not pass DC, these signals are presumed to be well below the gyrotron center line frequency. The technical noise in the gyrotron is apparent in the tens of kilohertz (*cf.* Fig. 7-6). The high voltage power supply is a likely source of the noise in this band. The specifications for the ripple on the power supply are 0.03% rms below 1 kHz and 0.75% rms above 1 kHz. In addition, the alternating current filament output is at 38 kHz. The gyrotron signal at higher frequencies shows little contamination [*cf.* Fig. 7-6(c)] indicating single mode operation.

7.2.6 Radiation Patterns

The first element in the quasi-optical transmission line is the quasi-optical antenna located internal to the gyrotron and collinear to the cross-bore of the superconducting magnet. Its function is to efficiently convert the operating $TE_{0,6}$ waveguide mode into a free-space Gaussian beam which will then be transmitted out of the vacuum tube to the DNP probe through a transmission line. That line can be either a corrugated metallic or hollow dielectric waveguide supporting the $HE_{1,1}$ quasi-Gaussian mode or a mirror line supporting the free-space Gaussian mode. This experiment employs an internal quasi-optical mode converter to efficiently separate the microwave beam from the energetic electron beam; the microwave beam is directed to the experiment through an orthogonal cross bore in the superconducting magnet, while the electron beam is collected in a compact, water-cooled collector region, far from any fragile microwave structures or windows. This in turn increases the vacuum pumping conductance and reduces the ohmic losses in the output waveguide. The mode converter consists of a cylindrical waveguide with a step cut and a cylindrical focusing mirror. The waveguide antenna converts the higher order transverse electric gyrotron output into a linearly polarized beam which is subsequently collimated by the focusing mirror. The mode converter works well for $TE_{m,p}$ modes where $m \ll p$.

Table 7.5: Beam waists of the mode converted radiation fields from Fig. 7-8 as calculated by the best fit Gaussian

$TE_{m,p}$ mode	Frequency (GHz)	x waist (mm)	y waist (mm)	Ellipticity (%)
$TE_{0,6}$	459	4.67 ± 0.04	4.91 ± 0.04	4
$TE_{2,6}$	456	6.42 ± 0.03	5.63 ± 0.02	12
$TE_{2,3}$	233	5.25 ± 0.02	6.60 ± 0.02	20
$TE_{2,2}$	157	3.00 ± 0.02	3.81 ± 0.02	21
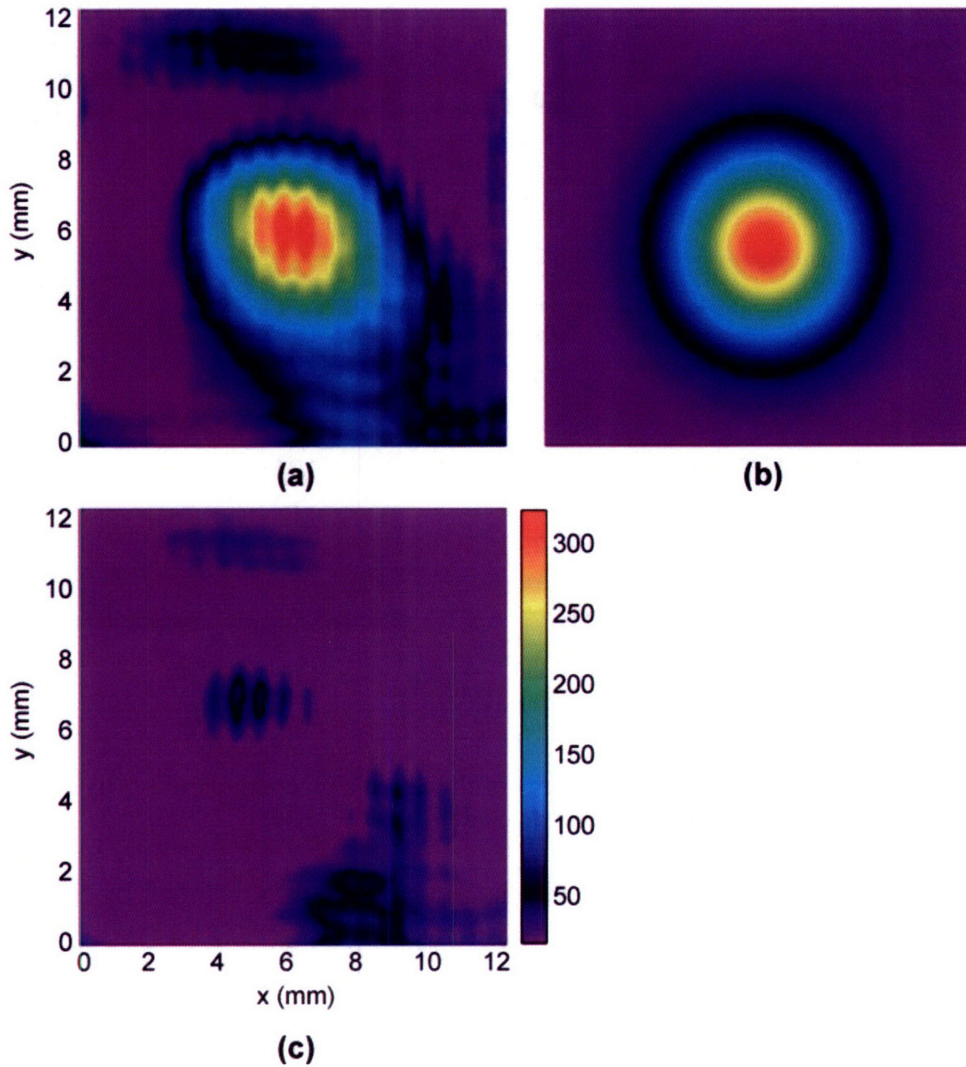
Figure 7-7: Planar section of the 460 GHz radiation intensity as recorded by a pyroelectric camera. (a) is the intensity 66 cm along the waveguide axis (b) is a Gaussian fit of the intensity data and (c) is the residual of the fit. The intensity is described on a linear scale in arbitrary units.
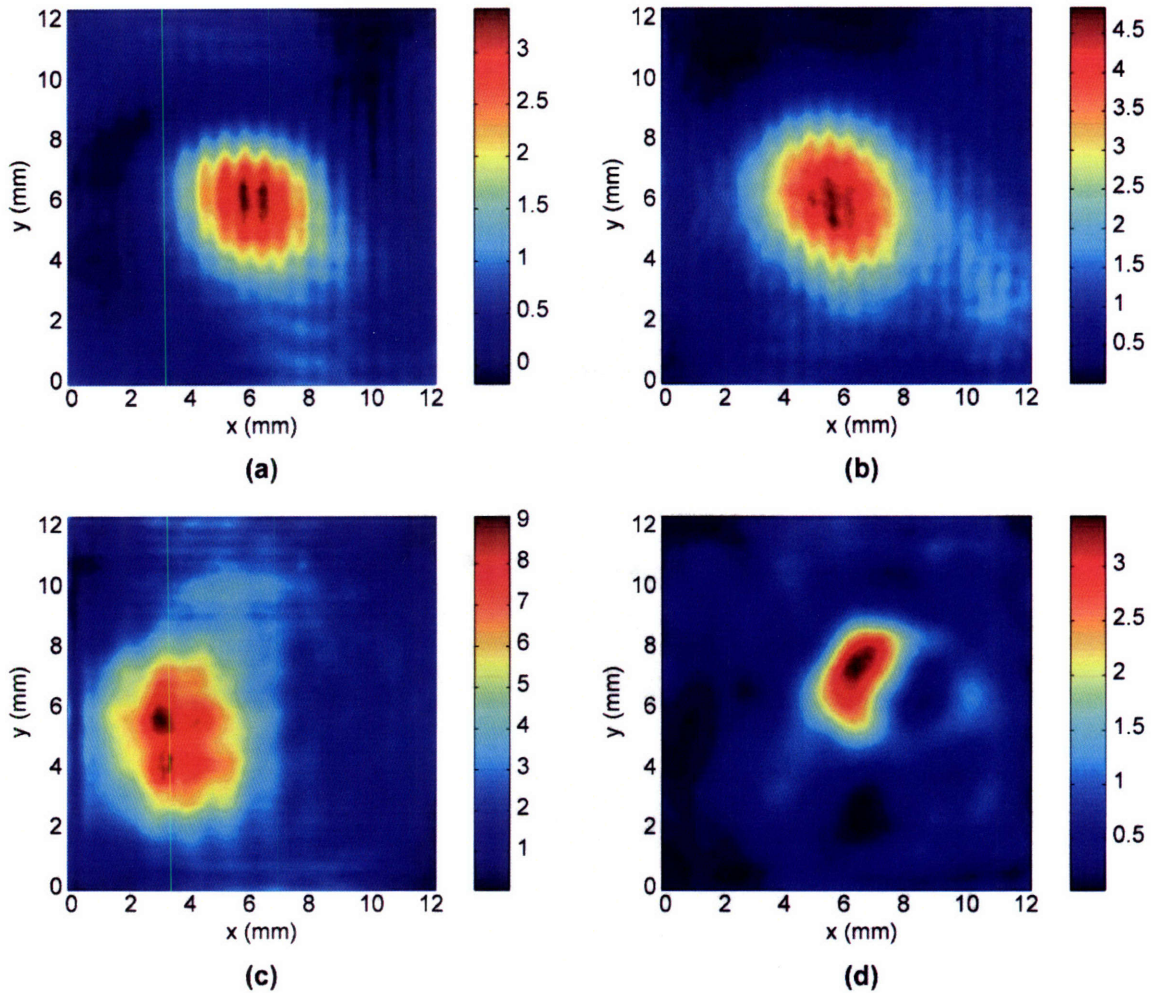
Figure 7-8: Linear radiation intensity patterns of the mode-converted (a) $TE_{0,6}$ (b) $TE_{2,6}$ (c) $TE_{2,3}$ and (d) $TE_{2,2}$ modes captured by a pyroelectric camera.

A pyroelectric camera laser beam diagnostic system developed by Spiricon, Inc. (Pyrocam III) was used for millimeter and submillimeter-wave radiation pattern measurements. The camera is a pyroelectric array consisting of 124 by 124 elements where the element spacing is 100 μm by 100 μm, yielding an active area of 12.4 by 12.4 mm. The pyroelectric camera has been previously used to image the output beams of 250 GHz [12] and 140 GHz [13] gyrotrons. During these measurements, the gyrotron was operated in CW mode with an output power of less than 2 W. Since a pyroelectric detector is sensitive only to alternating signals, the CW gyrotron beam was modulated at

48 Hz by an optical chopper housed in the body of the camera. Since the gyrotron window is 25.4 mm in diameter and set inside the cross bore of the superconducting magnet, an epoxyglass waveguide (supporting the $HE_{1,1}$ mode) with 25.4 mm inner diameter conveyed the output power to the pyroelectric camera over a distance of 66 cm. As a result, the detector aperture does not cover the entire area of the waveguide. The detector gain was set near the threshold of saturation to maximize the dynamic range of the measurement. Data were processed by subtraction of a separately recorded dark frame to eliminate systematic dead pixel artifacts and background noise, followed by averaging of 128 captured frames to improve the sensitivity of the measurement.

An image of the captured $TE_{0,6}$ mode-converted beam at 459 GHz is displayed in Fig. 7-7(a). A Gaussian fit [*cf.* Fig. 7-7(b)] determined that the measured beam is slightly elliptical with a waist size in y of 4.91 ± 0.04 mm and a waist size in x of 4.67 ± 0.04 mm, where the beam waist is given by $1/e^2$ from the maximum intensity or -8.7 dB. The 4% ellipticity indicates a good performance of the internal quasi-optical mode converter. The output field patterns of the converted $TE_{0,6}$, $TE_{2,6}$, $TE_{2,3}$, and $TE_{2,2}$ modes were also measured (*cf.* Fig. 7-8). These modes span 157 GHz through 459 GHz demonstrating that the pyroelectric camera functions continuously from millimeter to submillimeter wavelengths. The quasi-optical mode converter will convert most TE_{mp} modes to free-space Gaussian beams where $m \ll p$. In agreement with this prediction, images of the gyrotron operating in the $TE_{0,6}$ and $TE_{2,6}$ show a Gaussian beam, while images with the gyrotron operating in the $TE_{2,3}$ and $TE_{2,2}$ modes do not. Table 7.5 shows the beam waists of the four modes as calculated by a best-fit Gaussian with 95% confidence interval. A rectangular grid diffraction pattern is observed on the high frequency intensity patterns

345

that is not observed on the lowest frequency intensity pattern. The spacing of the elements in the pyroelectric array is 100 μm, which may cause interference effects with the gyrotron wavelengths in the hundreds of microns.

7.2.7 CW Stability

Operating under a computerized control system, the 460 GHz gyrotron is capable of stable CW emission for extended periods. The control system, implemented in the LabVIEW software package, is based upon similar principles as a computerized control system written for a low power CW 250 GHz gyrotron which has operated continuously for over twenty-one days and has been in service for seven years [12]. The stability of the emission in the $TE_{0,6,1}$ second harmonic mode near 460 GHz and, separately, the $TE_{2,3,1}$ fundamental mode near 230 GHz was monitored for a period of one hour during which the gyrotron ran in complete CW mode. During this period, a constant output power was maintained by proportional, integral, and derivative feedback adjustments to the filament current based on the difference between the set point and monitored power signal. The output power was monitored in two cases, first with a diode and later with a calorimeter. In the case of diode monitoring, the output power was referenced at the start and finish of the monitoring period with the calorimeter. All aspects of the experiment were monitored by the computerized control system and logged, including the output power, pressure, beam voltage, beam current, filament current, and gun coil current. The superconducting magnet was in persistent mode.

Table 7.6: Stability of the second harmonic $TE_{0,6,1}$ and fundamental $TE_{2,3,1}$ modes in the 460 GHz gyrotron

| | $TE_{0,6,1}$ (diode) | | $TE_{0,6,1}$ (calorimeter) | | $TE_{2,3,1}$ (diode) | |
	Avg.	Std. dev. (%)	Avg.	Std. dev. (%)	Avg.	Std. dev. (%)
Power (W)	3.76	0.3	3.13	0.4	4.69	0.2
Pressure ($\times 10^{-8}$ Torr)	4.34	3.4	3.80	1.7	1.21	1.7
Beam voltage (kV)	12.40	0.0	12.40	0.0	3.50	0.0
Filament current (A)	2.55	1.0	2.52	0.6	2.36	0.3
Beam current* (mA)	119.0	8.6	111.1	6.1	19.7	2.7
Gun coil current (A)	2.54	0.0	2.54	0.1	24.63	0.0

*Beam current was monotonically increasing in the second harmonic experiment.
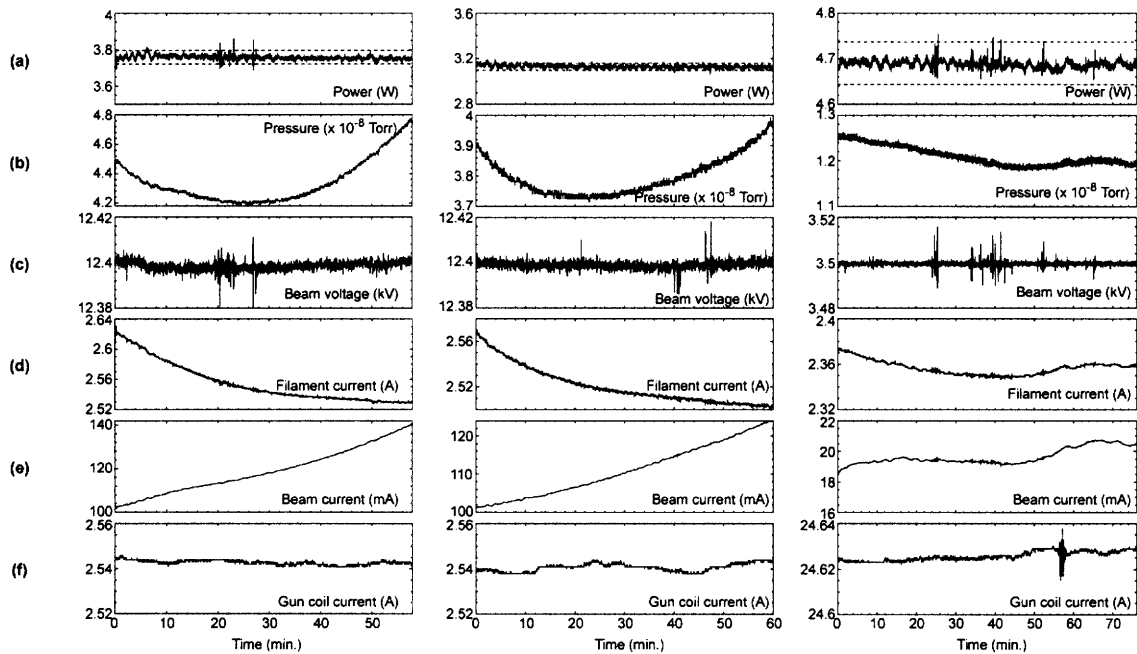
Figure 7-9: Three separate one hour duration stability tests of the (a) power, (b) pressure, (c) beam voltage, (d) filament current, (e) beam current, and (f) gun coil current for the $TE_{0,6,1}$ second harmonic mode at 459 GHz using a diode (left) and calorimeter (center) and for the $TE_{2,3,1}$ fundamental mode at 233 GHz using a diode (right) to monitor the output power. The dotted lines on (a) represent 1% stability.
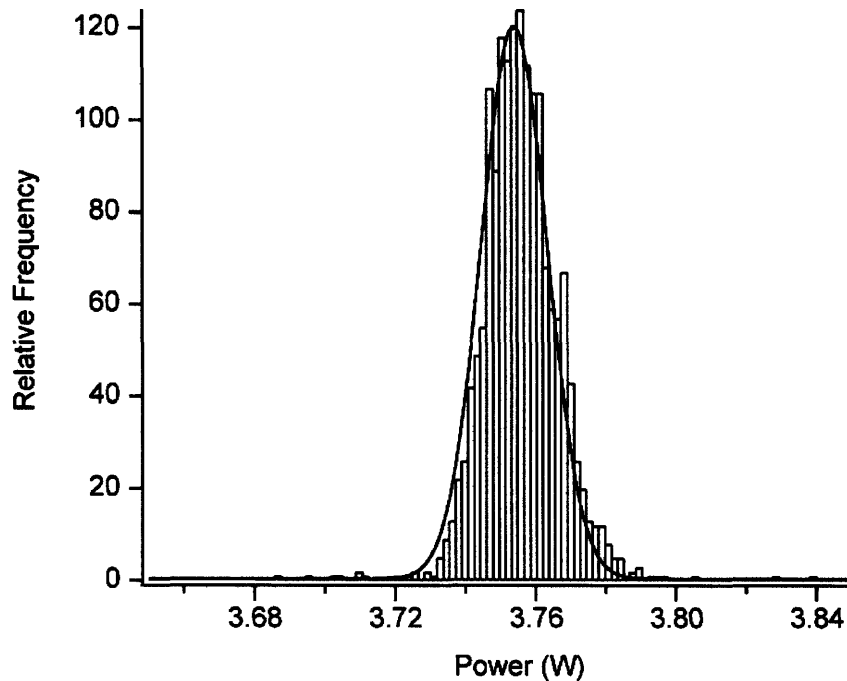
Figure 7-10: Statistical analysis of power fluctuations from set point for the diode controlled $TE_{0,6,1}$ hour long run. The solid line is a Gaussian fit to the data.

A summary of the $TE_{0,6,1}$ second harmonic and $TE_{2,3,1}$ fundamental results is shown in Fig. 7-9 and Table 7.6. A statistical analysis of excursions of the 459 GHz power signal from its set point over the hour long experiment using a diode for feedback (Fig. 7-10) shows that power fluctuations are normally distributed and that the tolerances of the DNP experiment are met by the control system. Notably, the power was stable to within 1% for all cases over the hour long period using feedback from either a diode or calorimeter, where the dotted lines in Fig. 7-9 represent ±1% of the power signal. The pressure in all cases was low, but showed a tendency to increase for second harmonic operation. This increase in pressure was directly related to the increase in beam current required to maintain the constant output power.

In both the fundamental and second harmonic operation, the output power is regulated through changes in the filament current, which, in turn, brings about proportional changes in the beam current. During constant power operation in the

fundamental mode, however, the beam current and filament current change much less than they do for similar operation at the second harmonic. While the rf output powers were comparable for both the fundamental and second harmonic controlled runs, their beam powers differed by a factor of 20 due to the difference in efficiency; where a beam power of 70 W was used for the fundamental, 1.4 kW of beam power was used for the second harmonic. Experimental runs of the gyrotron indicate that the increase in beam current required to maintain a constant second harmonic output power is likely due to the overheating of the electron gun. An improvement of the electron gun cooling system will be implemented in future runs.

7.3   Conclusion

The 460 GHz experiment has successfully demonstrated that a gyrotron can efficiently produce over 8 W of average power at the second electron cyclotron harmonic in low voltage operation. To our knowledge, this is the highest continuous-wave output achieved by a gyrotron this far into the submillimeter wavelength band. The efficiency of the gyrotron was verified with measurements of the cavity ohmic losses which also confirmed the ratio of diffractive to ohmic Q. The stability characteristics were studied over the duration of an hour, and demonstrated that the output power could be maintained stable to within 1% under computer control. The limiting factor in operating at longer periods of time is likely the overheating of the electron gun. This will be corrected in future operation. Frequency pulling measurements determined that the stability of the frequency with respect to the beam voltage, beam current, and magnetic field drift was sufficient for DNP. The radiation pattern of the second harmonic design mode at 460 GHz shows that the beam is Gaussian with a 4% ellipticity and that the mode converter

works reasonably well for several other observed second harmonic and fundamental modes. In addition, the gyrotron operates at useful CW output powers in several fundamental modes for which the design was not explicitly optimized; many of these modes also exhibit unusually broad magnetic tunability. The 460 GHz gyrotron will serve as a millimeter-wave source for sensitivity-enhanced nuclear magnetic resonance (dynamic nuclear polarization) experiments at a magnetic field of 16.4 T (700 MHz ^{1}H), which will be the highest frequency DNP experiments attempted to date.

7.4   References

[1] K. Hong, G. Brand, and T. Idehara, "A 150–600 GHz step-tunable gyrotron," *J. Appl. Phys.*, vol. 74, no. 8, pp. 5250–5258, Oct. 1993.

[2] T. Idehara, K. Yoshida, N. Nishida, I. Ogawa, M. L. Pereyaslavets, and T. Tatsukawa, "CW operation of a submillimeter wave gyrotron (gyrotron FU IV) for high stability of the output frequency," *Int. J. Infrared Millim. Waves*, vol. 19, no. 6, pp. 793–801, Jun. 1998.

[3] N. Zaytsev, T. Pankratova, M. Petelin, and V. Flyagin, "Millimeter- and submillimeter-wave gyrotrons," *Radio Eng. Electron. Phys.* (USA), vol. 19, no. 5, pp. 103–107, May 1974.

[4] V. Flyagin, A. Luchinin, and G. Nusinovich, "Submillimeter-wave gyrotrons: theory and experiment," *Int. J. Infrared Millim. Waves*, vol. 4, no. 4, pp. 629–637, July 1983.

[5] M. K. Hornstein, V. S. Bajaj, R. G. Griffin, K. E. Kreischer, I. Mastovsky, M. A. Shapiro, J. R. Sirigiri, and R. J. Temkin, "Second harmonic operation at 460 GHz and broadband continuous frequency tuning of a gyrotron oscillator," *IEEE Trans. Electron Devices*, vol. 52, no. 5, pp. 798–807, May 2005.

[6] K. Kreischer, C. Farrar, R. Griffin, R. Temkin, and J. Vieregg, "A 250 GHz gyrotron for NMR spectroscopy," *27th IEEE ICOPS Record Abstracts*. New Orleans, LA, Jun. 2000, p. 198.

[7] V. Bajaj, C. Farrar, M. Hornstein, I. Mastovsky, J. Vieregg, J. Bryant, B. Elena, K. Kreischer, R. Temkin, and R. Griffin, "Dynamic nuclear polarization at 9 Tesla using a novel 250 GHz gyrotron microwave source," *J. Mag. Res.*, vol. 160, no. 2, pp. 85–90, Feb. 2002.

[8] M. Botton, T. Antonsen, B. Levush, K. Nguyen, and A. Vlasov, "MAGY: A time-dependent code for simulation of slow and fast microwave sources," *IEEE Trans. Plasma Sci.*, vol. 26, no. 3, pp. 882–892, Jun. 1998.

[9] K. Kreischer, B. Danly, P. Woskoboinikow, W. Mulligan, and R. Temkin, "Frequency pulling and bandwidth measurements of a 140 GHz pulsed gyrotron," *Int. J. Elec.*, vol. 57, no. 6, pp. 851–862, Dec. 1984.

[10] O. Dumbrajs and G. Nusinovich, "Effect of technical noise on radiation linewidth in free-running gyrotron oscillators," *Phys. Plasmas*, vol. 4, no. 5, pp. 1413–1423, May 1997.

[11] G. Nusinovich and O. Dumbrajs, "Technical noise in gyroklystrons and phase-locked gyrotron oscillators," *Phys. Plasmas*, vol. 4, no. 5, pp. 1424–1433, May 1997.

[12] V. S. Bajaj, M. K. Hornstein, K. E. Kreischer, P. P. Woskov, M. L. Mak, J. Herzfeld, R. J. Temkin, and R. G. Griffin, "A continuous duty cycle 250 GHz gyrotron oscillator for dynamic nuclear polarization in biological solid state NMR," *J. Mag. Res.*, 2006.

[13] C. Joye, R. Griffin, M. Hornstein, K. Hu, K. Kreischer, M. Rosay, M. Shapiro, J. Sirigiri, R. Temkin, and P. Woskov, "Operational characteristics of a 14-W 140-GHz gyrotron for dynamic nuclear polarization," *IEEE Trans. Plasma Sci.*, vol. 34, no. 3, pp. 518–523, Jun. 2006.

Chapter 8   Efficient, Low Voltage Operation of a CW Gyrotron Oscillator at 233 GHz

The gyrotron oscillator is a source of high average power millimeter-wave through terahertz radiation. Here, we report low beam power and high efficiency operation of a tunable gyrotron oscillator at 233 GHz. The low voltage operating mode provides a path to further miniaturization of the gyrotron through reduction in the size of the electron gun, power supply, collector, and cooling system, which will benefit industrial and scientific applications requiring portability. Detailed studies of low voltage operation in the $TE_{2,3,1}$ mode reveal that the mode can be excited with less than 7 W of beam power at 3.5 kV. During CW operation with 3.5 kV beam voltage and 50 mA beam current, the gyrotron generates 12 W of RF power at 233.2 GHz. The EGUN electron optics code describes the low voltage operation of the electron gun. Using gun operating parameters derived from EGUN simulations, we show that a linear theory adequately predicts the low experimental starting currents.

8.1   Introduction

Since the power in a gyrotron oscillator increases strongly with beam voltage and current, gyrotrons tend toward operation with high voltage in the tens to hundreds of kilovolts generating tens of kilowatts to one or two megawatts in the microwave to millimeter-wave band. For example, a state-of-the-art commercial CW gyrotron oscillator at 140

GHz operating at 80 kV and 45 A has recently achieved a power level of 900 kW for a duration of several minutes [1], [2]. However, many high frequency applications, such as dynamic nuclear polarization (DNP) [3], require only a modest average rf output power of several watts to several tens of watts. In such cases, it is feasible to generate this amount of power under conditions of low voltage (<15 kV) and current operation. For instance, using a 140 GHz gyrotron oscillator (14 kV), it has been demonstrated that rf powers as low as 1 W can be sufficient to enhance the nuclear magnetic resonance signal using the dynamic nuclear polarization mechanism [4], [5] and 3-4 W (12 kV) has shown to be sufficient at 250 GHz [6].

In fact, there is no device as well suited to the generation of high average power submillimeter radiation as the gyrotron oscillator. Gyrotrons, whose interaction structures can be several times the operating wavelength, are more robust than conventional vacuum electron devices (such as the klystron, TWT, and BWO), whose circuit dimensions are limited to the order of a wavelength, thus restricting high power capabilities especially at higher frequencies. In a gyrotron, lowering the voltage at which oscillations occur while maintaining a good efficiency can result in a reduction of the size of the electron gun, power supply, collector, cooling system, and vacuum pumping system and can further reduce the length and complexity of the microwave tube processing and conditioning. Lowering the voltage of operation is therefore an important step toward miniaturization of the gyrotron.

In this work, we report a short wavelength gyrotron operating at a beam voltage as low as 3 kV and producing several watts of output power at 233 GHz. Previously, a gyrotron with a 5–15 kV, 2 mA beam has produced 5 W at 9.4 GHz with up to 2%

efficiency [7], and a gyrotron with a 20 kV, 2–3 mA beam in a 5 T magnet generated 1 W

of power at frequencies up to 140 GHz at an efficiency of up to 2% [8]. The gyrotron

reported here differs in several respects from this earlier work. It utilizes a magnetron

injection gun (MIG), which produces an annular beam. Such a beam has reduced space

charge forces and lower velocity spread than a Pierce gun, providing higher electron

beam quality and higher output efficiency. The present gyrotron was also optimized for

DNP with the requirements to operate continuously at the second electron cyclotron

harmonic at 460 GHz with 12 kV beam voltage and output powers of between several

watts and several tens of watts. A CW power level of over 8 W was observed near 460

GHz [9]. Results reported in this paper are for operation of this gyrotron at the

fundamental cyclotron harmonic.

The electromagnetic radiation in a gyrotron oscillator results from the interaction

of a mildly relativistic gyrating electron beam and transverse electric (TE) wave near

cutoff in an overmoded cavity resonator situated in a DC magnetic field. The oscillation

frequency ω of a TE$_{m,p,q}$ mode of a cylindrical cavity of effective length L and radius r_0 is

given by

$$\frac{\omega^2}{c^2} = k^2 = k_\perp^2 + k_z^2 \qquad (8.1)$$

where $k_\perp$ (= v_{mp}/r_0) and k_z (= $q\pi/L \ll k_\perp$) are the transverse and longitudinal propagation

constants of the TE$_{m,p,q}$ wave, c is the velocity of light, v_{mp} is the pth root of $J'_m(x)$, and m,

p, and q are, respectively, the azimuthal, radial, and axial mode numbers. The resonance

condition for the excitation of the cyclotron resonance maser instability is satisfied when

ω and k_z in (8.1) satisfy the beam mode dispersion relation,

$$\omega - k_z \beta_{z0c} \approx n\omega_{c0} \qquad (8.2)$$

where ω_{c0} ($=eB_0/\gamma\, m_e$) is the relativistic cyclotron frequency, $\gamma = (1 - \beta_z^2 - \beta_\perp^2)^{-1/2}$ is the relativistic mass factor, m_e and e are the electron rest mass and charge, $\beta_{\perp 0}$ and β_{z0} are, respectively, the transverse and longitudinal velocities of the electrons normalized to the velocity of light, n is the cyclotron harmonic number, B_0 is the magnitude of the static axial magnetic field, and the subscript "0" denotes that the value is taken at the start of the interaction region.

8.2   Low Voltage Experiment

In this experiment, the axis of the gyrotron lies along the vertical bore of a 9.2 T superconducting magnet, while the microwave power is extracted via a quasi-optical mode converter (optimized for $TE_{0,6}$ waveguide mode radiation) through an auxiliary, horizontal, room temperature bore which intersects with the main bore above the main coil of the superconducting magnet. The gyrotron is shown schematically in [9], [10]. The high voltage power supply used in the present experiment is 3 kW-limited with maximum output voltage of 25 kV and maximum output current of 192 mA.

The experiment employs a low voltage, diode-type electron gun which was analyzed using the EGUN electron optics and gun design program [11]; the results of this study over a range of 5-15 kV and 7.8-9.2 T were reported in [10]. For operating parameters corresponding to excitation of fundamental modes, EGUN simulations predict large variations in the velocity spread and velocity pitch ratio with changes in the beam voltage and the magnetic field.
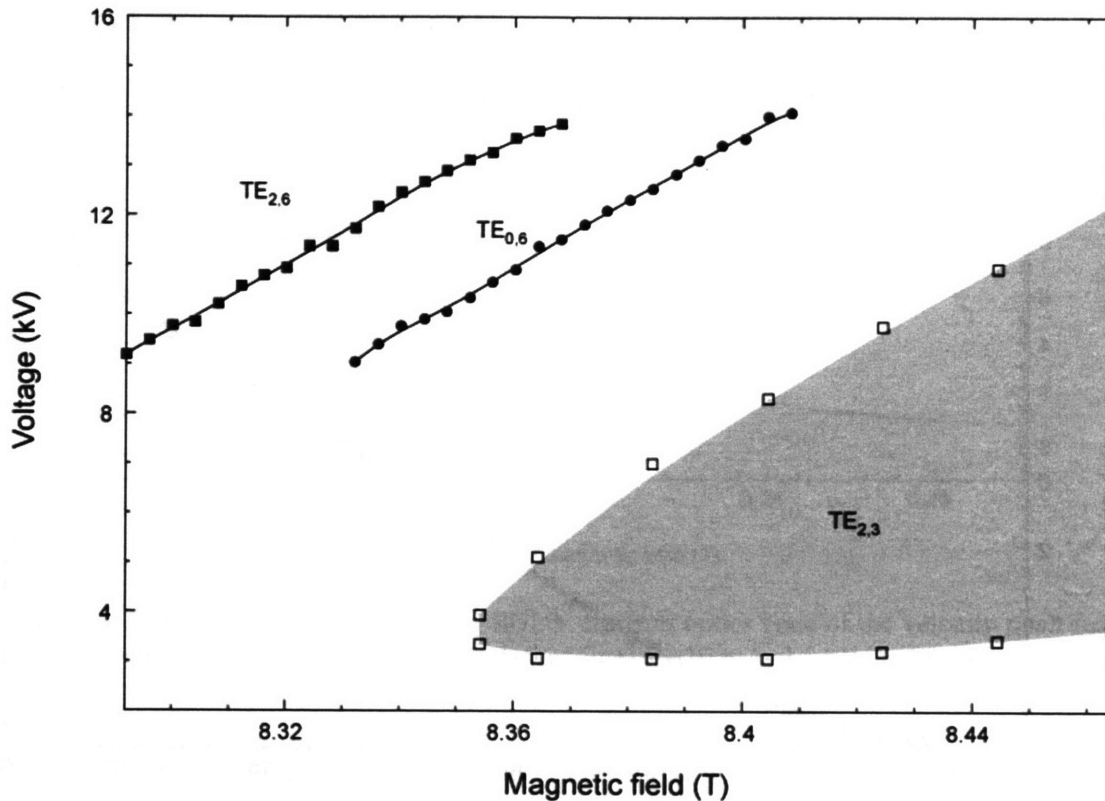
Figure 8-1: Mode excitation regions for two second harmonic modes ($TE_{2,6}$ and $TE_{0,6}$) and nearby fundamental harmonic mode ($TE_{2,3}$) over beam voltage, cavity, and, implicitly, cathode magnetic fields.

A parametric study of the gyrotron modes involves independent variation of the electron beam voltage and current, main magnetic field, and the gun magnetic field. Figure 8-1 is a plot of the mode excitation regime that was generated during microsecond-pulse, low-duty operation charting the regions of mode excitation in the parameter space of interest. For a fixed magnetic field, the excitation region is narrow in voltage-space for the second harmonic modes and has therefore been represented as a line. In Fig. 8-1, three main parameters have been varied – the main magnetic field, the beam voltage, and the cathode magnetic field for a fixed beam current of 100 mA – to determine the operational limits of each mode. The electron beam voltage was varied up to 15 kV, the main magnetic field was independently varied up to 8.5 T, and the cathode

357

magnetic field was varied by 30%. All measurements were taken at the end of a 2 m long copper waveguide of 2.54 cm inner diameter that couples directly to the output window.
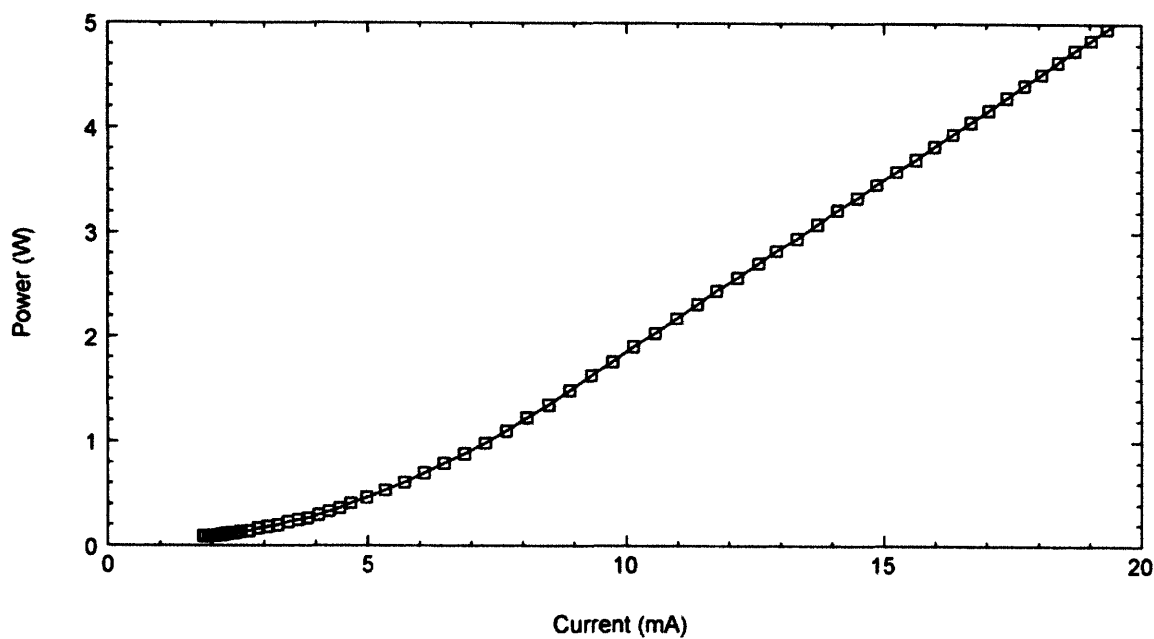
Figure 8-2: CW output power in the $TE_{2,3,1}$ mode as a function of beam current at 3.5 kV and 8.38 T.

In the region of interest, there are two second harmonic modes, the $TE_{2,6}$ at 456 GHz and the $TE_{0,6}$ at 459 GHz, and one fundamental mode, the $TE_{2,3}$, at 233 GHz. The studies of the $TE_{2,3}$ fundamental harmonic mode reveal that the mode can be excited at very low voltage, less than 3.5 kV, with less than 7 W of beam power. Calorimetric measurements of the rf power indicate that the mode begins oscillating at 2 mA at 8.38 T and 3.5 kV with 100 mW of output power (cf. Fig. 8-2). At the experimental magnetic field corresponding to the minimum measured starting current, a starting current of 2 mA can be obtained using linear theory [12] with electron velocity pitch factor α (ratio of transverse to longitudinal velocity of the electrons) of about 2.
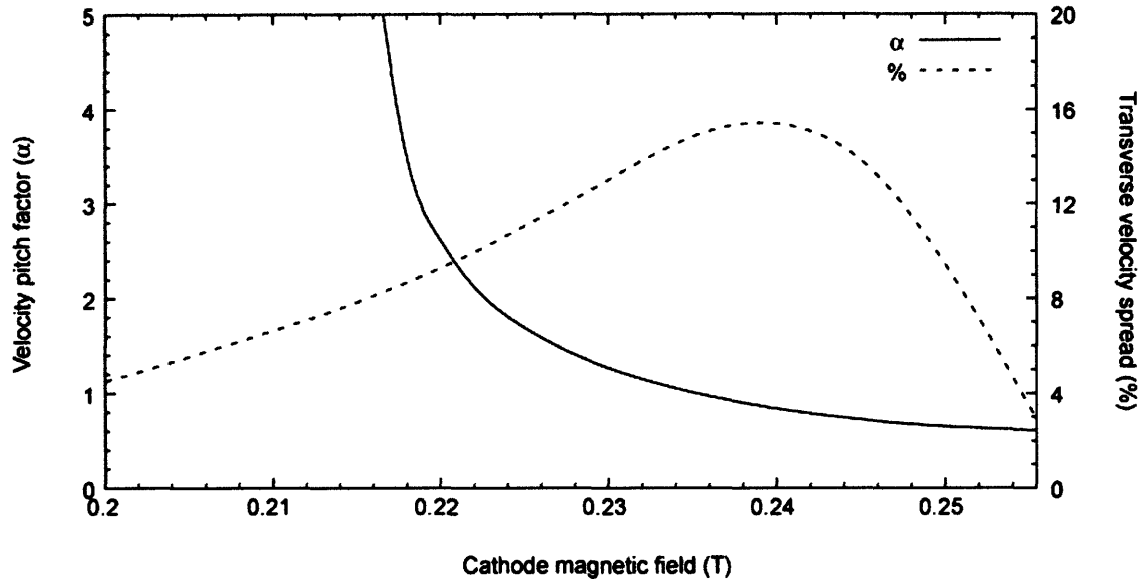
Figure 8-3: Electron gun simulation using EGUN electron optics code of the velocity pitch factor (solid line) and transverse velocity spread (dashed line) for 10 mA, 3.5 kV, and 8.38 T.

The low voltage operation of the electron gun can be adequately explained through simulation of the electron gun using the EGUN electron optics code. Depicted in Fig. 8-3 is an EGUN simulation for 10 mA beam current at 3.5 kV beam voltage. The cathode magnetic field used in these experiments is estimated to be less than 0.22 T, corresponding to an electron beam velocity pitch factor with a steep slope and a transverse velocity spread of 8%. The calculation in Fig. 8-3 depicts that a large range of alpha values can be obtained by comparatively small changes in the cathode magnetic field.
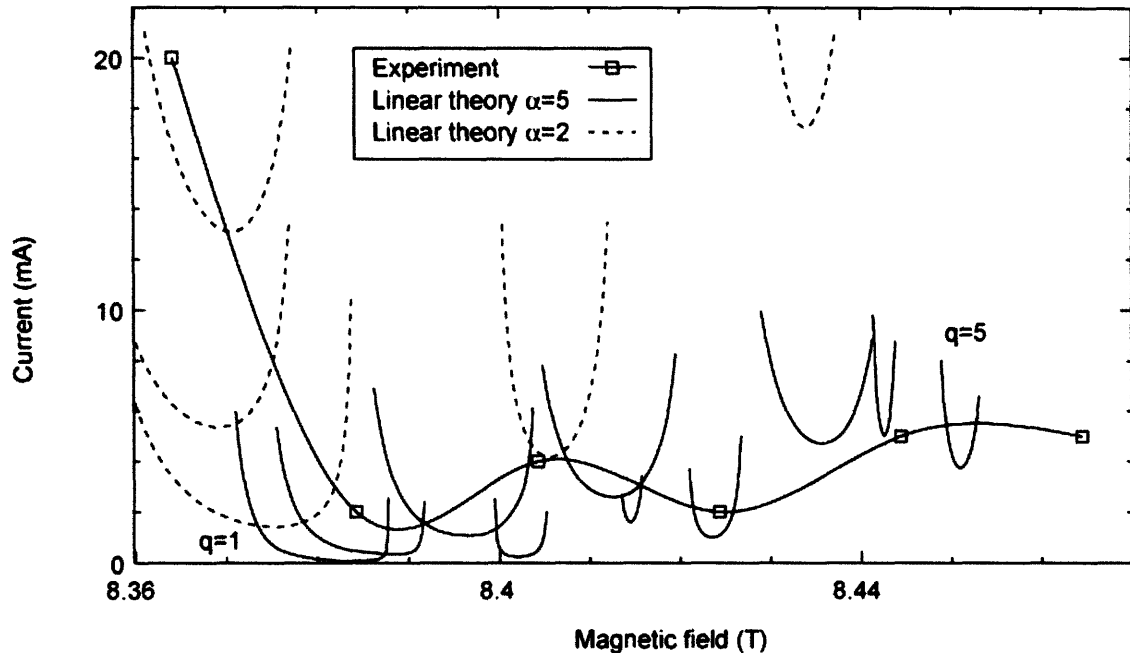
Figure 8-4: CW start current data in the $TE_{2,3,q}$ series of axial modes at 3.5 kV compared to linear theory using α equal to 2 and 5 and with 12% transverse velocity spread.

Using a range of alpha values between 2 and 5 and with 12% transverse velocity spread, the starting currents for the first five discrete integer longitudinal modes ($TE_{2,3,q}$, where q=1,2,3,4,5) have been calculated using linear theory [13] and are shown in Fig. 8-4. The experimental data in Fig. 8-4 are a representative sample of continuous start current data as a function of magnetic field. This phenomenon is a result of axial mode hybridization of the $TE_{2,3,q}$ modes and therefore the data cannot be assigned to discrete modes [10]. The starting current calculation uses electron beam parameters calculated by EGUN, cold cavity electric field profiles, cavity radius of 2 mm, and cavity beam radius of 0.85 mm. We have systematically increased the EGUN-derived velocity spread according to [14] to account for cathode surface roughness, thermal variations, and other effects not explicitly modeled in EGUN. While the experimental starting currents match well with linear theory for alpha equal to two at the lower magnetic fields, the calculation

360

shows that a higher alpha is required to provide good agreement at higher magnetic fields.
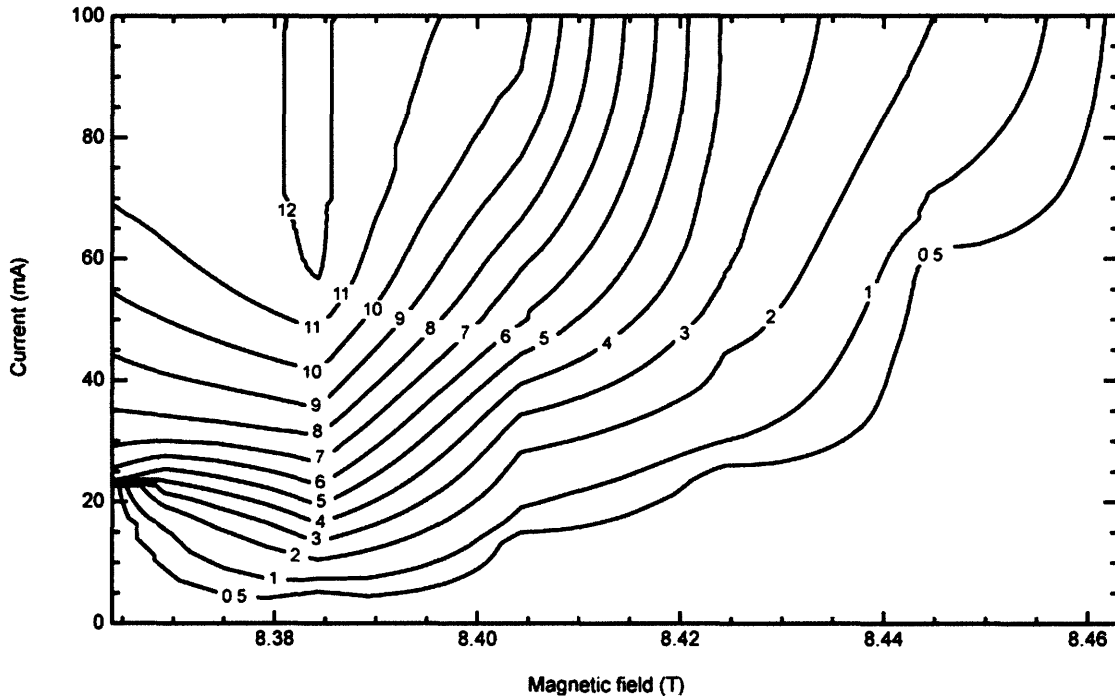
Figure 8-5: Contour plot of measured CW power data of the fundamental harmonic $TE_{2,3,q}$ modes in watts as a function of beam current and magnetic field for an electron beam voltage of 3.5 kV.

Average power measurements were made during the experiment using a laser calorimeter that was recalibrated for millimeter wavelengths. Figure 8-5 depicts measured CW power data of the fundamental harmonic $TE_{2,3,q}$ modes around 233 GHz as a function of beam current and magnetic field. A calorimeter was used to measure the radiation, and the beam voltage was fixed at 3.5 kV. Over 12 W of average power was recorded at 50 mA with an efficiency in excess of 7%. The mode also exhibits an experimentally wide frequency tuning range, shown in Fig. 8-6, nearly 2 GHz; this effect has been discussed in detail in [10], [15] and has been interpreted in terms of smooth transitions between higher order axial modes of the resonator.
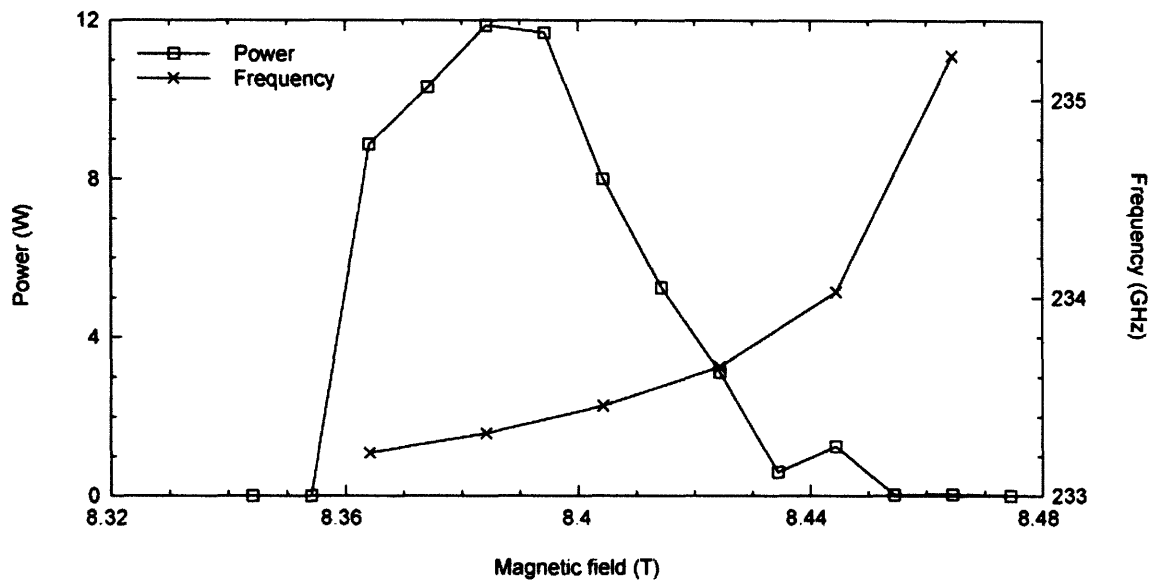
Figure 8-6: CW output power and frequency in the $TE_{2,3,q}$ modes as a function of magnetic field for 50 mA and 3.5 kV.

8.3 Conclusion

Gyrotron oscillators are capable of generating extremely high average powers (<1 MW) over a wide frequency range (typically 24-170 GHz). One challenge is to further develop compact gyrotron oscillators for moderate average power applications of millimeter-wave and submillimeter-wave radiation. In this work we have significantly lowered the operating voltage of a millimeter/submillimeter wavelength gyrotron while still producing several watts of average power. The fundamental harmonic $TE_{2,3,1}$ mode at 233 GHz was excited with low beam power (7 W), at a voltage below 3.5 kV while oscillations started with 2 mA of beam current. Linear theory provides an explanation to the low experimental starting currents at low voltage, and the EGUN electron optics code described the operation of the diode gun. Future low voltage gyrotron designs can then

incorporate a more compact electron gun and electron beam collector, and operate with significantly reduced cooling requirements.

8.4 References

[1] K. Felch, M. Blank, P. Borchard, P. Cahalan, S. Cauffman, T. S. Chu, and H. Jory, "Recent advances in increasing output power and pulse duration in gyrotron oscillators," in *Conference Digest. The Joint Thirtieth International Conference on Infrared and Millimeter Waves and Thirteenth International Conference on Terahertz Electronics (IEEE Cat. No. 05EX1150C)*, G. R. Neil and B. Danly, Eds., Williamsburg, VA, Sept. 2005, pp. 237–238.

[2] G. Dammertz, S. Alberti, A. Arnold, D. Bariou, P. Brand, H. Braune, V. Erckmann, O. Dumbrajs, G. Gantenbein, E. Giguet, R. Heidinger, J. P. Hogge, S. Illy, J. Jin, W. Kasparek, K. Koppenburg, H. P. Laqua, F. Legrand, W. Leonhardt, C. Lievin, G. Michel, G. Neffe, B. Piosczyk, O. Prinz, T. Rzesnicki, M. Schmid, M. Thumm, M. Q. Tran, X. Yang, and I. Yovchev, "High-power gyrotron development at Forschungszentrum Karlsruhe for fusion applications," *IEEE Trans. Plasma Sci.*, vol. 34, no. 2, pp. 173–186, Apr. 2006.

[3] L. Becerra, G. Gerfen, R. Temkin, D. Singel, and R. Griffin, "Dynamic nuclear polarization with a cyclotron resonance maser at 5 T," *Phys. Rev. Lett.*, vol. 71, no. 21, pp. 3561–3564, Nov. 1993.

[4] V. Weis, M. Bennati, M. Rosay, J. Bryant, and R. Griffin, "High-field DNP and ENDOR with a novel multiple-frequency resonance structure," *J. Magn. Reson.*, vol. 140, pp. 293–299, 1999.

[5] M. Rosay, V. Weis, K. E. Kreischer, R. J. Temkin, and R. G. Griffin, "Two-dimensional ^{13}C-^{13}C correlation spectroscopy with magic angle spinning and dynamic nuclear polarization," *J. Am. Chem. Soc.*, vol. 124, no. 13, pp. 3214–3215, Apr. 2002.

[6] V. Bajaj, C. Farrar, M. Hornstein, I. Mastovsky, J. Vieregg, J. Bryant, B. Elena, K. Kreischer, R. Temkin, and R. Griffin, "Dynamic nuclear polarization at 9 Tesla using a novel 250 GHz gyrotron microwave source," *J. Mag. Res.*, vol. 160, no. 2, pp. 85–90, Feb. 2002.

[7] B. Kulke, "Limitations on millimeter-wave power generation with spiraling electron beams," *IEEE Trans. Electron Devices*, vol. 19, no. 1, pp. 71–79, Jan. 1972.

[8] I. Bott, "A powerful source of millimetre wavelength electromagnetic radiation," *Phys. Lett.*, vol. 14, no. 4, pp. 293–294, Feb. 1965.

[9] M. Hornstein, V. Bajaj, R. Griffin, and R. Temkin, "Continuous-wave operation of a second harmonic gyrotron oscillator at 460 GHz," *IEEE Trans. Plasma Sci.*, vol. 34, no. 3, pp. 524–533, June 2006.

[10] M. K. Hornstein, V. S. Bajaj, R. G. Griffin, K. E. Kreischer, I. Mastovsky, M. A. Shapiro, J. R. Sirigiri, and R. J. Temkin, "Second harmonic operation at 460 GHz and broadband continuous frequency tuning of a gyrotron oscillator," *IEEE Trans. Electron Devices*, vol. 52, no. 5, pp. 798–807, May 2005.

[11] W. Herrmannsfeldt, "EGUN: An electron optics and gun design program," Stanford Linear Accelerator Center, Stanford, California, Technical Report SLAC-0331 UC-28, Oct. 1988.

[12] B. Danly and R. Temkin, "Generalized nonlinear harmonic gyrotron theory," *Phys. Fluids*, vol. 29, no. 2, pp. 561–567, Feb. 1986.

[13] M. Yeddulla, G. Nusinovich, and T. Antonsen, "Start currents in an overmoded gyrotron," *Phys. Plasma*, vol. 10, no. 11, pp. 4513–4520, Nov. 2003.

[14] K. Kreischer, T. Kimura, B. Danly, and R. Temkin, "High-power operation of a 170 GHz megawatt gyrotron," *Phys. Plasmas*, vol. 4, no. 5, pp. 1907–1914, May 1997.

[15] J. Zhao, G. Nusinovich, H. Guo, J. Rodgers, and V. Granatstein, "Axial mode locking in a harmonic-multiplying, inverted gyrotwystron," *IEEE Trans. Plasma Sci.*, vol. 28, no. 3, pp. 597–605, June 2000.

Chapter 9   Gradual Winding of the Bacteriorhodopsin Chromophore in the First Half of Its Ion-Motive Photocycle: a Dynamic Nuclear Polarization-Enhanced Solid State NMR Study

By exploiting sub-terahertz (250 GHz) radiation from a gyrotron oscillator, we have enhanced the sensitivity of NMR spectra of native bacteriorhodopsin samples using dynamic nuclear polarization. We report the first NMR spectra of the K intermediate in the ion-motive photocycle of bacteriorhodopsin. The intermediate is identified by its reversion to the resting state of the protein in red light and by its thermal decay to two successive substates of the L intermediate. The ^{15}N chemical shift of the Schiff base in K indicates that contact has been lost with its counterion. Under these circumstances, the visible absorption of K is expected to be more red-shifted than it is and this suggests torsion around single bonds of the chromophore. This is in contrast to the development of a strong counterion interaction and double bond torsion in L. Thus the storage of photon energy is primarily electrostatic in K and is transferred to torsional modes in L. This transfer is facilitated by the reduction in bond alternation that occurs with the initial loss of the counterion interaction, and is driven by the re-entrainment of the Schiff base under the influence of a new counterion interaction. The torsion developed in the chromophore in the first half of the photocycle is probably responsible for enforcing vectoriality in the pump by causing a decisive switch in the connectivity of the active site once the Schiff base counterion is neutralized by proton transfer.

9.1   Introduction

The light-driven ion pump, bacteriorhodopsin (bR), has been studied extensively since it was discovered in the 1970's. This effort has garnered a great deal of information about the structure of the protein and the changes that it undergoes during its functional photocycle. However, it remains unclear how the protein stores and channels energy to translocate ions and prevent backflow.

An important feature of the pump cycle (Figure 9-1) is that the change in the connectivity of the active site between the two sides of the membrane occurs midway through the photocycle (in the transition from the early M state to the late M state), long after the initial photoisomerization of the retinylidene chromophore from all-trans to 13-cis (Figure 9-2) and long before the thermal reisomerization of the chromophore at the end of the photocycle. Since the change in connectivity is divorced from the major isomerization events, much attention has been directed to the process(es) that might be responsible. However, in the fuller context, the more interesting question is how the active site remains connected to the extracellular surface for so long after the photoisomerization event, and what finally releases it from that set of interactions. In this light, it is not surprising that vibrational spectroscopy finds a strained chromophore in the K and L intermediates and a relaxed chromophore in the N intermediate [1]. Evidence of strain is also seen in solid state NMR spectra. Furthermore, solid state NMR has pinpointed the release of strain to the transition from early M to late M (i.e., coincident with the connectivity change) and determined that the strain in L and early M is dominated by torsion about double bonds [2, 3]. Of course, such torsion is expected to store more energy than torsion about single bonds. In the present work, we push further

back in the photocycle to learn how the torsion seen in the L and early M intermediates develops.
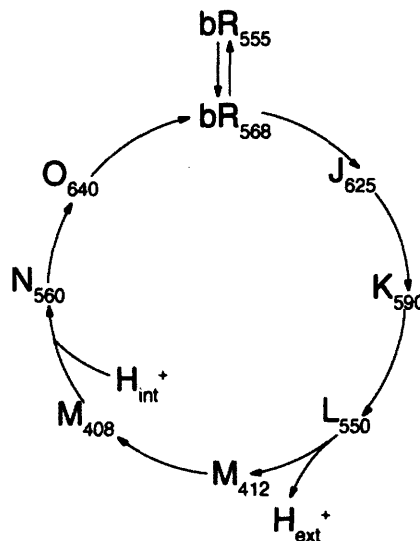
Figure 9-1: The ion-motive photocycle of bacteriorhodopsin. The subscript on each photocycle intermediate indicates wavelength of maximum visible absorbance.
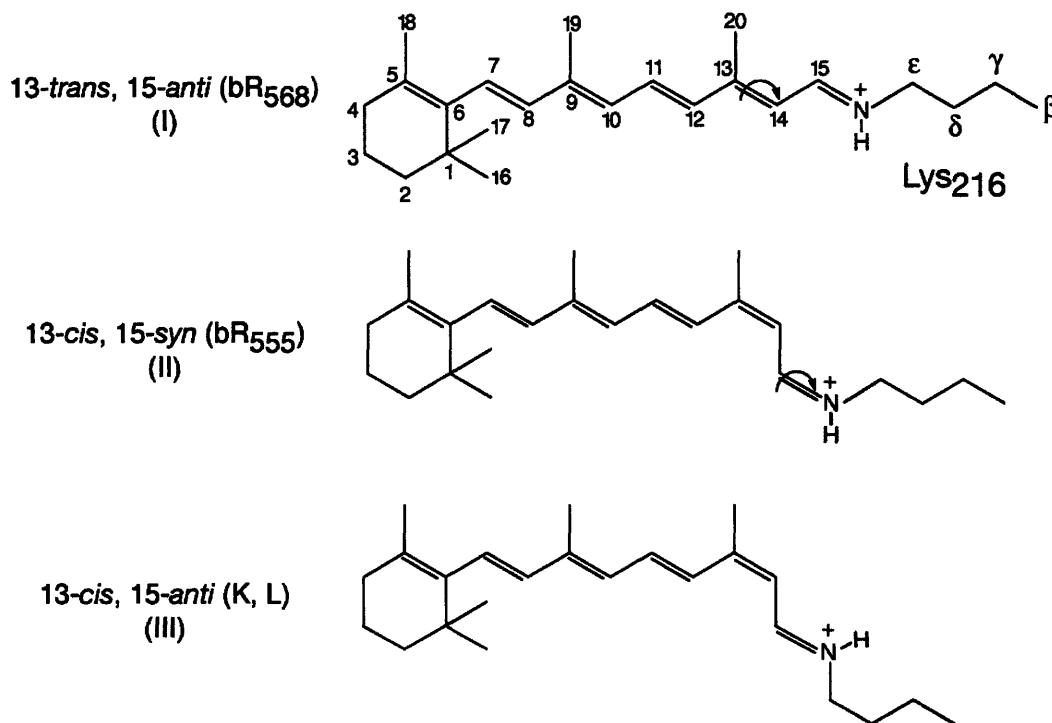
Figure 9-2: Retinal configurations in the early photocycle intermediates of bacteriorhodopsin.

NMR has the advantage of providing unique, non-perturbing, site-specific probes that are relatively readily applicable to mixtures of states, such as are obtained in studies of functional intermediates [4, 5]. On the other hand, NMR has the disadvantage of low sensitivity due to the small equilibrium polarization of nuclear spins. Recently, Dynamic Nuclear Polarization (DNP), in which the greater polarization of electron spins is transferred to the nuclear spins prior to the NMR experiment [6-8], has been demonstrated to provide large signal enhancements in bacteriorhodopsin in magnetic fields of 5 T [9]. Here we apply DNP at 9 T, the highest magnetic field at which DNP experiments have been performed to date [10]. The DNP experiment currently requires the application of a continuous radiofrequency field at, or near, the electron resonance frequency and cryogenic temperatures to attenuate spin-lattice relaxation processes that might otherwise compete with polarization transfer. Happily, the low temperatures are also useful for trapping the early photocycle intermediates of bR [11]. As a result, we have been able to observe the K state for the first time by NMR and identify two L substates according to their appearance in the thermal relaxation of K.

The ^{15}N chemical shift of the Schiff base in these three early photocycle intermediates suggests that the mode of energy storage is different in each. By comparison to halide salts of 13-*cis*,15-*anti* retinylidenes and bR variants in which the Schiff base counterion is neutralized, we conclude that the interaction between the chromophore and its counterion is lost in K, but becomes progressively restored and strengthened in the substates of L. At the same time, single bond torsion in the chromophore of the K intermediate is gradually superseded by double bond torsion in the L intermediates. These results suggest that photon energy is stored primarily in

electrostatic modes in K and is gradually transferred to torsional modes in the progression from L_1 to L_2. Since release of this torsion has previously been shown to coincide with the switch in the connectivity of the active site, it is likely responsible for enforcing vectoriality in the pump.

9.2 Methods and Materials

9.2.1 Sample Preparation

$[\zeta^{-15}N]$lysine-labelled bR was prepared by growing *Halobacterium salinarium* strain (JW-3) in a synthetic medium containing L-[$\zeta^{-15}N$]lysine [12]. The purple membrane, isolated and purified according to the method of Oesterhelt and Stoeckenius [13], was washed in 0.3M guanidinium hydrochloride at pH 10, until the supernatant had the same pH, and then washed further with 60% glycerol (v/v, for cryoprotection) containing 0.3 M guanidinium hydrochloride, and 40 mM 4-amino TEMPO (the exogenous nitroxide radical required for the DNP experiments [14]), at pH 10. The washed purple membrane was collected in a pellet by ultracentrifugation (1 hour at 323,000 g) and packed into the middle third of a 4 mm diameter single-crystal sapphire rotor which is transparent at both optical and millimeter-wave frequencies. The drive tip was bonded to the sapphire rotor using a low-temperature epoxy to avoid problems associated with thermal contraction at cryogenic temperatures. The sample was reversibly sealed using a vespel screw which threads into a Kel-F top spacer of a diameter such that it must be inserted under liquid nitrogen. The total sample volume was 57 mL.

9.2.2 Preparation of Photocycle Intermediates

In order to generate photocycle intermediates, light was delivered to the sample using a multimode fiber which penetrates the stator housing perpendicular to the rotor and projects a diffuse beam of diameter comparable to the sample size. The light sources were a 300 mW diode-pumped solid-state laser, operating at 532 nm (green), and an argon/krypton ion laser producing 1 W at 647 nm (red). Each photocycle intermediate was accumulated at the temperature which maximizes its yield relative to other states and then cooled (3-5 K/min) to 90 K to trap the intermediate for data acquisition. Operation of either laser raised the sample temperature by less than 0.5 K.

bR_{568}: bR_{568} (the "light adapted" state), was generated by irradiation of the dark-adapted mixture (bR_{568} and bR_{555}) with 532 nm light for 45 minutes at 278 K.

K intermediate: The K state was generated by irradiation of bR_{568} at 90 K with 532 nm light for 45 minutes.

L_1 and L_2: The L_1 and L_2 states were prepared, first, by thermal relaxation of the K intermediate at 150, 160, or 170 K. Both states were also prepared directly by irradiation of bR_{568} at 150 K with red light from a 647 nm laser for four hours.

M_o and M_n: The early M intermediate (M_o) was prepared by irradiation of bR_{568} with green light at 210 K for 45 minutes. The late M intermediate (M_n) was prepared by thermal relaxation of early M at 260 K.

In order to avoid interference with the generation of photocycle intermediates, the spinning frequency of the MAS rotor was monitored using weak IR light for illumination.

9.3 DNP/NMR Spectroscopy

All experiments were carried out at 9 T. The 250 GHz e⁻/380 MHz ^{1}H spectrometer includes a three RF channel (^{1}H, ^{13}C, ^{15}N) probe that incorporates matching transmission lines to provide remote tuning, high isolation between the channels, and high stability with respect to temperature variations in the sample chamber. Operation of the spectrometer employs custom-designed NMR data acquisition hardware and software (D.J. Ruben).

Millimeter-wave power is produced by a 250 GHz gyrotron oscillator. The beam is directed to the sample through a quasi-optical transmission circuit consisting of two HE_{11}-mode overmoded corrugated waveguides and an optical matching circuit between them [10, 15]. Gaussian mode purity is maintained throughout the transmission system, resulting in negligible transmission losses, and 2-4 W of power are delivered to the sample. The transmission circuit incorporates a quasi-optical beamsplitter for feedback regulation of the microwave power. A computer control system guarantees safe and unattended operation of the device with power stability of better than 1%.

Cryogenic magic angle spinning is accomplished through the use of bearing and drive nitrogen gas streams which have been cooled using a pressurized heat exchanger immersed in liquid nitrogen. The gas transfer lines incorporate integral heaters and calibrated resistive temperature sensors for feedback regulation of the temperature. However, the temperatures that we report are measured in the sample chamber using a Fabry-Perot interferometric thermometer, which is immune to magnetic and radiofrequency fields and is accurate to within 1 K. The spinning frequency was regulated to within 2-3 Hz by a pneumatic controller.

All ^{15}N chemical shifts are referenced indirectly to liquid ammonia by using adamantane as an external standard and following the procedure of Zilm and co-workers [[16]]. Due to the temperature dependence of the chemical shift, which can arise due to intrinsic and extrinsic (instrument-related) factors, we have referenced all spectra using the chemical shift of adamantane at the temperature of acquisition (usually 90 K).

One dimensional NMR spectra were recorded using cross-polarization [17, 18] with high power proton decoupling and magic angle spinning [19, 20] for high resolution. Typically, the cross polarization involved a ^{1}H field of 45 kHz, with the ^{13}C or ^{15}N power ramped linearly over the n=1 matching condition. Data were acquired with optimized TPPM [21] decoupling at 100 kHz field strength and magic angle spinning at a frequency of 6.25-6.5 kHz.

9.4　Results

Figure 9-3 shows ^{15}N spectra of [ζ-^{15}N]lysine-labelled bR under various conditions. The only change in these spectra, from one case to another, is in the signal from the Schiff base nitrogen of the retinylidene chromophore. These minor contributions to the spectrum can usually be detected within a few hours due to the 40-fold enhancement in sensitivity provided by DNP.

The spectrum of the dark-adapted sample [Figure 9-3(a)] shows bR_{555} and bR_{568} in the expected 60:40 proportion. Subsequent irradiation at 275 K with green light converts bR_{555} to bR_{568} [Figure 9-3(b)]. The following three spectra [Figure 9-3(c,d,e)] show that different intermediates accumulate depending on the temperature at which light adapted bR is irradiated.

Irradiation at 90K produces two new signals, the larger one upfield of bR_{568} and a smaller one downfield of bR_{568}. Neither of these has been detected by NMR previously. The major product can be assigned to the K state on multiple grounds: first, irradiation with red light results in the expected reversion to bR_{568}; second, as discussed further below, thermal relaxation (in the dark) at 150-170 K gives rise to the previously observed L photocycle intermediate, confirming that the newly observed species is an intermediate in the functional photocycle. The minor product disappears over a few hours at 90 K. Thus it appears to be an unstable side-product of the formation of K. According to visible spectroscopy, the generation of K is accompanied by the formation of iso-bR and pseudo-bR, both of which relax to bR_{568} in the dark at 77K [22]. Based on the yields reported in the literature, we tentatively assign the small, most downfield, signal in Figure 9-3(c) to iso-bR.

At 150K, the photocycle proceeds beyond the K intermediate, and the L intermediate accumulates. The two Schiff base signals observed under these conditions [Figure 9-3(d)] reproduce earlier observations [23]. The stronger of the two signals was previously assigned to the L state based on the wavelength dependence of its intensity and on thermal relaxation to the M state. However, for the weaker of the two signals, it was not possible to exclude the possibility of a photo-product of L. In the present work, access to lower temperatures allows us to unambiguously assign both signals as substates of L, according to their appearance as products of the thermal relaxation of the K intermediate (about which more below). It should be noted that Figure 9-3(d) shows no evidence of the K state, although the sample has been cooled to 90K for data acquisition. Previous observations of K on cooling L [24] may have been due to irradiation of

residual light adapted bR. In our experiments, cooling and data acquisition occur in the dark.
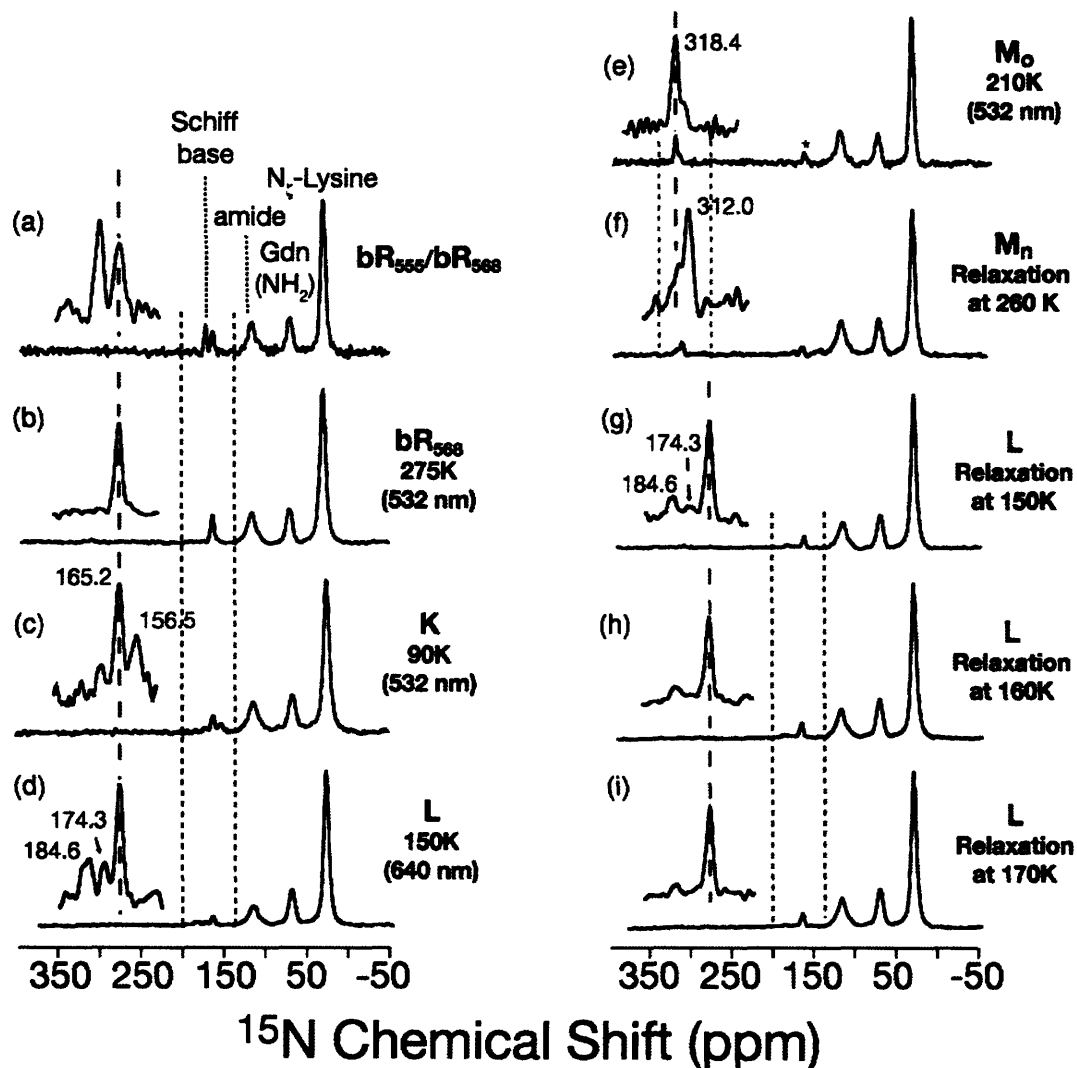
Figure 9-3: ^{15}N spectra of photocycle intermediates of [^{15}N]lys-bR. Insets expand the regions between the dashed blue lines and the red dashed lines clarify the relationships between the signals shown in the insets. All intermediates are accumulated by irradiation or thermal relaxation at the temperature of maximum yield, as indicated in the figure, and then trapped at 90K for sensitivity-enhanced detection with DNP: (a) dark-adapted thermal equilibrium mixture of bR$_{555}$ and bR$_{568}$; (b) light-adapted mixture produced by irradiation of the species in (a) with 532 nm green light at 275 K; (c) a mixture of the K intermediate with bR$_{568}$, produced by irradiation of bR$_{568}$ with 532 nm light at 90 K; (d) a mixture of the L$_1$ and L$_2$ states with bR$_{568}$, generated by direct excitation of bR$_{568}$ with 640 nm (red) light at 150 K; (e) the early M intermediate of bR, produced by irradiation of bR$_{568}$ with 532 nm (green) light at 210 K; (f) the late M photointermediate, produced by relaxation of the species in (e) at 260 K; (g-i) the products of the relaxation of the species in (c) at 150K, 160K, and 170K include intermediates L$_1$ and L$_2$ in proportions that reflect their order in the bR photocycle.

At higher temperatures, the photocycle progresses beyond the L intermediate, and the M intermediate accumulates. The extremely low-field signal of the Schiff base [Figures 9-3(e) and 9-3(f)] reflects the deprotonation of the Schiff base at this stage of the photocycle. At 210 K, the major product is the early M intermediate [Figure 9-3(e)]. Warming to 260 K yields the late M intermediate [Figure 9-3(f)]. This also reproduces previously observed behaviour [2, 3] and shows that the very high glycerol content of these samples has not significantly disturbed the progress of the photocycle.

The remaining spectra [Figures 9-3(g,h,i)] show the products of thermal relaxation of the K intermediate at 150 K, 160 K and 170 K. The fact that both of the signals produced by irradiation at these temperatures [Figure 9-3(d)] are also produced by thermal relaxation of a single K species suggests that the signals reflect two different L substates. At 150 K [Figure 9-3(g)], both L species are clearly evident. However, at higher temperatures [Figures 9-3(h,i)], the smaller, higher field, component gradually disappears. This suggests that the lower field component follows the higher field component in the photocycle and we therefore refer to the latter as L_1 and the former as L_2. This inference of two successive L states is in agreement with a recent analysis of time resolved visible spectra [25] and might explain the greater disorder found in x-ray crystallography of the L state at 150 K than at 170K [26].

In the foregoing spectra, linewidths for the ^{15}N Schiff base resonance are typically130-170 Hz. Since the chemical shift depends strongly on the electrostatic and electronic environment, these linewidths indicate a well-ordered chromophore structure and a distinct environment for each photocycle intermediate.

Table 9.1: ^{15}N chemical shifts of the Schiff base in bR

Intermediate	Chemical Shift (ppm vs. liquid NH_3)
bR_{555}	173.5 ± 0.65*
bR_{568}	165.2 ± 0.60
Iso-bR	175.4 ± 0.65*
K	156.5 ± 0.72
L_1	174.3 ± 1.02
L_2	184.6 ± 0.83
M_o	318.4 ± 0.63
M_n	312.0 ± 0.65*

* experimental uncertainty estimated by monitoring lysine resonance at 31.1 ppm

Chemical shifts for the Schiff bases of each of the eight species observed in the present work are summarized in Table 9.1. Most species were generated at least three times to provide a statistical measure of the uncertainty. However, for the less important species, we estimate the accuracy of the Schiff base chemical shifts from an analysis of the resonances of the free lysine sidechains in 61 independent ^{15}N spectra of three different samples. These chemical shift deviations were found to follow an approximately normal distribution, with a standard deviation of 0.65 ppm.

9.5   Discussion

9.5.1 Dynamic Nuclear Polarization

This work is the first application of dynamic nuclear polarization to functional intermediates of a protein. With signal enhancements of up to 40-fold, most 1D spectra can be acquired within an hour and longer data acquisition allows the detection of minor components. In spite of the necessity of doping with free radicals, the spectra are of comparable resolution to those obtained in earlier studies at higher temperatures, as long as cryoprotection conditions are adjusted to avoid phase separation of the sample with

repeated thermal cycling to liquid nitrogen temperatures. That these conditions are largely compatible with previous protocols for the generation and trapping of photocycle intermediates is demonstrated by the results in Figure 9-3.
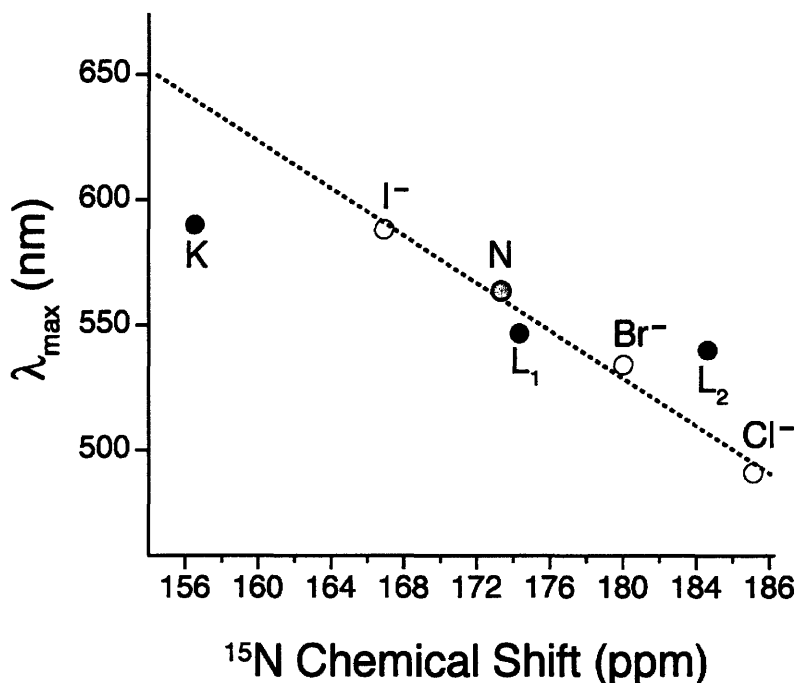
Figure 9-4: ^{15}N chemical shifts and wavelengths of maximum visible absorption for the Schiff base in halide salts of 13-*cis*,15-*anti* retinylidene model compounds [27] (O) and in the early photocycle intermediates of bacteriorhodopsin (●). The dashed line is a linear fit to the halide series data. For the L substates, we assign the reported wavelengths of maximum visible absorbance for the early, minor component and the major, late component [25] to our species L₁ and L₂, respectively.

9.5.2 Schiff Base-Counterion Interactions

The chemical shift of the Schiff base nitrogen in retinylidenes is extremely sensitive to the interactions of the Schiff base with hydrogen bonding and counterion partners [2, 3, 23, 27, 28]. In early work on bR, this sensitivity provided evidence for a hydrogen-bonded complex counterion in bR₅₆₈ [29-31] that was confirmed by x-ray crystallography a decade later [32]. It also indicates that the deprotonated Schiff base in each M

intermediate has a hydrogen bonding partner that has not yet been identified. In the present work, we find that the Schiff base signal is far upfield (small chemical shift) in the K intermediate and gradually moves downfield (larger chemicals shifts) in the L intermediate, as shown along the horizontal axis of Figure 9-4. Whereas the shifts of the L substates are comparable to those of 13-*cis*,15-*anti* retinylidene halides, the shift of the K intermediate is so far upfield that it only compares to the shifts of acid blue bR [31] and D85N bR [2], in which the Schiff base counterion has been neutralized by pH titration and mutation, respectively. This suggests that the Schiff base in K has lost contact with the original counterion, a result that is consistent with findings by FTIR [33]. Since both D85 and D212 remain unprotonated in K, the loss of the counterion interaction must reflect movement in the active site, as expected upon isomerization of the chromophore. However, the single narrow NMR signal of the K intermediate indicates a discrete state, in contrast to the considerable disorder seen in NMR spectra of the bR variants with a neutralized counterion.

Narrow NMR lines, indicative of order in the active site, persist through the rearrangements in the L substates that result in establishment of a counterion interaction which is intermediate in strength between that of the iodide and bromide salts in L_1 and between that of the bromide and chloride salts in L_2. As has been noted earlier [23], these counterion interactions are stronger than the counterion interaction in bR_{568} (the Schiff base ^{15}N resonance of which is farther upfield than the most upfield of the all-trans,15-anti retinylidene halides) and the candidates for the interactions in the active site of L are few. Either the Schiff base in L_1 and L_2 is approaching one of the two carboxylic acids in the active site more closely than in bR_{568}, or the water hydrogen bonded to the Schiff

base is becoming highly polarized. The latter seems more likely and has motivated speculation that bR may be acting as an inward-driven hydroxyl pump rather than an outward-driven proton pump [4, 5].

9.5.3 Polyene Torsion

The interactions of the Schiff base affect not only the chemical shift of the nitrogen, but also the visible spectrum of the chromophore. For a given configuration of the retinylidene, the relationship between the ^{15}N chemical shift and the frequency of maximum visible absorbance is linear [3, 23, 27, 28]. This is illustrated in Figure 9-4 for a set of halide salts of 13-*cis*,15-*anti* retinylidenes. In this series, the only variation from one model compound to the other is the counterion. Comparison with the data for the 13-*cis*,15-*anti* intermediates of the bR photocycle (also shown in Figure 9-4) must take into account other influences on the visible spectrum, particularly strain in the polyene chain. Distortion involving rotations about single bonds gives rise to wavelengths of maximum visible absorption that are shorter than expected based on the ^{15}N chemical shift; conversely, distortion involving torsion about double bonds yields wavelengths of maximum visible absorption that are longer than expected based on the ^{15}N chemical shift. These relationships were the basis of previous conclusions that the change in connectivity in the active site coincides with a release of double bond torsion in the chromophore [2].

Here, we extend this analysis to earlier stages of the photocycle. As shown in Figure 9-4, the K intermediate is blue shifted relative to expectations based on its Schiff base environment (*i.e.*, not as red shifted as expected) whereas the L_2 intermediate is red

379

shifted relative to expectations based on its Schiff base environment. This suggests that chromophore strain in the K intermediate is primarily about single bonds. Since torsion about single bonds does not store much energy, the data suggest that the energy in the K intermediate is stored primarily in the electrostatics of breaking the interaction between the Schiff base and its counterion. In contrast, chromophore strain in the L_2 intermediate appears to be primarily about double bonds. Such strain stores more energy and is presumably "paid" for by re-establishment of a counterion interaction. The L_1 intermediate falls between these two poles, with an intermediate counterion interaction and no significant shift in the visible spectrum. In this respect, it is like the N intermediate which is regarded as having a relaxed chromophore. However, since L_1 must have an energy intermediate between that of the K and L_2 states, it probably has a mixture of single and double bond torsion.

Table 9.2: Dihedral angles in the bR chromophore as determined by x-ray crystallography

intermediate	bR_{568}	K	L
pdb entry	1C3W	1MOK	1OOA
angle			
C14–C15=Nζ–Cε	–163°	131°	44°
C13=C14–C15=Nζ	179°	174°	161°
C12–C13=C14–C15	–157°	–56°	31°
C11=C12–C13=C14	178°	169°	151°
C10–C11=C12–C13	179°	179°	–178°

Table 9.2 shows torsion angles in bR found by fitting polyene coordinates to electron densities from x-ray diffraction [26, 34]. The results for the L intermediate agree with our qualitative conclusion that double bond torsion dominates just before Schiff base deprotonation ([23] and the present work). However, the fit to electron densities also finds double bond torsion dominating in the K intermediate, which is inconsistent with the NMR results.

The present overall picture is one of initial storage of energy in breaking the Schiff base-counterion interaction, with relatively little energy stored in polyene torsion, followed by stronger twisting of the chromophore, under the influence of new counterion interactions. The transfer of energy from electrostatic modes to torsional modes would be facilitated by the reduction of bond order alternation in the polyene (corresponding to delocalization of the retinylidene charge) when the counterion interaction is initially broken, and would be driven by the establishment of a new counterion interaction.

9.6   Conclusions

DNP-enhanced solid state NMR spectroscopy at cryogenic temperatures has provided the first NMR observation of the K intermediate of the ion-motive photocycle of bR, and afforded firm identification of the NMR signals of two, successive L intermediates. The ^{15}N chemical shifts of the chromophores of these species indicate that the Schiff base loses contact with its counterion in K and establishes a new counterion interaction in L_1 that becomes stronger in L_2. At the same time, low energy, single bond torsion in K evolves to high energy, double bond torsion in L_2. Thus photon energy initially stored in electrostatic form is transformed to torsion that is probably responsible for the decisive switch in the connectivity of the Schiff base when its counterion is neutralized by proton transfer. Such a switch is critical for preventing backflow in the pump.

9.7   References

[1]   Weidlich, O.; Siebert, F., Time-Resolved Step-Scan Ft-Ir Investigations of the Transition from Kl to L in the Bacteriorhodopsin Photocycle - Identification of Chromophore Twists by Assigning Hydrogen-out-of-Plane (Hoop) Bending Vibrations. *Applied Spectroscopy* **1993**, 47, (9), 1394-1400.

[2]   Hatcher, M. E.; Hu, J. G. G.; Belenky, M.; Verdegem, P.; Lugtenburg, J.; Griffin, R. G.; Herzfeld, J., Control of the pump cycle in bacteriorhodopsin: Mechanisms elucidated by solid-state NMR of the D85N mutant. *Biophysical Journal* **2002**, 82, (2), 1017-1029.

[3]   Hu, J. G.; Sun, B. Q.; Bizounok, M.; Hatcher, M. E.; Lansing, J. C.; Raap, J.; Verdegem, P. J. E.; Lugtenburg, J.; Griffin, R. G.; Herzfeld, J., Early and late M intermediates in the bacteriorhodopsin photocycle: A solid-state NMR study. *Biochemistry* **1998**, 37, (22), 8088-8096.

[4]   Herzfeld, J.; Lansing, J. C., Magnetic resonance studies of the bacteriorhodopsin pump cycle. *Annual Review of Biophysics and Biomolecular Structure* **2002**, 31, 73-95.

[5]   Herzfeld, J.; Tounge, B., NMR probes of vectoriality in the proton-motive photocycle of bacteriorhodopsin: evidence for an 'electrostatic steering' mechanism. *Biochimica Et Biophysica Acta-Bioenergetics* **2000**, 1460, (1), 95-105.

[6]   A. Abragam, W. P., *Compt. Rend.* **1958**, 246, 2253.

[7]   R.A.Wind; M. J. Duijvestijn, C. V. D. L., A. Manenschijn, J. Vriend, *Progress in NMR Spectroscopy* **1985**, 17, (1), 33-57.

[8]   Goldman, M., *Spin temperature and nuclear magnetic resonance in solids.* Clarendon Press: Oxford, 1970.

[9]   Rosay, M.; Lansing, J. C.; Haddad, K. C.; Bachovchin, W. W.; Herzfeld, J.; Temkin, R. J.; Griffin, R. G., High-frequency dynamic nuclear polarization in MAS spectra of membrane and soluble proteins. *Journal Of The American Chemical Society* **2003**, 125, (45), 13626-13627.

[10]   Bajaj, V. S.; Farrar, C. T.; Mastovsky, I.; Vieregg, J.; Bryant, J.; Elena, B.; Kreischer, K. E.; Temkin, R. J.; Griffin, R. G., Dynamic nuclear polarization at 9T using a novel 250 GHz gyrotron microwave source. *Journal of Magnetic Resonance* **2003**, 160, (2), 85-90.

[11]   Balashov, S. P.; Ebrey, T. G., Trapping and spectroscopic identification of the photointermediates of bacteriorhodopsin at low temperatures. *Photochemistry and Photobiology* **2001**, 73, (5), 453-462.

[12]   Argade, P. V.; Rothschild, K. J.; Kawamoto, A. H.; Herzfeld, J.; Herlihy, W. C., Resonance Raman-Spectroscopy of Specifically [Epsilon-15n]Lysine-Labeled Bacteriorhodopsin. *Proceedings of the National Academy of Sciences of the United States of America-Biological Sciences* **1981**, 78, (3), 1643-1646.

[13]   D. Oesterhelt, W. S., *Proceedings Of The National Academy Of Sciences Of The United States Of America* **1973**, 70, 2853-2857.

[14]   Gerfen, G. J.; Becerra, L. R.; Hall, D. A.; Griffin, R. G.; Temkin, R. J.; Singel, D. J., High-Frequency (140 Ghz) Dynamic Nuclear-Polarization - Polarization Transfer to a Solute in Frozen Aqueous-Solution. *Journal of Chemical Physics* **1995**, 102, (24), 9494-9497.

[15]   Woskov, P. P.; Bajaj, V. S.; Hornstein, M. K.; Temkin, R. J.; Griffin, R. G., Corrugated waveguide and directional coupler for CW 250-GHz gyrotron DNP experiments. *Ieee Transactions on Microwave Theory and Techniques* **2005**, 53, (6), 1863-1869.

[16]   Morcombe, C. R.; Zilm, K. W., Chemical shift referencing in MAS solid state NMR. *Journal of Magnetic Resonance* **2003**, 162, (2), 479-486.

[17]   Hediger, S.; Meier, B. H.; Ernst, R. R., Cross-Polarization under Fast Magic-Angle Sample-Spinning Using Amplitude-Modulated Spin-Lock Sequences. *Chemical Physics Letters* **1993**, 213, (5-6), 627-635.

[18]   Pines, A.; Gibby, M. G.; Waugh, J. S., Proton-Enhanced Nmr of Dilute Spins in Solids. *Journal of Chemical Physics* **1973**, 59, (2), 569-590.

[19]   Andrew, E. R.; Bradbury, A.; Eades, R. G., *Nature* **1958**, 182, 1659.

[20]   Lowe, I. J., *Physical Review Letters* **1959**, 2, 285.

[21]   Bennett, A. E.; Rienstra, C. M.; Auger, M.; Lakshmi, K. V.; Griffin, R. G., Heteronuclear Decoupling in Rotating Solids. *Journal of Chemical Physics* **1995**, 103, (16), 6951-6958.

[22]   Balashov, S. P., Photoreactions of the photointermediates of bacteriorhodopsin. *Israel Journal of Chemistry* **1995**, 35, (3-4), 415-428.

[23]   Hu, J. G. G.; Sun, B. Q. Q.; Petkova, A. T.; Griffin, R. G.; Herzfeld, J., The predischarge chromophore in bacteriorhodopsin: A N-15 solid-state NMR study of the L photointermediate. *Biochemistry* **1997**, 36, (31), 9316-9322.

[24]   Kouyama, T.; Nishikawa, T.; Tokuhisa, T.; Okumura, H., Crystal structure of the L intermediate of bacteriorhodopsin: Evidence for vertical translocation of a water molecule during the proton pumping cycle. *Journal of Molecular Biology* **2004**, 335, (2), 531-546.

[25]   Zimanyi, L.; Saltiel, J.; Brown, L. S.; Lanyi, J. K., A Priori Resolution of the Intermediate Spectra in the Bacteriorhodopsin Photocycle: The Time Evolution of the L Spectrum Revealed *Journal of Physical Chemistry, A* **2006**, 110, (7), 2318-2320.

[26]   Lanyi, J. K.; Schobert, B., Mechanism of proton transport in bacteriorhodopsin from crystallographic structures of the K, L, M-1, M-2, and M-2 ' intermediates of the photocycle. *Journal of Molecular Biology* **2003**, 328, (2), 439-450.

[27]   Hu, J. G.; Griffin, R. G.; Herzfeld, J., Synergy In The Spectral Tuning Of Retinal Pigments - Complete Accounting Of The Opsin Shift In Bacteriorhodopsin. *Proceedings Of The National Academy Of Sciences Of The United States Of America* **1994**, 91, (19), 8880-8884.

[28]   Hu, J. G. G.; Griffin, R. G.; Herzfeld, J., Interactions between the protonated Schiff base and its counterion in the photointermediates of bacteriorhodopsin. *Journal Of The American Chemical Society* **1997**, 119, (40), 9495-9498.

[29]   Degroot, H. J. M.; Harbison, G. S.; Herzfeld, J.; Griffin, R. G., Nuclear Magnetic-Resonance Study of the Schiff-Base in Bacteriorhodopsin - Counterion Effects on the N-15 Shift Anisotropy. *Biochemistry* **1989**, 28, (8), 3346-3353.

[30]   Harbison, G. S.; Roberts, J. E.; Herzfeld, J.; Griffin, R. G., Solid-State Nmr Detection Of Proton-Exchange Between The Bacteriorhodopsin Schiff-Base And Bulk Water. *Journal Of The American Chemical Society* **1988**, 110, (21), 7221-7223.

[31]   Degroot, H. J. M.; Smith, S. O.; Courtin, J.; Vandenberg, E.; Winkel, C.; Lugtenburg, J.; Griffin, R. G.; Herzfeld, J., Solid-State C-13 And N-15 Nmr-Study Of The Low Ph Forms Of Bacteriorhodopsin. *Biochemistry* **1990**, 29, (29), 6873-6883.

[32]   Luecke, H.; Schobert, B.; Richter, H. T.; Cartailler, J. P.; Lanyi, J. K., Structure of bacteriorhodopsin at 1.55 angstrom resolution. *Journal of Molecular Biology* **1999**, 291, (4), 899-911.

[33]   Kandori, H.; Belenky, M.; Herzfeld, J., Vibrational frequency and dipolar orientation of the protonated Schiff base in bacteriorhodopsin before and after photoisomerization. *Biochemistry* **2002**, 41, (19), 6026-6031.

[34]   Schobert, B.; Cupp-Vickery, J.; Hornak, V.; Smith, S. O.; Lanyi, J. K., Crystallographic structure of the K intermediate of bacteriorhodopsin: Conservation of free energy after photoisomerization of the retinal. *Journal of Molecular Biology* **2002**, 321, (4), 715-726.

Chapter 10 Complexities of Chromophore Isomerization in Bacteriorhodopsin Revealed by Polarization-Enhanced NMR of Uniformly Labeled Samples: Assignments of Stable and Transient States, Distance Measurements, Torsion Angle Experiments

In the archael membrane protein bacteriorhodopsin, photoisomerization of a retinal chromophore is coupled to ion translocation via a sequence of photocycle intermediates. In spite of decades of study by a wide variety of techniques, the mechanism of energy transduction is not well understood. Here, we elucidate the process by using multidimensional solid state NMR to assign chemical shifts of the chromophore in cryogenically trapped photocycle intermediates. In order to overcome intrinsic sensitivity limits, we enhance the NMR signals by a factor of ~120 using dynamic nuclear polarization (DNP), in which sub-terahertz (250 GHz) radiation from a cyclotron resonance maser is used to transfer spin polarization from electrons to nuclei, prior to the NMR experiment. Significant changes in chemical shifts report on chromophore rearrangement during the photocycle. The detection of four discrete substates of the L intermediate shows that the chromophore faces multiple barriers on the way to forming a fully planarized 13-cis C13=C14 bond in late L. Unexpected complexity is also seen in dark adaptation. These results demonstrate the capability of DNP to routinely extend the reach and range of NMR methods in membrane proteins.

10.1   Introduction

Bacteriorhodopsin (bR) is a 26-kDa integral membrane protein from *Halobacterium salinarum* that functions as a light-driven ion transporter. Seven transmembrane helices surround a transport channel in which the Schiff base (SB) formed between retinal and lysine 216 provides the binding site for a labile proton. The counterion of the protonated SB comprises a hydrogen bonded complex of two carboxyl groups (D85 and D212), one guanidyl group (R82), and several water molecules.

Absorption of a visible photon by the retinylidene chromophore initiates the photocycle,

$$bR_{568} \xrightarrow{h\nu} J_{625} \to K_{590} \to L_{550} \xrightarrow{-H^+} Mo_{412} \to Mn_{408} \xrightarrow{+H^+} N_{520} \to O_{640}{}^1 \tag{10.1}$$
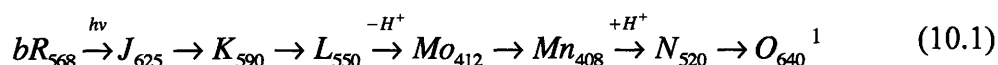
which results in the net translocation of a single proton across the membrane. The vectoriality and irreversibility of the pump cycle is enforced by a switch in connectivity of the SB from the extracellular to the cytoplasmic side between the early and late M states. On the other hand, photoisomerization of the chromophore occurs at the start of the photocycle, suggesting that an understanding of the structural rearrangements in early photocycle intermediates will be critical in understanding the impetus for the eventual switch in SB connectivity.

In order to obtain high-resolution structural information about bR photocycle intermediates, the photocycle must be arrested by cryogenic trapping. The accumulation of a desired intermediate can be favored by manipulation of the temperature and the wavelength of visible light irradiation. However, in most cases, the result is a mixture of photocycle intermediates. A unique advantage of NMR is that signals from these

---

[1] M_o and M_n in our nomenclature correspond respectively to early and late M, or M_1 and M_2 in the nomenclature of other investigators.

intermediates can be distinguished because of the dependence of the chemical shift interaction on local conformation. Studies of bR by solid state NMR (SSNMR) have distinguished the two M intermediates [1] previously only postulated and more L intermediates than previously inferred from time-resolved optical spectroscopy (as has been discussed previously in this thesis). In addition, SSNMR has elucidated details of the chromophore environment in various intermediates and provided evidence for an electrostatically-driven, torsion-based mechanism for enforcing vectoriality in the pump [2-4].

Multidimensional SSNMR has long been recognized as a promising and general tool in the structural biology of molecules that are inaccessible to X-ray crystallography and solution state NMR. Recent successes include determination of the structures, at atomic resolution, of a microcrystalline protein [5] and an 11-residue amyloid fibril [6] (and in this thesis). In analogy to successful approaches from solution state NMR [7], these studies involve uniformly isotopically enriched samples and multidimensional chemical shift correlation experiments for both resonance assignment and the collection of structural constraints. While this approach is tractable in small systems (<50 residues), it is not routine in larger systems. In higher molecular weight samples, the dispersion of signals in multiple chemical sites and across multiple dimensions of the experiment dramatically reduces the sensitivity of NMR, already low because of the small equilibrium polarization of nuclear spins at accessible temperatures. The sensitivity deficit is even more acute when NMR signals are further divided among multiple conformational states, as in trapped photocycle intermediates of bR. A one or two order

of magnitude enhancement of NMR sensitivity over the existing state of the art is required for broad application of multi-dimensional SSNMR methods.

Several methods have been developed to improve the sensitivity of NMR experiments. They include improvements in instrumentation and pulse sequence technology. An example is dynamic nuclear polarization (DNP), through which the ~660-fold greater spin polarization of unpaired electrons in a paramagnetically doped sample is transferred to nuclei prior to an NMR experiment [8-30]. Here, we demonstrate the utility of DNP as a general tool for biological SSNMR at 380 MHz (9T). These experiments rest on several recent developments: first, an understanding of the polarization transfer mechanisms operative at high magnetic fields [31] together with the development of optimized paramagnetic polarizing agents for doping diamagnetic biological samples [32]; second, the development of millimeter-wave gyrotrons (cyclotron resonance masers) capable of stable and continuous operation at frequencies above 250 GHz [8, 11, 14, 16, 33-38]; and, third , the development of cryogenic, variable-temperature NMR probes incorporating delivery of millimeter wave radiation for DNP and, for application to photocycle intermediates, visible radiation for excitation of the sample (this thesis). The application of DNP to bR has resulted in a signal enhancement of ~40 [8]. Further enhancement results purely due to the cryogenic cooling of the sample: because signal acquisition is conducted at 90 K, in order to both trap bR photointermediates and attenuate spin-lattice relaxation processes that interfere with electron-nuclear polarization transfer, the signals are enhanced by an overall Boltzmann factor of ~120 over room temperature experiments which do not incorporate DNP.

The present experiments on the intermediates of bR are designed to probe structural rearrangements in the chromophore early in the photocycle, when the absorbed energy is still relatively localized. Conformational changes can be deduced by monitoring changes in chemical shifts. Furthermore, chemical shift assignments are necessary for future direct measurement of conformational parameters, such as internuclear distances and torsion angles. Our approach entails frequency-selective heteronuclear magnetization transfer [39] from the SB nitrogen (K216 Nζ) to the C15 of retinal or the Cϵ of K216 , followed by homonuclear polarization transfer [40, 41] along the retinal polyene in the former case or along the K216 side chain in the latter case. Because of the extended topology of the chromophore, these experiments involve polarization transfer across up 4 to 5 ^{13}C-^{13}C bonds and distribution of the Schiff base magnetization across 6 to 7 ^{13}C sites in a single experiment, resulting in polarization transfer efficiencies of < 5% in the worst case. Due to the simultaneous presence of multiple photocycle intermediates, minor conformational intermediates are diluted by factors of 2 to 20. Nevertheless, two-dimensional spectra can be recorded in 12 to 48 hours in all photocycle intermediates of bR due to the high signal enhancement provided by DNP.
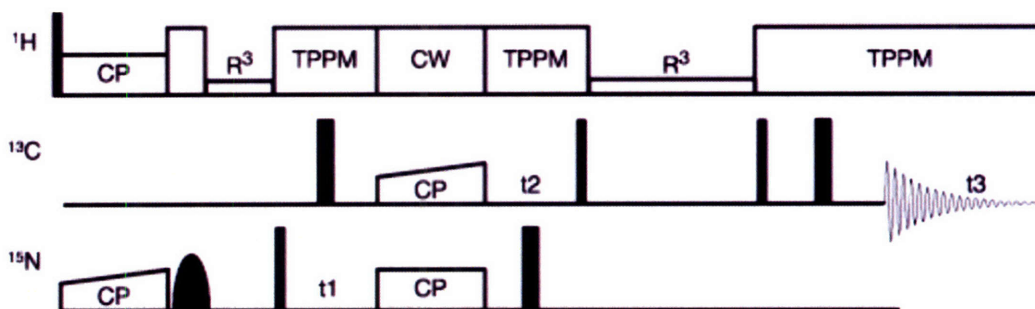
Figure 10-1: Pulse sequence for multidimensional, band-selective heteronuclear correlation experiment. Following ^{1}H-^{15}N cross-polarization, the Schiff base resonances are selected by a soft, band-selective ^{15}N pulse from the "E" family of selective excitation pulses optimized for solid state NMR. Signals corresponding to the Schiff base are along the z-axis, and all other signals are allowed to dephase. Following rotation to the transverse plane, the ^{15}N magnetization arising from the Schiff base resonances evolves under the ^{15}N chemical shift during t1 and then is transferred selectively to retinal-C15 or K216-Cε by SPECIFIC CP. The ^{15}N and ^{13}C fields are chosen to provide spectrally selective, chemical-shift dependent transfer to either directly bonded carbon, while a ramp of 5-6% in the ^{13}C RF field results in quasi-adiabatic transfer with improved efficiency. Following an optional t2 evolution period under the ^{13}C chemical shift, further correlations are established by homonuclear mixing using proton-driven spin diffusion with an R^{3} recoupling field or RFDR recoupling. Parameters were optimized using simplex optimization implemented in home-built NMR acquisition hardware and software (D. Ruben).

Figure 10-2: Nζ-C15-Cx heteronuclear correlation experiments for the retinylidene chromophore in the early photocycle intermediates of bR. Each row is the result of a single 2D experiment. (A) dark adapted state (…. H acquisition) (B) light-adapted state (12 h acquisition); (B) the K intermediate with residual bR$_{568}$ (12 h acquisition); (C) the L intermediate with residual bR$_{568}$ (48 h acquisition).
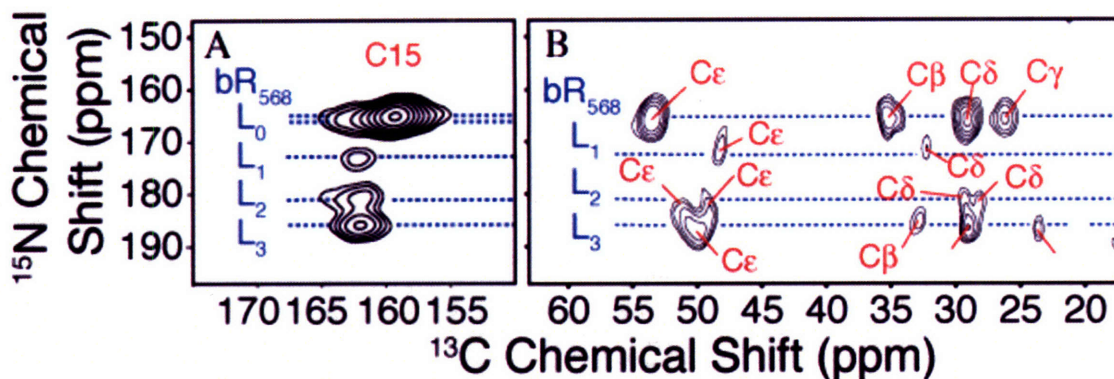
Figure 10-3: (A) Nζ-C15 and (B) Nζ-Cε-Cx heteronuclear correlation experiments for the L intermediate. The spectrum in (B) provides resonance assignments of K216 through magnetization transfer along its side chain.

A subset of the spectra obtained for various states of bR are shown in Figures 10-2 and 10-3. (The complete set of spectra is provided in Supporting Information.) In these spectra, the sensitivity of the ^{15}N chemical shift of the protonated SB to the strength of its counterion interaction resolves resonances from different intermediates in the nitrogen dimension of the 2D spectra. The combination of correlations via C15 (Figure 10-2) and Cε (Figure 10-3) result in 9 to 10 chemical shift assignments for each intermediate. The ^{13}C assignments are based on the relative intensities of the cross-peaks and the expected chemical shift range for each site. Not shown are non-chromophore regions of the spectra which contain some cross-peaks from long-range magnetization transfer to several nearby residues in the active site, including D85, D212, and nearby W86.

Examining the spectra in detail, we see that Figure 10-2B shows a single ^{13}C resonance for each accessible carbon in the light adapted (LA) chromophore. Similarly, Figure 10-2C shows a single ^{13}C resonance for each accessible carbon in the K photocycle intermediate (in addition to the resonances from the coexisting LA state). In contrast, the dark adapted (DA) state and the L state are unexpectedly heterogeneous.

Dark adaptation is generally considered to involve the equilibration of a bicycle pedal isomerization between all-trans,15-anti bR_{568} and 13-cis,15-syn bR_{555}. However, Figure 10-2A shows cross-peaks with the ^{15}N chemical shift of bR_{568} there are not seen in the light adapted state. Thus it seems that some chromophore isomerization occurs without perturbing the interactions of the SB. In addition, there is a cross peak at a ^{15}N chemical shift different from that of either bR_{568} or bR_{555}. However, the weakness of the signal suggests that there is very little of this species.

Until recently, the L state was considered to be a single species. However, a recent analysis of time-resolved optical spectra resolved two substates [42-44] and our own recent 1D DNP SSNMR spectra identified three substates [this thesis]. The present 2D spectra (Figure 10-2D and Figure 10-3) now show four L substates. The new one, L_0, has a ^{15}N chemical shift so similar to that of bR_{568} that its presence is only detectable by its C15 signal in the N-C15 correlation spectrum (Figure 10-3A). In the N-C15-Cx spectrum (Figure 10-2D) this signal is obscured by the C13 signal of bR_{568}. That each ^{15}N Schiff base resonance is correlated to a distinct manifold of ^{13}C resonances, reflects the presence of an ensemble of well-defined substates rather than conformational disorder.

Table 10.1: ^{13}C Chemical shifts (ppm) of retinal carbons in photocycle intermediates of bR.

^{13}C position	LA	DA	DA-2	K	L1	L2	L3	Mo1, Mo2
C11	136.4	139.8						129.7
C12	134.5	125.9		141.2	137.7	121.7	122.1	127.1,125.5
C13	166.8				169.6			
C14	123.9	111.5		119.4	123.9	116.4	117.5	124,123
C15	160	163.3	164.6	159.7	163.7	162.3	162.7	165.4
C20	14.27	23.36			17.26	24.88	24.77	20.62
	13.95	24.37						
	13.7							
	15.92							
	12.52							

Table 10.2: ^{13}C Chemical shifts (ppm) of carbons of the lysine 216 side chain in photocycle intermediates of bR.

^{13}C position	LA	DA	K	L1	L2	L3	Mo1, Mo2
K216-Ce	54.22	50.82	50.5	53.51	50.4	50.4	58.11,
	53.74	49.1	50.89	48.27	50.87, 48.97	49.89	58.12
	53.5	48.55					
K216-Cd	29.23	30.22	28.42	32.34	28.2, 29.37	29.05	
K216-Cg	26.51	28.51	24.6	29.13*		23.69	
K216-Cb	34.7					32.8	
K216-Ca	56.11						

The presence of mixtures of intermediates and their substates has important implications for crystallography. Refinement of crystallographic data requires *a priori* estimates of the reaction stoichiometry, in addition to the assumption of additive contributions to the diffraction. Since visible spectroscopy is of very limited use in this regard, the crystallographic refinement of L state structures accumulated between 150 K-170 K is probably subject to significant uncertainties. Similar arguments apply in the case of Mo: multiple conformational substates of Mo have been reported in one-dimensional spectra of specifically labeled samples and the additional resonances assigned here through correlation spectroscopy conclusively show discrete conformations of the retinal, rather than static disorder.

Several retinal chemical shifts are particularly informative because their dependence on specific structural parameters is well understood. As noted earlier, the progression of the ^{15}N shifts of the SB indicates that the electrostatic interaction of the Schiff base with its counterion is broken in the K intermediate and that a new, stronger counterion interaction is established in discrete steps as the photocycle progresses through the L substates. This supports earlier evidence that electrostatic steering is important in driving the photocycle forward [2, 45]. The experiments presented here also reveal changes in the ^{13}C chemical shifts that reflect steric interactions between protons

on carbons three bonds apart (the γ-effect). In particular, as seen earlier in M_o and M_n, retinal C12 in L2 and L3 is shifted up field relative to bR_{568} due to the steric interaction of its proton with that of retinal C15. (That there is no comparable shift of the C15 resonance is due to the fact that the C15 proton is in steric conflict already in bR568, in this case with the C20 protons.) The important feature of the present spectra is that the up field shift of C12 is not yet present in L0 or L1. Thus, at least one of the three bonds between C12 and C15 must be rotated from the fully planar 13-cis conformation and planarity is reached only as the photocycle progresses towards the late L and M photocycle intermediates. These changes in the torsional degrees of freedom of the retinal chromophore are consistent with the proposal that strain in the chromophore is responsible for the abrupt change in connectivity between early and late M that is responsible for enforcing the vectorial action of the pump [2, 4, 45].
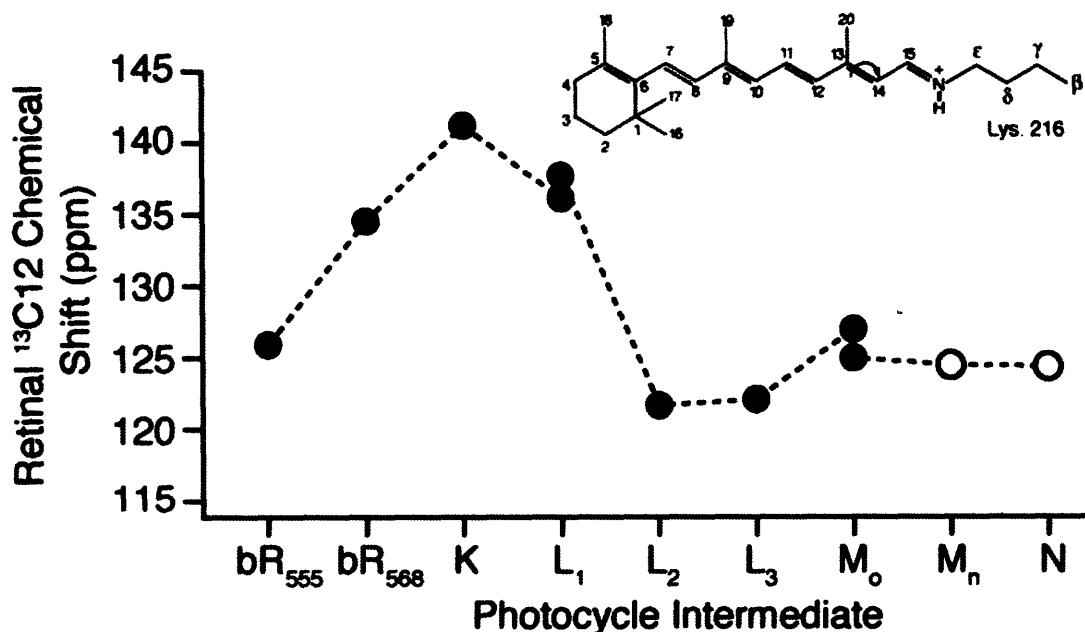
Figure 10-4: ^{13}C chemical shift of the C12 of retinal in the photocycle intermediates of bR (open circles denote previous measurements in selectively labeled samples).

In addition to providing important qualitative information about the active site, the present chemical shift assignments can be used to measure conformational constraints. Measurements in progress at this time focus on internuclear distances and torsion angles near the SB. Essential to this effort is the ~120-fold enhancement of spectral sensitivity afforded by DNP. Indeed the present application to bR demonstrates its potential value as a routine adjunct in high field solid state NMR experiments: Spectra from a substate of L that is present in ~5% yield in a protein/lipid complex of 35 kDa effective molecular weight suggest that spectra of a ~700 kDa system can be recorded in a similar amount of time, even at the modest magnetic field strength of 380 MHz. Recent extensions of this instrumentation to 460 GHz (700 MHz ^{1}H) [33, 34, 37] will aid applications in systems requiring greater chemical shift resolution. It should be noted that our efficiency of polarization transfer from electrons to nuclei is a fraction of its theoretical value (40/660 = ~6%) and a much higher DNP efficiency of ~40% has been realized at lower magnetic fields. By using improved polarizing agents, we anticipate that enhancements can be increased by at least a factor of 2. The enhancement may also be improved by using smaller samples or resonators optimized for aqueous samples, to increase the penetration of the microwaves into the sample. Finally, the DNP efficiency and total enhancement can be improved by operating at lower temperatures through the use of helium cooling gas, which is possible in the present apparatus without modification. The already important capabilities of DNP can thus easily be extended to enable new applications in the future.

10.2　Methods

10.2.1　Sample Preparation

The purple membrane, isolated and purified according to the method of Oesterhelt and Stoeckenius [46], was washed with 300 mM Gdn HCl, pH 10, and 40% (v/v) glycerol cryoprotectant as described in [1DPaper]. The sample was packed into a sapphire rotor that is transparent at both millimeter and optical wavelengths.

10.2.2　Accumulation of Different States

An optical fiber in the probe delivers green light (532 nm from a Coherent Verdi 6W DPSS laser) or red light (640 nm from a Coherent 599 dye laser pumped by the DPSS laser) to the rotating sample as needed. bR is dark-adapted by several hours of equilibration in the dark at room temperature and then light adapted by green light at 273 K. Different photocycle intermediates are accumulated by illumination of light adapted bR as follows:

  K:　　green light at 90K

  L's:　red light at 150K

  Mo:　green light at 210K.

The accumulated intermediates were cooled to 90K and their NMR spectra were acquired in the dark. The controlled cryogenic temperatures were achieved by using cooled dry nitrogen gas to drive magic angle spinning at 10 kHz.

10.3　Supporting Figures

Quasi-optical directional coupler
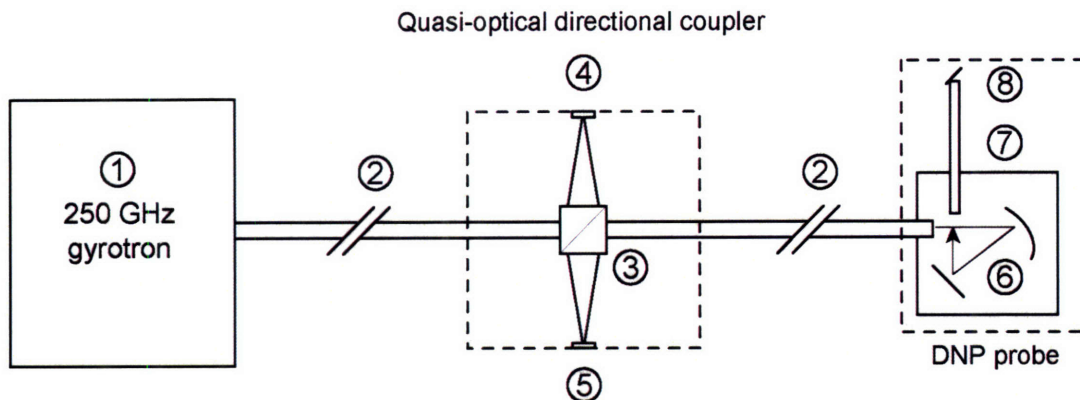
Figure 10-5(a): Schematic representation of the 250 GHz gyrotron, corrugated transmission system, and 380 MHz NMR probe. (1) 250 GHz gyrotron oscillator (2) Corrugated waveguide (22 mm i.d.). (3) Beam splitter; (4) Forward power detector; (5) Reflected power detector; (6) Focusing and reflecting mirror optics; (7) Helically corrugated waveguide (8 mm i.d.); and (8) Miter mirror.
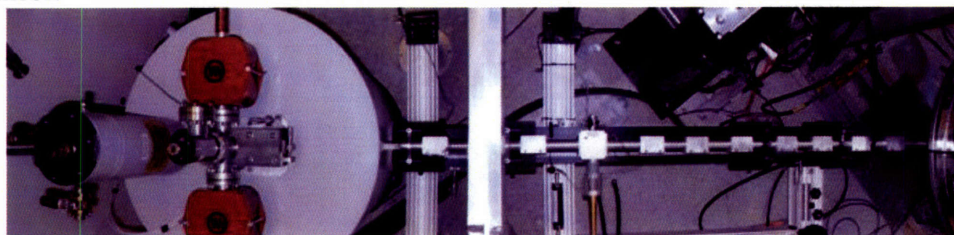
Figure 10-5(b): Composite photograph of the system illustrated schematically in Figure 10-5(a) *[left]* 250 GHz gyrotron the gyrotron tube is shown with vacion pumps in the gray superconducting magnet, *[center]* corrugated transmission system with the directional coupler visible in the center of the photograph, and *[right]* 380 MHz NMR magnet is visible on the edge of the photo. The NMR probe is not visible since it is under the magnet. The view in this photo is from above the gyrotron and waveguide looking down.
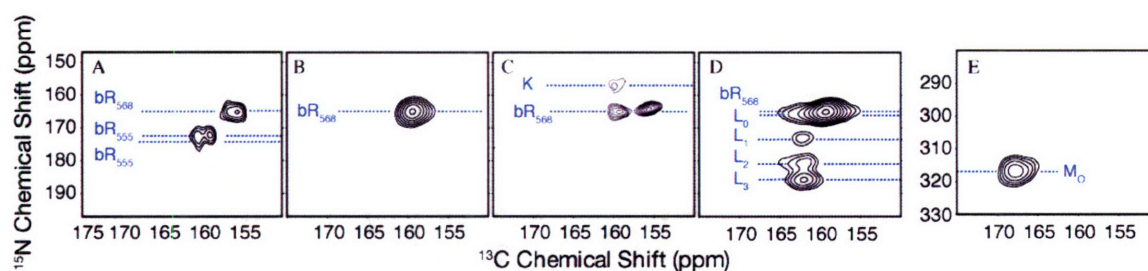
Figure 10-6: Nζ-C15 heteronuclear correlation experiments provide assignments of the K216-Nζ and retinal-C15 resonances in bR. (A) dark-adapted state ; (B) light-adapted state ; (C) the K intermediate with residual bR$_{568}$ and a short-lived side product with a ^{15}N chemical shift like that of bR$_{568}$; (D) the L intermediate with residual bR$_{568}$; (E) the Mo state. . This spectrum in C was acquired in 45 minutes with a non-uniform sampling of t1 to capture the signal of the side-product of K formation that decays within 1-2 hrs at 90K. Details of this approach and the reconstruction of the spectrum will be provided in a separate publication.

Figure 10-7: Nζ-C15 heteronuclear correlation experiments which trace the connectivity of resonances in the retinal chromophore of bR. (A) dark-adapted state ; (B) light-adapted state ; (C) the K state with residual bR$_{568}$; (D) the L state with residual bR$_{568}$; (E) The Mo state.
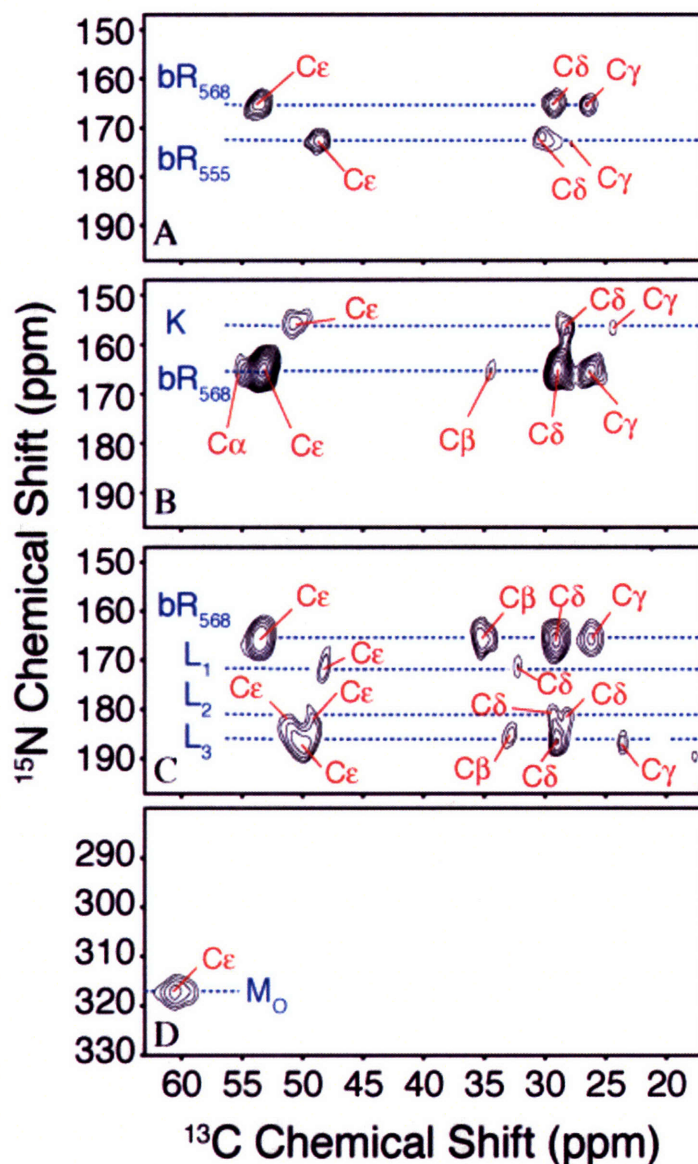
Figure 10-8: Nζ-Cε-Cx heteronuclear correlation experiments which trace the connectivity of resonances in K216 by magnetization transfer along its side chain. (A) light-adapted state; (B) the K state with residual bR_{568}; (C) the L state with residual bR_{568}; (D) The Mo state.

10.4 Unstable Photoproduct of Bacteriorhodopsin Probed by Dynamic Nuclear Polarization-Enhanced Solid State NMR with Non-Uniform Sampling

Bacteriorhodopsin (bR) is a 26 kDA integral membrane protein that functions as a light-driven ion pump in the archaea *Halobacterium salinarum*. Photoisomerization of the retinylidene chromophore initiates a sequence of changes that eventually results in the

expulsion of a single proton from the cell (or, equivalently, the uptake of a single hydroxyl). High-resolution structural information about these intermediates is necessary to discriminate between different models of the pump mechanism.

Structural studies of bR by crystallography or nuclear magnetic resonance (NMR) generally require trapping of photocycle intermediates through manipulation of the sample temperature and the frequency of irradiation. Rarely do the conditions favor one intermediate strongly over all others, and the result is generally a mixture of intermediates. Earlier studies of the bR photocycle using dynamic nuclear polarization (DNP)-enhanced NMR, in which the greater spin polarization of unpaired electrons is transferred to nuclei prior to the NMR experiment, have demonstrated that multidimensional NMR is capable of resolving even minor conformers in mixtures of intermediates.

Here, we combine reduced-dimensionality correlation spectroscopy with non-uniform sampling to record DNP-enhanced 2D spectra of the 532 nm photoproducts of [U-^{13}C,^{15}N]-bR in as little as 45 minutes. The short time scale of this acquisition permits observation not only of the K photocycle intermediate, but also of a transient side-product that decays within a few hours. Such side-products may complicate the interpretation of diffraction experiments which depend on knowledge of the reaction stochiometry. The present results demonstrate the utility of DNP NMR as a tool for rapid acquisition of structural information in membrane protein systems.

10.5   Non-linear sampling schemes

In its simplest manifestation, multidimensional Fourier transform NMR generates correlations by linear sampling of all incrementable time dimensions. While this is

acceptable for two and even three-dimensional NMR in stable biological samples, it results in prohibitively long acquisition times for spectra of higher dimensionality. It also has not been clear *a priori* that a linear sampling schedule produces optimal sensitivity and resolution per unit time. This problem, however, is not unique to NMR and has a rich history in many branches of science that deal with interferometry, including astronomy and radio astronomy. The reconstruction problem in interferometry involves obtaining the spectrum, S(f), given an observable O(f), where the instrument response is given by the matrix R, and the noise vector, N,

$$\vec{O}(f) = R \bullet \vec{S}(f) + \vec{N} \qquad (10.2)$$

The naïve mathematical inversion

$$\vec{S}(f) = R^{-1} \bullet \vec{O}(f) \qquad (10.3)$$

is appropriate only for invertible transformations, R, and in the absence of noise. A precise mathematical statement of well-posed inverse problems was provided by Hadamard in 1915: well-posed inverse problems require a unique solution which depends continuously on the parameters of the data. Inversion of non-linearly sampled data, however, is an ill-posed inverse problem that depends discontinuously on the data. Solution of such problems is generally impossible without introducing additional information about the data set into the inversion problem.

The process by which additional information is introduced into an inversion problem is called "regularization." For example, let us assume that the power spectrum of the perturbing noise is known. The Weiner filter, a kind of regularization method, then

suppresses the contributions of perturbed frequencies in the data reconstruction through the transformation

$$O'(f) = G(f) \bullet O(f) \qquad (10.4)$$

where

$$G(f) = \frac{PSF^*(f)}{PSF(f)^2 + \dfrac{P_n(f)}{P_s(f)}} \qquad (10.5)$$

The most common regularization transformation is the Tikhonov regularization. Given the aforementioned ill-posed inverse problem,

$$\vec{O}(f) = R \bullet \vec{S}(f) + \vec{N} \qquad (10.6)$$

the Tikhonov regularization instead involves solving a minimization problem to obtain S(f),

$$S = \min \left[R.S(f) - O(t) \right]^2 + \alpha \| S(f) \|^2 \qquad (10.7)$$

where α is a regularization parameter that penalizes solutions with a high norm. The Maximum Entropy Method (MEM) for reconstruction is a widely applied variant of this procedure in interferometry and NMR. In this process, the minimization problem is solved subject to the constraint that a Shannon-like entropy function,

$$S(f) = \sum_{j=0}^{N-1} R(|f_j|) \qquad (10.8)$$

is maximized. The precise form of the Entropy functional for an ensemble of spin-1/2 particles has been derived by Hoch, Stern and their co-workers [47-57].

While there have been numerous applications of the Maximum Entropy Method for spectral reconstruction, we note that it has the following unattractive features: (a) the physical basis of the entropy functional cannot be firmly justified; (b) solution of minimization problem for an N-dimensional dataset requires repeated operations on N-dimensional data matrices whose dimensionality can be quite high. As a compromise, Hoch proposed a row-wise reconstruction algorithm in which rows of a multidimensional data set are separately reconstructed. However, this approach suffers from uncontrolled nonlinearities which distort the spectra and prevent quantitative extraction of spectral intensities.

To search for a simpler spectral reconstruction method, we can employ linear algebraic techniques and determine how each candidate regularization transformation operates on the domain of singular values. Specifically, the singular value decomposition of matrix A,

$$A = USV^T \tag{10.9}$$

gives an expression for the nxn matrix A in terms of vectors $U=(U_1,U_2,\ldots,U_n)$, $V=(V_1,V_2,\ldots,V_n)$ and S, the diagonal matrix of singular values $S=diag(s_1,s_2,\ldots,s_n)$, defined by $AV_i=s_iU_i$ and $A^TU_i=s_iV_i$. Following the treatment of Vogel and co-workers, the formal solution of the Tikhonov inverse problem is

$$
\begin{aligned}
Y &= AX \\
X &= (A^T A + \alpha I)^{-1} A^T \\
&= (VS^T U^T USV^T + \alpha VIV^T)^{-1} VS^T U^T \\
&= V(S^T S + \alpha I)^{-1} S^T U^T \\
&= Vdiag(\frac{s_i^2}{s_i^2 + \alpha}\frac{1}{s_i})U^T
\end{aligned}
\tag{10.10}
$$

The expression in parentheses resembles a transfer function in the singular value domain: Tikhonov Regularization thus scales singular values in proportion to their size as compared to the regularization parameter, α. Since, in an ideal dataset, the first k linearly independent signal components will be represented by k singular values and vectors, this has the effect of removing noise from the reconstruction; the Maximum Entropy Method operates according to a similar principle.

In order to simplify the process of reconstruction, we elected to simply truncate the SVD at its first k terms, where k is an estimate of the number of cross peaks, and then solve the inverse reconstruction problem by global minimization using the truncated data set. This has the additional consequence of dramatically reducing the dimensionality of the minimization problem. For an N-dimensional experiment with ($n_1, n_2 ... n_n$) possible points in each dimension, programs for MEM generally operate on matrices of rank-(n_1 x n_2 x ... x n_n). In our rank-reduced approach, the solution domain is of rank-k, consisting of k n-element vectors and n singular values irrespective of the formal size of the data domain. The minimization algorithm operates efficiently, then, on the elements of the singular value decomposition directly. We note that a spectrum reconstructed this way can serve as an initial guess for subsequent minimization using MEM or other approaches, if this is desired.

10.6 Fast Detection of Transient Products in K Accumulation

In order to test the validity of this reconstruction approach, we recorded 2D spectra of bR immediately after production of the K photointermediate, using the pulse sequence previously described. Using the sampling schedule illustrated in Figure 10-8, we

recorded a 2D Nζ-C15 heteronuclear correlation experiment in the K photostate in less than 45 minutes with good sensitivity. Reconstruction of the spectrum reveals the presence of a transient photointermediate (Figure 10-9). We have therefore identified both the iso-bR and pseudo-bR side products of K accumulation that were previously inferred through their contributions to vibrational spectra at low temperatures[58].
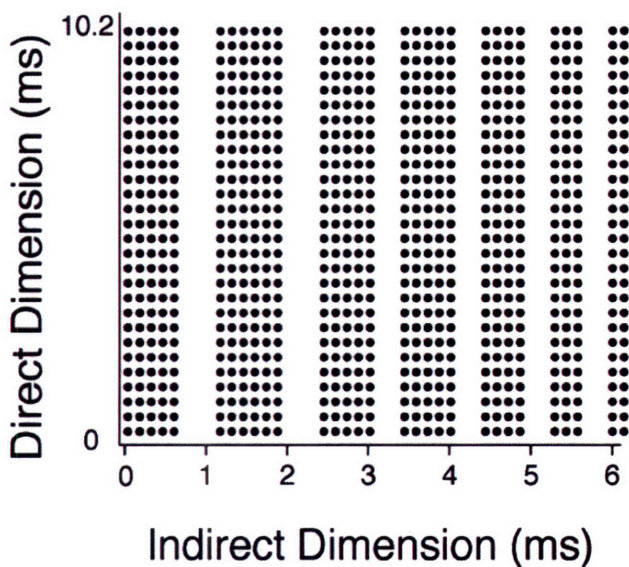
Figure 10-9: Sampling schedule used in non-linearly sampled 2D Nζ-C15 heteronuclear correlation experiment in the K photostate.
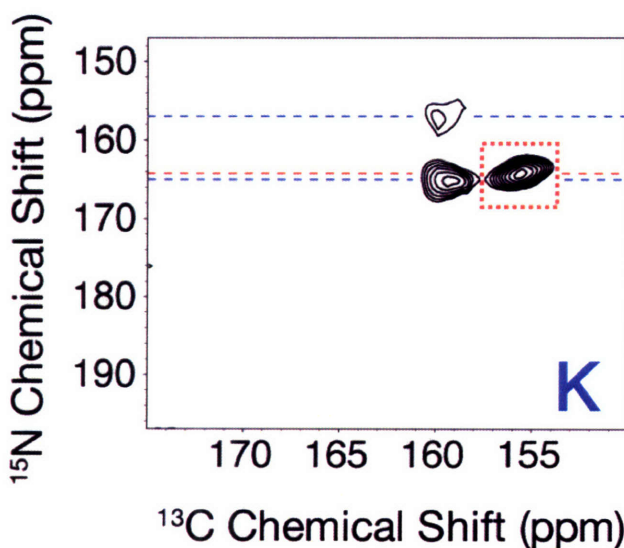
Figure 10-10: 2D Nζ-C15 heteronuclear correlation experiment in the K photostate. Note the presence of a transient photoproduct of K accumulation which decays within an hour.

10.7 Frequency-Selective TEDOR Experiments for Amino-Acid Selective Assignments and Heteronuclear Distance Measurements in bR

Distance measurements in uniformly labeled solids are complicated by the tendency of strong dipolar couplings between directly bonded spin pairs to obscure the weaker couplings of interest, a phenomenon called "dipolar truncation," which has been explained in earlier chapters. Even where dipolar truncation is absent due to the form of the recoupled Hamiltonian (*e.g.* REDOR experiments), strong heteronuclear dipolar couplings can compromise the sensitivity of the experiment. Further, evolution under the homonuclear ^{13}C-^{13}C J couplings in such systems imposes an overall modulation on the buildup or dephasing under the dipolar coupling, and it also can generate anti-phase coherences, which in turn give rise to phase-twisted line shapes. In order to circumvent these limitations, Jaroniec and co-workers introduced a frequency-selective REDOR [59, 60] experiment in which the detrimental effects of the J coupling are removed through the application of frequency-selective pulses. A logical extension of these techniques has been the 3D TEDOR experiment [61], in which multiple ^{13}C-^{15}N distances can be measured simultaneously or in a band selective manner in the context of a ^{13}C-^{15}N correlation experiment. In this case, the effects of the J coupling are respectively removed through the application of a coherence filter or frequency selective pulse.

Due to limited sensitivity, however, it has not yet been practical to apply this experiment to measure multiple weak dipolar couplings in membrane proteins. Further, in the case of bR, only distances in and around the chromophore and channel are of interest. This, in combination with the fact that several ^{15}N sites of interest are resolved in the ^{15}N dimension and have been assigned through previous DNP studies of bR, motivates a ^{15}N-frequency selective analog of the 3D TEDOR experiment (Figure 10-11).
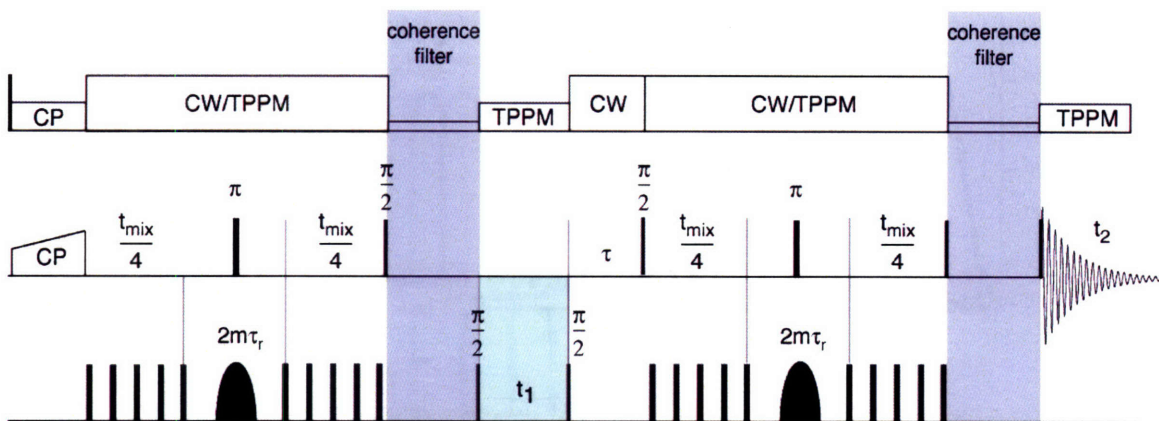
Figure 10-11: Pulse sequence for selective TEDOR transfer.

Following ramped, ^{1}H-^{13}C cross polarization, we apply a REDOR train to generate a ^{13}C-^{15}N antiphase coherence which evolves under the heteronuclear dipolar couplings. During the excitation period, a frequency selective pulse is applied on the nitrogen channel, with the result that only those ^{15}N nuclei within the pulse bandwidth contribute appreciably to the spin dynamics under REDOR. Following the excitation period, optional frequency labeling with the nitrogen chemical shift occurs during t_1. A second, frequency selective REDOR period converts the resulting coherence into observable magnetization on the ^{13}C channel, which is detected in t_2. A delay, t, is necessary to ensure that the time between REDOR periods is an integer number of rotor cycles. Finally, the ^{13}C-^{13}C J-couplings give rise to undesired zero-quantum and double-quantum coherences which, after the reconversion period, result in severe anti-phase distortions to the line shape and spurious cross-peaks in 2D spectra. Two variable-length coherence filters (z-filters) are applied to dephase these undesired coherences, resulting in undistorted and purely absorptive spectra.
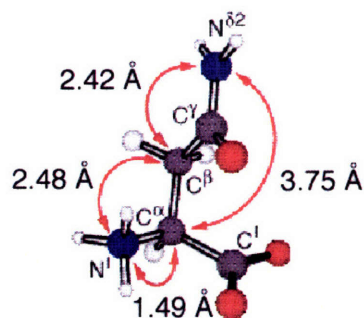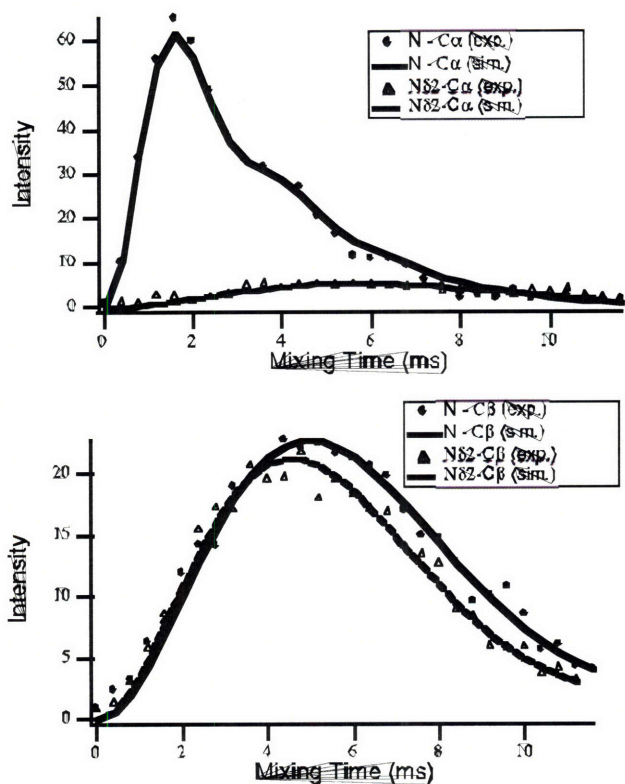
Figure 10-12: Application of fs-TEDOR experiment in asparagine.

Table 10.3: Heteronuclear distances measured with two-dimensional TEDOR experiment as applied to [U-^{13}C, ^{15}N]-Asparagine.

	fs-TEDOR (Å)	fs-REDOR (Å)	Neutron diffraction (Å)
N-C$^{\alpha}$	1.50	1.50	1.49
N$^{\delta 2}$-C$^{\alpha}$	3.24	3.58	3.75
N-C$^{\beta}$	2.46	2.49	2.48
N$^{\delta 2}$-C$^{\beta}$	2.41	2.44	2.42

As a test of fs-TEDOR, all heteronuclear distances in [U-^{13}C, ^{15}N]-asparagine were measured in two experiments, summarized in Figure 10-12 and Table 10.3, in good agreement with crystallographic distances. The sequence is currently being applied in [U-^{13}C, ^{15}N]-bR in combination with DNP for active site distance measurements. As a prelude to these measurements and to determine the capabilities of this sequence in DNP experiments, it was also applied to generate amino-acid specific side-chain assignments of the arginine region of bR, where six of the seven Arg. residues appear in the DNP-enhanced correlation spectra in Figure 10-13. In this case, the selective pulse was placed

on the arginine side chain ^{15}N resonances, and the TEDOR mixing time was set to favor two-bond (2.5 Å) couplings. Because directly bonded ^{13}C sites are coupled to several side chain ^{15}Ns, they are not expected to appear in this experiment.
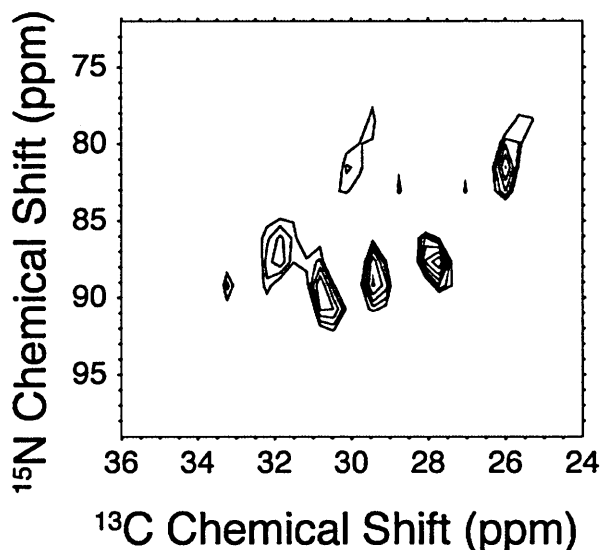
Figure 10-13: 2D heteronuclear correlation experiment of arginine side chain region of bR.

10.8 Measurement of the HNCH Torsion Angle and N-H Bond Distances in Uniformly Labeled bR with Dynamic Nuclear Polarization-Enhanced NMR

As outlined earlier in this chapter, vibrational spectroscopy and NMR chemical shift perturbation suggests that there are significant distortions in the planarity of the polyene chain in the vicinity of the Schiff base during the bR photocycle and support the electrostatic steering hypothesis for ion pumping in bR. The structure of retinal in the Schiff base region in photocycle intermediates of bR is therefore critically important to understanding the proton pumping mechanism. The internal coordinates of the retinal are, in principle, best constrained through the measurement of local torsion angles (see discussion in Chapter 11). Unfortunately, crystallographic structures are typically refined with planar retinal chromophores; even when they are not, extensive deconvolution of diffraction patterns is necessary to properly model mixtures of photointermediates, and

this produces uncertainty in the retinal conformation. The result, shown in Figure 10-17, is that the mechanistically important torsion angles are not reliably constrained by diffraction measurements. Solid state NMR, by contrast, is capable of direct determination of internuclear torsion angles with high accuracy [62-75], even in mixtures of photocycle intermediates. We defer a complete discussion of the tensor correlation experiments to Chapters 11 and 12 of this thesis and instead provide only a brief description here. In order to measure the H-Nζ-C15-H in the LA, L, and K states of bR, we utilized a Selective 3D HNCH experiment, shown in Figure 10-14. The sequence incorporates magnetization preparation steps for selective excitation of the Schiff base resonance as previously outlined. In the context of ^{13}C-^{15}N chemical shift correlation spectroscopy, the experiment measures correlated dephasing under the ^{1}H-^{15}N and ^{1}H-^{13}C dipolar interactions, recoupled using the γ-encoded TMREV [76] sequence. These dimensions are synchronously incremented to reduce the dimensionality of the experiment, resulting in a pseudo-3D sequence. As shown in Figure 10-15, this measurement is very similar to the HNCH measurements designed to provide constraints on the ϕ and ψ backbone torsion angles in peptides.
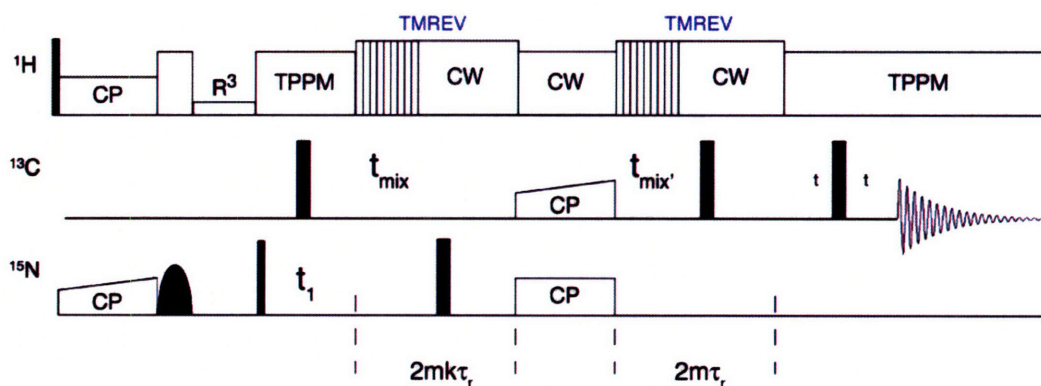
Figure 10-14: Sequence for selective 3D HNCH tensor correlation experiment.
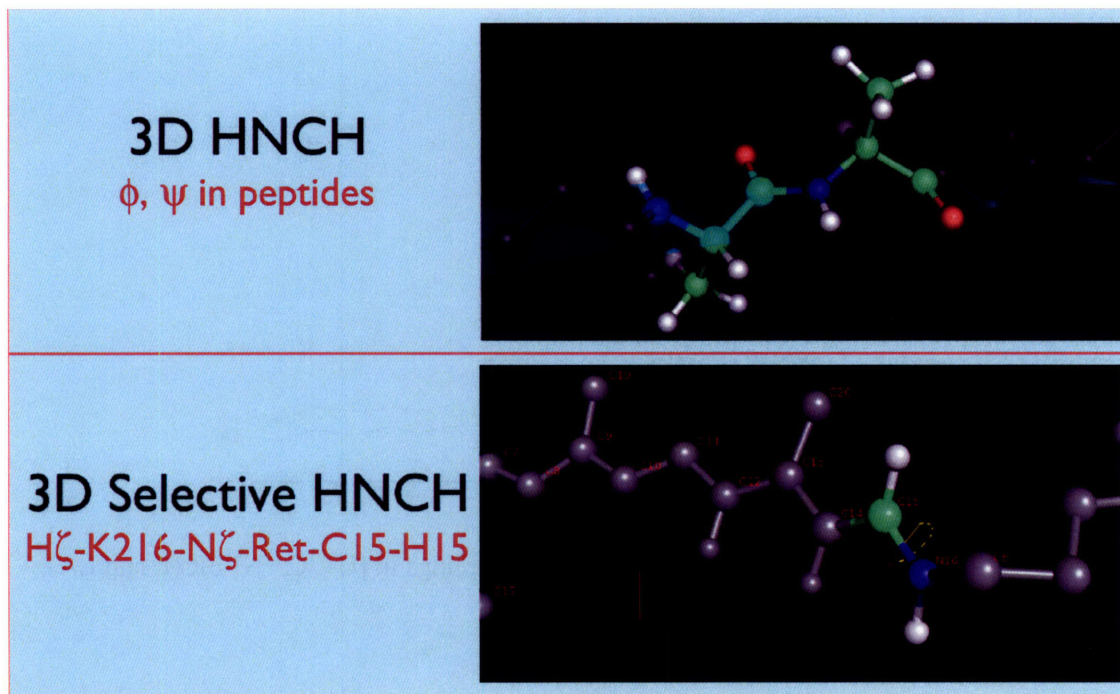
Figure 10-15: The relationship between 3D HNCH experiments in peptides and the 3D Selective HNCH experiment used in bR.

When either dipolar evolution time is set to zero, the result is a sequence that can be used for site-resolved heteronuclear distance measurements. An example of these measurements is shown in Figure 10-16, where the dephasing trajectory under TMREV has been Fourier transformed to yield a recoupled dipolar spectrum. The spectra demonstrate that the H-Nζ bond distance is identical in L2 and LA. In Figure 10-17, we illustrate the determination of the HNCH torsion angle in [U-^{13}C,^{15}N]-bR$_{568}$ in only 72 hours acquisition time, using Dynamic Nuclear Polarization. At the time of this writing, similar data have been collected in LA, L, and K photostates, and a global analysis is underway.
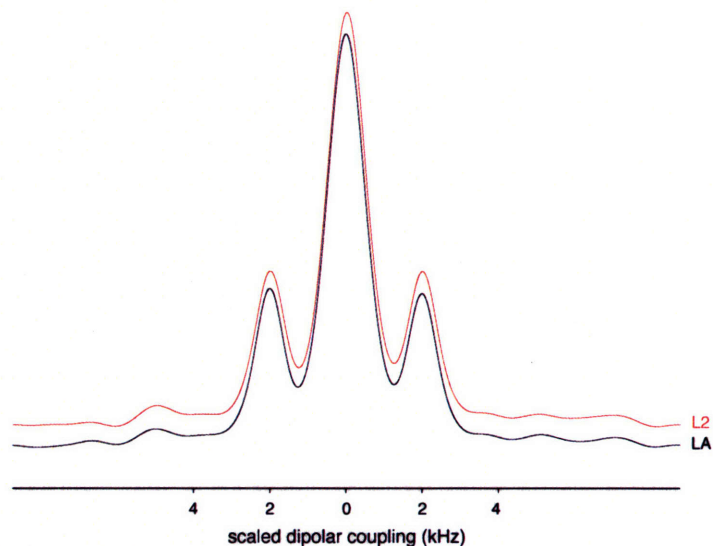
Figure 10-16: Recoupled dipolar lineshape for H-Nζ couplings in [U-^{13}C,^{15}N]-bR (L and LA).
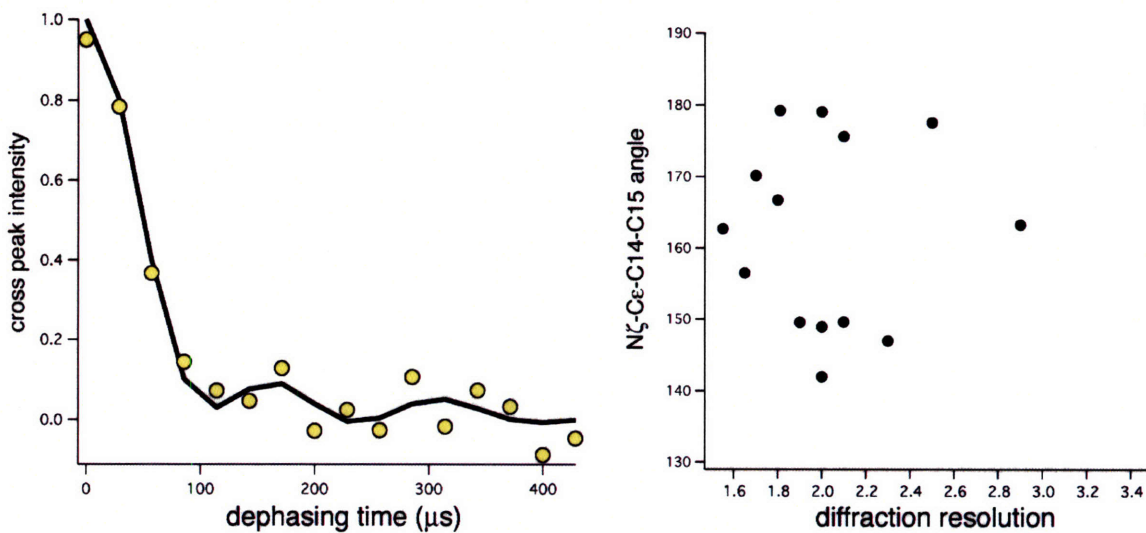
Figure 10-17: HNζ-C$_{15}$H torsion angle experiment conducted in [U-^{13}C,^{15}N]-bR in the L state. These data resulted from only 72 hours of acquisition time. The torsion angle is fit to 178±8° for bR$_{568}$. (right) the spread of torsion angle data in crystallographic studies of light-adapted bR.

10.9　　References

[1]　　Hu, J. G.; Sun, B. Q.; Bizounok, M.; Hatcher, M. E.; Lansing, J. C.; Raap, J.; Verdegem, P. J. E.; Lugtenburg, J.; Griffin, R. G.; Herzfeld, J., Early and late M intermediates in the bacteriorhodopsin photocycle: A solid-state NMR study. *Biochemistry* **1998,** 37, 8088-8096.

[2]   Hatcher, M. E.; Hu, J. G. G.; Belenky, M.; Verdegem, P.; Lugtenburg, J.; Griffin, R. G.; Herzfeld, J., Control of the pump cycle in bacteriorhodopsin: Mechanisms elucidated by solid-state NMR of the D85N mutant. *Biophysical Journal* **2002**, 82, (2), 1017-1029.

[3]   Herzfeld, J.; Hu, J. G.; Hatcher, M. E.; Belenky, M.; Verdegem, P.; Lugtenburg, J.; Griffin, R. G., NMR evidence for an electrostatically controlled, torsion-based switch in light-driven proton transport by bacteriorhodopsin. *Biophysical Journal* **2001**, 80, (1), 20a-20a.

[4]   Herzfeld, J.; Lansing, J. C., Magnetic resonance studies of the bacteriorhodopsin pump cycle. *Annual Review of Biophysics and Biomolecular Structure* **2002**, 31, 73-95.

[5]   Castellani, F.; van Rossum, B.; Diehl, A.; Schubert, M.; Rehbein, K.; Oschkinat, H., Structure of a protein determined by solid-state magic-angle-spinning NMR spectroscopy. *Nature* **2002**, 420, (6911), 98-102.

[6]   Jaroniec, C. P.; MacPhee, C. E.; Bajaj, V. S.; McMahon, M. T.; Dobson, C. M.; Griffin, R. G., High Resolution Molecular Structure of a Peptide in an Amyloid Fibril Determined by MAS NMR Spectroscopy. *Proc. Nat'l. Acad. Sci.* **2004**, 101, 711-716.

[7]   Cavanagh, J.; Fairbrother, W. J.; Palmer, A. G.; Skelton, N. J., *Protein NMR Spectroscopy: Principles and Practice*. Academic Press: San Diego, 1996.

[8]   Bajaj, V. S.; Hornstein, M. K.; Kreischer, K. E.; Sirigiri, J. R.; Woskov, P. P.; Mak, M.; Herzfeld, J.; Temkin, R. J.; Griffin, R. G., 250 GHz Gyrotron for Dynamic Nuclear Polarization in Biological Solid State NMR. *Journal of Magnetic Resonance* **2007**, 000, 0000-0000.

[9]   Joo, C.-G.; Hu, K.-N.; Bryant, J. A.; Griffin, R. G., In Situ Temperature Jump High-Frequency Dynamic Nuclear Polarization Experiments: Enhanced Sensitivity in Liquid-State NMR Spectroscopy. *J. Am Chem. Soc* **2006**, 128, 9428-9432.

[10]   Hu, K.-N.; Yu, H.-h.; Swager, T. M.; Griffin, R. G., Dynamic nuclear polarization with biradicals. *Journal of the American Chemical Society* **2004**, 126, (35), 10844-10845.

[11]   Bajaj, V. S.; Farrar, C. T.; Mastovsky, I.; Vieregg, J.; Bryant, J.; Elena, B.; Kreischer, K. E.; Temkin, R. J.; Griffin, R. G., Dynamic nuclear polarization at 9T using a novel 250 GHz gyrotron microwave source. *Journal of Magnetic Resonance* **2003**, 160, (2), 85-90.

[12]   Bajaj, V. S.; Farrar, C. T.; Hornstein, M. K.; Mastovsky, I.; Vieregg, J.; Bryant, J.; Elena, B.; Kreischer, K. E.; Temkin, R. J.; Griffin, R. G., Dynamic Nuclear Polarization at 9 Tesla Using a Novel 250 GHz Gyrotron Microwave Source. *J. Mag. Res.* **2002**, 160, (2), 85-90.

[13]   Rosay, M.; Zeri, A. C.; Astrof, N. S.; Opella, S. J.; Herzfeld, J.; Griffin, R. G., Sensitivity-enhanced NMR of biological solids: Dynamic nuclear polarization of Y21M fd bacteriophage and purple membrane. *Journal of the American Chemical Society* **2001**, 123, (5), 1010-1011.

[14]   Becerra, L. R.; Gerfen, G. J.; Bellew, B. F.; Bryant, J. A.; Hall, D. A.; Inati, S. J.; Weber, R. T.; Un, S.; Prisner, T. F.; Mcdermott, A. E.; Fishbein, K. W.; Kreischer, K. E.; Temkin, R. J.; Singel, D. J.; Griffin, R. G., A Spectrometer for Dynamic Nuclear-Polarization and Electron-Paramagnetic-Resonance at High-Frequencies. *Journal of Magnetic Resonance Series A* **1995**, 117, (1), 28-40.

[15]   Stevenson, S.; Dorn, H. C., C-13 Dynamic Nuclear-Polarization - a Detector for Continuous-Flow, Online Chromatography. *Analytical Chemistry* **1994**, 66, (19), 2993-2999.

[16]   Becerra, L. R.; Gerfen, G. J.; Temkin, R. J.; Singel, D. J.; Griffin, R. G., Dynamic Nuclear-Polarization with a Cyclotron-Resonance Maser at 5-T. *Physical Review Letters* **1993**, 71, (21), 3561-3564.

[17]   Un, S.; Prisner, T.; Weber, R. T.; Seaman, M. J.; Fishbein, K. W.; Mcdermott, A. E.; Singel, D. J.; Griffin, R. G., Pulsed Dynamic Nuclear-Polarization at 5-T. *Chemical Physics Letters* **1992**, 189, (1), 54-59.

[18]   Li, L. Y.; Qiu, J. Q.; Hu, S. G.; Liu, W. Y.; Ye, C. H., A Dnp Spectrometer at 1.94-T Magnetic-Field. *Science in China Series a-Mathematics Physics Astronomy* **1992**, 35, (10), 1214-1221.

[19]   Wind, R. A.; Li, L.; Lock, H.; Maciel, G. E., Dynamic Nuclear Polarization in the Nuclear Rotating Frame. *Journal of Magnetic Resonance* **1988**, 79, 577-582.

[20]   Duijvestijn, M. J.; Wind, R. A.; Smidt, J., A Quantitative Investigation of the Dynamic Nuclear Polarization Effect by Fixed Paramagnetic Centers of Abundant and Rare Spins in Solids at Room Temperature. *Physica* **1986**, 138B, 147-170.

[21]   Wind, R. A., Applications of Dynamic Nuclear Polarization in ^{13}C NMR in Solids. *Progress in NMR Spectroscopy* **1985**, 17, 33-67.

[22]   Wind, R. A.; Anthonio, F. E.; Duijvestijn, M. J.; Smidt, J.; Trommel, J.; Vette, G. M. C. d., Experimental Setup for Enhanced ^{13}C NMR Spectroscopy in Solids Using Dynamic Nuclear Polarization. *Journal of Magnetic Resonance* **1983**, 52, 424-434.

[23]   Wollan, D. S., Dynamic Nuclear Polarization with an Inhomogeneously Broadened ESR Line. I Theory. *Phys. Rev. B* **1976**, 13, 3671-3685.

[24]   Hausser, K. H.; Stehlik, D., Dynamic Nuclear Polarization in Liquids. *Advances in Magnetic Resonance* **1968**, 3, 79.

[25]   Bouffard, V.; Roinel, Y.; Roubeau, P.; Abragam, A., Dynamic Nuclear-Polarization in (Lid)-Li-6. *Journal De Physique* **1980,** 41, (12), 1447-1451.

[26]   Bleaney, B., Cross-relaxation and nuclear orientation in ytterbium vanadate. *Proceedings of the Royal Society of London Series a-Mathematical Physical and Engineering Sciences* **1999,** 455, (1988), 2835-2839.

[27]   Abragam, A.; Goldman, M., *Nuclear Magnetism: Order and Disorder*. Clarendon Press: Oxford, 1982.

[28]   Bouffard, V., Roinel, Y., Rousseau, P., and Abragam, A., Dynamic Nuclear Polarization in ^{6}LiD. *J. Physique* **1990,** 41., 1447-1451.

[29]   Abragam, A.; Proctor, W. G., Solid Effect. *C.R. Acad. of Sci.* **1959,** 246, 2253.

[30]   Goldman, M., *Spin Temperature in Nuclear Magnetic Resonance*. Oxor University Press: Oxford, 1973.

[31]   Hu, K.-N.; Bajaj, V. S.; Rosay, M. M.; Griffin, R. G., High Frequency Dynamic Nuclear Polarization Using Mixtures of TEMPO and Trityl Radicals. *J. Chem. Phys.* **2007,** 126, 044512.

[32]   Song, C.; Hu, K.-N.; Swager, T. M.; Griffin, R. G., TOTAPOL – A Biradical Polarizing Agent for Dynamic Nuclear Polarization Experiments in Aqueous Media. *J. Am Chem. Soc* **2006,** 128, 11385-90.

[33]   Hornstein, M. K.; Bajaj, V. S.; Griffin, R. G.; Kreischer, K. E.; Mastovsky, I.; Shapiro, M. A.; Sirigiri, J. R.; Temkin, R. J., Continuous-Wave Operation of a 460 GHz Second Harmonic Gyrotron Oscillator. *IEEE Trans. Electron Devices* **2005,** 52, (5), 798-807.

[34]   Hornstein, M. K.; Bajaj, V. S.; Griffin, R. G.; Temkin, R. J., Second Harmonic Operation at 460 GHz and Broadband Continuous Frequency Tuning of a Gyrotron Oscillator. *IEEE Trans. Electron Devices* **2005,** 52, (5), 798-807.

[35]   Joye, C. D.; Griffin, R. G.; Hornstein, M. K.; Hu, K.-N.; Kreischer, K. E.; Rosay, M.; Shapiro, M. A.; Sirigiri, J. R.; Temkin, R. J.; Woskov, P. P., Operational Characteristics of a 14 Watt, 140 GHz Gyrotron for Dynamic Nuclear Polarization. *IEEE Transactions on Plasma Science* **2006,** 34, 518-523.

[36]   Woskov, P. W.; Bajaj, V. S.; Hornstein, M. K.; Temkin, R. J.; Griffin, R. G., Corrugated Waveguide and Directional Coupler for CW 250 GHz Gyrotron DNP Experiments. *IEEE Transactions on Microwave Theory and Techniques* **2005,** 53, 1863-69.

[37]   Hornstein, M. K.; Bajaj, V. S.; Griffin, R. G.; Temkin, R. J., Efficient low-voltage operation of a CW gyrotron oscillator at 233 GHz. *IEEE Transactions on Plasma Science* **2007,** 35, (1), 27-30.

[38]   Hornstein, M. K.; Bajaj, V. S.; Griffin, R. G.; Temkin, R. J., Continuous-wave operation of a 460-GHz second harmonic gyrotron oscillator. *IEEE Transactions on Plasma Science* **2006,** 34, (3), 524-533.

[39]   Baldus, M.; Petkova, A. T.; Herzfeld, J.; Griffin, R. G., Cross polarization in the tilted frame: assignment and spectral simplification in heteronuclear spin systems. *Mol. Phys.* **1998,** 95, 1197-1207.

[40]   Bennett, A. E.; Rienstra, C. M.; Griffiths, J. M.; Zhen, W.; Lansbury, P. T.; Griffin, R. G., Homonuclear radio frequency-driven recoupling in rotating solids. *J. Chem. Phys.* **1998,** 108, 9463-9479.

[41]   Takegoshi, K.; Nakamura, S.; Terao, T., C-13-H-1 dipolar-assisted rotational resonance in magic-angle spinning NMR. *Chemical Physics Letters* **2001,** 344, (5-6), 631-637.

[42]   Zimanyi, L.; Saltiel, J.; Brown, L. S.; Lanyi, J. K., A priori resolution of the intermediate spectra in the bacteriorhodopsin photocycle: The time evolution of the L spectrum revealed. *Journal of Physical Chemistry A* **2006,** 110, (7), 2318-2321.

[43]   Zimanyi, L., Analysis of the bacteriorhodopsin photocycle by singular value decomposition with self-modeling: A critical evaluation using realistic simulated data. *Journal of Physical Chemistry B* **2004,** 108, (13), 4199-4209.

[44]   Nagle, J. F.; Zimanyi, L.; Lanyi, J. K., Testing Br Photocycle Kinetics. *Biophysical Journal* **1995,** 68, (4), 1490-1499.

[45]   Herzfeld, J.; Tounge, B., NMR probes of vectoriality in the proton-motive photocycle of bacteriorhodopsin: evidence for an 'electrostatic steering' mechanism. *Biochimica Et Biophysica Acta-Bioenergetics* **2000,** 1460, (1), 95-105.

[46]   D. Oesterhelt, W. S., *Proceedings Of The National Academy Of Sciences Of The United States Of America* **1973,** 70, 2853-2857.

[47]   Rovnyak, D.; Filip, C.; Itin, B.; Stern, A. S.; Wagner, G.; Griffin, R. G.; Hoch, J. C., Multiple-Quantum Magic-Angle Spinning Spectroscopy using Nonlinear Sampling. *J. Magn. Resonance* **2003,** 161, 43-55.

[48]   Mobli, M.; Stern, A. S.; Hoch, J. C., Spectral reconstruction methods in fast NMR: Reduced dimensionality, random sampling and maximum entropy. *Journal of Magnetic Resonance* **2006,** 182, (1), 96-105.

[49]   Rovnyak, D.; Frueh, D. P.; Sastry, M.; Sun, Z. Y. J.; Stern, A. S.; Hoch, J. C.; Wagner, G., Accelerated acquisition of high resolution triple-resonance spectra using non-uniform sampling and maximum entropy reconstruction. *Journal of Magnetic Resonance* **2004,** 170, (1), 15-21.

[50]   Stern, A. S.; Li, K. B.; Hoch, J. C., Modern spectrum analysis in multidimensional NMR spectroscopy: Comparison of linear-prediction extrapolation and maximum-entropy reconstruction. *Journal of the American Chemical Society* **2002,** 124, (9), 1982-1993.

[51]   Hoch, J. C.; Stern, A. S., Maximum entropy reconstruction, spectrum analysis and deconvolution in multidimensional nuclear magnetic resonance. *Nuclear Magnetic Resonance of Biologica Macromolecules, Pt A* **2001,** 338, 159-178.

[52]   Schmieder, P.; Stern, A. S.; Wagner, G.; Hoch, J. C., Quantification of maximum-entropy spectrum reconstructions. *Journal of Magnetic Resonance* **1997,** 125, (2), 332-339.

[53]   Hoch, J. C.; Stern, A. S.; Wagner, G., Maximum-Entropy Reconstruction of Nonlinearly Sampled-Data. *Journal of Cellular Biochemistry* **1995,** 76-76.

[54]   Schmieder, P.; Hoch, J. C.; Stern, A. S.; Wagner, G., Applications of Maximum-Entropy Reconstruction. *Journal of Cellular Biochemistry* **1993,** 300-300.

[55]   Stern, A. S.; Hoch, J. C., A New, Storage-Efficient Algorithm for Maximum-Entropy Spectrum Reconstruction. *Journal of Magnetic Resonance* **1992,** 97, (2), 255-270.

[56]   Donoho, D. L.; Johnstone, I. M.; Stern, A. S.; Hoch, J. C., Does the Maximum-Entropy Method Improve Sensitivity. *Proceedings of the National Academy of Sciences of the United States of America* **1990,** 87, (13), 5066-5068.

[57]   Hoch, J. C.; Stern, A. S.; Donoho, D. L.; Johnstone, I. M., Maximum-Entropy Reconstruction of Complex (Phase-Sensitive) Spectra. *Journal of Magnetic Resonance* **1990,** 86, (2), 236-246.

[58]   Balashov, S. P.; Ebrey, T. G., Trapping and spectroscopic identification of the photointermediates of bacteriorhodopsin at low temperatures. *Photochemistry and Photobiology* **2001,** 75, 453-62.

[59]   Jaroniec, C. P.; Tounge, B. A.; Rienstra, C. M.; Herzfeld, J.; Griffin, R. G., Measurement of C-13-N-15 distances in uniformly C-13 labeled biomolecules: J-decoupled REDOR. *Journal of the American Chemical Society* **1999,** 121, (43), 10237-10238.

[60]   Jaroniec, C. P.; Tounge, B. A.; Herzfeld, J.; Griffin, R. G., Frequency selective heteronuclear dipolar recoupling in rotating solids: accurate ^{13}C-^{15}N distance measurements in uniformly-^{13}C,^{15}N-labeled peptides. *J. Am. Chem. Soc.* **2001**, 3507-3519.

[61]   Jaroniec, C. P.; Filip, C.; Griffin, R. G., 3D TEDOR NMR experiments for the simultaneous measurement of multiple carbon-nitrogen distances in uniformly C-13, N-15- labeled solids. *Journal of the American Chemical Society* **2002**, 124, (36), 10728-10742.

[62]   Hong, M.; Gross, J. D.; Griffin, R. G., Site-resolved determination of peptide torsion angle phi from the relative orientations of backbone N-H and C-H bonds by solid-state NMR. *Journal of Physical Chemistry B* **1997**, 101, (30), 5869-5874.

[63]   SchmidtRohr, K., A double-quantum solid-state NMR technique for determining torsion angles in polymers. *Macromolecules* **1996**, 29, (11), 3975-3981.

[64]   Feng, X.; Eden, M.; Brinkmann, A.; Luthman, H.; Eriksson, L.; Gräslund, A.; Antzutkin, O. N.; Levitt, M. H., Direct determination of a peptide torsional angle ψ by double-quantum solid-state NMR. *J. Am. Chem. Soc.* **1997**, 119, 12006-12007.

[65]   Feng, X.; Verdegem, P. J. E.; Eden, M.; Sandstrom, D.; Lee, Y. K.; BoveeGeurts, P. H. M.; Grip, W. J. d.; Lugtenburg, J.; Groot, H. J. M. d.; Levitt, M. H., Determination of a molecular torsional angle in the metarhodopsin-I photointermediate of rhodopsin by double-quantum solid-state NMR. *J. Biomol. NMR* **2000**, 16, 1-8.

[66]   Feng, X.; Verdegem, P. J. E.; Lee, Y. K.; Sandström, D.; Edén, M.; Bovee-Geurts, P.; de Grip, W. J.; Lugtenburg, J.; de Groot, H. J. M.; Levitt, M. H., Direct determination of a molecular torsional angle in the membrane protein rhodopsin by solid-state NMR. *J. Am. Chem. Soc.* **1997**, 119, 6853-6857.

[67]   Hohwy, M.; Jaroniec, C. P.; Lansing, J.; Rienstra, C. M.; Griffin, R. G., ^{13}C-^{1}H recoupling in the HCCH torsion angle experiment in solid-state NMR. *Chem. Phys. Lett.* **1999**.

[68]   Hong, M.; Gross, J. D.; Griffin, R. G., Site-resolved determination of peptide torsion angle ϕ from the relative orientations of backbone N-H and C-H bonds by solid-state NMR. *J. Phys. Chem. B* **1997**, 101, 5869-5874.

[69]   Hong, M.; Gross, J. D.; Hu, W.; Griffin, R. G., Determination of the peptide torsion angle ϕ by ^{15}N chemical shift and ^{13}C$^{\alpha}$-^{1}H$^{\alpha}$ dipolar tensor correlation in solid-state MAS NMR. *J. Magn. Reson.* **1998**, 135, 169-177.

[70]   Hong, M.; Gross, J. D.; Rienstra, C. M.; Griffin, R. G.; Kumashiro, K. K.; Schmidt-Rohr, K., Coupling amplification in 2D MAS NMR and its application to torsion angle determination in peptides. *J. Magn. Reson.* **1997**, 129, 85-92.

[71]   Ladizhansky, V.; Jaroniec, C. P.; Diehl, A.; Oschkinat, H.; Griffin, R. G., Measurement of multiple y torsion angles in uniformly $^{13}C,^{15}N$-labeled a-spectrin domain using 3D ^{15}N-^{13}C-^{13}C-^{15}N MAS dipolar-chemical shift correlation spectroscopy. *J. Am. Chem. Soc.* **2003,** in press.

[72]   Ladizhansky, V.; Veshtort, M.; Griffin, R. G., NMR determination of the torsion angle ψ in α–helical peptides and proteins: the HCCN dipolar correlation experiment. *J. Magn. Reson.* **2002,** 154, (2), 317-324.

[73]   Rienstra, C. M.; Hohwy, M.; Mueller, L. J.; Jaroniec, C. P.; Reif, B.; Griffin, R. G., Determination of multiple torsion angle-constraints in U-^{13}C, ^{15}N-labeled peptides: 3D ^{1}H-^{15}N-^{13}C-^{1}H dipolar chemical shift spectroscopy in rotating solids. *J. Am. Chem. Soc.* **2002,** 124, 11908-11922.

[74]   Sack, I.; Balazs, Y. S.; Rahimipour, S.; S.Vega, Solid-State NMR Determination of Peptide Torsion Angles: Applications of ^{2}H-Dephased REDOR. *J. Am. Chem. Soc.* **2000,** 122, (49), 12263-12269.

[75]   Schmidt-Rohr, K., Torsion Angle Determination in Solid ^{13}C-Labeled Amino Acids and Peptides by Separated-Local-Field Double-Quantum NMR. *J. Am. Chem. Soc.* **1996,** 118, 7601-7603.

[76]   Hohwy, M.; Jaroniec, C. P.; Reif, B.; Rienstra, C. M.; Griffin, R. G., Local structure and relaxation in solid-state NMR: Accurate measurement of amide N-H bond lenghts and H-N-H bond angles. *J. Am. Chem. Soc.* **2000,** 122, 3218-3219.

Chapter 11   Structural and dynamic transitions of peptides and proteins monitored by solid state NMR

This chapter will appear in the following publication:
Vikram S. Bajaj, Patrick van der Wel, and Robert G. Griffin, "Structural and dynamic transitions of peptides and proteins monitored by solid state NMR," (2007).

11.1   Introduction

The central role of dynamics and flexibility in protein function has been clear since the very first crystal structure [1]. In order to bind substrate or channel a chemical reaction forward, an enzyme assumes one or more conformational states in sequence, such that energy is transduced in the desired direction. Transitions between these local energy minima, which are near the global minimum of the protein energy landscape, are mediated by concerted dynamical rearrangements at ambient temperatures [2, 3] [4]. At the same time, a protein must be able to adopt a unique conformation or set of conformations which are essential for its function. This balance between conformational flexibility and structural robustness has been optimized in each protein to allow it to function in the environment where it is normally active.

All dynamical processes in proteins are sensitive to temperature in varying degree. However, proteins undergo a *universal* dynamical transition at ~200 K and experience a concomitant loss of biological function. The transition is accompanied by reduced local atomic fluctuations and hence a change in the dynamics of the protein. In analogy to the dynamics encountered in disordered media such as liquids, this is called the "protein glass transition" [5-9] [10]. A similar transition has been observed in other biological macromolecules [11]. A detailed understanding of the physical basis for this phenomenon is important for several reasons. First, it will provide insight into the concerted dynamical rearrangements which are necessary for optimal biological function. Second,

a number of biophysical techniques, including x-ray crystallography, solid state NMR and cryo-electron microscopy, all require cooling of the sample to temperatures below the protein glass transition temperature. Since the protein in this state is not biologically active, it is important to understand how measured structural parameters change as a function of temperature. Finally, the dynamics of the glass transition, if better understood, may allow for trapping of mechanistically relevant conformational intermediates [6].

Several lines of evidence including x-ray crystallography [12] [13], FTIR [14], and molecular dynamics simulations [7] support the idea that the protein glass transition is due to a coupling of the protein motions with the dynamics of the solvent. The dynamical modes of the bulk water molecules, in particular, appear to influence the dynamics of the polypeptide chain; ordering of water at low temperatures is then associated with a loss of this dynamical activation [12] through a solvent caging effect. At temperatures slightly above the glass transition, ordering of bound waters results in increased local viscosity and prevents the anharmonic and concerted protein motions that gives rise to mechanistically significant rearrangements. However, several lines of evidence also show that a glass transition is possible in the absence of solvent: these include neutron scattering experiments in dehydrated films of myoglobin [15] and lysozyme [16], molecular dynamics simulations in the absence of solvent [17], and the extrapolated results of solution state NMR experiments at ambient temperatures [8]. These studies suggest that the glass transition is also an intrinsic property of the protein conformational energy surface alone. The glass transition is then associated with a loss of intrinsic mobility in internal (torsional) degrees of freedom, including dynamics in methyl groups, aromatic ring reorientation, and librational motions of side chains.

Recent molecular dynamics simulations by Vitkup and co-workers [7] suggest that solvent mobility dominates the glass transition until 180 K, and then intrinsic protein dynamics play the dominant role. The experimental evidence for these processes is currently insufficient.
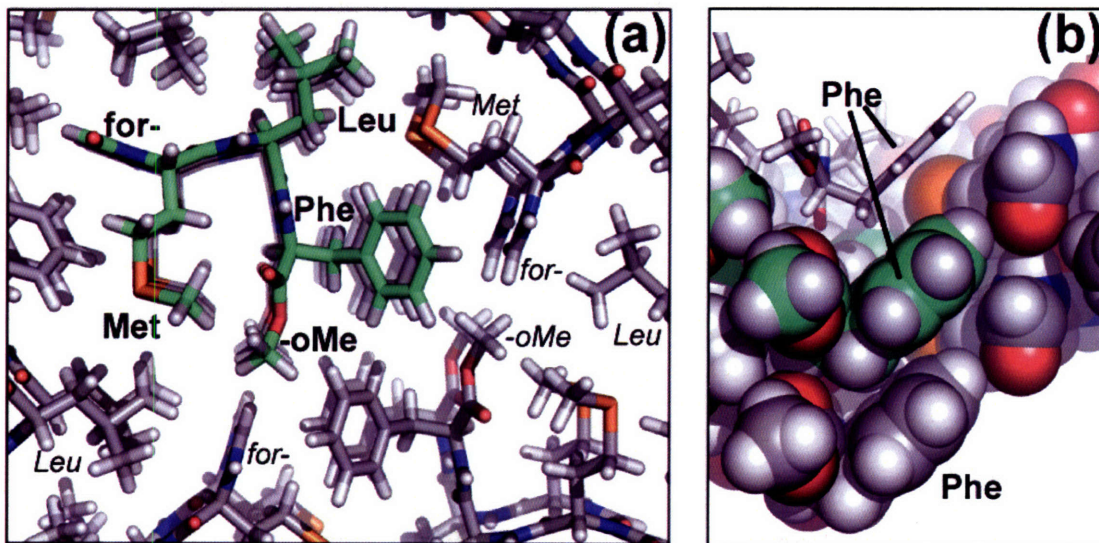
Figure 11-1: Lattice structure of *f-MLF-oMe* crystals [23]. Panel (a) shows a 'top-down' view of the crystal lattice. Panel (b) shows the steric crowding and relative orientation of the phenylalanine side chains, allowing aromatic π–π interactions.

Here, we aim to study that part of the protein glass transition which is due to the intrinsic dynamics of the peptide in the absence of solvent. To do so, we have performed solid-state NMR measurements of temperature-dependent structure and dynamics in a chemotactic tripeptide, *f*-MLF-OH, which is a model system for solid state NMR. It has been well-characterized in numerous previous experiments [18-21], resulting in an early solid-state NMR based structure [22]. In the current context, the system is particularly appropriate because it crystallizes in solvent-free microcrystals and yet experiences a representative range of dynamical phenomena. Indeed, a variety of conformational dynamics expected in this tripeptide, including rotamer interconversion, librational

motion of side chains, and three-fold "hopping" of methyl groups, as illustrated in Figure 11-2. Further, the addition of a single methyl group produces *f*-MLF-OMe, which yields very similar crystals whose structure has been solved by x-ray crystallography [23]. This form, however, the phenylalanine ring is static (Figure 11-1).
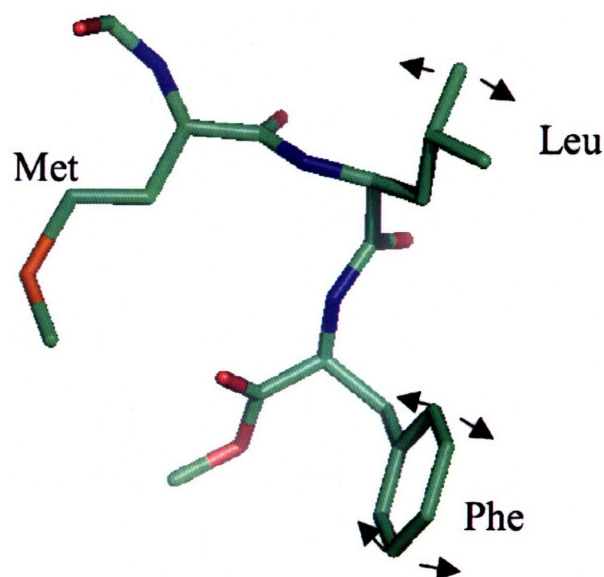
Figure 11-2: Representation of dynamical motions accessible to MLF. These motions include flipping of the phenylalanine ring about its symmetry axis, librational motions of the methionine side chain, rotamer interconversion of the leucine side chain, and three-fold hopping motion of the methyl groups.

Solid state NMR is a robust method of *ab initio* structure determination and is also capable of providing detailed information about motional processes over a wide range of time scales. Furthermore, there has been significant progress in the development of low-temperature MAS instrumentation in recent years, facilitating an investigation of the protein glass transition [24, 25]. In 1D spectra collected as a function of temperature, the effects of dynamics are readily observed. They include classical conformational exchange and interference phenomena that are manifest when dynamical process occur at rates similar to the magic angle spinning or ^{1}H decoupling. Further, the tripeptide *f*-MLF-OMe proves a rigid reference compounds, showing little effect of cooling to

temperatures as low as 90K. In contrast, similar cooling causes large changes in the NMR spectra of the *f*-MLF-OH crystals. These changes include the emergence of a structurally distinct substate of the peptide near the glass transition temperature, which we show is correlated to a remarkable motional transition occurring between 90 and 200 K. The observed dynamical transition is discussed in terms of its relation to the protein glass transition and protein low temperature dynamics in general.

11.2   Methods

11.2.1   Sample preparation

Unlabeled tripeptides *N*-formyl-Met-Leu-Phe-OH (*f*-MLF-OH) and *N*-formyl-Met-Leu-Phe-OCH$_3$ (*f*-MLF-OMe) were obtained from Bachem (King of Prussia, PA). Selectively deuterated f-MLF-OH containing ring-deuterated Phe-d$_5$ was prepared by solid phase peptide synthesis by SynPep Corporation (Dublin, CA). Uniformly labeled *f*-[U-^{13}C,^{15}N-MLF]-OH was synthesized by solid phase peptide synthesis by CS Bio Inc. (Menlo Park, CA). Isotopically labeled Phe-d$_5$, FMOC-[U-^{13}C,^{15}N-Met], FMOC-[U-^{13}C,^{15}N-Leu], and FMOC-[U-^{13}C,^{15}N-Phe] were obtained from Cambridge Isotope Laboratories (Andover, MA). F-MLF-OH and f-MLF-OMe were crystallized from isopropanol and benzene, respectively. Small, needlelike crystals were obtained after dissolution in warm solvent followed by slow evaporation to dryness.

11.2.2   NMR Measurements and Analysis

Magic angle spinning experiments were performed using a home-built spectrometer operating at 380 MHz ^{1}H frequency (designed by D. J. Ruben, Francis Bitter Magnet Laboratory, MIT) and a triple channel (^{1}H, ^{13}C, ^{15}N) 4 mm MAS probe designed for low temperature DNP experiments. Sample cooling was performed by using pre-cooled

nitrogen gas to provide the drive and bearing pressure for MAS. The spinning frequency of 6.25-7 kHz was controlled by a Bruker MAS controller (Billerica, MA). At each temperature, ^{13}C chemical shifts were referenced relative to dilute, aqueous DSS using external referencing via the ^{13}C chemical shifts of adamantine [26], and ^{15}N chemical shifts were referenced to liquid ammonia, via indirect referencing using the suggested IUPAC frequency ratios (^{13}C/^{1}H) of aqueous DSS and liquid NH$_3$ (^{15}N/^{1}H) [27, 28]. Spectra were processed and visualized using the NMRPipe [29], Sparky[30], and CCPNMR [31-34] software packages.

Static deuterium NMR spectra were obtained on a home-built spectrometer operating at 61 MHz ^{2}H frequency, courtesy of David Ruben (Francis Bitter Magnet Laboratory, MIT), using a quadrupolar echo pulse sequence. Simulation of the lineshapes was done using the TURBOPOWDER deuterium line shape simulation software [35].

11.3   Results

11.3.1   Room temperature measurements

Figure 11-2 shows the 1D solid-state MAS NMR spectra at room temperature for both f-MLF-OH and f-MLF-oMe. In f-MLF-oMe the chemical shifts of each carbon in the phenyl ring of MLF-OMe are distinct, indicating a static structure without dynamics that are observable on the NMR time scale. The ring in the f-MLF-OH peptide, on the other hand, is undergoing 180-degree flips, resulting in an averaging of the chemical shifts of Cδ and Cε ring carbons. Due to interference of the ring dynamics with the heteronuclear ^{1}H-^{13}C decoupling, these carbon signals are broad, unless the Phe side chain is deuterated (compare panels (c) and (d)).
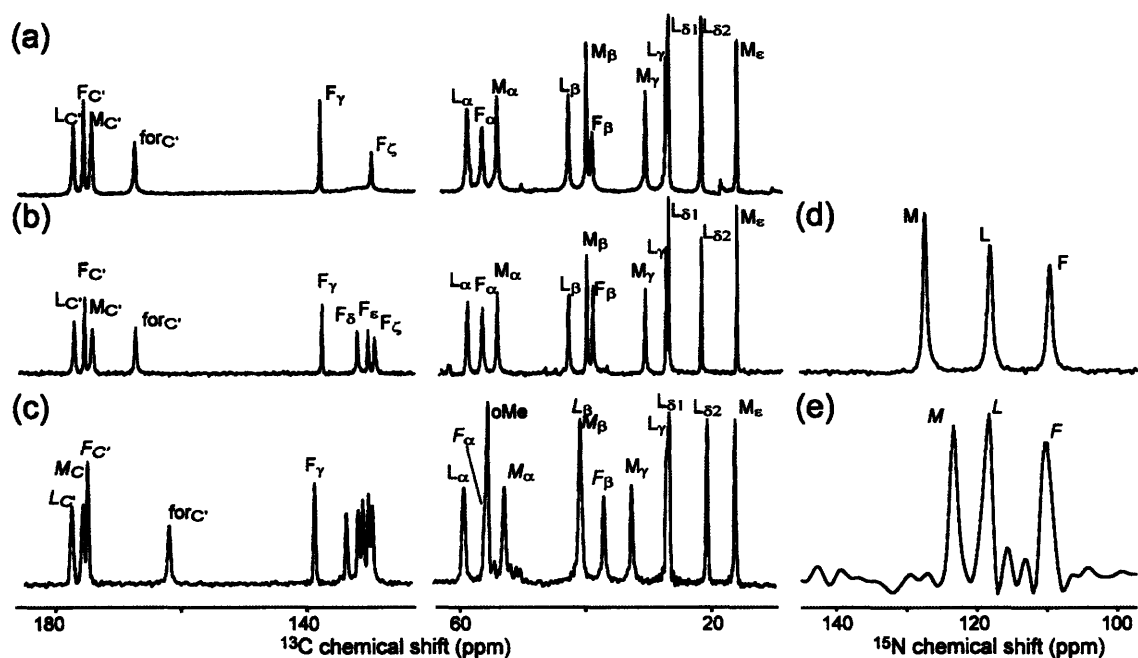
Figure 11-3: Room temperature 1D spectra and assignments. Panels (a)-(c) show the ^{13}C spectra of natural abundance f-MLF-OH, unlabeled f-MLF-OH with a ^{2}H-labeled side chain (Phe-d$_5$), and unlabeled f-MLF-OMe. Panels (d) and (e) contain the ^{15}N spectra of for-$[U$-$^{13}C,^{15}N]MLF$-OH and natural abundance f-MLF-OMe. Assignments for f-MLF-oMe are based on analogy with f-MLF-OH, with particular uncertainty in the italicized labels.

11.3.2   Cooling of f-MLF-oMe

Figure 11-3 shows the 1D spectra obtained for the f-MLF-oMe peptide, at temperatures ranging from 298 K down to 95 K. Neither the ^{15}N nor the ^{13}C resonances show a significant change in their chemical shifts, but significant changes in line width and peak intensity are observed. The largest effects are visible for the two methyl groups of leucine side chain (indicated with arrows in the figure). This is due to a change in the rate of the three-fold hopping motion of these methyl groups. Note that other methyl groups in the methionine side chain and capping the peptide's c-terminus experience less steric hindrance and as a result remain in the fast-motion regime in this temperature range.

427
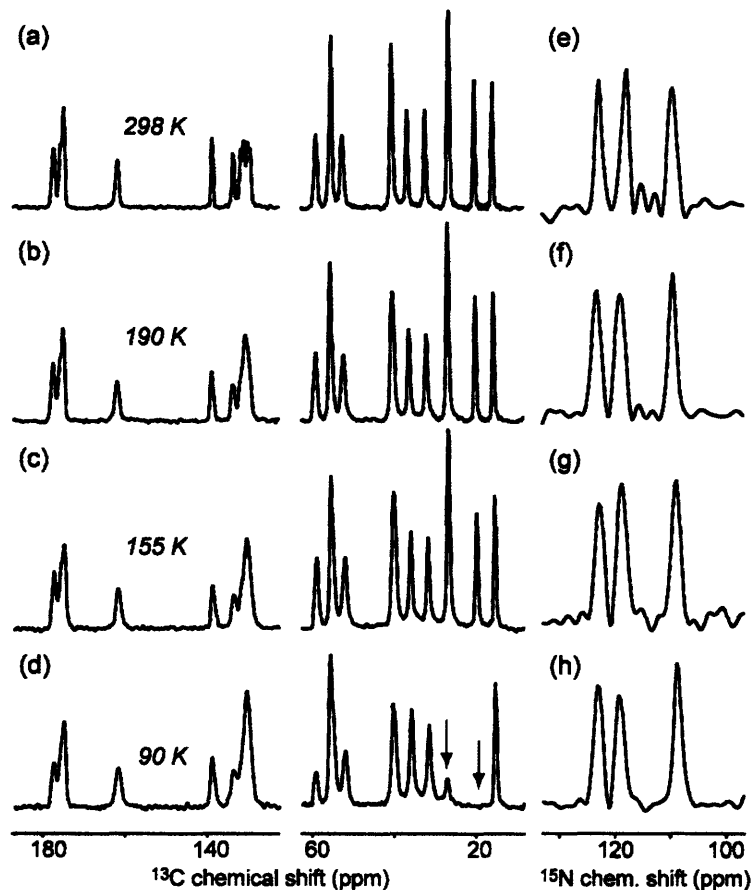
Figure 11-4: Variable temperature 1D spectra of unlabeled *f-MLF-oMe*, showing ^{13}C (a-d) and ^{15}N (e-h) measurements 298, 190, 155, and 95 K. Data were acquired at 380 MHz ^{1}H frequency and 6.25 kHz MAS. Arrows indicate Leu methyl resonances that are most strongly attenuated at low temperature.

11.3.3   Cooling of *f*-MLF-OH

Similar low temperature experiments were performed on the –OH variant. Figure 11-4 shows the ^{13}C 1Ds for natural abundance *f*-MLF-OH at various temperatures, ranging from room temperature to 90K. At 200K, there is no longer any averaging of the Phe ring carbons, indicating that the rapid flipping motion that it experiences at room temperature has slowed. Similar to *f*-MLF-oMe, those methyl groups that experience steric interactions (Leu side chain) disappear near 90K. Those that perform their three-fold hopping motion without steric hindrance (*e.g.* the –S-CH$_3$ of the Met side chain) remain mobile down to these temperatures. At 90K, most of the other resonances have a

chemical shift that is similar to their value at room temperature, with small shifts for just a few resonances. Interestingly, however, in the range between room temperature and 90K rather significant changes are observed, as shown in the column to the right. This apparent phase transition occurs at temperatures between 200K and 90K, and results in the formation of an additional, distinct spectroscopic 'form' of the peptide.
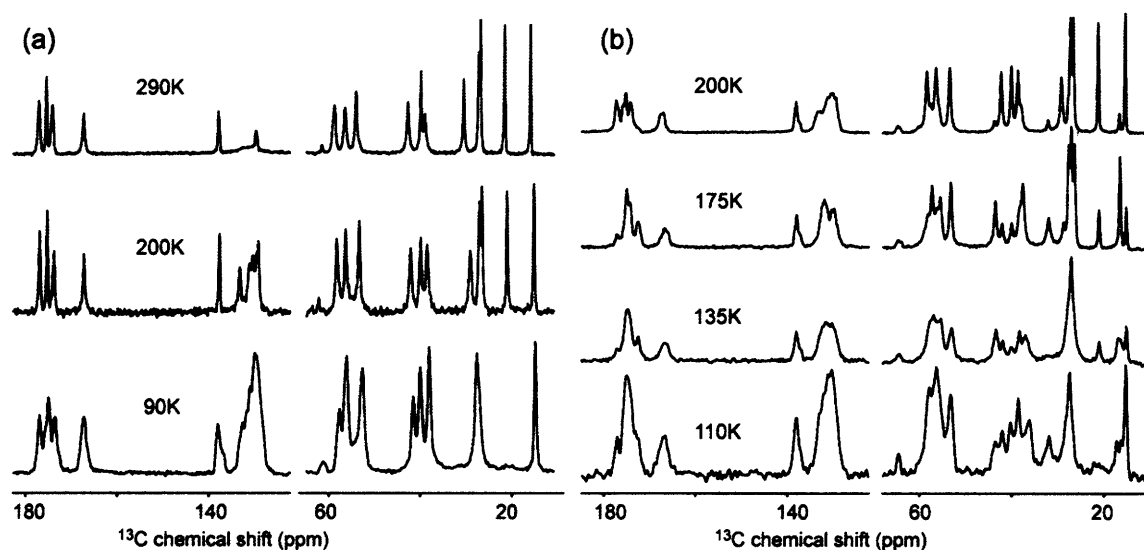
Figure 11-5: Variable temperature 1D spectra of unlabeled *f-MLF-OH*. Column (a) shows the coarse temperature dependence from room temperature down to 90K. The spectra on the right (b) illustrate the spectral changes indicative of a transition between 200K and 90K.

Similar trends are observed in Figure 11-6, showing the temperature dependent nitrogen spectra for 10% isotopically diluted [U-^{13}C, ^{15}N] f-MLF-OH. Upon cooling of the sample, the nitrogen resonances remain unaffected down to approximately 200K, after which we observe the appearance of a second set of resonances corresponding to a distinct conformational substate. Note that upon heating the sample (right column), the process is reversed, although there is a certain extent of hysteresis that affects the relative intensities (but not the chemical shifts). At the lowest temperatures, near 90K, the intensity of the 'second form' reduces again. The precise proportions vary slightly from sample to sample.
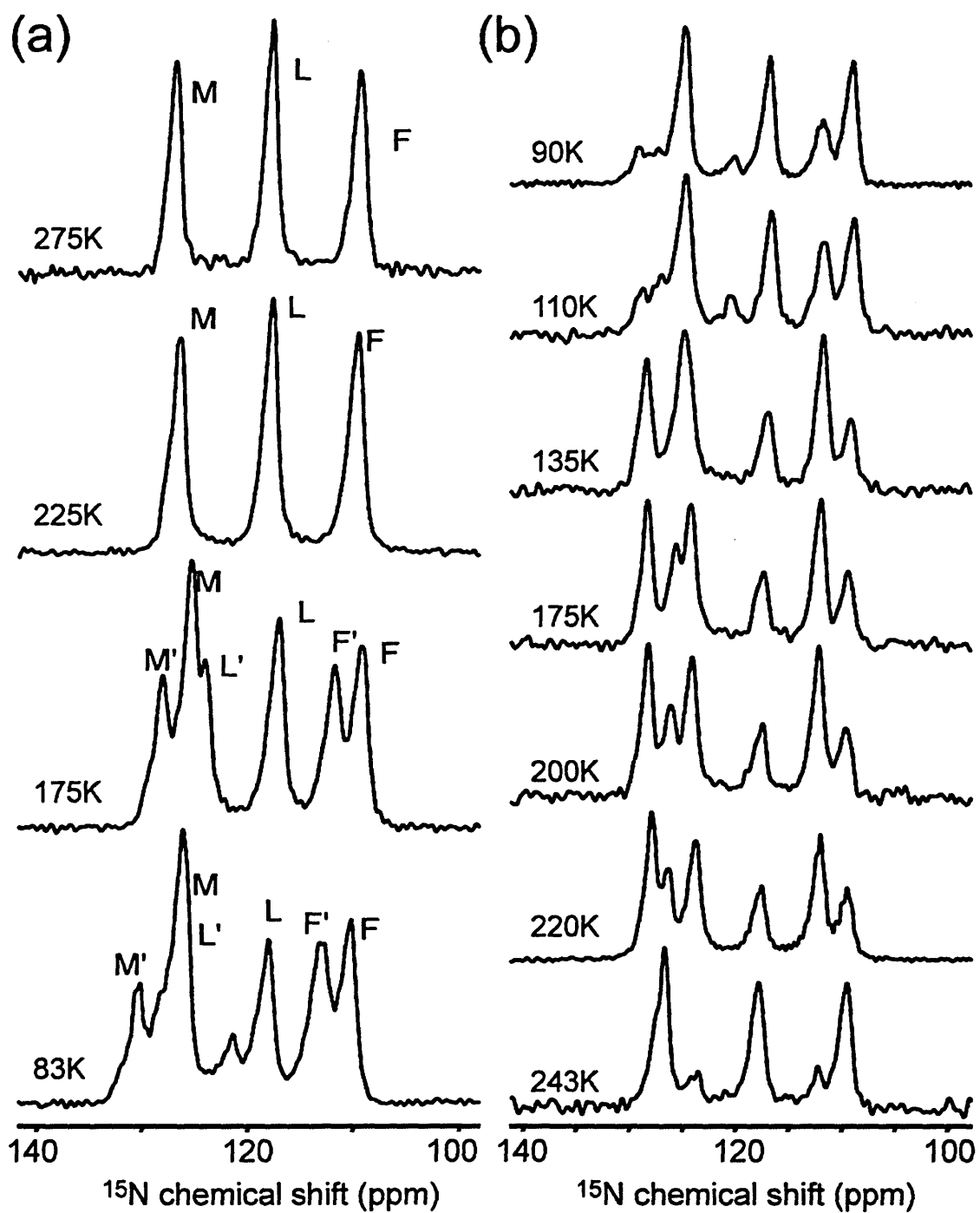
Figure 11-6: Variable temperature ^{15}N spectra of 10% [U-^{13}C, ^{15}N] f-MLF-OH. Column (a) shows the change occurring upon cooling from room temperature to 83K. Column (b) shows spectra obtained upon heating from 90K back to room temperature.
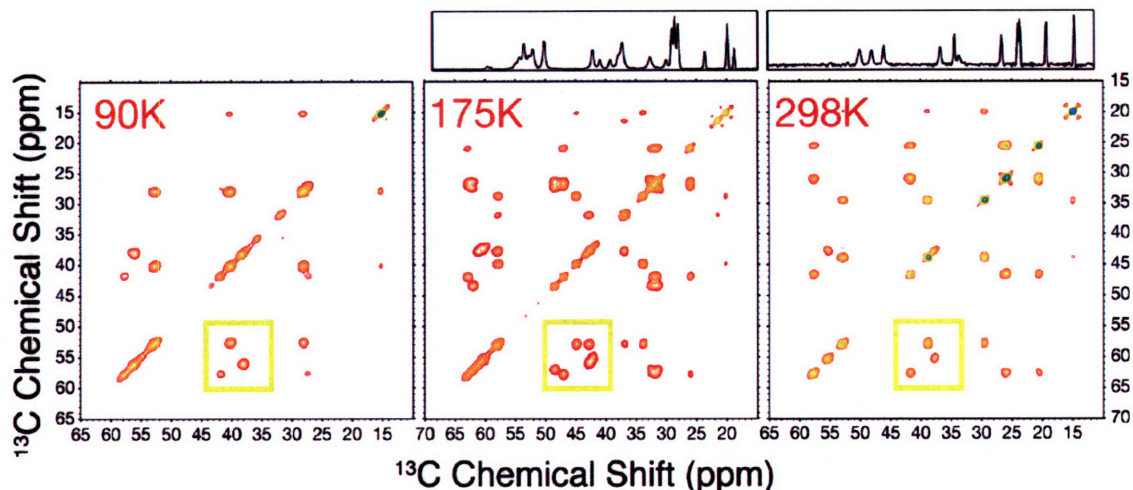
Figure 11-7: ^{13}C-^{13}C correlation spectra of 10% $^{13}C,^{15}N$ labeled f-MLF-OH at 298K (a), 175K (b), and 90K (c). A DARR/RAD mixing time of 10ms resulted in mostly single bond, and weaker two-bond correlations. The top and bottom panels show aliphatic-aliphatic and carbonyl-aliphatic cross-peaks, respectively. The novel form seen at 175K is highlighted in red.

The assignments of the different signals in the 1D spectra are based on assignment experiments performed at temperatures of 298K, 175K, and 90K. The results of these measurements are summarized in Figure 11-7 to Figure 11-10. Figure 11-7 illustrates that complete ^{13}C assignments can be obtained through 2D ^{13}C-^{13}C correlation spectroscopy. We observe a single form of the peptide at 298K and 90K, but a mixture of two forms at 175K. Of these, one form has chemical shifts which resemble those of the room temperature form of MLF, while the other form is a novel form that arises as the sample approaches a temperature of 175K. In Figure 11-8, these differences are highlighted for the aliphatic Cα-Cβ region of the correlation spectrum. It is further noteworthy that the apparent loss of resolution in the Cα region of the 1D spectrum is not due to line broadening but is instead due to the emergence of another structural form at intermediate temperatures. This transition is further illustrated in Figure 11-9, which highlights the C' region of the spectrum and shows that the emergence of a second form of MLF is accompanied by a pronounced change in the dynamics of the phenyalanine

ring. At room temperature, the timescale of the ring hopping motion interferes with either magic angle spinning or ^{1}H decoupling, and no cross peaks are seen. At low temperatures, the dynamics are attenuated and cross peaks emerge in the aromatic region of the spectrum. Complete ^{15}N and sequential assignments of the spectrum are possible through heteronuclear correlation spectroscopy, illustrated in Figure 11-10. Two-dimensional NCACX correlation experiments are sufficient to generate complete assignments of the peptide.
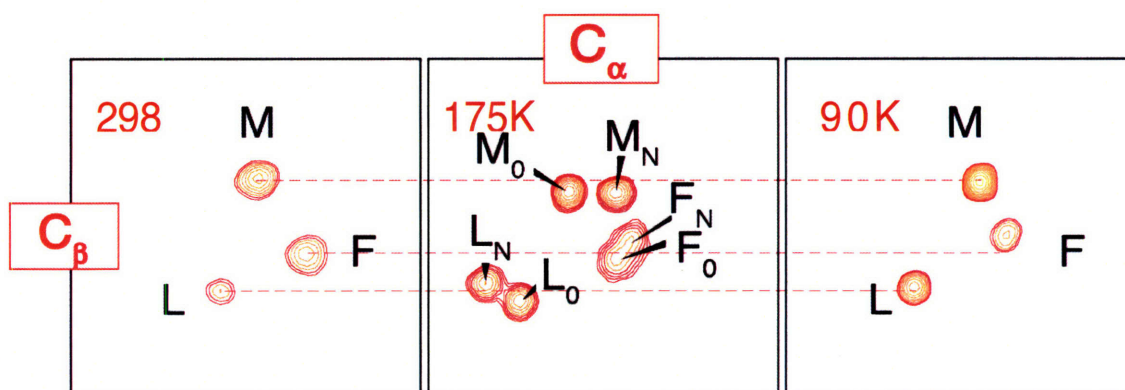
Figure 11-8: ^{13}C-^{13}C correlation spectra of 10% ^{13}C,^{15}N labeled f-MLF-OH as in Figure 11-7. The panels show correlated changes in the Cα-Cβ region and establish unambiguously that the line broadening in 1D spectra is actually due to a second structural form of MLF.

The assignment results and the 1D data can be combined to chart the change in chemical shift as a function of temperature, and the appearance of the transitional form below 200K. These results are summarized in Table 11.1, Table 11.2, and

Table 11.3, where the assignments for f-MLF-OMe, available only at natural abundance in this study, were made in analogy to f-MLF-OH.
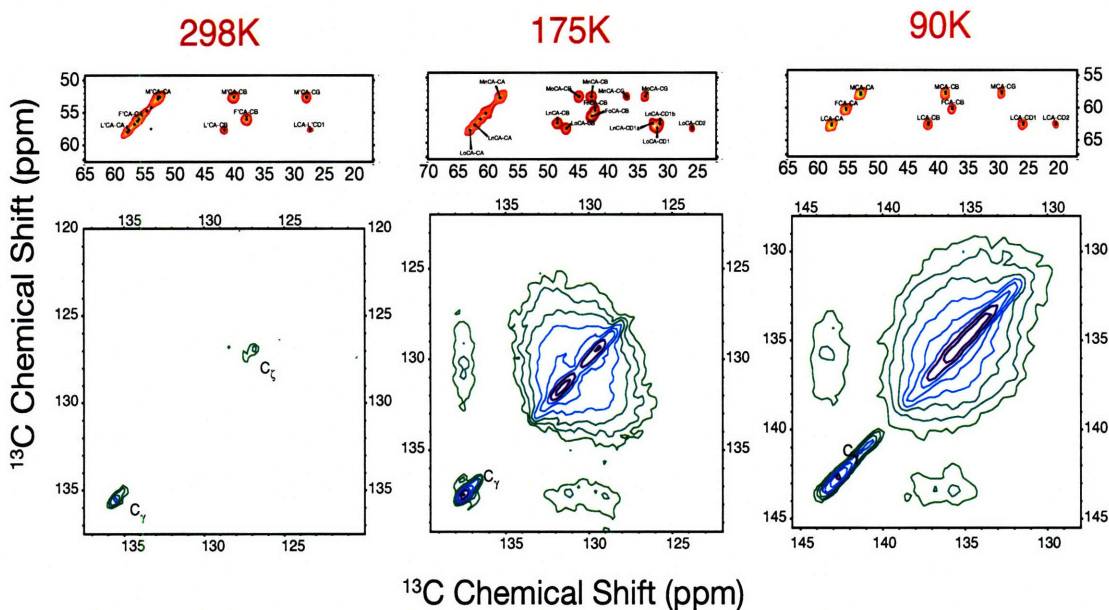
Figure 11-9: ^{13}C-^{13}C correlation spectra of 10% ^{13}C,^{15}N labeled f-MLF-OH as in Figure 11-7. The top panels highlight changes in the C-Ca region, and the lower panels highlight changes in the aromatic region of the spectrum. Note that aromatic cross peaks are completely absent at room temperature due to interfering dynamics and become visible at lower temperatures, where the dynamics are attenuated.
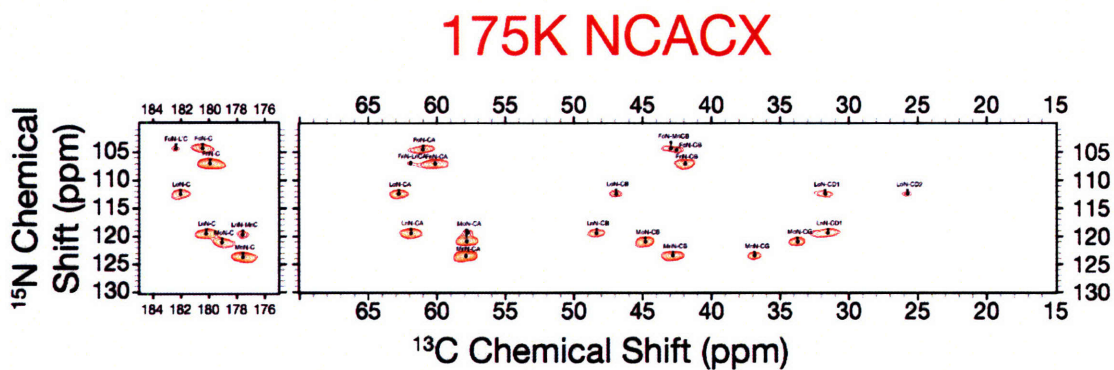
Figure 11-10: 2D ^{15}N-^{13}C NCACX-type correlation spectra which result in complete assignment of all resonances in MLF at 175K. Following ^{1}H-^{15}N cross polarization, the magnetization evolves under the ^{15}N chemical shift and then is transferred to the $^{13}C\alpha$ using band-selective cross polarization (SPECIFIC CP). Aliphatic cross-peaks are generated by proton-driven spin diffusion with an R^3 recoupling field (DARR).

Table 11.1: Tabulation of the ^{13}C and ^{15}N chemical shifts of f-MLF-OMe at various temperatures (referenced to DSS and liquid NH$_3$, respectively).

	Assignment	303K	192K	155K	95K
Carbonyl	Leu-C'	177.6	177.5	177.4	177.7
	Met-C'	175.8	175.8		
	Phe-C'	175.0	175.0	174.9	175.2
	Formyl-CO	162.1	162.0	161.9	161.9
Aromatic	Phe-CG	139.0	139.0	138.9	139.2
	Phe-?	134.0	133.9	133.8	134.0
	Phe-?	132.0	131.8		
	Phe-?	131.3			
	Phe-?	130.4	130.6	130.5	130.6
	Phe-?	129.8			
Aliphatic	Leu-CA	59.4	59.2	59.0	59.3
	Phe-CA & oMe	55.7	55.7	55.6	55.9
	Met-CA	53.0	52.4	52.1	52.2
	Leu-CB; Met-CB	41.0	40.6	40.3	40.6
	Phe-CB	37.2	36.5	36.1	36.2
	Met-CG	32.8	32.3	31.9	31.9
	Leu-CD	26.9	27.0	26.9	27.4
	Leu-CD	20.9	20.3	20.0	-
	Met-CE	16.4	15.9	15.6	15.6
^{15}N	Met-N	122.8	123.4	122.9	123.3
	Leu-N	117.6	119.3	118.9	119.8
	Phe-N	109.8	109.7	109.1	109.2

Table 11.2: Tabulation of ^{13}C chemical shifts of natural abundance f-MLF-OH at various temperatures (referenced to DSS). (aromatic chemical shifts are obtained from Phe-d$_5$ variant.)

	Assignment	303K	298K	200K	175K	135K	80K
Carbonyl	Leu-C'	177.1	177.1	177.3	177.1 / 175.0	177.0 / ?	176.9
	Phe-C'	175.5	175.4	175.8	174.3 / 174.3	174.8 / 174.8	174.9
	Met-C'	174.3	174.2	174.2	174.3 / 172.6	174.8 / 172.4	173.5
	Formyl-CO	167.4	167.3	167	166.7	166.7	167.0
Aromatic	Phe-CG	137.8	137.7	*138.1*	*138.0*	138.0	138.1
	Phe-CD?	132.1	132.3				
	Phe-CE?	130.4	130.4				
	Phe-CZ	129.4	129.3		*130.1*		
Aliphatic	Leu-CA	58.9	58.8	58.5 / 57.6	58.1 / 57.4	57.7 / 57.0	57.7
	Phe-CA	56.5	56.4	56.5	56.3 / 55.5	56.3 / 55.4	56.2
	Met-CA	54.2	54.1	53.5	53.2 / 53.2	53.0 / 53.0	52.6
	Leu-CB	42.9	42.7	42.3 / 43.8	42.1 / 43.6	42.0 / 43.5	41.6
	Met-CB	40.0	39.9	40.1	40.0 / 37.6*	40.2 / 37.1*	40.0
	Phe-CB	39.0	38.9	38.7 / 38.1	37.6* / 37.6	37.1* / 37.1*	38.1
	Met-CG	30.8	30.6	29.3 / 32.2	28.8 / 32.0	27.1* / -	27.8
	Leu-CG	27.3	27.2	27.3 / 27.3*	27.2 / 27.7	27.1*	27.8
	Leu-CD1	26.9	26.8	26.7	26.5 / 26.5	27.1*	-
	Leu-CD2	21.8	21.6	21.3	21.1 / ?	21.1 / ?	-
	Met-CE	16.1	16.0	15.4 / 16.7	15.2 / 16.6	15.2 / 17.0	15.0

* Resonances showing (severe) overlap, large uncertainty in exact frequency & intensity

434

Table 11.3: Tabulation of 15N chemical shifts for 10% [U-^{13}C,^{15}N]-labeled f-MLF-OH at various temperatures (indirectly referenced to liquid NH3 via the adamantane ^{13}C resonances).

Assignment	298K	225K	200K	175K	135K	90K
Met-N	127.5	126.3		125.5		124.8
Met-N'	n/a			128.2	128.3	129.0 / 127.3
Leu-N	118.2	117.5		117.1		116.7
Leu-N'	n/a			124.1		? / 120.1?
Phe-N	109.7	109.3		109.2		108.8
Phe-N'	n/a			111.8		111.7

11.3.4   Structure Determination

In order to determine the high resolution structure of two forms of MLF which co-exist at 175K, we have followed a strategy that has been applied successfully in the case of MLF at room temperature and, more recently, in amyloid fibrils from transthyretin [36] and its L111M mutant (in this thesis). This strategy involves the application of dipolar recoupling experiments in uniformly labeled systems to measure heteronuclear ^{13}C-^{15}N distances [20, 37, 38] and homonuclear [39-42] distances, and tensor correlation experiments [19, 43-53] to constrain backbone and sidechain torsion angles. All measurements were conducted in a sample diluted to 10% in natural abundance peptide prior to crystallization in order to minimize the effects of intermolecular dipolar couplings (see Figure 11-11). In this case, we have used the 3D TEDOR [38] and Rotational Resonance Width [42] experiments to obtain distance constraints. The backbone ϕ and ψ torsion angles were constrained through HNCH and HN$_{i+1}$C$_i$H tensor correlation experiments, respectively, which incorporate the TMREV sequence for γ-encoded heteronuclear recoupling; secondary constraints on ψ were obtained through the NCCN dipolar correlation experiment. Side chain torsion angles were constrained through the HCCH tensor correlation experiment.
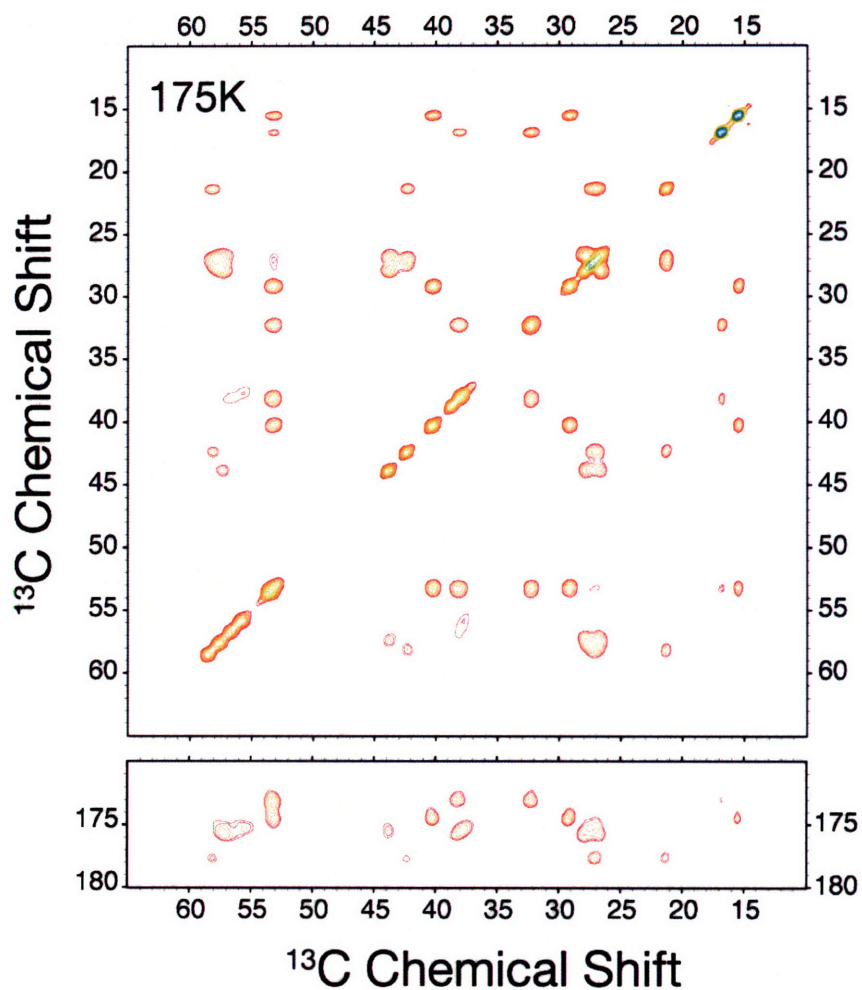
Figure 11-11: CHHC experiment in 10% [U-^{13}C,^{15}N]-MLF, which was subsequently used for experiments designed to measure structural parameters. The absence of intermolecular cross peaks at long mixing times demonstrates that all structural constraints measured in these experiments are not influenced by intermolecular packings in the diluted sample.

The details of the 3D TEDOR pulse sequence are described in Figure 11-12, while Figure 11-13 is a 2D projection of the 3D experiment that illustrates the number of cross peaks from which meaningful distances can be extracted. The data are fit using an approximate analytical model of the spin dynamics for multiple, coupled spins under TEDOR [38] using a Levenberg-Marquardt algorithm for minimization of the χ^2 fit parameter. An example of the fit for weak dipolar couplings corresponding to distances of 5.4 Å and 6.4

Å is shown in Figure 11-15. The approximate analytical model used to fit these data neglects the orientational dependence of the spin dynamics and hence introduces a systematic error of approximately 10%-20%, which is greater than the random error in these data in all cases.
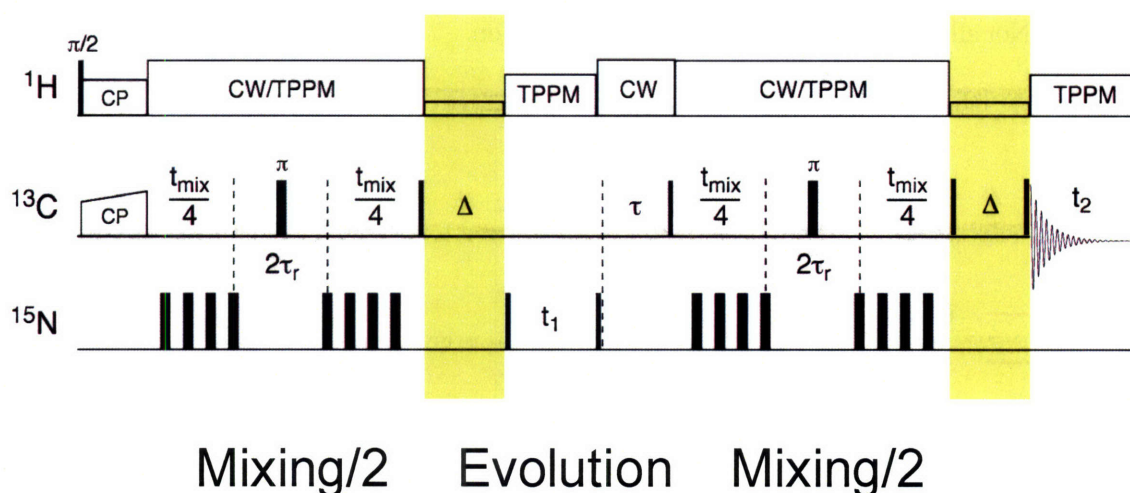
Figure 11-12: 3D TEDOR experiment use for ^{15}N-^{13}C distance measurements in MLF, in which transferred echo double resonance is used to produce quantitative heteronuclear polarization transfer in the context of a chemical shift correlation experiment [38].
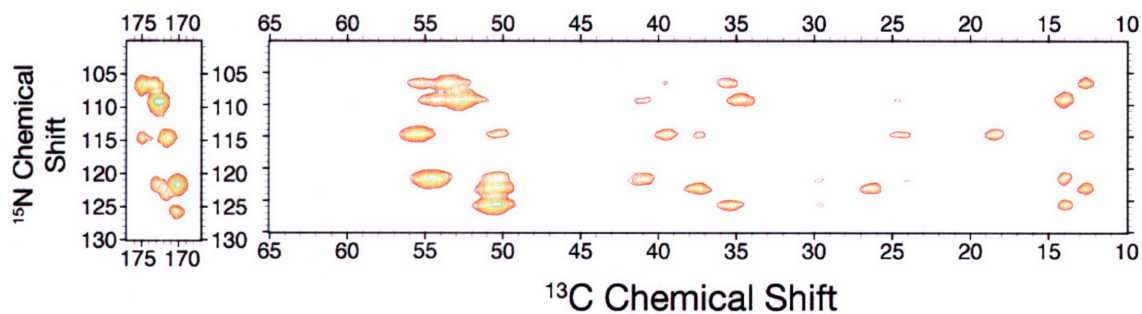
Figure 11-13: Projection of dipolar dimension of 3D TEDOR experiment in MLF (175 K). The intensity of each cross peak was fit as a function of the mixing time to obtain an accurate estimate of the heteronuclear distance.
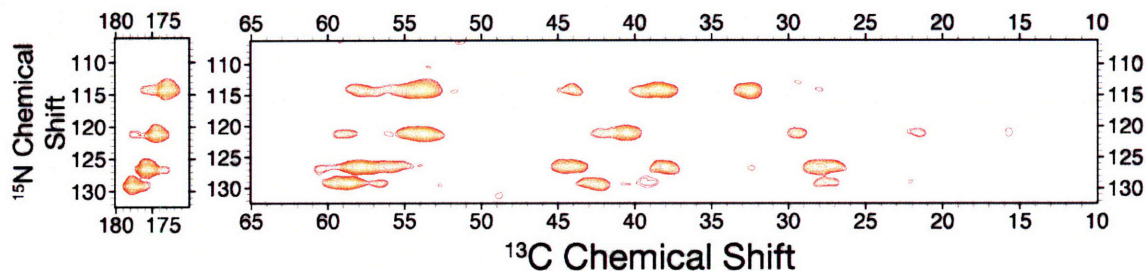
Figure 11-14: Projection of dipolar dimension of 3D Rotational Resonance Width experiment in MLF (175 K). With the exception of $C\alpha$ and $C\beta$ atoms, the intensity of each cross peak was fit as a function of the spinning frequency to obtain an accurate estimate of the homonuclear distance. Not all cross peaks are visible in this projection.
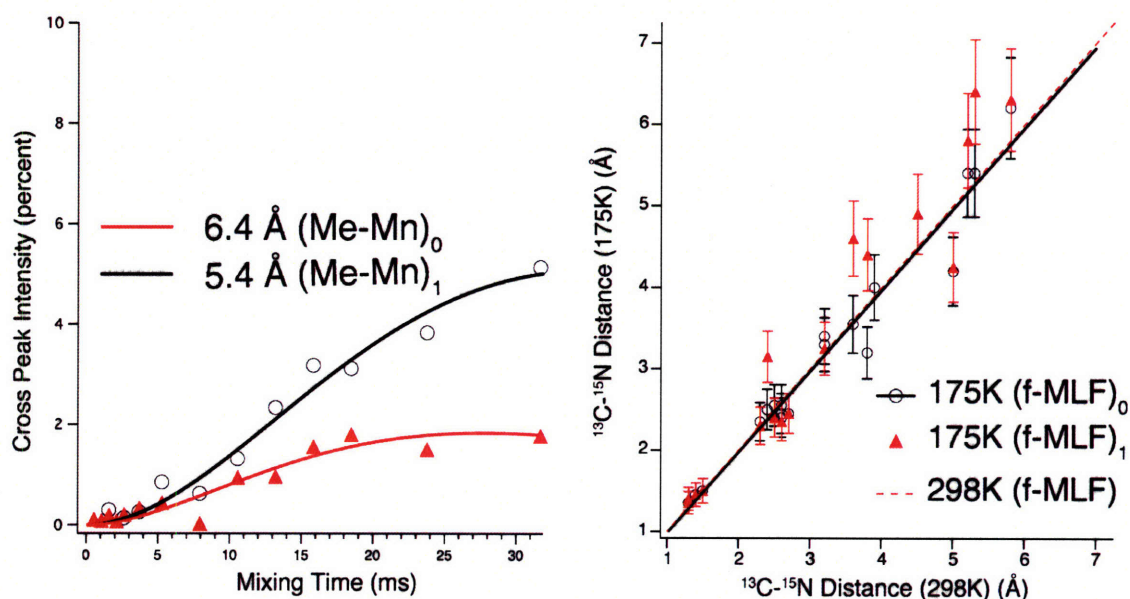
Figure 11-15: (left) Example of fitting of long distances in TEDOR experiments. (right) The N-form of MLF (MLF-1) has systematically longer distances than the O-form, which closely resembles both the room temperature and 90K MLF structures.

HNCH and $HN_{i+1}C_iH$ tensor correlation experiments are illustrated in Figure 11-16. The correlated dephasing under ^1H-^{15}N and ^1H-^{13}C couplings is monitored through the intensity of the ^{15}N-^{13}C cross peaks as a function of the synchronously incremented dipolar mixing time. The relative rate of incrementation is chosen to optimize the sensitivity of the experiment (in this case, n=2). In these experiments, TMREV-4 was applied at a spinning frequency of 8.333 kHz. The resulting trajectories can be fit to obtain constraints on the backbone torsion angles (Figure 11-21).
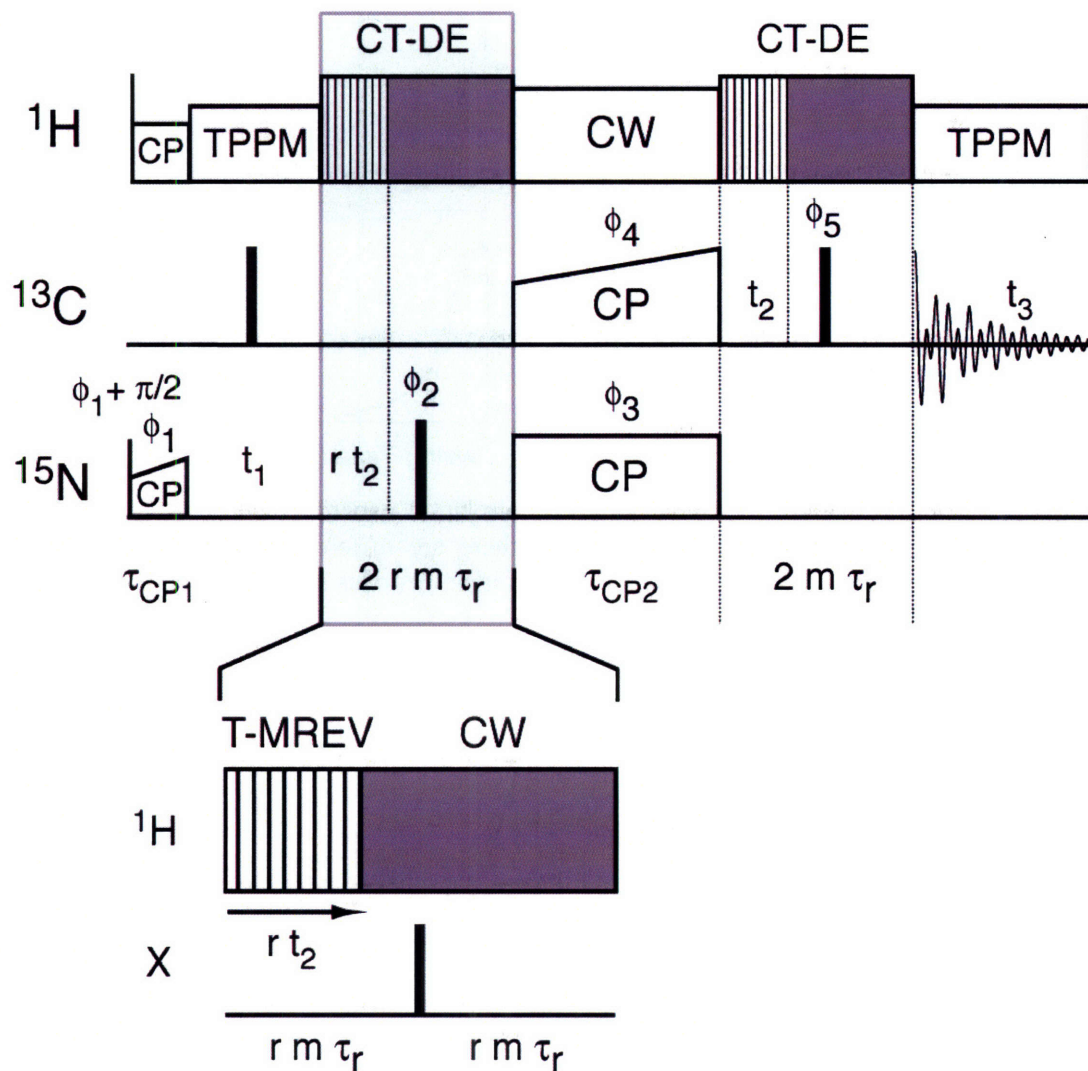
Figure 11-16: 3D HNCH experiments for measurement of backbone ϕ torsion angles in uniformly labeled peptides [52]. Heteronuclear couplings are reintroduced using constant-time TMREV [54] recoupling sequences which are synchronously incremented during ^{1}H-^{13}C and ^{1}H-^{15}N recoupling periods. A similar experiment to measure the ψ torsion angle instead involves correlation of the ^{1}H-^{15}N$_{(i+1)}$ dipolar tensor with the ^{1}H-^{13}Cα tensor.
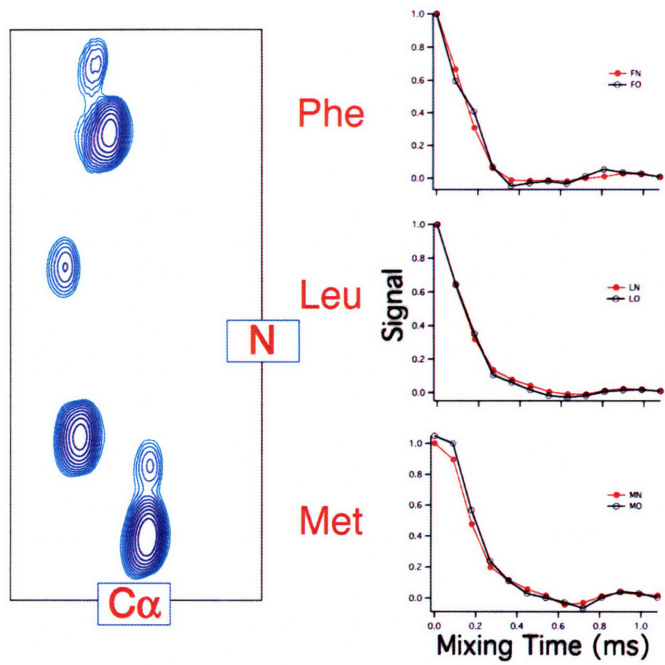
Figure 11-17: Experimental data for HNCH tensor correlation experiment designed to measure the ϕ torsion angle in MLF at 175K. Note that there are differences in the experimental dephasing trajectories for the methionine and phenylalaine residues between the two forms of MLF but minimal differences for the leucine.
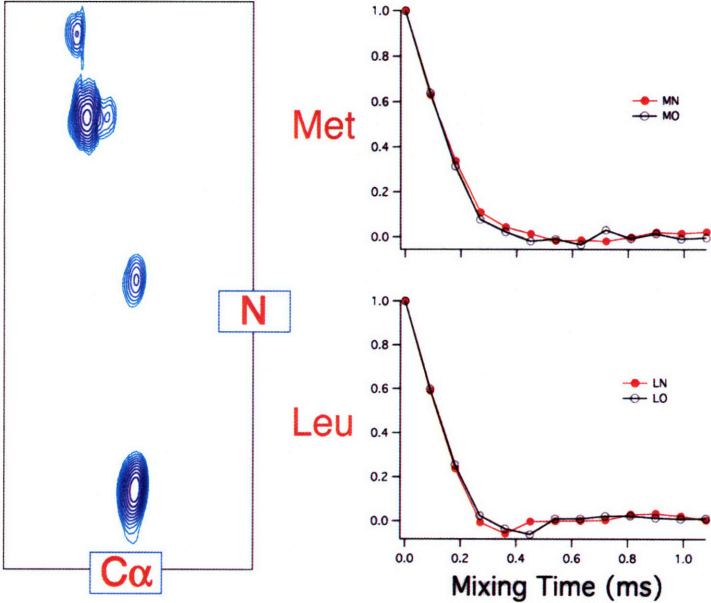
Figure 11-18: Experimental data for $HN_{i+1}C_iH$ tensor correlation experiment designed to measure the ψ torsion angle in MLF at 175K. No constraints on the phenylalanine residue can be obtained from this experiment. The results suggest only minimal differences in this backbone ψ torsion angle between the N-form and O-form of MLF. The HNCH ψ measurements were supplemented with an NCCN dipolar correlation experiment that constrains the same torsion angle.

440
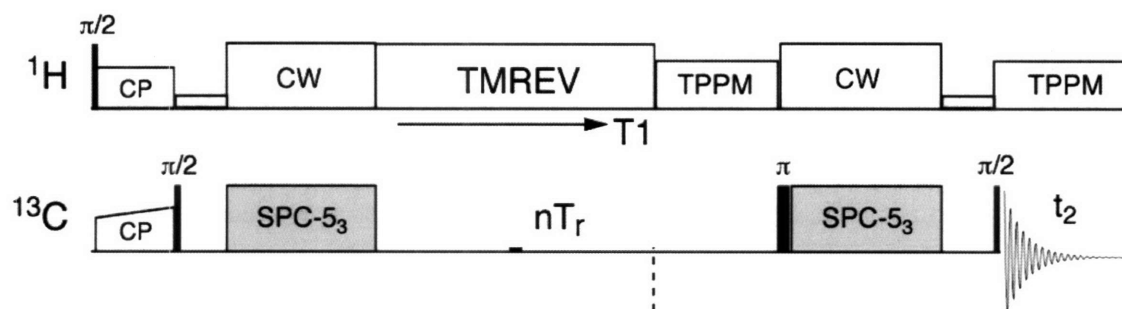
Figure 11-19: 3D HCCH experiments for measurement of side chain χ_n torsion angles in uniformly labeled peptides. Double quantum coherence is created using the band-selective SPC-5_3 recoupling sequence [55] and allowed to dephase under the ^{1}H-^{13}C dipolar interactions, reintroduced by TMREV [54].

The 3D HCCH experiment for side chain torsion angle measurements can be implemented in one of two ways: in one implementation, show in Figure 11-19, a double quantum coherence dephases under the recoupled ^{1}H-^{13}C dipolar interactions. A second implementation involves two separate synchronous dipolar recoupling periods. In both cases, the narrowband homonuclear recoupling sequence SPC5$_3$ is used to generate double quantum coherence or polarization transfer. The results of these experiences, show in Figure 11-20, suggest that there are differences in the side chain torsion angles of N-form and O-form MLF. However, because of systematic degeneracies in the data analysis, these constraints have not been included at this stage of the structural refinement. In the related NCCN experiment, which provides constraints on the ψ backbone torsion angle, SPC5$_3$ is used to generate double quantum coherence between C'-Cα, and this is allowed to dephase under the N-C' and N-Cα interactions which are recoupled simultaneously using REDOR. The resulting dephasing trajectories can be fit to obtain constraints on the torsion angle, as shown in Figure 11-21 for the case of the Leucine residue in MLF.

The structural data resulting from these experiments is summarized in Table 11.4 and Table 11.5. Solutions for the torsion angle inherently dependent on the precise value of the heteronuclear ^{1}H-^{15}N and ^{1}H-^{13}C couplings and on the three-atom bond angles used in the calculation of the projection angles. For all fits, we used the equilibrium parameters specified in the X-Plor NIH NMR refinement forcefield for consistency. The expected variation of bond angles about these average values can induce a ±10-15 degree uncertainty in the solution for the projection angle, which in all cases is greater than the random error in these experiments.
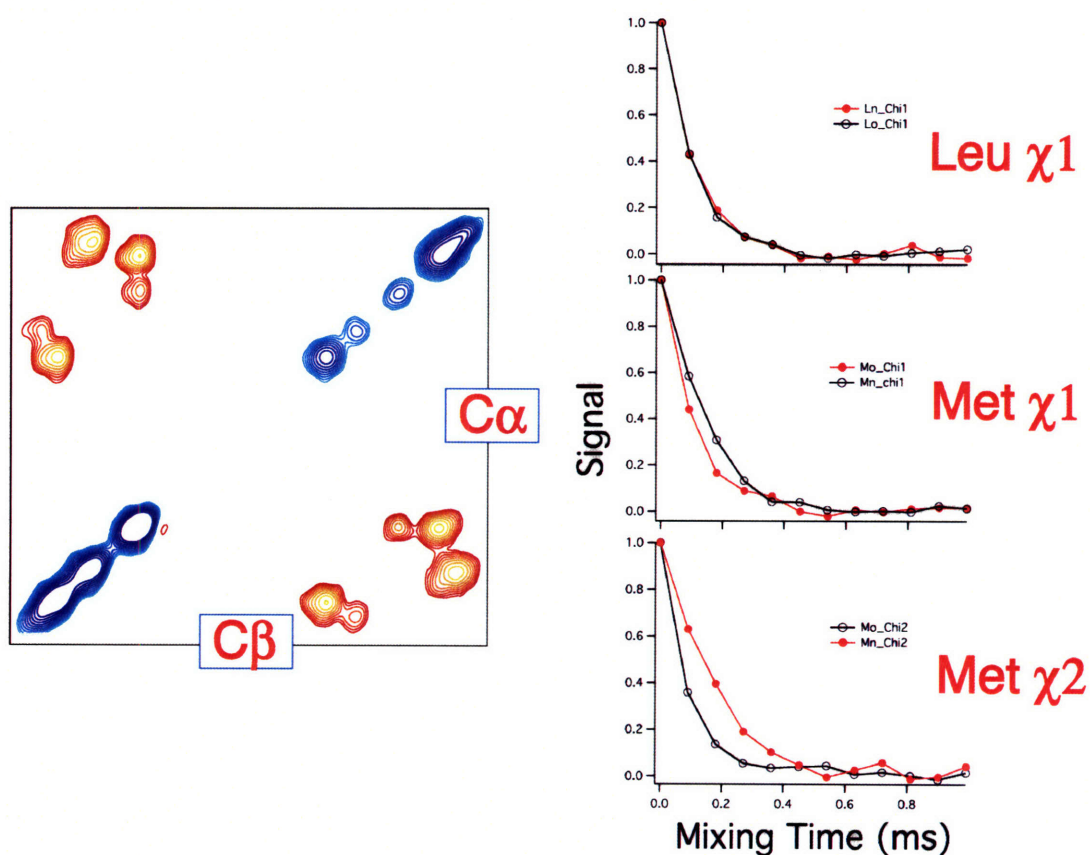
Figure 11-20: Experimental data for HCCH tensor correlation experiment designed to measure the χ_n torsion angles in MLF at 175K. The results show significant differences in side chain conformation between the two forms of MLF which co-exist at 175K.
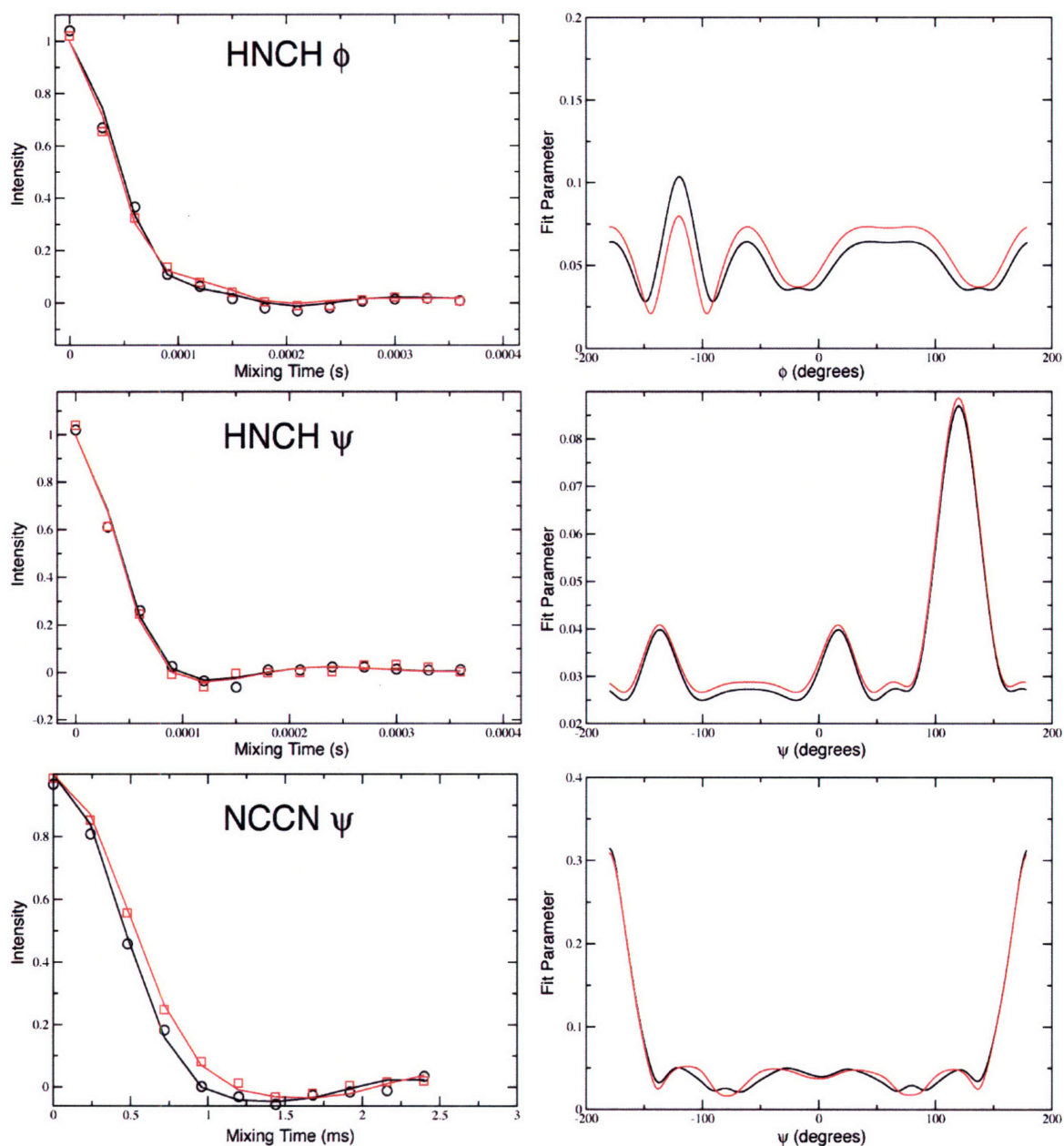
Figure 11-21: Examples of data fitting and resulting solution surfaces for the backbone torsion angles of Leucine in N-form (red) and O-form (black) f-MLF-OH as measured in HNCH (ϕ), $HN_{i+1}C_iH$ (ψ), and NCCN (ψ) tensor correlation experiments.

Table 11.4: Summary of torsion angle measurements resulting from HNi-CiH (f), HNi+1-Ci-H (y) and NCCN (y) dipolar tensor correlation experiments.

	ϕ H-N$_i$-Cα_i-H	ψ H-N(i+1)-Cα-H	N-Cα-C'-N
Mn	-150, -90 (-17, 137)	144, 95	-154, 154
Mo	164, 105, (-46, -164)	-160, -110,40, 157	-159, 159
Ln	-144, -96	-100, -19, 48	-78, 78
Lo	-149, -91	-101, -18, 46	-69, 69
Fn	156, 117; 3, -36; -84, -157	n/a	n/a
Fo	171, 97; 21, -55; -72, -167	n/a	n/a

Table 11.5: Summary of distance measurements resulting from 3D TEDOR experiments [38].

		Distance (nm)		
		RT form (298K)	Form-0 (175 K)	Form-N (175K)
Met. N	MC-MN	250	240	240
	Mα-MN	150	150	150
	Mβ-MN	250	255	240
	Mγ-MN	380	320	440
	Mϵ-MN	530	540	640
Leu. N	MC-LN	130	135	135
	Mα-LN	260	255	235
	Mβ-LN	320	330	
	Mγ-LN	500	420	425
	Mϵ-LN	580	620	630
	LC-LN	240	250	315
	Lα-LN	150	150	150
	Lβ-LN	260	240	235
	Lγ/δ-LN	360	355	460
	Lδ2-LN	390	400	
Phe. N	Mϵ-FN	520	540	580
	LC-FN	130	135	140
	Lα-FN	230	235	230
	Lβ-FN	320	340	325
	Lγ/δ-FN	450		490
	Lδ2-FN	600		
	FC-FN	270	245	245
	Fα-FN	140	145	145
	Fβ-FN	260	245	235
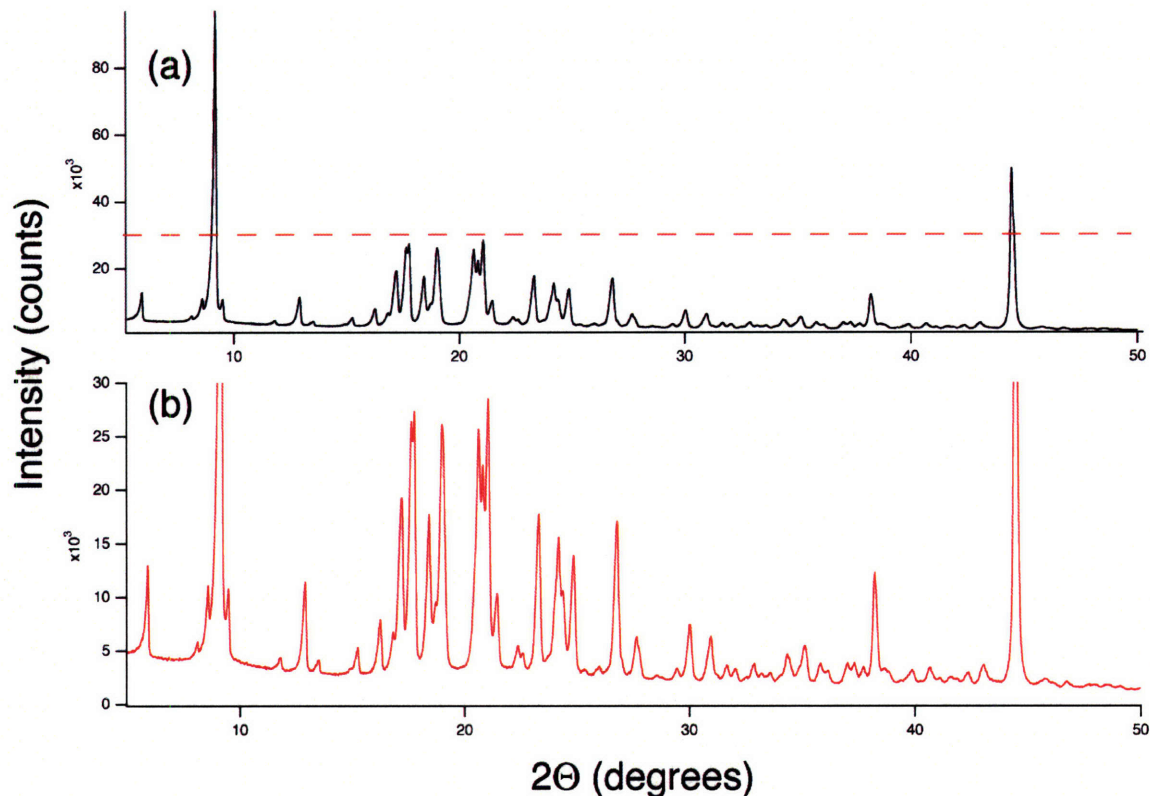
Figure 11-22: Powder diffraction pattern of *f*-MLF-OH sample used in NMR studies. The unit cell parameters (P2₁2₁2₁, a=21.9, b=20.7, c=5.3) were obtained through indexing in CRYSFIRE and rigid body refinement in the program UNITCell.

11.3.5   Powder diffraction

While there is a high resolution diffraction structure of *f*-MLF-OMe, *f*-MLF-OH does not

yield crystals of sufficient size for diffraction experiments. Nevertheless, we expect that

the dynamics might be influenced by crystal packing, and so it is important to determine

if the crystal packing arrangement is similar in both peptides. In order to verify that the

crystallographic parameters of *f*-MLF-OH are similar to those of *f*-MLF-OMe, we

conducted powder diffraction experiments (MIT CMSE), show in Figure 11-22.

Following indexing, analysis, and refinement, we obtained unit cell parameters of

P2₁2₁2₁, with a=21.9, b=20.7, c=5.3. The published parameters for *f*-MLF-OMe are

P2₁2₁2₁ with a=21.7, b=21.8, c=5.1. The slightly larger unit cell of *f*-MLF-OH may

explain its greater ring dynamics, and this is also suggested by greater equilibrium

displacements in short-time molecular dynamics simulations of the MLF crystal in the program GROMACS (not shown). However, it was computationally infeasible to extend these simulations to the timescales probed by NMR experiments.

11.3.6   Direct Probe of Dynamics

If a dynamical process imparts time-dependence to a dipolar coupling, the dipolar coupling may be averaged from its static value. In turn, the magnitude of a recoupled dipolar interaction will also be averaged. Thus, by monitoring the magnitude of dipolar couplings through recoupling experiments as a function of temperature, the thermal activation and other parameters of the process can be identified, if there is a model to explain the motion. We have monitored the ^{1}H-^{13}C dipolar couplings as a function of temperature using the TMREV recoupling sequence (Figure 11-23).
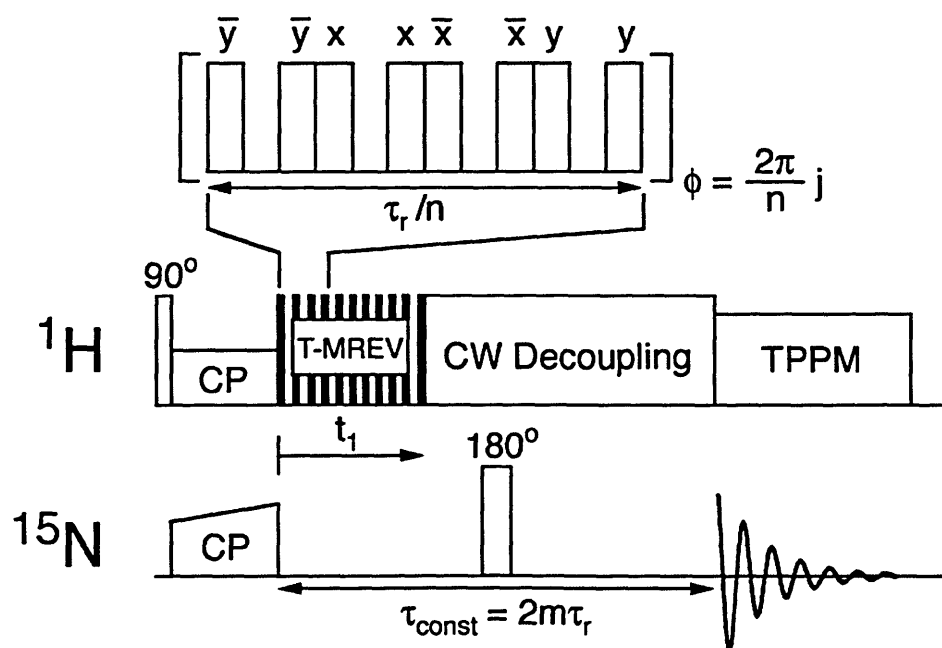
Figure 11-23: TMREV [54] experiment to probe averaging of ^{1}H-^{13}C dipolar couplings as a function of temperature.

The dipolar lineshapes, shown in Figure 11-24 and Figure 11-25 change significantly as a function of temperature. In particular, they indicate that methyl and aromatic motions slow down progressively as the temperature is reduced, and that the dipolar couplings, shown in Figure 11-25, reach a limit near the value of the glass transition temperature. This change in the averaging of the dipolar coupling strength, which is directly related to the dynamics, is correlated to the emergence of a second form of MLF at low temperatures.
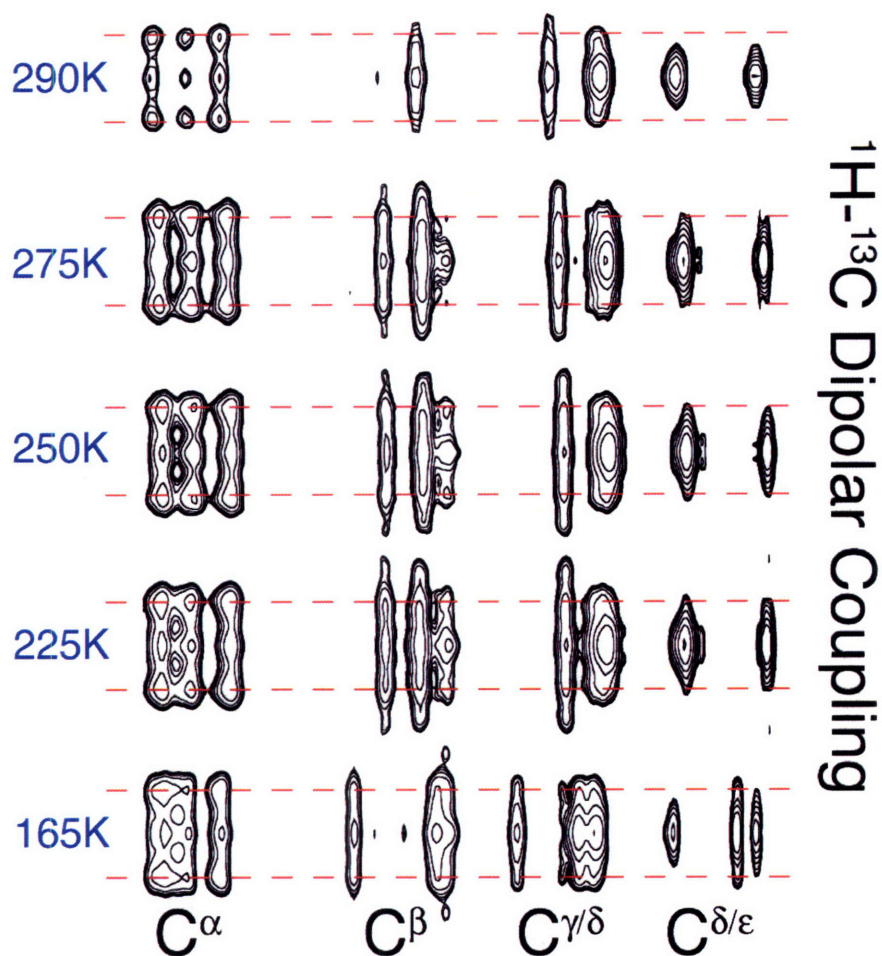
Figure 11-24: Span of recoupled dipolar interaction as a function of temperature. The second dimension is generated from a Fourier transform of the dipolar dephasing curve under TMREV recoupling. Note the increase in apparently methyl group dipolar couplings as the temperature is reduced.
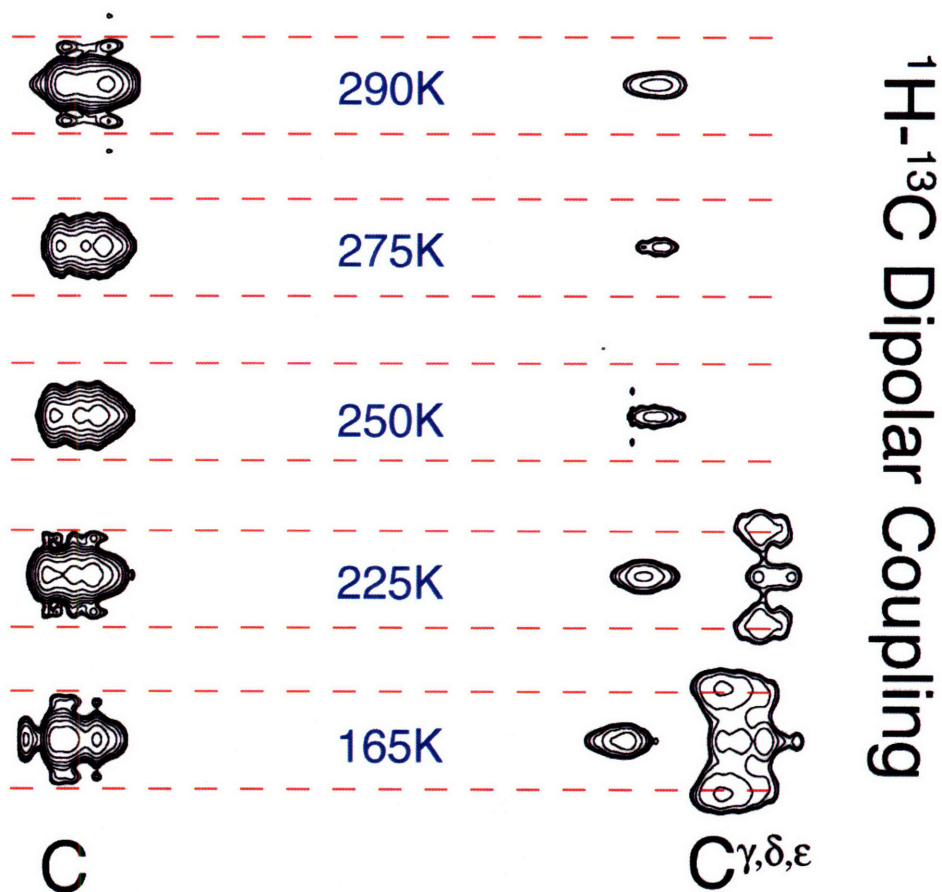
Figure 11-25: Span of recoupled dipolar interactions in TMREV experiments as a function of temperature. The dramatic change in the dipolar lineshape of the aromatic carbons clearly indicates a change in their dynamics with temperature.

11.4   Discussion

The NMR data show a remarkable difference in dynamical behavior between the two tripeptide crystals, despite their similar chemical structure and crystallization behavior. As expected for a largely rigid system, the changes in the NMR spectra of the methylated peptide *f*-MLF-OMe are relatively small. They are limited to changes in the methyl group intensities, with the variations correlated to the steric hindrance encountered by the methyl group during its three-fold jump. The interference of the ^{1}H-^{13}C decoupling due to a reduction in CH_3 jump rate occurs at a higher temperature for the Leu side chain methyls. At 90K, the Met CH_3 group rotation remains fast enough to prevent such

destructive interference. The various ^{15}N and ^{13}C resonance frequencies remain unaffected, including those of the Phe side chain (which is immobile up to room temperature).
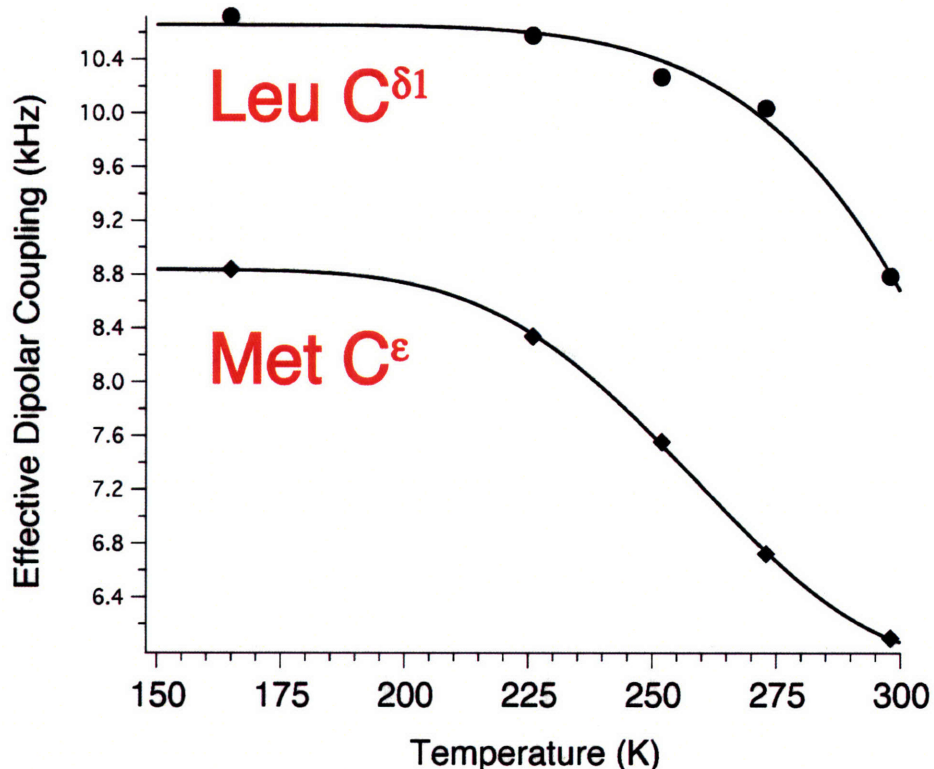
Figure 11-26: Effective (scaled) dipolar couplings for two methyl groups as a function of temperature. The methionine Cε methyl appears to be in a less hindered environment than the Leu Cδ1, though both experience an apparent loss of dynamics near the glass transition temperature.

Spectra of the *f*-MLF-OH peptide show the same manifestations of methyl group dynamics (disappearance of Leu methyls), but significant additional effects of cooling are also visible. These effects include the temperature-correlated emergence of a second conformational substate which is correlated to the dynamical transition. In order to study this further, we applied several solid state NMR methods to measure structural parameters of the peptide at 175K. The variable temperature structural measurements

were complicated by the disappearance of the Leu methyl groups at lower temperatures, but the chemical shifts suggest that the peptide is structurally similar.

In the conventional picture of temperature-activated conformational exchange as monitored by NMR, a transition between two states results in spectra with an averaged, narrow resonance at high temperature, a broad, single resonance at intermediate temperatures, and separate narrow resonances at temperatures low enough to arrest the dynamics. Interestingly, *f*-MLF-OH does not display this behavior, but rather shows a distribution between two distinct, similarly narrow sets of NMR lines. Even more atypical seems the observation that the form that appears upon cooling, again disappears at even lower temperatures.

The phase transition in *f*-MLF-OH takes place between 200 and 100K. Concomitantly, there is a drastic reduction in the intensity of the methyl group resonances. The temperature range of the transition is below the canonical protein glass transition, which is generally observed at 200-230K [10]. The observed dynamical event does correlate with the observed onset of anharmonic motion at temperatures above 100K, which was proposed to be associated with methyl group dynamics [7, 11, 16, 56]. Our system highlights the fact that another potentially important source of side chain motions in proteins can be associated with the aromatic side chains, such as phenylalanine. The predominant difference between the *f*-MLF-OH and *f*-MLF-OMe crystals revolves around the dynamic of the Phe ring. As illustrated in Figure 11-1, the aromatic ring in *f*-MLF-OMe is prevented from flipping by the close proximity of a number of bulky groups, including the C-terminal methyl group (OMe). The lack of this group in *f*-MLF-OH allows the Phe 180° flip, which must play a role in the observed phase behavior.
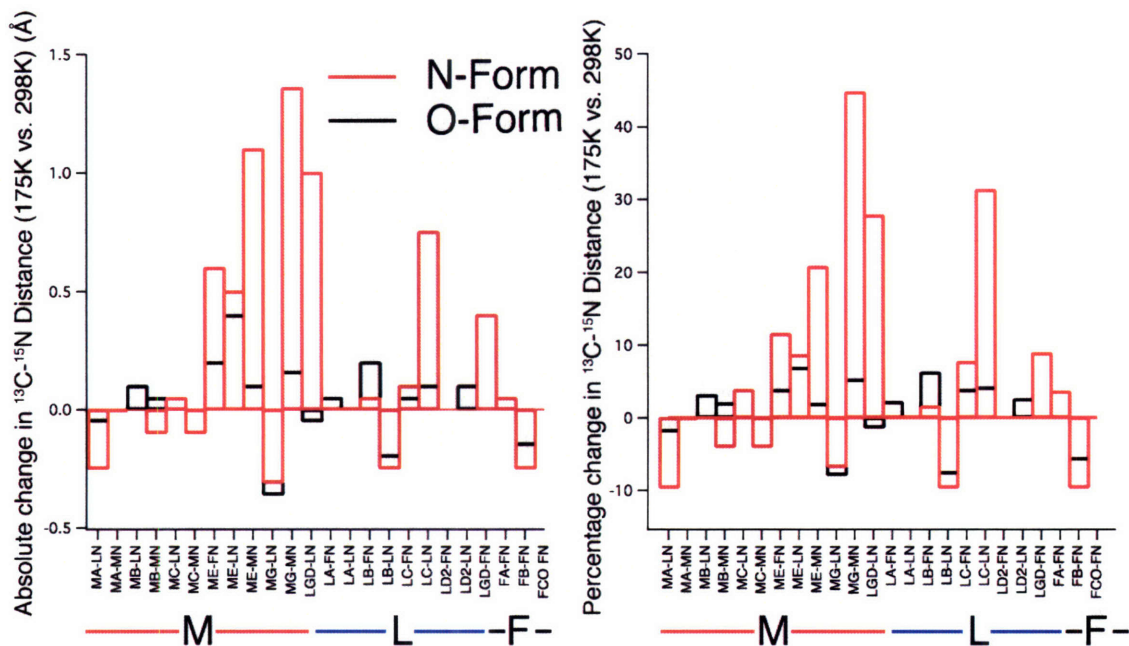
Figure 11-27: Deviation in heteronuclear distances in two forms of MLF at 175K from their room temperature values (indicated by red line at y=0). The N-form of MLF has systematically longer distances than the O-form, which closely resembles both the room temperature and 90K MLF structures.

Aside from the implications for low temperature protein dynamics, our results are also relevant to low temperature solid state NMR applications. We observe that line broadening as a result of cooling to low temperatures (even in a dynamical system) does not preclude low temperature NMR experiments. As previously observed in a number of other peptide and protein systems, one can obtain relatively narrow spectral lines at temperatures down to 90K. While there might be solvent-dependent mechanisms which result in broadening of NMR lines near the glass transition, it may be possible to manipulate these through solvent composition and cooling rate. As has already been demonstrated, the attenuation of signals from sites in intermediate-rate conformational exchange can be ameliorated through specific deuteration.
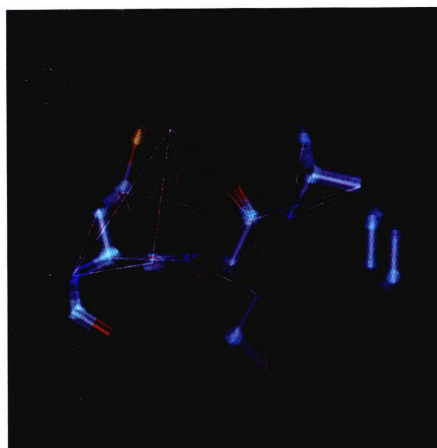
Figure 11-28: Density of structural constraints for N-form of MLF superimposed on MLF structure.

11.4.1   Refinement

The high resolution structures of two forms of MLF, the N-form and the O-form, were refined based on solid state NMR constraints using previously established protocols for simulated annealing molecular dynamics [36] as implemented in the program X-Plor-NIH [57]. Due to the lack of intensity in the methyl resonances at 90K, no side chain constraints could be obtained for the Leucine residue, and hence no structural refinement was attempted for MLF at this temperature. However, its chemical shifts suggest that this form closely resembles the room temperature form of MLF. As shown in Figure 11-28, solid-state NMR measurements provide approximately 9 constraints/residue, which is sufficient to yield structural ensembles characterized by a root mean squared deviation in heavy atom coordinates of 0.53 Å for O-form MLF. The lack of constraints on the terminal Phe. residue allows it to assume a variety of conformations in the refinement. While it is possible to further constrain its conformation by applying either an excluded volume restraint or periodic boundary conditions representing the MLF crystal lattice, no such approaches were attempted here. Representative members of the structural ensemble for N-form and O-form MLF are shown in Figure 11-29.

O-form   **N-form**
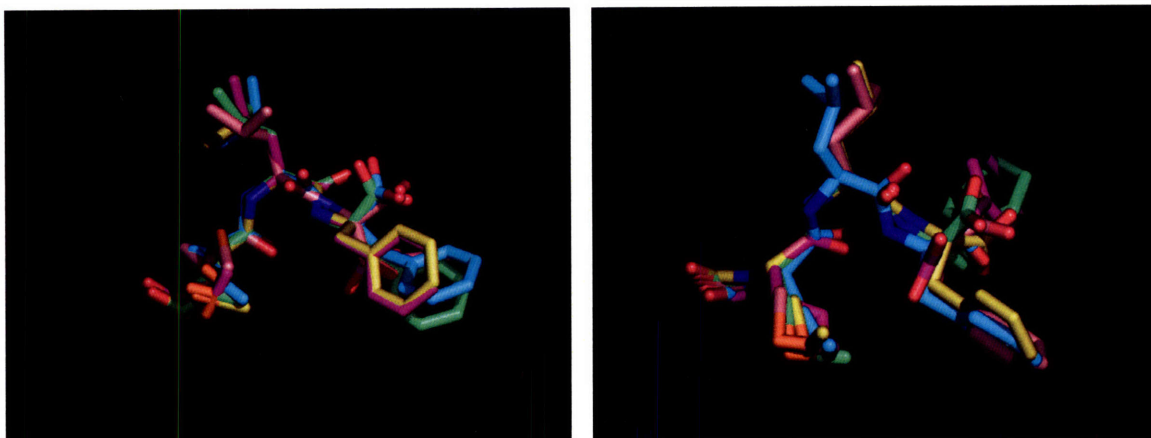
Figure 11-29: Preliminary refinement of MLF structures on the basis of experimental data at 175K. It is anticipated that inclusion of additional side-chain torsion angle data in the refinement data set will improve the ensemble. Differences between the O-form and N-form structures are most pronounced in the side chains. The ensembles are generated by selecting the five structures which represent the conformational space spanned by the 100 lowest energy conformers in the refined ensembles. Alignments are generated to all heavy atoms.
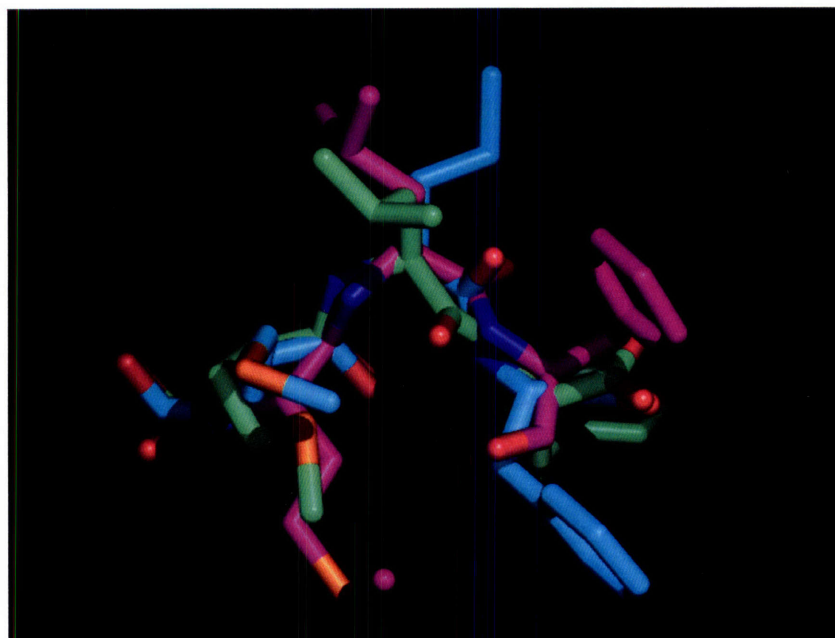
Figure 11-30: Superposition of 298K, N-form, and O-form MLF average structures as determined by solid state NMR. Structural coordinates were averaged and then subjected to minimization in Cartesian coordinates (in X-PLOR-NIH) to eliminate inappropriate geometries and steric clashes.

Average structures for three forms of MLF are superimposed in Figure 11-30. Though there are differences in the backbone torsion angles, the structures predominantly differ in side chain conformation. The structure of the O-form of MLF is similar to the room temperature form, while the N-form has systematically longer distances and a different conformation of the Leucine side chain, in particular.

A cooperative and reversible structural transition occurs between these forms as the sample is cooled from ambient to cryogenic temperatures. The structural phase transition is accompanied by a coupled transition in the range of dynamics experienced by the sample, and both have similar temperature dependence. There are no intermediate range exchange dynamics as would be expected if the N-form and O-form of MLF existed and were in conformational exchange at room temperature. Further, in the related *f*-MLF-OMe peptide, whose crystal lattice excludes a subset of the ring motions experienced by *f*-MLF-OH at room temperature, no such phase transition occurs. It is reasonable to ask whether or not the activation of these dynamical modes is necessary for the structural phase transition to occur, or if the reverse is true. Our measurements elucidate the endpoints of this phase transition but do not provide information about its mechanism. In order to understand this further, it may be possible to conduct molecular dynamics simulations to assess the stability and range of motion in the MLF lattice, using these structures as a starting points or for comparison. We conducted molecular dynamics simulations in the program GROMACS [58, 59] to confirm a greater degree of dynamics at short time scales in *f*-MLF-OH as compared to *f*-MLF-OMe, but it was not computationally feasible to extend these approaches to monitor the dynamical timescales associated with NMR measurements. Using replica exchange or parallel tempering molecular dynamics [60-62] and periodic boundary conditions to represent the MLF

lattice, it appears computationally practical to extend this approach to the millisecond timescale. Such a study may reveal the connection between the dynamical and structural phase transitions seen here. Further, molecular dynamics simulations may be used for ensemble averaging of NMR restraints, and thus might be helpful in generating more accurate estimates of dipolar couplings and torsion angles in the presence of dynamics.

11.4.2 Protein Applications

The tripeptide MLF is model system for a subset of the range of dynamics experienced by proteins near the glass transition temperature. It may be a model for, in particular, the part of the glass transition which is due to the loss of anharmonic motional modes of the protein. While methyl dynamics have been invoked to explain the glass transition in the past [8], it is increasingly clear that the transition also involves coupling to the range of structures and dynamics experienced by the solvent. In the context of low-temperature NMR studies such as those involving Dynamic Nuclear Polarization, the source of line broadening observed at low temperatures in some microcrystalline protein systems [63] [64] is of particular interest. Several explanations are possible: first, it may be possible that the crystal structure of the system is being damaged by freezing at low temperature. The observation that temperature-induced line broadening is reversible in microcrystalline systems tends to exclude this hypothesis. Second, temperature-induced or so-called "cold denaturation" of the protein may be responsible for the line broadening. Indeed, there may be structural heterogeneity without static disorder, as shown in the case of MLF, which would only become visible in multidimensional correlation spectra and would appear as line broadening in 1D spectra of a protein with hundreds or thousands of chemical sites. Finally, the freezing of the solvent at low

temperature may induce static disorder in the sites with which it interacts structurally; equivalently, it may introduce line broadening through its interaction with these sites via the magnetic dipolar coupling.

Table 11.6: Plasmid sequence of pet30-GB1 plasmid and translated amino acid sequence of GB1 fusion peptide crystallized and used for these experiments (legend: EcoRI sites; NdeI sites; cac C-terminal HIS tag). (bottom) SDS PAGE (18-20% gradient) gel illustrating purification of polypeptide following cell lysis.

```
cat ATG CAG TAC AAA CTG ATC CTG AAC GGT AAA ACC CTG AAA GGT
GAA ACC ACC ACC GAA GCT GTT GAC GCT GCT ACC GCG GAA AAA GTT
TTC AAA CAG TAC GCT AAC GAC AAC GGT GTT GAC GGT GAA TGG ACC
TAC GAC GAC GCT ACC AAA ACC TTC ACC GTT ACC GAA GGA TCC CAC
CAC CAC CAC CAC CAC TAA gaa ttc
```

1-MQYKLILNGK TLKGETTTEA VDAATAEKVF KQYANDNGVD GEWTYDDATK TFTVTEGSHHHHHH-64

marker | pellet - 2.5 hrs | pellet - 5 hrs | pellet - 5 hrs detergent lysis | pellet - 5 hrs detergent lysis | pellet - 5 hrs control | purified fractions
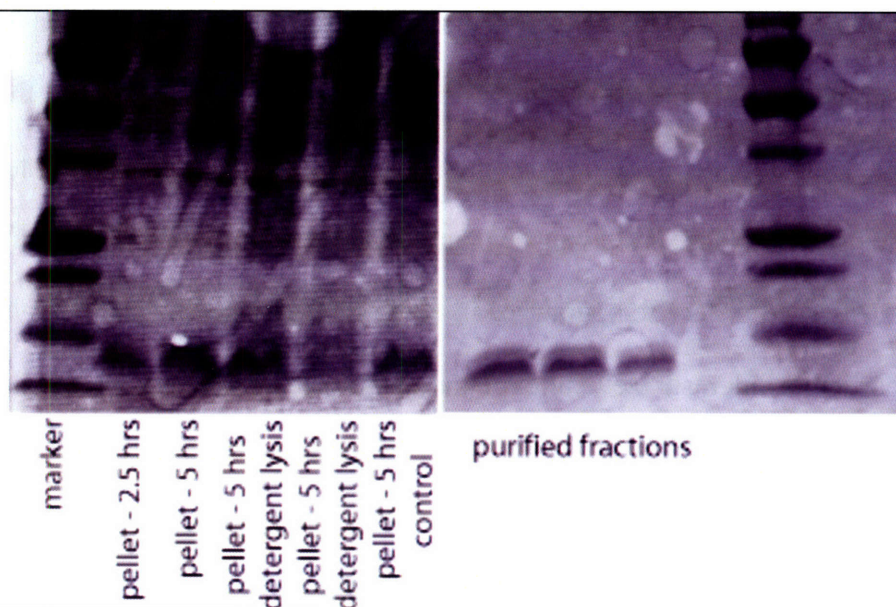
In order to study this problem, we began an investigation of immunoglobulin binding (B1) domain of Protein G, a small, thermally stable protein that has been characterized previously by crystallography [65], solution state NMR [66], and solid state NMR [64]. The protein (see Table 11.6) was overexpressed in e.coli as a fusion peptide with a 6-residue, N-terminal HIS tag that was used for affinity purification of the lysate. The

lysate was produced by detergent lysis, as this gave the best yield of purified product. It is important to note that these experiments have involved a different protein construct, and hence a protein with different physical properties, than that used in the solid state NMR experiments of Rienstra and colleagues. Following affinity chromatography, the polypeptide was further purified using gel filtration chromatography and then dialyzed into the crystallization buffer (25 mM sodium acetate, pH 4.5). Crystallization conditions were established by hanging drop vapor exchange methods starting from a protein concentration of 30 mg/mL. Batch crystallization was accomplished using two approaches. First, the sample was crystallized using PEG 2000 (50% w/v) as a crowding agent and by using a SpeedVac centrifugal evaporation unit to bring the sample gradually to a concentration at which precipitation can occur [63]. Cryoprotectants such as glycerol were added to the initial crystallization buffer in a concentration that resulted in bulk glass formation upon freezing at the target concentration of precipitant. A second approach utilizes methylpentanediol (MPD) as a precipitant and has been described in the solid state NMR literature [64]. Following crystallization, the samples were packed by centrifugation into 3.2 mm or 4 mm NMR rotors.

The samples were initially characterized at room temperature using a 700 MHz NMR spectrometer. We have recorded 2D ^{13}C-^{13}C correlation spectra at 700 MHz using proton driven spin diffusion with an R^3 recoupling field (DARR[67]). Two-dimensional NCA and NCACX-type ^{15}N-^{13}C correlation spectra were recorded using approaches described earlier. The spectra, shown in Figure 11-31, Figure 11-32, and Figure 11-33, show resolution typical of microcrystalline proteins, with the majority of cross peaks resolved in a two-dimensional experiment.
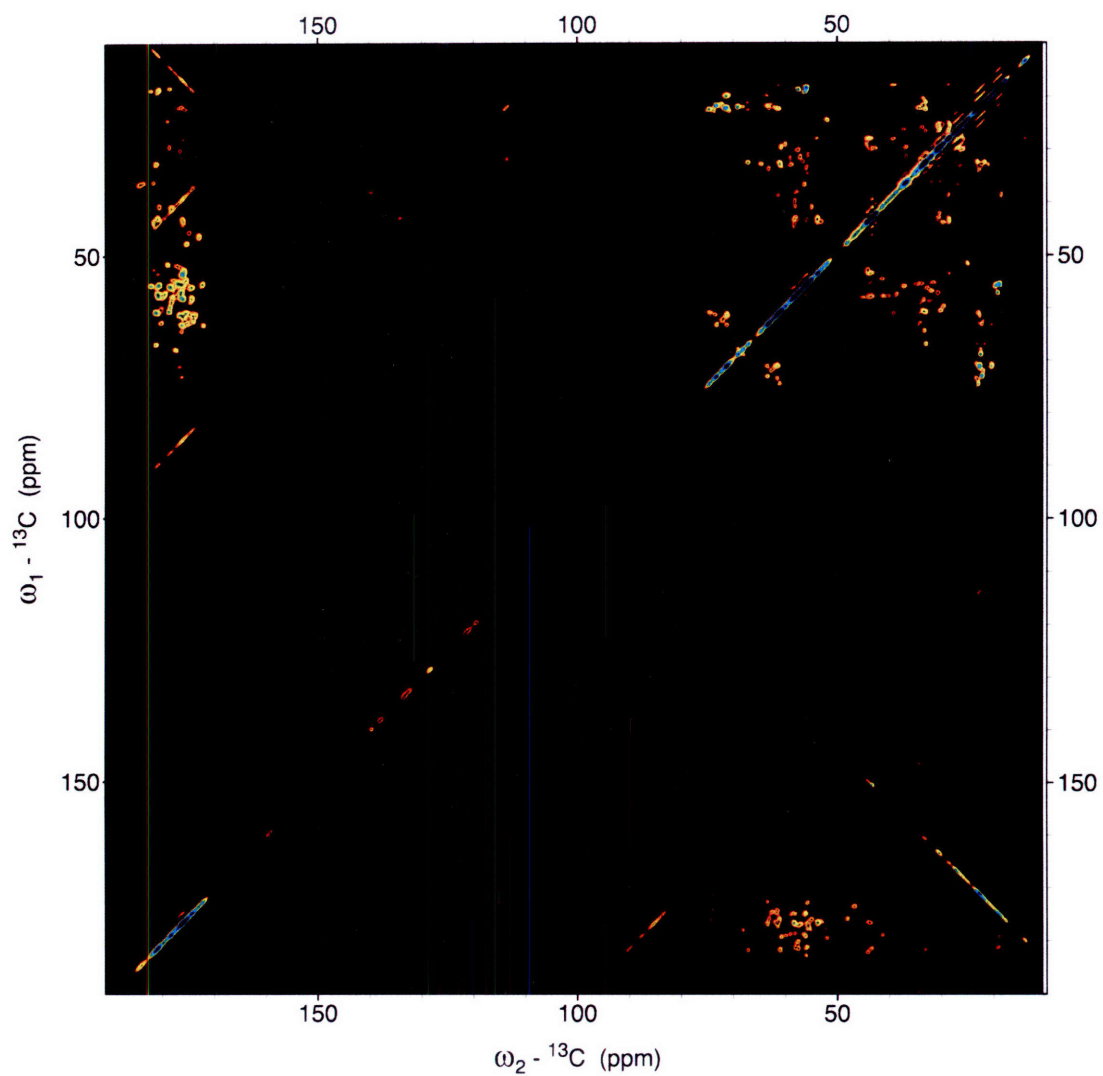
Figure 11-31: Homonuclear ^{13}C-^{13}C correlation experiment in nanocrystalline protein GB1 recorded at 700 MHz with DARR. The protein was prepared through precipitation in polyethylene glycol. Note the excellent resolution, which is typical of microcrystalline proteins.
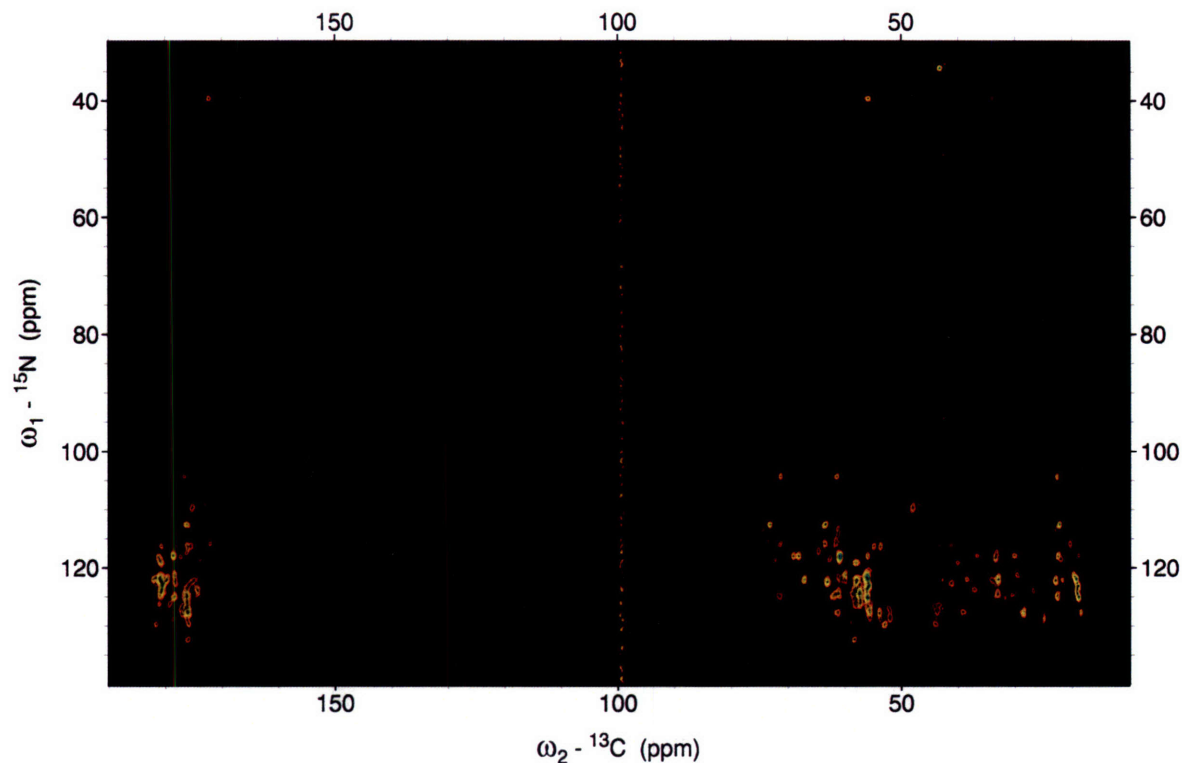
Figure 11-32: Heteronuclear ^{13}C-^{15}N NCACX-type correlation experiment in nanocrystalline protein GB1 recorded at 700 MHz.

The low-temperature dynamics of this system were studied on the 380 MHz DNP spectrometer, which is able to access a wide variety of temperatures. The results of this very initial study for samples of GB1 cryoprotected with 20% glycerol are shown in Figure 11-34. The resolution for this microcrystalline sample is surprisingly high even at 380 MHz, a comparatively low field for biomolecular NMR applications. Upon cooling, there is a loss of resolution due to line broadening (see for example, the Threonine Cα-Cβ region), but detailed analysis of 3D spectra for resolved regions (*e.g.* proline, threonine) will be required to understand the basis for these effects. In Figure 11-35, one-dimensional spectra of a ^{15}N-labeled GB1 sample precipitated from MPD show a more dramatic loss of resolution with temperature, indicating that solvent dynamics may play a role in these processes.
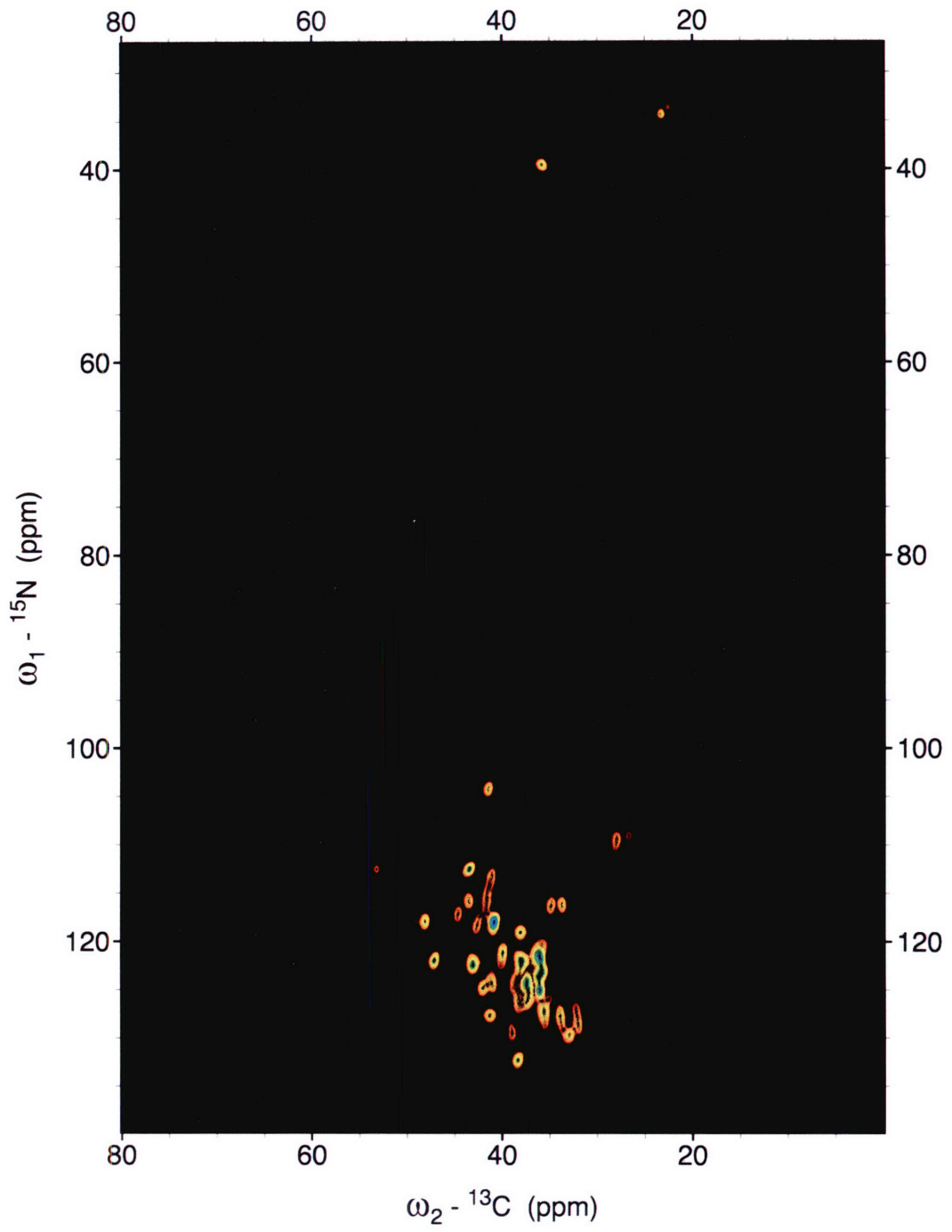
Figure 11-33: Heteronuclear ^{13}C-^{15}N NCA-type correlation experiment in nanocrystalline protein GB1 recorded at 700 MHz.
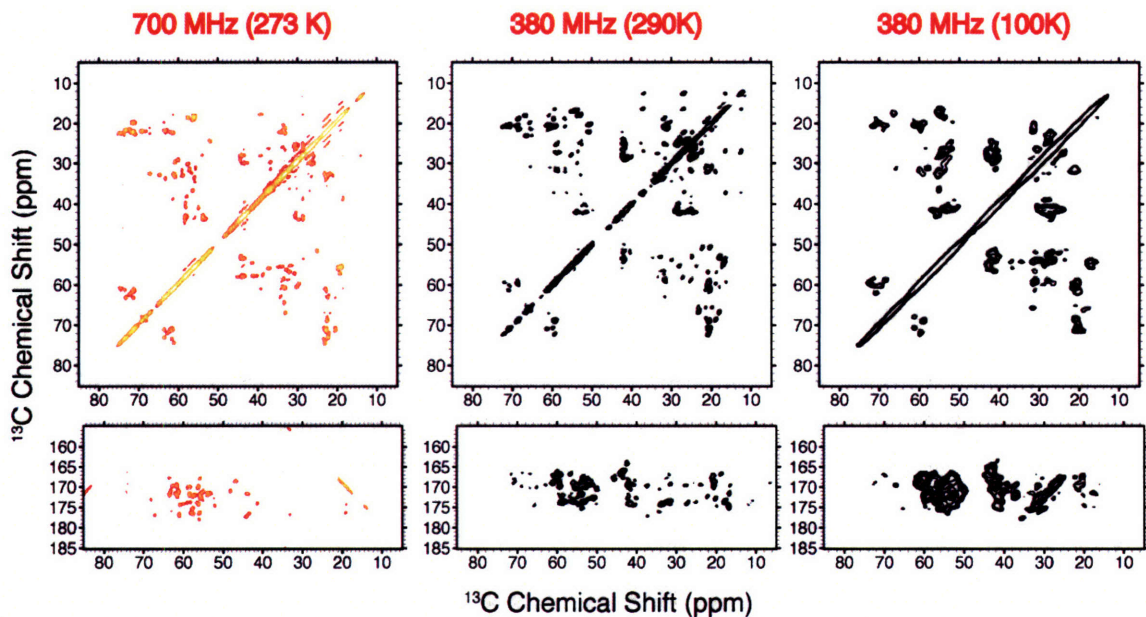
Figure 11-34: A comparison of homonuclear correlation spectra of protein GB1. (left) PEG-precipitated sample of GB1 at 700 MHz, 273K; (middle) homonuclear correlation spectrum of a sample of GB1 precipitated from PEG and cryoprotected with glycerol, recorded at 380 MHz; (right) the same sample, cooled to 100K.
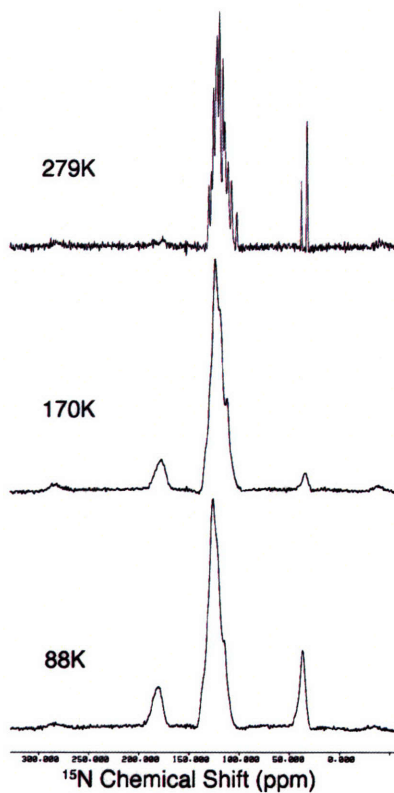
Figure 11-35: 1D ^{15}N spectra of U-^{15}N-MLF microcrystals prepared by precipitation in MPD. Note the loss of resolution at lower temperatures.

A complete study of these effects was not attempted here. At the very least, such a study will involve recording resolved 2D or 3D correlation spectra in GB1 samples at a variety of intermediate temperatures from 290K to 90K. The role of cryoprotection can be explored by measuring spectra in samples prepared with different cryoprotectants or different concentrations of a single effective cryoprotectant, such as glycerol. Further, the direct or indirect involvement of the solvent can be tested by preparing samples from highly deuterated solvents. Ultimately, the degree of chemical shift resolution and sensitivity realized in these initial experiments suggests that all of the approaches used for the elucidation of the structural phase transition in MLF can be applied to probe the structural and dynamical basis of the glass transition in a protein such as GB1.

11.5   References

[1]   Kendrew, J. C.; Bodo, G.; Dintzis, H. M.; Parrish, R. G.; Wyckoff, H.; Phillips, D. C., A Three-Dimensional Model of the Myoglobin Molecule Obtained by X-Ray Analysis. *Nature* **1958,** 181, (4610), 662-666.

[2]   Elber, R.; Karplus, M., Multiple Conformational States of Proteins - a Molecular-Dynamics Analysis of Myoglobin. *Science* **1987,** 235, (4786), 318-321.

[3]   Elber, R.; Karplus, M., Low-Frequency Modes in Proteins - Use of the Effective-Medium Approximation to Interpret the Fractal Dimension Observed in Electron-Spin Relaxation Measurements. *Physical Review Letters* **1986,** 56, (4), 394-397.

[4]   Kushida, T.; Kanematsu, Y.; Kurita, A., Studies on the liquid-glass transition of proteins and their structural changes by site selective fluorescence. *Kobunshi Ronbunshu* **1996,** 53, (10), 614-627.

[5]   Ringe, D.; Petsko, G. A., The 'glass transition' in protein dynamics: what it is, why it occurs, and how to exploit it. *Biophysical Chemistry* **2003,** 105, 667–680.

[6]   Petsko, G. A.; Ringe, D., Understanding and exploiting the "glass transition" in protein dynamics. *Abstracts of Papers of the American Chemical Society* **2003,** 225, U781-U781.

[7]   Vitkup, D.; Ringe, D.; Petsko, G. A.; Karplus, M., Solvent mobility and the protein 'glass' transition. *Nature Structural Biology* **2000**, 7, (1), 34-38.

[8]   Lee, A. L.; Wand, A. J., Microscopic origins of entropy, heat capacity and the glass transition in proteins. *Nature* **2001**, 411, (6836), 501-504.

[9]   Gutin, A.; Sali, A.; Abkevich, V.; Karplus, M.; Shakhnovich, E. I., Temperature dependence of the folding rate in a simple protein model: Search for a "glass" transition. *Journal of Chemical Physics* **1998**, 108, (15), 6466-6483.

[10]   Mok, K. H.; Nagashima, T.; Day, I. J.; Jones, J. A.; Jones, C. J. V.; Dobson, C. M.; Hore, P. J., Rapid sample-mixing technique for transient NMR and photo-CIDNP spectroscopy: Applications to real-time protein folding. *Journal of the American Chemical Society* **2003**, 125, (41), 12484-12492.

[11]   Caliskan, G.; Briber, R. M.; Thirumalai, D.; Garcia-Sakai, V.; Woodson, S. A.; Sokolov, A. P., Dynamic transition in tRNA is solvent induced. *Journal of the American Chemical Society* **2006**, 128, (1), 32-33.

[12]   Teeter, M. M.; Yamano, A.; Stec, B.; Mohanty, U., On the nature of a glassy state of matter in a hydrated protein: Relation to protein function. *Proceedings of the National Academy of Sciences of the United States of America* **2001**, 98, (20), 11242-11247.

[13]   Rassmussen, B. F.; Stock, A. M.; Wallon, G.; Lovat, S.; Oshima, T.; Kanaoka, M.; Zavodsky, P.; Ringe, D.; Petsko, G. A., Probing the Relationship between Protein Flexibility and Protein Function through the Glass-Transition in Dynamic Behavior at 220-K. *Faseb Journal* **1992**, 6, (1), A411-A411.

[14]   Mayer, E., Ftir Spectroscopic Study of the Dynamics of Conformational Substates in Hydrated Carbonyl-Myoglobin Films Via Temperature-Dependence of the Co Stretching Band Parameters. *Biophysical Journal* **1994**, 67, (2), 862-873.

[15]   Doster, W.; Bachleitner, A.; Dunau, R.; Hiebl, M.; Luscher, E., Thermal-Properties of Water in Myoglobin Crystals and Solutions at Subzero Temperatures. *Biophysical Journal* **1986**, 50, (2), 213-219.

[16]   Boswell, P. G.; Lugert, E. C.; Rabai, J.; Amin, E. A.; Buhlmann, P., Coordinative properties of highly fluorinated solvents with amino and ether groups. *Journal of the American Chemical Society* **2005**, 127, (48), 16976-16984.

[17]   Smith, J.; Kuczera, K.; Karplus, M., Dynamics of Myoglobin - Comparison of Simulation Results with Neutron-Scattering Spectra. *Proceedings of the National Academy of Sciences of the United States of America* **1990**, 87, (4), 1601-1605.

[18]   Hong, M.; Griffin, R. G., Resonance assignments for solid peptides by dipolar-mediated $^{13}C/^{15}N$ correlation solid-state NMR. *J. Am. Chem. Soc.* **1998**, 120, 7113-7114.

[19]   Ladizhansky, V.; Veshtort, M.; Griffin, R. G., NMR determination of the torsion angle ψ in α–helical peptides and proteins: the HCCN dipolar correlation experiment. *J. Magn. Reson.* **2002**, 154, (2), 317-324.

[20]   Jaroniec, C. P.; Tounge, B. A.; Herzfeld, J.; Griffin, R. G., Frequency selective heteronuclear dipolar recoupling in rotating solids: accurate ^{13}C-^{15}N distance measurements in uniformly-^{13}C,^{15}N-labeled peptides. *J. Am. Chem. Soc.* **2001**, 3507-3519.

[21]   Sun, B. Q.; Rienstra, C. M.; Costa, P. R.; Williamson, J. R.; Griffin, R. G., 3D ^{15}N-^{13}C-^{13}C chemical shift correlation spectroscopy in rotating solids. *J. Am. Chem. Soc.* **1997**, 119, 8540-8546.

[22]   Rienstra, C. M.; Tucker-Kellogg, L.; Jaroniec, C. P.; Hohwy, M.; Reif, B.; McMahon, M. T.; Tidor, B.; Lozano-Perez, T.; Griffin, R. G., *De Novo* Determination of Peptide Structure with Solid-State MAS NMR. *Proc. Nat. Acad. Sci. USA* **2002**, 99, 10260-10265.

[23]   Gavuzzo, E.; Mazza, F.; Pochetti, G.; Scatturin, A., Crystal structure, conformation, and potential energy calculations of the chemotactic peptide N-formyl-L-Met-L-Leu-L-Phe-OMe. *Int. J. Peptide Protein Res.* **1989**, 34, 409-415.

[24]   Bajaj, V. S.; Farrar, C. T.; Mastovsky, I.; Vieregg, J.; Bryant, J.; Elena, B.; Kreischer, K. E.; Temkin, R. J.; Griffin, R. G., Dynamic nuclear polarization at 9T using a novel 250 GHz gyrotron microwave source. *Journal of Magnetic Resonance* **2003**, 160, (2), 85-90.

[25]   Bajaj, V. S.; Hornstein, M. K.; Mak, M. L.; Herzfeld, J.; Griffin, R. G., A Magic Angle Spinning NMR Probe for Dynamic Nuclear Polarization Experiments at 9T (in preparation. *J. Mag. Res.* **2005**.

[26]   Morcombe, C. R.; Zilm, K. W., Chemical shift referencing in MAS solid state NMR. *Journal of Magnetic Resonance* **2003**, 162, (2), 479-486.

[27]   Markley, J. L.; Bax, A.; Arata, Y.; Hilbers, C. W.; Kaptein, R.; Sykes, B. D.; Wright, P. E.; Wüthrich, K., Recommendations for the presentation of NMR structures of proteins and nucleic acids. *Pure & Appl. Chem.* **1998**, 70, 117-142.

[28]   Levitt, M. H., Symmetry-Based Pulse Sequences in Magic Angle Spinning Solid State NMR. In *Encyclopedia of Nuclear Magnetic Resonance*, Harris, D. M. G. a. R. K., Ed. John Wiley & Sons: 2002; Vol. 9, pp 165-196.

[29]   Delaglio, F.; Grzesiek, S.; Vuister, G. W.; Pfeifer, J.; Bax, A., NMR PIPE. *J. Biomol. NMR* **1995**, 6, 277-293.

464

[30]   Goddard, T. D.; Kneller, D. G., SPARKY - NMR Assignment Program (http://www.cgl.ucsf.edu/home/sparky/). 2006.

[31]   Fogh, R. H.; Vranken, W. F.; Boucher, W.; Stevens, T. J.; Laue, E. D., A nomenclature and data model to describe NMR experiments. *Journal of Biomolecular Nmr* 2006, 36, (3), 147-155.

[32]   Vranken, W. F.; Boucher, W.; Stevens, T. J.; Fogh, R. H.; Pajon, A.; Llinas, P.; Ulrich, E. L.; Markley, J. L.; Ionides, J.; Laue, E. D., The CCPN data model for NMR spectroscopy: Development of a software pipeline. *Proteins-Structure Function and Bioinformatics* 2005, 59, (4), 687-696.

[33]   Fogh, R. H.; Boucher, W.; Vranken, W. F.; Pajon, A.; Stevens, T. J.; Bhat, T. N.; Westbrook, J.; Ionides, J. M. C.; Laue, E. D., A framework for scientific data modeling and automated software development. *Bioinformatics* 2005, 21, (8), 1678-1684.

[34]   Pajon, A.; Ionides, J.; Diprose, J.; Fillon, J.; Fogh, R.; Ashton, A. W.; Berman, H.; Boucher, W.; Cygler, M.; Deleury, E.; Esnouf, R.; Janin, J.; Kim, R.; Krimm, I.; Lawson, C. L.; Oeuillet, E.; Poupon, A.; Raymond, S.; Stevens, T.; van Tilbeurgh, H.; Westbrook, J.; Wood, P.; Ulrich, E.; Vranken, W.; Li, X. L.; Laue, E.; Stuart, D. I.; Henrick, K., Design of a data model for developing laboratory information management and analysis systems for protein production. *Proteins-Structure Function and Bioinformatics* 2005, 58, (2), 278-284.

[35]   Wittebort, R. J.; Olejniczak, E. T.; Griffin, R. G., Analysis of Deuterium Nuclear-Magnetic-Resonance Line-Shapes in Anisotropic Media. *Journal of Chemical Physics* 1987, 86, (10), 5411-5420.

[36]   Jaroniec, C. P.; MacPhee, C. E.; Bajaj, V. S.; McMahon, M. T.; Dobson, C. M.; Griffin, R. G., High-resolution molecular structure of a peptide in an amyloid fibril determined by magic angle spinning NMR spectroscopy. *Proceedings of the National Academy of Sciences of the United States of America* 2004, 101, (3), 711-716.

[37]   Gullion, T.; Schaefer, J., Rotational-echo double-resonance NMR. *J. Magn. Reson.* 1989, 81, 196-200.

[38]   Jaroniec, C. P.; Filip, C.; Griffin, R. G., 3D TEDOR NMR experiments for the simultaneous measurement of multiple carbon-nitrogen distances in uniformly ^{13}C, ^{15}N-labeled solids. *J. Am. Chem. Soc.* 2002, 124, (36), 10728-10742.

[39]   Costa, P. R.; Sun, B.; Griffin, R. G., Rotational resonance tickling: accurate internuclear distance measurement in solids. *J. Am. Chem. Soc.* 1997, 119, 10821-10836.

[40]   Costa, P. R.; Sun, B.; Griffin, R. G., Rotational resonance width experiment. *J. Magn. Reson.* 2003, in press.

[41]   Ladizhansky, V.; Griffin, R. G., Band selective ^{13}C-^{13}C distance measurements in uniformly ^{13}C,^{15}N labeled peptides using solid state MAS NMR. *J. Am. Chem. Soc.* **2003,** submitted.

[42]   Ramachandran, R.; Ladizhansky, V.; Bajaj, V. S.; Griffin, R. G., C-13-C-13 rotational resonance width distance measurements in uniformly C-13-labeled peptides. *Journal of the American Chemical Society* **2003,** 125, (50), 15623-15629.

[43]   Hong, M.; Gross, J. D.; Griffin, R. G., Site-resolved determination of peptide torsion angle phi from the relative orientations of backbone N-H and C-H bonds by solid-state NMR. *Journal of Physical Chemistry B* **1997,** 101, (30), 5869-5874.

[44]   Reif, B.; Hohwy, M.; Jaroniec, C. P.; Rienstra, C. M.; Griffin, R. G., NH-NH vector correlation in peptides by solid-state NMR. *Journal of Magnetic Resonance* **2000,** 145, (1), 132-141.

[45]   Feng, X.; Eden, M.; Brinkmann, A.; Luthman, H.; Eriksson, L.; Gräslund, A.; Antzutkin, O. N.; Levitt, M. H., Direct determination of a peptide torsional angle ψ by double-quantum solid-state NMR. *J. Am. Chem. Soc.* **1997,** 119, 12006-12007.

[46]   Feng, X.; Lee, Y. K.; Sandström, D.; Eden, M.; Maisel, H.; Sebald, A.; Levitt, M. H., Direct determination of a molecular torsional angle by solid-state NMR. *Chem. Phys. Lett.* **1996,** 257, 314-320.

[47]   Hohwy, M.; Jaroniec, C. P.; Lansing, J.; Rienstra, C. M.; Griffin, R. G., ^{13}C-^{1}H recoupling in the HCCH torsion angle experiment in solid-state NMR. *Chem. Phys. Lett.* **1999.**

[48]   Hong, M.; Gross, J. D.; Griffin, R. G., Site-resolved determination of peptide torsion angle ϕ from the relative orientations of backbone N-H and C-H bonds by solid-state NMR. *J. Phys. Chem. B* **1997,** 101, 5869-5874.

[49]   Hong, M.; Gross, J. D.; Hu, W.; Griffin, R. G., Determination of the peptide torsion angle ϕ by ^{15}N chemical shift and ^{13}C$^{\alpha}$-^{1}H$^{\alpha}$ dipolar tensor correlation in solid-state MAS NMR. *J. Magn. Reson.* **1998,** 135, 169-177.

[50]   Hong, M.; Gross, J. D.; Rienstra, C. M.; Griffin, R. G.; Kumashiro, K. K.; Schmidt-Rohr, K., Coupling amplification in 2D MAS NMR and its application to torsion angle determination in peptides. *J. Magn. Reson.* **1997,** 129, 85-92.

[51]   Ladizhansky, V.; Jaroniec, C. P.; Diehl, A.; Oschkinat, H.; Griffin, R. G., Measurement of multiple y torsion angles in uniformly ^{13}C,^{15}N-labeled a-spectrin domain using 3D ^{15}N-^{13}C-^{13}C-^{15}N MAS dipolar-chemical shift correlation spectroscopy. *J. Am. Chem. Soc.* **2003,** in press.

[52]   Rienstra, C. M.; Hohwy, M.; Mueller, L. J.; Jaroniec, C. P.; Reif, B.; Griffin, R. G., Determination of multiple torsion angle-constraints in U-^{13}C, ^{15}N-labeled peptides: 3D ^{1}H-^{15}N-^{13}C-^{1}H dipolar chemical shift spectroscopy in rotating solids. *J. Am. Chem. Soc.* **2002**, 124, 11908-11922.

[53]   Hong, M.; Gross, J. D.; Hu, W.; Griffin, R. G., Determination of the peptide torsion angle phi by N-15 chemical shift and C-13(alpha)-H-1(alpha) dipolar tensor correlation in solid-state MAS NMR. *Journal of Magnetic Resonance* **1998**, 135, (1), 169-177.

[54]   Hohwy, M.; Jaroniec, C. P.; Reif, B.; Rienstra, C. M.; Griffin, R. G., Local structure and relaxation in solid-state NMR: Accurate measurement of amide N-H bond lenghts and H-N-H bond angles. *J. Am. Chem. Soc.* **2000**, 122, 3218-3219.

[55]   Hohwy, M.; Rienstra, C. M.; Griffin, R. G., Band-selective homonuclear recouplng in solid state NMR for improved performance in uniformly isotope-labeled peptides. *J. Chem. Phys.* **2002**, 117, 4973-4987.

[56]   Cottone, G.; Giuffrida, S.; Ciccotti, G.; Cordone, L., Molecular dynamics simulation of sucrose- and trehalose-coated carboxy-myoglobin. *Proteins-Structure Function and Bioinformatics* **2005**, 59, (2), 291-302.

[57]   Schwieters, C. D.; Clore, G. M., Internal coordinates for molecular dynamics and minimization in structure determination and refinement. *Journal of Magnetic Resonance* **2001**, 152, (2), 288-302.

[58]   Van der Spoel, D.; Lindahl, E.; Hess, B.; Groenhof, G.; Mark, A. E.; Berendsen, H. J. C., Gromacs: Fast, Flexible, and Free. *Journal of Computational Chemistry* **2005**, 26, (16), 1701-1718.

[59]   Lindahl, E.; Hess, B.; van der Spoel, D., GROMACS 3.0: a package for molecular simulation and trajectory analysis. *Journal of Molecular Modeling* **2001**, 7, (8), 306-317.

[60]   Beauvais, C.; Guerrault, X.; Coudert, F. X.; Boutin, A.; Fuchs, A. H., Distribution of sodium cations in faujasite-type zeolite: A canonical parallel tempering simulation study. *Journal of Physical Chemistry B* **2004**, 108, (1), 399-404.

[61]   Cheng, X. L.; Cui, G. L.; Hornak, V.; Sinnnerling, C., Modified replica exchange simulation methods for local structure refinement. *Journal of Physical Chemistry B* **2005**, 109, (16), 8220-8230.

[62]   Earl, D. J.; Deem, M. W., Parallel tempering: Theory, applications, and new perspectives. *Physical Chemistry Chemical Physics* **2005**, 7, (23), 3910-3916.

[63]   Martin, R. W.; Zilm, K. W., Preparation of protein nanocrystals and their characterization by solid state NMR. *Jour. Magn. Resonance* **2003**, 164, 162-174.

[64] Franks, W. T.; Zhou, D. H.; Wylie, B. J.; Money, B. G.; Graesser, D. T.; Frericks, H. L.; Sahota, G.; Rienstra, C. M., Magic-Angle Spinning Solid-State NMR Spectroscopy of the b1 Immunoglobulin Binding Domain of Protein G (GB1): 15N and 13C Chemical Shift Assignments and Conformational Analysis. *J. Am Chem. Soc* **2005,** 127, 12291.

[65] Gallagher, T.; Alexander, P.; Bryan, P.; Gilliland, G. L., Two Crystal Structures of the B1 Immunoglobulin-Binding Domain of Streptococcal Protein G and Comparison with NMR. *Biochemistry* **1994,** 33, 4721-4729.

[66] Gronenborn, A. M.; Filpula, D. R.; Essig, N. Z.; Achari, A.; Whitlow, M.; Wingfield, P. T.; Clore, G. M., A Novel Highly Stable Fold of the Immunoglobulin Binding Domain of Streptococcal Protein G. *Science* **1991,** 253, 657-661.

[67] Takegoshi, K.; Nakamura, S.; Terao, T., C-13-H-1 dipolar-assisted rotational resonance in magic-angle spinning NMR. *Chemical Physics Letters* **2001,** 344, (5-6), 631-637.

Chapter 12   Resonance width measurements of homonuclear and heteronuclear dipolar couplings

Parts of this chapter are based on:

Ramachandran, R., Ladizhansky, V., Bajaj, V. S. and Griffin, R. G. " 13C–13C rotational resonance width distance measurements in uniformly C-13-labeled peptides." Journal of the American Chemical Society 125, 15623-15629 (2003).

Bajaj, V.S., Ramachandran, R., Ladizhansky, V., Griffin, R.G. " N-C Cross Polarization Resonance Width Experiments for Accurate Measurement of Heteronuclear Dipolar Couplings in Solid State NMR." (in preparation).

Bajaj, V.S., Caporini, M, van der Wel, P., Griffin, R.G. "Quasi-Adiabatic Passage Experiments for Measurement of Heteronuclear and Homonuclear Distances in Solid State NMR" (in preparation).

12.1   3D Rotational Resonance Width Experiments

The rotational resonance width (R^2W) experiment is a constant-time version of the rotational resonance (R^2) experiment, in which the magnetization exchange is measured as a function of sample spinning frequency rather than the mixing time. The significant advantage of this experiment over conventional R^2 is that both the dipolar coupling and the relaxation parameters can be independently and unambiguously extracted from the magnetization exchange profile. In this paper we combine R^2W with two-dimensional ^{13}C-^{13}C chemical shift correlation spectroscopy, and demonstrate the utility of this technique for the site-specific measurement of multiple ^{13}C-^{13}C distances in uniformly labeled solids. The dipolar truncation effects, usually associated with distance measurements in uniformly labeled solids, are considerably attenuated in R^2W experiments. Thus, R^2W experiments are applicable to uniformly labeled biological systems. To validate this statement, multiple ^{13}C-^{13}C distances (in the range of 3-6 Å) were determined in N-acetyl-[U-^{13}C,^{15}N]L-Val-L-Leu with an average precision of

±0.5 Å. Furthermore, the distance constraints extracted using a two-spin model agree well with the X-ray crystallographic data.

12.2   Introduction

Recent innovations and technological advances in the field of solid-state NMR (SSNMR) spectroscopy have brought it to the point where it shows considerable promise as a technique for studying problems of biological relevance that are not accessible via solution NMR or diffraction techniques [1-10]. In particular the combination of magic angle spinning (MAS) [11-13], cross-polarization (CP) [14, 15] and heteronuclear decoupling techniques [16-18], yielded increased spectral resolution and sensitivity in studies of such systems. At the same time MAS attenuates the dipolar interactions among the nuclear spins. Since these are the primary parameters of interest in structure determinations, it is necessary to reintroduce the dipolar interactions in order to retrieve the desired structural information. This fact has provided the impetus for the development of a suite of recoupling techniques that result in the reintroduction of the dipolar couplings during MAS in a controlled manner [19-24]. In such recoupling schemes (the rotational resonance technique consider here being an exception), the spin component of the dipolar interaction is modulated with radio-frequency pulses to constructively interfere with the MAS modulated spatial component, thereby resulting in the re-introduction of the dipolar interaction. Using such approaches, distance constraints have been obtained in a number of selectively labeled systems [20]. These distance measurements are essential in determining the molecular structure of biological samples such as membrane proteins [2-5, 25, 26] and insoluble peptide aggregates [9, 10, 27, 28],

470

whose structures are not easily accessible with conventional structural techniques such as solution-state NMR spectroscopy and X-ray crystallography.

Dipolar recoupling techniques can be conveniently classified as either broad-banded or selective. To date broad-banded recoupling techniques are used extensively for spectral assignments, but the deleterious effects of dipolar truncation [29] and other multi-spin interactions on the spin dynamics limit their utility in distance measurements in uniformly ^{13}C labeled solids. In particular, the strong couplings among directly bonded spins, attenuate polarization transfer to weakly coupled neighbors and it is precisely these distances that are essential in structure determination. Quantifying multi-spin effects in uniformly labeled systems is difficult and usually results in inaccurate distance measurements. Moreover, such techniques are sensitive to pulse imperfections and require intense radio frequency modulations on the low-γ nuclei, which interfere with the proton decoupling, leading to a loss of signal intensity during the recoupling period [30]. In contrast, with selective recoupling techniques such as rotational resonance (R^2) [31-39], and its related variants [40-43] such problems are circumvented because the applied rf fields are either weak or non existent.

In the case of R^2 experiments, the dipolar interaction between the members of a pair of spins is reintroduced selectively by matching the isotropic chemical shift difference, δ (in Hz), to an integer multiple of the sample spinning frequency (υ_r) – *i.e.* $\delta = n\upsilon_r$ (where *n* is a small integer representing the order of resonance) – and monitoring the exchange dynamics as a function of the mixing time. This leads to a coherent interaction between the nuclear spins and the macroscopic sample rotation, leading to magnetization exchange between the spins of interest. Since the recoupling during R^2 is

rotor-driven, it is, in contrast to radio frequency driven recoupling techniques, less sensitive to interference from ^{1}H decoupling. Moreover, the spectral selectivity of the R^2 phenomenon is often advantageous in quantitative studies, as multiple and relayed polarization transfers are minimized. Most importantly, as a direct consequence of the selectivity, the dipolar truncation effects are significantly attenuated in R^2 experiments.

In addition to the dependence on the internuclear distance, the magnetization exchange dynamics at R^2 are sensitive to the homogeneous and inhomogeneous contributions to the zero quantum line-width parameters [42-46]. The homogeneous contribution is described by a phenomenological relaxation parameter T_2^{ZQ}, which characterizes the decay of the ZQ coherences created during the magnetization exchange. In addition, the chemical shift distribution (CSD) [47] represents an inhomogeneous contribution that arises mainly from variations in intermolecular packing and results in a distribution of chemical shifts at each of the recoupled spin sites. Quantifying these two zero-quantum contributions is an important and non-trivial task since they must be separated from the dipolar couplings if structural parameters are to be measured accurately. Only recently have experiments been devised to measure the homogeneous and inhomogeneous contributions to such effects [42, 43, 48-50].

In the usual R^2 magnetization exchange experiments, the dipolar couplings are extracted by fitting the experimental exchange curves with different sets of dipolar (and in some cases the magnitude and orientation of CSA tensors) and relaxation parameters. However, the accuracy of such distance measurements is limited by the accuracy with which the zero quantum line-width parameters (especially T_2^{ZQ}) are estimated and accounted for in the numerical simulations. The value of T_2^{ZQ} has a significant influence

on the exchange dynamics, and depending on its relative magnitude (with respect to the effective dipolar interaction), the form of the magnetization exchange trajectories vary from damped oscillations in the "under-damped" regime ($\omega_{eff} \gg 1/T_2^{ZQ}$), to monotonic decays in the opposite over-damped case (($\omega_{eff} \ll 1/T_2^{ZQ}$).[38] Short distances often fall in the under-damped category and can be measured accurately [39], even absent an accurate estimate of the zero quantum relaxation parameters. However, in the context of measurements intended to constrain the structure of biomolecules, the most interesting constraints arise from long-range dipolar contacts between residues that are also distant in primary structure. These distances tend to correspond to the over-damped case. Consequently, the accuracy of such long-range distance measurements using the R^2 magnetization exchange method can be significantly compromised by the uncertainties associated with the estimation of the ZQ relaxation parameters. This necessitates the need for developing experiments with a reduced dependence on the relaxation parameters.

With this goal in mind, Costa *et al.* proposed an experiment based on rotational resonance technique where the magnetization exchange was monitored under a constant mixing time as a function of spinning frequency (rotational resonance width, R^2W) [43] which shows a reduced dependence on relaxation parameters. In a similar vein, Goobes *et al.* [45, 46] proposed observation of the magnetization exchange as a function of spinning frequency in a constant time, narrow-band radio frequency driven recoupling (nb-RFDR) experiment. Both approaches involve the observation of the ZQ resonance transition, with its intensity and width dependent on the dipolar coupling and relaxation parameters. The simultaneous analysis of both (or alternatively the resonance shape) allows independent extraction of distance and relaxation parameters without ambiguity when

compared to the conventional R^2 experiments. Using this technique, internuclear distances in selectively labeled samples have been determined with a reduced dependence on zero-quantum line-width parameters and with much improved accuracy and precision.
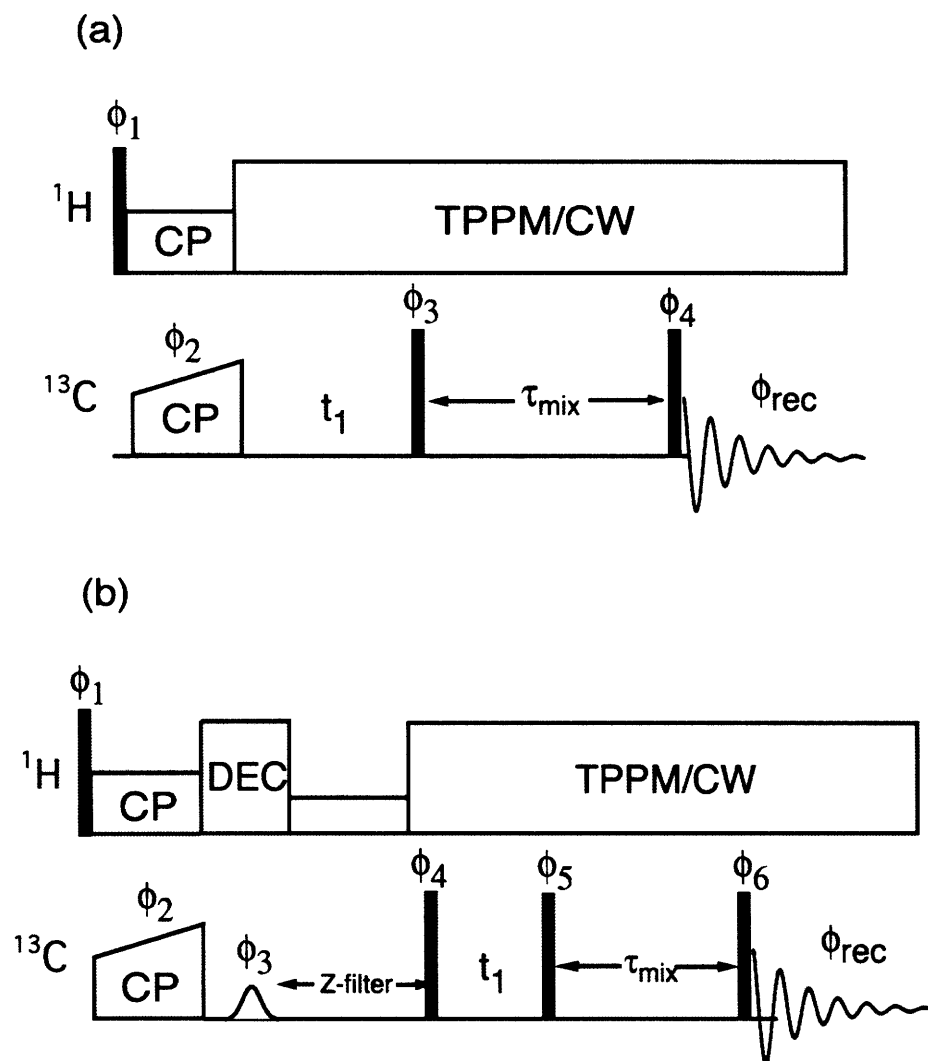
Figure 12-1: Pulse sequences for 3D-R^2W experiment. Solid rectangles represent $\pi/2$ pulses. (a) Represents a general ^{13}C-^{13}C correlation experiment performed as a function of spinning frequency with the following phase cycling scheme: $\varphi_1=1$, $\varphi_2=1313$, $\varphi_3=2$, $\varphi_4=1122\ 3344$, $\varphi_{rec}=1324\ 3142\ 3142\ 1324$. (b). In this scheme a selective Gaussian flip-up pulse is employed to select the carbonyl region of the spectrum. The following phase cycles were employed: $\varphi_1=8\times1$, 8×3; $\varphi_2=1$; $\varphi_3=8\times2$, 8×4; $\varphi_4=1$; $\varphi_5=4\times3$, 4×1; $\varphi_6=1234$; $\varphi_{rec}=1234\ 3412\ 3412\ 1234\ 3412\ 1234\ 1234\ 3412$. The labels 1,2,3,4 correspond to the phases x,y,-x,-y respectively. In all the above experiments the phase of the ^1H-CP pulse was fixed along the y-axis and the dipolar mixing time (τ_{mix}) was 30 ms.

The primary aim of the experiments reported here is to extend the applicability of the R^2W technique to uniformly ^{13}C-labeled systems and to investigate the dependence of the accuracy of R^2W measurements in the presence of multiple spin couplings. To address these issues we have measured multiple distance constraints (in the range of 3-6 Å) in the dipeptide N-acetyl-[U-^{13}C,^{15}N]L-Val-L-Leu using 3D dipolar-chemical shift correlation spectroscopy. Using an approximate model of the spin dynamics that considers only two coupled spins, a total of 9 distances were extracted in good agreement with the diffraction distances. The excellent agreement of all the measured distances with X-ray data justifies the use of this simplified model. The ability of the R^2W approach to separate the effects of relaxation and dipolar couplings, and simultaneously attenuate dipolar truncation, makes it an invaluable tool in structural studies of uniformly labeled biological systems.

12.3   Experimental

The experiments were performed on a sample N-acetyl-[U-^{13}C,^{15}N]L-Valine-L-Leucine (the N-acetyl group was not labeled). For measuring intramolecular distances, the above uniformly labeled compound was diluted to 9% in natural abundance to attenuate intermolecular dipolar couplings. The NMR spectra were recorded at 8.4 T (360.336 MHz for ^1H, 90.607 MHz for ^{13}C) using a Cambridge Instruments spectrometer (courtesy of Dr. D. J. Ruben) with a commercial Chemagnetics triple resonance MAS probe. The probe was equipped with 4.0 mm Chemagnetics spinning module. Spinning frequencies in the range 5.8–7.5 kHz were used in the experiments and were regulated to ±2Hz with a Bruker spinning frequency controller. The standard approach for site-specific measurement of multiple ^{13}C-^{13}C distances is illustrated in Figure 12-1(a). Ramped cross-

polarization [51] from ^{1}H creates the initial ^{13}C magnetization. The magnetization is then encoded by the t_1 evolution, followed by a preparatory $\pi/2$ pulse, which creates the initial longitudinal polarization (along z-axis) for dipolar mixing. The second $\pi/2$ pulse creates transverse polarization for detection. The period between the two $\pi/2$ pulses constitutes the dipolar mixing time and is maintained constant in the experiment. In our implementation of the R^2W experiment, a series of two-dimensional experiments are performed using different sample spinning frequencies. Due to the larger ^{13}C spectral width, the t_1 increments in such 2D experiments are generally short in order to avoid spectral folding. Since the total number of scans is limited by the number of t_1 points (which in turn is needed to establish high resolution in the indirect dimension) as well as by phase cycling, such experiments are often time consuming, unnecessarily in small peptides where high signal-to-noise can be expected. This problem, however can be circumvented by employing the pulse sequence illustrated in Figure 12-1(b) and has been implemented in our experiments. Here, following ^{1}H-^{13}C CP, the carbonyl region of the ^{13}C spectrum is selected by a 90° Gaussian pulse which restores the ^{13}C=O magnetization to the z-axis of the rotating frame. This is followed by application of a z-filter, during which all unwanted coherences are dephased via transverse relaxation processes and removed through phase cycling. After the dephasing period, the carbonyl magnetization is restored to the transverse plane by a $\pi/2$ pulse. Since the spectral width of the residual ^{13}C (only carbonyl region) spectrum is reduced, larger t_1 increments are possible during the evolution period thereby minimizing the total acquisition time. The chemical shifts of the carbonyl resonances are then encoded during t_1 evolution, which is then followed by a preparatory $\pi/2$ pulse for the magnetization exchange. The influence of the heteronuclear

^{13}C-^{1}H dipolar interaction during the t_1 evolution, ^{13}C–^{13}C recoupling period and acquisition is minimized by employing the two-pulse phase modulation (TPPM) decoupling scheme [18] ($\sim$ 83 kHz, ϕ = 12°, τ = 6 µs), while CW proton decoupling of $\sim$ 100 kHz was employed during the $\pi/2$ pulses. The length of ^{13}C $\pi/2$ pulses was 5 µs, and Gaussian pulse of 300 µs and recycle delays of 3 s were employed in all our experiments.

12.4   Numerical Simulations

The spin dynamics under rotational resonance conditions have been well described by several authors [34, 36, 38, 40-43, 48, 50] and will not be considered in detail in this article. We therefore only present modifications of the theory relevant to our experimental scheme. In the high field approximation the spin Hamiltonian for an isolated spin pair during MAS is given by

$$H = \omega_1(t)I_{1z} + \omega_2(t)I_{2z} + \omega_d(t)[2I_{1z}I_{2z} + \tfrac{1}{2}(I_1^+I_2^- + I_1^-I_2^+)] \qquad (12.1)$$

where $\omega_i(t)$, $\omega_d(t)$ denote the periodic time-dependent coefficients (due to MAS) of the chemical shift and dipolar interactions respectively. Such periodic time-dependent interactions may be conveniently expressed using a Fourier series expansion given below

$$\omega_\lambda(t) = \sum_{m=-2}^{2} \omega_\lambda^{(m)} e^{i2\pi m\nu_r t} \qquad (12.2)$$

where $\omega_\lambda^{(m)}$ (for $\lambda = 1$, 2 or d) denotes the time-independent Fourier component associated with a particular interaction. The orientation dependence [52] of the chemical shift interaction is expressed through the coefficients

$$\omega_\lambda^{(m)} = \omega_{iso}^\lambda \delta_{m=0} + \omega_{aniso}^\lambda \left\{ D_{0,-m}^2(\Omega_{PR}^\lambda) - \frac{\eta^\lambda}{\sqrt{6}} \left[D_{-2,-m}^2(\Omega_{PR}^\lambda) + D_{2,-m}^2(\Omega_{PR}^\lambda) \right] \right\} d_{-m,0}^2(\beta_{RL}) \qquad (12.3)$$

where $\omega_{iso}^{\lambda} = -\omega_0 \sigma_{iso}^{\lambda}$ and $\omega_{aniso}^{\lambda} = -\omega_0 \sigma_{aniso}^{\lambda}$ represent the isotropic and anisotropic components of the interaction. The chemical shielding parameters (such as isotropic chemical shift, anisotropy and asymmetry parameter) are related to the principal values of the shielding tensor according to $\sigma_{iso}^{\lambda} = \frac{1}{3}\left(\sigma_{xx}^{\lambda} + \sigma_{yy}^{\lambda} + \sigma_{zz}^{\lambda}\right)$, $\sigma_{aniso}^{\lambda} = \sigma_{zz}^{\lambda} - \sigma_{iso}^{\lambda}$, and

$\eta^{\lambda} = \dfrac{\sigma_{yy}^{\lambda} - \sigma_{xx}^{\lambda}}{\sigma_{zz}^{\lambda} - \sigma_{iso}^{\lambda}}$ respectively. $D_{p,q}^{2}(\Omega_{PR}^{\lambda})$ is an element of the Wigner rotation matrix (of rank 2) describing the transformation from the principal axis frame P^{λ} of the interaction λ through a given crystal fixed frame C (which in our case is chosen to coincide with the dipolar principal axis system) to the rotor frame R, *i.e.*

$$D_{p,q}^{2}(\Omega_{PR}^{\lambda}) = \sum_{k=-2}^{2} D_{p,k}^{2}(\Omega_{PC}^{\lambda}) D_{k,q}^{2}(\Omega_{CR}^{\lambda}) \tag{12.4}$$

where $\Omega_{XY} = \left\{\alpha_{XY}, \beta_{XY}, \gamma_{XY}\right\}$ denotes the Euler angles relating the frames X and Y. Ω_{PC}^{λ} specifies the orientation of the interaction tensor relative to the crystal fixed frame and Ω_{CR}^{λ} represents the so called powder angles describing the individual crystallite orientation relative to the rotor frame. The reduced Wigner matrix element $d_{-m,0}^{2}(\beta_{RL})$ relates the transformation from the rotor frame R to the laboratory frame L with $\beta_{RL} = \tan^{-1}(\sqrt{2})$ being the magic angle. The definition of the dipolar coefficients is analogous to the above description and is represented by,

$$\omega_{d}^{(m)} = b_{jk} \sum_{m1=-2}^{2} D_{0,m1}^{2}(\Omega_{PC}^{jk}) \times D_{m1,m}^{2}(\Omega_{CR}^{\lambda}) d_{m,0}^{2}(\beta_{RL}) \tag{12.5}$$

where b_{jk} is the through-space dipole coupling constant given by $b_{jk} = \left(-\frac{\mu_0}{4\pi}\right)\gamma^2\hbar\frac{1}{r_{jk}^3}$ in units of rad s^{-1}. For the sake of clarity and convenience, the above Hamiltonian is

rewritten using the single transition operator basis [53]. In this basis the Hamiltonian is written as a sum of two interaction terms, namely

$$H = H_0 + H_1 \qquad (12.6)$$

where

$$H_0 = \omega_\Sigma(t) I_z^{14} + \omega_A(t)(I_z^{12} - I_z^{34}) \qquad (12.7)$$

$$H_1 = \delta(t) I_z^{23} + \omega_B(t) I_x^{23} \qquad (12.8)$$

and $\omega_\Sigma(t) = \omega_1(t) + \omega_2(t)$, $\delta(t) = \omega_1(t) - \omega_2(t)$ denote the sum and the difference of the chemical shift terms. Since the exchange dynamics under the R^2 condition is described in the zero quantum subspace, the spin system is only governed by the interaction term H_1 and is represented by

$$H_1 = \delta\, I_z^{23} + \omega_B(t) I_x^{23}, \qquad (12.9)$$

where the time-dependent CSA coefficients have been omitted for the sake of simplicity and $\delta = \omega_1^{iso} - \omega_2^{iso}$ denotes the isotropic chemical shift difference between the spin pair of interest. In order to describe the observed interference effect between the MAS modulated spatial component (of the dipolar interaction) and the chemical shift modulated spin component of the interaction the above Hamiltonian is transformed into an interaction frame (defined by the transformation function $U = \exp\{i(2\pi n \upsilon_r t) I_z^{23}\}$). In this frame the Hamiltonian is represented by

$$H^T = U H_1 U^{-1} = (\delta - n\upsilon_r) I_z^{23} + \omega_B(t)\left[I_x^{23} \cos(2\pi n \upsilon_r t) + I_y^{23} \sin(2\pi n \upsilon_r t) \right] \qquad (12.10)$$

Inserting the dipolar time-dependent coefficients in the above expression, the interaction Hamiltonian can be re-expressed as

$$H^T = (\delta - n\upsilon_r)I_z^{23} + \sum_{m=-2}^{2} \omega_B^{(m)}\left[I_+^{23} e^{i(n-m)2\pi\upsilon_r t} + I_-^{23} e^{i(n+m)2\pi\upsilon_r t} \right] \tag{12.11}$$

which can further be simplified to

$$H^T = (\delta - n\upsilon_r)I_z^{23} + \tfrac{1}{2}\sum_{n=-2}^{2} \omega_B^n I_x^{23} \tag{12.12}$$

So far, we have neglected the time-dependence of the chemical shift anisotropy. Although it is true that the CSA interaction would affect the lineshape of cross-peaks of a correlation spectrum, their effect on polarization transfer is less significant.[54] The unitary operator described above may be modified to include the time-dependent CSA interaction as and has been described in detail by Karlsson et al. [48]:

$$U(t) = \exp\{-i[2\pi n\upsilon_r t + \Phi_\Delta^{aniso}(t,0)]I_z^{23}\}, \tag{12.13}$$

where $\Phi_\Delta^{aniso}(t_a, t_b) = \int_{t_a}^{t_b} \omega_\Delta^{aniso}(t)dt$. In this frame the Hamiltonian is represented by

$$H^T = (\delta - n\upsilon_r)I_z^{23} + \tilde{\omega}_B(t)I_x^{23} \tag{12.14}$$

where $\tilde{\omega}_B(t) = \omega_B(t)\exp[-i\Phi_\Delta^{aniso}(t,0)]$. Usually, the exchange dynamics is governed by the interaction Hamiltonian and depends on the experimental scheme employed. In the conventional R^2 experiments ($\delta = n\upsilon_r$) the above interaction Hamiltonian has only a transverse component and is purely dipolar in nature whereas in the case of R^2W experiments, since the exchange dynamics is monitored as a function of spinning frequency, the interaction Hamiltonian has both the longitudinal (described by the resonance mismatch terms) as well as a transverse component (described by the dipolar terms). Since the exchange dynamics are influenced by both coherent (described by the Hamiltonian operator) as well as incoherent interactions (described by the relaxation

operator), the spin dynamics is best studied using the Liouville formalism. In this approach a new set of basis operators are defined (also known as super-operators) and the time evolution of the spin system (represented by the spin density operator, $\rho(t)$) is studied by solving the Liouville-von Neumann equation

$$\frac{d}{dt}\rho(t) = -i[H,\rho(t)] - \hat{\Gamma}\rho(t) .$$

(12.15)

Using the Liouville super-operator $\hat{L}$ (represented by $\hat{L} = -i\hat{H} - \hat{\Gamma}$), the above equation can be further simplified and rewritten as a first order homogeneous differential equation

$$\frac{d}{dt}\rho(t) = \hat{L}\rho(t)$$

(12.16)

The term $\hat{H}$ in the Liouville super-operator $\hat{L}$ denotes the Hamiltonian commutation super-operator whose matrix elements are defined by

$$\hat{H}_{ab} = \langle Q_a | \hat{H} | Q_b \rangle = Tr\{Q_a^+[H,Q_b]\}$$

(12.17)

where $|Q_a\rangle$, $|Q_b\rangle$ etc. are orthonormal basis operators defined in the Liouville space, and $\hat{\Gamma}$ denotes the relaxation super-operator, which is usually diagonal for all practical purposes (neglecting cross-relaxation terms) and is formally represented by

$$\hat{\Gamma} = \sum_i \frac{|Q_i\rangle\langle Q_i|}{T^i \langle Q_i | Q_i \rangle}$$

(12.18)

The term T^i in the above equation denotes the relaxation time associated with a given coherence i. The R^2W experiments described here involve polarization transfer from spin 1 to spin 2; the relevant Liouville subspace is therefore spanned by the operators $\{|I_{1z}\rangle, |I_{2z}\rangle, |\sqrt{2}I_x^{23}\rangle, |\sqrt{2}I_y^{23}\rangle\}$ and the Liouville super-operator $\hat{L}$, can be represented by a $4 \otimes 4$ matrix. Using the explicit form of the operators mentioned above, Eq. (12.14) can be expanded as follows

$$\frac{d}{dt}\begin{pmatrix} \langle I_{1z}(t) \rangle \\ \langle I_{2z}(t) \rangle \\ \langle \sqrt{2}I_x^{23}(t) \rangle \\ \langle \sqrt{2}I_y^{23}(t) \rangle \end{pmatrix} = \begin{pmatrix} \frac{-1}{T_1^{(1)}} & 0 & 0 & \sqrt{2}\omega_B^n \\ 0 & \frac{-1}{T_1^{(2)}} & 0 & -\sqrt{2}\omega_B^n \\ 0 & 0 & \frac{-1}{T_2^{ZQ}} & -(\delta-n\nu_r) \\ -\sqrt{2}\omega_B^n & \sqrt{2}\omega_B^n & (\delta-n\nu_r) & \frac{-1}{T_2^{ZQ}} \end{pmatrix}\begin{pmatrix} \langle I_{1z}(t) \rangle \\ \langle I_{2z}(t) \rangle \\ \langle \sqrt{2}I_x^{23}(t) \rangle \\ \langle \sqrt{2}I_y^{23}(t) \rangle \end{pmatrix}. \qquad (12.19)$$

Here, T_1^i denotes the longitudinal relaxation time associated with spin i and is determined experimentally by measuring the intensity (or magnetization) as a function of mixing time far from rotational resonance conditions. In our case the measured T_1^i were long and have been neglected in the calculations. The term T_2^{ZQ} refers to the zero quantum relaxation parameter, and accounts for effects that are not directly correlated to the chemical shift or the dipolar interactions. The spin dynamics are then evaluated by solving Equation (12.19). Usually the distance information for a particular spin pair is obtained by calculating the root mean square deviation between the experimental and simulated data that is represented as

$$RMSD = \frac{1}{N}\sum_{i=1}^{N}(E^i - S^i)^2. \qquad (12.20)$$

Here E^i and S^i denote the experimental and simulated data (integrated cross peak intensities in our case) for a particular spin pair of interest. The summation index here refers to the number of points (denoted by N, corresponding to different sample spinning frequencies) performed. The internuclear distance r and the zero-quantum relaxation T_2^{ZQ} constitute the fit parameters in such calculations.

12. 5   Data Analysis

The experimental data from the R^2W experiments were processed using NMRPipe[55], and the cross peak volumes were extracted by automated fitting to two-dimensional

Gaussians. Analysis of the magnetization exchange curves involved: (i) normalization of all data points to initial carbonyl intensities derived from cross-polarization reference experiments conducted at identical spinning frequencies to compensate for the dependence of CP enhancements on the sample spinning frequency, (ii) normalization of cross peak volumes to carbonyl intensity at a spinning frequency which is free from any recoupling conditions, and (iii) estimation of model parameters using a Liouville-space formalism (Equation 12.19) of the spin dynamics (*vide supra*) which considers only two coupled spins. For model estimation, the root mean squared deviation between the calculated and measured magnetization exchange curves was minimized; confidence intervals reflected in the contour plots were derived on the basis of an F-test[57] in which only points above the noise floor were used to enumerate the degrees of freedom in the model fitting. The experimental details and results obtained using this method are discussed in the next section.
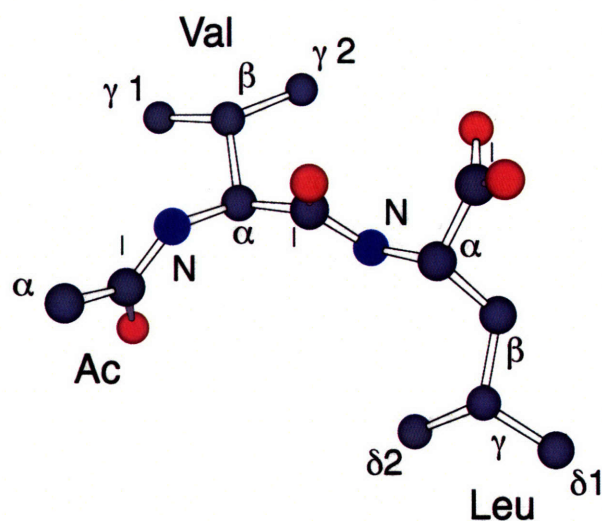
Figure 12-2: Diagram of the peptide N-Ac-Val-Leu derived from the crystal structure. The nomenclature used to label measured distances in the text is indicated.
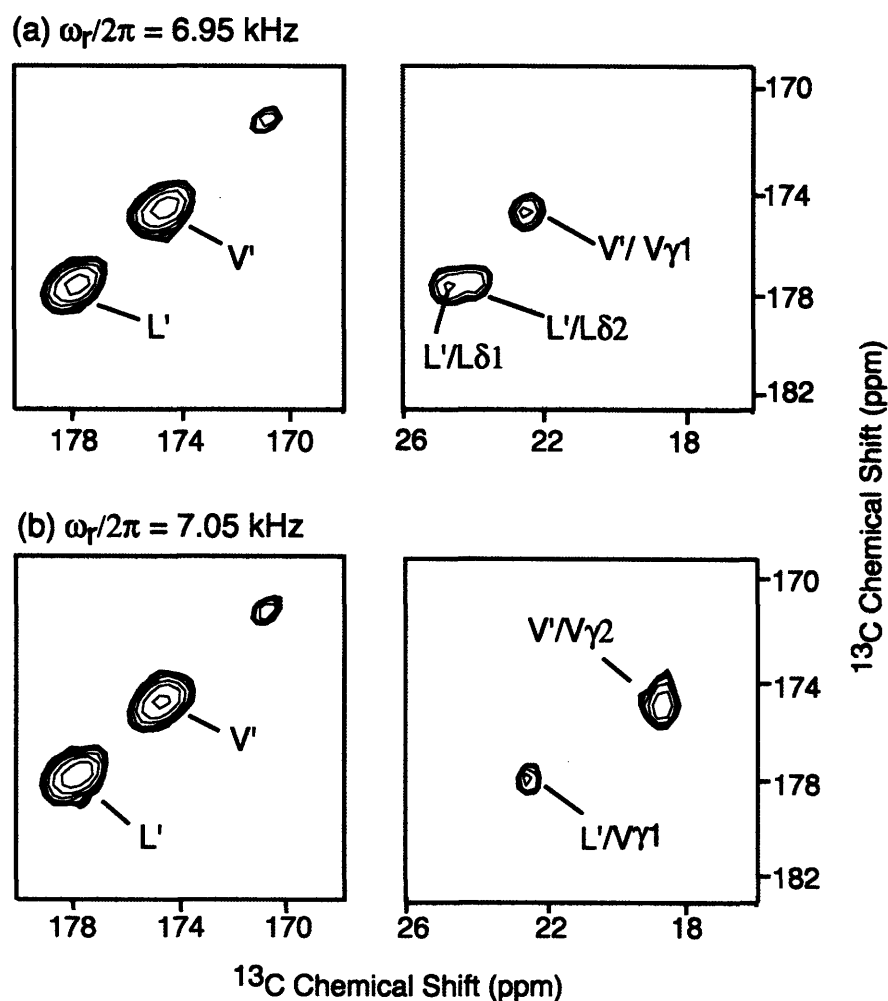
Figure 12-3: Representative two-dimensional slices from the ^{13}C-^{13}C R^2W experiment in N-Acetyl [U-^{13}C,^{15}N]L-Val-L-Leu recorded on 360 MHz spectrometer at (a) $\omega_r/2\pi$=6.95 kHz and (b) $\omega_r/2\pi$=7.05 kHz. The pulse sequence of Figure 12-1(b) was used with the mixing time of 30 ms. Different cross peaks appear at different spinning frequencies, thereby demonstrating the selectivity of the polarization transfer. In (a) cross-peaks corresponding to the medium range V'-Vγ1 dipolar coupling (R=3.879 Å according to the crystal structure) appear in the spectrum, along with long-range couplings between the L'-Lδ1 (R=4.675 Å) and L'-Lδ2 (R=4.872 Å). These cross peaks are not present in (b) (note that the spinning frequency changes by just 100 Hz), but two additional cross-peaks appear between L' and Vγ1 (R=6.464 Å) and V' and Vγ2 (R=2.969 Å).

12.6   Results and Discussion

To validate our approach, the proposed 3D R^2W experiment was applied to carbonyl-side chain distance measurements in N-acetyl-[U-^{13}C,^{15}N]L-Val-L-Leu. The three-dimensional structure of this dipeptide had been previously determined using X-ray crystallography[57] and is illustrated in Figure 12-2. In combination with 2D ^{13}C-^{13}C

correlation spectroscopy, the R^2W methodology allows the measurement of multiple distance constraints in a site-specific manner.

The R^2W experiments were performed at 360 MHz (^1H frequency) and at spinning frequencies ranging from 5.8-7.5 kHz, incremented in steps of 25 Hz. The sweep range of the sample spinning frequencies employed in the 2-D experiments were chosen to satisfy appropriate resonance conditions ($n=2$) between all carbonyl and side-chain carbons. Figure 12-3 illustrates representative two-dimensional slices from the R^2W experiment corresponding to spinning frequencies 6.95 kHz and 7.05 kHz, and to a mixing time of 30 ms.

The cross-peaks in the aliphatic region are labeled with the carbonyl and side chain carbon frequencies. When the spinning frequency corresponds or is sufficiently close to the R^2 condition for a particular carbonyl-side chain spin pair, the magnetization exchange between the spins results in the appearance of cross-peaks in the aliphatic region of the spectrum. The aliphatic regions of the spectra demonstrate that these polarization exchange processes are highly selective. In particular, at $\omega_r/2\pi$=6.95 kHz, the V'-Vγ1 (medium-range; R=3.879 Å according to crystal structure), L'-Lδ1 (long-range; R=4.675 Å), and L'-Lδ2 (long range; R=4.872 Å) interactions are recoupled. However, at a slightly higher spinning frequency, $\omega_r/2\pi$=7.05 kHz, the corresponding cross peaks disappear, and cross peaks corresponding to L'-Vγ1 (long range; R=6.46 Å), and V'-Vγ2 (short-range; R=2.969 Å) appear. The varying cross peak intensities associated with a particular spin pair of interest provide a measure of polarization transfer as a function of sample spinning frequency and can be used as a tool to estimate the distance between the spins of interest. The dependence of the cross peak intensity on the spinning frequency is

shown in Figure 12-4 for the L'-Lδ2 and V'-Vγ1 spin pairs together with the best fit

simulations and confidence plots. The T_1 relaxation times were calibrated in separate

experiments. In all the experiments described in this article, the peak intensities were

referenced with respect to the intensity of the carbonyls (that were polarized initially). In

addition, the above intensities were corrected for the dependence of CP enhancement on
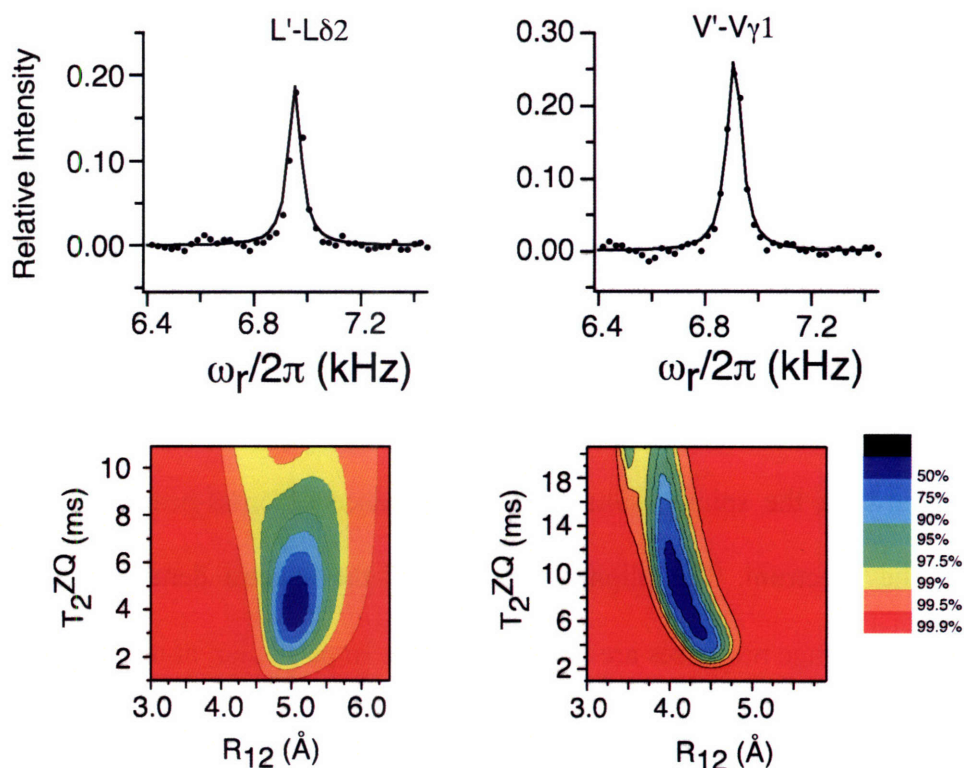
Figure 12-4: Representative plots of the cross peak intensities as a function of the spinning frequency for the L'-Lδ2 and V'-Vγ1 rotational resonances, and corresponding graphs of the model estimator in which contour levels are confidence intervals determined from an F-test. The volume intensities of the cross-peaks are given relative to the corresponding carbonyl peaks. The parameters in the best fit simulations were as follows. For L'-Lδ2: $T_2^{ZQ} = 4.0\ ms$, $R = 5.0\ \text{Å}$. For V'-Vγ1: $T_2^{ZQ} = 8.9\ ms$, $R = 4.25\ \text{Å}$. The confidence limits of the contour levels are indicated on the figure.

the sample spinning frequency. The experimentally observed polarization transfer

efficiency is quite high for stronger coupling and is on the order of 20% for longer (L'-

Lδ2) distances. Using the numerical procedure described in the previous section and

from the RMSD plots, a total of 9 distances were extracted with high precision and are presented in Table 12.1. As is clear from the table, the distances measured using NMR are in good agreement with X-ray data, despite the fact that multi-spin effects have been neglected in our calculations. The agreement between the two data sets further justifies our use of a simplified two-spin model for data analysis. It also is in agreement with the earlier reported effect of the reduction of dipolar truncation in the presence of multiple quantum relaxation.[58]
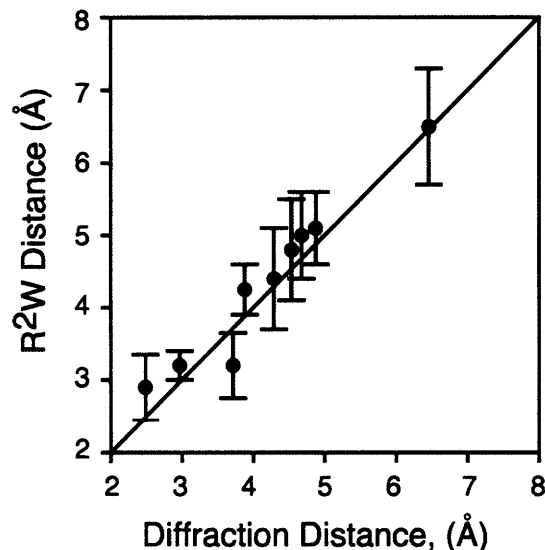
Figure 12-5: Comparison of ^{13}C-^{13}C distances measured by using X-ray diffraction and R^2W experiments. NMR results account for random errors.

In order to investigate other sources of systematic error, the dependence of the spin dynamics on the magnitude and orientation of the CSA was studied. For a given set of typical CSA parameter, a series of numerically exact simulations were performed and then fit using the approximate treatment presented here. The results of the simulations indicate an overestimation of the inter-nuclear distances of at worst 0.2 Å using NMR when the CSA magnitude and orientation are not known *a priori*. Such dependence on CSA parameters can however be minimized at the $n=1$ R^2 condition.

487

One of the limitations of this approach is the stringent condition imposed on the sample spinning frequency. This restricts the applicability of this technique to systems in which the CSA's are small compared to the chemical shift differences. Where this condition is not met, the resolution is often obscured by the presence of crowded sidebands, which in turn affects the selectivity. Such problems can be partially alleviated

Table 12.1. ^{13}C-^{13}C Internuclear Distances and ZQ relaxation times determined in N-Ac-L-Val-L-Leu

Atoms		^{13}C-^{13}C Distance (Å)		T_2^{ZQ}, ms
		$R^2W^{(1)}$	Xray	
V′	Vγ2	3.20±0.20	2.969	5.9
	Vγ1	4.25±0.35	3.879	8.9
	Lδ1	4.40±0.70	4.290	13.0
	Lβ	3.25±0.45	3.715	9.3
L′	Vγ2	4.80±0.70	4.535	4.3
	Vγ1	6.50±0.80	6.460	0.1$^{(2)}$
	Lδ1	5.00±0.60	4.675	6.0
	Lδ2	5.10±0.50	4.872	4.0
	Lβ	2.95±0.45	2.487	7.0

[1]The error bars are given with 95% confidence level.
[2] The R^2W data for L'-Vγ1 spin pair could be fit with T_2^{ZQ} relaxation 0.1-10 ms. The polarization transfer efficiency for this cross peak was very weak because of the long distance, and could be fit with broad distribution of the ZQ relaxation parameter.

by employing the R^2TR technique (rotational resonance in the tilted frame) introduced by Terao *et al.* [40, 41]. This approach relaxes the restrictions on the sample spinning frequency in addition to eliminating the broadening effects observed under rotational resonance conditions.

12.7   Conclusions

We have demonstrated the application of 3-D R^2W technique for simultaneous site-specific measurement of multiple ^{13}C-^{13}C (carbonyl-side chain) distances in uniformly

^{13}C-labeled solids. The method relies on ^{13}C chemical shift resolution and is expected to benefit from higher static magnetic fields with better selectivity and reduced dependence on multi-spin effects. Since the recoupling is chemical shift modulated, its application is limited to systems with spin pairs having significant isotropic chemical shift differences. Fortunately, many interesting biological systems satisfy this criterion. Further, the effects of dipolar truncation are significantly reduced in this approach and enable the extraction of distance constraints even in weaker (or long range) couplings. Moreover, in systems with favorable chemical shift resolution the distance information can be extracted without ambiguity using a simple two-spin approximation model. Thus, the reduced dependence on relaxation and other multi-spin parameters makes this a suitable approach for measuring distances in larger uniformly labeled biological systems.

12.8 ^{15}N-^{13}C Cross Polarization Resonance Width Experiments for Accurate Measurements of Heteronuclear Dipolar Couplings in Solid State NMR

We present a three-dimensional magic angle spinning experiment, Cross Polarization Resonance Width (CPRW), for the measurement of multiple heteronuclear dipolar couplings in uniformly labeled solids. CPRW is a constant-time experiment that records the passage through a DQ ^{13}C-^{15}N Hartmann-Hahn [54, 55] match condition as a function of the RF field on either channel. The resulting exchange trajectories can be fit to obtain both the dipolar coupling and the double-quantum lineshape parameter (T_2^{DQ}) independently, yielding an accurate estimate of the internuclear distance. We further show that a simple two-spin treatment, both numerical and analytical, can be used to fit the experimental data, greatly simplifying analysis in crowded spectra. Finally, we apply the Multipole-Multimode Floquet Theory [56-58] (MMFT) approach to incorporate the

effects of CSA-induced depolarization into the two-spin treatment. The experiments are demonstrated in the dipeptide N-acetyl-[U-^{13}C, ^{15}N]-Val-Leu and the tripeptide [U-^{13}C-^{15}N]-N-formyl-Met-Leu-Phe, in which structurally informative backbone ^{15}N to side-chain ^{13}C distances have been obtained. Here, we briefly describe this sequence and the initial results with reference to the previous description of resonance width phenomena in the context of rotational resonance width experiments.

As described in the previous section, experiments designed for the simultaneous measurement of multiple distances in uniformly labeled compounds share several features. First, they are generally pseudo-3D experiments in which an anisotropic interaction is recoupled in one dimension of the experiment, while other dimensions involve chemical shift correlation. The build up or decay of the cross peak intensities then encodes information about the anisotropic coupling. Second, the experiment must be designed in such a way that the dipolar couplings of interest can be independently and reliably fit even in the presence of decoherence effects such as depolarization and relaxation. Finally, they must be free from both the effects of dipolar truncation, in which a stronger coupling dominates the weaker couplings of interest in a multispin system, and from signal evolution under the J-couplings, which are not structurally informative in this context. This criteria can be met either by applying a recoupling sequence whose Hamiltonian is commuting for different spin pairs (and hence does not suffer from truncation) or by using a frequency-selective approach that selectively recouples only the weak dipolar couplings of interest. The transferred-echo double resonance (3D TEDOR [59]) experiment is an example of the former, and rotational resonance width [60] (R2W) and R2TR [61] experiment of the latter.

The 3D TEDOR experiment gives reliable estimates of the heteronuclear dipolar couplings and has been applied to peptides and amyloid fibrils, including in this thesis. However, while the form of the recoupled Hamiltonian precludes dipolar truncation, the experiment is nevertheless sensitive to multi-spin effects. In order to extract the distance from a given ^{13}C, I, to a nitrogen, S, the build up and decay of all I-S$_n$ cross peaks to which the carbon is coupled must be monitored and simultaneously fit. This means that all such cross peaks must be resolved in a 2D ^{13}C-^{15}N correlation experiment. Further, for multiple couplings, the polarization transfer is scaled according to the number of couplings and their magnitudes, resulting in weak intensities particularly for residues whose side chains contain nitrogen. Finally, the spin dynamics are sensitive to the orientation of the dipolar tensors as well as their magnitudes. Jaroniec and co-workers used the first, orientationally-independent terms of a formal analytical expansion of the spin dynamics under REDOR[62-66] to approximate the spin dynamics. This approximation introduces a systematic error of up to 20% in the measured distances. In spite of these limitations, 3D TEDOR is an extremely effective tool for structure determination in peptides and proteins with resolved chemical shifts.

To overcome these limitations, an ideal sequence would generate spin dynamics that are approximately governed by bilinear, two-spin interactions. This precludes the use of broadband recoupling sequences. Following the successful resonance width approaches for homonuclear distance measurements, the CPRW experiment makes use of weak irradiation on both ^{13}C and ^{15}N channels as first introduced by Terao and Costa, and later in the heteronuclear context by Baldus and co-workers. The experiment is spectrally selective because it relies on a modified Hartmann-Hahn matching conditions between

effective RF fields under weak, off-resonant irradiation. Two conditions can occur: [40, 41] the ZQ conditions for a (i,j)-spin pair occur at radio-frequency intensities satisfying the equality

$$\left| \omega_i^{eff} - \omega_j^{eff} \right| = n\omega_R, \ n = 1,2 \ (ZQ), \tag{12.21}$$

and the double quantum (DQ) conditions satisfy the equality:

$$\omega_i^{eff} + \omega_j^{eff} = n\omega_R, \ n = 1,2 \ (DQ). \tag{12.22}$$

In this context, the DQ condition with weak RF fields results in spectral selectivity which is sufficient to recouple aliphatic resonances in the range 0-30 ppm without introducing strong couplings to the Cα and Cβ of the amino acid side chain. The experiment is then particularly useful for the measurement of structurally informative ^{15}N to side-chain methyl distances.

Considering only two coupled spins, the Hamiltonian for this experiment near the DQ matching condition is:

$$H = -\Delta_1 S_z - \Delta_2 I_z + \omega_{12}^{eff} (S^+ I^+ + S^- I^-), \tag{12.23}$$

where

$$\Delta_i = \omega_i^{eff} - \omega_R \tag{12.24}$$

$$\omega_i^{eff} = \sqrt{\Delta \omega_i^2 + \omega_1^2} \tag{12.25}$$

The recoupled dipolar coupling is scaled by geometrical factors under off-resonance irradiation according to

$$\omega_{ij}^{eff} = \frac{1}{4} D_{ij} (1 + 2 \sin \beta_i \sin \beta_j - \cos \beta_i \cos \beta_j) \tag{12.26}$$

where:

$$\beta_j = \arctan\left(\frac{\omega_1}{\Delta\omega_j}\right) \tag{12.27}$$

and D_{ij} depends on the Euler angles.

In order to properly account for the effects of relaxation on the spin dynamics, we follow the polarization transfer in the operator space,

$$\frac{d}{dt}\rho(t) = \hat{L}\rho(t) \tag{12.28}$$

where the Liouville superoperator is $\hat{L} = -i\hat{H}_{eff} - \hat{\Gamma}$. The superoperators have matrix elements where are defined as follows,

$$\left(Q_i\middle|\hat{H}_{eff}\middle|Q_j\right) = Tr\left\{Q_i\left[H_{eff}, Q_j\right]\right\},$$

$$\left(Q_i\middle|\hat{\Gamma}\middle|Q_j\right) = \frac{\delta_{ij}}{T_i}. \tag{12.29}$$

In the fictitious operator approach, the operators, Q, are chosen to satisfy the commutation relations of two-spin basis operators [67]:

$$Q_1 = I_z, \quad Q_2 = S_z,$$

$$Q_3 = \sqrt{2}(I^+S^+ + I^-S^-), \tag{12.30}$$

$$Q_4 = -i\sqrt{2}(I^+S^+ - I^-S^-)$$

Explicit calculation of the commutators yields the following expansion of the master equation, in which the relaxation elements appear purely on the diagonal:

$$\frac{d}{dt}\begin{pmatrix} \langle Q_1(t)\rangle \\ \langle Q_2(t)\rangle \\ \langle Q_3(t)\rangle \\ \langle Q_4(t)\rangle \end{pmatrix} = \begin{pmatrix} -1/T_{1\rho}^{(1)} & & & \sqrt{2}\omega_{12}^{eff} \\ & -1/T_{1\rho}^{(2)} & & \sqrt{2}\omega_{12}^{eff} \\ & & -1/T_2^{DQ} & -(\Delta_1 + \Delta_2) \\ -\sqrt{2}\omega_{12}^{eff} & -\sqrt{2}\omega_{12}^{eff} & \Delta_1 + \Delta_2 & -1/T_2^{DQ} \end{pmatrix}\begin{pmatrix} \langle Q_1(t)\rangle \\ \langle Q_2(t)\rangle \\ \langle Q_3(t)\rangle \\ \langle Q_4(t)\rangle \end{pmatrix} \tag{12.31}$$

To simulate the spin dynamics, this system of differential equations is solved subject to the initial condition:

$$\langle Q_1(0) \rangle = 1, \ \langle Q_2(0) \rangle = 0, \ \langle Q_3(0) \rangle = 0, \ \langle Q_4(0) \rangle = 0 \qquad (12.32)$$

The spin dynamics thus depend on several empirical parameters: the dipolar coupling, $T_{1\rho}$ for each spin, and T_2^{DQ}. Of these, $T_{1\rho}$ can be experimentally determined in a separate spin-locking experiment, while the dipolar coupling and T_2^{DQ} must be fit. Due to a Bloch-Siegert-like shift in the resonance condition due to the CSA, the position of the resonance is allowed to vary slightly during the fit in treatments which do not incorporate the CSA. The experiment is conducted in a regime which minimizes transverse elements of the CSA, as they also contribute to depolarization effects.

12.9 Experimental Methods

12.9.1 Uniformly labeled peptides

The dipeptide N-acetyl-[U-^{13}C,^{15}N]L-Val-L-Leu (N-Ac-VL) and tripeptide N-formyl-[U-^{13}C,^{15}N]L-Met-L-Leu-L-Phe (N-f-MLF-OH) were produced by solid phase synthesis and crystallized as described elsewhere [68-70]. N-Ac-VL and N-f-MLF-OH peptides were diluted to 9% and 10%, respectively, in the respective natural abundance peptides to minimize the effects of intermolecular dipolar couplings.

12.9.2 NMR experiments

The NMR experiments were performed on NMR spectrometers operating at 11.7 T (500 MHz ^{1}H) and 8.42 T (360 MHz ^{1}H) using spectrometer hardware that was designed by

D.J. Ruben and co-workers at Cambridge Instruments. All experiments were performed on 4-mm triple resonance Chemagnetics (Fort Collins, CO) probes at spinning frequencies from 13.5 – 16 kHz. The CPRW pulse sequence is shown in Figure 12-6.
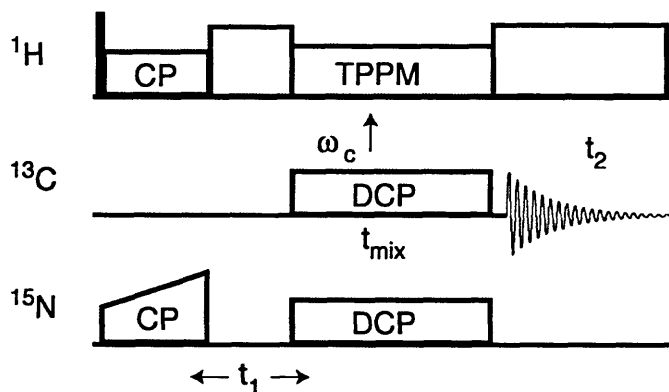
Figure 12-6: Pulse sequence for 3D CPRW experiment. Following polarization transfer from the ^{1}H to ^{15}N spins, the magnetization evolves under the ^{15}N chemical shift during t1 and is then transferred to the ^{13}C spins through a constant-time Hartmann-Hahn cross polarization period. A pseudo-3D experiment is conducted as a function of the ^{13}C RF field.

12.10   Results and Data Analysis

Experimental data were processed using RNMR or NMRPipe and integrated in NMRPipe using the NlinLS lineshape fitting utility. The $T_{1\rho}$ relaxation parameters were measured in separate spin-locking experiments, and the experimental data were simulated by numerical solution of the system of four differential equations that describe the spin dynamics in the fictitious operator subspace. Random errors were estimated through the diagonal elements of the covariance matrix of the fit. The results for experiments conducted in [U-^{13}C,^{15}N]-VL at 360 MHz are shown in Figures 12-7 and 12-8. They demonstrate that conformationally significant distances can be accurately measured in 3D CPRW experiments. Indeed, Figure 12-7 shows that distance measurements can be accurate even in the case of nearly complete resonance overlap. This is an experimental

demonstration of previous observations of the diminished importance of dipolar truncation in three-spin systems in the presence of multiquantum relaxation [71].
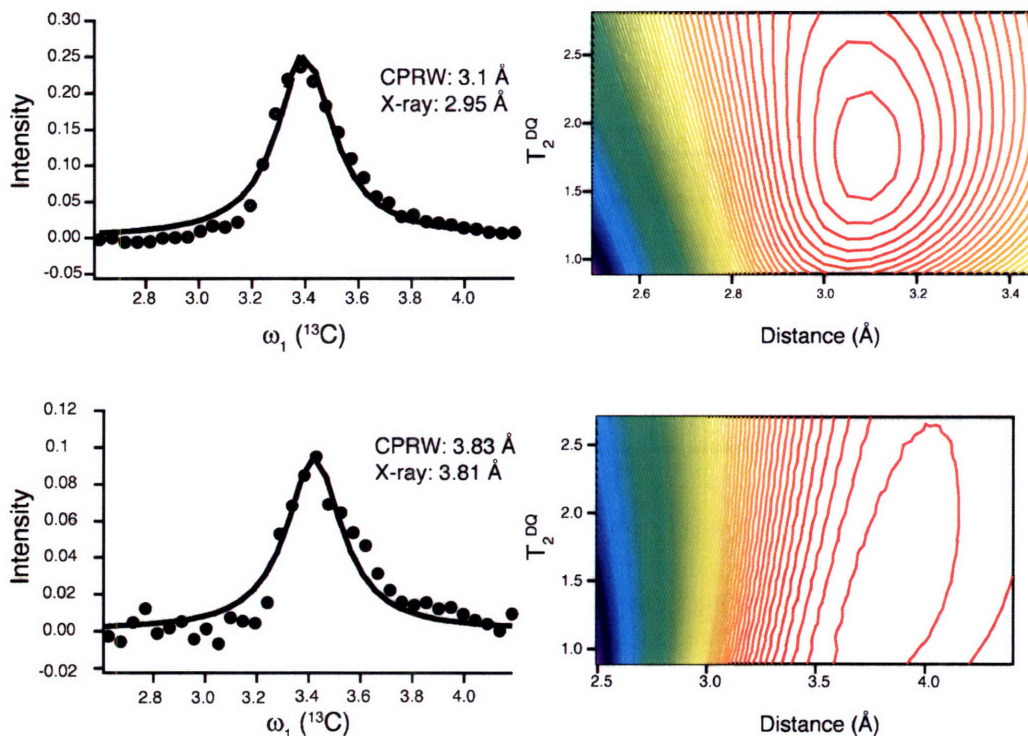
Figure 12-7: Accuracy of distance measurements in the presence of chemical shift overlap. The matching conditions which result in Val γ1-VN and Val γ 2-VN cross peaks are fulfilled nearly simultaneously, but the two-spin approximation still gives an accurate estimate of the internuclear distance.
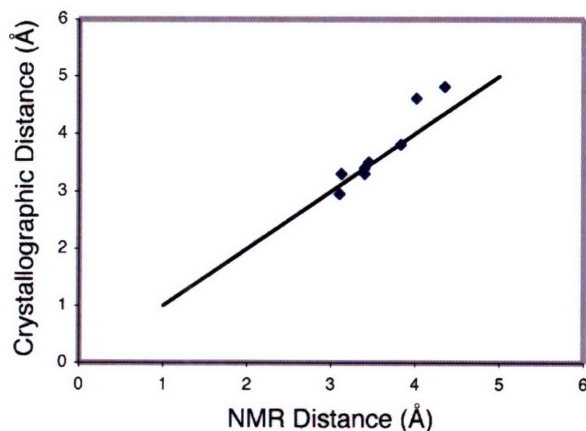
Figure 12-8: Comparison of distances determined in [U-^{13}C,^{15}N]-Val-Leu by CPRW and x-ray crystallography.

12.11   Kinetic Approximations to the Spin Dynamics

Because the CPRW experiment can be interpreted in terms of a two-spin approximation, it should be possible to approximate the spin dynamics in terms of simple kinetic relationships, in analogy to NOE-spectroscopy in solution state NMR. To do this, we make the approximation that operators which do not give rise to observable magnetization reach steady-state values. This results in an analytically soluble system of differential equations which yields, for the observable operators,

$$S_{1z} = \frac{1}{2}(1 + e^{-2kt})$$

$$S_{2z} = \frac{1}{2}(-1 + e^{-2kt}) \qquad (12.33)$$

$$k = \frac{2\omega^2 R}{(\Delta_1 + \Delta_2)^2 + R^2}; R = \frac{1}{T_2^{DQ}}$$

The difference between the exact and approximate treatment, shown in Figure 12-9, suggests that this approximation is valid over the entire range of experimentally relevant parameters.
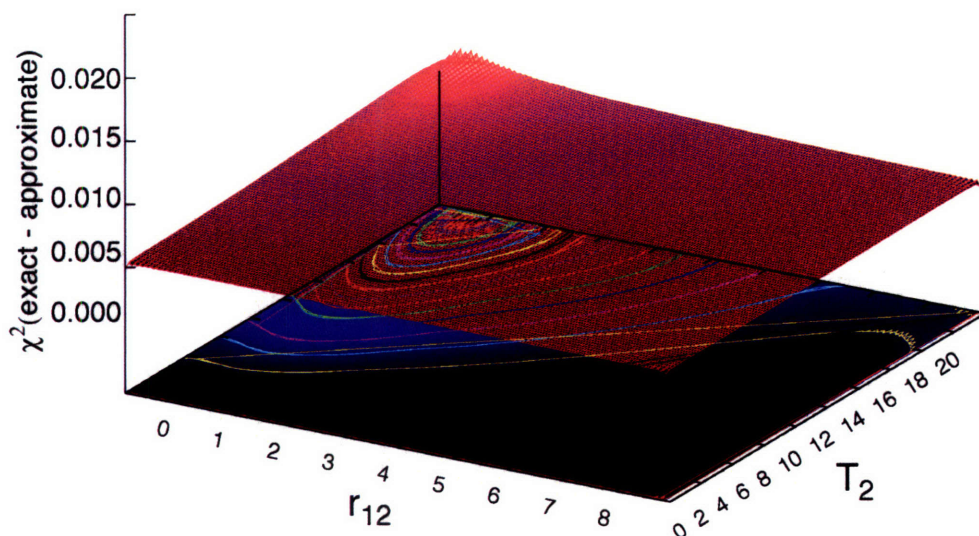
Figure 12-9: Agreement of analytical approximation treatment with two-spin numerical approach. The agreement is good over the entire range of relevant distances and relaxation parameters.

While the data in Figure 12-7 demonstrate the reduced importance of dipolar truncation for overlapping couplings of comparable magnitude in the presence of multiquantum relaxation, it is not always possible to arrange the experiment so that strong couplings are absent from the spin dynamics. In this case, an analytical treatment would require an enlarged operator space. The kinetic approach, as shown in Figure 12-10, simplifies the simulation of such experiments. In this picture, the spin dynamics are solved by numerical integration of two coupled rate equations. The simulations in Figure 12-11 show that it is an appropriate mechanism to consider polarization transfer among multiple coupled spins.
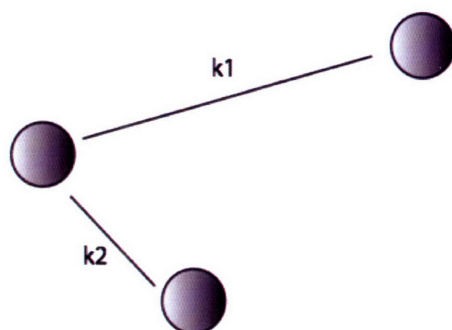
Figure 12-10: Kinetic approach for estimating weak couplings in the presence of a strong coupling with partial resonance overlap.
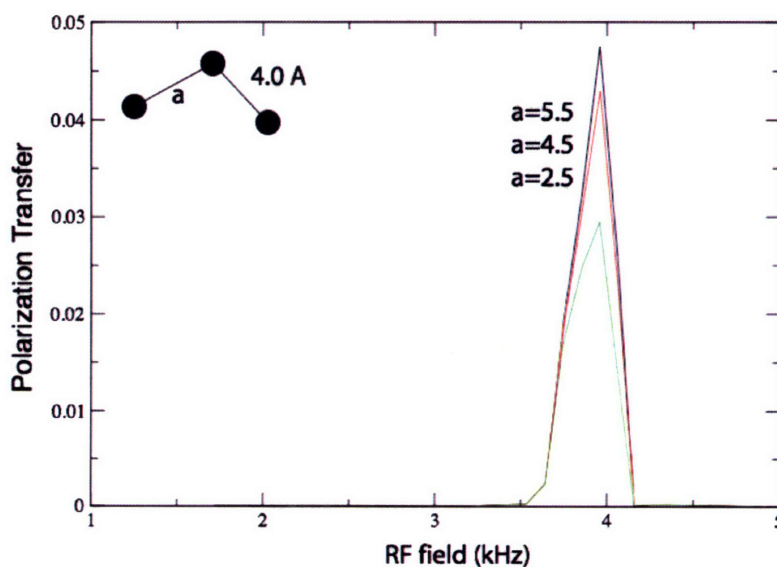
Figure 12-11: Attenuation of magnetization transfer for weak coupling (4.0 Å) in the presence of an additional overlapping resonance (5.5, 4.5, 2.5 Å).

12.12   The Influence of CSA on the Spin Dynamics[1]

As has been pointed out earlier, the transverse component of the CSA results in a Bloch-Siegert-like shift in the heteronuclear Hartmann-Hahn resonance condition. However, it also contributes to the multiquantum relaxation and may thus result in depolarization. It is therefore particularly important to conduct the experiment to avoid the transverse components of the ^{13}C CSA and far from the ^{15}N CSA recoupling condition, which in practice requires fast magic angle spinning. The effects of the CSA are summarized in Figure 12-12.
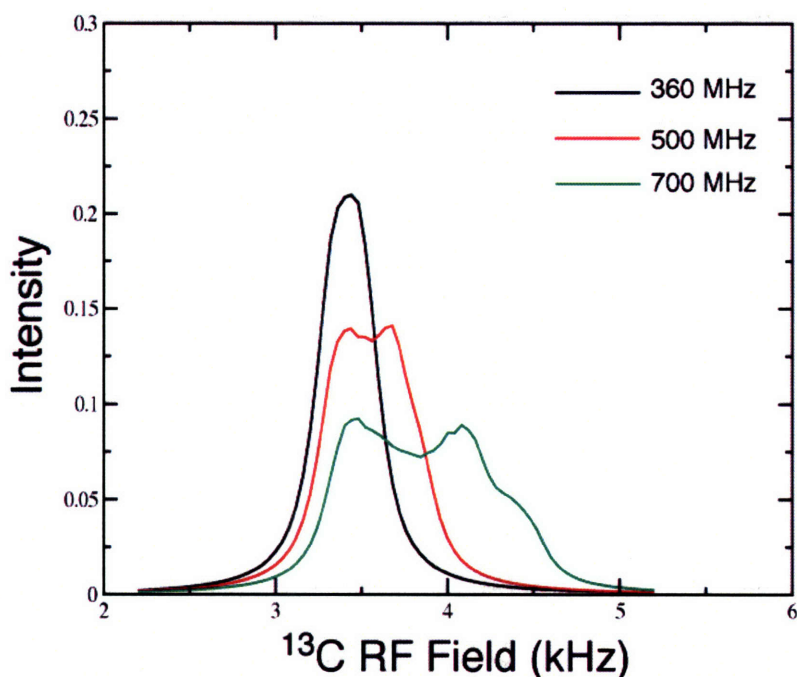
Figure 12-12: The effects of CSA under conditions where the transverse CSA elements are not minimized. CSA parameters corresponding to amide ^{15}N and ^{13}Cβ were assumed.

While it is possible to approximately account for the effects of the CSA using average Hamiltonian theory in a fictitious-spin basis, we instead apply the more general Multipole

---

[1] The MMFT approach and its application to heteronuclear decoupling, rotational resonance width and depolarization in double-quantum recoupling experiments are due to Dr. Ramesh Ramachandran and are summarized in several papers on this topic.

theory of Ramachandran *et al.*, which allows for a complete description of the dynamics and can be readily extended to describe multiple spin dynamics.

12.12.1   Basic theory

The spin Hamiltonian of a heteronuclear two spin system under MAS is represented by

$$H(t) = \left(\omega_I(t) + \omega_I\right)I_z + \left(\omega_S(t) + \omega_S\right)S_z + 2\omega_{IS}(t)I_zS_z + \omega_{1I}I_x + \omega_{1S}S_x \qquad (12.1A)$$

where the isotropic chemical shifts are represented by $\omega_{I(S)}$ and the time-dependent

anisotropic interactions (spatial terms) are represented by $\omega_\lambda(t) = \sum_{\substack{m=-2, \\ m \neq 0}}^{2} \omega_\lambda^{(m)} e^{im\omega_r t}$ with λ

characterizing the spin interactions (*i.e.* $\lambda = I, S, IS$). Since the spatial terms ω_λ (often

expressed in terms of spatial tensor operators, $R_\lambda^{(k)0}$), are often expressed in their

respective principal axes, the following sets of transformations describe the dynamics in

the lab frame.

$$\text{PAS} \xrightarrow{D(\Omega_{PM})} \text{molAS} \xrightarrow{D(\Omega_{MR})} \text{RAS} \xrightarrow{D(\Omega_{RL})} \text{Lab} \qquad (12.2A)$$

Employing the properties of Wigner rotation matrices, the spatial tensors defined in the

principal axis system (PAS) are transformed in to the lab frame (represented by

$D^{(k)}(\Omega_{PL})$) as follows,

$$D^{(k)}(\Omega_{PL})R^{(k)0}\left(D^{(k)}\right)^{-1}(\Omega_{PL}) = \sum_{q_1,q_2,q=-k}^{k} R^{(k)q_1}D_{q_1q_2}^{(k)}(\Omega_{PM})D_{q_2q}^{(k)}(\Omega_{MR})D_{q0}^{(k)}(\Omega_{RL}) \qquad (12.3A)$$

where $D^{(k)}(\Omega_{PM})$ represents the Wigner rotation matrix describing the transformation

from the PAS to the molecular axis system (molAS) and $D^{(k)}(\Omega_{MR})$ the transformation

from the molecular axis to the rotor axis (RAS). The transformation from the rotor axis to

the lab frame is time-dependent (due to sample spinning) and is represented by the Euler

angles $\Omega_{RL} = \left(\alpha_0 - \omega_r t, \beta_m, 0 \right)$ with β_m representing the magic angle and ω_r the sample

spinning frequency. In the case of chemical shift anisotropy (CSA), the spatial

components in the lab frame are represented by,

$$\underbrace{R_{L,I(S)}^{(2)0}(t)}_{\omega_{I(S)}(t)} = \sum_{m_1=0,\pm2} R_{P,I(S)}^{(2)m_1} \underbrace{\sum_{m_2=-2}^{2} D_{m_1 m_2}(\Omega_{PM}) \sum_{\substack{m=-2 \\ m\neq0}}^{2} D_{m_2 m}(\Omega_{MR})\; D_{m0}(\Omega_{RL})}_{\omega_{I(S)}^{(m)}}$$

(12.4A)

where $R_{P,I(S)}^{(2)m_1}$ ($R_{P,(I(S)}^{(2)0} = \delta_{anis}$, $R_{P,(I(S)}^{(2)\pm2} = -\frac{1}{\sqrt{6}}\delta_{anis}\eta$ where δ_{anis}, η represent the chemical

shift anisotropy and asymmetry parameter) represents the non-zero spatial terms defined

in the principal axis frame. In a similar vein the dipolar spatial terms are represented by,

$$\underbrace{R_{L,IS}^{(2)0}(t)}_{\omega_{IS}(t)} = \sum_{m_2=-2}^{2} R_{P,IS}^{(2)0} D_{0 m_2}(\Omega_{PM}) \underbrace{\sum_{\substack{m=-2 \\ m\neq0}}^{2} D_{m_2 m}(\Omega_{MR})\; D_{m0}(\Omega_{RL})}_{\omega_{IS}^{(m)}}$$

(12.5A)

where only $R_{P,IS}^{(2)0}$ ($R_{P,IS}^{(2)0} = b_{jk}$, and $b_{jk} = \dfrac{\mu_0 \gamma_I \gamma_S \hbar}{4\pi r_{IS}^3}$ (rad / s) represents the dipolar

coupling constant) is non-zero in the dipolar principal axis frame.

To describe the effects of RF irradiation, the Hamiltonian (Eq. 12.1A) in the

rotating frame is transformed in to a tilted frame defined by the transformation operator

$U_1 = \exp(i\beta_I I_y)\exp(i\beta_S S_y)$, with $\beta_{I(S)} = \arctan\left(\dfrac{\omega_{1I(S)}}{\omega_{I(S)}} \right)$ representing the tilt angle.

Employing the multipole operator basis (Table 12.2), the Hamiltonian in the tilted

rotating frame is represented by

$$H_T = U_1 H U_1^{-1}$$

$$= \omega_{I,eff} I_z + \omega_{S,eff} S_z + \omega_I(t) \sum_{q=-1}^{1} \alpha^{(1)q}{}_{(10)} \, iT^{(1)q}{}_{(10)} + \omega_S(t) \sum_{q=-1}^{1} \alpha^{(1)q}{}_{(01)} \, iT^{(1)q}{}_{(01)} +$$

$$- 2\omega_{IS}(t) \sum_{q=-1}^{1} \alpha^{(1)q}{}_{(10)} \, iT^{(1)q}{}_{(10)} \times \sum_{q=-1}^{1} \alpha^{(1)q}{}_{(01)} \, iT^{(1)q}{}_{(01)} \tag{12.6A}$$

where α represents the Wigner rotation matrix elements corresponding to a tensor of rank 1 (*i.e.* $\alpha^{(1)0} = \cos\beta$, $\alpha^{(1)\pm 1} = \mp \frac{1}{\sqrt{2}} \sin\beta$, with β representing the flip angle) and $\omega_{I(S),eff}$ the effective field (*i.e.* $\omega_{I(S),eff} = \sqrt{\omega_{I(S)}^2 + \omega_{1I(S)}^2}$) along the z-axis .

Table 12.2. Operator basis for two spin system

Operator basis	Number of operators
1. Identity operator	
$T^{(0)0}{}_{(00)}$	1
2. Single spin operators	
$T^{(1)q}{}_{(10)}$	3
$T^{(1)q}{}_{(01)}$	3
3. Two spin operators	
$T^{(2)q}{}_{(11)}$	5
$T^{(1)q}{}_{(11)}$	3
$T^{(0)0}{}_{(11)}$	1
Total	16

In the CPRW approach, the polarization transfer is established through a series of experiments under constant mixing times as opposed to the traditional NMR experiments, wherein the polarization transfer is monitored as a function of mixing time under a single effective Hamiltonian. Since the coherent averaging due to MAS is compensated through a series of experiments with different RF fields; the modifications in the spin Hamiltonian are conveniently described in the interaction frame defined by the transformation operator, $U_2 = \exp(in\omega_r t I_z) \exp(in\omega_r t S_z)$ represented below,

$$\tilde{H}(t) = U_2 H_T U_2^{-1}$$

$$= \left(\omega_{I,\text{eff}} - n\omega_r\right) iT^{(1)0}{}_{(10)} + \left(\omega_{S,\text{eff}} - n\omega_r\right) iT^{(1)0}{}_{(01)} +$$

$$\omega_I(t) \sum_{q=-1}^{1} \alpha^{(1)q}{}_{(10)} e^{iqn\omega_r t} \; iT^{(1)q}{}_{(10)} + \omega_S(t) \sum_{q=-1}^{1} \alpha^{(1)q}{}_{(01)} e^{iqn\omega_r t} \; iT^{(1)q}{}_{(01)} - \qquad \text{(12.7A)}$$

$$2\omega_{IS}(t) \sum_{q=-1}^{1} \alpha^{(1)q}{}_{(10)} e^{iqn\omega_r t} \; iT^{(1)q}{}_{(10)} \times \sum_{q=-1}^{1} \alpha^{(1)q}{}_{(01)} e^{iqn\omega_r t} \; iT^{(1)q}{}_{(01)}$$

The spin dynamics in the interaction frame could be solved analytically, either employing the Average Hamiltonian theory (AHT) or the Floquet theory. In the zero order Average Hamiltonian treatment, the effective Hamiltonian describing the spin dynamics neglecting the effects of CSA interactions may be represented by,

$$\tilde{H}_{0,\text{AHT}} = \left(\omega_{I,\text{eff}} - n\omega_r\right) iT^{(1)0}{}_{(10)} + \left(\omega_{S,\text{eff}} - n\omega_r\right) iT^{(1)0}{}_{(01)}$$
$$+ G_{IS,-1}^{(2)2} T^{(2)2}{}_{(11)} + G_{IS,1}^{(2)-2} T^{(2)-2}{}_{(11)} \qquad \text{(12.8A)}$$

where the G coefficients represent the dipolar spatial terms $\omega_{IS}^{(m)}$, illustrated in Eq. (5).

Expressing the density operator in the multipole basis i.e. $\rho(t) = \Phi_q^{(k)}{}_{(k_1 k_2}, t) \, T^{(k)q}{}_{(k_1 k_2)}$, the spin dynamics in the operator (or Liouville) space is described by the following set of differential equations.

$$i\hbar \frac{d}{dt} \begin{bmatrix} \hat{\Phi}_0^{(1)}{}_{(10)\,[t]} \\ \hat{\Phi}_0^{(1)}{}_{(01)\,[t]} \\ \hat{\Phi}_2^{(2)}{}_{(11)\,[t]} \\ \hat{\Phi}_{-2}^{(2)}{}_{(11)\,[t]} \end{bmatrix} = \begin{bmatrix} 0 & 0 & -iG_{12,1} & iG_{12,-1} \\ 0 & 0 & -iG_{12,1} & iG_{12,-1} \\ iG_{12,-1} & iG_{12,-1} & -\left(\omega_{I,\text{eff}} + \omega_{S,\text{eff}} - \omega_r\right) & 0 \\ -iG_{12,1} & -iG_{12,1} & 0 & \left(\omega_{I,\text{eff}} + \omega_{S,\text{eff}} - \omega_r\right) \end{bmatrix} \begin{bmatrix} \hat{\Phi}_0^{(1)}{}_{(10)\,[t]} \\ \hat{\Phi}_0^{(1)}{}_{(01)\,[t]} \\ \hat{\Phi}_2^{(2)}{}_{(11)\,[t]} \\ \hat{\Phi}_{-2}^{(2)}{}_{(11)\,[t]} \end{bmatrix} \qquad \text{(12.9A)}$$

where the $\hat{\Phi}_q^{(k)}{}_{(10)\,[t]}$'s represent the time-dependent spin polarizations in the interaction frame. The expectation value of the observable is given by

$$\langle \hat{S}_x(t) \rangle = \text{Tr}\left[\hat{S}_x \hat{\rho}(t) \right]$$
$$= \hat{\Phi}_0^{(1)}{}_{(01,t)} \sin \beta_S \qquad \text{(12.10A)}$$

where $\hat{S}_x = U_2 U_1 S_x U_1^{-1} U_2^{-1}$ represents the observable in the interaction frame. It is important to note here that the spin dynamics is described in the Schrödinger picture. The incoherent effects due to relaxation are incorporated in to the exchange dynamics by including a phenomenological decaying rate constant, T_{DQ} corresponding to the double quantum polarizations $\hat{\Phi}_{\pm 2}^{(2)}(11,t)$. Although the proposed model provides a qualitative explanation of the underlying phenomena, quantitative agreement with the experimental data often requires a complete description of the CSA effects in addition to the contributions from the second order terms in the Hamiltonian. To this end several researchers have derived expressions for evaluating the higher order corrections based on the Magnus expansion. Although such approaches yield results, they are often numerical in nature and fail to provide analytical insights of the underlying phenomena. Furthermore, existing basis employed for spin description in such treatments do not elucidate the exact contributions of the higher order terms in the spin dynamics.

Alternatively we present an approach based on Floquet theory (MMFT) for evaluating the higher order terms in addition to describing the dynamics incorporating both the coherent as well as incoherent effects. In the MMFT approach the spin dynamics is described in the Floquet-Liouville space and the higher order corrections are evaluated in terms of an effective Hamiltonian derived using the contact (or van Vleck) transformation procedure. The complexities involved in the conventional Floquet treatments are significantly minimized in the MMFT approach. In the next section we describe the CPRW experiments using the MMFT approach.

12.12.2 Spin dynamics using the MMFT approach

Employing the Floquet theorem for solving differential equations involving time-dependent coefficients, Shirley proposed a general description in the form of Floquet theory for studying periodic time-dependent phenomena in quantum mechanics. In this approach a time-dependent Hamiltonian, which is periodic is transformed in to a time-independent Hamiltonian via Fourier series expansion. The transformed Hamiltonian (also referred as Floquet Hamiltonian) is described in an infinite dimensional Floquet state space (of dimension $(2I_1 + 1)(2I_2 + 1)...(2I_N + 1)(2n + 1)$, where I_i represents the spin quantum number and n the Fourier index ($n = -\infty, \infty$)) using a basis set constructed by a direct product of the spin basis with the Fourier index. Since the evolution of a quantum system is constrained by both coherent (due to the spin Hamiltonian) as well as incoherent (relaxation) processes, an adequate interpretation of the experimental results entails a Floquet-Liouville space $((2I_1 + 1)^2 (2I_2 + 1)^2 ...(2I_N + 1)^2 (2n + 1))$ treatment. Since the density operator defines a state in the operator (or Liouville) space analogous to the spin eigenfunctions in the state space, an appropriate choice of the basis has often limited the description in the Floquet-Liouville space. The problem is circumvented in the MMFT approach by expressing both the density operator and the spin Hamiltonian using an operator basis constructed by a direct product of the irreducible spherical tensor operator basis (which is finite and represented in Table 12.2) with the Fourier index (which in principle is infinite). The multipole operators $T^{(k)q}{}_{(k_1 k_2)}$ (in Table 12.2) define the spin part while the Fourier operators F_r define the Fourier part of the basis. Such an approach provides a convenient basis that is independent of spin magnitude and quite elegant for analytical treatments involving multiple spins. Employing the MMFT

approach the spin Hamiltonian in the interaction frame (Eq. 12.7A) is transformed in to a

time-independent Hamiltonian represented in the Floquet –Liouville space.

$$H_F = \omega_r N + \omega_{I,off} \; iT^{(1)0}{}_{(10)}F_0 + \omega_{S,off} \; iT^{(1)0}{}_{(01)}F_0 + \sum_{\substack{m=-2,\,q=-1\\m\neq0}}^{2\quad1} G^{(1)q}_{I,m} \; iT^{(1)q}{}_{(10)}F_{m+qn} +$$

$$\sum_{\substack{m=-2,\,q=-1\\m\neq0}}^{2\quad1} G^{(1)q}_{S,m} \; iT^{(1)q}{}_{(01)}F_{m+qn} + \sum_{\substack{m=-2,\,q=-1,\\m\neq0\quad q\neq0}}^{2\quad1} G^{(1)q}_{IS,m} \; T^{(1)q}{}_{(11)}F_{m+qn} + \hspace{2cm} (12.11A)$$

$$\sum_{\substack{m=-2,\,q=-2\\m\neq0}}^{2\quad2} G^{(2)q}_{IS,m} \; T^{(2)q}{}_{(11)}F_{m+qn} + \sum_{\substack{m=-2,\\m\neq0}}^{2} G^{(0)0}_{IS,m} \; T^{(0)0}{}_{(11)}F_m$$

where the indices q and r denote the off-diagonality in the spin and Fourier dimensions

respectively. The operator N is diagonal both in the spin as well as in the Fourier

dimension and is obtained from the derivation of the Floquet Hamiltonian. In the above

representation of the Floquet Hamiltonian only the non-zero Fourier components are

represented with the G coefficients having the following definitions:

$$G^{(1)q}_{I,m} = \omega^{(m)}_I \alpha^{(1)q}{}_{(10)}, G^{(1)q}_{S,m} = \omega^{(m)}_S \alpha^{(1)q}{}_{(01)}, G^{(1)\pm1}_{IS,m} = \omega^{(m)}_{IS} \tfrac{1}{2}\sin\left(\beta_I - \beta_S\right),$$

$$G^{(2)\pm1}_{IS,m} = \pm\omega^{(m)}_{IS} \tfrac{1}{2}\sin\left(\beta_I + \beta_S\right), G^{(2)0}_{IS,m} = -\omega^{(m)}_{IS}\left(\sqrt{\tfrac{2}{3}}\cos\beta_I \cos\beta_S - \tfrac{1}{\sqrt{6}}\sin\beta_I \sin\beta_S\right),$$

$$G^{(2)\pm2}_{IS,m} = -\omega^{(m)}_{IS} \tfrac{1}{2}\sin\beta_I \sin\beta_S, \qquad G^{(0)0}_{IS,m} = \omega^{(m)}_{IS}\left(\tfrac{1}{\sqrt{3}}\cos\beta_I \cos\beta_S + \tfrac{1}{\sqrt{3}}\sin\beta_I \sin\beta_S\right) \qquad \text{and}$$

$\omega_{I(S),off} = \omega_{I(S),eff} - n\omega_r$ the off-sets of the individual spins. Each element $\left[H^j_i\right]$

represents a matrix of dimension 16×16 defined in the Liouville space. The off-

diagonality in both spin and Fourier dimensions often complicates the dynamics and

often necessitates spin description in the entire Floquet-Liouville space. The standard

approach in such cases involves numerical diagonalization of a truncated Floquet

Hamiltonian matrix with the order of truncation fixed based on the convergence of

eigenvalues for increasing matrix dimensions. Though such numerical approaches yield

results; physical insights in to the dynamics often entail analytical treatments. To this end we employ the contact transformation procedure for deriving an effective Hamiltonian, which is nearly diagonal both in the spin as well as in the Fourier dimension. The advantages associated with such an approach have been described in earlier works and would not be elaborated upon any further in this article. In the next section we derive the effective Hamiltonian using the contact transformation procedure.

12.12.3   Effective Floquet Hamiltonians

The contact (or van Vleck) transformation procedure is an operator equivalent of the traditional Rayleigh-Schrödinger perturbation theory in which perturbation corrections to the zero order eigenvalues and eigenvectors are obtained in terms of operators as opposed to matrix elements. The method employs a series of unitary transformations chosen carefully such that the off-diagonal contributions (operators) due to the interaction Hamiltonians (perturbations) are folded back to give diagonal corrections to the zero order Hamiltonian. As a result, one obtains a new Hamiltonian whose eigenvalues are comparable to those of the exact Hamiltonian.

In order to apply the contact transformation procedure the Floquet Hamiltonian (Eq. (12.11A)) is rewritten as a sum involving a zero order and a perturbing Hamiltonian. Generally, the zero order Hamiltonian is represented using operators, which are diagonal both in the spin as well as in the Fourier dimension (*i.e.* terms involving $T^{(k)0}$ and F_0 operators). Nevertheless, depending on the nature of experiments, the definition of the zero order Hamiltonian needs to be modified accordingly. For *e.g.* in the case of double-quantum recoupling experiments (both homonuclear and heteronuclear) the zero order Hamiltonian should involve the $T^{(2)\pm2}_{(11)}$ operators. The definition of the zero order

Hamiltonian plays a vital role in averting the problem of degeneracy (or Poincare's catastrophe) in quantum mechanical treatments based on perturbation theory. It is important to realize that the zero order Hamiltonian is both a dominant as well as a time-independent interaction and should be defined carefully according to the experiment of interest. In the CPRW approach the resonance condition ($\omega_{I,eff} + \omega_{S,eff} = n\omega_r$) is scanned through a series of experiments by varying the effective fields under constant mixing times. Such an approach more or less compensates the effects of chemical shift dispersion as well as minimizes the dependence of the experimental data on the relaxation parameters. The catastrophic (or degeneracy) condition in the CPRW experiments is obviated by the following choice of the zero order (H_0) and perturbing Hamiltonian (H_1).

$$
\begin{aligned}
H_0 = {} & \omega_r N + \omega_{I,off}\, iT^{(1)0}{}_{(10)}F_0 + \omega_{S,off}\, iT^{(1)0}{}_{(01)}F_0 + \\
& G^{(2)2}_{IS,-1}T^{(2)2}{}_{(11)}F_0 + G^{(2)-2}_{IS,1}T^{(2)-2}{}_{(11)}F_0
\end{aligned}
\tag{12.12A}
$$

$$
\begin{aligned}
H_1 = {} & \sum_{\substack{m=-2,\, q=-1 \\ m\neq 0}}^{2\ \ 1} G^{(1)q}_{I,m}\, iT^{(1)q}{}_{(10)}F_{m+qn} + \sum_{\substack{m=-2,\, q=-1 \\ m\neq 0}}^{2\ \ 1} G^{(1)q}_{S,m}\, iT^{(1)q}{}_{(01)}F_{m+qn} + \\[6pt]
& \sum_{\substack{m=-2,\, q=-1, \\ m\neq 0 \quad q\neq 0}}^{2\ \ 1} G^{(1)q}_{IS,m}\, T^{(1)q}{}_{(11)}F_{m+qn} + \sum_{\substack{m=-2, \\ m\neq 0}}^{2} G^{(0)0}_{IS,m}\, T^{(0)0}{}_{(11)}F_m + \\[6pt]
& \sum_{\substack{m=-2,\, q=-1 \\ m\neq 0}}^{2\ \ 1} G^{(2)q}_{IS,m}\, T^{(2)q}{}_{(11)}F_{m+qn} + \sum_{\substack{m=-2,\, q_1=\pm 2 \\ m\neq 0}}^{2} G^{(2)q_1}_{IS,m}\, T^{(2)q_1}{}_{(11)}F_{m+qn}
\end{aligned}
\tag{12.13A}
$$

Such a choice should not be misinterpreted as a clever manipulation of the theory to suit the experiment, but rather a fundamental definition of the zero order Hamiltonian in quantum mechanics.

Employing the method of contact transformation, the transformation function S_1 is expressed as a linear combination of spin operators used to describe the perturbing Hamiltonian H_1.

$$S_1 = i \left[\begin{array}{l} \displaystyle\sum_{\substack{m=-2,\,q=-1 \\ m\neq 0}}^{2}\sum_{q=-1}^{1} C_{I,m}^{(1)q}\, iT^{(1)q}{}_{(10)}F_{m+qn} + \displaystyle\sum_{\substack{m=-2,\,q=-1 \\ m\neq 0}}^{2}\sum_{q=-1}^{1} C_{S,m}^{(1)q}\, iT^{(1)q}{}_{(01)}F_{m+qn} + \\[4mm] \displaystyle\sum_{\substack{m=-2,\,q=-1, \\ m\neq 0\quad q\neq 0}}^{2}\sum^{1} C_{IS,m}^{(1)q}\, T^{(1)q}{}_{(11)}F_{m+qn} + \displaystyle\sum_{\substack{m=-2, \\ m\neq 0}}^{2} C_{IS,m}^{(0)0}\, T^{(0)0}{}_{(11)}F_{m} + \\[4mm] \displaystyle\sum_{\substack{m=-2,\,q=-1 \\ m\neq 0}}^{2}\sum_{q=-1}^{1} C_{IS,m}^{(2)q}\, T^{(2)q}{}_{(11)}F_{m+qn} + \displaystyle\sum_{\substack{m=-2,\,q_1=\pm2 \\ m\neq 0}}^{2}\sum C_{IS,m}^{(2)q_1}\, T^{(2)q_1}{}_{(11)}F_{m+qn} \end{array} \right] \qquad (12.14A)$$

The C coefficients involved in the transformation function are suitably chosen to compensate the off-diagonality (both in the spin as well as in the Fourier dimension) by solving equation (12.15A).

$$H_1^{(1)} = H_1 + i\big[S_1, H_0\big] \qquad (12.15A)$$

Since the perturbation H_1 is chosen to contain only off-diagonal terms, the first order correction $H_1^{(1)}$ is zero and the C coefficients are obtained by solving a set of linear equations (Eq. 12.16A) corresponding to a particular operator and have been tabulated in Table 12.3.

$$\begin{aligned} H_1^{(1)} &= H_1 + i\big[S_1, H_0\big] \\ &= iT^{(1)q}{}_{(10)}F_{m+qn}\Big[G_{I,m}^{(1)q} - \big\{(m+qn)\omega_r + q\omega_{I,off}\big\} C_{I,m}^{(1)q} \Big] + \\ &\quad iT^{(1)q}{}_{(01)}F_{m+qn}\Big[G_{S,m}^{(1)q} - \big\{(m+qn)\omega_r + q\omega_{S,off}\big\} C_{S,m}^{(1)q} \Big] + \\ &\quad T^{(0)0}{}_{(11)}F_{m}\Big[G_{IS,m}^{(0)0} - m\omega_r C_{IS,m}^{(0)0} \Big] + \\ &\quad T^{(2)q}{}_{(11)}F_{m+qn}\Big[G_{IS,m}^{(2)q} - \big\{(m+qn)\omega_r - q\tfrac{1}{2}\big(\omega_{I,off}+\omega_{S,off}\big)\big\} C_{IS,m}^{(2)q} - \tfrac{1}{2}\big(\omega_{I,off}-\omega_{S,off}\big) C_{IS,m}^{(1)q} \Big] + \\ &\quad T^{(1)q}{}_{(11)}F_{m+qn}\Big[G_{IS,m}^{(1)q} - \tfrac{1}{2}\big(\omega_{I,off}-\omega_{S,off}\big) C_{IS,m}^{(2)q} - \big\{(m+qn)\omega_r + q\tfrac{1}{2}\big(\omega_{I,off}+\omega_{S,off}\big)\big\} C_{IS,m}^{(1)q} \Big] \end{aligned} \qquad (12.16A)$$

Table 12.3. C coefficients involved in the transformation function. The indices involved in the coefficients have the following values, $q = \pm 1, q_1 = 0, \pm 1, q_2 = \pm 2$ and $m = \pm 1, \pm 2$.

$$C_{I(S),m}^{(1)q_1} = \frac{G_{I(S),m}^{(1)q_1}}{\left\{(m+q_1 n)\omega_r + q_1 \omega_{I(S),off}\right\}}$$

$$C_{IS,m}^{(2)0} = \frac{G_{IS,m}^{(2)0}}{m\omega_r}, \quad C_{IS,m}^{(0)0} = \frac{G_{IS,m}^{(0)0}}{m\omega_r}$$

$$C_{IS,m}^{(2)q_2} = \frac{G_{IS,m}^{(2)q_2}}{\left\{(m+q_2 n)\omega_r - q_2 \frac{1}{2}\left(\omega_{I,off} + \omega_{S,off}\right)\right\}},$$

$$C_{IS,m}^{(2)q} = \frac{\frac{1}{2}\left(\omega_{I,off} - \omega_{S,off}\right)G_{IS,m}^{(1)q} - \left\{(m+qn)\omega_r + q\frac{1}{2}\left(\omega_{I,off} + \omega_{S,off}\right)\right\}G_{IS,m}^{(2)q}}{\frac{1}{4}\left(\omega_{I,off} - \omega_{S,off}\right)^2 - \left\{(m+qn)\omega_r - q\frac{1}{2}\left(\omega_{I,off} + \omega_{S,off}\right)\right\}\left\{(m+qn)\omega_r + q\frac{1}{2}\left(\omega_{I,off} + \omega_{S,off}\right)\right\}}$$

$$C_{IS,m}^{(1)q} = \frac{\frac{1}{2}\left(\omega_{I,off} - \omega_{S,off}\right)G_{IS,m}^{(2)q} - \left\{(m+qn)\omega_r - q\frac{1}{2}\left(\omega_{I,off} + \omega_{S,off}\right)\right\}G_{IS,m}^{(1)q}}{\frac{1}{4}\left(\omega_{I,off} - \omega_{S,off}\right)^2 - \left\{(m+qn)\omega_r - q\frac{1}{2}\left(\omega_{I,off} + \omega_{S,off}\right)\right\}\left\{(m+qn)\omega_r + q\frac{1}{2}\left(\omega_{I,off} + \omega_{S,off}\right)\right\}}$$

Table 12.4. Coefficients involved in the second order correction terms. The indices involved in the coefficients have the following values, $q = \pm 1, q_1 = \pm 1, \pm 2$ and $m = \pm 1, \pm 2$.

$$A_1 \quad \frac{1}{2}\left[\underbrace{-qC_{I,m}^{(1)q}G_{I,-m}^{(1)-q}}_{csa-csa} + \underbrace{(-1)^{-q_1}\frac{q_1}{2}C_{IS,m}^{(2)q_1}G_{IS,-m}^{(2)-q_1} + \frac{1}{2}qC_{IS,m}^{(1)q}G_{IS,-m}^{(1)-q} - \frac{1}{2}\left(C_{IS,m}^{(2)q}G_{IS,-m}^{(1)-q} - C_{IS,m}^{(1)-q}G_{IS,-m}^{(2)q}\right)}_{dipolar-dipolar}\right]$$

$$A_2 \quad \frac{1}{2}\left[\underbrace{-qC_{S,m}^{(1)q}G_{S,-m}^{(1)-q}}_{csa-csa} + \underbrace{(-1)^{-q_1}\frac{q_1}{2}C_{IS,m}^{(2)q_1}G_{IS,-m}^{(2)-q_1} + \frac{1}{2}qC_{IS,m}^{(1)q}G_{IS,-m}^{(1)-q} + \frac{1}{2}\left(C_{IS,m}^{(2)q}G_{IS,-m}^{(1)-q} - C_{IS,m}^{(1)-q}G_{IS,-m}^{(2)q}\right)}_{dipolar-dipolar}\right]$$

$$A_3 \quad \frac{1}{2}\left[\underbrace{\begin{array}{l}-\frac{1}{\sqrt{2}}\left\{\left(C_{I,m}^{(1)1} + C_{S,m}^{(1)1}\right)G_{IS,-m}^{(2)1} + \left(G_{I,-m}^{(1)1} + G_{S,-m}^{(1)1}\right)C_{IS,m}^{(2)1}\right\} + \frac{1}{\sqrt{2}}\left\{\left(C_{I,m}^{(1)1} - C_{S,m}^{(1)1}\right)G_{IS,-m}^{(1)1} - \left(G_{I,-m}^{(1)1} - G_{S,-m}^{(1)1}\right)C_{IS,m}^{(1)1}\right\} \\ + \left\{\left(C_{I,-2}^{(1)0} + C_{S,-2}^{(1)0}\right)G_{IS,1}^{(2)2} + \left(G_{I,-2}^{(1)0} + G_{S,-2}^{(1)0}\right)C_{IS,1}^{(2)2}\right\} + \left\{\left(C_{I,1}^{(1)0} + C_{S,1}^{(1)0}\right)G_{IS,-2}^{(2)2} + \left(G_{I,1}^{(1)0} + G_{S,1}^{(1)0}\right)C_{IS,-2}^{(2)2}\right\}\end{array}}_{csa-dipolar}\right]$$

$$A_4 \quad \frac{1}{2}\left[\underbrace{\begin{array}{l}\frac{1}{\sqrt{2}}\left\{\left(C_{I,m}^{(1)-1} + C_{S,m}^{(1)-1}\right)G_{IS,-m}^{(2)-1} + \left(G_{I,-m}^{(1)-1} + G_{S,-m}^{(1)-1}\right)C_{IS,m}^{(2)-1}\right\} + \frac{1}{\sqrt{2}}\left\{\left(C_{I,m}^{(1)-1} - C_{S,m}^{(1)-1}\right)G_{IS,-m}^{(1)-1} - \left(G_{I,-m}^{(1)-1} - G_{S,-m}^{(1)-1}\right)C_{IS,m}^{(1)-1}\right\} \\ -\left\{\left(C_{I,2}^{(1)0} + C_{S,2}^{(1)0}\right)G_{IS,-1}^{(2)-2} + \left(G_{I,2}^{(1)0} + G_{S,2}^{(1)0}\right)C_{IS,-1}^{(2)-2}\right\} - \left\{\left(C_{I,-1}^{(1)0} + C_{S,-1}^{(1)0}\right)G_{IS,2}^{(2)-2} + \left(G_{I,-1}^{(1)0} + G_{S,-1}^{(1)0}\right)C_{IS,2}^{(2)-2}\right\}\end{array}}_{csa-dipolar}\right]$$

It is important to realize here that in the evaluation of the C coefficients corresponding to the double quantum operators $T^{(2)\pm 2}{}_{(11)}$, the catastrophic condition $(\omega_{I,eff} + \omega_{S,eff} = n\omega_r, m = -qn)$ has been avoided by the definitions employed in

Equations 12.12A and 12.13A. The second order (or diagonal) corrections to the zero order Hamiltonian are obtained by evaluating $H_2^{(1)}$,

$$
\begin{aligned}
H_2^{(1)} &= H_2 + i\left[S_1, H_1\right] - \tfrac{1}{2}\left[S_1, \left[S_1, H_0\right]\right] \\
&= \tfrac{i}{2}\left[S_1, H_1\right] \\
&= iT^{(1)0}{}_{(10)}F_0 A_1 + iT^{(1)0}{}_{(01)}F_0 A_2 + T^{(2)2}{}_{(11)}F_0 A_3 + iT^{(2)-2}{}_{(11)}F_0 A_4
\end{aligned}
\tag{12.17A}
$$

with the A coefficients (Table 12.4) representing the second order corrections. The second order corrections are evaluated using the general commutator relations between the tensor operators and the Fourier operators illustrated in earlier works. The cross-terms between the CSA-CSA and dipolar-dipolar interactions result in corrections to single spin operators (represented by the coefficients A_1, A_2) while the cross-terms between the CSA-dipolar interactions result in corrections to two spin operators (represented by the coefficients A_3, A_4).

The effective Hamiltonian derived from the contact transformation procedure is block-diagonal in our approach and simplifies the dynamics considerably in the Floquet-Liouville space.

$$
\begin{aligned}
H_F^{\mathit{eff}} &\approx H_0 + H_2^{(1)} \\
&= \omega_r N + \left(\omega_{I,\mathit{off}} + A_1\right) iT^{(1)0}{}_{(10)}F_0 + \left(\omega_{S,\mathit{off}} + A_2\right) iT^{(1)0}{}_{(01)}F_0 + \\
&\quad \left(G_{IS,-1}^{(2)2} + A_3\right) T^{(2)2}{}_{(11)}F_0 + \left(G_{IS,1}^{(2)-2} + A_4\right) T^{(2)-2}{}_{(11)}F_0
\end{aligned}
\tag{12.18A}
$$

12.12.4   Spin dynamics in the Floquet-Liouville space

Following the MMFT approach, the density operator for a two-spin system in the Floquet-Liouville space is represented by,

$$\rho_F(t) = \sum_{n=-\infty}^{\infty} \sum_{\substack{k,q,k_1, \\ k_2}} \Phi_{q,n}^{(k)}{}_{(k_1 k_2},t) T^{(k)q}{}_{(k_1 k_2)} F_n \qquad (12.19A)$$

and the dynamics in the Floquet-Liouville space is described by Equation 12.20A.

$$i\hbar \frac{d}{dt} \hat{\Phi}_{q,n}^{(k)}{}_{(k_1 k_2},t) = \left[\left[A \right]_{kq,k'q'} \right]_{n,n'} \hat{\Phi}_{q',n'}^{(k')}{}_{(k_1' k_2'},t) \qquad (12.20A)$$

where $\hat{\Phi}_{q,n}^{(k)}{}_{(k_1 k_2},t)$ represents the spin polarization (defined in the interaction frame) and

$\left[\left[A \right]_{kq,k'q'} \right]_{n,n'}$ the supermatrix defined in the Floquet-Liouville space. The index k denotes

the total rank and q its component. The ranks of the individual spins are represented by

k_1, k_2 respectively and range from $0, 2I_i$. The derivation of the matrix elements in the

supermatrix is described in the original article describing the MMFT approach.

Employing the effective Floquet Hamiltonians (Eq. 12.18A), the spin dynamics in

the Floquet-Liouville space can in principle be described using a set of differential

equations corresponding to a particular Fourier mode.

$$i\hbar \frac{d}{dt} \begin{bmatrix} \vdots \\ \hat{\Phi}^{(2)}(t) \\ \hat{\Phi}^{(1)}(t) \\ \hat{\Phi}^{(0)}(t) \\ \hat{\Phi}^{(-1)}(t) \\ \hat{\Phi}^{(-2)}(t) \\ \vdots \end{bmatrix} = \begin{bmatrix} \ddots & & & & & \\ & [A_0]_2^* & & & & \\ & & [A_0]_1^* & & & \\ & & & [A_0]_0^* & & \\ & & & & [A_0]_{-1}^* & \\ & & & & & [A_0]_{-2}^* \\ & & & & & & \ddots \end{bmatrix} \begin{bmatrix} \vdots \\ \hat{\Phi}^{(2)}(t) \\ \hat{\Phi}^{(1)}(t) \\ \hat{\Phi}^{(0)}(t) \\ \hat{\Phi}^{(-1)}(t) \\ \hat{\Phi}^{(-2)}(t) \\ \vdots \end{bmatrix} \qquad (12.21A)$$

$$i\hbar \frac{d}{dt} \hat{\Phi}^{(i)}(t) = [A]_i \hat{\Phi}^{(i)}(t) \qquad (12.22A)$$

$$\hat{\Phi}_a^{(i)}(t) = \sum_{jk} \Gamma_{ak}^{(i)} e^{it\lambda_k^{(i)}t} \left[\Gamma_{kj}^{(i)} \right]^{-1} \hat{\Phi}_j^{(i)}(0) \qquad (12.23A)$$

where $\hat{\Phi}^{(i)}(t)$ represents a column vector (of dimension 16×1) corresponding to a particular Fourier mode i defined in the Liouville space using the operator basis described in Table 12.2. In the above expression $\Gamma_{ak}^{(i)}$ and $\lambda_k^{(i)}$ represent the eigenvectors and eigenvalues corresponding to a particular mode (denoted by the superscript) respectively. The subscript in $\hat{\Phi}_a^{(i)}(t)$ is representative of all the quantum numbers (such as the rank, component etc) employed in the description of the spin polarization in the operator space.

It is important to realize here that such simplifications in the Floquet-Liouville space result only from the effective Hamiltonians obtained from the contact transformation procedure.

At time $t=0$ the Floquet density matrix is represented by spin polarizations whose Fourier indices are zero $i.e.$ $\hat{\rho}_F(0) = \hat{\Phi}^{(0)}(0)$. Such a choice of the initial condition is appropriate as no evolution takes place at $t=0$, and is consistent with other standard theoretical approaches employed for spin description in a finite dimensional space. Since the Floquet Hamiltonian has been transformed into a new frame (in which it is diagonal) , it becomes essential for the initial condition, $\hat{\rho}_F(0)$, to be described in a common frame. This is illustrated by the following transformation,

$$\begin{aligned}\hat{\rho}_F^{eff}(0) &= e^{i\lambda S_1}\hat{\rho}_F(0)e^{-i\lambda S_1} \\ &= \hat{\rho}_F(0) + \left[S_1, \hat{\rho}_F(0)\right] + ...\end{aligned} \tag{12.24A}$$

In this new frame, in addition to the $\hat{\Phi}^{(0)}(0)$ term, initial conditions for other polarizations ($\hat{\Phi}^{(i)}(0)$, $i \neq 0$) result from the evaluation of higher order terms in Eq. (12.24A) (such as $\left[S_1, \hat{\rho}_F(0)\right] + ..$ etc.). However, these polarizations ($\hat{\Phi}^{(i)}(0)$, $i \neq 0$) are

scaled accordingly (approximately by a factor $\dfrac{1}{n\omega_r}$, due to the transformation function

S_1), thereby minimizing their contributions in the Floquet-Liouville space. This enables

an approximate description of the spin dynamics in a reduced subspace, corresponding to

the super-block $\left[A_0\right]_0^*$ (i.e. block whose Fourier indices are zero), illustrated below.

$$
i\hbar\frac{d}{dt}\hat{\Phi}^{(0)}(t) = \left[A_0\right]_0^* \hat{\Phi}^{(0)}(t)
$$

$$
\hat{\Phi}_a^{(0)}(t) = \sum_{jk}\Gamma_{ak}e^{i\lambda_k t}\Gamma_{kj}^{-1}\hat{\Phi}_j^{(0)}(0)
$$

(12.25A)

In a similar vein the Floquet detection operator (S_x^F) is transformed in the new frame

defined by the transformation function S_1. Since the entire dynamics is described in the

Schrödinger picture, the time dependence is retained only on the density operator.

$$
\left\langle \hat{S}_{x,eff}^F(t)\right\rangle = \mathrm{Tr}\left[\hat{S}_{x,eff}^F(0)\hat{\rho}_F^{eff}(t)\right]
$$

(12.26A)

where $\hat{S}_{x,eff}^F(0) = e^{-i\lambda S_1}\hat{S}_x^F(0)e^{i\lambda S_1}$. The $\hat{S}_x^F(0)$ represents the Floquet operator at time $t = 0$

and analogous to $\hat{\rho}_F(0)$ is represented via spin polarizations whose Fourier indices are

zero. Such simplifications in the description of the spin dynamics in the Floquet-Liouville

space are possible only due to the effective Hamiltonians derived from the contact

transformation procedure. In the next section we describe the dynamics in the Liouville

space corresponding to the super-block $\left[A_0\right]_0^*$.

12.12.5   Spin dynamics in the Liouville space

Although the description of a two-spin system in the operator space involves a matrix of

dimension 16×16; the effective Hamiltonian (Eq. 12.18A) reduces the complexity of the

514

problem in the Liouville space. Accordingly the spin dynamics in the interaction frame is governed by the following sets of differential equations,

$$
i\hbar \frac{d}{dt}
\begin{bmatrix}
\hat{\Phi}_0^{(1)}{}_{(10)\,[t]} \\
\hat{\Phi}_0^{(1)}{}_{(01)\,[t]} \\
\hat{\Phi}_2^{(2)}{}_{(11)\,[t]} \\
\hat{\Phi}_{-2}^{(2)}{}_{(11)\,[t]}
\end{bmatrix}
=
\begin{bmatrix}
0 & 0 & -iA_4' & iA_3' \\
0 & 0 & -iA_4' & iA_3' \\
iA_3' & iA_3' & -(A_1'+A_2') & 0 \\
-iA_4' & -iA_4' & 0 & (A_1'+A_2')
\end{bmatrix}
\begin{bmatrix}
\hat{\Phi}_0^{(1)}{}_{(10)\,[t]} \\
\hat{\Phi}_0^{(1)}{}_{(01)\,[t]} \\
\hat{\Phi}_2^{(2)}{}_{(11)\,[t]} \\
\hat{\Phi}_{-2}^{(2)}{}_{(11)\,[t]}
\end{bmatrix}
\qquad (12.27A)
$$

where $A_1' = \omega_{I,off} + A_1$, $A_2' = \omega_{S,off} + A_2$, $A_3' = A_3 + G_{IS,-1}^{(2)2}$ and $A_4' = A_4 + G_{IS,1}^{(2)-2}$. The equation illustrated above is exactly identical to the one derived using the zero order Average Hamiltonian treatment sans the second order corrections.

In the interaction frame, the density operator is represented by $\hat{\rho}(t) = \hat{\Phi}_q^{(k)}{}_{(k_1 k_2,\,t)} T^{(k)q}{}_{(k_1 k_2)}$ and the initial conditions for the various polarizations are obtained by solving Eq. (12.28A)

$$
\hat{\rho}(t) = U_2 U_1 \rho(t) U_1^{-1} U_2^{-1}
\qquad (12.28A)
$$

where the density operator in the rotating frame is represented by $\rho(0) = I_x$. Employing the above relations the following initial conditions are obtained $\hat{\Phi}_0^{(1)}{}_{(10)[0]} = i$, $\hat{\Phi}_0^{(1)}{}_{(01)[0]} = 0$ in accord with the experiments. Since the entire dynamics is described in the interaction frame, the final detection operator (S_x) is also transformed in to the tilted frame (i.e. $\hat{S}_x = U_2 U_1 S_x U_1^{-1} U_2^{-1}$)

$$
\begin{aligned}
\langle \hat{S}_x(t) \rangle &= \mathrm{Tr}\left[\hat{S}_x \hat{\rho}(t) \right] \\
&= \Phi_0^{(1)}{}_{(01,\,t)} \sin \beta_S
\end{aligned}
\qquad (12.29A)
$$

In order to describe the incoherent effects, a simple exponential relaxation model is employed in our calculations to describe the dynamics during the CPRW experiments. In

515

this approach the relaxation is modeled as a damping term along the diagonal corresponding to each of the polarizations involved in the dynamics.

$$i\hbar\frac{d}{dt}\begin{bmatrix}\hat{\Phi}_0^{(1)}{}_{(10)\,[t]}\\\hat{\Phi}_0^{(1)}{}_{(01)\,[t]}\\\hat{\Phi}_2^{(2)}{}_{(11)\,[t]}\\\hat{\Phi}_{-2}^{(2)}{}_{(11)\,[t]}\end{bmatrix}=\begin{bmatrix}-iT_{1\rho,I}^{-1} & 0 & -iA_4' & iA_3'\\0 & -iT_{1\rho,S}^{-1} & -iA_4' & iA_3'\\iA_3' & iA_3' & -\left(A_1'+A_2'\right)-iT_{DQ}^{-1} & 0\\-iA_4' & -iA_4' & 0 & \left(A_1'+A_2'\right)-iT_{DQ}^{-1}\end{bmatrix}\begin{bmatrix}\hat{\Phi}_0^{(1)}{}_{(10)\,[t]}\\\hat{\Phi}_0^{(1)}{}_{(01)\,[t]}\\\hat{\Phi}_2^{(2)}{}_{(11)\,[t]}\\\hat{\Phi}_{-2}^{(2)}{}_{(11)\,[t]}\end{bmatrix}\quad(12.30A)$$

The complex factor ' i' in the relaxation terms originate from the definition in the Liouville-von Neumann equation ($i\hbar\frac{d\rho(t)}{dt}=\left[H,\rho(t)\right]-i\left[R,\rho(t)\right]$ where R represents the relaxation matrix). $T_{1\rho}$ represents the relaxation time in the rotating frame and T_{DQ} the relaxation associated with the double quantum coherence. In the next section we describe the results obtained using this model.

In order to demonstrate the utility and accuracy of the MMFT description, we conducted two CPRW experiments at 500 MHz (^{1}H). In the first, described in Figure 12-13, conditions for a CPRW experiment in [U-^{13}C-^{15}N]-VL were chosen so that the applied ^{15}N RF field was near that required for CSA recoupling. In spite of the CSA-induced dynamics, several distances are measured in VL, albeit with reduced accuracy. A second experiment was conducted in [U-^{13}C-^{15}N]-f-MLF-OH with conditions chosen to minimize CSA recoupling, resulting in 11 conformationally significant distance measurements in good agreement with crystallographic data.
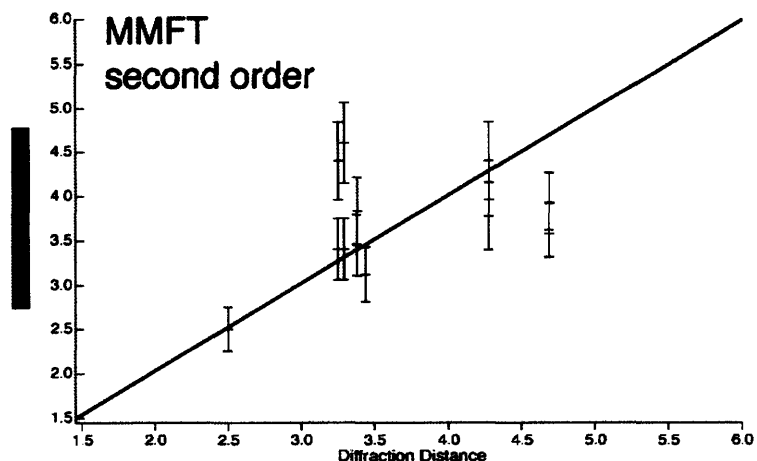
Figure 12-13: Accuracy of the distance estimation when the experiment is conducted near the CSA recoupling condition. The data are fit using a second order MMFT treatment which takes into account the CSA.
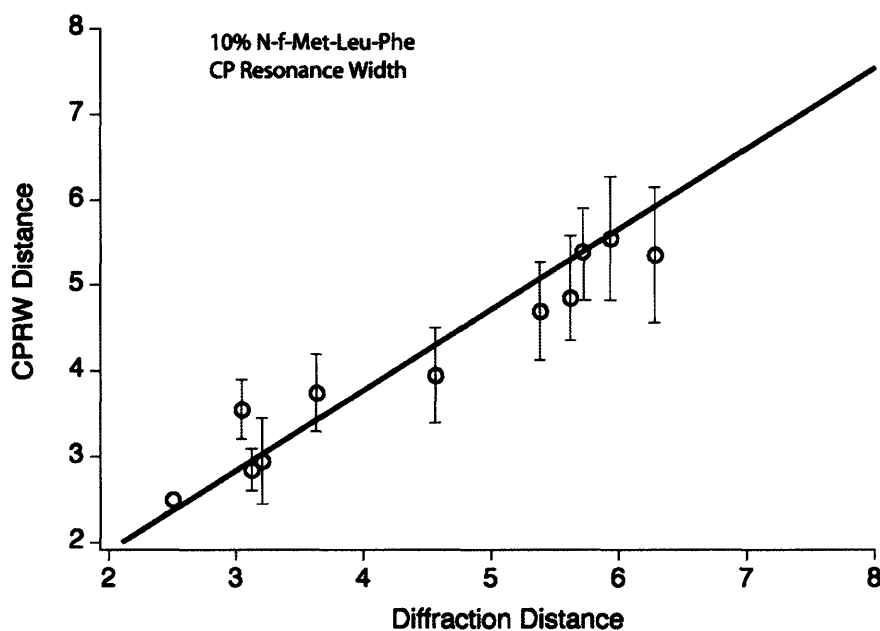
Figure 12-14: Comparison of distances determined in $[U-^{13}C,^{15}N]$-f-Met-Leu-Phe by CPRW and x-ray crystallography.

12.13 Quasi-Adiabatic Passage Experiments for Homonuclear and Heteronuclear Distance Measurements

We have introduced two new sequences for the measurement of homonuclear and heteronuclear distances in uniformly labeled compounds. These sequences, called quasi-adiabatic DQ CP and quasi-adiabatic R2TR/HORROR respectively, make use of frequency-selective recoupling to overcome the effects of dipolar truncation, and are

517

described in Figures 12-15 and 12-16. Unlike conventional resonance width experiments, which typically require 60-80 points in the dipolar dimension to fully record each exchange curve, here all matching conditions are successively fulfilled at different times during ramped RF excitation. A complete experiment requires as few as 8 points in the dipolar dimension, collected as a function of the ramp rate (the adiabatic parameter). Analytical and numerical results, shown in Figure 12-17, demonstrate that the ramp also reduces the dependence of the experiment on the CSA, CSA orientation, and experimental imperfections such as RF inhomogeneity. By using a HORROR matching field, the experiment can used for aliphatic distance measurements (methyl-methyl, methyl-side chain), for which the only present options are all based on proton-driven spin diffusion. The same approach has been applied for carbonyl-to-side-chain distance measurements, where it can be used instead of R2Width when the experiment duration is limiting. These distance measurements are attractive because the aliphatic region is generally more resolved than the carbonyl region (probed with R2Width and R2TR), and because constraints to methyl groups probe the hydrophobic core of folded proteins. These constraints are particularly important for determining the intermolecular packing arrangement of peptide aggregates such as amyloid fibrils. For that reason, we have chosen 100%-labeled peptide crystals, in which both intermolecular and intramolecular couplings can be measured, to demonstrate these experiments.
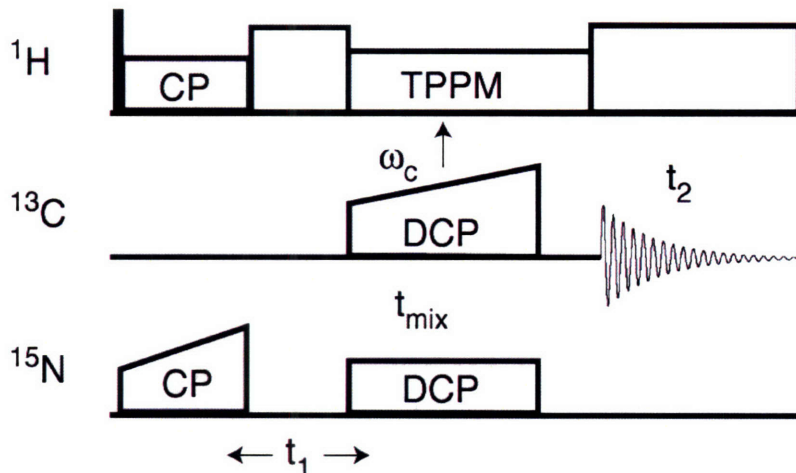
Figure 12-15: Pulse sequence for 3D quasi-adiabatic CPRW experiment. The ^{13}C RF field is ramped linearly through all recoupling conditions for aliphatic spins of interest.
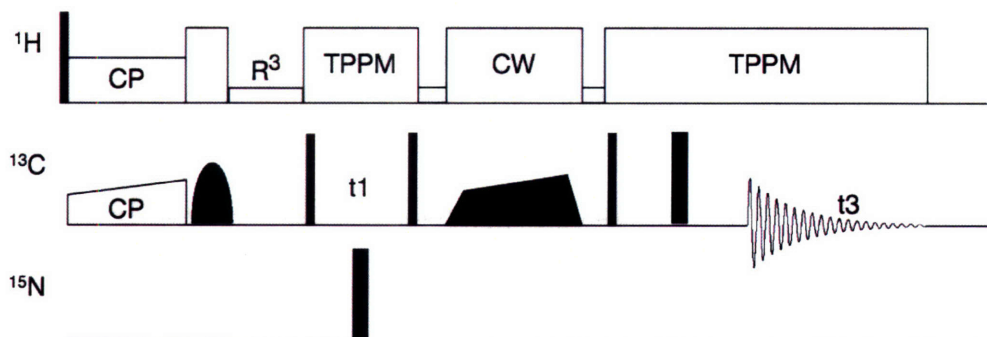
Figure 12-16: Pulse sequence for quasi-adiabatic DQ R2TR/HORROR experiment for homonuclear distance measurements. Following selection of the initial magnetization, the system evolves under the ^{13}C chemical shift during T1. Magnetization is then transferred using a ramped radiofrequency field selected to span the HORROR or n=1/n=2 R2TR DQ matching conditions for the spins of interest, depending on the chemical shift separation of the carbons involved, and detected in T2 following an echo.
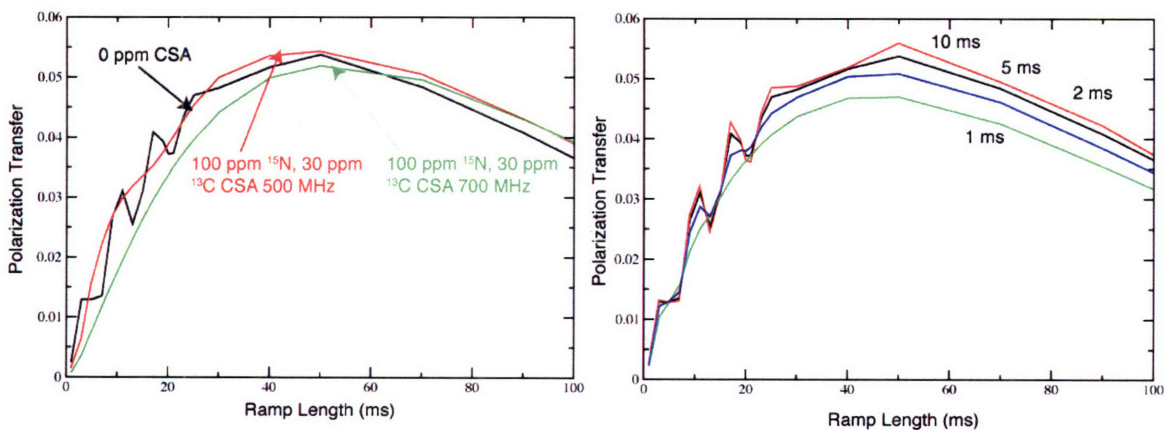
Figure 12-17: Spin dynamics during the ramp for several values of the CSA and (b) T_2 relaxation parameter. Quasi-adiabatic polarization transfer during the ramp is less influenced by the CSA and DQ relaxation than the equivalent "sudden" experiment.
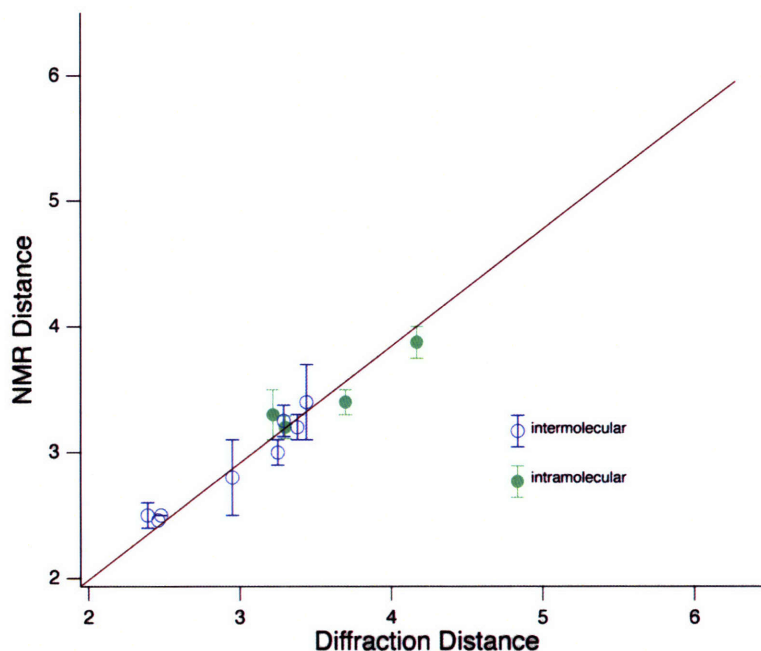
Figure 12-18: Plot of intramolecular and intermolecular distances in [U-^{13}C,^{15}N]-Val. Leu measured using 3D quasi-adiabatic CPRW.

Figure 12-18 demonstrates the result of applying this experiment to [U-^{13}C,^{15}N]-Val. Leu, in which 10 intermolecular and intramolecular distances were measured in good agreement with the crystal structure. The results were analyzed using numerical integration of the kinetic, two-spin approximate model of the spin dynamics, as outlined in the last section.

Figures 12-19 and 12-20 illustrate an application of the homonuclear experiment to methyl-methyl and methyl-aliphatic distance measurements in n-formyl-[U-^{13}C,^{15}N]-MLF. Several distances up to ~5.5 Å are accurately fit even in a *simple two-spin model which has one fit parameter and neglects relaxation and CSA effects*. A more realistic model will improve the accuracy of this analysis. Further, we note that the magnetization transfer efficiency for weak couplings continues to improve with increasing mixing time. Thus, the capabilities of the commercial NMR probe used here limit the sensitivity of this experiment for applications to weak dipolar couplings.
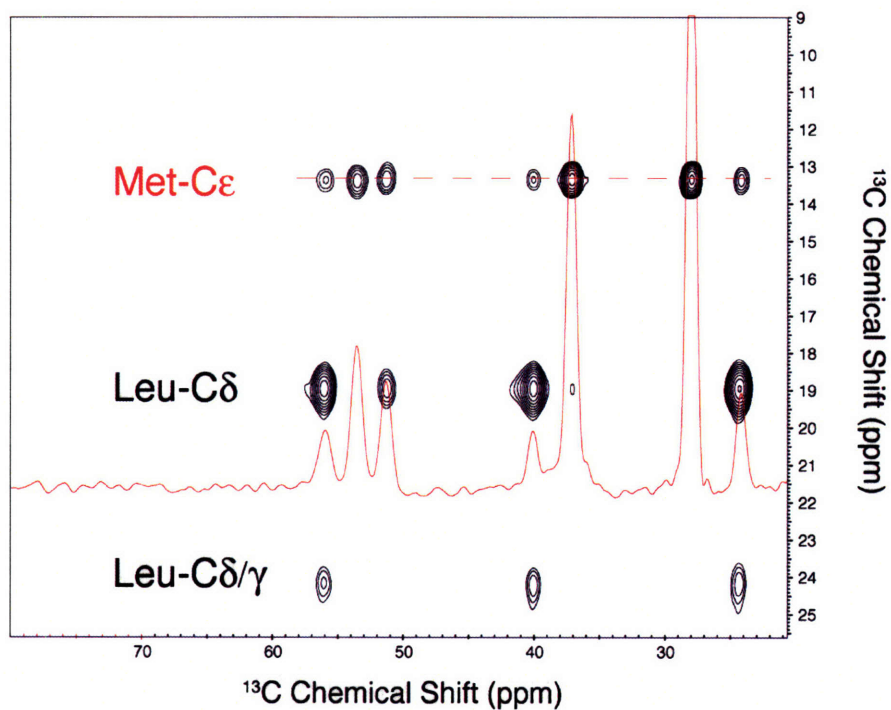
Figure 12-19: DQ HORROR spectrum in which magnetization from the methyl groups (Met-Cε, Leu-Cδ1, and Leu-Cδ2/Cγ) is selected and transferred to other aliphatic resonances.
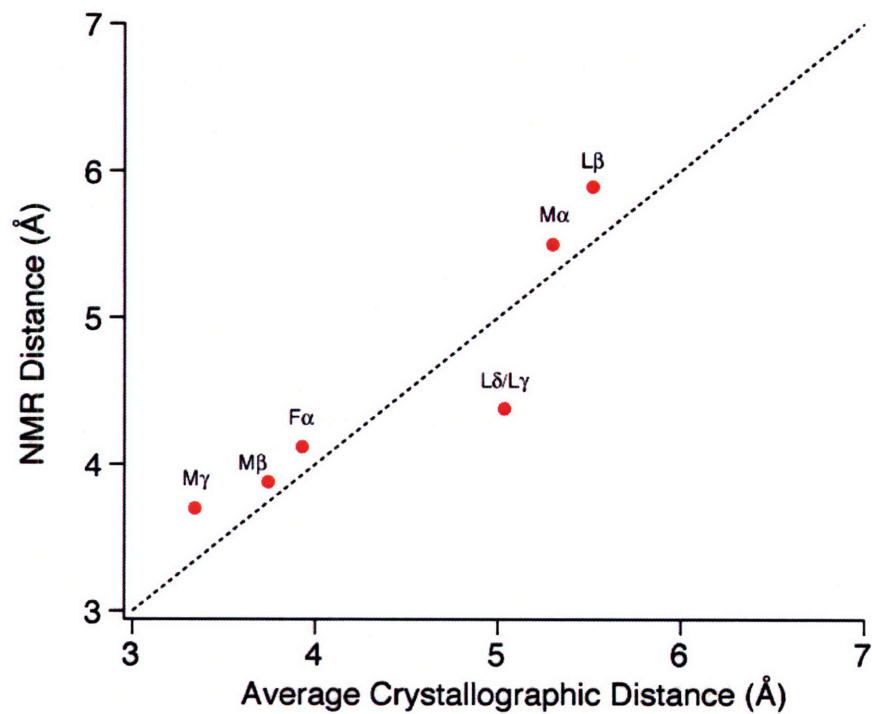
Figure 12-20: A plot of distances obtained by fitting exchange trajectories to a simple two-spin model which neglects relaxation.

Because of their simplicity, robustness towards experimental imperfections and relaxation, and the straightforward analytical approaches used to extract internuclear distances, we anticipate that the quasi-adiabatic passage methods outlined here will be useful adjuncts to spin diffusion and other methods whose spin dynamics are more complex and less amenable to quantitative analysis.

12.14   References

[1]   McDermott, A.; Creuzet, F.; Griffin, R. G.; Zawadzke, L. E.; Ye, Q. Z.; Walsh, C. T., Rotational resonance determination of the structure of an enzyme-inhibitor complex: phosphorylation of an (amino alkyl) phosphonate inhibitor of D-alanyl-D-alanine ligase by ATP. *Biochemistry* **1990**, 29, 5567-5574.

[2]   Creuzet, F.; McDermott, A.; Gebhard, R.; van der Hoef, K.; Spijker-Assink, M. B.; Herzfeld, J.; Lugtenburg, J.; Levitt, M. H.; Griffin, R. G., Determination of membrane protein structure by rotational resonance NMR: Bacteriorhodopsin. *Science* **1991**, 251, 783-786.

[3]   McDermott, A.; Creuzet, F.; Gebhard, R.; van der Hoef, K.; Levitt, M. H.; Herzfeld, J.; Lugtenburg, J.; Griffin, R. G., Determination of Internuclear Distances and the Orientatation of Functional Groups by Solid-State NMR: Rotational Resonance Study of the Conformation of Retinal in Bacteriorhodopsin. *Biochemistry* **1994**, 33, 6129-6136.

[4]   McDowell, L. M.; Klug, C. A.; Beusen, D. D.; Schaefer, J., Ligand Geometry of the Ternary Complex of 5-Enolpyruvylskikimate-3-phospate Synthase from Rotational-Echo Double-Resonance NMR. *Biochemistry* **1996**, 35, 5395-5403.

[5]   McDowell, L. M.; Lee, M.; McKay, A.; Anderson, K. S.; Schaefer, J., Intersubunit Communicaltion in Tryptophan Synthase by Carbon-13 and Fluorine-19 REDOR NMR. *Biochemistry* **1996**, 35, 3328-3334.

[6]   Marassi, F. M.; Opella, S. J., NMR structural studies of membrane proteins. *Curr. Opin. Struct. Biol.* **1998**, 8, 640-648.

[7]   Griffin, R. G., Dipolar recoupling in MAS spectra of biological solids. *Nature Struct. Biol.* **1998**, 5, 508-512.

[8]   Watts, A., NMR of drugs and ligands bound to membrane receptors. *Curr. Opin. Biotech.* **1999**, 10, 48-53.

[9]   Tycko, R., Solid State NMR as a Probe of Amyloid Fibril Structure. *Curr. Opin. Chem. Biol.* **2000**, 4, 500.

[10]   Petkova, A. T.; Ishii, Y.; Balbach, J. J.; Antzutkin, O. N.; Leapman, R. D.; Delaglio, F.; Tycko, R., A structural model for Alzheimer's β-amyloid fibrils based on experimental constraints from solid state NMR. *Proc. Nat. Acad. Sci. USA* **2002**, 99, 16742-16747.

[11]   Andrew, E. R.; Bradbury, A.; Eades, R. G., Nuclear magnetic resonance spectra from a crystal rotated at high speed. *Nature* **1958**, 182, 1659.

[12]   Lowe, I. J., Free induction decay of rotating solids. *Phys. Rev. Lett.* **1959**, 2, 285.

[13]   Long, J. R.; Sun, B. Q.; Bowen, A.; Griffin, R. G., Molecular dynamics and magic angle spinning NMR. *J. Am. Chem. Soc.* **1994**, 116, 11950-11956.

[14]   Pines, A.; Gibby, M. G.; Waugh, J. S., Proton-enhanced NMR of dilute spins in solids. *J. Chem. Phys.* **1973**, 59, 569-590.

[15]   Schaefer, J. S., E. O, CPMAS. *J. Am. Chem. Soc.* **1976**, 98, 1030.

[16]   Mehring, M.; Pines, A.; Rhim, W.-K.; Waugh, J. S., *J. Chem. Phys.* **1971**, 54, 3239.

[17]   Mehring, M.; Sinning, G., Dynamics of heteronuclear spin coupling and decoupling in solids. *Phys. Rev.* **1977**, B15, (5), 2519-2532.

[18]   Bennett, A. E.; Rienstra, C. M.; M., A.; Lakshmi, K. V.; Griffin, R. G., Heteronuclear decoupling in rotating solids. *J. Chem. Phys.* **1995**, 103, 6951-6957.

[19]   Bennett, A. E. Dipolar Recoupling and Decoupling in Solid State Nuclear Magnetic Resonance Spectroscopy. Massachusetts Institute of Technology, 1995.

[20]   Dusold, S.; Sebald, A., Dipolar recoupling under magic-angle spinning conditions. *Annu. Rep. Nucl. Magn. Reson. Spectr.* **2000**, 41, 185-264.

[21]   Hohwy, M.; Rienstra, C. M.; Jaroniec, C. P.; Griffin, R. G., Fivefold symmetric homonuclear dipolar recoupling in rotating solids: Application to double quantum spectroscopy. *J. Chem. Phys.* **1999**, 110, 7983-7992.

[22]   Carravetta, M.; Edén, M.; Zhao, Z.; Brinkmann, A.; Levitt, M. H., Symmetry principles for the design of radiofrequency pulse sequences in the nuclear magnetic resonance of rotating solids. *Chem. Phys. Lett.* **2000**, 321, 205-215.

[23] Carravetta, M.; Eden, M.; Zhao, X.; Brinkmann, A.; Levitt, M. H., Symmetry principles for the design of radiofrequency pulse sequences in the nuclear magnetic resonance of rotating solids. *Chemical Physics Letters* **2000**, 321, (3-4), 205-215.

[24] Brinkmann, A.; Edén, M.; Levitt, M. H., Symmetry principles in the nuclear magnetic resonance od spinning solids: Heteronuclear recoupling by generalized Hartmann-Hahn sequences. *J. Chem. Phys.* **2001**, 115, 357-384.

[25] Weliky, D. P.; Bennett, A. E.; Zvi, A.; Anglister, J.; Steinbach, P. J.; Tycko, R., Solid-state NMR evidence for an antibody-dependent conformation of the V3 loop of HIV-1 gp120. *Nat. Struct. Biol.* **1999**, 6, 141-145.

[26] Thompson, L. K.; McDermott, A. E.; Raap, J.; van der Wielen, C. M.; Lugtenburg, J.; Herzfeld, J.; Griffin, R. G., Rotational resonance NMR study of the active site structure in bacteriorhodopsin: Conformation of the Schiff base linkage. *Biochemistry* **1992**, 31, 7931-7938.

[27] Gregory, D. M.; Benzinger, T. L. S.; Burkoth, T. S.; Miller-Auer, H.; Lynn, D. G.; Meredith, S. C.; Botto, R. E., Dipolar recoupling NMR of biomolecular self-assemblies: determining inter- and intrastrand distances in fibrilized Alzheimer's β-amyloid peptide. *Solid State Nucl. Magn. Reson.* **1998**, 13, 149-166.

[28] Tycko, R., Biomolecular solid state NMR: advances in structural methodology and Applications to peptide and protein fibrils. *Annu. Rev. Phys. Chem.* **2001**, 52, 575-606.

[29] Baldus, M. M., B.H., Broadband recoupling. *J. Magn. Reson.* **1997**, 128, 172.

[30] Ishii, Y.; Ashida, J.; Terao, T., ^{13}C-^{1}H dipolar recoupling dynamics in ^{13}C multiple-pulse solid-state NMR. *Chem. Phys. Lett.* **1995**, 246, 439-445.

[31] Andrew, E. R.; Clough, S.; Farnell, L. F.; Gledhill, T. A.; Roberts, I., Resonant rotational broadening of NMR spectra. *Phys. Lett.* **1966**, 21, 505-506.

[32] Andrew, E. R.; Bradbury, A.; Eades, R. G.; T, W. V., related to rotational resoanance. *Phys. Lett.* **1963**, 4, 99.

[33] Raleigh, D. P.; Harbison, G. S.; Neiss, J. E.; Roberts, J. E.; Griffin, R. G., Rotational Resonance. *Chem. Phys. Lett.* **1987**, 138, 285.

[34] Meier, B. H.; Earl, W. L., Rotational resonance. *J. Am. Chem. Soc.* **1987**, 109, 7937.

[35] Raleigh, D. P.; Levitt, M. H.; Griffin, R. G., Rotational resonance in solid state NMR. *Chem. Phys. Lett.* **1988**, 146, 71-76.

[36] Colombo, M. G. M., B.H.; Ernst, R.R., Rotational resonance. *Chem. Phys. Lett.* **1988,** 146, 189.

[37] Raleigh, D. P. C., F.; Das Gupta, S. K.; Levitt, M. H.; Griffin, R. G., Rotational resonance. *J. Am. Chem. Soc.* **1989,** 111, 4502.

[38] Levitt, M. H.; Raleigh, D. P.; Creuzet, F.; Griffin, R. G., Theory and simulations of homonuclear spin pair systems in rotating solids. *J. Chem. Phys.* **1990,** 92, 6347-6364.

[39] Williamson, P. T. F.; Verhoeven, A.; Ernst, M.; Meier, B. H., Determination of internuclear distances in uniformly labeled molecules by rotational-resonance solid-state NMR. *J. Am. Chem. Soc.* **2003,** 125, (9), 2718-2722.

[40] Takegoshi, K.; Nomura, K.; Terao, T., Rotational resonance in the tilted rotating frame. *Chem. Phys. Lett.* **1995,** 232, 424-428.

[41] Takegoshi, K.; Nomura, K.; Terao, T., Selective Homonuclear Polarization Transfer in the Tilted Rotating Frame under MAgic Angle Spinning in Solids. *J. Magn. Reson.* **1997,** 127, 206-216.

[42] Costa, P. R.; Sun, B.; Griffin, R. G., Rotational resonance tickling: accurate internuclear distance measurement in solids. *J. Am. Chem. Soc.* **1997,** 119, 10821-10836.

[43] Costa, P. R.; Sun, B.; Griffin, R. G., Rotational resonance width experiment. *J. Magn. Reson.* **2003,** in press.

[44] Kubo, A. M., C. A, spectral spin diffusion. *J. Chem. Soc. Faraday Trans. I* **1988,** 84, 3713.

[45] Goobes, G.; Boender, G. J.; Vega, S., Spinning frequency-dependent narrowband RF-driven dipolar recoupling. *J. Magn. Reson.* **2000,** 146, 204-219.

[46] Goobes, G.; Vega, S., Improved narrowband dipolar recoupling for homonuclear distnqace measurements. *J. Magn. Reson.* **2002,** 146, 236-251.

[47] Vander Hart, D. L. E., W. L.; Garroway, A. N., Line broadening in C13. *J. Magn. Reson.* **1981,** 44, 361.

[48] Karlsson, T.; Levitt, M. H., Longitudinal rotational resonance echoes in solid state nuclear magnetic resonance: Investigation of zero quantum spin dynamics. *J. Chem. Phys.* **1998,** 109, 5493-5507.

[49] Karlsson, T.; Brinkmann, A.; Verdegem, P. J. E.; Lugtenburg, J.; Levitt, M. H., Multiple-quantum relaxation in the magic-angle-spinning NMR of ^{13}C spin pairs. *Solid State Nucl. Magn. Reson.* **1999,** 14, 43-58.

[50] Helmle, M.; Lee, Y. K.; Verdegem, P. J. E.; Feng, X.; Karlsson, T.; Lugtenburg, J.; de Groot, H. J. M.; Levitt, M. H., Anomalous rotational resonance spectra in magic-angle spinning NMR. *J. Magn. Reson.* **1999**, 140, 379-403.

[51] Metz, G.; Wu, X.; Smith, S. O., Ramped-amplitude cross-polarization in magic-angle-spinning NMR. *J. Magn. Reson. A* **1994**, 110, 219-227.

[52] Spiess, H. W., Rotation of molecules and nuclear spin relaxation. In *Dynamic NMR Spectroscopy*, Diehl, P.; Fluck, E.; Kosfeld, R., Eds. Springer-Verlag: Berlin, 1978; Vol. 15, pp 55-214.

[53] Vega, S., Fictitious spin operator formalism. *J. Chem. Phys.* **1978**, 68, 5518.

[54] Schaefer, J.; Stejskal, E. O., Double Cross Polarization NMR in Solids. *J. Magnetic Resonance* **1979**, 34, 443-447.

[55] Baldus, M. A.; Petkova, A. T.; Herzfeld, J.; Griffin, R. G., Cross Polarization in the Tilted Frame: Assignment and Spectral Simplification in Heteronuclear Spin Systems. *Mol. Phys.* **1997**, 95, (6), 1197-1207.

[56] Ramachandran, R.; Griffin, R. G., Multipole-Based Multimode Floquet Theory in NMR. **submitted (2003)**.

[57] Ramachandran, R.; Griffin, R. G., Description of depolarization effects in double-quantum solid state nuclear magnetic resonance experiments using multipole-multimode Floquet theory. *Journal of Chemical Physics* **2006**, 125, (4), -.

[58] Ramachandran, R.; Lewandowski, J. R.; van der Wel, P. C. A.; Griffin, R. G., Multipole-multimode Floquet theory of rotational resonance width experiments: C-13-C-13 distance measurements in uniformly labeled-solids. *Journal of Chemical Physics* **2006**, 124, (21), -.

[59] Jaroniec, C. P.; Filip, C.; Griffin, R. G., 3D TEDOR NMR experiments for the simultaneous measurement of multiple carbon-nitrogen distances in uniformly ^{13}C, ^{15}N-labeled solids. *J. Am. Chem. Soc.* **2002**, 124, (36), 10728-10742.

[60] Ramachandran, R.; Ladizhansky, V.; Bajaj, V. S.; Griffin, R. G., ^{13}C-^{13}C Rotational Resonance Width Distance Measurements in Uniformly ^{13}C-Labeled Peptides. *J. Amer. Chem. Soc.* **2003**, 125, 15623-15629.

[61] Ladizhansky, V.; Griffin, R. G., Band selective ^{13}C-^{13}C distance measurements in uniformly ^{13}C,^{15}N labeled peptides using solid state MAS NMR. *J. Am. Chem. Soc.* **2003**, submitted.

[62]   Mueller, L. J.; Elliott, D. W., Correlated tensor interactions and rotational-echo double resonance of spin clusters. *Journal of Chemical Physics* **2003**, 118, (19), 8873-8881.

[63]   Vogt, F. G.; Gibson, J. M.; Mattingly, S. M.; Mueller, K. T., Determination of molecular geometry in solid-state NMR: Rotational-echo double resonance of three-spin systems. *Journal of Physical Chemistry B* **2003**, 107, (5), 1272-1283.

[64]   Vogt, F. G.; Mattingly, S. M.; Gibson, J. M.; Mueller, K. T., Measurement of internuclear distances in solid-state NMR by a background-filtered REDOR experiment. *Journal of Magnetic Resonance* **2000**, 147, (1), 26-35.

[65]   Vogt, F. G.; Aurentz, D. J.; Mueller, K. T., Determination of internuclear distances from solid-state nuclear magnetic resonance: dipolar transforms and regularization methods. *Molecular Physics* **1998**, 95, (5), 907-919.

[66]   Mueller, K. T.; Jarvie, T. P.; Aurentz, D. J.; Roberts, B. W., The REDOR transform: Direct calculation of internuclear couplings from dipolar-dephasing NMR data (vol 242, pg 535, 1996). *Chemical Physics Letters* **1996**, 254, (3-4), 281-282.

[67]   Ernst, R. R.; Bodenhausen, G.; Wokaun, A., *Principles of Nuclear Magnetic Resonance in One and Two Dimensions*. Clarendon Press: Oxford, 1991.

[68]   Stewart, P. L.; Tycko, R.; Opella, S. J., Peptide backbone conformation by solid-state nuclear magnetic resonance spectroscopy. *J. Chem. Soc. Faraday Trans. I* **1988**, 84, 3803-3819.

[69]   Rienstra, C. M.; Hohwy, M.; Hong, M.; Griffin, R. G., 2D and 3D ^{15}N-^{13}C-^{13}C NMR chemical shift correlation spectroscopy of solids: Assignment of MAS spectra of peptides. *J. Am. Chem. Soc.* **2000**, 122, 10979-10990.

[70]   Jaroniec, C. P.; Tounge, B. A.; Herzfeld, J.; Griffin, R. G., Frequency selective heteronuclear dipolar recoupling in rotating solids: accurate ^{13}C-^{15}N distance measurements in uniformly-^{13}C,^{15}N-labeled peptides. *J. Am. Chem. Soc.* **2001**, 3507-3519.

[71]   Ladizhansky, V.; Griffin, R. G., Band-selective Carbonyl to Side Chain ^{13}C-^{13}C Distance Measurements in U-^{13}C,^{15}N-Labeled Solid Peptides by Magic Angle Spinning NMR. *J. Amer. Chem. Soc.* **2003**, 125, (in press).

Chapter 13   Solid State NMR Structure of the L111M Mutant of Transthyretin$_{105\text{-}115}$ in an Amyloid Fibril

Portions of the following chapter have been adapted from a manuscript in preparation: "Solid State NMR Structure of the L111M Mutant of Transthyretin$_{105\text{-}115}$ in an Amyloid Fibril" Vikram Bajaj, Marc Caporini, Cait MacPhee, Anthony Fitzpatrick, Christopher Dobson, Robert Griffin. To be submitted (2007).

13.1   Introduction

In general, proteins adopt regular tertiary structures which encapsulate enzymatic active sites and project binding or interacting surfaces. This regular tertiary structure, or protein fold, is thus essential for native protein function, and the mechanistic basis of protein folding is the thus the target of both experimental and computational investigation [1]. Protein folding is also of considerable medical interest, as many significant diseases are caused by mutations which perturb or eliminate the native function of a protein by influencing its propensity to fold correctly [2]. While misfolded proteins generally trigger cellular mechanisms through which they are targeted for decay, most proteins are also able to enter a conformational state in which they aggregate and accumulate in amyloid deposits. At least 25 clinical disorders are associated with amyloidosis and protein aggregation [3].

Amyloid diseases are caused by extracellular deposits of long, unbranched protein fibrils which give a characteristic green birefringence upon binding Congo Red dye. Amyloid fibrils have been characterized by electron microscopy [4], mass spectrometry [5], cryo-EM reconstruction [6], atomic force microscopy [7], x-ray diffraction [8], circular dichroism [9-11], and NMR spectroscopy [12, 13], but, until recently, their precise three-dimensional structure has been unknown. In order to understand the structural basis for amyloid fibril accumulation, we have studied several short peptides

which form amyloid fibrils. Peptide fragments of transthyretin (see Figure 13-2), an extracellular transporter of thyroid hormone, form amyloid fibrils [14-18] *in vitro*, and we have recently solved the structure of $TTR_{105-115}$ using MAS NMR methods [19, 20] [21]. Mutations in the wild-type TTR sequence are responsible for inheritable amyloid disorders; the L111M mutant genotype, in particular, causes a hereditary amyloid-related cardiomyopathy [22-53]. Here, we investigate the structure of the L111M mutant which, in addition to its clinical significance, displays differences in fibril morphology (Figure 13-3) and fibril formation kinetics (Figure 13-6). A comparison of the WT and L111M structures may provide information about the molecular basis of supramolecular fibril assembly.

In order to solve the three-dimensional structure of amyloid fibrils of L111M TTR, we have applied the solid state NMR methodology outlined in the previous chapter, which is based on the successful strategy employed for WT TTR. This has involved measurement of heteronuclear [54-56] and homonuclear [57-59] dipolar couplings in uniformly labeled samples to generate distance constraints, and tensor correlation [60-70] experiments to generate constraints on the backbone and side chain torsion angles. Here, we characterize the fibril morphology and formation kinetics using EM, AFM, and NMR, report the intramolecular or monomer structure of the peptide fragment.

13.2   Materials and Methods

13.2.1   Synthesis of Samples

Samples for experiments designed to probe the fibril morphology were prepared by solid phase synthesis [71] (FMOC chemistry) by CS Bio Inc. Samples for NMR experiments

were prepared from FMOC-protected and O-T-Butyl (where applicable) protected, U-^{13}C,^{15}N-labeled amino acids purchased from Cambridge Isotope Laboratories. Two segmentally U-^{13}C,^{15}N-labeled fragments were prepared, as shown in Figure 13-1, corresponding to the peptide fragment shown in Figure 13-2.

Figure 13-1: Samples used for solid-state NMR measurements in L111M TTR. Two segmentally [U-^{13}C, ^{15}N]-labeled samples were prepared by solid phase synthesis.

Figure 13-2: Ribbon diagram of native transthyretin monomer backbone. The segment corresponding to the native structure of residues 105-115 is highlighted in blue.

13.2.2   Formation of Amyloid Fibrils [7, 72]

The peptides were dissolved without further purification in a solution of 10% acetonitrile in water (v/v), adjusted to pH 2.0, at a concentration of 18 mg/mL. The solutions were

incubated in sealed containers at 37°C for 48 hours, after which they became turbid, indicating the formation of amyloid fibrils. The fibrilization solutions were then left undisturbed for 14 days at ambient temperatures (23°C ± 5°C). Concentrated pellets of the amyloid fibrils were formed by two cycles of centrifugation at 300,000xg, followed by washing in distilled water. The concentrated pellets were packed into 4 mm Varian NMR rotors that were sealed to prevent dehydration of the pellet.

13.2.3   NMR Experiments

All NMR experiments were performed on a 500 MHz NMR console with a home-built spectrometer console (D.J. Ruben). The sample temperature was maintained at 2°C during the experiments to prevent sample damage due to RF and aerodynamic heating. The spinning frequencies ranged from 8.6-10.0 kHz, depending on the experiment. TPPM [73] decoupling (83-125 kHz) was employed during acquisition and during multiple pulse sequences where appropriate. Chemical shifts were referenced indirectly to solid adamantane following the recommendations of Morocombe and co-workers [74].

13.3   Results

13.3.1   Fibril Morphology and Kinetics

Amyloid fibrils can adopt a variety of morphologies which may, *a priori*, correspond to different structures on the NMR length scale. These morphologies may also have different NMR spectra and may therefore be responsible for broad NMR lines seen in other amyloid fibril systems [12, 75, 76]. Several morphologies seen in images of WT $TTR_{105-115}$ amyloid fibrils are shown in Figure 13-5. They include rope-like twisted fibrils, ribbon like structures with various degrees of pitch, and flat, untwisted, laterally-

associated protofilaments that are characteristic of denatured or immature fibril samples [72]. The morphology of L111M TTR$_{105-115}$ samples were characterized using negative stain transmission electron microscopy (Figure 13-3) and atomic force microscopy (Figure 13-4). Both techniques reveal that L111M amyloid fibrils have a twisted, ribbon-like morphology which differ in pitch and width from WT amyloid fibrils. The pitch and width of WT amyloid fibrils is approximately 950 ± 100 Å and 108 ± 12 Å, respectively; for L111M, these are 1200 ± 100 Å and 173 ± 15 Å.
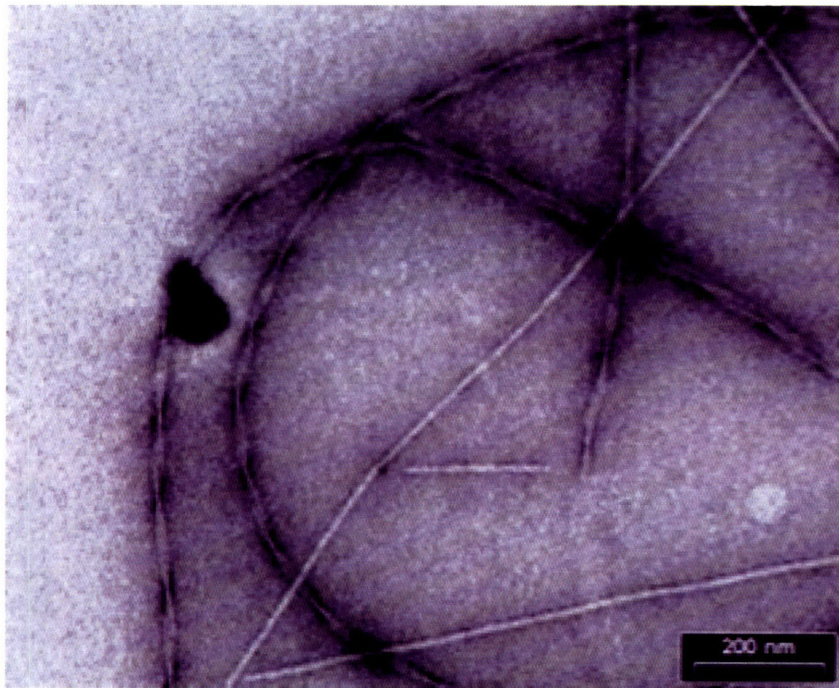
Figure 13-3: Negative stain TEM image of amyloid fibrils prepared from peptides of L111M TTR$_{105-115}$. The predominant morphology is that of a twisted ribbon.
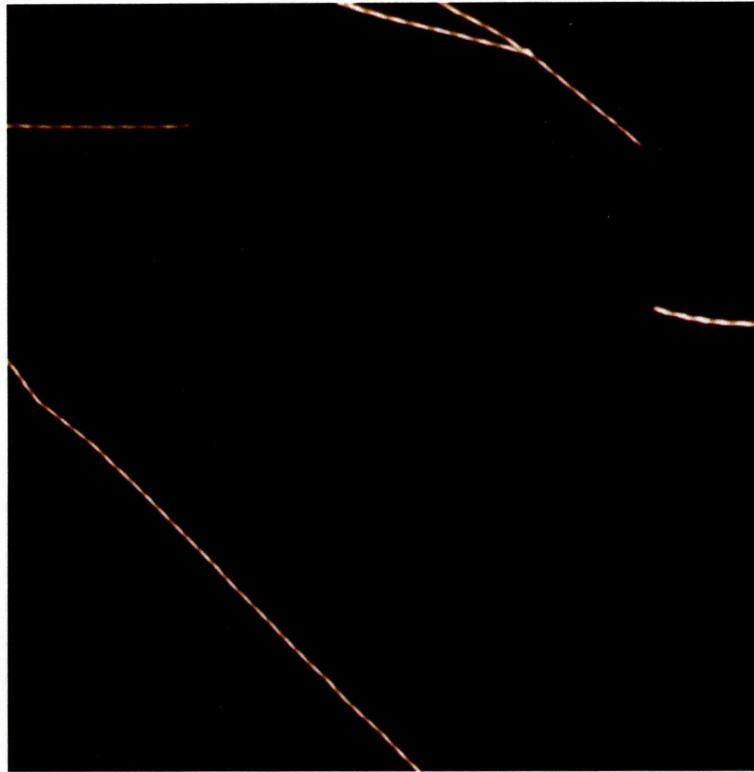
Figure 13-4: AFM image of mature amyloid fibrils from prepared from L111M TTR$_{105-115}$. The sample was dehydrated and imaged on the surface of freshly cleaved mica substrate.
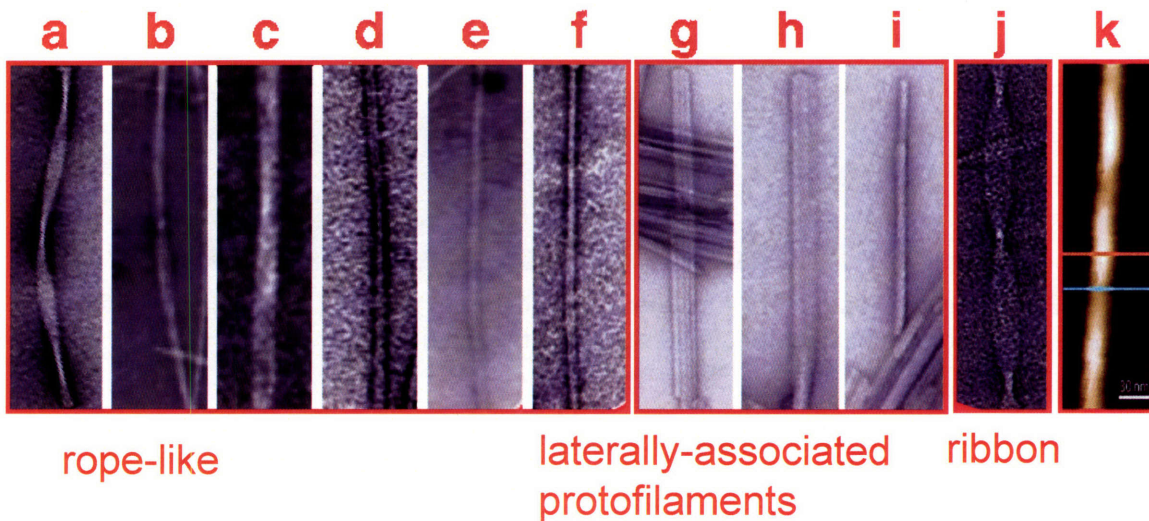
Figure 13-5: The range of fibril polymorphism represented in samples of WT TTR$_{105-115}$. Sample morphology observed during maturation and in mature fibrils ranges from rope-like extended fibrils to ribbon-like fibrils which appear to have a hollow core. Laterally associated protofilaments are also visible in some samples. NMR samples are inspected to confirm that one morphology dominates prior to NMR experiments.
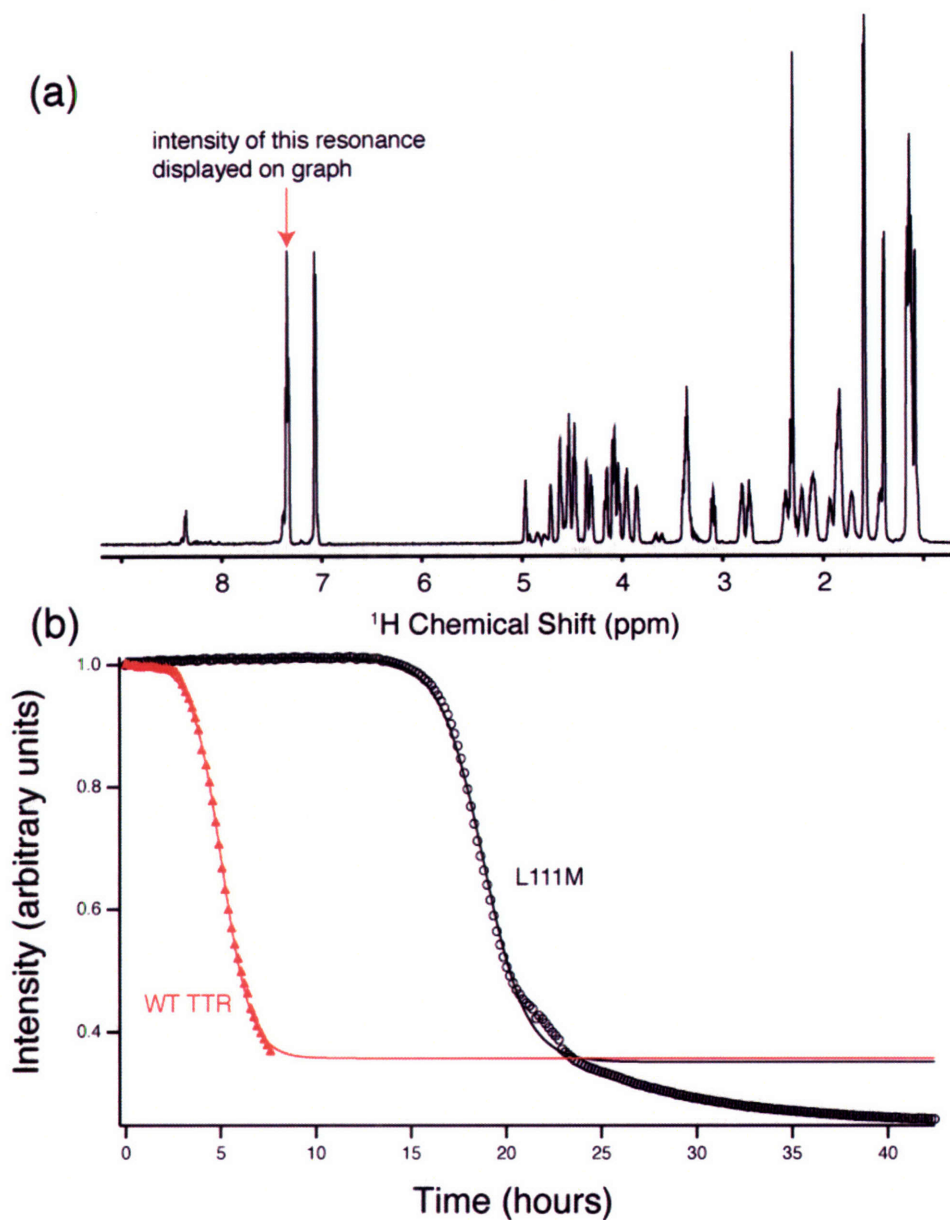
Figure 13-6: The kinetics of amyloid fibril formation in WT $TTR_{105-115}$ and its L111M monitored by ^1H solution state NMR (spectrum in (a)) (10% d-acetonitrile in D_2O; 4 scans with presaturation for solvent suppression). Because the NMR spectra change only in intensity, we assume that any intermediates of fibril formation are too dilute or short-lived to be observed. The results demonstrate dramatic differences in the kinetics of amyloid fibril formation in the WT and L111M peptides.

13.3.2   X-ray fiber diffraction measurements

Jarvis and co-workers [15] have recorded x-ray fiber diffraction patterns from amyloid-

forming peptides of transthyretin. These measurements, which are summarized in Table

535

13.1, are sensitive to length scales longer than the NMR measurements and therefore indicate differences in the packing of monomers into the protofilament and the protofilaments into an NMR fibril. However, they do not encode any information about the monomer structure.

Table 13.1: Summary of diffraction measurements in WT and L111M peptides reported by Jarvis and co-workers [15].

WT TTR$_{105-115}$ equivalent resolution (Å)	L111M TTR$_{105-115}$ equivalent resolution (Å)
4.7	4.7
9.7	8.4
17.1	15.5
31.0	28.0

13.3.3   Fibril Formation Kinetics

The kinetics of amyloid fibril formation can be assessed by monitoring optical turbidity, binding of amyloid fibrils to a fluorescent dye such a thioflavin T, dynamic light scattering, time-resolved circular dichroism, or NMR [10, 77-79]. In all cases, kinetic measurements in a wide variety of systems show that fibril formation is preceded by a characteristic lag or nucleation phase, followed by a period of rapid growth, and then finally fibril maturation. Solution state NMR is a particularly attractive method of following fibril formation kinetics, because completely formed amyloid fibrils precipitate as solids and do not contribute to the NMR spectra in solution. The loss of intensity in the NMR spectra can thus be followed as a direct indicator of the fibril formation kinetics. Because the NMR line widths and positions do not change, any intermediate oligomers of fibril formation must be too dilute or, equivalently, short-lived to be observed in these experiments. Samples for solution state NMR were prepared by dissolving WT TTR (pI 5.52, MW=1198.38) at 15 mg/mL concentration, or L111M TTR (pI=5.52, MW=1216.41) at 15 mg/mL or 15.2 mg/mL concentration in 10% deuterated

acetonitrile in D_2O (v/v). The kinetics of fibril formation were monitored by ^1H solution state NMR at 591 MHz; the pulse sequence incorporate presaturation for suppression of the residual water, and all experiments were conducted at a constant temperature of 37°C. The measurements were repeated to guarantee their reproducibility. The results indicate that the L111M and WT TTR fibrils differ in the kinetics of the lag or nucleation phase of fibril formation. The next phase of rapid fibril growth is similar in both cases, but this phase is diffusion-limited in many models of fibril growth, and so is not expected to be significantly different for two peptides with similar physical properties. Finally, the slower, fibril maturation phase occurs at a faster rate for the L111M peptide than for the WT TTR peptide.

13.3.4   One Dimensional Solid State NMR

One-dimensional solid-state NMR spectra were recorded with high power proton decoupling (100 kHz TPPM) on a 500 MHz NMR spectrometer. The spectra, shown in Figure 13-7, are characterized by narrow line widths, which demonstrate that the sample is microscopically well ordered and contains one conformation of the peptide. Further, differences in the aromatic intensities and line shapes between the N-terminal and C-terminal segmentally labeled samples point to differences in the dynamics of the N-terminal and C-terminal tyrosine. The greater line widths and reduced intensities for the C-terminal tyrosine suggests that the rate of ring flipping or other motion is different in that case from that of the tyrosine on the N-terminus. One-dimensional NMR spectra were recorded before and after each subsequent multidimensional experiment to insure that the sample was not damaged by RF heating or other effects.
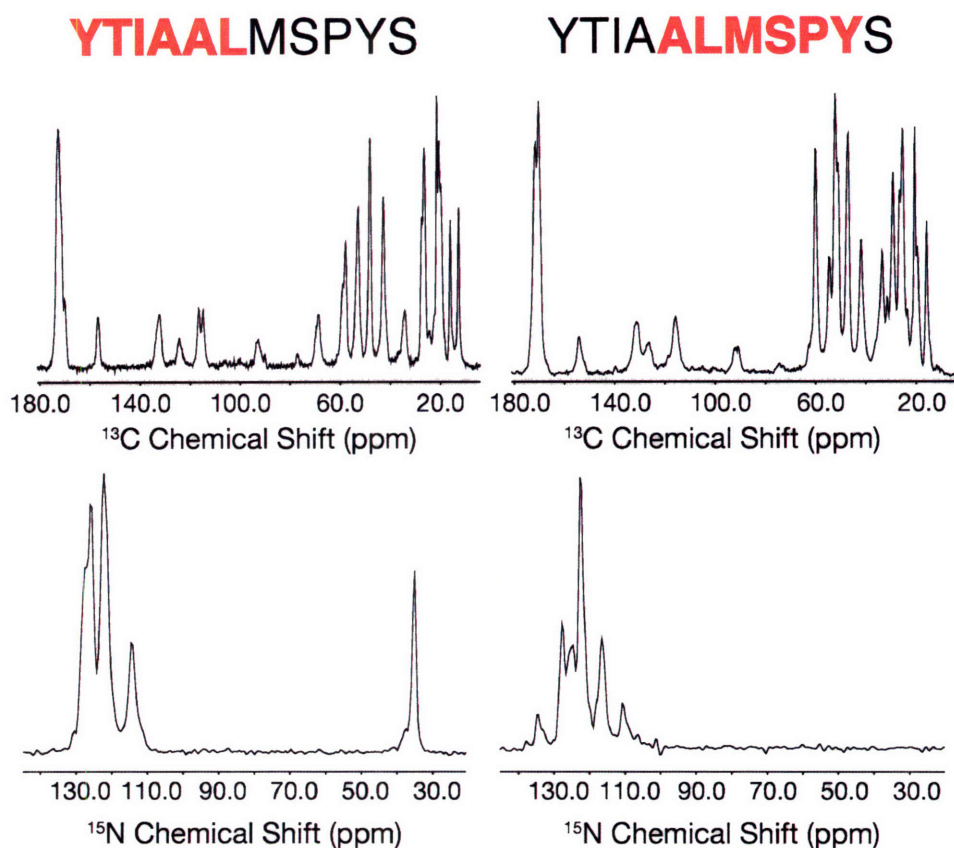
Figure 13-7: One-dimensional ^{13}C and ^{15}N NMR spectra of the two segmentally labeled peptide samples used in this study. The spectra demonstrate that the sample is microscopically well ordered. Differences in the aromatic line intensities are due to different aromatic ring dynamics experienced by the N and C-terminal tyrosines.

13.3.5 Chemical Shift Assignments

Chemical shift assignments were obtained on the basis of 2D ^{13}C-^{13}C and ^{15}N-^{13}C correlation spectroscopy [80, 81]. Complete side chain connectivity and sequential assignments were possible on the basis of three spectra for each sample: 2D ^{13}C-^{13}C, which provide connectivity between side chain carbons, 2D NCACX, which provides intraresidue correlation between the amide nitrogen and side chain carbons, and 2D NCOCX, which gives interresidue correlations between the side chain carbons and the amide nitrogen of the subsequent residue, in complete analogy to well-established solution state NMR experiments [82].

538

Figure 13-8: Pulse sequence for 2D ^{13}C-^{13}C homonuclear correlation spectroscopy through proton-driven spin diffusion with the application of a ^1H R^3 recoupling field (DARR).

Figure 13-9: Two-dimensional ^{13}C-^{13}C correlation experiments in L111M TTR$_{105-115}$. The spectra demonstrate that the samples are microscopically ordered. All ^{13}C sites can be assigned on the basis of a single 2D correlation experiment in each sample.

Homonuclear correlation spectroscopy was accomplished through either proton-driven spin diffusion [83-85] with the application of an R^3 recoupling field [86] or application of the SPC5 double quantum mixing sequence [87] for polarization transfer

among aliphatic carbons (Figure 13-8). The mixing times were set to 10 ms and 0.8 ms (8 τ_r), respectively, to favor polarization transfer to directly bonded carbons. The spinning frequency was 10 kHz and 83 kHz TPPM decoupling was applied during acquisition. Assignments and 2D spectra are shown in Figure 13-9 for both samples. Due to dynamical processes which interfere with the proton decoupling or magic angle spinning, site-specific assignments of aromatic resonances was only possible for the N-terminal peptide, as shown in Figure 13-10.
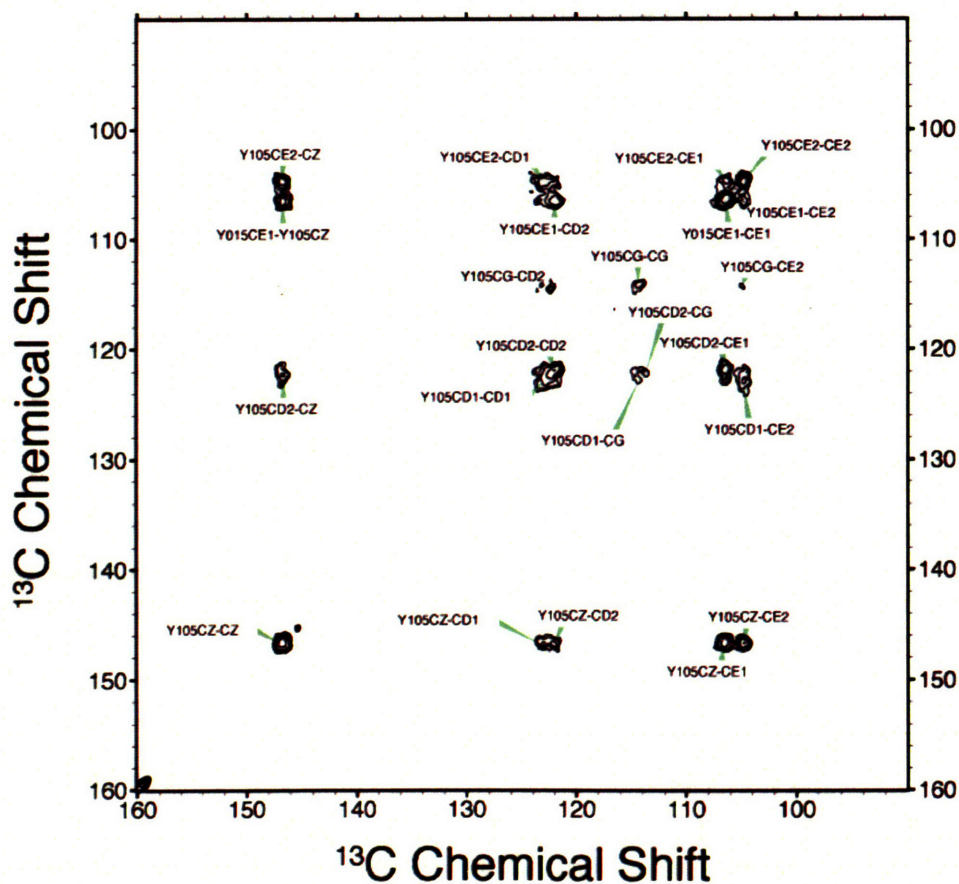
Figure 13-10: Aromatic region of 2D ^{13}C-^{13}C correlation experiment in YTIAAL-labeled sample of L111M TTR$_{105-115}$. Since the timescale of the aromatic ring dynamics for the C-terminal tyrosine does not interfere with the decoupling or magic angle spinning, nor does it render ring carbons equivalent through conformational exchange, it is possible to obtain a complete set of assignments for its ^{13}C sites.

Heteronuclear correlation spectroscopy was accomplished through spectrally selective ^{15}N-^{13}C polarization transfer (SPECIFIC CP [88]) from the amide nitrogen to the Cα of the same residue or to the C' carbon of the following residue in NCACX and NCOCX experiments, respectively. Aliphatic polarization transfer was accomplished using proton-driven spin diffusion with the application of an R^3 recoupling field (Figure 13-11). The mixing times were set to 20 ms to give uniform polarization transfer to all sites in the side chain. The spinning frequency was 10 kHz and 83 kHz TPPM decoupling was applied during acquisition. NCACX and NCOCX spectra, shown in Figure 13-12, confirm ^{13}C assignments and provide assignments for all backbone ^{15}N sites. Both the homonuclear and heteronuclear correlation spectra also confirm that each monomer in the amyloid fibril exists in the same chemical and conformational environment.
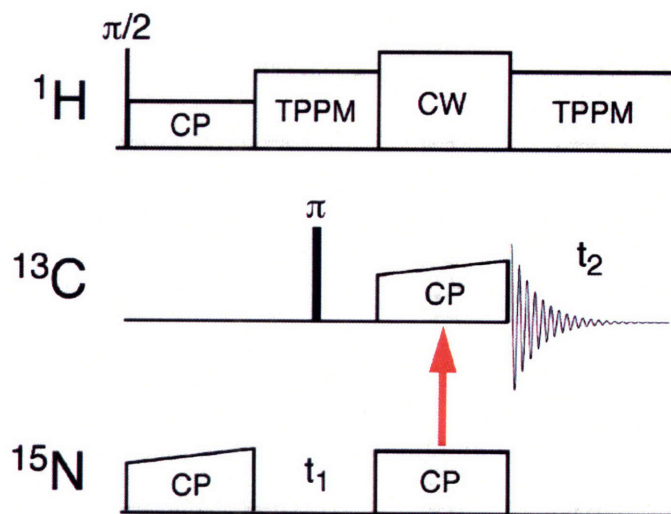
Figure 13-11: Pulse sequence for 2D ^{15}N-^{13}C homonuclear correlation spectroscopy. Following ^{1}H-^{15}N cross polarization, magnetization evolves under the ^{15}N chemical shift during T_1 and then is transferred to the $^{13}C\alpha$ or $^{13}C'$ via band-selective cross polarization (SPECIFIC CP). Aliphatic homonuclear mixing is accomplished through proton-driven spin diffusion with the application of a ^{1}H R^3 recoupling field (DARR).
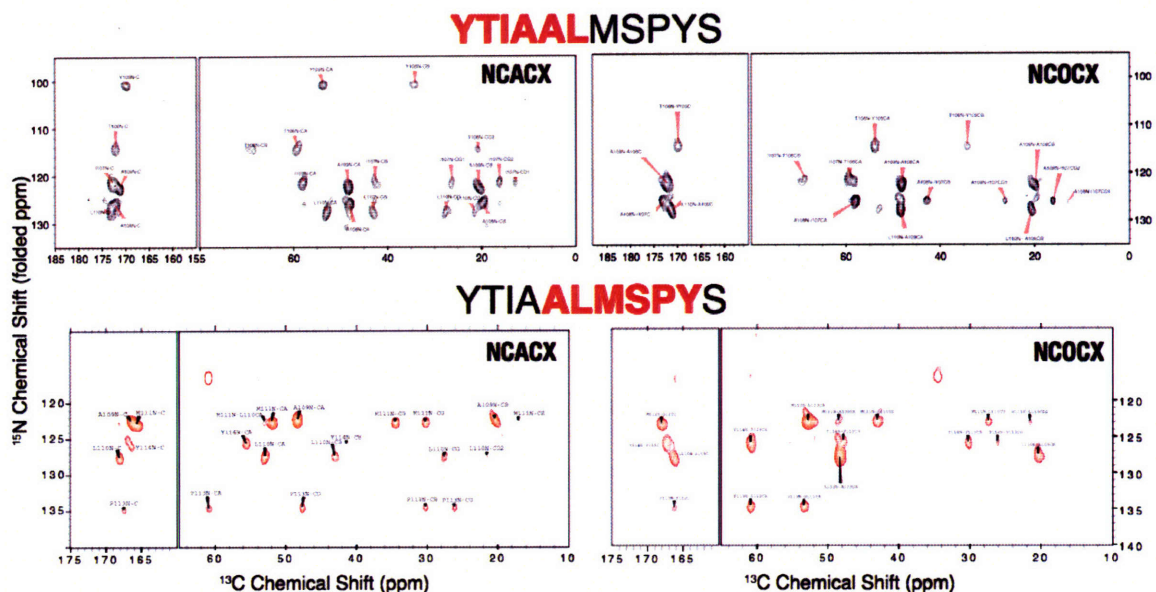
Figure 13-12: Two-dimensional ^{15}N-^{13}C correlation experiments in L111M TTR$_{105-115}$. Complete sequential assignments have been obtained through 2D NCACX and NCOCX-type correlation spectra, shown above for each sample.

13.3.6   Measurement of Distances

Structural constraints in the form of internuclear distances were obtained by 3D TEDOR [54] (^{15}N-^{13}C) and Rotational Resonance Width [57-59] (^{13}C-^{13}C) methods, both of which report on the dipolar couplings by monitoring the evolution of cross-peak intensities as a function of an incrementable parameter. In the case of 3D TEDOR, which is a broadband experiment, the intensities of ^{13}C-$^{15}N_i$ cross peaks as a function of the TEDOR mixing time are simultaneously fit to obtain all heteronuclear dipolar couplings to a given carbon atom. The R^2W experiment is spectrally selective due to its reliance on the rotational resonance [89-91], in which spin pairs separated approximately by the spinning frequency or twice the spinning frequency are recoupled. The evolution of ^{13}CO-^{13}C cross peak intensities are fit as a function of the spinning frequency at constant mixing time to obtain an estimate of the homonuclear distance.

542

Examples of 2D planes from 3D TEDOR experiments are shown in Figure 13-13, for the YTIAAL sample, and in Figure 13-14, for the ALMSPY-labeled sample (only the aliphatic regions are shown). Each cross peak corresponds to a unique ^{15}N-^{13}C dipolar coupling and leads to a structural constraint. An example of data fitting is illustrated in Figure 13-15, in which cross peaks between I107Cγ2 and T106N/I107N are simultaneously fit to yield two distances. The modulation of cross peak intensities at long mixing times is due to the influence of homonuclear J couplings; the data fitting assumes that they take canonical published values for peptides [92].
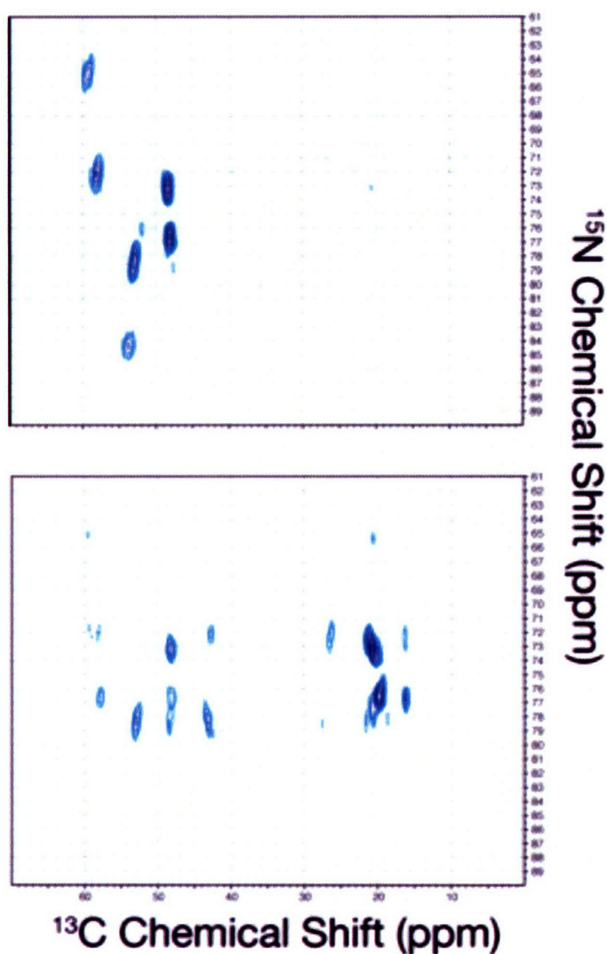
Figure 13-13: 2D planes from 3D TEDOR experiment in YTIAAL-labeled L111M TTR$_{105-115}$ sample corresponding to 1 ms (top) and 10 ms (bottom) TEDOR mixing times. The intensity of each cross peak as a function of the mixing time can be fit to obtain the heteronuclear dipolar couplings.
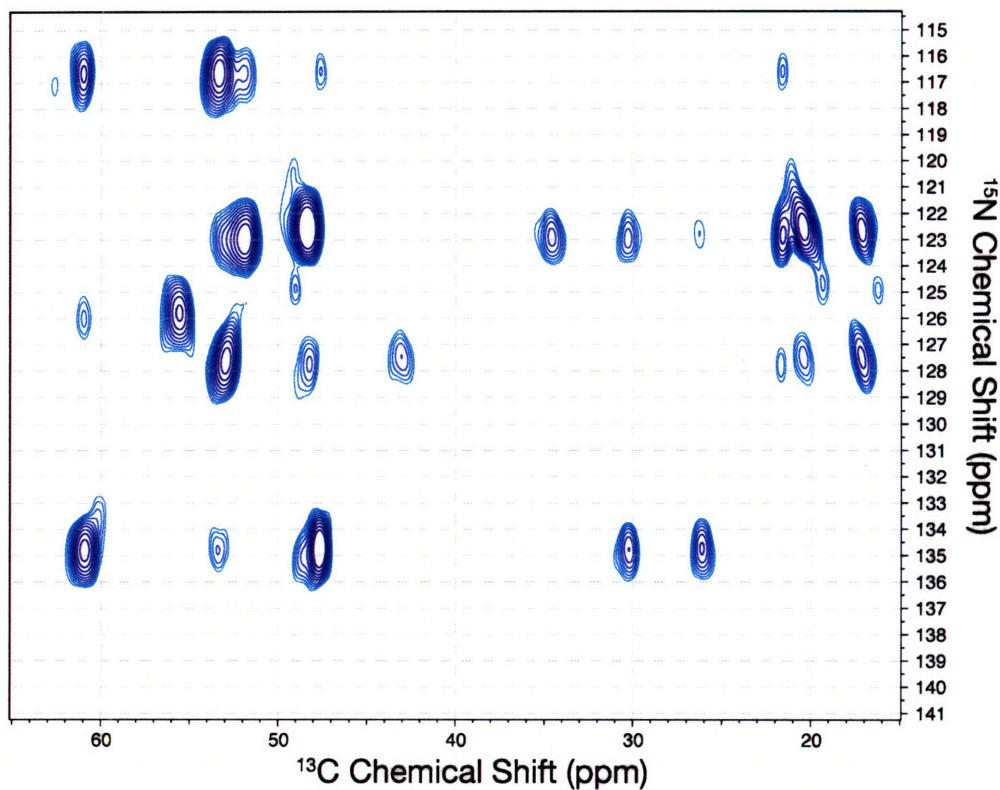
Figure 13-14: 2D plane from 3D TEDOR experiment in ALMSPY-labeled L111M TTR$_{105-115}$ sample corresponding to a 10 ms TEDOR mixing time. The intensity of each cross peak as a function of the mixing time can be fit to obtain the heteronuclear dipolar couplings.
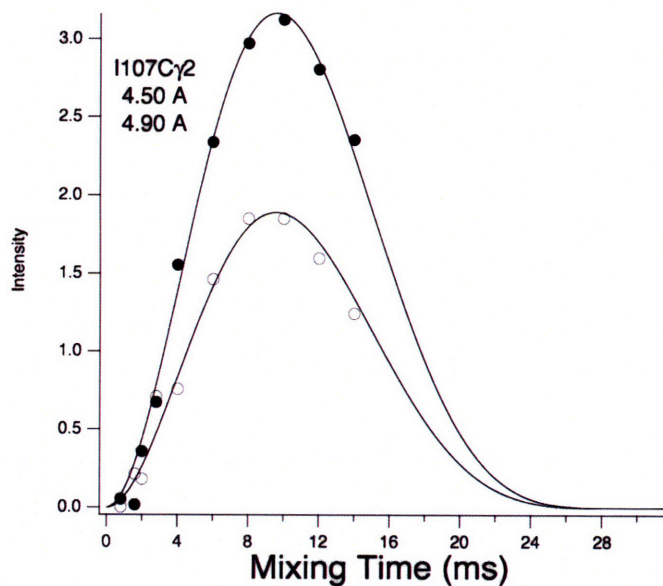
Figure 13-15: Example of data fitting for I107Cγ2 ^{13}C-^{15}N cross peaks to I107N and T106N. The modulation of TEDOR intensity at long mixing times is due to the J-coupling. Experimental data extends to 16 ms.

13.3.7 Measurement of Torsion Angles

Constraints on backbone torsion angles can be obtained through tensor correlation experiments, in which the spin evolution due to one anisotropic element of the nuclear spin Hamiltonian (*e.g.* CSA, dipolar coupling) is correlated to that of another. The mutual orientation of the anisotropies is then inferred from the combined dynamics. This approach is most useful for dipolar tensors, which have an orientation with respect to the molecular segment that is known by definition. The dipolar tensor correlation experiments utilized here follow two patterns: in one, a correlated spin state is created between two directly bonded nuclei, and that state is allowed to dephase under recoupled heteronuclear dipolar couplings. Examples of this include HCCH [64] tensor correlation experiment, which is useful for constraining side chain torsion angles, and the NCCN experiment for the backbone torsion angle ψ. Alternatively, polarization transfer can be used to correlate the dynamics at one site with those of another, such as in the HNCH (ϕ) experiment [65] and the $HN_{i+1}CH$ (ψ) experiment [61]. In these cases, two separate incrementable heteronuclear evolution periods are employed during which the system evolves separately under the H-N and H-Cα dipolar couplings. When combined with chemical shift evolution, such an experiment is, in principle, four dimensional. To avoid prohibitively long acquisition times, the two dimensions are instead synchronously incremented in a ratio that maximizes the sensitivity of the experiment. All experiments make use of $SPC5_3$[93] for narrowband homonuclear double quantum mixing and the γ-encoded TMREV[94] sequence (TMREV-4) for heteronuclear ^1H-^{15}N and ^1H-^{13}C recoupling. The NCCN correlation experiment makes use of REDOR[95] for ^{15}N-^{13}C recoupling.

Thr106 Backbone Torsion Angles
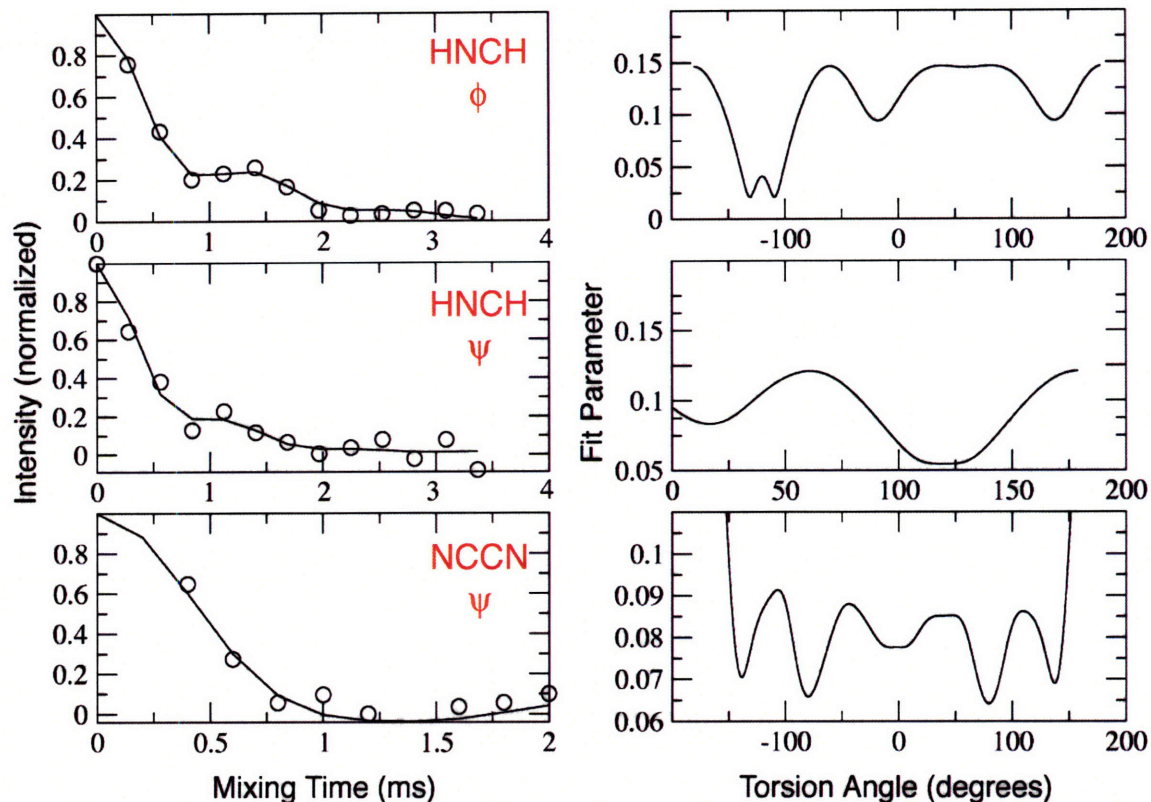
Figure 13-16: Experimental constraints on backbone torsion angles of Threonine 106 from HNCαH (ϕ), HN$_{i+1}$CαH (ψ), and NCCN (ψ) tensor correlation experiments. Fits as a function of mixing time are indicated on the left, and the solution surfaces are plotted on the right.

For the HNCH experiments, data analysis involves simultaneous fitting of torsion angle and a constant which describes exponential relaxation, subject to assumptions about the ^{1}H-^{15}N and ^{1}H-Cα bond lengths and equilibrium bond angles. The NCCN experiment is dependent on assumptions about the N-Cα and Cα-CO distances in addition to the N-Cα-CO and Cα-C'-N bond angles. These parameters are fixed at there equilibrium values from the forcefield used in the NMR refinement (XPlor-NIH [96]); however, statistically reasonable variations in these parameters introduce a potential 10-15 degree error in the torsion angle measurement, which in all cases exceeds the random error recovered from the data fit [19]. In particular, pairs of nearly degenerate solutions

in the HNCH experiments coalesce effectively into a single solution if the bond angles

and other parameters are not precisely defined. While global Monte Carlo simulation

can, in principle, uncover the true confidence intervals that describe the data, we have not

attempted this approach here. An example of torsion angle experiments which constrain

the backbone torsion angles in T106 is provided in Figure 13-16. Since the solution

space may contain multiple acceptable minima (particularly for the ψ measurements),

multiple torsion angle measurements are combined where possible to yield a consistent

solution.

Table 13.2: Experimental constraints on backbone torsion angles in L111M TTR$_{105-115}$ fibrils.

| | ϕ | ψ | |
	H-N$_i$-Cα_i-H	H-N(i+1)-Cα-H	N-Cα-C$'$-N
Y105	n/a	99.0, 140.8	±158
T106	-130.6, -109.3	119	±138, ±80
I107	-130.0, -110.0	120	±138
A108	-130.1, -109.9	104.8. 135.2	±132
A109	-138.8, -101.1	109.8, 129.4	±134
L110	-129.4, -110.5	112.5, 126.0	±152
M111	-135.0, -104.3	106.9, 130.8	±130
S112	-136.3, -103.6	n/a	±136
P113	n/a	120	±144
Y114	-140.7, -100.5	n/a	n/a
S115	n/a	n/a	n/a

Table 13.3: Distance constraints measured in 3D TEDOR experiments in L111M TTR$_{105\text{-}115}$.
Potetentially intermolecular couplings are colored in red.

Spin 1	Spin 2	Distance (nm)	Spin 1	Spin 2	Distance (nm)
Y105 Cα	Y105 N	150	L110 Cβ	L110N	240
Y105 Cα	T106 N	260	L110 Cβ	M111N	355
Y105 C'	Y105 N	245	L110 Cγ	L110 N	450
Y105 C'	T106 N	140	L110 Cδ1	L110N	460
T106 Cα	T106 N	150	L110 Cδ1	M111 N	320
T106 Cα	I107 N	275	L110 Cδ1	S112 N	440
T106 Cγ	T106 N	370	L110 Cδ2	A108 N	470
T106 Cγ	I107 N	310	L110 Cδ2	A109 N	470
T106 C'	T106 N	315	L110 Cδ2	L110 N	445
T106 C'	I107 N	140	L110 Cδ2	M111 N	440
I107 Cα	I107 N	150	L110 C'	A108 N	320
I107 Cα	A108 N	235	L110 C'	L110 N	145
I107 Cβ	I107 N	260	M111 Cα	M111 N	150
I107 Cβ	A108 N	320	M111 Cα	S112 N	235
I107 Cγ	I107 N	300	M111 Cβ	A109 N	315
I107 Cγ2	I107 N	400	M111 Cβ	M111 N	260
I107 Cγ2	A108 N	470	M111 Cβ	S112 N	355
I107 Cγ2	A109 N	510	M111 Cγ	M111 N	255
I107 Cδ	I107 N	500	M111 Cε	A109 N	390
I107 Cδ	A108 N	650	M111 Cε	L110 N	380
I107 Cδ	A109 N	880	M111 Cε	M111 N	440
A108 Cα	A108 N	150	S112 Cα	S112 N	150
A108 Cα	A109 N	480	S112 Cα	P113 N	255
A108 Cβ	A108 N	265	S112 Cβ	S112N	255
A108 Cβ	A109 N	335	P113 Cα	P113 N	145
A108 C'	A108 N	240	P113 Cα	Y114 N	270
A108 C'	A109 N	140	P113 Cβ	P113 N	250
A109 Cα	A109 N	145	P113 Cγ	P113 N	280
A109 Cα	L110 N	250	P113 Cδ	S112 N	305
A109 Cα	M111 N	310	P113 Cδ	P113 N	150
A109 Cβ	A108N	370	Y114 Cα	Y114 N	150
A109 Cβ	A109N	265	L110 Cα	M111 N	220
A109 Cβ	L110N	340	L110 Cα	A108 N	335
A109 Cβ	M111 N	360	L110 Cα	L110 N	150
A109 C'	A109 N	240			
A109 C'	L110 N	135			

548

13.4 Discussion

13.4.1 Structural Refinement

The structure was refined using simulated annealing molecular dynamics [97] in the internal variable minimizer implemented in XPlor-NIH [96], roughly following protocols developed in the refinement of MLF at Low Temperature and the WT TTR structure [21]. Distance restraints were represented as harmonic potentials, while torsion angle restraints were represented as square-well potentials during the later stages of the refinement. No database-derived restraints were used in the process. Acceptable solutions contained no violations of the distance or torsion angle restraints. The density of restraints is depicted in Figure 13-17. Since the C-terminal serine was not isotopically labeled, there are far fewer constraints on the C-terminus than at other sites. Many conformations of the C-terminus are thus reflected in the structural ensemble, and this is not an indication of either static or dynamic disorder. Refinement of the structure using periodic boundary conditions or excluded volume restraints designed to simulate the packing of the amyloid fibril monomer into a generic β-sheet would further constrain the conformation, but no such approaches were attempted in this refinement. A representative set of structures from an ensemble of 100 acceptable structures is shown in Figure 13-18. The average root mean square deviation of coordinates of heavy atoms is 0.51 Å, which is slightly better than what was possible in the refinement of the related WT $TTR_{105-115}$ structure. Side chain torsion angles were not included at this stage of the refinement, but it is anticipated that their inclusion will improve the quality of the refined structural ensemble. Finally, a preliminary conformational analysis of quality of the structural ensemble, shown in Figure 13-19, shows that all residues adopt conformations

in the favored or most-favored regions of the conformational space corresponding to β-

sheet secondary structure.
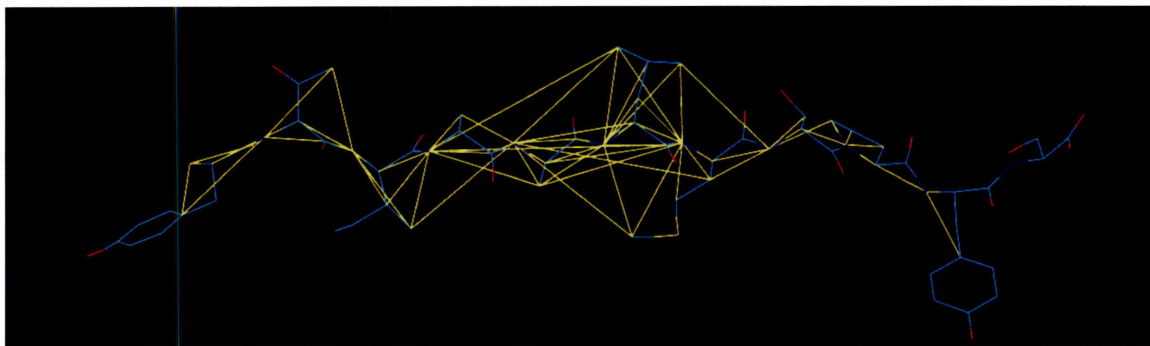
Figure 13-17: Representation of the density of structural constraints used in the refinement of the L111M structure. Note the lower density of constraints in the N-terminal tyrosine and on the C-terminus, which was not labeled due to the expense of attaching labeled, protected, Serine to the resin.
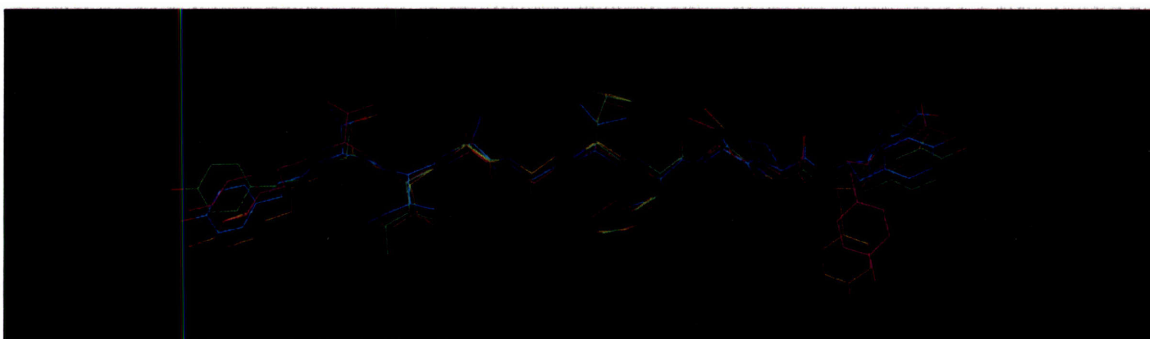
Figure 13-18: Representative members of the L111M structural ensemble. These conformers span the conformational space defined by the 100 lowest energy structures in the minimization.
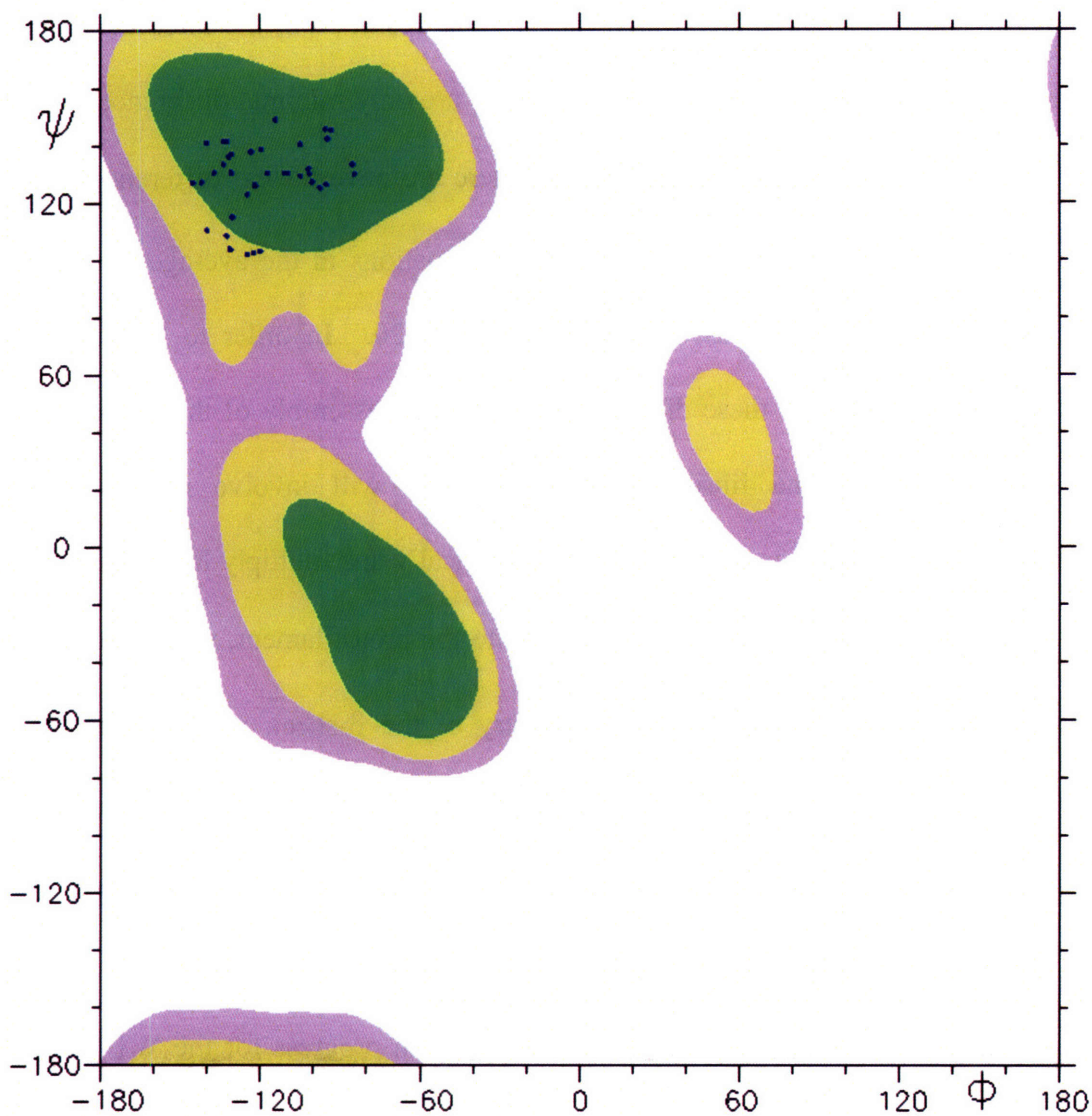
Figure 13-19: Ramachandran plot formed from the ensemble depicted in Figure 13-18. All residues lie within the favored, β-sheet region of the conformational space.

13.4.2   Differences from WT Structure

Both the WT $TTR_{105-115}$ peptide and its L111M mutant adopt the conformation of an extended β-strand in the amyloid fibril, with no indication of the β-turn conformation that it adopts in the native transthyretin protein. That they have β-sheet content was known from diffraction and circular dichroism experiments [14-16], and this is characteristic of all amyloid fibril samples. The diffraction experiments further indicate different periodic

spacings in the L111M peptide, which may in part result from the alternate excluded volume of the methionine side chain. While there are only minimal differences possible in conformation between extended β-strands, there are nevertheless differences in both the backbone torsion angles and side chain conformations in the average structures of WT and L111M TTR$_{105-115}$, as shown in Figure 13-20. In order to understand the structural consequences of these differences for the self-assembly of the entire amyloid fibril, a structure of the fibril is required. This will involve measurement of intermolecular conformational parameters in specifically and multiply labeled samples to determine the parameters of β-strand packing into the protofilament, which includes the orientation (parallel or antiparallel) and registry of the β-sheet, and the number and relative topology of β-sheets in the protofilament. The length scales on which the protofilaments twist and assemble into fibrils are inaccessible to solid state NMR and must therefore be studied by cryo-electron microscopy, atomic force microscopy, and other techniques. These measurements are currently in progress for the WT TTR$_{105-115}$ peptide and will also be completed for the case of the L111M mutant. A comparison of these structures may provide insights into the different physical properties of these two amyloid fibrils, including their different fibril formation kinetics and differences in pitch and width of the fibrils.
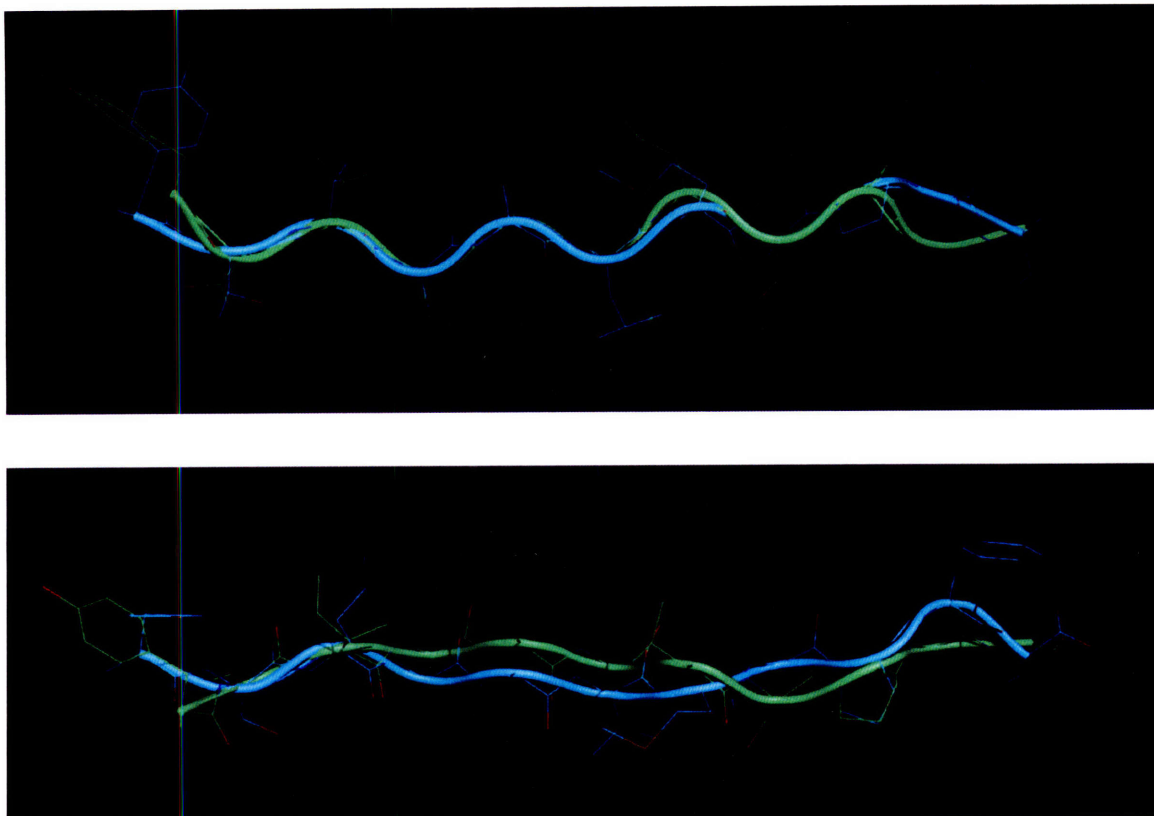
Figure 13-20: Comparison of the WT TTR structure with the structure of L111M TTR (two views).

13.5   References

[1]   Lyon, C. E.; Suh, E. S.; Dobson, C. M.; Hore, P. J., Probing the exposure of tyrosine and tryptophan residues in partially folded proteins and folding intermediates by CIDNP pulse-labeling. *Journal of the American Chemical Society* **2002,** 124, (44), 13018-13024.

[2]   Dobson, C. M., Protein Misfolding, Evolution and Desease. *Trends in Biochemical Sciences* **1999,** 24, 329-332.

[3]   Sunde, M.; Blake, C. C. F., From the globular to the fibrous state: protein structure and structural conversion in amyloid formation. *Quarterly Reviews of Biophysics* **1998,** 31, (1), 1-+.

[4]   Serpell, L. C.; Sunde, M.; Fraser, P. E.; Luther, P. K.; Morris, E. P.; Sangren, O.; Lundgren, E.; Blake, C. C. F., Examination of the Structure of the Transthyretin Amyloid Fibril by Image-Reconstruction from Electron-Micrographs. *Journal of Molecular Biology* **1995,** 254, (2), 113-118.

[5]   Nettleton, E. J.; Tito, P.; Sunde, M.; Bouchard, M.; Dobson, C. M.; Robinson, C. V., Characterization of the oligomeric states of insulin in self-assembly and amyloid fibril formation by mass spectrometry. *Biophysical Journal* **2000**, 79, (2), 1053-1065.

[6]   Jimenez, J. L.; Guijarro, J. I.; Orlova, E.; Zurdo, J.; Dobson, C. M.; Sundae, M.; Saibil, H. R., Cryo-electron Microscopy Structure of an SH3 Amyloid Fibril and Model of the Molecular Packing. *EMBO J.* **1999**, 18, (4), 815-821.

[7]   Chamberlain, A. K.; MacPhee, C. E.; Zurdo, J.; Morozova-Roche, L. A.; Hill, H. A. O.; Dobson, C. M.; Davis, J. J., Ultrastructural Organization of Amyloid Fibrils by atomic force microscopy. *Biophys. J.* **2000**, 79, (6), 3282-3293.

[8]   Diaz-Avalos, R.; Long, C.; Fontano, E.; Balbirnie, M.; Grothe, R.; Eisenberg, D.; Caspar, D. L., Cross-beta order and diversity in nanocrystals of an amyloid-forming peptide. *J Mol Biol* **2003**, 330, (5), 1165-75.

[9]   McParland, V. J.; Kad, N. M.; Kalverda, A. P.; Brown, A.; Kirwin-Jones, P.; Hunter, M. G.; Sunde, M.; Radford, S. E., Partially unfolded states of beta(2)-microglobulin and amyloid formation in vitro. *Biochemistry* **2000**, 39, (30), 8735-8746.

[10]   Guijarro, J. I.; Sunde, M.; Jones, J. A.; Campbell, I. D.; Dobson, C. M., Amyloid fibril formation by an SH3 domain. *Proceedings of the National Academy of Sciences of the United States of America* **1998**, 95, (8), 4224-4228.

[11]   Olofsson, A.; Ippel, H. J.; Baranov, V.; Horstedt, P.; Wijmenga, S.; Lundgren, E., Capture of a dimeric intermediate during transthyretin amyloid formation. *Journal of Biological Chemistry* **2001**, 276, (43), 39592-39599.

[12]   Tycko, R., Solid State NMR as a Probe of Amyloid Fibril Structure. *Curr. Opin. Chem. Biol.* **2000**, 4, 500.

[13]   Petkova, A. T.; Ishii, Y.; Balbach, J. J.; Antzutkin, O. N.; Leapman, R. D.; Delaglio, F.; Tycko, R., A structural model for Alzheimer's β-amyloid fibrils based on experimental constraints from solid state NMR. *Proc. Nat. Acad. Sci. USA* **2002**, 99, 16742-16747.

[14]   Jarvis, J. A.; Munro, S. L. A.; Craik, D. J., Structural-Analysis of Peptide Fragment-71-93 of Transthyretin by Nmr-Spectroscopy and Electron-Microscopy - Insight into Amyloid Fibril Formation. *Biochemistry* **1994**, 33, (1), 33-41.

[15]   Jarvis, J. A.; Craik, D. J.; Wilce, M. C. J., X-Ray Diffraction Studies of Fibrils Formed From Peptide Fragments of Transthyretin. *Biochemical and Biophysical Research Comm.* **1993**, 192, (3), 991-998.

[16]   Jarvis, J.; Munro, S.; Craik, D., Nmr Structural Studies of Fragments of the Thyroid-Hormone Transport Protein Transthyretin Involved in Amyloid Formation. *Journal of Cellular Biochemistry* **1993**, 276-276.

[17]   Gustavsson, A.; Engstrom, U.; Westermark, P., Normal Transthyretin and Synthetic Transthyretin Fragments Form Amyloid-Like Fibrils Invitro. *Biochemical and Biophysical Research Communications* **1991**, 175, (3), 1159-1164.

[18]   Gustavsson, A.; Engstrom, U.; Westermark, P., Normal Transthyretin and Synthetic Transthyretin Fragments Form Amyloid Like Fibrils *in vitro*. *Biochem. Biophys. Res. Commun.* **1991,** 175, 1159-1164.

[19]   Jaroniec, C. P.; MacPhee, C. E.; Bajaj, V. S.; McMahon, M. T.; Dobson, C. M.; Griffin, R. G., High-resolution molecular structure of a peptide in an amyloid fibril determined by magic angle spinning NMR spectroscopy. *Proceedings of the National Academy of Sciences of the United States of America* **2004,** 101, (3), 711-716.

[20]   Jaroniec, C. P.; MacPhee, C. E.; Astrof, N. S.; Dobson, C. M.; Griffin, R. G., Molecular conformation of a peptide fragment of transthyretin in an amyloid fibril. *Proceedings of the National Academy of Sciences of the United States of America* **2002,** 99, (26), 16748-16753.

[21]   Jaroniec, C. P.; MacPhee, C. E.; Bajaj, V. S.; McMahon, M. T.; Dobson, C. M.; Griffin, R. G., High Resolution Molecular Structure of a Peptide in an Amyloid Fibril Determined by MAS NMR Spectroscopy. *Proc. Nat'l. Acad. Sci.* **2004,** 101, 711-716.

[22]   De Carvalho, M.; Moreira, P.; Evangelista, T.; Ducla-Soares, J. L.; Bento, A.; Fernandes, R.; Saraiva, M. J., New transthyretin mutation V28M in a Portuguese kindred with amyloid polyneuropathy. *Muscle & Nerve* **2000,** 23, (7), 1016-1021.

[23]   Nakamura, Y.; Yutani, C.; Nakazato, M.; Date, Y.; Baba, T.; Goto, Y., A case of hereditary amyloidosis transthyretin variant Met 30 with amyloid cardiomyopathy, less polyneuropathy, and the presence of giant cells. *Pathology International* **1999**, 49, (10), 898-902.

[24]   Lashuel, H. A.; Wurth, C.; Woo, L.; Kelly, J. W., The most pathogenic transthyretin variant, L55P, forms amyloid fibrils under acidic conditions and protofilaments under physiological conditions. *Biochemistry* **1999,** 38, (41), 13560-13573.

[25]   Zolyomi, Z.; Benson, M. D.; Halasz, K.; Uemichi, T.; Fekete, G., Transthyretin mutation (Serine 84) associated with familial amyloid polyneuropathy in a Hungarian family. *Amyloid-International Journal of Experimental and Clinical Investigation* **1998,** 5, (1), 30-34.

[26]   Utsugisawa, K.; Tohgi, H.; Nagane, Y.; Yamagata, M.; Saito, K.; Mihara, M., Familial amyloid polyneuropathy related to transthyretin mutation VAL30 to Leu in a Japanese family. *Muscle & Nerve* **1998,** 21, (12), 1783-1785.

[27]   Sebastiao, M. P.; Saraiva, M. J.; Damas, A. M., The crystal structure of amyloidogenic Leu(55) -> Pro transthyretin variant reveals a possible pathway for

transthyretin polymerization into amyloid fibrils. *Journal of Biological Chemistry* **1998**, 273, (38), 24715-24722.

[28]   Myers, T. J.; Kyle, R. A.; Jacobson, D. R., Familial amyloid with a transthyretin leucine 33 mutation presenting with ascites. *American Journal of Hematology* **1998**, 59, (3), 249-251.

[29]   Ikeda, K.; Kinoshita, M.; Takamiya, K.; Iwasaki, Y.; Tomita, Y.; Nakano, I.; Nakazato, M., Bulbar palsy in senile onset familial amyloid polyneuropathy ((30)Val -> Met): transthyretin-amyloid deposits in the hypoglossal nerve root. *European Journal of Neurology* **1998**, 5, (2), 211-214.

[30]   Blanco-Jerez, C. R.; Jimenez-Escrig, A.; Gobernado, J. M.; Lopez-Calvo, S.; De Blas, G.; Redondo, C.; Villanueva, M. G.; Orensanz, L., Transthyretin Tyr77 familial amyloid polyneuropathy: A clinicopathological study of a large kindred. *Muscle & Nerve* **1998**, 21, (11), 1478-1485.

[31]   Ikeda, S.; Tokuda, T.; Nakamura, A.; Ueno, I.; Taketomi, T.; Yanagisawa, N.; Li, Y. F., Transthyretin Met 30 familial amyloid polyneuropathy in China. Usefulness of mass spectrometry for screening a variant TTR in serum. *Amyloid-International Journal of Experimental and Clinical Investigation* **1997**, 4, (2), 104-107.

[32]   Goebel, H. H.; Seddigh, S.; Hopf, H. C.; Uemichi, T.; Benson, M. D.; McKusick, V. A., A European family with histidine 58 transthyretin mutation in familial amyloid polyneuropathy. *Neuromuscular Disorders* **1997**, 7, (4), 229-230.

[33]   Bordeneuve, V. P.; Bicetre, L. E. K.; Lalu, T.; Misrahi, M.; Said, G., Identification of 3 new variants of the transthyretin (TTR) and study of haplotypes in familial amyloid polyneuropathy (FAP). *Neurology* **1997**, 48, (3), 6089-6089.

[34]   Uemichi, T.; Gertz, M. A.; Benson, M. D., A New Transthyretin Variant (Ser-24) Associated with Familial Amyloid Polyneuropathy. *Journal of Medical Genetics* **1995**, 32, (4), 279-281.

[35]   Toyooka, K.; Fujimura, H.; Ueno, S.; Yoshikawa, H.; Kaido, M.; Nishimura, T.; Yorifuji, S.; Yanagihara, T., Familial Amyloid Polyneuropathy Associated with Transthyretin Gly42 Mutation - a Quantitative Light and Electron-Microscopic Study of the Peripheral Nervous-System. *Acta Neuropathologica* **1995**, 90, (5), 516-525.

[36]   Nordvag, B. Y.; Ranlov, I.; ElGewely, M. R.; Husby, G., Two transthyretin variants, Ser 6 and Met 111, in a Danish kindred with familial amyloid cardiomyopathy: Implications for serum TTR and thyroxine hormone levels. *Amyloid-International Journal of Experimental and Clinical Investigation* **1995**, 2, (4), 241-250.

[37]   Gustavsson, A.; Jahr, H.; Tobiassen, R.; Jacobson, D. R.; Sletten, K.; Westermark, P., Amyloid Fibril Composition and Transthyretin Gene Structure in Senile Systemic Amyloidosis. *Laboratory Investigation* **1995**, 73, (5), 703-708.

[38]   Zeldenrust, S. R.; Skinner, M.; Skare, J.; Benson, M. D., A New Transthyretin Variant (His-69) Associated with Vitreous Amyloid in an Fap Family. *Amyloid-International Journal of Experimental and Clinical Investigation* **1994**, 1, (1), 17-22.

[39]   Nordvag, B. Y.; Riise, H. M. F.; Husby, G., Verification of the Transthyretin Met-111 Mutation in Familial Amyloid Cardiomyopathy of Danish Origin by DNA Sequening. *Human Genetics* **1994**, 93, (4), 484-485.

[40]   Fiori, M. G.; Salvi, F.; Plasmati, R.; Tessari, F.; Bianchi, R.; Tassinari, C. A., Amyloid Deposits inside Myocardial Fibers in Transthyretin-Met30 Familial Amyloidotic Polyneuropathy - a Histological and Biochemical-Study. *Cardiology* **1994**, 85, (3-4), 145-153.

[41]   Bhatia, K.; Reilly, M.; Adams, D.; Davis, M. B.; Hawkes, C. H.; Thomas, P. K.; Said, G.; Harding, A. E., Transthyretin Gene-Mutations in British and French Patients with Amyloid Neuropathy. *Journal of Neurology Neurosurgery and Psychiatry* **1993**, 56, (6), 694-697.

[42]   Ueno, S.; Fujimura, H.; Yorifuji, S.; Nakamura, Y.; Takahashi, M.; Tarui, S.; Yanagihara, T., Familial Amyloid Polyneuropathy Associated with the Transthyretin Cys114 Gene in a Japanese Kindred. *Brain* **1992**, 115, 1275-1289.

[43]   Uemichi, T.; Ueno, S.; Fujimura, H.; Umekage, T.; Yorifuji, S.; Matsuzawa, Y.; Tarui, S., Familial Amyloid Polyneuropathy Related to Transthyretin Gly42 in a Japanese Family. *Muscle & Nerve* **1992**, 15, (8), 904-911.

[44]   Uemichi, T.; Murrell, J. R.; Zeldenrust, S.; Benson, M. D., A New Mutant Transthyretin (Arg-10) Associated with Familial Amyloid Polyneuropathy. *Journal of Medical Genetics* **1992**, 29, (12), 888-891.

[45]   Takahashi, N.; Ueno, S.; Uemichi, T.; Fujimura, H.; Yorifuji, S.; Tarui, S., Amyloid Polyneuropathy with Transthyretin Arg50 in a Japanese Case from Osaka. *Journal of the Neurological Sciences* **1992**, 112, (1-2), 58-64.

[46]   Saraiva, M. J. M.; Almeida, M. R.; Sherman, W.; Gawinowicz, M.; Costa, P.; Costa, P. P.; Goodman, D. S., A New Transthyretin Mutation Associated with Amyloid Cardiomyopathy. *American Journal of Human Genetics* **1992**, 50, (5), 1027-1030.

[47]   Saeki, Y.; Ueno, S.; Takahashi, N.; Soga, F.; Yanagihara, T., A Novel Mutant (Transthyretin Ile-50) Related to Amyloid Polyneuropathy - Single-Strand Conformation Polymorphism as a New Genetic-Marker. *Febs Letters* **1992**, 308, (1), 35-37.

[48]   Nordvag, B. Y.; Husby, G.; Ranlov, I.; Elgewely, M. R., Molecular Diagnosis of the Transthyretin (Ttr) Met(111) Mutation in Familial Amyloid Cardiomyopathy of Danish Origin. *Human Genetics* **1992**, 89, (4), 459-461.

[49]   Kametani, F.; Ikeda, S.; Yanagisawa, N.; Ishi, T.; Hanyu, N., Characterization of a Transthyretin-Related Amyloid Fibril Protein from Cerebral Amyloid Angiopathy in

Type-I Familial Amyloid Polyneuropathy. *Journal of the Neurological Sciences* **1992**, 108, (2), 178-183.

[50]   Ippolito, J. A.; Mechanic, L.; Heiman, A., Transthyretin Amyloid - a Case-Report. *Journal of Histotechnology* **1992**, 15, (4), 325-327.

[51]   Koeppen, A. H.; Wallace, M. R.; Benson, M. D.; Altland, K., Familial Amyloid Polyneuropathy - Alanine-for-Threonine Substitution in the Transthyretin (Prealbumin) Molecule. *Muscle & Nerve* **1990**, 13, (11), 1065-1075.

[52]   Maury, C. P. J.; Teppo, A. M.; Karinemi, A. L.; Koeppen, A. H., Amyloid Fibril Protein in Familial Amyloidosis with Cranial Neuropathy and Corneal Lattice Dystrophy (Fap Type-Iv) Is Related to Transthyretin. *American Journal of Clinical Pathology* **1988**, 89, (3), 359-364.

[53]   Saraiva, M. J. M.; Birken, S.; Costa, P. P.; Goodman, D. S., Amyloid Fibril Protein in Familial Amyloidotic Polyneuropathy, Portuguese Type - Definition of Molecular Abnormality in Transthyretin (Prealbumin). *Journal of Clinical Investigation* **1984**, 74, (1), 104-119.

[54]   Jaroniec, C. P.; Filip, C.; Griffin, R. G., 3D TEDOR NMR experiments for the simultaneous measurement of multiple carbon-nitrogen distances in uniformly C-13, N-15- labeled solids. *Journal of the American Chemical Society* **2002**, 124, (36), 10728-10742.

[55]   Michal, C. A.; Jelinski, L. W., REDOR 3D: Heteronuclear distance measurements in uniformly labeled and natural abundance solids. *J. Am. Chem. Soc.* **1997**, 119, 9059-9060.

[56]   Gullion, T.; Schaefer, J., Rotational Echo Double Resonance NMR. *J. Magn. Reson.* **1989**, 81, 196-200.

[57]   Costa, P. R.; Sun, B.; Griffin, R. G., Rotational resonance width experiment. *J. Magn. Reson.* **2003**, in press.

[58]   Ramachandran, R.; Lewandowski, J. R.; van der Wel, P. C. A.; Griffin, R. G., Multipole-multimode Floquet theory of rotational resonance width experiments: C-13-C-13 distance measurements in uniformly labeled-solids. *Journal of Chemical Physics* **2006**, 124, (21), -.

[59]   Ramachandran, R.; Ladizhansky, V.; Bajaj, V. S.; Griffin, R. G., C-13-C-13 rotational resonance width distance measurements in uniformly C-13-labeled peptides. *Journal of the American Chemical Society* **2003**, 125, (50), 15623-15629.

[60]   Ladizhansky, V.; Jaroniec, C. P.; Diehl, A.; Oschkinat, H.; Griffin, R. G., Measurement of multiple y torsion angles in uniformly $^{13}C,^{15}N$-labeled a-spectrin domain using 3D ^{15}N-^{13}C-^{13}C-^{15}N MAS dipolar-chemical shift correlation spectroscopy. *J. Am. Chem. Soc.* **2003**, in press.

[61]   Rienstra, C. M.; Hohwy, M.; Mueller, L. J.; Jaroniec, C. P.; Reif, B.; Griffin, R. G., Determination of multiple torsion angle-constraints in U-^{13}C, ^{15}N-labeled peptides: 3D ^{1}H-^{15}N-^{13}C-^{1}H dipolar chemical shift spectroscopy in rotating solids. *J. Am. Chem. Soc.* **2002,** 124, 11908-11922.

[62]   Ladizhansky, V.; Veshtort, M.; Griffin, R. G., NMR determination of the torsion angle Psi in alpha-helical peptides and proteins: The HCCN dipolar correlation experiment. *Journal of Magnetic Resonance* **2002,** 154, (2), 317-324.

[63]   Hong, M., Determination of Multiple Phi Torsion Angles in Solid Proteins by Selective and Extensive ^{13}C Labeling and Two-Dimensional Solid-State NMR. *J. Magnetic Reson.* **1999,** 139, 389-401.

[64]   Hohwy, M.; Jaroniec, C. P.; Lansing, J.; Rienstra, C. M.; Griffin, R. G., ^{13}C-^{1}H recoupling in the HCCH torsion angle experiment in solid-state NMR. *Chem. Phys. Lett.* **1999.**

[65]   Hong, M.; Gross, J. D.; Hu, W.; Griffin, R. G., Determination of the peptide torsion angle phi by N-15 chemical shift and C-13(alpha)-H-1(alpha) dipolar tensor correlation in solid-state MAS NMR. *Journal of Magnetic Resonance* **1998,** 135, (1), 169-177.

[66]   Hong, M.; Gross, J. D.; Rienstra, C. R.; Griffin, R. G.; Kumashiro, K. K.; Schmidt-Rohr, K., Coupling Amplification in 2D MAS NMR and its Application to Torsion Angle Determination in Peptides. *Journal of Magnetic Resonance* **1997,** 129, 85-92.

[67]   Hong, M.; Gross, J. D.; Griffin, R. G., Site-resolved determination of peptide torsion angle phi from the relative orientations of backbone N-H and C-H bonds by solid-state NMR. *Journal of Physical Chemistry B* **1997,** 101, (30), 5869-5874.

[68]   Feng, X.; Verdegem, P. J. E.; Lee, Y. K.; Sandström, D.; Edén, M.; Bovee-Geurts, P.; de Grip, W. J.; Lugtenburg, J.; de Groot, H. J. M.; Levitt, M. H., Direct determination of a molecular torsional angle in the membrane protein rhodopsin by solid-state NMR. *J. Am. Chem. Soc.* **1997,** 119, 6853-6857.

[69]   Feng, X.; Eden, M.; Brinkmann, A.; Luthman, H.; Eriksson, L.; Graslund, A.; Antzutkin, O. N.; Levitt, M. H., Direct determination of a peptide torsional angle psi by double-quantum solid-state NMR. *J. Am. Chem. Soc.* **1997,** 119, (49), 12006-12007.

[70]   Schmidt-Rohr, K., Torsion Angle Determination in Solid C(13)-Labelled Amino Acids and Peptides by Separated-Local-Field Double-Quantum NMR. *J. Am. Chem. Soc.* **1996,** 118, 7601-7603.

[71]   Stewart, G.; Young, G., *Solid Phase Peptide Synthesis.* 2nd ed.; Pierce Chemical Co.: Rockford, IL, 1984.

[72]   Macphee, C. E.; Dobson, C. M., Chemical dissection and reassembly of amyloid fibrils formed by a peptide fragment of transthyretin. *Journal of Molecular Biology* **2000,** 297, (5), 1203-1215.

[73]   Bennett, A. E.; Rienstra, C. M.; Auger, M.; Lakshmi, K. V.; Griffin, R. G., Heteronuclear Decoupling in Rotating Solids. *J. Chem. Phys.* **1995,** 103, 6951.

[74]   Morcombe, C. R.; Zilm, K. W., Chemical shift referencing in MAS solid state NMR. *Journal of Magnetic Resonance* **2003,** 162, (2), 479-486.

[75]   Tycko, R., Prospects for resonance assignments in multidimensional solid-state NMR spectra of uniformly labeled proteins. *J. Biomol. NMR* **1996,** 8, 239-251.

[76]   Tycko, R.; Antzutkin, O.; Balbach, J.; Ishii, Y.; Blanco, F.; Reed, J. In *Multiple-quantum NMR of Alzheimer's β-amyloid fibrils and other topics*, 41st Experimental Nuclear Magnetic Resonance Conference, Asilomar, CA, 2000; Asilomar, CA, 2000.

[77]   Thorn, D. C.; Meehan, S.; Sunde, M.; Rekas, A.; Gras, S. L.; MacPhee, C. E.; Dobson, C. M.; Wilson, M. R.; Carver, J. A., Amyloid fibril formation by bovine milk kappa-casein and its inhibition by the molecular chaperones alpha(s-) and beta-casein. *Biochemistry* **2005,** 44, (51), 17027-17036.

[78]   Liu, L.; Murphy, R. M., Kinetics of inhibition of beta-amyloid aggregation by transthyretin. *Biochemistry* **2006,** 45, (51), 15702-15709.

[79]   Maleknia, S. D.; Reixach, N.; Buxbaum, J. N., Oxidation inhibits amyloid fibril formation of transthyretin. *Febs Journal* **2006,** 273, (23), 5400-5406.

[80]   Aue, W.; Bartholdi, E.; Ernst, R. R., Two Dimensional Spectroscopoy. Application to Nuclear Magnetic Resonance. *J. Chem. Phys.* **1976,** 64, 2229-2246.

[81]   Ernst, R. R.; Bodenhausen, G.; Wokaun, A., *Principles of Nuclear Magnetic Resonance in One and Two Dimensions.* Clarendon Press: Oxford, 1991.

[82]   Cavanagh, J.; Fairbrother, W. J.; Palmer, A. G.; Skelton, N. J., *Protein NMR Spectroscopy: Principles and Practice.* Academic Press: San Diego, 1996.

[83]   McDermott, A.; Polenova, T.; Bockmann, A.; Zilm, K. W.; Paulsen, E. K.; Martin, R. W.; Montelione, G. T., Partial NMR assignments for uniformly (C-13, N-15)-enriched BPTI in the solid state. *Journal of Biomolecular Nmr* **2000,** 16, (3), 209-219.

[84]   Meier, B. H., Polarization Transfer and Spin Diffusion in Solid-State NMR. *Advances in Magnetic and Optical Resonance* **1994,** 18, 1-116.

[85]   Suter, D.; Ernst, R. R., Spin diffusion in resolved solid-state NMR spectra. *Phys. Rev. B* **1985,** 32, 5608-5627.

[86]   Takegoshi, K.; Nakamura, S.; Terao, T., C-13-H-1 dipolar-assisted rotational resonance in magic-angle spinning NMR. *Chemical Physics Letters* **2001**, 344, (5-6), 631-637.

[87]   Hohwy, M.; Rienstra, C. M.; Jaroneic, C. P.; Griffin, R. G., Fivefold symmetric homonuclear dipolar recoupling in rotating solids: application to double quantum spectroscopy. *J. Chem. Phys* **1999**, 110, 7983.

[88]   Baldus, M. A.; Petkova, A. T.; Herzfeld, J.; Griffin, R. G., Cross Polarization in the Tilted Frame: Assignment and Spectral Simplification in Heteronuclear Spin Systems. *Mol. Phys.* **1997**, 95, (6), 1197-1207.

[89]   Meier, B. H.; Earl, W. L., Rotational resonance. *J. Am. Chem. Soc.* **1987**, 109, 7937.

[90]   Colombo, M. G. M., B.H.; Ernst, R.R., Rotational resonance. *Chem. Phys. Lett.* **1988**, 146, 189.

[91]   Raleigh, D. P.; Levitt, M. H.; Griffin, R. G., Rotational Resonance in Solid-State Nmr. *Chemical Physics Letters* **1988**, 146, (1-2), 71-76.

[92]   Jaroniec, C. P.; Filip, C.; Griffin, R. G., 3D TEDOR NMR experiments for the simultaneous measurement of multiple carbon-nitrogen distances in uniformly ^{13}C, ^{15}N-labeled solids. *J. Am. Chem. Soc.* **2002**, 124, (36), 10728-10742.

[93]   Hohwy, M.; Rienstra, C. M.; Griffin, R. G., Band-selective homonuclear dipolar recoupling in rotating solids. *Journal of Chemical Physics* **2002**, 117, (10), 4973-4987.

[94]   Hohwy, M.; Jaroniec, C. P.; Reif, B.; Rienstra, C. M.; Griffin, R. G., Local structure and relaxation in solid-state NMR: Accurate measurement of amide N-H bond lengths and H-N-H bond angles. *Journal of the American Chemical Society* **2000**, 122, (13), 3218-3219.

[95]   Gullion, T.; Schaefer, J., Rotational-echo double-resonance NMR. *J. Magn. Reson.* **1989**, 81, 196-200.

[96]   Schwieters, C. D.; Clore, G. M., Internal coordinates for molecular dynamics and minimization in structure determination and refinement. *Journal of Magnetic Resonance* **2001**, 152, (2), 288-302.

[97]   Brunger, A. T.; Adams, P. D.; Clore, G. M.; DeLano, W. L.; Gros, P.; Grosse-Kunstleve, R. W.; Jiang, J. S.; Kuszewski, J.; Nilges, M.; Pannu, N. S.; Read, R. J.; Rice, L. M.; Simonson, T.; Warren, G. L., *Crystallography and NMR system*: A new software suite for macromolecular structure determination. *Acta Cryst.* **1998**, D54, 905-921.

Chapter 14   The Supramolecular Structure of Amyloid Fibrils formed from Transthyretin$_{105-115}$.

This chapter is based on work conducted in collaboration with Marc Caporini, at MIT, and Anthony Fitzpatrick, Cait Macphee, and Professor Christopher Dobson, in Cambridge, UK.

14.1   Introduction

Solid state NMR has been applied to elucidate the structure adopted by monomers of TTR$_{105-115}$ [1] and its amyloidogenic L111M [2] mutant at atomic resolution. These are the first high-resolution structures of amyloid fibrils solved by any technique. While informative in that respect, a structure of the monomeric unit alone is insufficient to provide a complete picture of fibril self-assembly. The self-association of monomers into amyloid fibrils has been studied by solution state NMR [3], solid state NMR [4-13] [14], electron microscopy and diffraction, [15-17] cryo-EM reconstruction [18, 19], and atomic force microscopy [20, 21], but a high resolution atomic structure has yet to emerge. Recent micro-scale x-ray diffraction studies of crystals formed from amyloid-forming peptides by Eisenberg [3, 22-24] and co-workers have provided an intriguing insight into the structural basis of amyloid assembly. However, the crystals are not themselves amyloid fibrils, and recent solid state NMR evidence [25] calls into question the structural relationship between the crystals and the fibrils formed from the same peptides.

Fibrils are difficult structural targets because they are structured on length scales ranging from the atomic to the microscopic. Fibrils themselves, as shown in Figure 14-1, are microscopic objects which are 100-200 nm wide and microns long. Peptide monomers form β-sheets, either parallel or antiparallel, which are stabilized by the canonical hydrogen bonding forces. One or more β-sheets then associate into a

563

protofilament, and the winding of protofilaments results in assembly of the microscopic

fibril (Figure 14-2).
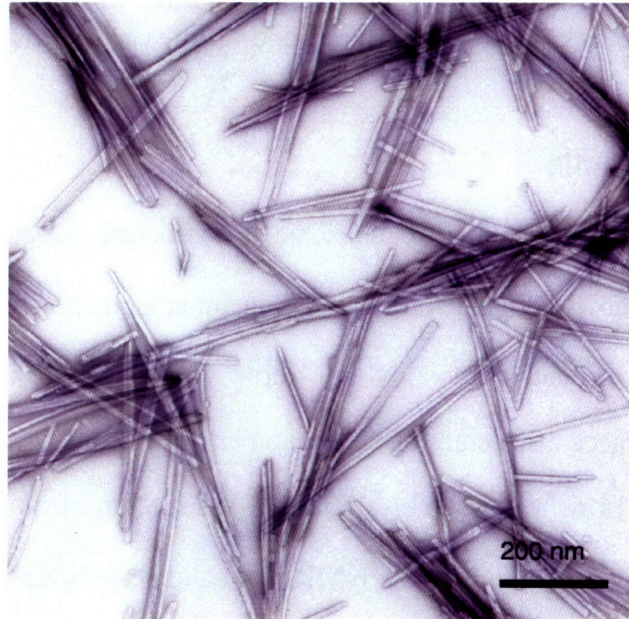
Figure 14-1: Electron micrograph (negative stain) of amyloid fibrils from $TTR_{105-115}$.
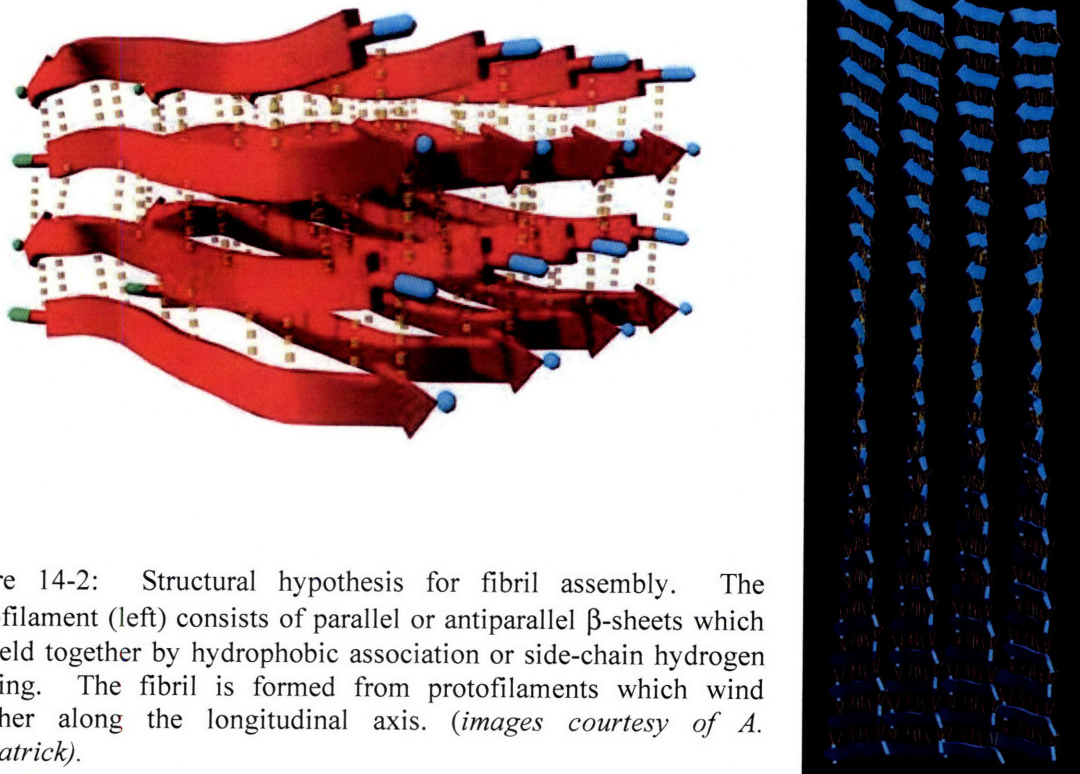
Figure 14-2: Structural hypothesis for fibril assembly. The protofilament (left) consists of parallel or antiparallel β-sheets which are held together by hydrophobic association or side-chain hydrogen bonding. The fibril is formed from protofilaments which wind together along the longitudinal axis. (*images courtesy of A. Fitzpatrick*).
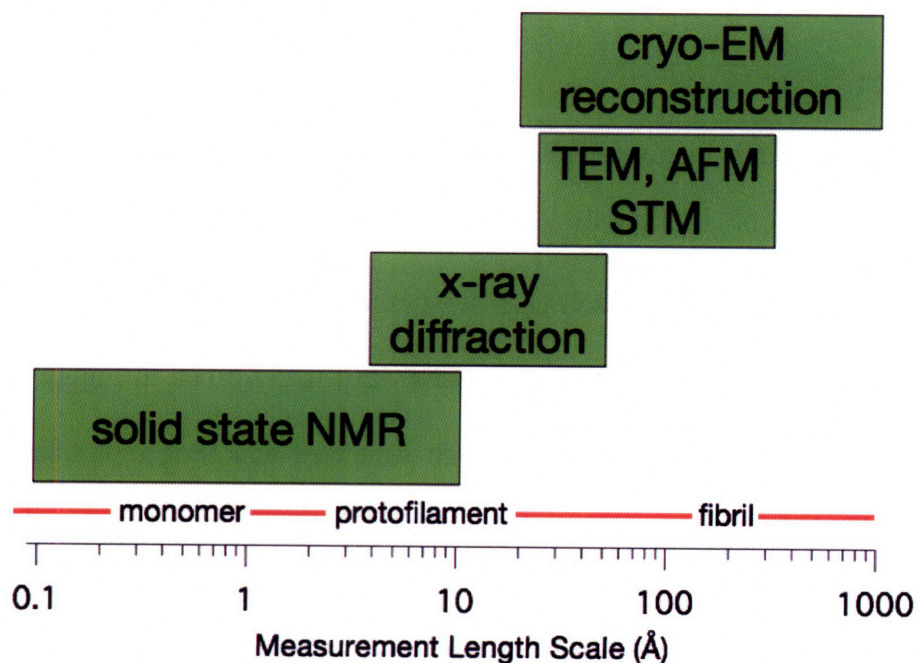
Figure 14-3: Length scale of experimental methods used in the TTR structure determination.

Solid-state NMR measurements are based on intermolecular dipolar couplings whose strength declines rapidly with the distance between interacting centers. While they effectively constrain the structure of the monomer and may provide constraints on the interaction between monomers, solid-state NMR methods cannot be extended to provide information about length scales greater than 10 Å. X-ray fiber diffraction, by contrast, provides information about periodic structural features such as the repeated spacing between monomers in a protofilament and between protofilaments, typically on the 5-50 Å length scale for amyloid fibril samples. Above 100 Å, imaging techniques such as electron microscopy and atomic force microscopy can image the fibril surface. Mass-per-unit length measurements can be obtained through quantitative STEM experiments with known mass calibration standards, such as tobacco mosaic virus. Finally, cryo-electron tomography operates on the longest length scales and can result in three-dimensional information about amyloid fibril morphology in favorable cases [18].

The length scales at which these methods yield information about fibril structure are summarized in Figure 14-3.

In principle, information from all the aforementioned structural methods can be combined to yield a complete, high-resolution structure of an amyloid fibril. A structural protocol which accomplishes the self-consistent combination of these diverse data using simulated annealing molecular dynamics in CNS [26] is described in Figure 14-4. The protofilament structure will be refined through simulated annealing molecular dynamics subject to NMR-derived distance constraints and symmetry constraints produced from fiber diffraction measurements. STEM-based mass per unit length measurements provide constraints on the number of β-sheets in a protofilament and the number of protofilaments in the transverse axis of the fibril, both of which are *a priori* inputs to the structure refinement. The resulting protofilament structure can then be used as a template to fit the electron density map resulting from cryo-EM image reconstruction. Provided that all the data are consistent, the structure that will emerge will be the first high resolution structure of an amyloid fibril. This chapter summarizes our progress towards refining this structure.
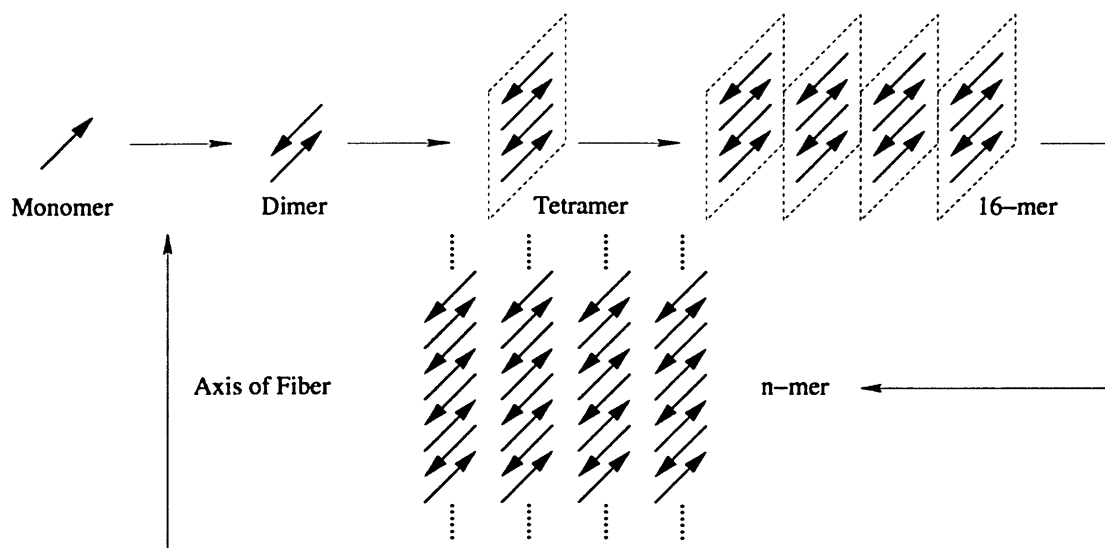
Figure 14-4: Strategy of hierarchical structure determination of TTR amyloid fibrils.

14.2   Solid State NMR Constraints on the Structure of the β-sheet

The fundamental secondary structural element of amyloid fibril structure is the β-sheet, as verified by the structure of the monomer. Adjacent β-strands assemble into β-sheets primarily through intermolecular hydrogen bonds to form an axis which is approximately perpendicular to the orientation of the side chains. Though energetically disfavored, β-strands may pack into a parallel fashion as well as an antiparallel one. In addition, as shown in Figure 14-5, the orientation of the strands in a sheet may vary: they may be exactly in register, exactly out of register, or some combination or mixture of registers. Though significant perturbations in peptide registry have been observed in at least one system [27] as a function of sample preparation conditions, this is due primarily to the presence of ionizable side chains. The lack of acidic or basic side chains in TTR suggests that the register will be fixed by hydrophobic compatibility or other forces.
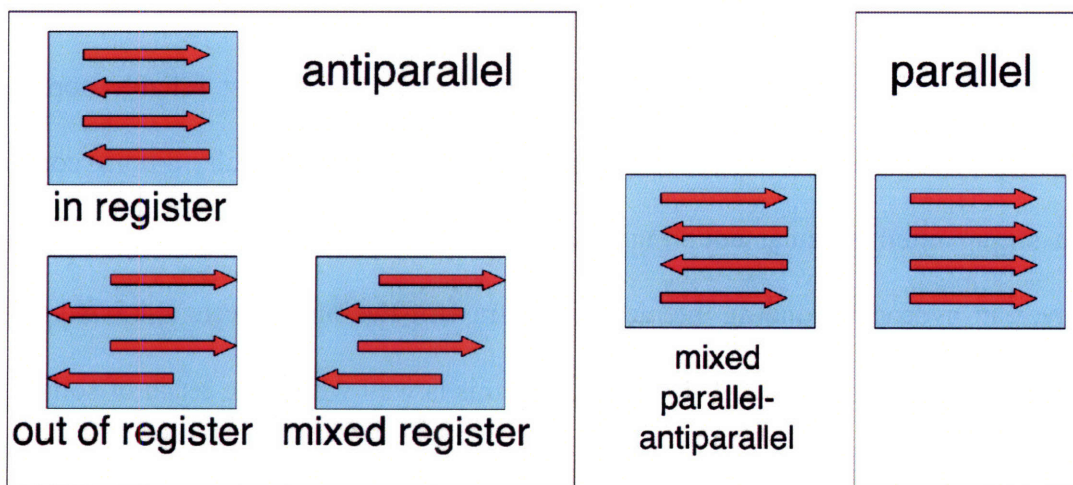
Figure 14-5: Several possibilities for β-sheet registry in amyloid fibrils.

14.2.1   Monomers are in a Single Chemical Environment

A structure of the peptide monomer is a prerequisite for refinement of a fibril structure; it also provides indirect information about the fibril topology. First, the quality of the

refined structural ensemble suggests that every β-strand in the amyloid fibril adopts the same structure. Second, each site in the monomer has a single, well-defined chemical shift and narrow resonance widths, suggesting that each monomer is also in the same chemical environment. This implies that fibril geometries which call for mixed registries are less likely; such geometries would result in multiple chemical shifts for each site or broad spectral features (*i.e.* a continuum of shifts). Further, these results demonstrate that each monomer is identically solvated and rule out fibril configurations which call for differential solvation of protofilament surface.

14.2.2   Tests of the Antiparallel Hypothesis: REDOR Experiments

Antiparallel β-sheets fulfill a greater number of backbone hydrogen bonds, and therefore they are energetically favored over parallel sheets. On the other hand, both antiparallel and parallel registries of the TTR peptide are equivalent in terms of hydrophobic complementarity. Ideal solid state NMR measurements of antiparallel sheet geometry must unambiguously probe intermolecular interactions. The most reliable approach, then, involves labeling sites that experience a very weak intramolecular dipolar coupling but a strong intermolecular coupling, such as backbone $^{13}C'$ and ^{15}N sites which are involved in hydrogen bonding interactions. X-ray diffraction suggests a 4.7 Å spacing between adjacent strands in a β-sheet [28], and this is well within the reach of solid state NMR methods designed to measure heteronuclear dipolar couplings. Rotational Echo Double Resonance (REDOR), in particular, is a well-established method for the measurement of ^{13}C-^{15}N dipolar couplings [29-36], and we have previously described its use in the context of distance measurements in the monomer. The REDOR measurements presented here make use of TPPM decoupling [37] in the evolution

periods between REDOR pulses to minimize dephasing due to relaxation [38] but otherwise do not differ from previously published techniques. As shown in Figure 14-6, inter-strand ^{15}N-$^{13}C'$ distances lie in the 3.9-5.5 Å range and can easily be probed in spin-pair labeled samples.
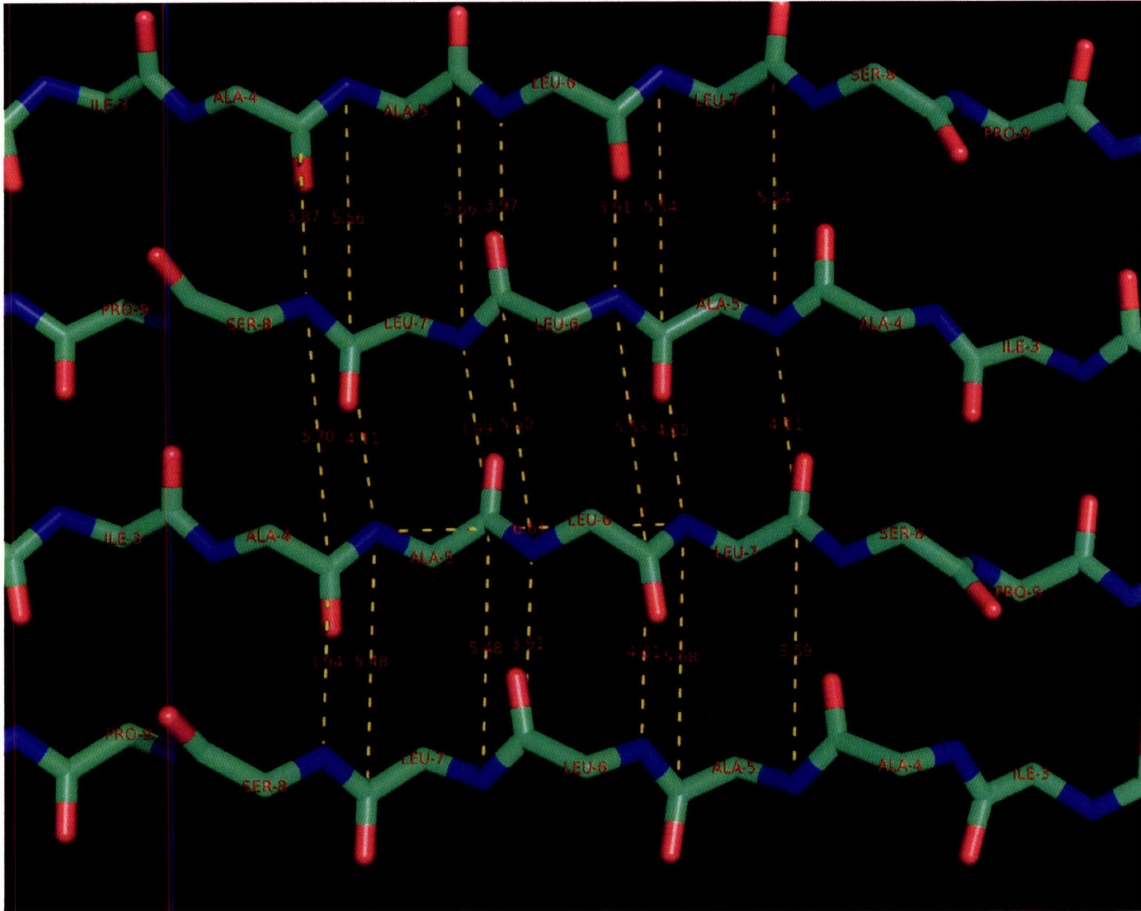
Figure 14-6: Antiparallel model of TTR$_{105-115}$ amyloid fibrils showing key backbone-to-backbone heteronuclear distances.

The expected dephasing curves for spin geometries shown in Figure 14-6 are tabulated in Figure 14-7, where an average coupling corresponding to a 4.7 Å distance has been assumed. The REDOR signals, normalized on the basis of an intrinsic reference which compensates for relaxation and for some experimental imperfections, are expected to dephase by approximately 40% at 20 ms for an spin pair in an antiparallel beta sheet

orientation. Three spin pair samples, listed in Table 14.1, were synthesized to test the antiparallel, antiparallel+1, and antiparallel-1 configurations. The results, which are illustrated in Figure 14-8 and Figure 14-9, show minimal dephasing due to REDOR and suggest that the orientations probed in these experiments do not occur in the fibril. Peptides corresponding to registry indices greater than +/- 1 were not prepared.
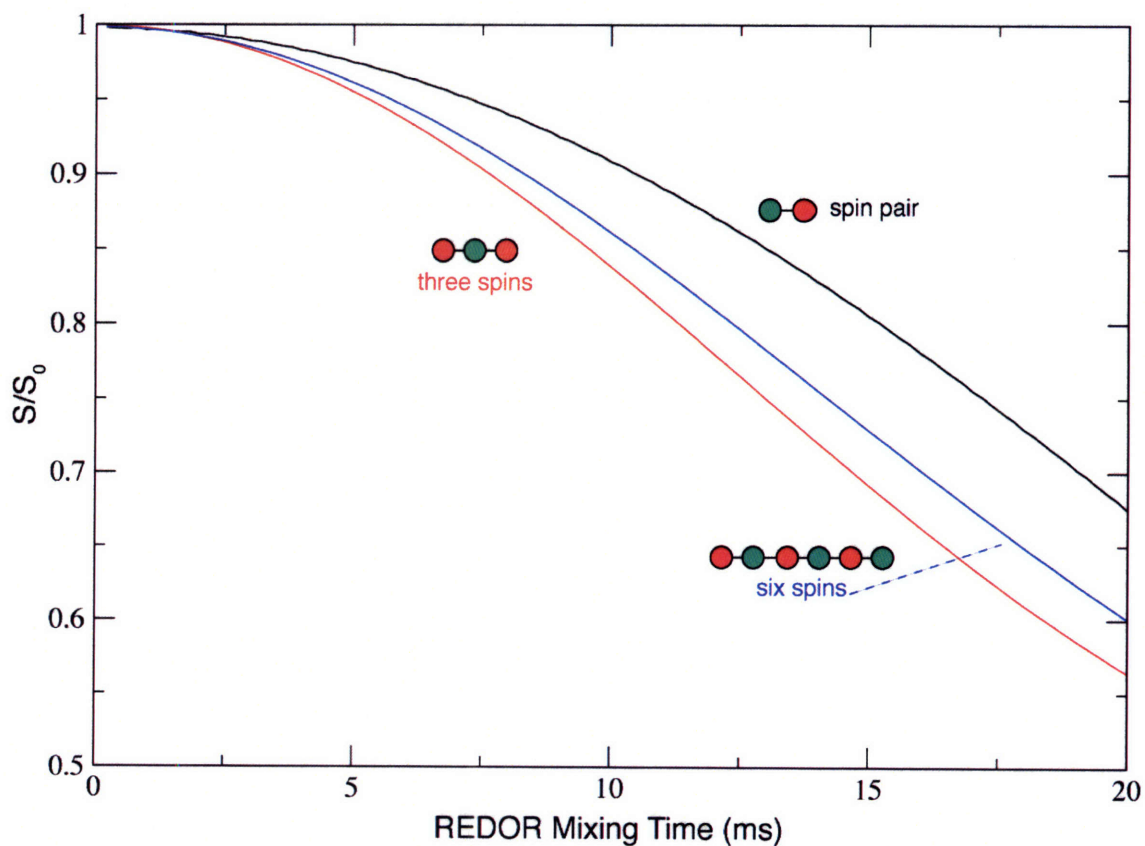
Figure 14-7: Analytical simulations of REDOR dephasing corresponding to spin geometries in TTR$_{105-115}$. (black) spin pair, 4.7 Å; (red) spin triplet, 4.7 Å; (blue) six spins, 4.7 Å.
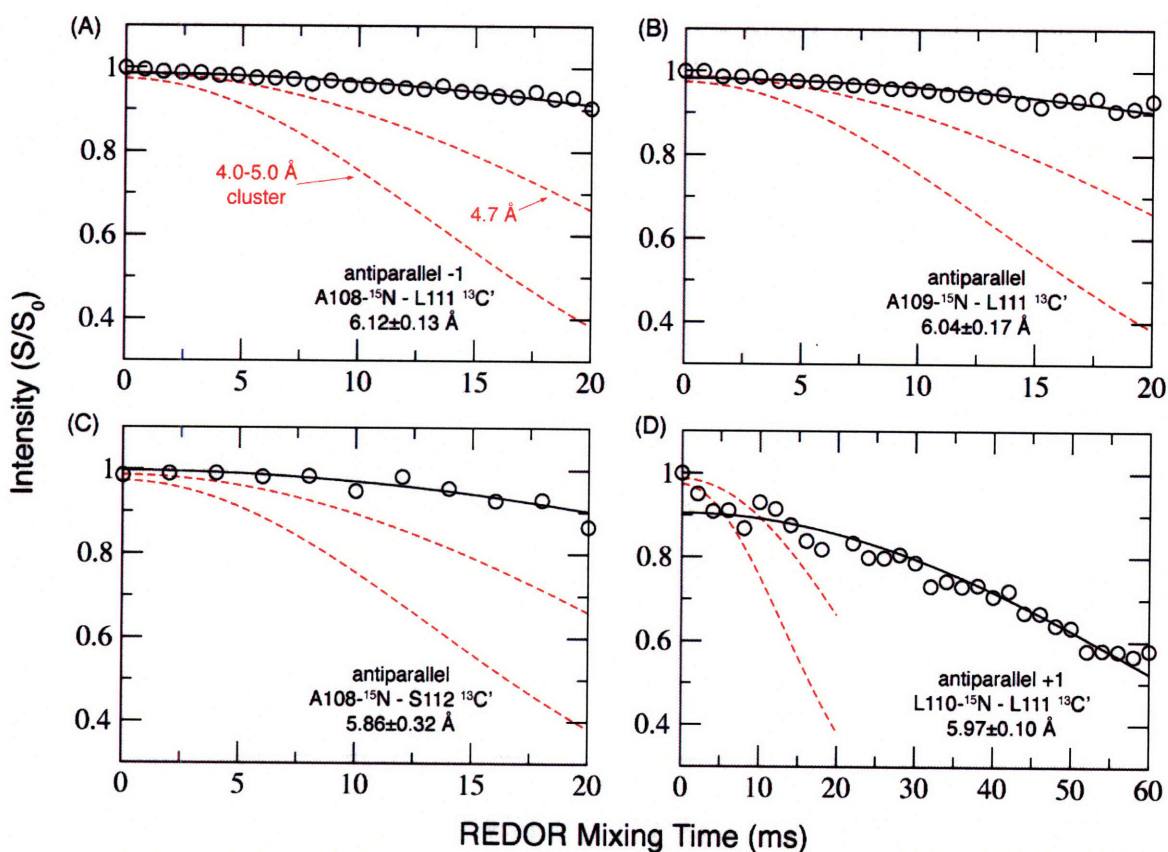
Figure 14-8: Summary of REDOR measurements designed to test the hypothesis of antiparallel β-sheet packing. The dashed red lines correspond to simulations of the dephasing in a spin pair separated by 4.7 Å and a cluster of four spins with two inequivalent distances of 4.1 Å and 5.6 Å respectively. (A) Ala108-[15]N—Leu111-[13]C', antiparallel -1 register; (B) Ala109-[15]N—Leu111-[13]C', antiparallel and in register; (C) Ala108-[15]N—Ser112-[13]C', antiparallel and in register; (D) Leu110-[15]N—Leu111-[13]C', antiparallel +1 register. The expected dephasing is not observed in these experiments.

571
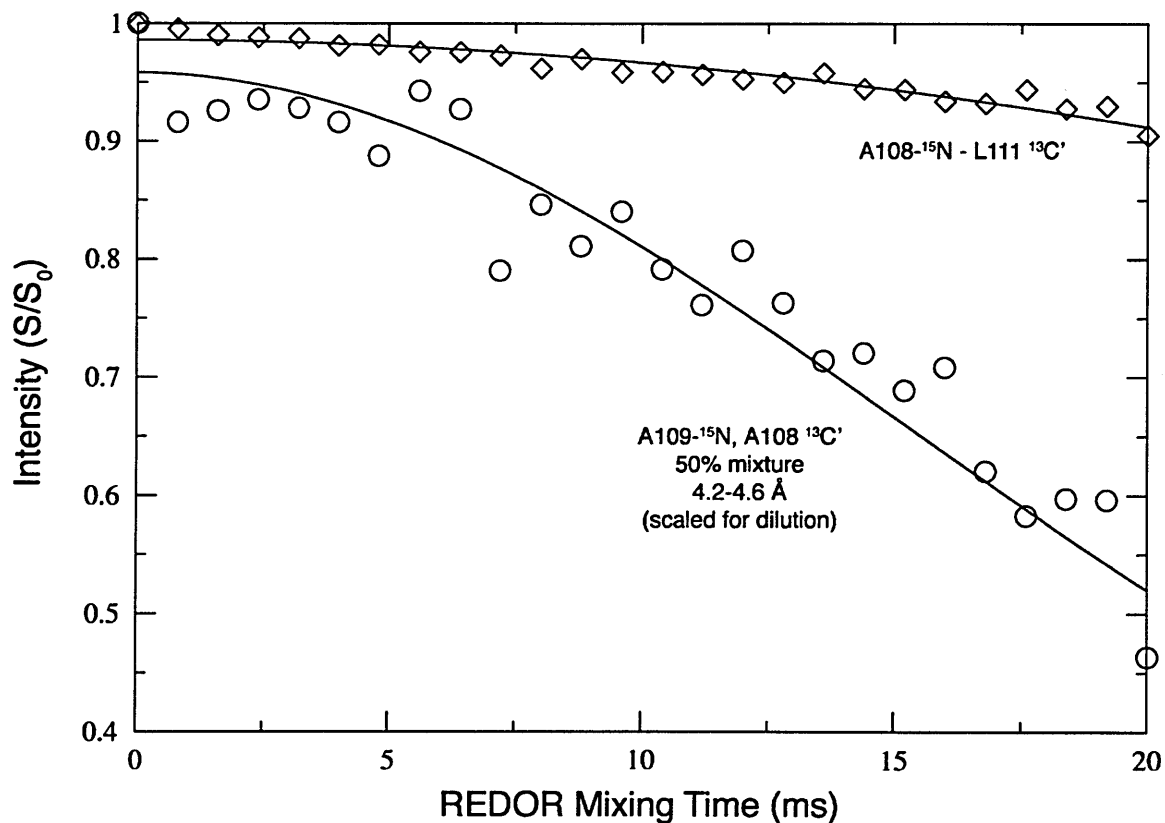
Figure 14-9: REDOR measurements in Ala108-^{15}N—Leu111-^{13}C' spin pair sample and in a mixture of Ala108-^{15}N and Ala109111-^{13}C' labeled peptides designed to probe parallel strand packing. The dephasing in the mixed sample has been adjusted to account for the 50% dilution of all intermolecular couplings. In both absolute and scaled terms, the dephasing is greater in this sample. A four-spin model with two unequal couplings fits the data in agreement with the hypothesis of parallel, in register packing, subsequently verified in other experiments (see below).

Table 14.1: Spin pair samples for intermolecular measurements in TTR amyloid fibrils. ^{15}N spins are colored blue and ^{13}C' spins red.

Parallel – In Register

$Y_{105}\ T_{106}\ I_{107}\ A_{108}\ A_{109}\ L_{110}\ L_{111}\ S_{112}\ P_{113}\ Y_{114}\ S_{115}$
$Y_{105}\ T_{106}\ I_{107}\ A_{108}\ A_{109}\ L_{110}\ L_{111}\ S_{112}\ P_{113}\ Y_{114}\ S_{115}$

Parallel – 1 Out of Register

$Y_{105}\ T_{106}\ I_{107}\ A_{108}\ A_{109}\ L_{110}\ L_{111}\ S_{112}\ P_{113}\ Y_{114}\ S_{115}$
$Y_{105}\ T_{106}\ I_{107}\ A_{108}\ A_{109}\ L_{110}\ L_{111}\ S_{112}\ P_{113}\ Y_{114}\ S_{115}$

Antiparallel – In Register

$Y_{105}\ T_{106}\ I_{107}\ A_{108}\ A_{109}\ L_{110}\ L_{111}\ S_{112}\ P_{113}\ Y_{114}\ S_{115}$
$S_{115}\ Y_{114}\ P_{113}\ S_{112}\ L_{111}\ L_{110}\ A_{109}\ A_{108}\ I_{107}\ T_{106}\ Y_{105}$
$Y_{105}\ T_{106}\ I_{107}\ A_{108}\ A_{109}\ L_{110}\ L_{111}\ S_{112}\ P_{113}\ Y_{114}\ S_{115}$

$Y_{105}\ T_{106}\ I_{107}\ A_{108}\ A_{109}\ L_{110}\ L_{111}\ S_{112}\ P_{113}\ Y_{114}\ S_{115}$
$S_{115}\ Y_{114}\ P_{113}\ S_{112}\ L_{111}\ L_{110}\ A_{109}\ A_{108}\ I_{107}\ T_{106}\ Y_{105}$
$Y_{105}\ T_{106}\ I_{107}\ A_{108}\ A_{109}\ L_{110}\ L_{111}\ S_{112}\ P_{113}\ Y_{114}\ S_{115}$

Antiparallel – +1 Out of Register

$Y_{105}\ T_{106}\ I_{107}\ A_{108}\ A_{109}\ L_{110}\ L_{111}\ S_{112}\ P_{113}\ Y_{114}\ S_{115}$
$S_{115}\ Y_{114}\ P_{113}\ S_{112}\ L_{111}\ L_{110}\ A_{109}\ A_{108}\ I_{107}\ T_{106}\ Y_{105}$
$Y_{105}\ T_{106}\ I_{107}\ A_{108}\ A_{109}\ L_{110}\ L_{111}\ S_{112}\ P_{113}\ Y_{114}\ S_{115}$

Antiparallel – -1 Out of Register

$Y_{105}\ T_{106}\ I_{107}\ A_{108}\ A_{109}\ L_{110}\ L_{111}\ S_{112}\ P_{113}\ Y_{114}\ S_{115}$
$S_{115}\ Y_{114}\ P_{113}\ S_{112}\ L_{111}\ L_{110}\ A_{109}\ A_{108}\ I_{107}\ T_{106}\ Y_{105}$
$Y_{105}\ T_{106}\ I_{107}\ A_{108}\ A_{109}\ L_{110}\ L_{111}\ S_{112}\ P_{113}\ Y_{114}\ S_{115}$

14.3 Tests of the Parallel Hypothesis: DRAWS Experiments and REDOR Experiments

The design of experiments to probe the geometry of parallel β-strands is complicated by the overlap of intermolecular and intramolecular couplings. For example, labeling ^{15}N$_i$ and ^{13}C'$_{i-1}$ sites (*e.g.* Ser112 and Pro113), which are hydrogen bonding partners, would result in an observable intermolecular coupling but a much stronger intramolecular coupling. The intramolecular coupling of a directly bonded spin pair would obscure the measurement of the weak dipolar coupling of interest. This is true even for sequences such as REDOR, which do not suffer from dipolar truncation, because the sites involved

in intermolecular and intramolecular interactions are identical and therefore have the same chemical shifts. Two alternatives are possible: first, instead of labeling the ^{15}N-^{13}C spin pair in a single sample, two samples may be prepared, each with one labeled site. Fibrils prepared from a physical mixture of these samples would then be free of intramolecular couplings, albeit at the expense of the statistical dilution of the intermolecular coupling between monomers. A second approach involves measuring homonuclear distances in a singly labeled site. As shown in Figure 14-10, the carbonyl sites have a unique topology with a regular, 4.6-4.7 Å, distance in a parallel, in register β-sheet. Because similar couplings may be manifest in an out-of-register antiparallel β-sheet (Figure 14-10), at least two measurements will be required to unambiguously establish this geometry. The L111-$^{13}C'$ and S112-$^{13}C'$ spin pair samples are suitable for this kind of measurement.

Parallel, in register 4.69-4.74 Å **Antiparallel, in register** 10.3-10.9 Å

Antiparallel, +1 7.68-7.78 Å **Antiparallel, +2** 4.87-6.61 Å
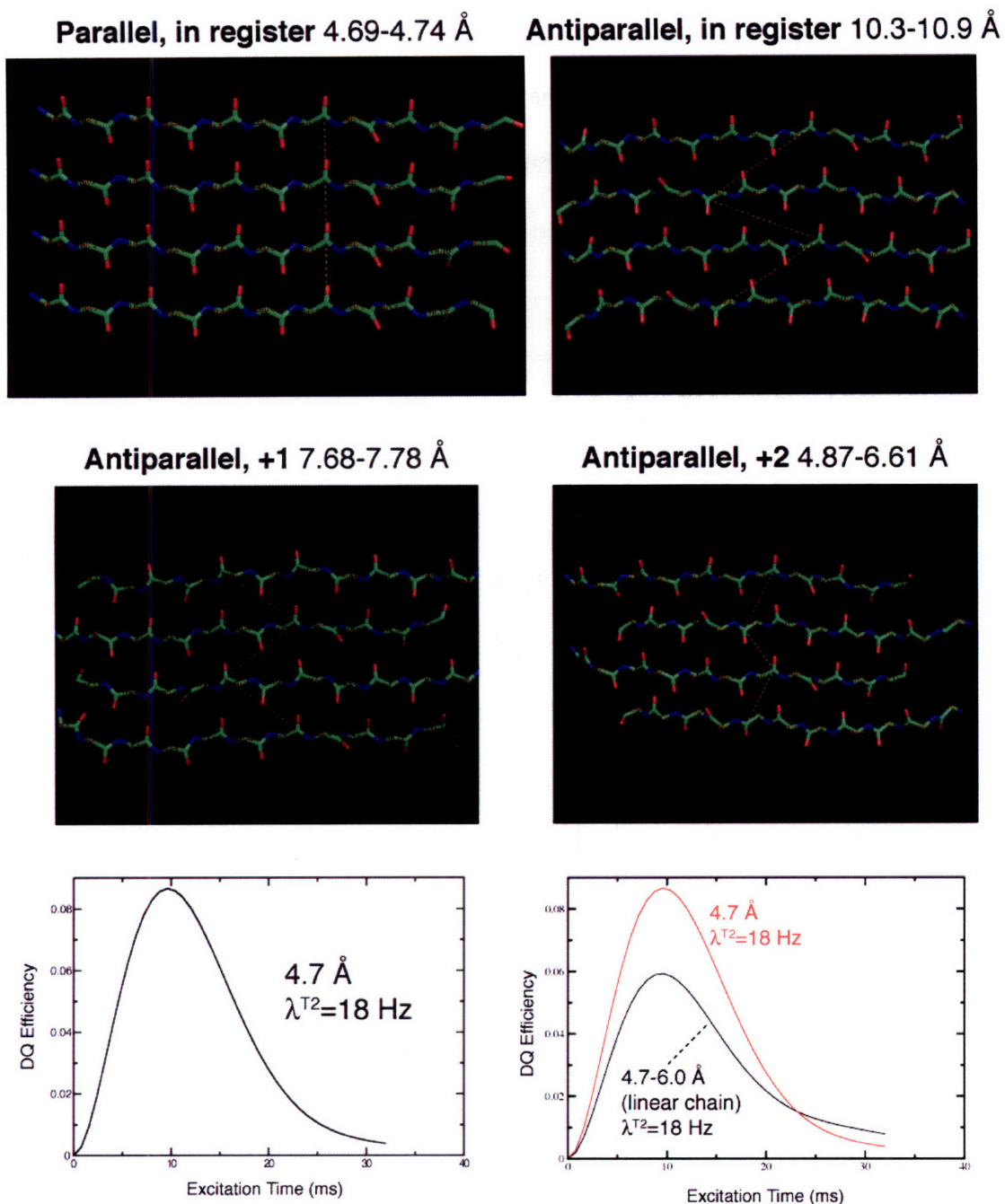
Figure 14-10: Peptide geometry corresponding to parallel β-sheet packing. Note that antiparallel+2 and antiparallel+3 packing produces some carbonyl-carbonyl distances which are similar to those in a parallel strand. (below) DQ DRAWS spin dynamics for spin geometries found in TTR.

Several recoupling sequences have been applied for homonuclear distance measurements between spins of degenerate chemical shift. The finite-pulse RFDR zero-quantum (ZQ) recoupling sequence has been applied at high MAS frequencies and in a constant-time

implementation (which produces a static dipolar Hamiltonian) by Tycko and co-workers [39] for homonuclear distance measurements in multispin systems. This approach has the advantage of being applicable at arbitrary MAS frequencies. Instead, we have chosen to investigate approaches based on double quantum (DQ) spin pair filters. While SPC5 [40] and other γ-encoded DQ recoupling sequences based on C7 symmetry are effective as mixing sequences in assignment experiments, they suffer from reduced efficiency for the case of weak dipolar couplings in the presence of the chemical shift anisotropy [41] [42]. Sequences based on $R22^9_4$ symmetry have been applied by Levitt and co-workers [43] [44] for homonuclear distance measurements in systems with large CSAs; however, this family of sequences is known to be extremely sensitive to experimental artifacts such as spectrometer phase errors and switching transients. The DRAWS sequence [41, 45, 46] has been frequently used in this application, has reduced sensitivity to the CSA, and is less sensitive to experimental artifacts. In spite of its high RF field requirement of 8.5 times the MAS frequency, DRAWS can be successfully applied to homonuclear distance measurements in singly labeled samples at low magnetic fields.

In order to minimize the RF requirements and minimize the contribution of the CSA, we conducted all DRAWS measurements at 360 MHz ($\omega_r/2\pi = 5.882$ kHz, $w_{RF}{\sim}50$ kHz, $\omega_{TPPM} = 83\text{-}125$ kHz). Previous studies have involved analytical simulations incorporating phenomenological transverse relaxation of the observed signal [41, 47] for data fitting. However, numerous investigators [48, 49] [50-52] and our previous work on this subject [53] demonstrate the importance of multi-quantum relaxation parameters in solid state NMR distance measurements. Further, the spin topologies involved in TTR measurements require simulation of coupled spin networks, which is analytically

576

difficult. For these reasons, our data analysis involves an exact numerical treatment of the spin dynamics in the program SPINEVOLUTION [42]. Since the CSA is known to contribute to MQ relaxation effects [51], the simulations explicitly include the experimentally determined CSA. In order to further investigate the validity of this model, we recorded DQ DRAWS trajectories in a dicarboxylic acid model compound as a function of the decoupling field, as shown in Figure 14-13. At different decoupling field strengths, the data are fit with an identical dipolar coupling but with unique transverse relaxation parameters, suggesting that the effects of insufficient decoupling and similar experimental imperfections are effectively modeled by this treatment. We note that the best-fit distance of 3.76 Å, while significantly shorter than the crystallographic distance of 3.91 Å, agrees with previously reported solid state NMR measurements of this compound with DRAWS and the $SR22_4^9$ recoupling sequence [41].

Simulations of linear spin topologies are shown in Figure 14-11, where it is apparent that the simulated DQ DRAWS trajectories do not converge as a function of the number of spins, particularly at long mixing times. In the cross-β model for amyloid structure, the β-sheets extend along the axis of the fibril, which we assume to be longer than the NMR length scale. Thus, the spin dynamics can be approximated by a periodic boundary condition which renders all spins in the cluster equivalent. Simulations of spin chain geometries, shown in Figure 14-12, rapidly converge in the initial rate regime (< 10 ms) and show reduced dependence on the simulation geometry at long mixing times. Thus, we anticipate that this approximation will be an effective treatment of the spin dynamics in the initial rate regime, while the build-up at longer mixing times may depend on the precise details of the fibril topology. Expected DQ DRAWS build-up trajectories

577

for spin topologies corresponding to various parallel β-sheet registries are shown in Figure 14-14.
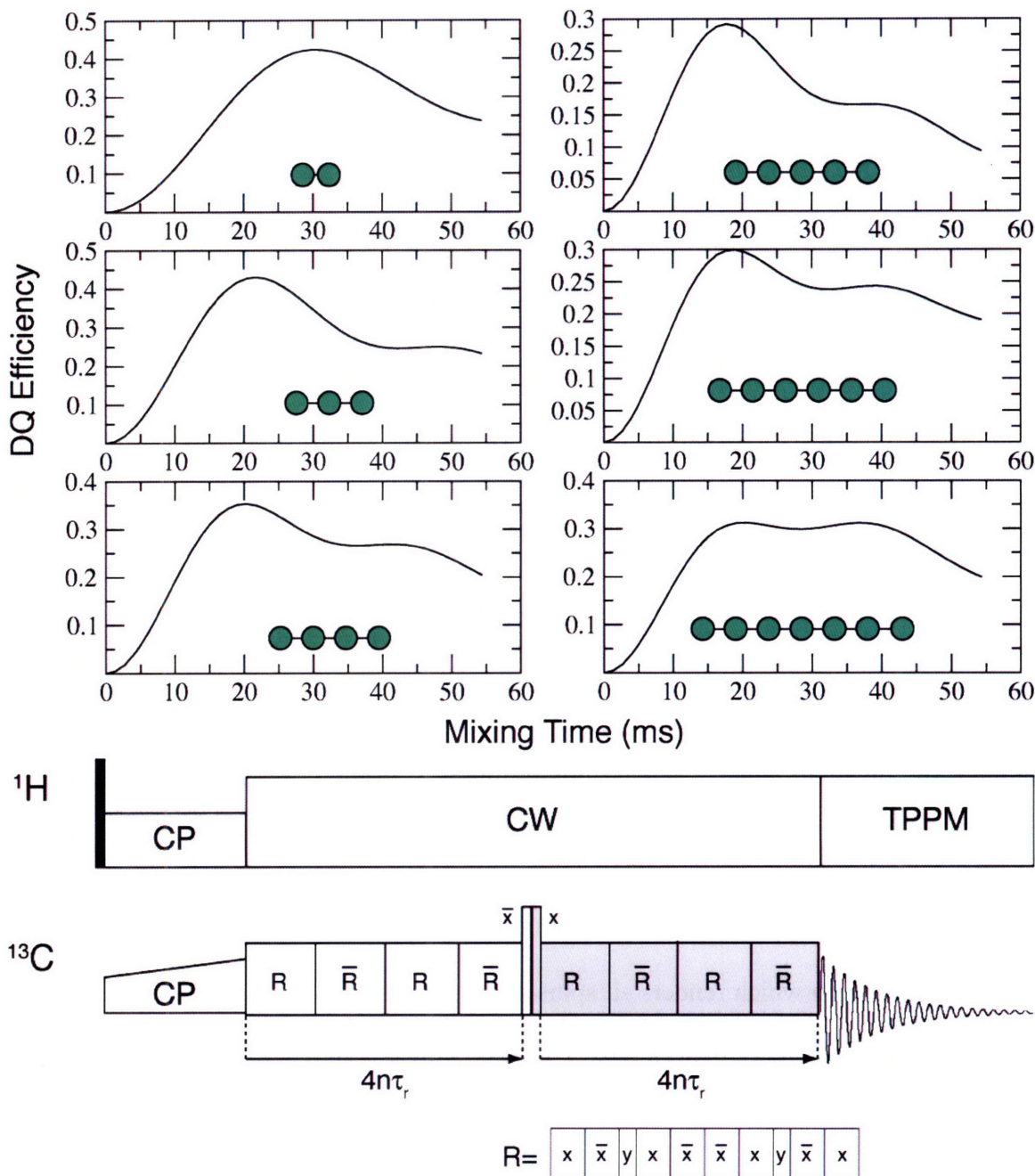

Figure 14-11: Numerical simulation of DQ DRAWS experiment in linear spin clusters with a topology similar to that of a parallel β-sheet. Note the lack of convergence as a function of the number of spins. No T_2 relaxation has been included in these simulations, but the CSA is explicitly included. (bottom) the DQ DRAWS pulse sequence used in these experiments.
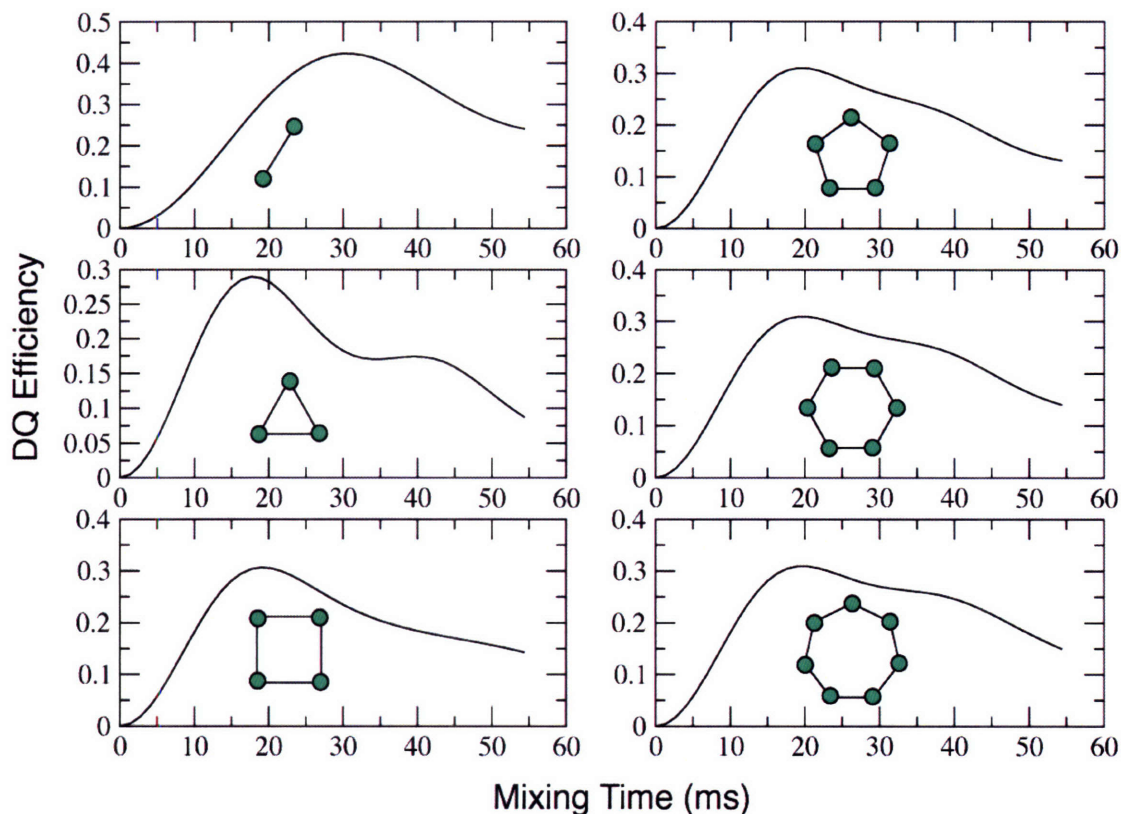
Figure 14-12: Numerical simulation of DQ DRAWS experiment in clusters of spins with a periodic boundary condition that renders all spins equivalent. The simulations rapidly converge in the initial rate regime (< 10 ms). No T_2 relaxation has been included in these simulations, but the CSA is explicitly included.
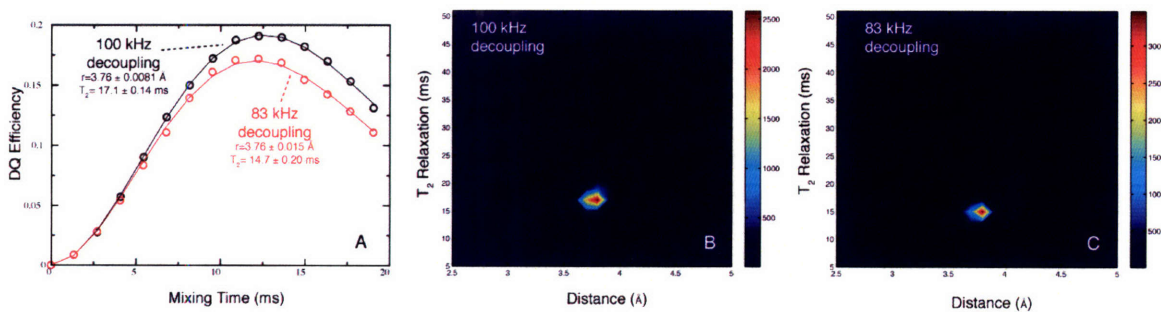
Figure 14-13: The dependence of DQ DRAWS efficiency on CW decoupling power during the mixing. Because damping of DQ coherences by CSA-induced dynamics is implicitly accounted for in the numerical simulations, the experimental model contains only a single transverse relaxation parameter. The model results in an unambiguous fit of the distance and the relaxation parameter.
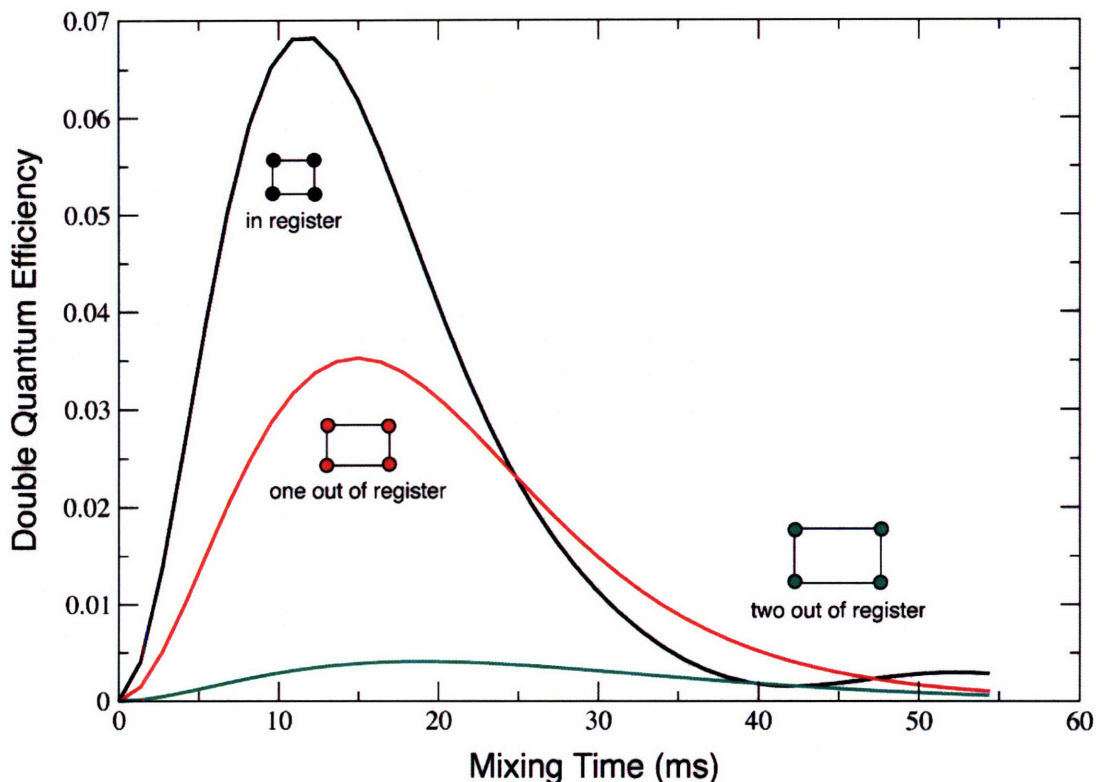
Figure 14-14: Expected DQ DRAWS build-up trajectory for spin geometries corresponding to parallel, parallel+1, and parallel+2 β-sheets. Note that out of register parallel β-sheets have inequivalent sets of intermolecular couplings which have been included in this simulation. T_2=15ms, 360 MHz ^{1}H, 5.882 kHz MAS. The maximum filtering efficiency will vary depending on the magnitude of the T_2 relaxation, which is expected to be stronger in the amyloid fibril than in succinate (succinate parameters were used here).

The experimental DQ DRAWS curves are shown for several compounds in Figure 14-15. The model compound 1,4-^{13}C-Succinate, with a crystallographically determined internuclear distance of 3.9 Å, is fit with a distance of 3.81 Å and agrees with numerical simulations over the entire range of the exchange curve. Two TTR samples – L111 ^{13}C' and S112 ^{13}C' – result in DQ DRAWS curves which are fit, using a cluster of four spins with periodic boundary conditions, to 4.5±0.1 Å and 4.48 ±0.06 Å, respectively, where the errors represent random errors and do not take into account possible systematic errors. These couplings and exchange trajectories are most consistent with a parallel, in-register arrangement of the monomers to form β-sheets in the amyloid fibril. For self-consistency,

it will be useful to confirm these measurements with REDOR experiments in diluted samples. An example of such a measurement in a sample made from a mixture of A108-^{13}C' labeled and A109-^{15}N-labeled peptide is shown in Figure 14-16. Adjusting for the 50% dilution of intermolecular dipolar couplings, the distance between the two labeled sites fits to 4.22-4.7Å, which is also consistent only with a parallel, in-register β-sheet. Thus, all experimental DQ DRAWS and REDOR data are consistent with this topology.
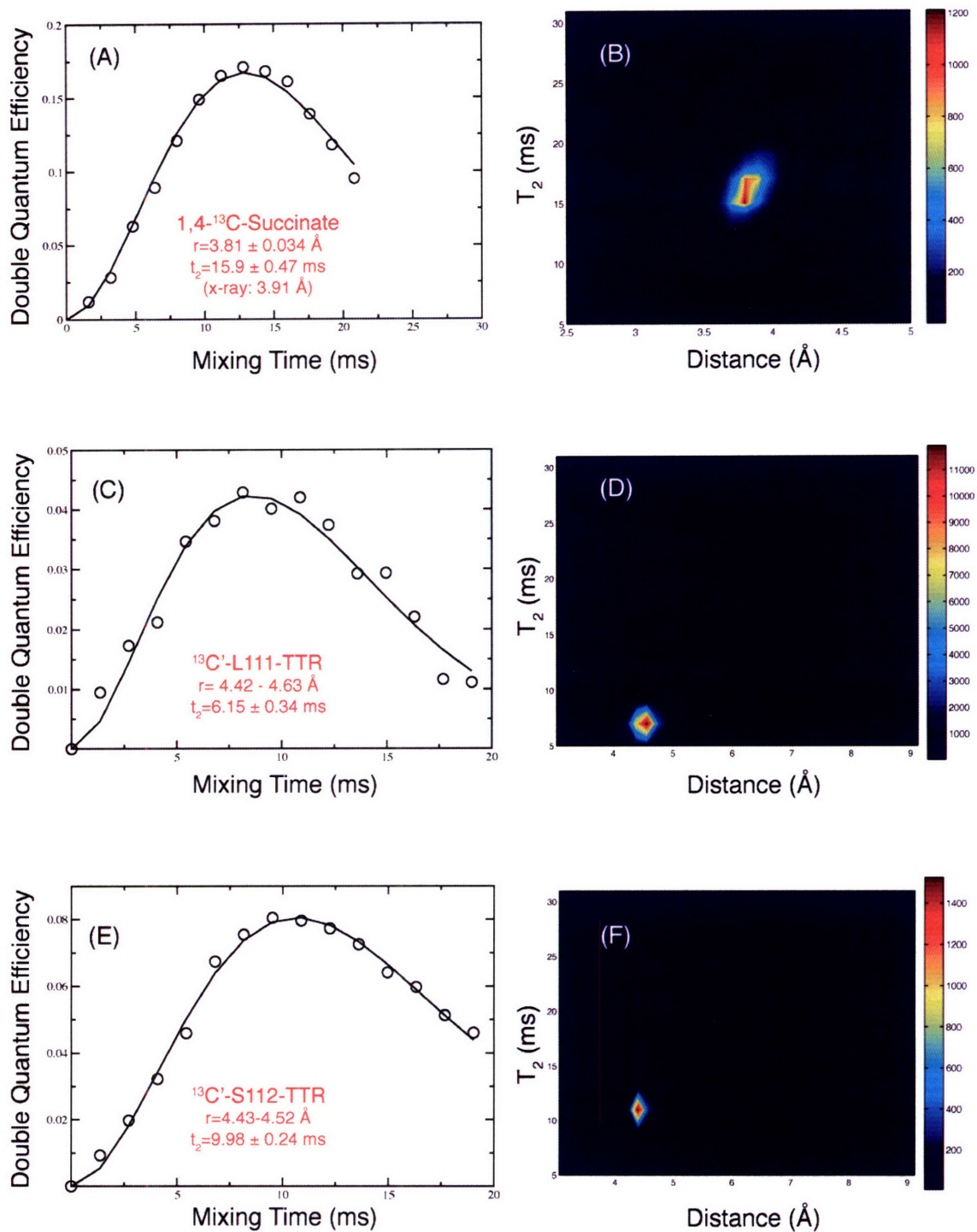
Figure 14-15: DQ DRAWS experimental data, theoretical fits, and probability surfaces for (a,b) 1,4-^{13}C-succinate model compound, fit using a two-spin numerical model with literature values for the CSA; (c,d) L111-^{13}C' TTR$_{105-115}$, fit (solid line) using a four-spin model incorporating a periodic boundary condition (~83 kHz decoupling); (e,f) S112-^{13}C' TTR$_{105-115}$ fit in the same way (~105 kHz decoupling).
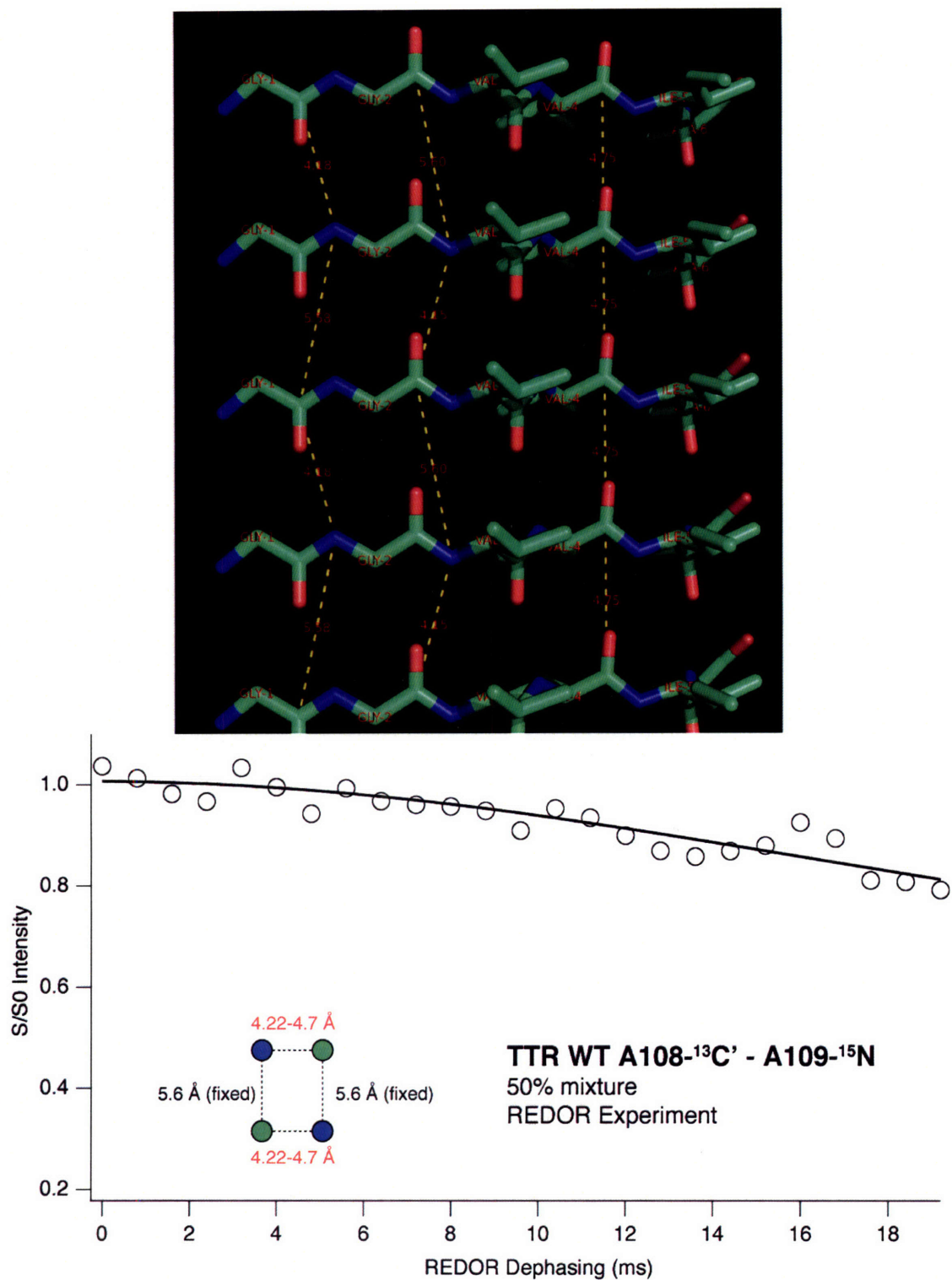
Figure 14-16: (top) Intermolecular distances in dry-GGVVIA crystal structure of Eisenberg and co-workers; (bottom) REDOR experiment in 50% mixture of A108-[13]C' and A109-^{15}N-labeled WT TTR.

14.4 Solid State NMR Constraints on the Structure of the Protofilament

While the structure of the β-sheet is best probed through interactions between sites labeled on the backbone of adjacent monomers, the protofilament architecture can only be probed through side-chain interactions. This is because the spacing between β-sheets in the protofilament is greater than 10 Å, as confirmed by x-ray diffraction measurements. The spectral regions corresponding to aliphatic side chains are spectrally resolved, unlike the $^{13}C'$ region. Thus, it is possible to probe these interactions in multiply labeled samples. Such measurements provide a higher density of constraints as compared to those in spin pair samples. As illustrated in Figure 14-17, two samples were initially prepared for this type of measurement, both corresponding to the hypothesis of an antiparallel spin-spin coupling. Five experimental approaches were applied to these samples: (1) Heteronuclear distance measurements with 3D TEDOR [54]; Homonuclear distance measurements with (2) CHHC [55], (3) DARR [56], (4) R^2TR and R^2W [57, 58], (5) quasi-adiabatic HORROR experiments. A subset of these experiments is described here.

1. $Y_{105}T_{106}I_{107}A_{108}A_{109}L_{110}L_{111}S_{112}P_{113}Y_{114}S_{115}$ TTR$_{105-115}$ WT

2. $Y_{105}T_{106}I_{107}A_{108}A_{109}L_{110}L_{111}S_{112}P_{113}Y_{114}S_{115}$ TTR$_{105-115}$ WT
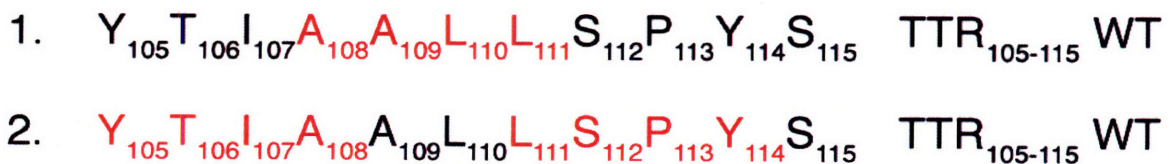
Figure 14-17: Samples for intermolecular measurements of protofilament architecture in TTR$_{105-115}$.

14.4.1   Measurements Based on Spin Diffusion

Magnetization exchange between protons or magnetization exchange between ^{13}C sites mediated by their interactions with nearby ^{1}H sites (proton-driven spin diffusion) are semi-quantitative indicators of internuclear proximity.   They have been applied extensively for the elucidation of intermolecular complexes [59, 60] and, recently, for structure determination in microcrystalline proteins [61, 62].   The application of the CHHC [1]H-^{1}H magnetization exchange experiment to AALL, shown in Figure 14-18, reveals Ala-Hα-Leu-Hα cross peaks which are likely intermolecular in origin.   In an antiparallel β-sheet, the Hα-Hα distance approaches 2.25 Å, while, in a parallel sheet, the Hα-Cα distance is ~3.1 Å; the corresponding intramolecular distance is 4.3 Å.   A separate control experiment in a YTIA-labeled sample demonstrates that no intramolecular crosspeaks are observed at this mixing time, as do internal controls in this sample (*e.g.* lack of Leu Hβ–Ala-Hα cross peaks).   The presence of these crosspeaks is thus most consistent with parallel or antiparallel configuration of the amyloid fibrils which is, at most, +/-1 out of register.   The measurements also illustrate some features of experiments based on spin diffusion: namely, while it is possible to quantitatively interpret spin diffusion exchange trajectories, the analysis requires numerical simulations of the nearby spin geometry, typically including 7-9 spins (Veshtort, private communication).   Exact numerical simulations are therefore computationally infeasible unless the exact spin geometry is known *a priori*.   Analytical approaches for the approximate simulation of spin diffusion have been developed but have not yet been explored here [55].
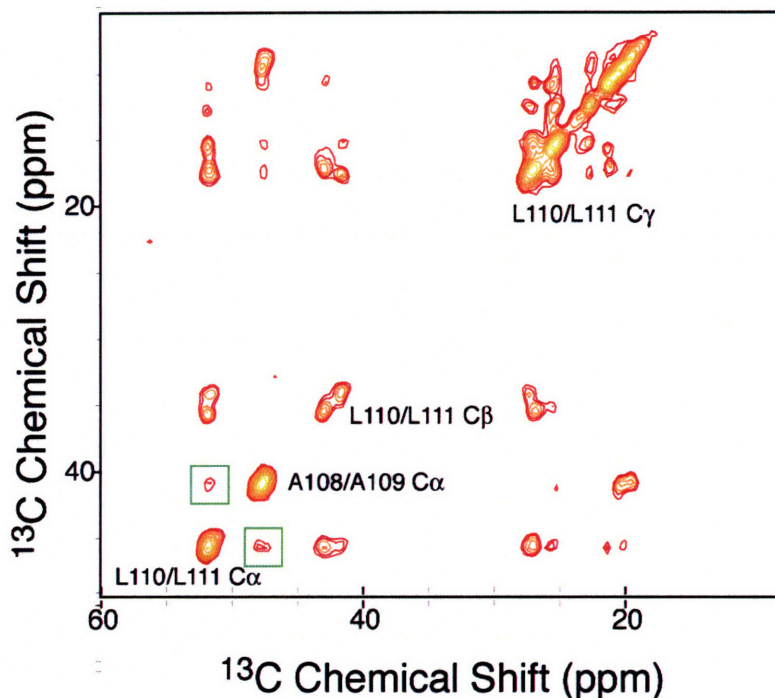
Figure 14-18: 2D plane of CHHC experiment conducted in AALL-labeled TTR sample.

Instead of these approaches, we have elected to perform experiments in a sample labeled so that all interesting cross peaks are unambiguously intermolecular. While it is possible to probe interfaces by specific labeling of one binding partner with ^{13}C and the other with ^{15}N, such a labeling pattern would result in dilution of intermolecular couplings in this system. Instead, we probed the antiparallel protofilament packing hypothesis in a sample that was uniformly labeled at the N and C-termini (Figure 14-17). Irrespective of the experiment, any magnetization exchange between the labeled "YTIA" and "LSPY" segments of the peptide is therefore intermolecular. Proton-driven spin diffusion experiments (DARR-type) are illustrated in Figure 14-19 and Figure 14-20. At short mixing times, only intramolecular cross peaks appear; at longer mixing times, however, intramolecular cross peaks are clearly visible. Approximately 15-20 intermolecular cross peaks have been observed in this experiment. While efforts to quantify them are

underway, they can be classified as between 3-6 Å by using known intramolecular couplings as an internal calibration, following procedures used by other investigators [62]. The results, analyzed in Figure 14-21, are most consistent with an antiparallel interface between β-sheets in the protofilament. A quantitative analysis of the cross peak intensities which takes into account the possibility of relayed transfer is underway and may result in improved differentiation of the conformational possibilities.
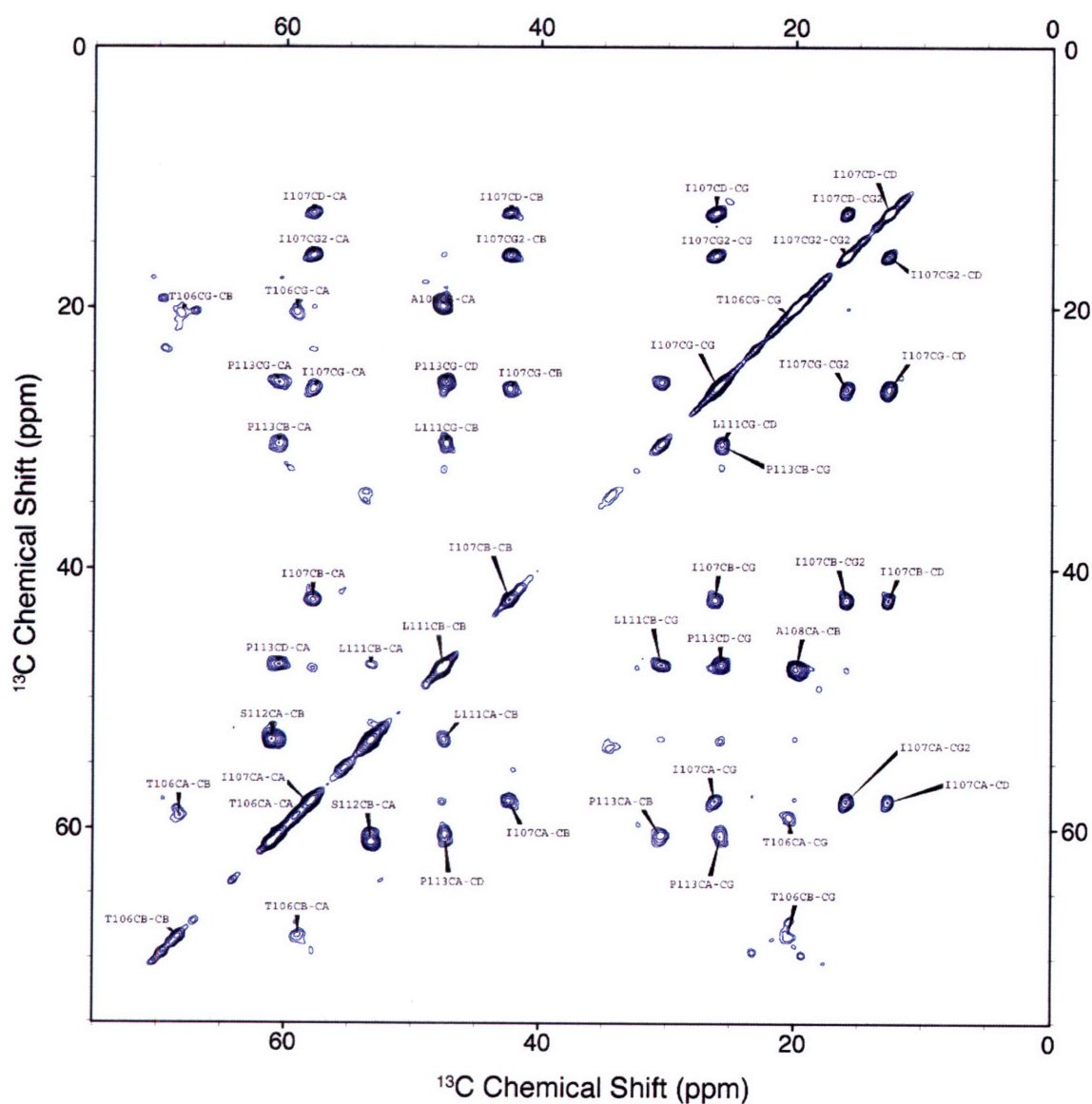
Figure 14-19: 2D plane of 3D DARR experiment corresponding to 25 ms mixing time in YTIA—LSPY TTR$_{105-115}$ sample. All cross peaks are intramolecular.
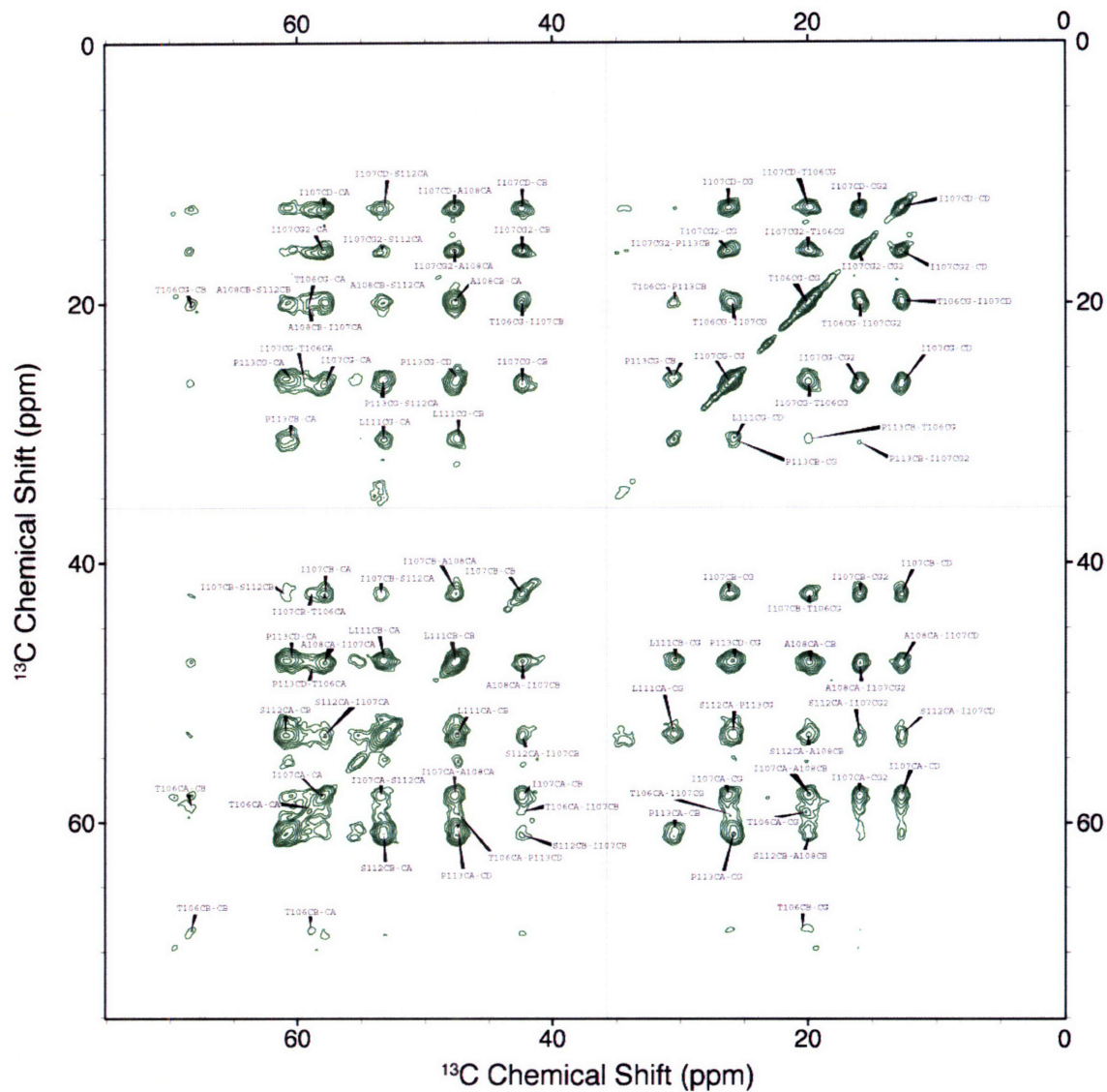
Figure 14-20: 2D plane of 3D DARR experiment corresponding to 250 ms mixing time in YTIA—LSPY TTR$_{105-115}$ sample. Many intermolecular cross peaks emerge at long mixing times.
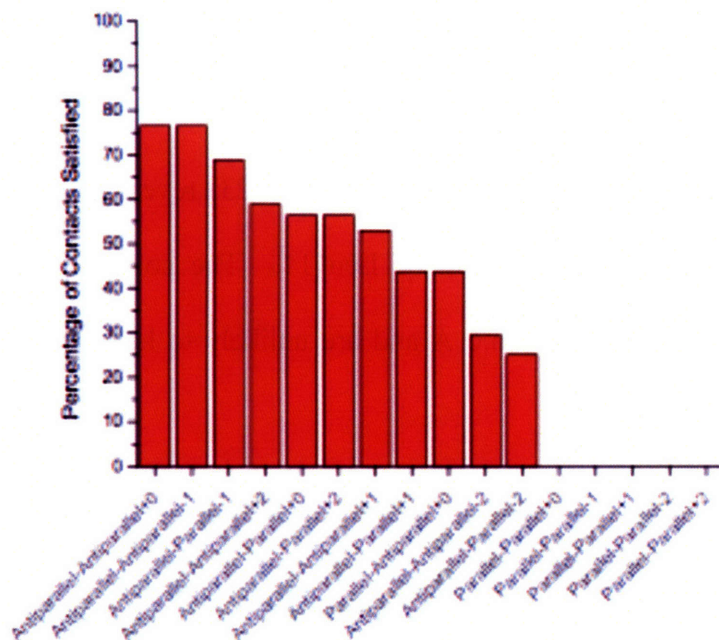
Figure 14-21: Consistency of DARR results with preliminary family of TTR models (*courtesy of A. Fitzpatrick*).
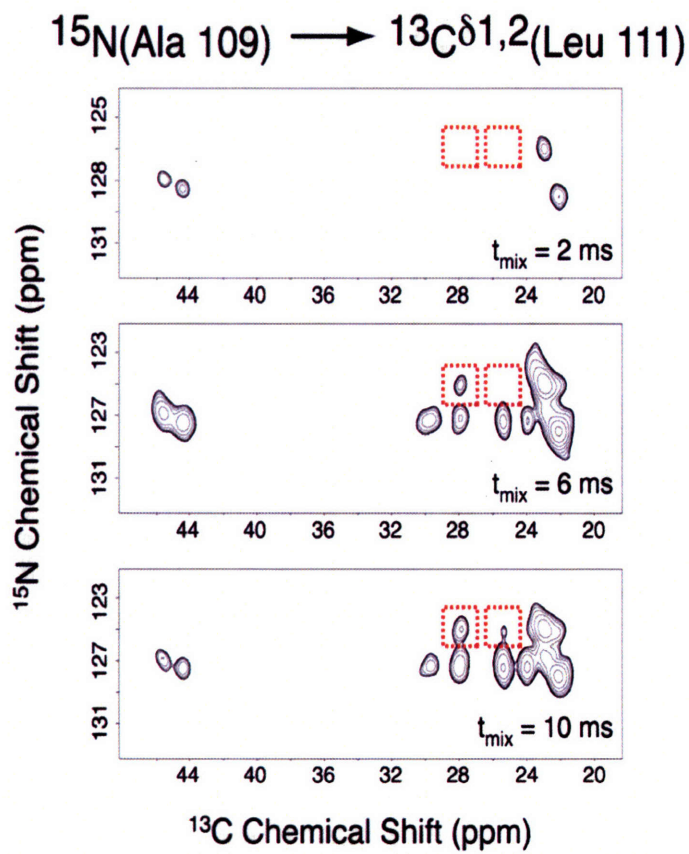
Figure 14-22: 3D TEDOR experiment in AALL-labeled sample which demonstrates intermolecular cross peaks that report on the protofilament packing geometry.

Several other structural measurements are also consistent with an antiparallel packing of β-sheets in the protofilament. 3D TEDOR and R^{2}TR experiments in the AALL labeled sample (Figure 14-22 and Figure 14-23) reveal cross peaks between the Ala108 backbone and the side chain of Leu111. The corresponding intramolecular distances lie in the range of 5.9-6.6 Å and are unlikely to have been detected in these experiments.
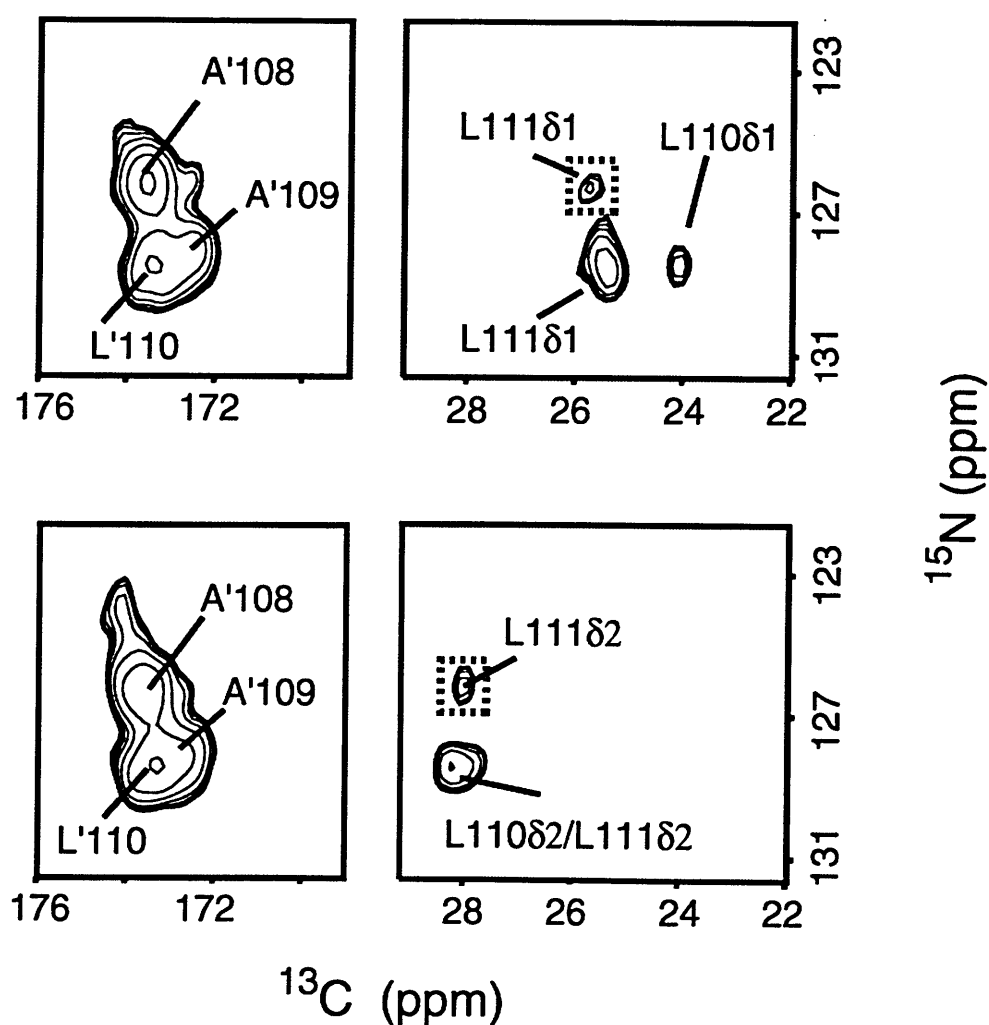
Figure 14-23: 3D R^{2}TR experiment in AALL-labeled sample which demonstrates intermolecular cross peaks that report on the protofilament packing geometry.

The ^{15}N-^{13}Cδ1 and ^{15}N-^{13}Cδ2 distances are fit to 4.1 Å and 5.2 Å, respectively, while the ^{13}C'-^{13}Cδ1,2 distances fit to 4.3-5.4 Å. As shown in Figure 14-24 and Figure 14-25, these distances are expected to lie in the 4.5-4.8 Å range for in-register, antiparallel sheet-sheet packing. The corresponding ^{15}N-^{13}Cδ1 distances lie in the range 5.2-5.6 Å ^{13}C'-^{13}Cδ1,2 for a parallel sheet-sheet packing, while the ^{13}C'-^{13}Cδ1,2 distances are 4.9-5.2 Å. Because these distances may change as a function of the peptide registry, we cannot use a single distance alone to rule out parallel packing of the interface. However, antiparallel packing is most consistent with the totality of information. Similar constraints have been observed between the A108N backbone and M111 side chain of the L111M mutant of TTR.
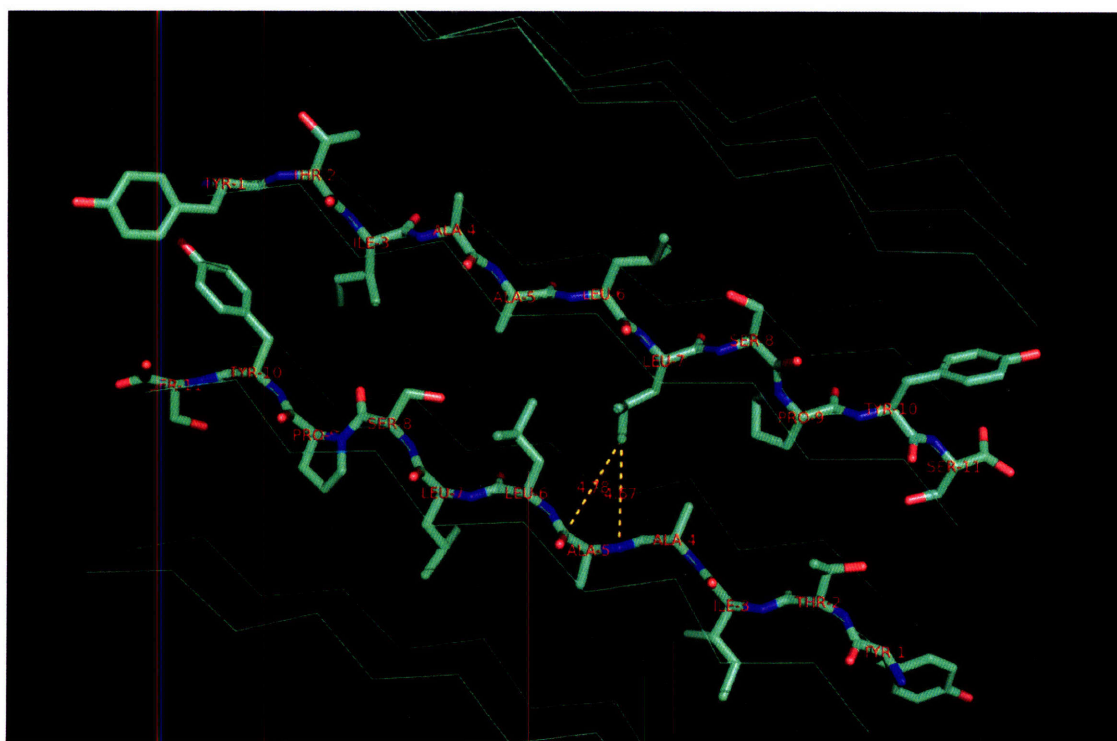
Figure 14-24: Distances between A108 backbone and L111 side chain in antiparallel-antiparallel configuration of TTR amyloid fibrils.
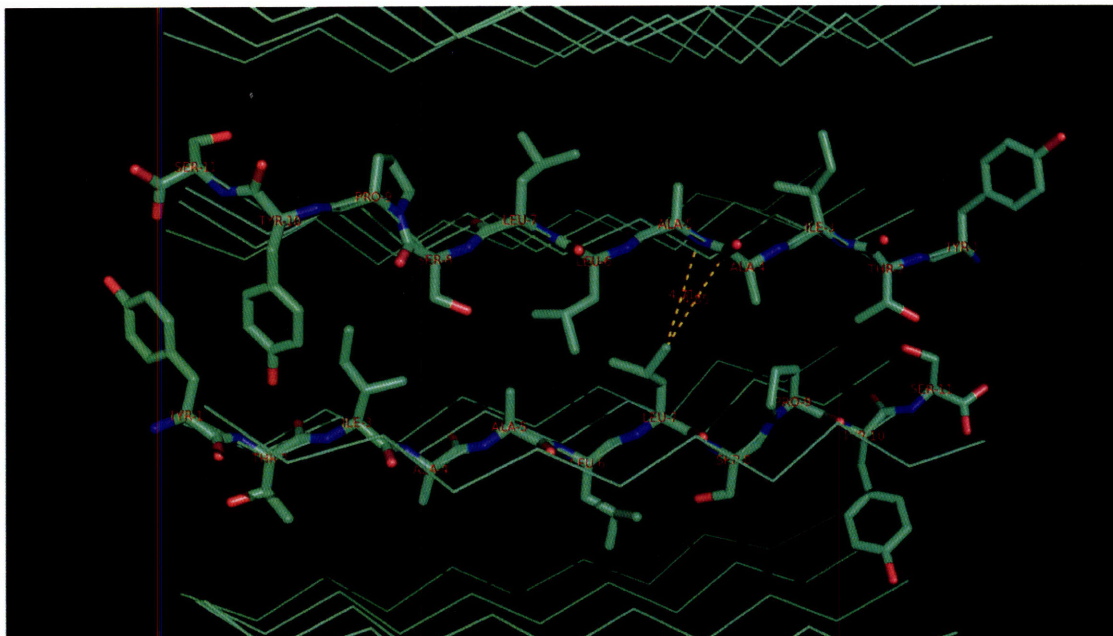
Figure 14-25: Distances between A108 backbone and L111 side chain in parallel-antiparallel configuration of TTR amyloid fibrils.
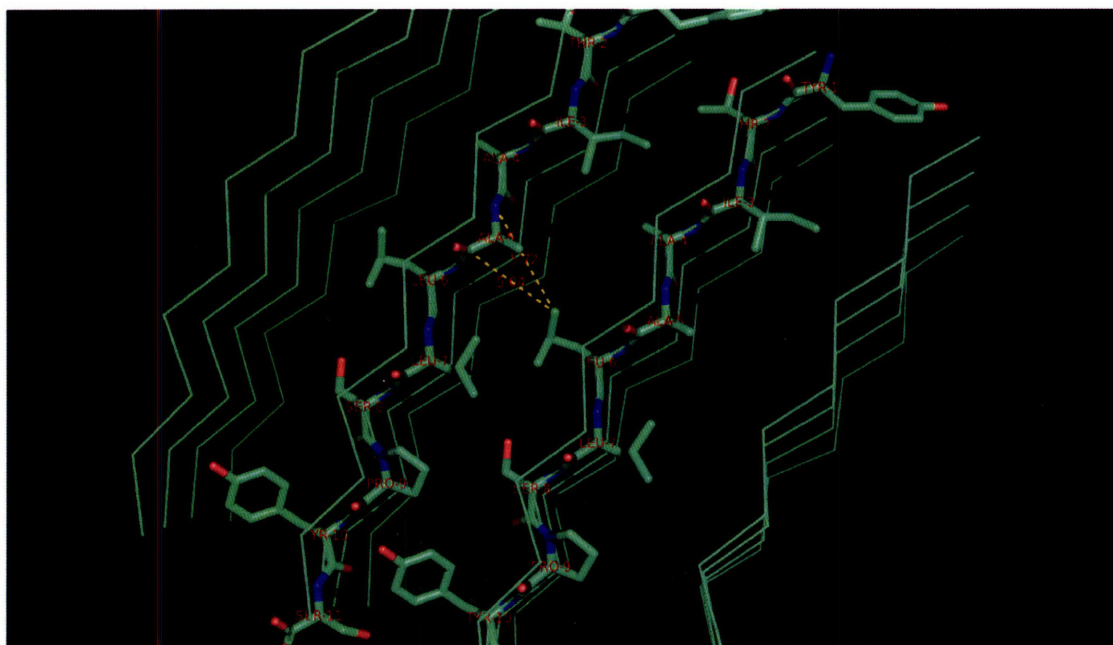
Figure 14-26: Distances between A108 backbone and L111 side chain in parallel-parallel configuration of TTR amyloid fibrils.
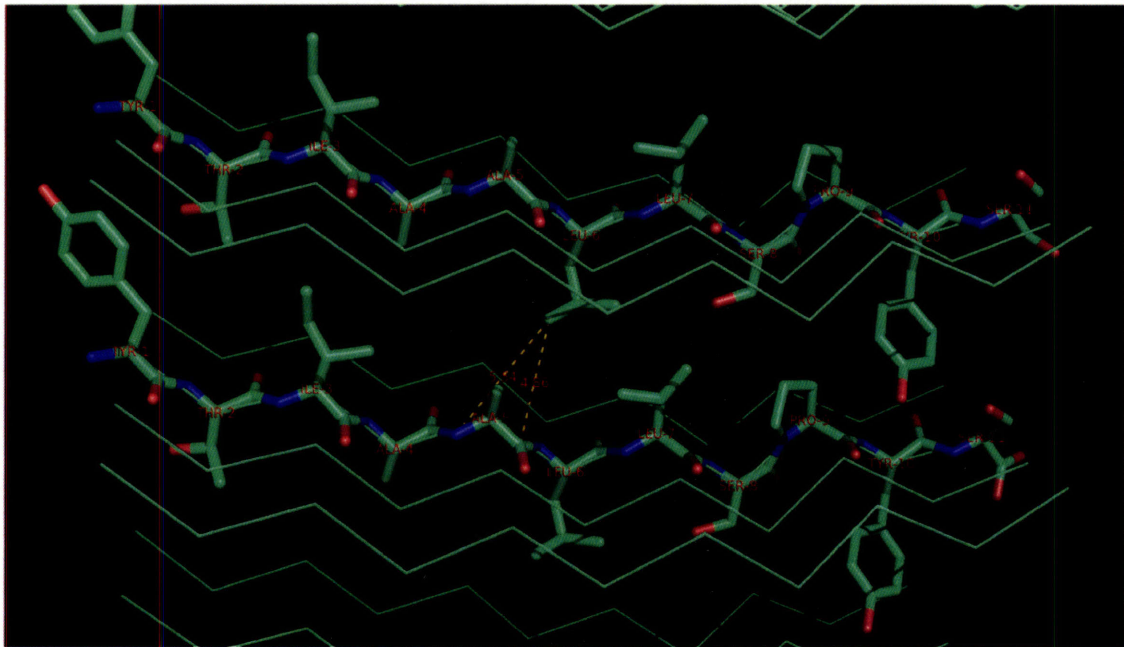
Figure 14-27: Distances between A108 backbone and L111 side chain in parallel-parallel configuration of TTR amyloid fibrils (alternate distances).

Table 14.2: Table of intermolecular restraints in TTR$_{105\text{-}115}$ amyloid fibrils.

| Assignment	Distance Estimate	Method
T106CA-P113CD	3-5 Å	DARR
T106CG-P113CB	3-5 Å	DARR
I107CA-S112CA	3-5 Å	DARR
I107CB-S112CA	3-5 Å	DARR
I107CB-S112CB	3-5 Å	DARR
I107CD-S112CA	3-5 Å	DARR/HORROR
I107CD-P113CA	3-5 Å	DARR
I107CG2-S112CA	3-5 Å	DARR
I107CG2-P113CA	3-5 Å	DARR
I107CG2-P113CB	3-5 Å	DARR
A108CB-S112CA	3-5 Å	DARR
A108CB-S112CB	3-5 Å	DARR
S112CA-T106CG	3-5 Å	DARR/HORROR
S112CB-I107CA	3-5 Å	DARR
P113CA-I107CA	3-5 Å	DARR
P113CA-T106CG	3-5 Å	DARR
A109N-L111CD1	4.1 Å	3D TEDOR
A109N-L111CD2	5.2 Å	3D TEDOR
P113N-A108CB	4-5.5 Å	3D TEDOR
S112N-A108CB	4-5.5 Å	3D TEDOR
Y114N-I107CA	4-5.5 Å	3D TEDOR
A108CO-L111CD1	4.3-5.25Å	R^2TR
A108CO-L111CD2	4.3-5.25Å	R^2TR
A108/A109CA	2.0-4.0Å	CHHC

14.5   Refinement of the Protofilament Structure

Refinement of an NMR structure of the protofilament, which involves self-consistent evaluation of all the distance restraints, will result in a family of structures that is most consistent with the observed data. The first step in this process is the refinement of a dimeric interface between two monomers. This has been accomplished using Cartesian-space simulated annealing molecular dynamics in the program X-Plor NIH [63], and a preliminary family of refined structures is presented in Figure 14-28. Starting from extended strands, the structure refinement used intramolecular and intermolecular distance restraints. The conformational analysis shown in Figure 14-29 demonstrates that

all residues occupy favored regions of the β-sheet conformational space. In order to refine the protofilament structure completely, side chain distance restraints can be incorporated into the refinement. However, this can only be accomplished once the number of sheets in the protofilament are known through other measurements (such as STEM). The inclusion of hydrogen bonding potentials, which was not done in this refinement, is a logical step in improving the geometry of this ensemble.
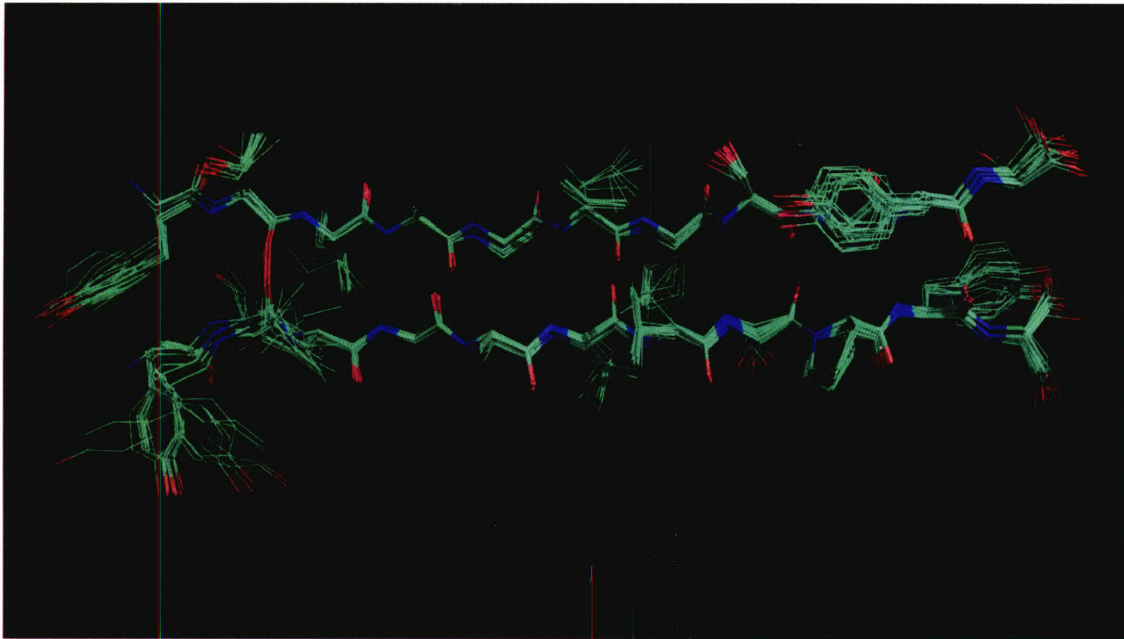
Figure 14-28: Structure of TTR dimer refined from extended strands using intermolecular and intramolecular structural constraints.
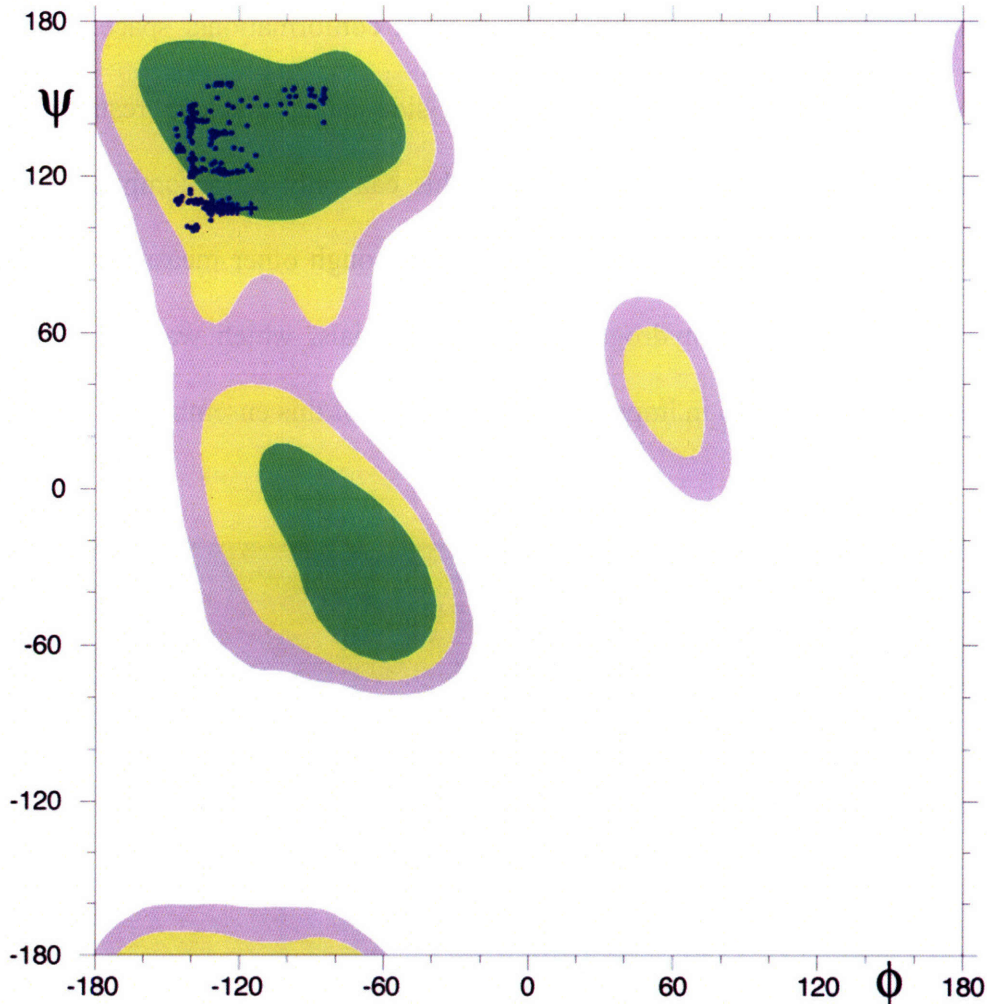
Figure 14-29: Ramachandran plot illustrating the quality of the structural ensemble in Figure 14-28.

14.6   Structural Approaches for Fibril Architecture on Long Length Scales

Several experimental approaches are being applied to extend these structural measurements to the length scale of the microscopic amyloid fibril. As previously mentioned, these include x-ray fiber diffraction, atomic force microscopy, STEM mass per length measurements, and cryo-EM tomography. STEM mass per unit length measurements are required to obtain an estimate of the number of β-sheets in the protofilament. Cryo-EM experiments, which are in progress, will provide an electron

density map that can be fit using the structure of the protofilament, refined by NMR and other methods (Anthony Fitzpatrick, private communication). An example of the current reconstruction is shown in Figure 14-30, in which the pattern of dark-light-dark regions in the fibril crossover is characteristic of a fibril that has a hollow core.
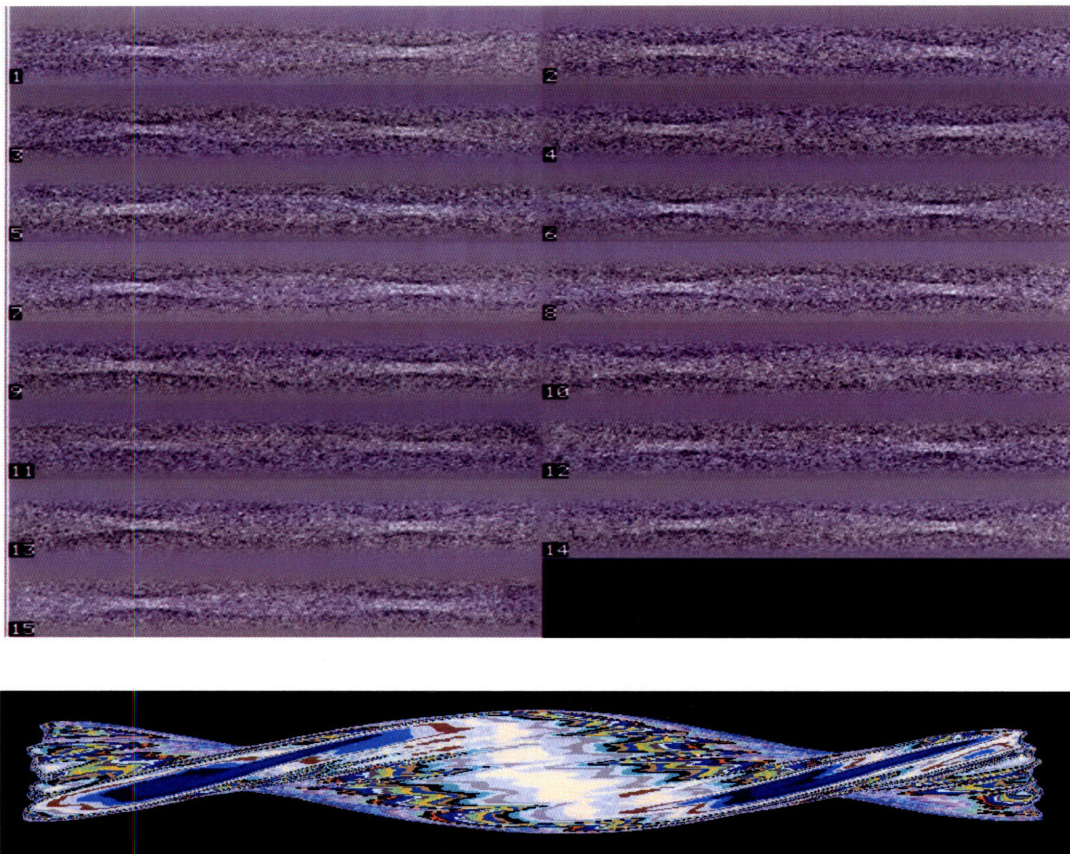
Figure 14-30: Examples of structural refinement from cryo-EM experiments (*courtesy of A. Fitzpatrick*).

14.7   References

[1]   Jaroniec, C. P.; MacPhee, C. E.; Bajaj, V. S.; McMahon, M. T.; Dobson, C. M.; Griffin, R. G., High-resolution molecular structure of a peptide in an amyloid fibril determined by magic angle spinning NMR spectroscopy. *Proceedings of the National Academy of Sciences of the United States of America* **2004,** 101, (3), 711-716.

[2]   Bajaj, V. S.; Caproini, M.; MacPhee, C. E.; Dobson, C. M.; Griffin, R. G., Molecular Structure Determination of the L111M Amyloid Peptide from Transthyretin with Solid State NMR. *J. Am Chem. Soc* **2007,** (submitted for publication).

[3]   Nelson, R.; Saway, M. R.; Balbirnie, M.; Madsen, A. O.; Riekel, C.; Grothe, R.; Eisenberg, D., Structure of the cross-b spine of amyloid-like fibrils. *Nature* **2005,** 435, 773-778.

[4]   Sharpe, S.; Yau, W.-M.; Tycko, R., Expression and purification of a recombinant peptide from the Alzheimer's beta-amyloid protein for solid-state NMR. . *Prot Expr Purif.* **2005,** 42, 200-10.

[5]   Tycko, R., Insights into the Amyloid Folding Problem from Solid-State NMR. *Biochemistry* **2003,** 42, (11), 3151-3159.

[6]   Petkova, A. T.; Ishii, Y.; Balbach, J. J.; Antzutkin, O. N.; Leapman, R. D.; Delaglio, F.; Tycko, R., Structural Model for Alzheimer's beta-Amyloid Fibrils Based on Experimental Constraints from Solid State NMR. *Proc. Nat'l Acad Sci* **2002,** 99, 16742-16747.

[7]   Tycko, R.; Antzutkin, O.; Balbach, J.; Ishii, Y.; Blanco, F.; Reed, J. In *Multiple-quantum NMR of Alzheimer's β-amyloid fibrils and other topics*, 41st Experimental Nuclear Magnetic Resonance Conference, Asilomar, CA, 2000; Asilomar, CA, 2000.

[8]   Tycko, R., Solid State NMR as a Probe of Amyloid Fibril Structure. *Curr. Opin. Chem. Biol.* **2000,** 4, 500.

[9]   Spencer, R. G. S.; Halverson, K. J.; Auger, M.; McDermott, A. E.; Griffin, R. G.; Lansbury, P. T., An unusual peptide conformation may precipitate amyloid formation in Alzheimer's disease: Application of solid-state NMR to the determination of protein secondary structure. *Biochemistry* **1991,** 30, 10382-10387.

[10]   Jarrett, J. T.; Costa, P. R.; Griffin, R. G.; Lansbury, P. T., Models of the Beta-Protein C-Terminus - Differences in Amyloid Structure May Lead to Segregation of Long and Short Fibrils. *Journal of the American Chemical Society* **1994,** 116, (21), 9741-9742.

[11]   Griffiths, J. M.; Ashburn, T. T.; Auger, M.; Costa, P. R.; Griffin, R. G.; Lansbury, P. T., Rotational resonance solid-state NMR elucidates a structural model of pancreatic amyloid. *J. Am. Chem. Soc.* **1995,** 117, 3539-3546.

[12]   Lansbury, P. T.; Costa, P. R.; Griffiths, J. M.; Simon, E. J.; Auger, M.; Halverson, K. J.; Kocisko, D. A.; Hendsch, Z. S.; Ashburn, T. T.; Spencer, R. G. S.; Tidor, B.; Griffin, R. G., Structural Model for the b Amyloid Fibril: Interstrand Alignment of an Antiparallel b Sheet Comprising a C-terminal Peptide. **1995,** 2, 990-997.

[13]   Costa, P. R.; Kocisko, D. A.; Sun, B. Q.; Lansbury, P. T.; Griffin, R. G., Determination of peptide amide configuration in a model amyloid fibril by solid-state NMR. *J. Am. Chem. Soc.* **1997,** 119, 10487-10493.

[14]   Siemer, A. B.; Ritter, C.; Ernst, M.; Riek, R.; Meier, B. H., High-Resolution Solid-State NMR Spectroscopy of the Prion Protein HET-s in Its Amyloid Conformation. *Angew. Chem. Int. Ed.* **2005,** 44, 2–5.

[15]   Nettleton, E. J.; Tito, P.; Sunde, M.; Bouchard, M.; Dobson, C. M.; Robinson, C. V., Characterization of the oligomeric states of insulin in self-assembly and amyloid fibril formation by mass spectrometry. *Biophysical Journal* **2000,** 79, (2), 1053-1065.

[16]   Serpell, L. C.; Sunde, M.; Fraser, P. E.; Luther, P. K.; Morris, E. P.; Sangren, O.; Lundgren, E.; Blake, C. C. F., Examination of the Structure of the Transthyretin Amyloid Fibril by Image-Reconstruction from Electron-Micrographs. *Journal of Molecular Biology* **1995,** 254, (2), 113-118.

[17]   Sunde, M.; Blake, C., The structure of amyloid fibrils by electron microscopy and X-ray diffraction. *Advances in Protein Chemistry, Vol 50* **1997,** 50, 123-159.

[18]   Jimenez, J. L.; Guijarro, J. L.; Orlova, E.; Zurdo, J.; Dobson, C. M.; Sunde, M.; Saibil, H. R., Cryo-electron microscopy structure of an SH3 amyloid fibril and model of the molecular packing. *Embo Journal* **1999,** 18, (4), 815-821.

[19]   Guijarro, J. I.; Sunde, M.; Jones, J. A.; Campbell, I. D.; Dobson, C. M., Amyloid fibril formation by an SH3 domain. *Proceedings of the National Academy of Sciences of the United States of America* **1998,** 95, (8), 4224-4228.

[20]   Chamberlain, A. K.; MacPhee, C. E.; Zurdo, J.; Morozova-Roche, L. A.; Hill, H. A. O.; Dobson, C. M.; Davis, J. J., Ultrastructural Organization of Amyloid Fibrils by atomic force microscopy. *Biophys. J.* **2000,** 79, (6), 3282-3293.

[21]   Cardoso, I.; Goldsbury, C. S.; Muller, S. A.; Olivieri, V.; Wirtz, S.; Damas, A. M.; Aebi, U.; Saraiva, M. J., Transthyretin fibrillogenesis entails the assembly of monomers: A molecular model for in vitro assembled transthyretin amyloid-like fibrils. *Journal of Molecular Biology* **2002,** 317, (5), 683-695.

[22]   Balbirnie, M.; Grothe, R.; Eisenberg, D. S., An amyloid-forming peptide from the yeast prion Sup35 reveals a dehydrated beta-sheet structure for amyloid. *Proc Natl Acad Sci U S A* **2001,** 98, (5), 2375-80.

[23]   Diaz-Avalos, R.; Long, C.; Fontano, E.; Balbirnie, M.; Grothe, R.; Eisenberg, D.; Caspar, D. L., Cross-beta order and diversity in nanocrystals of an amyloid-forming peptide. *J Mol Biol* **2003,** 330, (5), 1165-75.

[24]   Nelson, R.; Eisenberg, D., Recent atomic models of amyloid fibril structure. *Current Opinion in Structural Biology* **2006,** 16, 260-265.

[25] van der Wel, P. C. A.; Lewandoswki, J.; Griffin, R. G., Solid state NMR study of amyloid nanocrystals and fibrils formed by the peptide GNNQQNY from yeast prion protein Sup35p. *J. Am Chem. Soc* **2007**, (in press).

[26] Brunger, A. T.; Adams, P. D.; Clore, G. M.; DeLano, W. L.; Gros, P.; Grosse-Kunstleve, R. W.; Jiang, J. S.; Kuszewski, J.; Nilges, M.; Pannu, N. S.; Read, R. J.; Rice, L. M.; Simonson, T.; Warren, G. L., *Crystallography and NMR system*: A new software suite for macromolecular structure determination. *Acta Cryst.* **1998**, D54, 905-921.

[27] Kammerer, R. A.; Kostrewa, D.; Zurdo, J.; Detken, A.; García-Echeverría, C.; Green, J. D.; Müller, S. A.; Meier, B. H.; Winkler, F. K.; Dobson, C. M.; Steinmetz, M. O., Exploring amyloid formation by a de novo design. *Proc Natl Acad Sci U S A* **2004**, 101, 4435-4440.

[28] Jarvis, J. A.; Craik, D. J.; Wilce, M. C. J., X-Ray DiffractionStudies of Fibrils Formed FromPeptide Fragments ofTransthyretin. *Biochemical and Biophysical Research Comm.* **1993**, 192, (3), 991-998.

[29] Gullion, T.; Schaefer, J., Rotational-echo double-resonance NMR. *J. Magn. Reson.* **1989**, 81, 196-200.

[30] Merritt, M. E.; Sigurdsson, S. T.; Drobny, G. P., Long-range distance measurements to the phosphodiester backbone of solid nucleic acids using ^{31}P-^{19}F REDOR NMR. *J. Am. Chem. Soc.* **1999**, 121, 6070-6071.

[31] Jaroniec, C. P.; Tounge, B. A.; Rienstra, C. M.; Herzfeld, J.; Griffin, R. G., Measurement of C-13-N-15 distances in uniformly C-13 labeled biomolecules: J-decoupled REDOR. *Journal of the American Chemical Society* **1999**, 121, (43), 10237-10238.

[32] Hatanaka, M.; Hu, J. G.; Petkova, A. T.; Bizounok, M.; Verhoeven, M.; Lugtenburg, J.; Griffin, R. G.; Herzfeld, J., Active site changes in the early M -> late M transition of the photocycle of bacteriorhodopsin detected by ^{13}C-^{15}N REDOR NMR. *Biochemistry* **1999**.

[33] Nishimura, K.; Naito, A.; Tuzi, S.; Saito, H.; Hashimoto, C.; Aida, M., Determination of the three-dimensional structure of crystalline Leu-enkephalin based on six sets of accurately determined interatomic distances from ^{13}C-REDOR NMR and the conformation-dependent ^{13}C chemical shifts. *J. Phys. Chem. B* **1998**, 102, 7476-7483.

[34] Michal, C. A.; Jelinski, L. W., REDOR 3D: Heteronuclear distance measurements in uniformly labeled and natural abundance solids. *J. Am. Chem. Soc.* **1997**, 119, 9059-9060.

[35] Mcdowell, L. M.; Klug, C. a.; Studelska, D. R.; Tasaki, K.; Beusen, D. D.; Mckay, R. a.; Schaefer, J., Applications of Redor Nmr-Spectroscopy. *Journal of Cellular Biochemistry* **1995**, 18-18.

[36]   Li, Y.; Appleyard, R. J.; Shuttleworth, W. A.; Evans, J. N. S., Time-Resolved Solid-State REDOR NMR Measurements of 5-enolpyruvylshikimate 3-phosphate synthase. *J. Am. Chem. Soc.* **1994,** 116, (23), 10799-10800.

[37]   Bennett, A. E.; Rienstra, C. M.; Auger, M.; Lakshmi, K. V.; Griffin, R. G., Heteronuclear Decoupling in Rotating Solids. *J. Chem. Phys.* **1995,** 103, 6951.

[38]   Mitchell, D. J.; Evans, J. N. S., Improved heteronuclear decoupling in REDOR with the use of TPPM. *Chemical Physics Letters* **1998,** 292, (4-6), 656-660.

[39]   Ishii, Y.; Balbach, J. J.; Tycko, R., Measurement of dipole-coupled lineshapes in a many-spin system by constant-time two-dimensional solid state NMR with high-speed magic-angle spinning. *Chemical Physics* **2001,** 266, (2-3), 231-236.

[40]   Hohwy, M.; Rienstra, C. M.; Jaroneic, C. P.; Griffin, R. G., Fivefold symmetric homonuclear dipolar recoupling in rotating solids: application to double quantum spectroscopy. *J. Chem. Phys* **1999,** 110, 7983.

[41]   Karlsson, T.; Popham, J. M.; Long, J. R.; Oyler, N.; Drobny, G. P., A study of homonuclear dipolar recoupling pulse sequences in solid-state nuclear magnetic resonance. *Journal of the American Chemical Society* **2003,** 125, (24), 7394-7407.

[42]   Veshtort, M.; Griffin, R. G., SPINEVOLUTION: a powerful tool for simulations of solid and liquid state NMR experiments. *J. Magn. Resonance* **2003,** (submitted for publication).

[43]   Levitt, M. H., Symmetry-Based Pulse Sequences in Magic Angle Spinning Solid State NMR. In *Encyclopedia of Nuclear Magnetic Resonance*, Harris, D. M. G. a. R. K., Ed. John Wiley & Sons: 2002; Vol. 9, pp 165-196.

[44]   Carravetta, M.; Eden, M.; Zhao, X.; Brinkmann, A.; Levitt, M. H., Symmetry principles for the design of radiofrequency pulse sequences in the nuclear magnetic resonance of rotating solids. *Chemical Physics Letters* **2000,** 321, (3-4), 205-215.

[45]   Mehta, M. A.; Gregory, D. M.; Kiihne, S.; Mitchell, D. J.; Hatcher, M. E.; Shiels, J. C.; Drobny, G. P., Distance measurements in nucleic acids using windowless dipolar recoupling solid state NMR. *Solid State Nuclear Magnetic Resonance* **1996,** 7, (3), 211-228.

[46]   Gregory, D. M.; Mitchell, D. J.; Stringer, J. A.; Kiihne, S.; Shiels, J. C.; Callahan, J.; Mehta, M. A.; Drobny, G. P., Windowless dipolar recoupling--The detection of weak dipolar couplings between spin-1/2 nucleic with large chemical-shift anisotropies. *Chem. Phys. Lett.* **1995,** 246, 654.

[47]   Drobny, G. P.; Long, J. R.; Karlsson, T.; Shaw, W.; Popham, J.; Oyler, N.; Bower, P.; Stringer, J.; Gregory, D.; Mehta, M.; Stayton, P. S., Structural studies of biomaterials using double-quantum solid-state NMR spectroscopy. *Annual Review of Physical Chemistry* **2003,** 54, 531-571.

[48]   Karlsson, T.; Hughes, C. E.; Schmedt auf der Gunne, J.; Levitt, M. H., Double-quantum excitation in the NMR of spinning solids by pulse assisted rotational resonance. *J. Magn. Reson.* **2001**, 148, 238-247.

[49]   Karlsson, T.; Brinkmann, A.; Verdegem, P. J. E.; Lugtenburg, J.; Levitt, M. H., Multiple-quantum relaxation in the magic-angle-spinning NMR of ^{13}C spin pairs. *Solid State Nucl. Magn. Reson.* **1999**, 14, 43-58.

[50]   Ramachandran, R.; Griffin, R. G., Multipole-Based Multimode Floquet Theory in NMR. **submitted (2003).**

[51]   Ramachandran, R.; Griffin, R. G., Description of depolarization effects in double-quantum solid state nuclear magnetic resonance experiments using multipole-multimode Floquet theory. *Journal of Chemical Physics* **2006**, 125, (4), -.

[52]   Ramachandran, R.; Lewandowski, J. R.; van der Wel, P. C. A.; Griffin, R. G., Multipole-multimode Floquet theory of rotational resonance width experiments: C-13-C-13 distance measurements in uniformly labeled-solids. *Journal of Chemical Physics* **2006**, 124, (21), -.

[53]   Ramachandran, R.; Ladizhansky, V.; Bajaj, V. S.; Griffin, R. G., C-13-C-13 rotational resonance width distance measurements in uniformly C-13-labeled peptides. *Journal of the American Chemical Society* **2003**, 125, (50), 15623-15629.

[54]   Jaroniec, C. P.; Filip, C.; Griffin, R. G., 3D TEDOR NMR experiments for the simultaneous measurement of multiple carbon-nitrogen distances in uniformly C-13, N-15- labeled solids. *Journal of the American Chemical Society* **2002**, 124, (36), 10728-10742.

[55]   Filip, C.; Ladizhansky, V.; Jaroniec, C. P.; Bajaj, V.; Griffin, R. G., Measurement of ^{1}H-^{1}H distances in uniformly labeled peptides: a spin diffusion approach. *J. Am. Chem. Soc.* **2002**, manuscript in preparation.

[56]   Takegoshi, K.; Nakamura, S.; Terao, T., C-13-H-1 dipolar-assisted rotational resonance in magic-angle spinning NMR. *Chemical Physics Letters* **2001**, 344, (5-6), 631-637.

[57]   Ramachandran, R.; Ladizhansky, V.; Bajaj, V. S.; Griffin, R. G., ^{13}C-^{13}C Rotational Resonance Width Distance Measurements in Uniformly ^{13}C-Labeled Peptides. *J. Amer. Chem. Soc.* **2003**, 125, 15623-15629.

[58]   Ladizhansky, V.; Griffin, R. G., Band-selective Carbonyl to Side Chain ^{13}C-^{13}C Distance Measurements in U-^{13}C,^{15}N-Labeled Solid Peptides by Magic Angle Spinning NMR. *J. Amer. Chem. Soc.* **2003**, 125, (in press).

[59]   Heise, H.; Hoyer, W.; S, B.; Andronesi, O.; Riedel, D.; Baldus, M., Molecular-level secondary structure, polymorphism, and dynamics of full-length alpha-synuclein fibrils studied by solid-state NMR. *Proc Natl Acad Sci U S A* **2005**, 102, 15871-76.

[60]   Lange, A.; Luca, S.; Baldus, M., Structural constraints from proton-mediated rare-spin correlation spectroscopy in rotating solids. *J. Am. Chem. Soc.* **2002,** 124, (33), 9704-9705.

[61]   de Boer, I.; Bosman, L.; Raap, J.; Oschkinat, H.; de Groot, H. J. M., 2D ^{13}C-^{13}C MAS NMR correlation spectroscopy with mixing by true ^{1}H true spin diffusion reveals long-range intermolecular distance restraints in ultra-high magnetic fields. *J. Magn. Reson.* **2002,** 157, 286-291.

[62]   Castellani, F.; van Rossum, B.-J.; Diehl, A.; Schubert, M.; Rehbein, K.; Oschkinat, H., Structure of a protein determined by solid-state magic-angle-spinning NMR spectroscopy. *Nature* **2002,** 420, 98-102.

[63]   Schwieters, C. D.; Clore, G. M., Internal coordinates for molecular dynamics and minimization in structure determination and refinement. *Journal of Magnetic Resonance* **2001,** 152, (2), 288-302.

curriculum vitae

Education

University of Pennsylvania, B.A., Biochemistry	2000
University of Pennsylvania, M.S., Chemistry	2000
(Advisor: Professor Stanley J. Opella)	
Massachusetts Institute of Technology, Ph.D., Chemistry,	2007
(Advisor: Professor Robert G. Griffin)	
University of California at Berkeley and Lawrence Berkeley National Laboratory	2007-
Postdoctoral Training. (Advisor: Professor Alexander Pines)	

Academic Honors and Awards

PGS Fellowship, Natural Sciences and Engineering Research Council of Canada	2001-2003
Phi Beta Kappa; Dean's List; magna cum laude, University of Pennsylvania	2000

Publications

Bajaj, V. S. Farrar, C.T., *et al.* "Dynamic nuclear polarization at 9T using a novel 250 GHz gyrotron microwave source." *Journal of Magnetic Resonance* 160, 85-90 (2003).

Ramachandran, R., Ladizhansky, V., Bajaj, V. S. and Griffin, R. G. "^{13}C rotational resonance width distance measurements in uniformly C-13-labeled peptides." *Journal of the American Chemical Society* 125, 15623-15629 (2003).

Jaroniec, C. P., MacPhee C.E., Bajaj, V.S., *et al.* "High-resolution molecular structure of a peptide in an amyloid fibril determined by magic angle spinning NMR spectroscopy." *Proceedings of the National Academy of Sciences of the United States of America* 101, 711-716 (2004).

Ramachandran, R., Bajaj, V. S. and Griffin, R. G. "Theory of heteronuclear decoupling in solid-state nuclear magnetic resonance using multi pole-multimode Floquet theory". *Journal of Chemical Physics* 122 (2005).

Woskov, P. P., Bajaj, V. S., Hornstein, M. K., Temkin, R. J. and Griffin, R. G. "Corrugated waveguide and directional coupler for CW 250-GHz gyrotron DNP experiments." *IEEE Transactions on Microwave Theory and Techniques* 53, 1863-1869 (2005).

Hornstein, M. K., Bajaj, V.S., *et al.* "Second harmonic operation at 460 GHz and broadband continuous frequency tuning of a gyrotron oscillator." *IEEE Transactions on Electron Devices* 52, 798-807 (2005).

Hornstein, M. K., Bajaj, V.S., Griffin, R.G., Temkin, R.J. "Continuous-wave operation of a 460 GHz second harmonic gyrotron oscillator." *IEEE Transactions on Plasma Science* 34(3):524-533 (2006).

Hornstein, M. K., Bajaj, V.S., Griffin, R.G., Temkin, R.J. "Efficient, low voltage operation of a CW gyrotron oscillator at 233 GHz." *IEEE Transactions on Plasma Science* 35(1):27-30 (2007).

Hu, K-N., Bajaj, V.S., Rosay, M.M, Griffin, R.G. "High frequency dynamic nuclear polarization using mixtures of TEMPO and trityl radicals." *Journal of Chemical Physics* 126, 044512 (2007)

Bajaj, V.S., Hornstein, M.K., Kreischer, K.E., Woskov, P.P, Mak-Jurkauskas, M.K., Herzfeld, J., Griffin, R.G. "A continuous duty cycle 250 GHz gyrotron oscillator for dynamic nuclear polarization in biological solid state NMR." *Journal of Magnetic Resonance.* (submitted)

Bajaj, V.S., Mak-Jurkauskas, M.L., Belenky, M., Herzfeld, J., Griffin, R.G. "Conformational heterogeneity in Early intermediates of the bacteriorhodopsin photocycle." (submitted)

Bajaj, V.S., Mak-Jurkauskas, M.L., Hornstein, M.K., Herzfeld, J., Griffin, R.G. "The active site of early intermediates in the proton-motive photocycle of bacteriorhodopsin: a dynamic nuclear polarization-enhanced solid state NMR study." (submitted)